3-2022

Directionally Sensitive Gamma Imaging Using Rotating Scatter Masks and Inexpensive, Scintillation Detectors

Christopher S. Charles

DIRECTIONALLY SENSITIVE GAMMA IMAGING USING ROTATING SCATTER MASKS AND INEXPENSIVE, SCINTILLATION DETECTORS

DISSERTATION

Christopher S. Charles, Major, USAF
AFIT-ENP-DS-22-M-08

DEPARTMENT OF THE AIR FORCE
AIR UNIVERSITY

AIR FORCE INSTITUTE OF TECHNOLOGY

Wright-Patterson Air Force Base, Ohio

AFIT-ENP-DS-22-M-08

DIRECTIONALLY SENSITIVE GAMMA IMAGING USING ROTATING SCATTER MASKS AND INEXPENSIVE, SCINTILLATION DETECTORS

DISSERTATION

Presented to the Faculty

Graduate School of Engineering and Management

Air Force Institute of Technology

Air University

Air Education and Training Command

in Partial Fulfillment of the Requirements for the

Degree of Doctor of Philosophy in Nuclear Engineering

Christopher S. Charles, B.S., M.S.

Major, USAF

30 September 2021

AFIT-ENP-DS-22-M-08

DIRECTIONALLY SENSITIVE GAMMA IMAGING

USING ROTATING SCATTER MASKS

AND

INEXPENSIVE, SCINTILLATION DETECTORS

Christopher S. Charles, B.S., M.S.
Major, USAF

Committee Membership:

Dr. Larry W. Burggraf
Chairman

Dr. Matthew C. Fickus
Member

Dr. Darren E. Holland
Member

Dr. Benjamin R. Kowash
Member

Dr. James C. Petrosky
Member

ADEDJI B. BADIRU, PhD

Dean, Graduate School of Engineering and Management

Abstract

Wide-area and omnidirectional gamma survey and source direction determination is often constrained by detector size, weight, complexity, and system cooling requirements, or limited by resolution or Field-of-View constraints. The primary goal of this work was to demonstrate the first instantiation of the FitzGerald design [1] Rotating Scatter Mask (RSM) as a proof-of-concept for two-dimensional source direction determination using a single, inexpensive, non-cooled scintillator, as well as an alternate mask design for comparison. A large FitzGerald RSM was additively manufactured from a low-Z, acrylic like material and rotated around the ubiquitous standard 3"x3" NaI(Tl) or NaI(Tl)/CsI(Tl) phoswich detector internal to the mask. Smaller versions of the FitzGerald and alternate RSM designs were also 3D printed for testing and used in conjunction with a $LaBr_3$ detector to characterize the RSM system's performance with a size and weight reduction applied. The rotation angle of the system was recorded and associated to each recorded gamma event, to encode and subsequently bin the recorded energy spectra by the known RSM rotational position. The resultant experimental scattergrams were then compared to a library of computational generated modulation curves to predict the point-source direction.

A simplified, analytic, attenuation by Compton scatter of the Full-Energy Peak (FEP) model, based on a Beer-Lambert's law relationship was built, developed, and applied to the design geometry of the RSMs using a Cs-137 662 keV gamma. This modeling method was developed employing the known gamma attenuation and scattering physics for High-density Polyethylene (HDPE), which was the planned mask material, to enable determination and verification of the major influences of RSM design and to interpret experimental measurements. This modeling technique was later parameterized and used in conjunction with initial experimental results to

create detector response matrix (DRM) libraries for both the FEP and Compton continuum portions of the acquired spectra. The code runs significantly faster than other MCNP® or GEANT codes developed for this RSM due to its simplifying assumptions, while producing results comparable to later Monte Carlo code methods [2] [3]. Resolution and accuracy results, using both the Modal Assurance Criterion and a Least-Squares comparison approach, to the numerically modeled libraries of the FitzGerald design RSM system were made. Source directions were successfully predicted over the nearly 3π steradian acceptance angle of the system, with an average resolution determined to be ~4° when using the FEP attenuation by scatter-out based library for comparison.

RSM design considerations, two original SolidWorks drawings, and the construction are catalogued in this work, as are the laboratory equipment used, RSM configuration(s), and source placement(s). In addition to the single-source investigations, sources of different energies at the same location of placement are shown to be distinguishable by energy binning of their FEPs in the spectra when constructing the experimental scattergrams. Same energy sources but placed at two distinct locations, are shown to be distinguishable through a modulation curve convolution/deconvolution schema utilizing a gridded pattern search algorithm. This work also shows that approximate point-source direction determination can be made when only using the Compton portion of the spectra for comparison. As well, two small RSMs having different designs are compared over a range of source placements to characterize performance dependence of design changes. Recommendations for construction of a hybrid RSM/Rotational Modulation Collimator (RMC) system to further enhance the forward looking ~15° FOV of the system and operational considerations for expanding the utility of the system in real-world conditions are suggested. A full summary of the scattergrams and source direction predictions are presented in the Appendices.

Dedicated to my best friend and our wonderful kids. I am so thankful the Creator made us for each other!

Thank you for the time and patience…… You really are the best!

Kids let's hang out again, I've missed so much.

No rose without a thorn but many a thorn without a rose
— Arthur Schopenhauer

Acknowledgements

It is with great thanks and appreciation that I acknowledge the following people. Some gave tremendous help; others a quick look. Some have seen me through this whole time; others just briefly checked in. Some have saved my career; others have no idea what I am talking about. Some have given incredible counsel; others have offered a much-needed ear to listen. Some I will miss, or not give the extensive and profuse thanks that I should. But all know that they can show up, at any time, and will be welcome at my table.

In no particular order (except for the first one):

Ms. Julie Logan – None of this work would have been possible without Ms. Logan very kindly repositioning and resetting the RSM data-acquisition system between collection runs. I had already PCS'd to a new assignment on the other side of the country, and so data was shared via Google Drive and by FedEx'ing a 1TB USB hard drive back and forth. Her work extended into collecting the multinuclide source data sets and the elevated background data sets of the large RSM, even though she did not need to use them for her Thesis work. Thank you Julie!

Dr. David Wehe of the University of Michigan and Dr. Benjamin Kowash – The data-acquisition computer and support peripherals from Kowash's Dissertation were loaned to AFIT for this work. It is with great appreciation that I recognize their contribution(s) from the University of Michigan. So glad I had a starting point…

Dr. Jim Petrosky – Got me all the $$$ money $$$ I needed and shepherded my work through reporting and milestones with the sponsor: DTRA. This ended up being completely transparent to me and allowed for better focus on the task at hand.

Everyone in the AFIT Modeling and Machine Shop – I am extremely grateful for the assistance of "Crabby" and consider him a good friend. His extended and voluntary efforts helped move the RSM out of theory and into a physical reality! One time that stands out was over a rainy, cold Ohio weekend in 2016, he built the torque-multiplication system. His extra effort allowed the gearing system to be designed, machined, fitted, and operational in record time! An over 2-week delay was averted, by moving the production request up in the queue, while not affecting others' efforts. All the others there deserve a SHOUT OUT too, thank you: Boston Dan and The Kid.

George, Todd, Ned, Nancy, Jen, and Karen – I did not end up needing your help, but I certainly appreciate the motivation!

Dr. Larry Burggraf & Dr. Darren Holland – You are the ones who saved me. Your support and guidance cannot be quantified. Thank you for going to bat for me and for all the great guidance!

Mom, Ramblin' Wreck, Dad (Bandit #263), Grammie, Bros! & Sis, Gramp, Grandma and Babci – You really are the best family a kid could ever ask for. I miss you GATOR.

Angelo, Wooddy, AJ, PJ, Tracy, TK, Corrie, Joel, Jimmy, Ryan, Carson, Mike, Murwais and Whalid – Thanks for always checking in on me and pushing me to continue to produce through the exhausting times.

The Swedish Auto Maker Volvo & the Superstore of IKEA – They must have collaborated on a laydown seat and trunk/twin mattress size and design… There is simply no other explanation.

COL Ken Letcher, always better to have to hold one back! Just move out and get it done.

To my very best teachers Mrs. Diaz and Mr. Guerrero – Thanks for both years (all 3 of them), the excellent prep, and the best advice I ever got!

Colonels Tom, Fee, Suriano, Ziegler, Kiziah, Glitz (Bandit #210), Bergren and Wacker, and Drs. Brennan, Bedeaux, Clinton, Kelly, McClory and Turinetti, and Misters Del Barga, Miller & Rothenbush – your understanding and mentorship is genuinely appreciated. I owe each of you something different, but I am grateful to God that you came into my life at the time I needed one thing or another the most. I especially appreciate the after-hours chats, music advice, random email check-ins, sending me home from work to get this thing done, and so much more. You did it out of care and with no benefit to yourselves. Thank you for the time you've spent.

Mr. Phil Smith – Your efforts to teach me SolidWorks (and in creating the .dxf for the point-cloud data import) were instrumental in realizing the CAD drawings that kick started the build. You ROCK dude!

Mr. Eric Taylor – always there for me and always came through with the resources I needed.

To all the other resources, friends, and family I have drawn on over the years – *Thank You*. It has taken far too long and I'm sincerely hoping I can be of use to you one day; if not, then just swing by for a BBQ.

Kimi Räikkönen – It's a hobby to me too. You're my hero!

Christopher S. Charles
Patrick SFB, March 2022
Home Sweet Home

Contents

List of Figures

Figure Page

List of Tables

Table Page

DIRECTIONALLY SENSITIVE GAMMA IMAGING

USING ROTATING SCATTER MASKS

AND

INEXPENSIVE, SCINTILLATION DETECTORS

I. Introduction

1.1 Motivation, Approach, and Results Overview

The size, weight, expense, cooling requirement, limited field-of-view (FOV), and complexity of traditional gamma imaging systems make the Rotating Scatter Mask (RSM) system a very appealing alternative for wide-area radiological survey. The RSM system offers a quick, inexpensive, and portable radiological source direction determination with comparable spatial resolution to current, two-dimensional, multi-array gamma imaging technologies [4] due to its increase in collection efficiency, lower weight, and simplicity. As well, it can be miniaturized for Unmanned Aerial Vehicle (UAV) mounting and used for neutron detection operation as already demonstrated by Holland [5]. The attenuation-based Rotating Mask Collimator (RMC) system used by Kowash [6] and the scatter-based RSM system, proposed by FitzGerald [1] and developed here, are shown in Figure 1. This work modified Kowash's RMC hardware as the basis for demonstrating the first ever RSM measurements and analysis of those results.

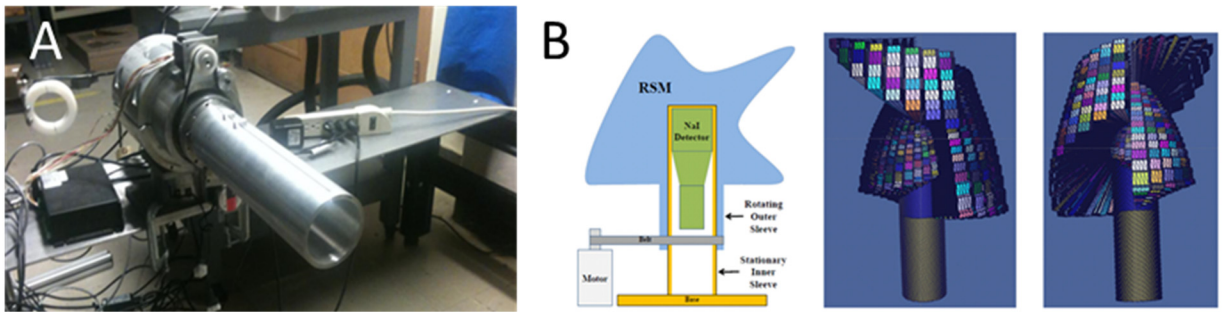

Figure 1. (A) Kowash's RMC imaging mount, drive motor, holographic position encoder ring and associated electronics, and absorption slit mounting/spacing tube are shown here. Out of view are the tungsten attenuator slit masks; (B) The RSM system as originally conceived of by FitzGerald [1], and his initial MCNP® modeling work. Reprinted with FitzGerald's permission.

The ultimate objective of this RSM work is to provide the Warfighter a small, robust, and inexpensive alternative to traditional multi-array 2D gamma imagers. By using a novel approach, based on gamma scattering as the primary gamma attenuation mechanism and a small, non-cooled, off-the-shelf point source detector(s), the goal of this work is to provide proof-of-concept of FitzGerald's RSM concept and to characterize its performance. Methods applied to do this, the theory of RSM design, manufacturing, and the engineering modifications to Kowash's equipment are discussed in later sections. A full-sized version of FitzGerald's design, incorporating both a standard 3"x3" NaI(Tl) and a NaI(Tl)/CsI(Tl) phoswich type detector to suppress backscatter from mounting hardware and photo-multiplier tube (PMT), was tested. Multiple source locations using a variety of gamma energies to characterize this novel system's function and performance were utilized. Further, it is shown that multiple small test sources in the FOV of the RSM are distinguishable, including two of the same energy but at different locations. This work uses both the information contained in the Full-Energy Peak (FEP) and Compton continuum portions of the recorded spectra to independently match the experimentally obtained scattergrams to the most similar numerically modeled expected modulation curve (or Detector Response Curve: DRC) for each portion of the spectra. This search occurs over all the 64,440 allowed source placement positions/DRCs in the RSM's FOV defined for this work. Both a Least-Squares (LS) differencing approach and the Modal Assurance Criterion (MAC) method are used to select the best matched source direction prediction, which is defined by spherical polar coordinates as the angular direction originating at the center of the detector to the center of the source. The results and efficacy of both methods is compared.

Further, a lightweight, field- or UAV-portable system is ultimately desired for rapid acquisition and identification of lost or diverted gamma emitting sources. This is also investigated

here by the construction and testing of two smaller, additively manufactured RSMs to fulfill this objective. One is of FitzGerald's original RSM design [1]. The other is a novel alternate design developed for this work which utilizes FitzGerald's design criteria for ensuring modulation curve uniqueness over all RSM viewing angle (φ) and rotational angle (θ) possibilities but with added material discontinuities to the RSM geometry. Both designs are then compared to each other using the same data acquisition schema. It is shown that good agreement of the source direction prediction to the known placement, through comparison with the Detector Response Matrix (DRM) lookup library is obtained. The DRM is a compilation of all allowed source position DRCs. However, these smaller RSMs exhibited a noticeable decrease in overall system resolution when compared to the larger RSM characterization. Additionally, when miniaturizing the RSMs, it is noted that the shape of the $LaBr_3$ detector (extruded cube) does not match the intrinsic RSM design geometry used in construction. The decrease in overall size is also shown to decrease the small RSM's sensitivity (defined as the ratio of the maximum and minimum of the scattergram modulation curve) as expected due to having a shorter mask material length for interaction. These data sets are also observed to have a higher relative counting statistics error compared to the larger RSM results due to their shorter acquisition time and the relative decrease in scintillator volume of the $LaBr_3$ detector used when compared to the overall dimensions of the smaller RSMs. These differences could explain the decrease in resolution.

Model development for the expected DRC at a specific angular direction (φ,θ) and the subsequent lookup library DRM (compilation of all DRCs) is discussed in Chapter II. Specifics of the RSMs geometric designs, the coordinate system utilized, and the additive manufacturing construction is discussed in Chapter III. Chapter IV explores the laboratory equipment set-up and data processing methods, while Chapter V presents the Results, Analysis and Conclusions of the

individual setups and detector configurations. Chapter VI presents a Summary of the novel efforts recorded here, as well as a Continuing Work section associated with the Air Force Institute of Technology's (AFIT) current investigation of RSM technologies which was enabled by these results. Finally, recommendations for future areas of investigation in both RSM system employment and design changes is made.

1.2 Photon Interactions with Matter Review

Gamma and x-ray photons interact with matter through three primary mechanisms in which electrons are freed or created to further interact with their surroundings. They are photoelectric absorption, Compton scattering, and pair production.

In the photoelectric absorption of a photon, the kinetic energy of the once bound orbital electron is equal to the energy of the incident photon, minus the binding energy (B_e) needed to free it as is shown in Equation (1).

$$T_e = E_\gamma - B_e \tag{1}$$

In other words, it is calculated as an elastic collision, where the momentum of the photon has been neglected when compared to the relatively massive "at rest" heavy atom. It is interesting to note that a free electron cannot absorb a photon and recoil under this mechanism. As well, the energy required to free the electron and the probability of absorption is difficult to calculate from first principles, as it is a complicated quantum mechanics problem. We do know however from experimentation that it is most significant for photon energies around ~100 keV, rapidly increases with the atomic number of the absorber atom (as Z^4) and also decreases quickly with incident photon energy (E_γ^{-3}) [7]. Therefore, these photoelectric type interactions play a significant role in down-scattered photon absorption in high-Z, scintillation type detector crystal materials such as NaI(Tl). The probability of absorption (photoelectric cross-section: σ_e) is not linear with energy

and shows significant, sudden changes in structure at the binding energies associated with the corresponding electron shells of the material, such as the M-, L-, and K-shells. These are known as "absorption edges". An example of this shown from the National Institute for Standards (NIST) of the United States Department of Commerce are seen in Figure 2. Notice here that the probability of absorption is falling off significantly after 100 keV.

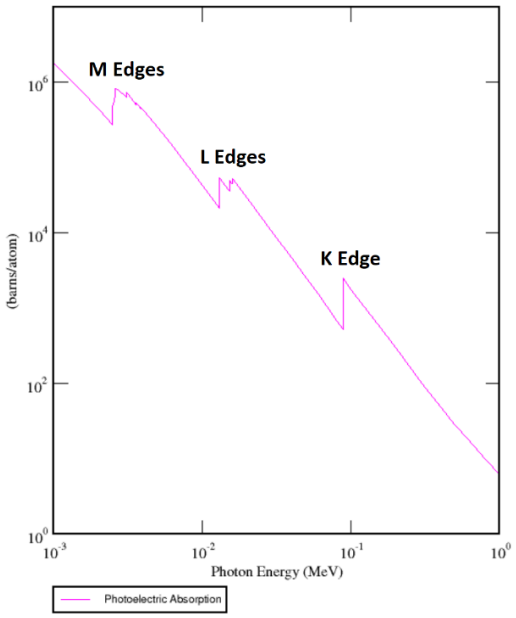

Figure 2. The photoelectric cross-section of Lead (Pb) from NIST [8]. Notice the discrete discontinuities in the probability of absorption at the M-, L-, and K-electron shell binding energies. Reprint of a U.S. government owned website display, with labels of the shell edges added by the author.

The second interaction is that of the so-called *Compton*[1] scattering effect. The effect is most often observed to be accompanied by the recoil of an electron, as the charged particle of interaction with the photon. If it is assumed that very little photon energy is transferred to the nucleus of the atom from whence the electron came, simple derivations lead to a convenient

[1] Named after Arthur H. Compton, a professor at Washington University in St. Louis. In 1922, he discovered the effect in x-rays which directly showed the quantized particle nature of electromagnetic radiation, as oppose to the previously accepted wave only nature. He found that individual x-rays incident on a "light" element would very often have a longer wavelength (i.e. lower energy) when measured after passing through a material [5].

expression for finding the energy transfer and resultant change to the angle of incidence of the photon. The discussion of Compton scattering here will be limited to that focus.

When developing the governing equations for Compton scattering, a convenient substitution can be made for the momentum ($\boldsymbol{p}$)/energy (E) relationship of the recoiled electron (β) and can be replaced with the relativistic relationships $p_e = E_e/c$ and $\beta = v_e/c$ when mathematically articulating the collision using conservation of total energy and linear momentum. By assuming a relatively small binding energy for the electron (compared to that of its rest mass energy) and that it is in fact at rest initially, a governing equation can be developed. A visual schematic for Compton scattering is shown in Figure 3.

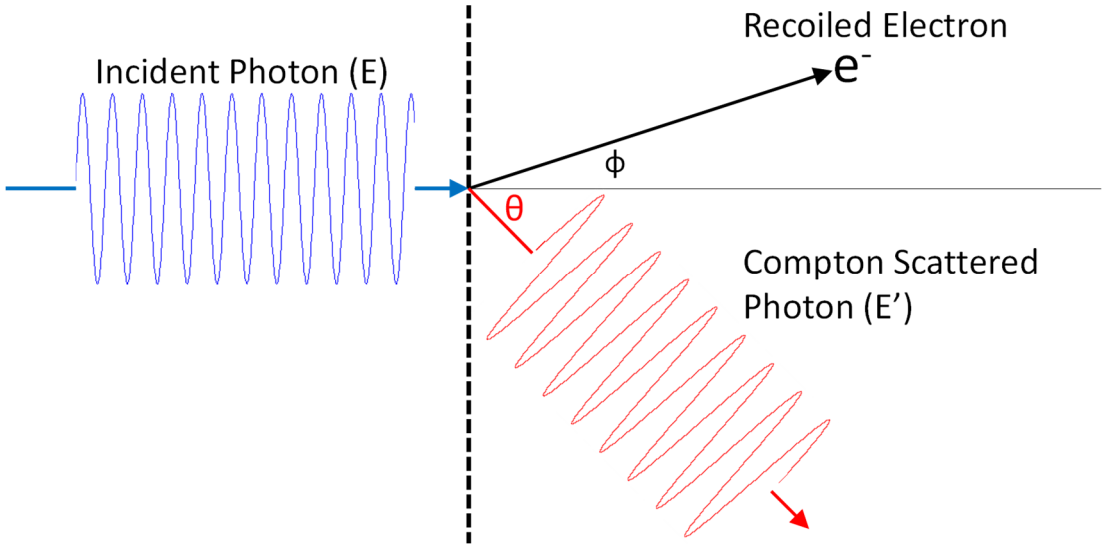

Figure 3. Reference geometry for Compton scattering. A higher energy incident ray is down scattered in energy with a coincident change in direction. A recoiled electron accounts for conservation of energy and linear momentum.

Solving the conservation equations $E_\gamma = E'_\gamma + E_e$ and $\boldsymbol{p}_\gamma = \boldsymbol{p}'_\gamma + \boldsymbol{p}_e$ using the previous substitutions for β and the general definitions of relativistic momentum and energy defined by:

$$\boldsymbol{p} = \frac{m\boldsymbol{v}}{\sqrt{1 - \frac{\boldsymbol{v}^2}{c^2}}} \tag{2}$$

and

$$E = \sqrt{\boldsymbol{p}^2c^2 + m^2c^4} \tag{3}$$

where the energy definition for a gamma, can be simplified to $E_\gamma = \boldsymbol{p}_\gamma c$ (since photons are massless) leads to the following system of equations:

X-axis momentum components:

$$\frac{E_\gamma}{c} = \frac{E'_\gamma}{c} cos\theta + \frac{mc\beta\ cos\varphi}{\sqrt{1-\beta^2}} \tag{4}$$

Y-axis momentum components:

$$0 = \frac{E'_\gamma}{c} sin\theta - \frac{mc\beta\ sin\varphi}{\sqrt{1-\beta^2}} \tag{5}$$

Conservation of Energy equation:

$$E_\gamma + mc^2 = E'_\gamma + \frac{mc^2}{\sqrt{1-\beta^2}} \tag{6}.$$

If we are interested only in the energy of the scattered photon and neglect the ejected electron's energy and momentum, the above three equations can be combined to find:

$$E'_\gamma = \frac{E_\gamma}{1 + (E_\gamma/mc^2)(1 - cos\theta)} \tag{7}$$

where mc^2 is the rest mass energy of the electron, which carries a value of ~511 keV. Thus, if one knows the incoming photon's energy and measures its outgoing energy, the scattering angle can be determined. Conversely, if the outgoing scattering angle is measured, the average scattered gamma energy can be inferred. Compton scattering is therefore considered a form of incoherent elastic scattering.

From Equation (7), we can see that the maximum resultant gamma energy occurs at θ = 0° which corresponds to no interaction with the material and therefore no change in energy. A minimum occurs at θ = 180°, where the gamma backscatters exactly in the direction from which

it originated. For the 662 keV emission of Cs-137, this means the resultant gamma energy can therefore range from its original energy to ~184 keV below incident energy when Compton scattered inside a material. If the Compton scattering event happens inside a detector and the freed electron contributes completely to the forming of electron-hole pairs within the scintillation material, a spectra feature known as the Compton continuum is formed. This feature starts at a lower energy than the original FEP because the recoiled gamma escapes the crystal without further interaction. For Cs-137, this feature will start with the Compton edge at an energy of 478 keV (184 keV below the 662 keV FEP). The remaining Compton continuum can then continue down to the lower limit of the recorded spectrum depending on subsequent interactions and how much of the original gamma's energy was deposited (or escaped), which is highly dependent on the design and size of the detector. Of note, due to the probability distribution of the Klein-Nishina formula (and the higher likelihood of 180° backscatter), a 184 keV peak is often observed within the Compton continuum itself [9]. Further development of the Compton scattering phenomenon can be conducted to find the Klein-Nishina formula for the differential cross-section per electron but is beyond the scope of this work. All that was needed is the total cross-section of interaction for the material used at the energies considered. Total cross-sections, taken from the NIST XCOM database [10], are presented in the model development section. Use of total cross-sections is justifiable, since the relative contribution of either photelectric absorption or pair production over the energy range considered in this work is orders of magnitude less than that of Compton scattering.

The last interaction of photons with matter needing consideration is that of pair production. This process starts at gamma energies above 1.022 MeV, where an electron-positron pair is created while the original gamma disappears in the process. Pair production can only occur in the presence

of the nucleus, where the strong force is present. In the process, the incident gamma's energy is converted directly into the masses of the electron-positron pair, and little energy or momentum is transferred to the secondary particle. The remaining energy of the initial photon not converted into mass or transferred to the secondary particle is carried off in the kinetic energy of the electron-positron pair. Subsequently, the most common contribution to the recorded spectra in this case is that of a positron/electron annihilation event, in which two photons of 511 keV are then released and free to interact with a detector. Pair production is not a concern for this work as it is only important for gamma energies much larger than 1.2 MeV, as seen in the Figure 4. Its effect on the spectra recorded in this work are negligible compared to the other Compton continuum contributors.

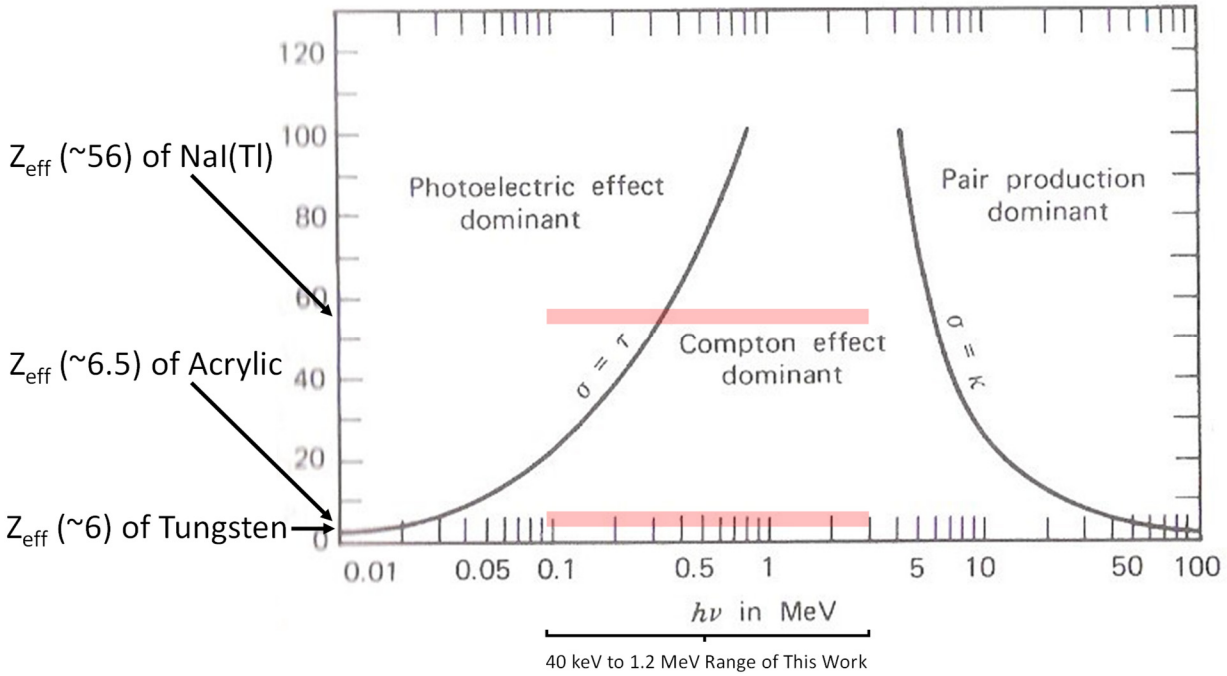

Figure 4. From Knoll [11], this figure shows the relative importance of the three major gamma interaction types as a function of energy and Z of the absorber material. It has been modified to show the energy range used in this work (shaded red bar regions), and points out the Z_{eff} of the acrylic (RSM material) and the NaI(Tl) (scintillator material) used in this work. The Z_{eff} of Tungsten (W) has also been pointed out for comparison, as it is a commonly used absorption mask material. Figure is reprinted with publisher's permission.

Figure 4 shows the relative importance of the three main gamma/material interaction types just discussed as a function of the Z value (atomic number of protons) of the interaction medium.

For a low-Z material, such as the acrylic (theoretical Z_{eff} of ~6.5) [12] used for scattering in the RSM, the Compton scattering effect is dominant over the energy range considered (40 keV to 1.2 MeV marked in red shading). High-Z NaI(Tl) has a Z_{eff} of ~56 [13]. This indicates that an incident gamma is more likely to be fully absorbed in the scintillator material of the detector, compared to the acrylic of the RSM off which it is more likely to scatter. If Compton scatter does occur inside the detector, then the remaining down scattered gamma is likely to interact via photoelectric absorption and deposit its remaining energy within the detector, depending on the interaction location and overall size of the detector. As a commonly used absorber material, it is interesting to note that Tungsten (W) has a Z_{eff} of ~6. While a high-Z material, the Z_{eff} is calculated with respect to the valence electrons. In the case of W, the tightly bound nature of the inner shells negates their individual electron contributions to the Z_{eff} calculation. However, due to its high-density (1.7 times that of lead) it ultimately serves as an excellent absorber, through multiple Compton interactions and finally photoelectric absorption.

To illustrate the differences in attenuation for the major RSM system materials used, a side-by-side comparison of the mass attenuation coefficients for both acrylic and NaI is shown in Figure 5. The energy range has been limited to be representative of this investigation. Notice that the y-axis scale of the right-hand figure has been adjusted for uniformity and direct comparison to the left-hand side. Since Cs-137 is the primary source used for this investigation, the 662 keV gamma is also of principal interest. In both materials, Compton scattering is the dominant mechanism of interaction at this 662 keV energy. For acrylic, the next most probable interaction is that of coherent scattering, but it is approximately three orders-of-magnitude lower. In this process, the incident photon is scattered by the entire electron cloud of an atom. Any recoil of this atom is equally shared between the electrons and nucleus. From an energy and momentum conservation

perspective, the deflected photon undergoes a negligible loss. Therefore, the wavelength of the photon remains the same and only a resultant change in direction of the incident photon is measured [14].

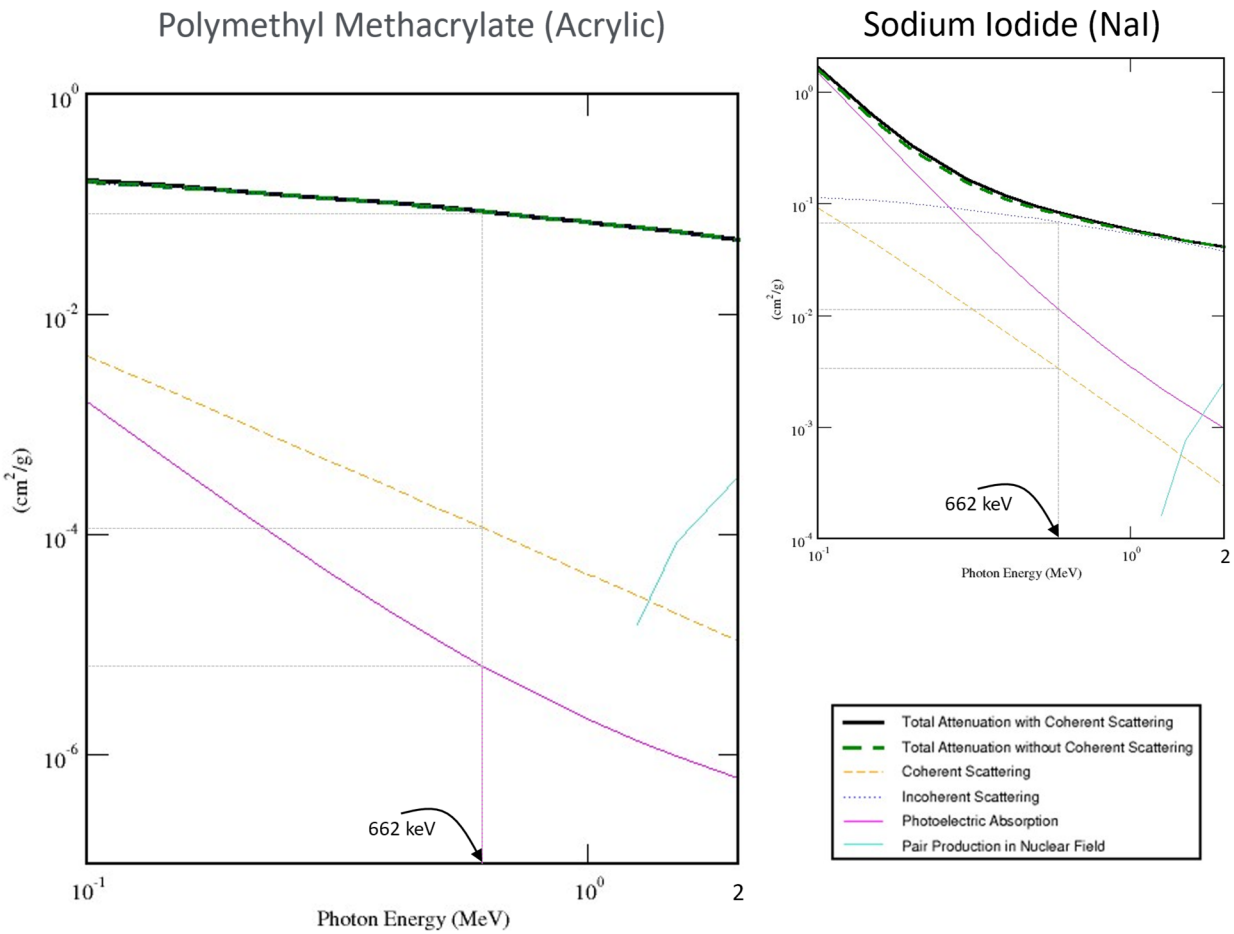

Figure 5. Side-by-side comparison of the mass attenuation coefficients for acrylic and NaI from NIST XCOM [15]. The Cs-137 662 keV gamma emission line is marked, and the grey lines are superimposed as an overlay to help the reader review the coefficient values of the different mechanisms. Notice that both graphs are log-log scales, and that the right-hand figure is adjusted for axis-scale alignment to the left-hand side. As well, notice that the photoelectric absorption (pink line) of the NaI is about 3 orders of magnitude greater than the acrylic. Reprint of U.S. government owned website display.

Based on the size of the data sets recorded in this experimental work, it is estimated that the uncertainty associated with counting statistics is roughly an order of magnitude greater than any contribution made by coherent scattering, so it was convenient to neglect when developing the computational models of Chapter II. While a full treatment of this Rayleigh-type scattering needs to be included in any complete model (especially in high-Z absorbers), it is neglected in the

practical application of this work because its probability of occurrence is orders of magnitude lower than the primary interactions.

Also, while the total mass attenuation coefficient (μ/ρ) of each material appears to be about the same for an incident photon energy of 662 keV, the linear attenuation coefficient (μ), which is related to the fractional loss in intensity of the photon crossing any distance *dx* of the material is approximately 8 times higher for NaI. This is due to its higher density (ρ), when compared to acrylic. This higher density also makes it a good choice for use as the primary scintillator crystal material of the detectors used in this research. To show the mathematical relationship of density to the linear attenuation coefficient of a material, it must be understood that the total cross-section of a material is formed by summing all individual cross-sections (i.e. $\sigma_{tot} = \sigma_{pe} + \sigma_{coh} + \sigma_{incoh} + \sigma_{pair} + \sigma_{trip} + \sigma_{ph.n}$). This total can then be related to the attenuation coefficient as: $\mu = \sigma\rho/uA$, where u is the atomic mass unit and A is the relative atomic mass of the target element (in amu) [16]. For completeness, the subscripts listed for the total cross-section correspond to: *pe* for photoelectric absorption, *coh* for coherent scattering, *incoh* for incoherent scattering (Compton), *pair* and *trip* for the cross-sections of electron-positron pair production in the fields of the nucleus and the atomic electron respectively, and *ph.n.* is the photonuclear cross-section (not previously mentioned, but also negligible for this research).

Attempts are made to simplify, approximate, and reduce the computational modeling efforts here to the primary RSM spectra contributors, as any complete treatment of the possible interactions involved is a complicated process. In that way, when comparing the expected modulation curves of the DRM library to experimental scattergram results, the primary model contributors can in fact be deduced to be the main components necessary to describe the RSM system's Physics to the first order. This was later proved by the more computationally intensive

MCNP® and GEANT modeling efforts conducted by both Logan [2] and Condon [3], which either used the same data presented in this work or repeated the experiments.

1.3 Gamma Imaging Methods Review

Gamma imaging can nominally be divided into two main groups. That of true (or direct) gamma imagers and Compton imagers. True gamma imagers are defined by the direct measurement of the photon's energy after deposition in a detector, while Compton imagers use information gathered about photon/material interactions to measure the start and end points of interaction. In conjunction with the scattering angle(s) data, the original source position and energy can be inferred using a variety of projection techniques.

Collimator Type

For true gamma imaging type detectors, pinhole imagers allow a small portion of the source generated photons through to either a segmented detector configuration or to multiple small detectors. Since the focal length through a pinhole is infinite, the detector can be placed at any distance from the pinhole, which with the right detector configuration allows for high-resolution image construction. However, due to its relatively small aperture, the efficiency of such a system is limited and can require long collection times. To increase efficiency, the aperture can be made larger, but this then comes at the expense of the resolution of the system [4].

On the other hand, collimator type imagers allow a narrow portion (i.e. limited acceptance angle) of the source photons to enter the detector. Photons entering off the primary collimator axis are attenuated through absorption by the high-Z "wall" materials, such as Tungsten or Lead from which it is usually constructed, during the photon's transit through the length of the collimator. Thus, only photons travelling parallel to the collimator axis are transmitted. This limited FOV can

then be used in conjunction with a single detector or with a segmented detector for constructing high-resolution images. In the case of multiple, closely spaced collimators (also known as a parallel hole system) measurement of the source can be made to generate a high-resolution, two-dimensional picture of the active region. Limitations include short useable focal lengths and limited efficiency due to the collection time necessary to collect enough counts for accurately determining the source intensity. If the pinhole diameters are increased to allow more photons to pass (increase efficiency) or the parallel hole collimator gets too large, the resolution of the system will be reduced. While the efficiency increases, it comes at the cost of photons from other than the location of interest to be passed to the detector(s). In all cases though, the operation is in that of the near field. Moving the source to a far field distance (parallelizing the incoming rays), causes a washout in resolution and negates the effect of the placement of the collimator with its parallel slits in the first place [4]. This limitation is addressed by the invention of the Anger camera where multiple detectors are utilized.

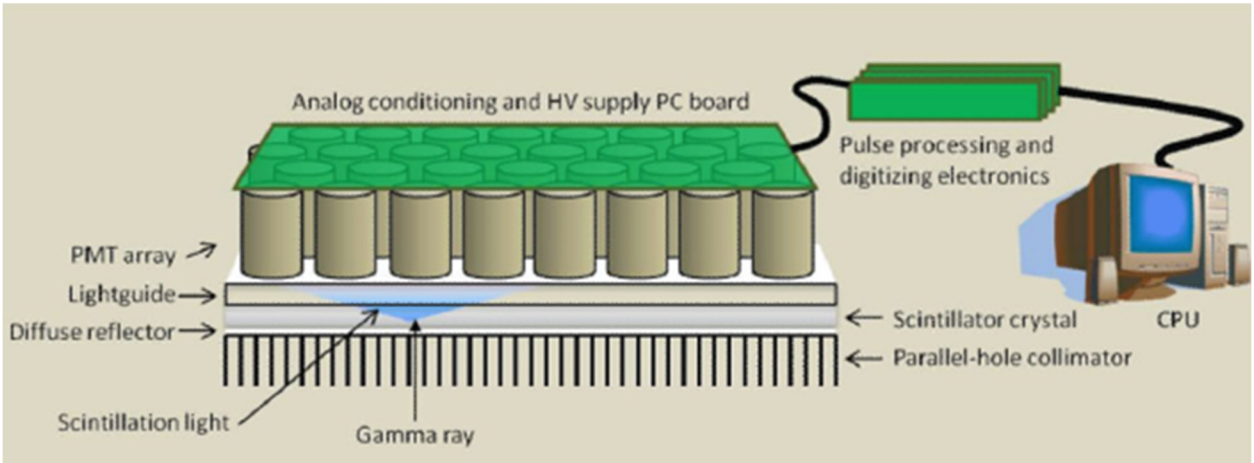

Figure 6. Schematic view of the Anger camera and its support equipment, reprinted with permission from Peterson [17]. Notice the large parallel hole collimator, scintillator/diffuser/lightguide geometry, and the 2-D PMT array.

An example of the Anger Camera system is shown in Figure 6. The genius of the Anger camera, developed by Hal O. Anger in 1952, is that a large array of pinholes could be used to

image objects in the far field, while still maintaining high resolution [17]. By placing a large, parallel hole collimator in front of a large slab of scintillating material, then optically coupling multiple, closely packed PMTs to the back side, gamma photons from all areas of the object to be imaged could be done so simultaneously. This greatly expanded the FOV of the imager, while keeping its resolution on par with that of a pinhole type imager. Since the subsequent interaction of the scintillating material with that of the incident photon creates isotropically generated light, the PMT nearest the interaction registers the highest voltage value, while adjacent PMTs detect lower signals. The generated signals in all PMTs per interaction are then ratioed and the results evaluated to determine which slit in the collimator the far field photon (incident parallel) passed through. Since relatively large NaI crystals can be grown compared to other types of scintillating crystals, this greatly increased the FOV while maintaining sufficiently good resolution over a large area compared to other collimator systems. The Anger camera has therefore been used as the mainstay in body-sized imaging applications since its inception [17]. However, even with relatively thick collimators, the background leakage can be significant for higher energy sources and can cause a noisy spectrum to be recorded.

More true gamma imagers, but with the added caveat of having to in some way decode the resultant signal, can be found in the description of coded aperture, rotating modulator (RM), and RMC gamma imaging systems. By far, the coded aperture setup is the most complicated. It requires a pixilated detector, the discretization of which is highly influential on the resolution of the system, and it utilizes a complicated image signal processing deconvolution algorithm. RM and RMC setups are simpler, as described below, but can lack the resolution afforded by a coded aperture system.

Coded aperture systems use a many pinhole mask (collectively called the aperture), through which photons from the source emitter are filtered and a shadow is cast on the detector. Depending on the pattern used (or multiple patterns) and the subsequent processing, an image can be deduced that should resemble the original object, while maintaining a high-angular resolution with a Signal-to-Noise (SNR) ratio that scales as the square root of the number of open channels [4]. 50% photon attenuations (i.e. equal hole and attenuator material areas) are normally used in these coded aperture setups, but at the expense of complicated algorithms and potential ghost image formations. These are possible if the construction of the mask is not in perfect agreement with the numeric model used for deconvolution. The entire system can also be quite heavy (in some cases hundreds of pounds). This is due to the majority (> 90%) of the mass being credited to the attenuator material [4]. Previous work by FitzGerald, the originator of the RSM design used in this work, explored the imaging properties of a coded aperture system consisting of a static (i.e. non-rotating) selectable grid of pinholes allowing gamma deposition to take place on a pixilated Double-Sided Strip Detector (DSSD). Since his novel grid holes could be reconfigured on each subsequent image effort, the source location was determined by convolving/correlating the detectors' response to these various grid patterns (using previously collected information to enhance subsequent image collection attempts) [18].

In contrast, the RM and RMC systems use attenuation of gamma radiation through a mask (or masks), along with relative angular position changes between the source and detector, to change the source image intensity presented to the detector over a full rotation. The main differences between the RM and RMC systems are the number of attenuation masks and number of detectors. In the case of the RMC, two separated slit attenuators (usually manufactured from Tungsten or another high-Z material), which may have dissimilar slit spacing between the forward and aft

pieces are mechanically linked and rotated along the axis of the detector, which remains static. The intensity of the gammas received by the detector are then recorded with respect to the rotation angle of the masks. An example of these types of modulation curves can be seen in Figure 7 when the RMC work of Kowash [6] is discussed. Knowing the slit spacing, material attenuation properties and mask spacing, the recorded modulation curve can be inferred as a superposition of individual source points (of an extended source) for imaging. This happens to be equivalent to a problem in radio interferometry and the same algorithms can be used in image reconstruction [4].

For the RM system, only one slit mask is needed, but usually an array of detectors below the mask now collect intensity data as the mask is rotated. These systems offer good angular resolution of closely spaced sources, in some cases less than 2º, but are limited by FOV (based on attenuator mask spacing) to a solid angle of ~15º. They may also require greater dwell time for image construction, in that an attenuation-based system normally reduces the gammas arriving at the detector by 50% or more, compared to other imaging systems [19].

RMCs use the principle of attenuating the source photon count profile by varying the transmission function (using a set of 2 or more slitted masks separated by some distance) over a 2π rotation about the longitudinal axis of a single cylindrical detector. The masks, made of a high-Z attenuating material with regularly spaced slit openings, are separated by a fixed distance and rotated. Due to the pattern of the slits and the separation distance, the front area of the detector that is exposed to the transmitted radiation varies uniquely over a single rotation for a certain source position. This modulation pattern is then used to identify the source location or produce an image based on superposition deconvolution. Drawbacks include needing to use non-symmetric slit patterns to eliminate the often produced symmetric "ghost" images (referred to as degeneracies

in this work) of the possible source locations [6]. Further, the FOV of the detector system is limited due to the size of the attenuating masks and their separation distance in the collimator.

The RMC system was the subject of Kowash's work [6] in searching for orphaned gamma-emitting radioactive sources where he improved upon the position accuracy and resolution (especially in the near field) by incorporating physical distance parameters of the mask thickness(es) and the ability of higher energy photons to penetrate the masks into his model [6]. Kowash showed that the transmission function changes as a function of mask rotation, using both in-phase and an slit off-set asymmetric front mask to create an out-of-phase configuration. Some symmetry due to the spacing of the slits in the front and rear attenuator masks is seen in Figure 7 for the in-phase case; however this symmetry, and the subsequent location ambiguity during source image reconstruction, was eliminated with the out-of-phase mask configuration [6]. His RMC was shown to work well (system resolution of about 1°) for identifying the location of the source in two-dimensions and was extended to imaging an extended source. The RMC was also found to have some utility in predicting the range from the detector at which the source was located. However, the FOV was limited (~17°) [6]. RMC systems are in general related to the RSM, in that a single detector is used in combination with a rotating attenuator to create/measure a source photon modulation curve for further analysis.

There is further precedence for using singular point-source detectors in imaging applications, as they have been used for many years in astronomical imaging techniques, by way of RMs and RMCs. It is interesting to point out that the DOE has funded NASA [4] to build and refine RM and RMC systems for stellar imaging in the past. One can only suppose that their intent is to scale down the technology and use it for effective terrestrial investigation of radioactive sources.

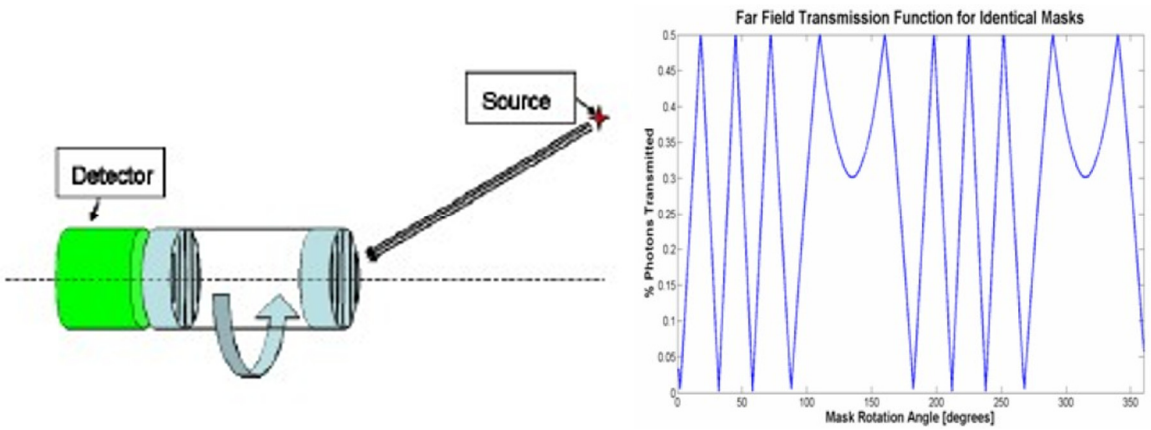

Figure 7. RMC set-up and modulation curve from Kowash's dissertation [6]**. Reprinted with permission of the author.**

Compton Type Imagers

Gamma imaging devices are often composed of a stacked two-dimensional array of scintillator type detectors and their associated PMTs for detection of radiation. In a Compton camera type imager, there are two distinct arrays of individual detectors separated by some distance as seen in Figure 8.

Gamma radiation interacts in the first plane of detectors and is assumed to Compton scattered to the second plane. Accounting for the energy deposited during both interactions (and also assuming that detector #2 was an absorption event), the angle of the first scatter can be calculated. The source location of the gamma radiation can then be inferred to lie along a circular region, based on a cone projection of the most-likely scattering angle of the gamma ray, since it is assumed to Compton scatter and the relative change (ΔE) in energy of the gamma can be measured as determined by Equation (7). With careful configuration, the FOV of these detectors can be nearly 4π steradians (i.e. the "1st" scatter can occur in either of the detector arrays). After multiple interactions, the intersection of these circles can be used to locate the source in three-dimensions. The mathematics are similar to GPS triangulation (but based on the measured change of a single photon's energy instead of the arrival time difference of multiple signals), where the intersection

of a minimum of three timing signals can fix a location on a two-dimension ellipsoid surface to within the uncertainty of the detector/transmitter location and timing signal propagation delays. A fourth signal can then be used to determine elevation (in this case the distance between the detector and the source).

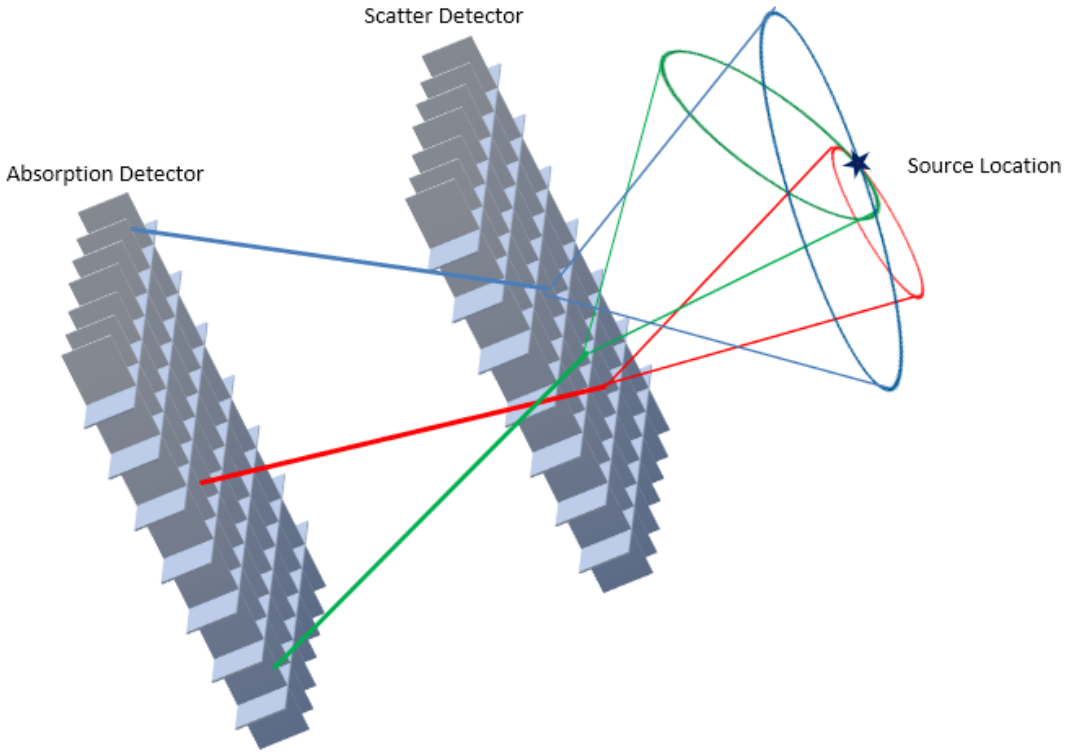

Figure 8. Compton Camera. In this case, the circles of "probable" location are made from the average scattering angle, determined by the Compton equation for the energy difference and flight path trajectory that was measured between the two planes of the detector.

Compton cameras and their associated support equipment, such as cooling units (if high-purity Germanium (HPGe) is used), the power supplies for the arrays of PMTs, and the sheer size of the support brackets necessary to hold the array configurations in place can cause their overall size to be significant. They are often fixed in a particular location and not considered a mobile unit [20]. Smaller, portable units are available and in development, but they often lack the resolution and FOV of their larger counterparts [21]. The first practical Compton camera for identifying source direction was demonstrated by Martin in his PhD research at the University of

Michigan [22]. In follow-on research at AFIT by Dr. Martin et al., a single HPGe array was used to demonstrate the first backscatter Compton imaging of near-surface material defects which had the potential for field use [23] [24].

Other Work Related to the Goals of this Research

Other work has been done to turn single, standard scintillation type detectors into directionally sensitive devices. Work from 2004 in Japan, used a tandem NaI(Tl)/BGO crystal detector in a phoswich configuration (i.e. optically coupled primary and "guard" scintillator slabs). Along with the NaI(Tl) and BGO decay constants, which compare the ratios of the gammas that interacted in either the NaI(Tl), BGO, or both, path length analysis (i.e. orientation of the crystal to the source) was used to determine the position of a source relative to the detector.

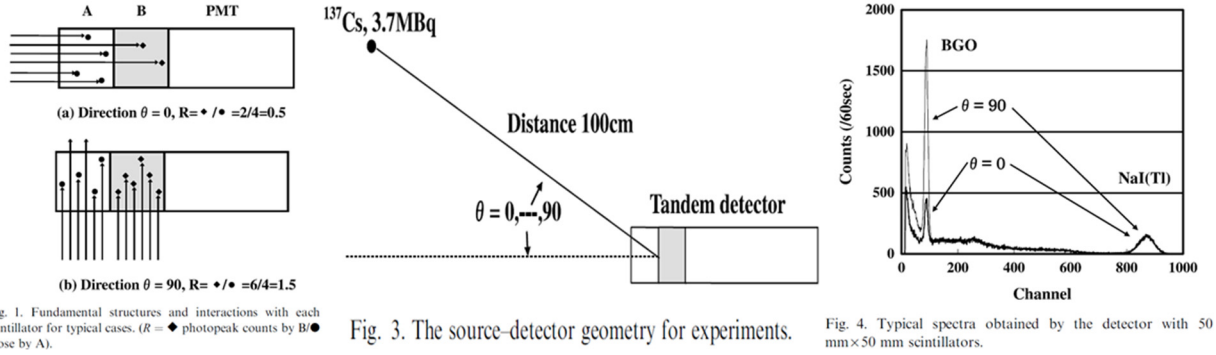

Fig. 1. Fundamental structures and interactions with each scintillator for typical cases. (R = ◆ photopeak counts by B/● those by A).

Fig. 3. The source–detector geometry for experiments.

Fig. 4. Typical spectra obtained by the detector with 50 mm×50 mm scintillators.

Figure 9. Previous phoswich work for source location identification through path length analysis [25]**. Shirakawa used a single scintillator, on a rotational platform to characterize both the direction and distance to the gamma source. Reprinted with publisher's permission.**

It should be noted that a setup like this is inherently 2-dimensional as seen in Figure 9, and leaves ambiguity as to where the source is located on a circle around the axial dimension. This method still requires waveform acquisition/analysis, and a mount on which to change the detectors' orientation. In fact, this method could be combined with an RSM (in an initially non-rotating state) containing a phoswich to identify at what viewing angle (relative to the collinear RSM and detector crystal axes) the source of interest is probably located. Some RSM orientation angles have been seen to perform better than others through experimentation, the results of which

are presented in Chapter V, so setting up the initial conditions based on a quick, initial directional survey leveraging the referenced work of Shirakawa [25], may ultimately lead to optimized operational results when using the RSM. As well, initial RSM data using the total spectra counts may provide a quicker, more accurate general source direction than using fewer FEP counts to identify a source direction due to lower statistical uncertainty [26]. At some time after initiating data collection, one could switch to using only the FEP information to find the source direction, as lower energy scatter-in contributions to the Compton continuum affects the accuracy of the "combined" method. The information content in different energy regions of the spectra is discussed in Chapter II.

Finally, work has already been done to mount radiation detectors on UAVs to map fallout near the Chernobyl reactor site. It illustrated the value of gamma imaging, as well as the need for a more effective approach than proximity detection for mapping large areas. In early 2019, scientists from the University of Bristol in the UK [27] partnered with their Ukrainian counterparts to use a UAV, equipped with both gamma and neutron sensors, to map radioactive hotspots in Chernobyl's *Red Forest*[2]. This was the first ever use of a fixed-wing UAV with multiple types of radiation detectors to map a radioactive area and done as a continued effort to characterize and mitigate the consequences of this accident. The drone spent a total of 24 hours in the air over a 50 sortie, 10-day period and mapped about 6 square-miles of contaminated forest in the fallout area, using a gridded, patterned search method. Previously unknown hotspots were discovered at a location used for "soil separation" activities during the cleanup operations because of this mapping survey. Therefore, aerial identification operations of this type are still vitally important, as the

[2] The forest surrounding the area is now known by this colorful moniker, based on the "ginger-brown" color that the foliage has permanently changed to due to radiation exposure following the April 1986 disaster.

Chernobyl exclusion zone is over 1,000 square miles in area, and dangerous levels of radiation are still being found in soil and animal samples hundreds of miles away (one wild boar in Sweden was found to have over 10 times the safe radiation limit as recently as 2017) over 30 years after this accident. Miniaturized RSM technology, mounted on UAVs, offers an efficient way to broadly maps areas like this, and allow workers to keep their personal radiation exposure "as low as reasonably achievable" (ALARA).

1.4 Radiation Imaging is Historically Needed

One might return to the underlying assumption of this work and wonder about the utility of such a system, when asked if such a system is indeed needed. The following historical examples show that it is. Radioactive sources will continue to be used for a variety of applications, and if they are, a robust, inexpensive, and ubiquitous system(s) will be needed to guarantee their safe use and security.

Current uses of radioactive materials account for power generation, industrial radiography (inspections of build sites and materials using gamma "shine though" to identify deficiencies), medical isotopes used for imagery or treatment, and safety monitoring of the environment (i.e. smoke detectors). Yet, with all the uses and proliferation of radioactive materials in society, the majority of the public has a general concern (or even distrust) of being in the presence of such sources. This probably stems from the concerning stories that have been documented and publicized over the last 70+ years. From the obvious effects of nuclear weapons, to the less well-known environmental pollution that was caused by the development of both jet and rocket engines based on miniature nuclear reactor designs, to terrorists trying to acquire radioactive material for either an explosive radiological dispersal device (RDD) or radiological exposure device (RED), to simply losing track of the material all raise the concern of having access to robust imaging/locating

methods. The possibility of exposure without consent is a genuine issue, and monitoring/early detection of problems should be considered [28].

The following are abbreviated examples of radiological incidents in history (of the most commonly used sources like: Co-60, Cs-137, and Ir-192), that support the need for an integrated detector network for continuous monitoring of hazards and movement(s) of radioactive material to keep the public safe [28].

- In Estonia, a "lump" of Cs-137 was discovered in a family's kitchen cabinet. Due to lax security measures in the former Soviet Bloc country, a man was able to climb a perimeter fence and gain access to the facility where it was stored. While it is unknown for how long the family kept the material before discovery, it was long enough for the man to accumulate almost 4 times (1,500 R) the characteristic LD_{50} dose and eventually pass away. His wife and son also suffered significant "burns" consistent with radiation exposure, and the family dog was thought to have died from radiation sickness too. An interesting unintended consequence of the dog's passing was that the local police force also took to hunting feral dogs in the area, over concerns that the radioactive "disease" could spread.
- In Mexico, an incident occurred where over 4,000 people were exposed to a Co-60 source. While no hospitalization or deaths were reported in this event, body and head aches, nosebleeds and upset stomachs were reported. This accidental release of radioactivity into the environment was discovered when a radiation detector (at the entrance to the Los Alamos National Lab in the United States) activated. The source of the radiation was found to be metal support structure parts used in construction (i.e. rebar, and other metal that had been previously recycled in Mexico and shipped to the U.S.). An investigation was started and found that the original source of radioactive material came from a medical warehouse in Ciudad Juarez, where a teletherapy (external beam radiotherapy) machine had been stored. The unit was obtained by metal salvagers and at some

point, the sealed Co-60 container was breached. This resulted in the spilling of the Co-60 pellets into the back of a pick-up truck and subsequently along the roadway into the environment. By chance, the pick-up broke down and was abandoned in a working-class neighborhood where it sat for some time. During this time, residents of the neighborhood experienced the problems previously described. While the truck was eventually removed, the Co-60 did scatter, and some ended up at a recycling smelting facility where they were inadvertently incorporated into the recycled building materials. It was only by chance that the driver of the transportation truck stopped at Los Alamos to ask for directions, otherwise the incident would have gone without notice or investigation.

- In Brazil, a similar incident occurred where medical grade Cesium Chloride (CsCl) was scavenged from an abandoned clinic. The finder had assumed that because it could no longer be used for medical purposes that it must be "empty". The source was separated from the scrap metal and eventually taken to the man's home, where he broke it open. CsCl has an iridescent glow, which further compounded the exposure issues. The substance was passed around to curious observers and even rubbed onto skin in some cases. This led to significant exposure and in some cases was fatal. Further, members of the surrounding community came to live with prejudice toward the affected people. They thought the radiation sickness may be contagious, similar to the Estonia incident, leading to both personal stigmas applied towards the victims and a fear of buying products produced by them.
- In the United States in 1979, a California construction inspector left an Ir-192 "pigtail" source used for weld radiography outside of its container and unattended. A worker proceeded to pick it up and place it in his back pocket for approximately 45 minutes. While the unaware worker was not permanently impaired, another Ir-192 incident occurred in Morocco in 1984 where eight people ended up dying from exposure. Both were similar in the fact that a passer-by picked up the metal cylinder, which was unmarked.

Clearly, these incidents show that there is a lack of public knowledge regarding radiation and its sources. Sources are often not labeled as well as they should be, and early detection (which would greatly minimize the spread and harm) is essentially nonexistent. While we in the United States already have high-trained personnel and stringent standards to deal with any potential radiological situation based on intelligence gathering resources, we have limited resources and mapping/tracking ability for finding lost and diverted sources (which is probably the more likely scenario of significant concern). A network of RSMs, along with integrated cell phone solid-state detectors [29], combined with the current remote sensing [30] and Port-of-Entry resources [31], would give much better situational awareness for the avoidance of every scenario discussed so far.

These incidents also show that it is of paramount importance to track (and identify) lost or absconded radiation sources quickly and correctly. The RSM system represents a novel method for quickly, inexpensively (low-cost, ubiquitous detectors with no cooling requirements), and portably (no bulk issues normally associated with Compton detector arrays or Port-of-Entry scanners) to implement a high-resolution, 2D imaging technology applied over a wide-area to quickly locate sources.

1.5 Recent Gamma Imaging Needs Suitable to the RSM System

Because of the Fukushima Daiichi nuclear reactor damage in 2011, recent "hot spot" imaging work has occurred in Japan to develop a "low-cost, high-sensitivity" Compton camera for area search and situational awareness. It was quickly realized while responding to the damaged Fukushima structure, that standard survey meters had serious limitations for the identification of hot spots. In the recently published work of Kagaya, et al. [21], a forward and aft array (4 rows by 2 columns) of commercially available CsI(Tl) scintillators was constructed, to make a Compton camera. Characterization of the system was conducted, and it was found to have a viewing angle

of about 1π steradians, with a 3.5º resolution (or about a 1 m^2 coverage at a 10 m distance). This is arguably better than a handheld detector (and like the RSM system, does not require a previous background measurement to identify source hot spots) and it is suitable for a stand-off measurement of an area. However, the size, weight, complexity in design, and expense (16 detectors, totaling > $67K), is still a detractor when compared to the RSM system. Plus, the limited FOV, requires more operator interaction/exposure than just setting up an RSM to rotate and collect the gamma interactions and angular rotation data and then returning at a later time.

Searching remote or larger areas can be a significant undertaking when it comes to locating radiological sources, since these sources may not readily stand out from everyday objects (if not marked properly). Even if they are marked appropriately, it may be difficult to locate their position due to a variety of reasons (intentional obfuscation, proper archiving/tracking of location, and unexpected natural occurrences). Consider for example, a 2002 IAEA mission to recover Sr-90 thermoelectric generators, used to power communications equipment in the former Soviet Bloc country of Georgia. The sources were scattered at various sites over a 550 km^2 (212 mi^2) area, but the exact location information was no longer available. The search lasted for 2-weeks and was comprised of over 80 people. It required the use of both vehicles and horses to access remote wooded areas, where searchers would often proceed on foot to investigate potential generator sites. Over 280 were discovered and recovered, but it is still unknown how many more might be left unaccounted for. An UAV mounted RSM, with a loitering capability (combined with differential GPS technology to accurately capture orientation information of the system) may have significantly reduced both the manpower and costs associated with the search, as well as contributing to a higher confidence that all the Sr-90 generators had been located and removed [32].

1.6 RSM Literature Review

FitzGerald's Original Work [1]

The original paper by FitzGerald published in 2014 [1] described the method of creation of the RSM shape, the detector placement, proposed coordinate system for source direction identification, and initial MCNP® modeling to show the theoretical system response. In it, he developed two distinct response curves at three source positions (one was a shift in the theta rotational angle, θ, but at the same viewing angle phi, φ). These response curves are henceforth referred to as modulation curves (i.e. number of gammas received by the detector are proportionally different according to the thickness of the intermediate RSM material and are a function of the rotation angle for any given viewing angle source placement) if numerically generated. They are referred to as scattergrams if experimentally collected.

His work suggested High-Density Polyethylene (HDPE) as a construction material, but he also recognized that in future configurations other low-Z (but higher density materials) such as: graphite, carbon composites, and Beryllium should be investigated. This opens the door to making the RSM of a more compact configuration. Low-Z material is necessarily chosen to maximize scattering and minimize absorption, because photoelectric absorption scales as Z^4, while Compton scattering scales as the Z_{eff} of the material, as described earlier. He also briefly investigated the RSM radius value on collection efficiency, addressed the SNR limit necessary for extended source image reconstruction techniques, and explored the FOV of the proposed system. Here, he also realized the possibility of *ghost* imaging, seen in this work as degeneracies (or similarities) in the RSM modulation curves at two or more allowable source angular positions. He suggested that a scattering method using a low-Z scatter mask would have advantages over high-Z attenuation-based masks because gammas from the same source could scatter into the detector from an off

detector/source line-of-sight material interaction, which would allow for source direction information to be determined using the Compton continuum information. Combined with the information contained in the FEP portion of the spectra, his low-Z material RSM construction and internal detector placement design effectively allows for an increased acceptance angle of the detector and an overall increase in the efficiency of the system.

This research was started to confirm and extend the theoretical RSM imaging approach that FitzGerald proposed for this new class of gamma imagers. The equipment and concepts developed in this research were then employed and extended by several other AFIT graduate students.

Logan's 2017 Thesis Work [2]

Logan used the SolidWorks CAD design for the FitzGerald design RSM developed in this work, as well as the same 18 primary data sets presented in Chapter V (with the exception of viewing angle $\varphi = 135°$, which was later retaken by the author due to position encoder reader issues). Ms. Logan's MCNP® and GEANT modeling efforts are briefly addressed in section 5.3, where the results of her computational (i.e. library) modulation curves for given source positions are compared to the experimental data. However, her work also included a more robust statistical effort to more appropriately model both the detector energy resolution (i.e. imperfect and in need of FEP broadening to match the experimental spectra) and to incorporate the expected Compton down-scattering of higher energy sources from the surrounding lab environment into the FEP range used to generate her scattergrams [33]. Her work focused exclusively on using the FEP portion of the spectra for source direction identification and is the underpinning of all follow-on AFIT work that has so far been done with both the FitzGerald class of RSM designs and other classes.

Her work used the standard MAC matching methodology presented in this work when making comparisons between the scattergram and DRM library, but she also used both the Anderson-Darling and Kolmogorov-Smirnov tests to determine how well her computational library iterations statistically matched each other. This furthered the work she was able to do in modeling the broadening of the spectra due to the nature of the NaI(Tl) detector at more than one energy value (i.e. detector response was characterized across the complete energy spectrum). With these modeling improvements, she found that her prediction of point-source direction was similar to this work when using a particle simulation set of only 500,000 [34]. She also addressed the RSM system resolution and found it to be approximately 3.5° in both φ and θ. While this number is slightly better than the value found in this work, it does set a good precedence to show how the resolution of the lookup library can affect the angular position determination. In her case, the φ scale of the library was developed in increments of 10°, while the θ scale was in increments of 5°. Therefore, in many instances, the predicted source direction was in exact agreement with the actual source angular position, when searching over her 2,592 DRM options. This resulted in a measured overall system resolution value less than what is expected if using the "half-the-distance" between the smallest scale increments added in quadrature metric. So, even though her library search would be considered sparse (compared to the method and discretization presented in this work) it does show that a determination of the source direction can be made without extensive RSM dwell time or post-processing/imaging that is sometimes computationally expensive, if optimal "sparse" DRM search parameters are chosen.

Finally, her work enabled further advanced imaging work by Oleson et al. [35] as part of a parametric optimization study in RSM design, which discussed the minimum particle interactions needed to determine an accurate source position.

Condon's 2018 Thesis Work [3]

Condon's thesis work essentially repeated the work done here and by Logan, using the system designed and built for this research, with the original large, FitzGerald class RSM. However, he investigated the development of multiple modulation curve libraries (DRMs) based on different energy sources. He correctly found that while the normalized shape of a DRC for a given source position is the same at all energies, the relative intensity and therefore resultant peak and trough amplitudes of the modulation curves and scattergrams were minorly effected based on energy. The number of FEP attenuations by scattering of the higher-energy source model libraries he developed decreased. This is expected and due to the lower probability of RSM material interaction. The lower interaction probability (mass attenuation coefficient) for Compton scattering in these cases resulted in "shallower" scattergram troughs for higher energy sources. This highlights the need to correctly fit each DRC reference curve to the experimental scattergram when calculating the MAC value used when determining the most probable source direction. However, it also shows that the same DRC can be used across a variety of incident gamma energies. The correction/fit work presented here in Chapter V facilitates the use of the same complete DRM with RSMs of different material(s) and size(s), or when using a different detector so long as the relative geometries of the RSM and detector remain the same.

As well, he incorporated trapezoidal background subtraction into the spectra results used to identify the source's FEP, which resulted in better fidelity experimental scattergram production than shown in this baseline work. He also showed for the first time that three distinct sources of different energies at different positions could be identified by the RSM successfully.

Holland's 2018 RSM Design Optimization Work [5]

Dr. Holland's follow-on work showed that the FitzGerald design, while a good proof-of-concept, may not be the optimal solution for RSM geometry (of course this is scenario dependent). The uniqueness of the modulation curves across all possible source positions could be improved. His work addressed this optimization problem and led to a series of alternate designs, most of which outperformed the FitzGerald design based on a series of metrics, including improved post-processing times for the data sets and increases in detector efficiency. His development of alternate RSM designs were based on orthogonal basis sets and eigenvector value problems to minimize the degeneracies found in the FitzGerald class of designs. While his MCNP® modeling investigation showed no perfect design over all RSM use scenarios, the configurations discovered improved the accuracy of the source direction determination, reduced the necessary collection dwell time, and improved the speed (computational effort) at which the source direction could be determined all while significantly reducing the RSM size and weight compared to this work.

Holland found that it is not necessary to use a square filling matrix for the RSM design as was done by FitzGerald and carried over to this work. Holland's work on RSM designs and Olesen et al.'s characterization of such (eight total RSMs in two different design groups/classes) [35] led to advances in RSM design theory that reduce the natural degeneracies found in the FitzGerald class of designs (production rules for the FitzGerald class are discussed in Chapter III).

Olesen's Thesis Work [36]

Olesen followed the optimization work by Holland and tested the 8 new designs developed through extensive modeling evaluation, using metrics anchored in comparing all library modulation curves/DRCs using the MAC method, as initiated by FitzGerald (and used in all subsequent work). He discovered that the along with size reduction, simplification could be made

to the complexity of analysis necessary for identifying the source's position. Specifically, by decoupling the rotation angle, θ, from the viewing angle, φ, he found that a much smaller subset ($1/360^{th}$) of the DRM library look-up modulation curves could be used, as a shifting and comparison over all θ was not necessary. All these new designs had a lower measure of degeneracy compared to the FitzGerald design and maintained the uniqueness of the modulation curves at all allowed source positions (but without implementing FitzGerald's strict design rules). Six of the eight showed better efficiencies, while only one of the new designs had better sensitivity (i.e. larger ratio of the max/min peak/trough amplitudes of the recorded scattergrams) compared to the FitzGerald design. This work focused on a total mass reduction for an additively manufactured RSM in general, so the sensitivity (scatter-out of the FEP source term from the source line-of-sight to the detector) differences were expected. These new designs did not maintain the same average amount of scattering material over a full rotation, as in the original FitzGerald class of designs, but proved smaller and lighter with similar source direction prediction results to the FitzGerald class. They were therefore categorized into 2 new design classes (named Spartan and Mace) based on their geometric shapes and theory of operation.

The Figures of Merit (FOM) used by Olesen were only applied to the FEP portion of the spectra for the cases presented, as no Compton scatter-in libraries were generated. Therefore, the work presented in Chapter V here is the first to report on the use of the Compton continuum portion of the spectra for source direction determination. Specifically, this statement is true not only regarding the FitzGerald design but also in general for all classes of RSM.

Egner's 2019 Thesis Work [37]

Egner showed that RSMs are good candidates for mixed-radiation (i.e. gammas and neutrons) directional imaging [37] [38]. Egner et al. [37] built, tested, and reported on the next

generation RSM "Spartan I" class design by Holland [5]. Not only did they show good system performance for gamma detection along with miniaturization and automation of the entire unit, inclusion of an EJ-309 Boron loaded liquid scintillator for neutron detection was done. Egner showed that effective post-processing of the pulse waveform outputted from the PMT was conducted to discriminate between neutron-induced proton recoil events and those of gamma-induced electron events and their contributions to the PMT light yield. In this way, a separation of the gamma and neutron source events was made, the data parsed, and source direction(s) determined. This shows that further work to add spectroscopy (through total spectrum bracketing), source activity, source distance, isotopic composition, and the identification of any possible shielding materials, is within the realm of possibility for next-generation RSM designs.

Olesen's 2020 Dissertation Work [39]

Olesen et al. [40] used his previous work in the characterization of RSM designs [35], based on Holland's classes [5] [41] and RSM optimization work, to conduct a series of studies to determine the feasibility and performance of three imaging algorithms: Maximum-Likelihood Expectation-Maximization (ML-EM), Locally Competitive Algorithm (LCA), and Convolutional Neural Network (CNN) with RSM scattergrams created by an extended source (i.e. exists at more than one discrete point in the RSM FOV).

While the ML-EM algorithm is widely used and established for imaging in medical community and coded-aperture imaging, the LCA and CNN are newer, novel techniques when dealing with problems where a convolution of many point sources (i.e. extended source) lead to a near infinite combination of weighted modulation curves due to the degeneracies of the RSM systems. His coordinate system was setup to cover φ from 5° – 170°, and θ from 0° – 355° in increments of 5°, for a total of 2,448 possible angular positions for a point source, and so creating

a master DRM of weighted sums of all the possible positions of the extended source(s) contributing to the experimentally captured scattergram is quite challenging and not easily done. The complexity of simplistically dealing with a superposition of DRCs is shown in Chapter V and in Condon's [3] work. The problem quickly becomes too computationally expensive to use brute force methods, and so it is recognized that Olesen's work represents the path forward for an extended source (true imagining techniques) visualization with regard to future RSM invention.

Backed by the point-source validation of Ms. Logan's modeling results of the FitzGerald design, MCNPX® models of the RSM design by Holland known as Mace II were extended to include four geometrically extended sources in the shapes of a: Disc, Ring, Junction ("X" shape), and a Square. The four sources were placed at varying distances and sizes in relation to the RSM and simulated scattergrams were recorded in the digital environment. Post-processing then showed good imaging characteristics by the LCA method, followed closely by the ML-EM technique. It is interesting to note that ML-EM outperformed LCA for sources near the equator ($\varphi = 90°$), but LCA was ultimately the clear winner for imaging point-sources in any direction. The simple neural network of the CNN technique had lower resolution than the other two but will serve as an added basis for comparison with follow-on RSM image reconstruction work.

Holland's Continuing Work [42]

Efforts are currently ongoing to refine and optimize the design space, and make comparisons of such results, for more complex variations of RSMs in future instantiations. In short, rapid progress has been made in reducing the necessary computational time to compare hundreds of thousands of design variations over a six-parameter design space based on a Beer-Lambert's law surrogate transport model (similar to what is used in the RSM response model used

in this work and discussed in Chapter II), instead of the more traditional (and computationally expensive) Monte Carlo type approach of either MCNP® or GEANT.

1.7 Summary

The primary goal of this research was to conduct the initial verification and validation that a RSM of the FitzGerald class of designs can successfully use the FEP portion of the spectra to locate a point source emitter. Secondarily however, scattering-in of non-line of sight gammas, recorded in the Compton continuum, and their subsequent use to direct the user to the gamma source's location with a high degree of accuracy over a variety of background conditions was desired. This distinguishes the work here from previous and subsequent AFIT research. It is the first to show source direction information can be deduced from the Compton continuum portion of the spectra.

This was the genius of FitzGerald's original idea. He suggested that a scattering method using a low-Z scatter mask would have advantages over high-Z attenuation-based masks because gammas from the same source could scatter into the detector from an off detector/source line-of-sight material interaction. This effectively increased the size of the acceptance angle of these types of systems. In fact, efficiency was shown to increase, and next-generation RSM designs also continued to explore the efficiency increases and optimizations available due to the use of low-Z material and unique scattering geometries [36].

II. RSM Computational Modeling Development

2.1 Introduction

Simple analytic models based on gamma attenuation by Compton scattering within the RSM material out-of-the-path of the detector, were developed to closely match the numerical Monte-Carlo Neutral Particle *(MCNP®)*[3] simulations conducted by FitzGerald [1] for his RSM design. These deterministic models were used to predict the FEP material scattering interactions and resultant attenuation-by-scattering affect to the source intensity as recorded by the detector set interior to the RSM. The models were later parameterized and modified to incorporate experimental results for calibration, and they served as the foundation for the scatter-in library development, which uses the Compton continuum portion of the spectrum for point source direction determination and performance analysis. This is presented at the end of Chapter II.

The intent of the numerical development presented here was to build a catalog of library lookup curves for future comparison with experiment scattergrams when making the source direction determination. Lookup library files (or DRM) are constructed for each allowed source angular position ($\theta = 0° – 359°$ and $\varphi = 1° – 179°$ for a total comparison file value of 64,440 DRCs). Because statistically significant MCNP® results can take a significant amount of computational time, close to 6 hours per DRC in Logan's work [34], a quick analytic method was desired to characterize and study the expected differences in modulation curves over a variety of RSM geometrical configurations and source positions prior to finalization and production. In

[3] As an interesting aside, MCNP® was originally designed to only predict neutral particle transport, as it's name implies (Monte Carlo N-Particle). However, it is now fully capable of modeling the transport and interaction of charged particles as well as photons. It has been in use for so long however, with so many upgardes, that its name no longer reflects the capabilities of the code. MCNP® is a registered trademark owned by Los Alamos National Laboratory.

addition, no RSM SolidWorks CAD models yet existed for importation into more advanced modeling environments. Finally, the FEP attenuation-by-scattering response functions were later stochastically modified to investigate system design parameters by simulating the expected scattergram results with varying degrees of noise/uncertainty. These were used to test and refine the direction prediction software prior to and during experimental data collection.

While Monte Carlo models do in general provide the detailed "gold standard" of gamma scattering physics needed in RSM geometries, analytic models enable us to gain better understanding of the primary interaction contributors regarding RSM design changes. Monte Carlo techniques do not readily produce an understanding of what interactions are most important in producing modulation curve differences, something the initial RSM design development presented here was meant to address. Therefore, the insights introduced here may have the potential to replace the DRM search library with an infinite resolution analytical algorithm. This would make investigating distributed sources more tractable in future RSM research.

2.2 Original Simple FEP Attenuation Models

Two analytical models were developed: one which described the geometric positioning of an external point source term compared to a point detector internal to the RSM and the other which considered the finite size of the RSM and detector. The first analytic model was developed to only show general agreement to the MCNP® simulation as a steppingstone, by considering the source as a point at infinity and the detector as a point exactly in the center of the RSM. A second iteration of the model was developed to account for the finite size of the NaI(Tl) detector crystal and the near field source location on a ray from a point at infinity, which takes into account the statistical nature of the energy range of the arriving gammas and their average scattering angle by incorporating a detector response function. The development of both versions is described here,

and results are presented in the order in which they were produced. In both cases, only the source, RSM, and detector were modeled to exist. No work was done to include any other structure.

In the first simplistic model, only the material depth of the RSM in a single straight-line path from the source's angular position to the center of the NaI(Tl) detector crystal was considered in the attenuation-by-scattering calculation. The gamma radiation intensity at the detector is described by a parameterized Beer-Lambert's Law, as shown in Equation (8). I_0 is the initial intensity of the source. $\frac{\mu}{\rho}$ is the incoherent scattering, linear mass attenuation coefficient for a 662 keV gamma in HDPE, with a value of $8.851 \cdot 10^{-2}$ cm^2/g. This value was calculated using the *XCOM: Photon Cross-Sections Database* from NIST [10]. ρ is the density of the HDPE, with a value of 0.97 g/cm^3, and x is the length of RSM material between the surface of the detector and the surface of the RSM, which varies according to the filling matrix. ε is a coefficient weighting factor that was used to empirically scale the model to match experimental results. For the first model, ε was set to 1. This model fundamentally assumes any gamma energy incident on the detector is recorded.

$$I = I_0 e^{-\varepsilon\left(\frac{\mu}{\rho}\right)\rho x} \tag{8}$$

Comparison of the normalized peak amplitude of the generated modulation curves, with respect to unity, and the MCNP® results of FitzGerald [1] is shown in Figure 10. Here, the simple model results for equivalent source placements shows qualitative agreement. However, the sharp discontinuities of the simple model are unphysical, as the detector is not a point, and the amplitude of the curve(s) at various points throughout the full rotation do not match to the original FitzGerald MCNP® results. Of note, the original MCNP® results generated by FitzGerald are no longer available in numerical, discretized form for further comparison. The freeware version of WebPlotDigitizer [43] was tried on his graphics to partially remedy this, but the uncertainty in

aligning individual degree positions of the theta, θ, rotation of the RSM for numeric quantitative comparison was found to be inconsistent.

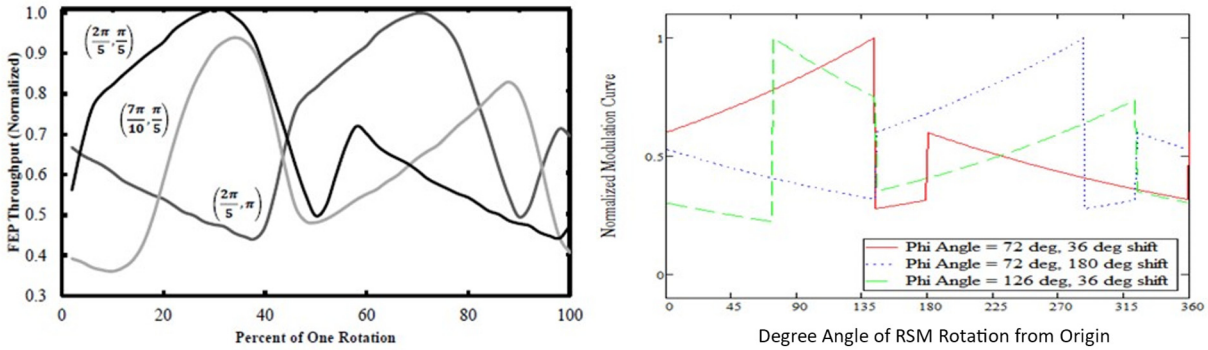

Figure 10. Detector response curves from FitzGerald's initial MCNP® modeling (left, reprinted with his permission) compared to simple line-of-sight attenuation by scatter only model (right) developed in this work. The same three source placements are shown in both.

The sharp discontinuities see on the right panel of Figure 10, which are due to RSM geometry, are physical but need to transition more smoothly if a useable model, to mimic the MCNP® generated curves was to be found. The finite size of the detector crystal, the geometry of both the surface shape and depth of the RSM material, and the different probabilities of absorption for the FEP gamma through different thicknesses of the NaI(Tl) crystal (which depend on source orientation to the cylindrical crystal) needed to be considered for accuracy. Developing this functional response of the system to a distance point source was empirically modeled through a parameterized, scalable, blurring function around the source/detector center direct line-of-sight. So, while the computational speed and qualitative amplitude of the first model was ideal, the necessary modifications needed for accuracy and scaling of a more advanced model will be developed later in Chapter II.

The initial modeling work undertaken investigated a smoothly filled matrix, as opposed to the one with an introduced discontinuity, as discussed in FitzGerald's paper [1]. In the paper, it was not directly addressed as to why FitzGerald chose to not consider the simplest form of the filling matrix. While many ways of filling the RSM surface cylinder matrix exists, only one of

them varies in a relatively smooth way. An example of this is shown in the smooth alternate design representative matrix on the lower portion of Figure 11. A full treatment of filling matrices and their considerations are presented in Chapter III.

The original design presented by FitzGerald modified the smooth filling matrix by inverting the bottom half of the rows (corresponding to θ) at the 180° point, thereby creating a discontinuity in the smoothness of the RSM's outer surface values over the range of RSM rotation angle. Examples of the smooth (1st alternate design) surface matrix and FitzGerald's design are shown in Figure 11. Both have the same design values in each row, but because of the introduced discontinuities in the filling matrix, the octants of FitzGerald's design do not transition smoothly. This produced unique modulation curves in the simulation of the FitzGerald design compared to the smooth alternate design.

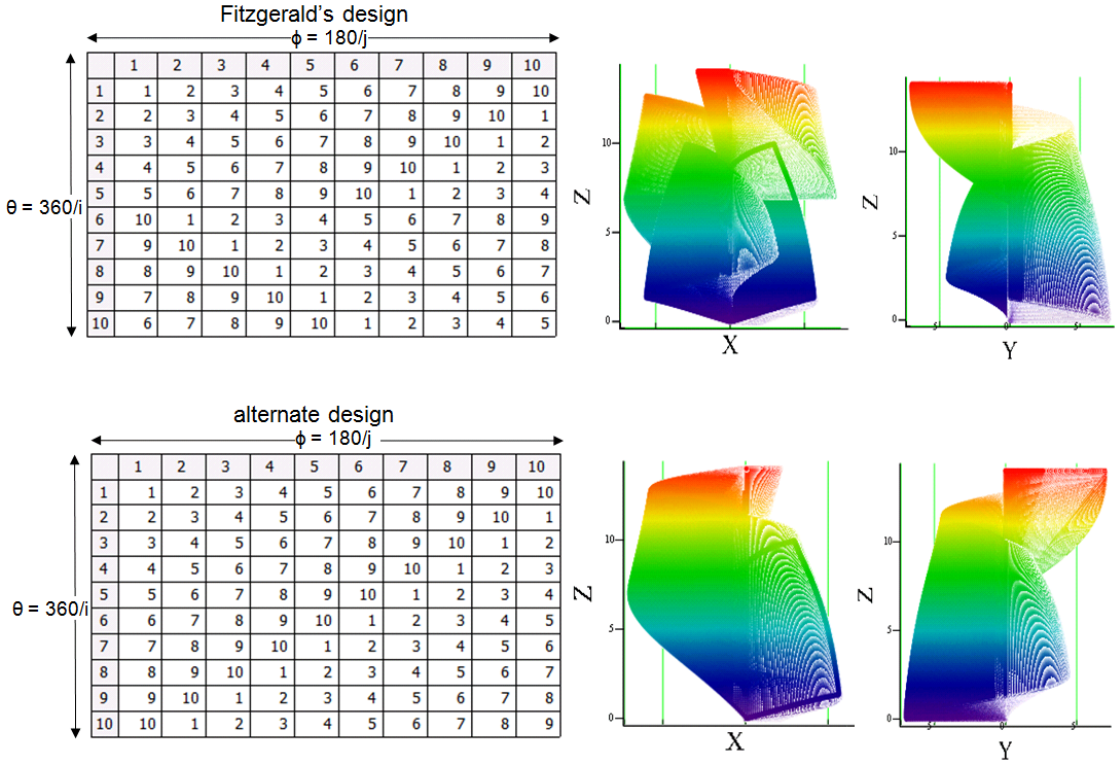

Figure 11. The FitzGerald RSM design filling matrix and RSM outer surface point cloud (top); compared to a relatively continuous (no induced discontinuities) 1st alternate design (bottom). Notice that the summation of each row and column is the same, and that the integers values are never repeated in either row or column. This is a defining characteristic of the FitzGerald class of RSM designs.

To graphically show this, the simple first-order model of the shape of the expected modulation curves was run for both designs. A comparison of the two RSM design's modulation curves verified the uniqueness of the modulation curves over the range of possible φ and θ point source position combinations. However, these results raised concern that the smooth design would produce degenerate scattergram results throughout the entire system, leading to ambiguity in the source position determination, when experimental uncertainty was accounted for.

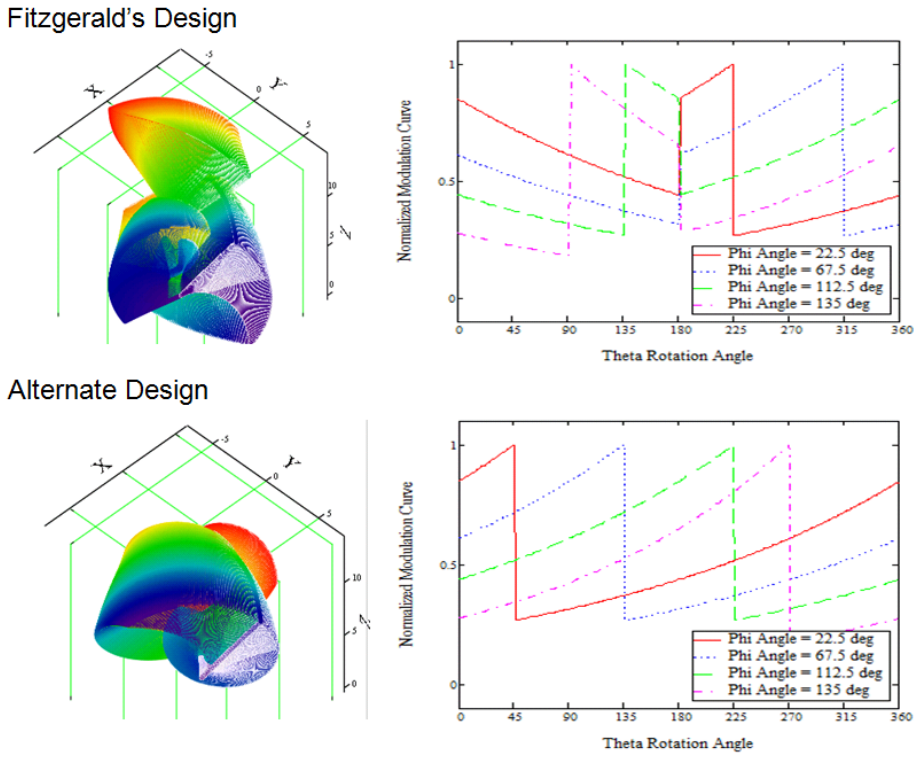

Figure 12. Initial modulation curve modeling showed that a smooth RSM design would have repetition across a full rotation (bottom), while the FitzGerald design (top) might have apparent degeneracies over the RSM rotation angle theta, θ, when realistic smoothing was added to the model.

In addition, it was observed that the FitzGerald design also produced modulation curves that had a mirrored symmetry about a full rotation (θ) as seen in Figure 12. From inspection of the first-order model compared to the MCNP® results, it was speculated that this may also cause an ambiguity in the source direction for the viewing angle (φ) region near φ = 90° due to discontinuity smoothing that is present in a real system. This would lead to decreased system

resolution in source direction prediction around this angular region, compared to the rest of the potential viewing angles. Regardless, a proposal to manufacture both designs and test/compare them by focusing on each design's effective FOV was submitted, but with the caveat that the simple analytic model limitations were recognized and that steps to refine it should be taken.

2.3 Development of the Advanced Model

A second numerical model was developed with the assumption that the source being imaged by the RSM system was in the near field. In this case, non-parallel rays define interactions at the edges of the detector. Hence, more than a single material path length should be used for the response generation at each allowed angular position. This being the case, combined with the finite size of the 3"x3" NaI(Tl) detector and the dimensions of the RSM, a region on the surface of the RSM that gammas from the source would pass through on their way to the detector was estimated. This surface area was named the "active area" for a defined position and is seen as a black circular region in Figure 13.

It had already been hypothesized that the dominant FEP attenuation mechanism for gammas from the source is due to photons Compton scattering out of the path to the detector. Therefore, only the gammas that passed through the active area needed to be considered in the FEP modulation curve simulation, and absorption in the mask material could be neglected. This active area on the surface was modeled by distributing a faux source, with an intensity of $I_o = 1$, at every defined RSM surface point (φ,θ) encompassed by the subtended solid angle (Ω) defining the active area. With the origin of the RSM system being defined as the center of the detector, this allowed for an estimate of the solid angle necessary to encompass the active region, in terms of φ and θ. In other words, an area on the surface of the RSM through which the gamma rays would pass from the source on their way to interacting with the detector crystal could be estimated. This was in

turn used to specify the solid angle components of the source viewing angle and RSM rotational angle necessary to include into the numeric averaging of the model about the centerline to predict the expected scattergrams more accurately.

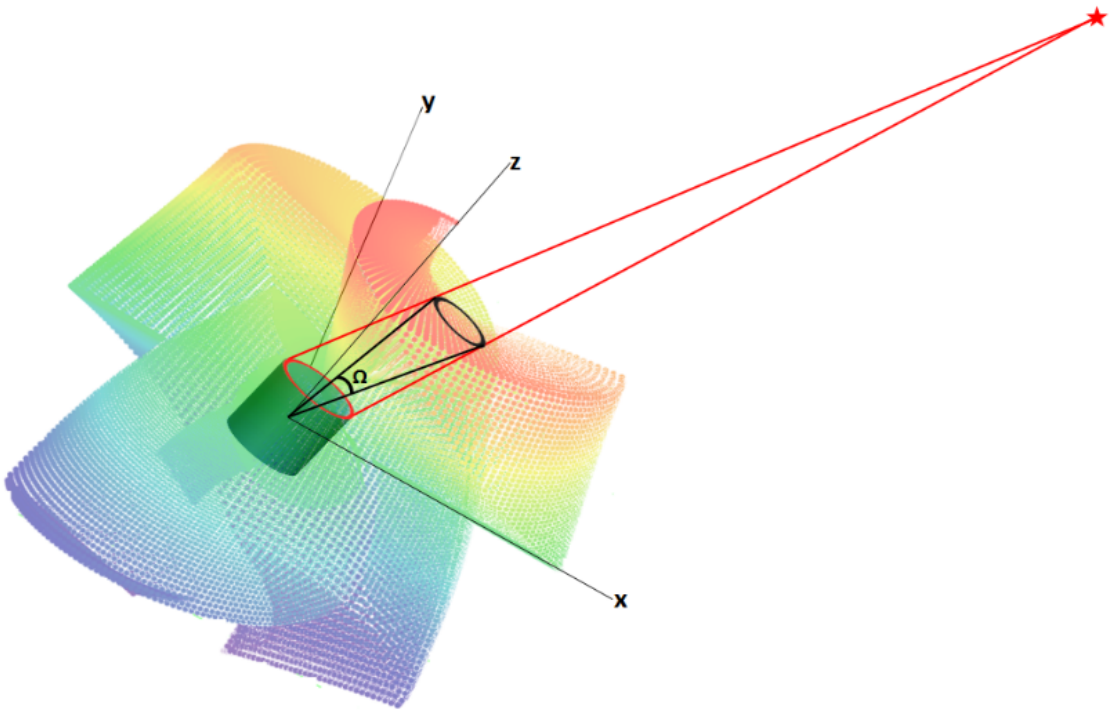

Figure 13. Solid angle (Ω) depiction of the probable source gamma interaction/scattering active region of the RSM.

(φ, θ) pairs define the direction of a ray intersecting the detector center and the source center. Because of the definition of θ (0° – 359°) and φ (0° – 180°) in the geometry of the RSM configuration (showed later in Chapter III), and the fact that the surface filling matrix was chosen to be square, there are twice as many φ indices for every unit of solid angle as there are θ indices. The θ indices for this advanced model correspond to 1° increments, while the φ indices correspond to ½° increments. Therefore, an indexing system to account for this difference was developed and implemented to account for every possible combination that defined a ray that intersected the active area of interest, when building the advanced model FEP modulation curve for a defined angular position. The contribution of each available ray within the solid angle to the total modulation curve was then investigated.

The same attenuation by scattering calculation as before was used to determine the gamma intensity reaching the detector crystal. These results were then summed over the solid angle range of φ and θ, according to Equation (9), for a specified source centerline value. This accounted for the finite size of the detector crystal and the contribution of the off-centerline components when predicting the modulation curve values over a full rotation of the RSM.

$$ModulationCurve_{\phi,\theta} = \sum_{\phi,\theta}^{\phi,\theta \pm \Omega_{index}} I_{\phi,\theta} \tag{9}$$

When normalized, the results of Figure 14 were produced.

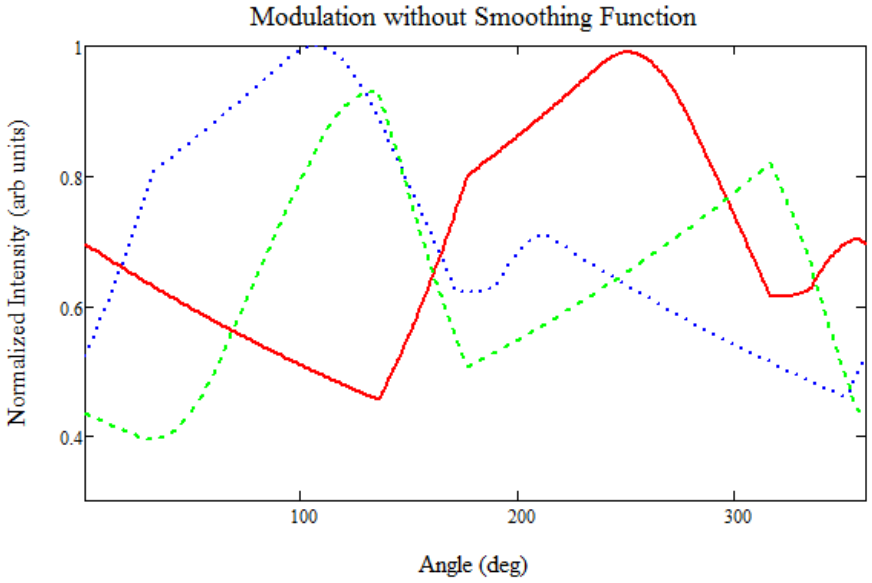

Figure 14. Modulation curves for the same three source positions as modeled by FitzGerald, generated by the advanced model. Notice that they are in better qualitative agreement to Figure 10, and so this modification was considered a step in the right direction.

Notice a better qualitative agreement in Figure 14 to FitzGerald's MCNP® results on the left-hand side of Figure 10. The steep amplitude transitions are more consistent with the expected experimental results, but a few sharp discontinuities still required smoothing to improve the agreement. After close examination of the peak and trough transitions of the modulation curve over a full RSM rotation, it was realized that because of the cylindrical geometry of the NaI(Tl) crystal, a higher probability of absorption through the thick center of the crystal, as opposed to that

of the edges, needed to be considered. Therefore, a variable parameter for FEP absorption in the detector, which fell off towards the edges of the detector (i.e. the border of the active area solid angle), was incorporated into the model for further smoothing.

Various absorption "fall-off" functions describing the detector response were tried such as: linear, exponential and an inverted parabola. The best observed fit to the FitzGerald MCNP® model was accomplished using a form of sinusoidal fall off as described by the equations:

$$WF_{\varphi} = 1 - \alpha \cdot \left(\frac{2\Omega + 1}{index}\right) \cdot Sin\left(\frac{index - \Omega + 1}{\Omega}\right) \tag{10}$$

and

$$WF_{\theta} = 1 - \beta \cdot \left(\frac{\Omega + 1}{index}\right) \cdot Sin\left(\frac{index - \frac{\Omega}{2} + 1}{\frac{\Omega}{2}}\right) \tag{11}.$$

These equations allowed for the same general shape to be applied to both the φ and θ directions as a weighting function (WF_{φ} and WF_{θ}) to cause the total value for any off-centerline contribution to take on any value between 1 and 0 if the adjustment parameters, α and β, are less than 1. The weighting function was also designed so that the maximum and minimum values are the same for both parameters, but of course this is only strictly true if the adjustment parameters for both the φ and θ versions are the same. It should be noted that while the functional forms for these weighting equations in φ and θ looks different in their indexing scheme, they are evenly spaced in degree and produce the same difference (Δ) at any particular φ or θ from the source/detector centerline. In other words, their value at a unique solid angle measured from the centerline is the same in both directions. This is because the number of φ points in the system are sampled twice as frequently as the θ points, as previously discussed. The α and β parameters were built as part of the code for flexibility in doing the final empirical fitting to the MCNP® or

experimentally generated curves. Both were initially set to 0.9 for both the φ and θ weighting functions. It is seen in Figure 15 that the total weighting function at this value ranged between 0.25 and 1. The values were not varied for the rest of the initial investigation, but they did become a fine-fitting parameter that was used in subsequent model iterations to calibrate the advanced model to the empirical experimental results. The value of the parameters however was always the same (i.e. $\alpha = \beta$).

The weighting functions were used to moderate the contribution of the outlying φ and θ active surface area point contributions to account for angle-dependent changes in the detector crystal material interaction length (i.e. orientation of the edges of the detector compared to the thick center as seen by the emitted ray). In retrospect, it was recognized that this approximation is only physically true when the subtended angle (Ω) exceeds a minimum of 45°, which it never does in this model, and is also highly dependent on the orientation of the detector crystal because of the cylindrical shape, so a different weighting scheme should be investigated in the future.

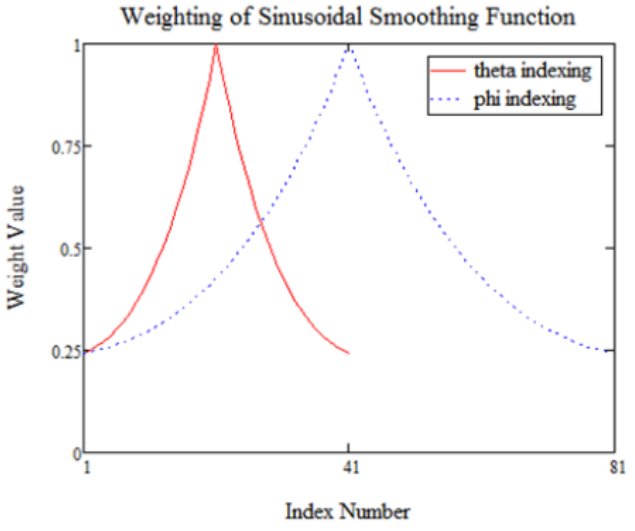

ThetaIndex =

	1
1	0.24268
2	0.28982
3	0.37889
4	0.51809
5	0.71902
6	1
7	0.71902
8	0.51809
9	0.37889
10	0.28982
11	0.24268

PhiIndex =

	1
1	0.24268
2	0.25976
3	0.28642
4	0.32357
5	0.37225
6	0.43368
7	0.50933
8	0.60105
9	0.71117
10	0.84276
11	1
12	0.84276
13	0.71117
14	0.60105
15	0.50933
16	0.43368
17	0.37225
18	0.32357
19	0.28642
20	0.25976
21	0.24268

Figure 15. Weighting functions used to "smooth" simple model modulation curve results.

Because of the weighting function modification to the model, the resultant averaged summation of the modulation curves considered for contribution (i.e. inside the active area) showed peak and trough amplitudes differences to be consistently smaller than for the FitzGerald's MCNP® simulations, across the entire RSM rotation. However, the sharp transitions at material discontinuities disappeared, and the model's predictions more closely matched the MCNP® simulation over the entire rotation range for the original three source placements specified in FitzGerald's paper [1]. The general shape was nonetheless found to be in better agreement with the FitzGerald simulations, so a method for fitting the experimental scattergram amplitudes (once acquired) to the DRM library individual modulation curves was concurrently developed. This is discussed later in Chapter IV.

In addition, a reduction factor, ε, to the linear mass attenuation coefficient was incorporated and varied in the advanced model. This modification parameter likely represents the statistical nature of gamma emission and allows for a range of energies to fall under the FEP and contribute to the modulation curve (as it would in a physical detector system). In other words, it does not restrict the interaction of the photon, scattering material, and detector to be constrained by a singularly defined gamma FEP energy. Conversely, it could be that the reduction factor was needed to account for the actual attenuation coefficient of the material, finite size of the detector and its efficiency, and the ratio of mask size to detector size of the final RSM build. Thus, variations in the attenuation coefficient of the material(s) for a range of emitted gamma energies can be empirically accounted for, and built-in to change the library of modulation curves addressing different energy regimes and RSM source viewangles, φ. The final libraries for this work did not include this parameterization option, as a normalization and scaling/stretching routine

was implemented to overcome peak and valley differences of the library data, before comparing and matching to the experimental scattergram data.

After this last modification was accomplished, the available fitting parameters consisting of the solid angle for the active area of interest, weighting shape, and linear attenuation reduction factor were iteratively adjusted until what appeared to be a best fit was converged upon. This laid the adjustable parameters values' baseline for a brute force search method regarding library calibration to experiment. Modeling efforts which occurred after the experimental results were available further refined the adjustable fitting parameters and are described later. Also of note, a higher-resolution model with more discretized angular positions in φ and θ, could have easily been developed by simply expanding the matrix used to create the surface point-cloud of the RSM. However, it is still the highest resolution model developed to date.

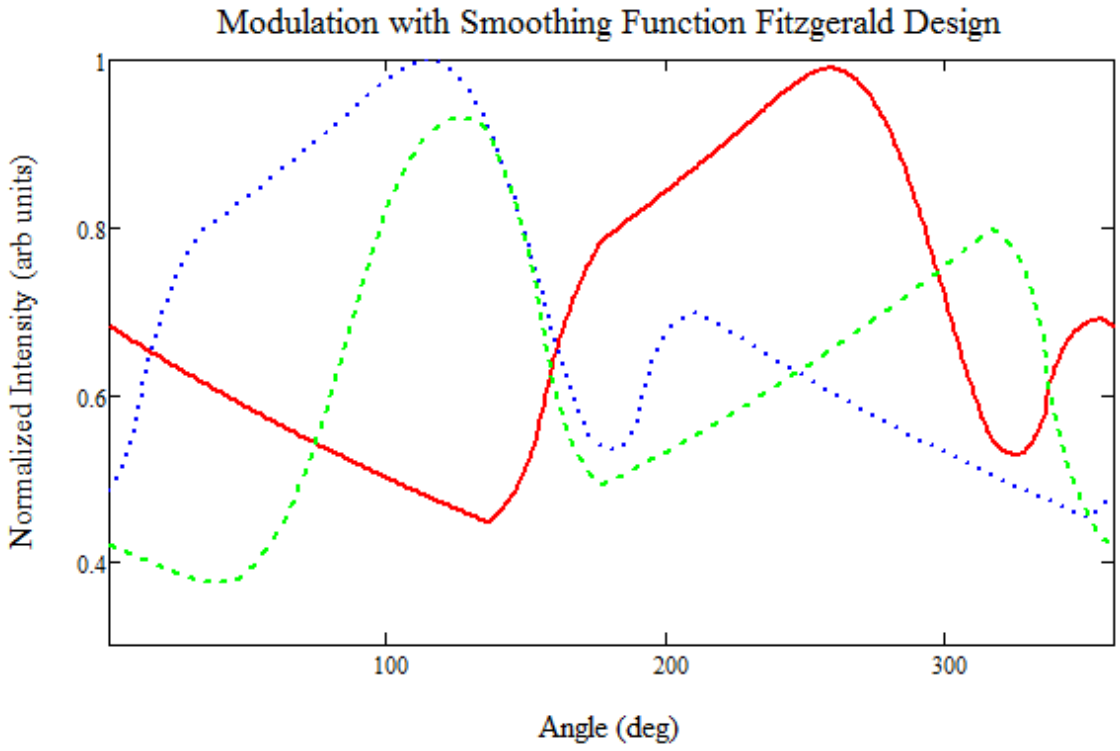

Figure 16. Final modulation curves for a near field source, generated by the weighted advanced model, to be used as a comparison to the FitzGerald MCNP® model.

The final results of this advanced model overlaid with the FitzGerald's MCNP® output (grey scale) [1] and the analytical model (color scale) are shown in Figure 17.

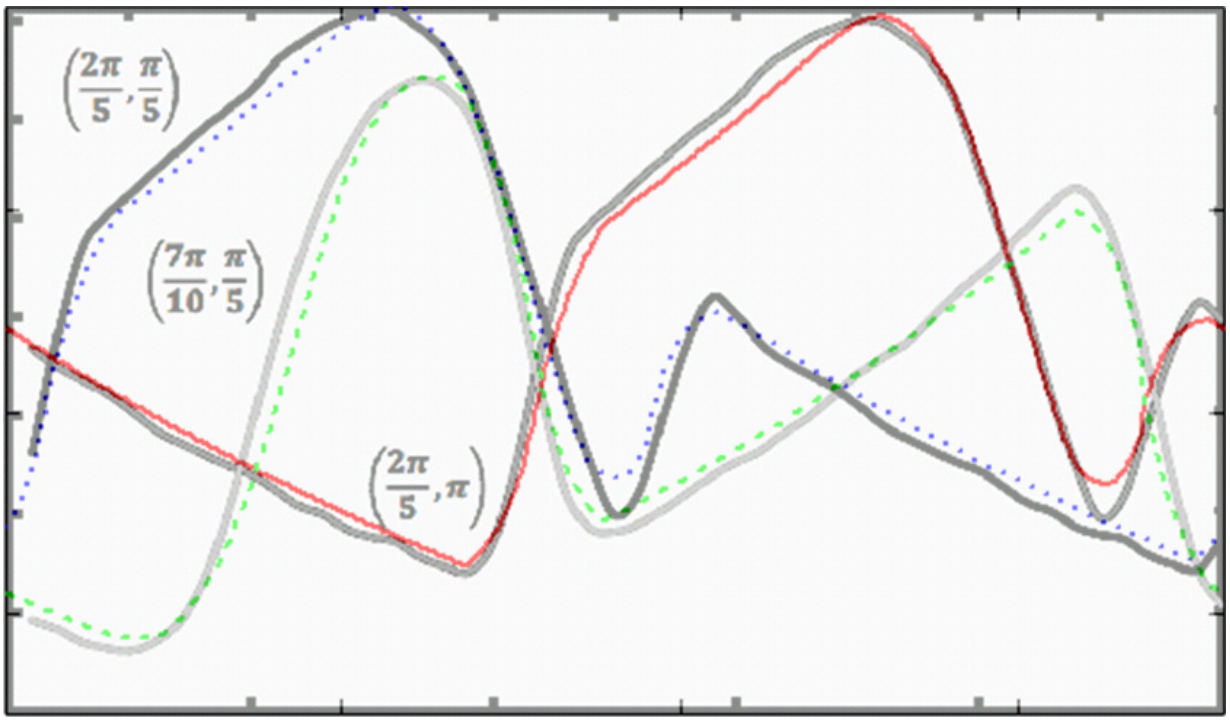

Figure 17. Final fit of the advanced modulation curve model (color) overlaid with FitzGerald's MCNP® results (grey scale) [1]**.**

2.4 RSM Design Investigation

The advanced model, now validated by a few MCNP® calculations, was then used to expeditiously generate modulation curves to refine the selection of the various FitzGerald class RSM designs, sizes, and materials options. The first comparison made was that of the smooth alternate design (discussed later in Chapter III) for the same source positions as FitzGerald's paper [1]. It is interesting to note how similar the modulation curves are for this design, varying only slightly in amplitude. Figure 18 shows the results for the first alternate RSM design.

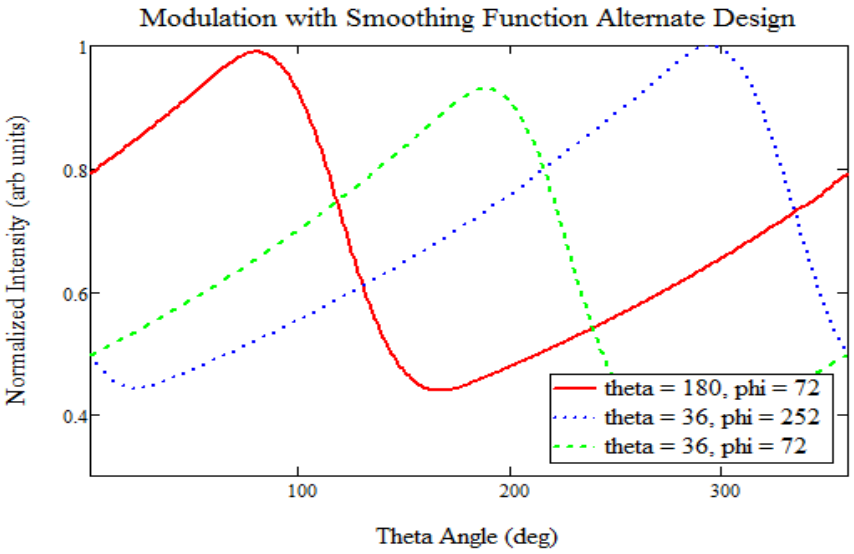

Figure 18. Advanced modulation curve model for the smooth alternate RSM design. Notice that the modulation curves at φ = 2π/5 (72°) should be equivalent but are not. This is due to a WF indexing error (1 bin shift) when crossing θ = 0° that was not immediately recognized.

Figure 19 shows both the FitzGerald RSM design and the first alternate smooth design at a specific φ viewing angle of 45° over a full rotation for θ source positions of 0°, 60°, 120°, 180°, 240° and 300°. An expected symmetry is seen in both cases because the rotation about the RSM axis is defined by θ.

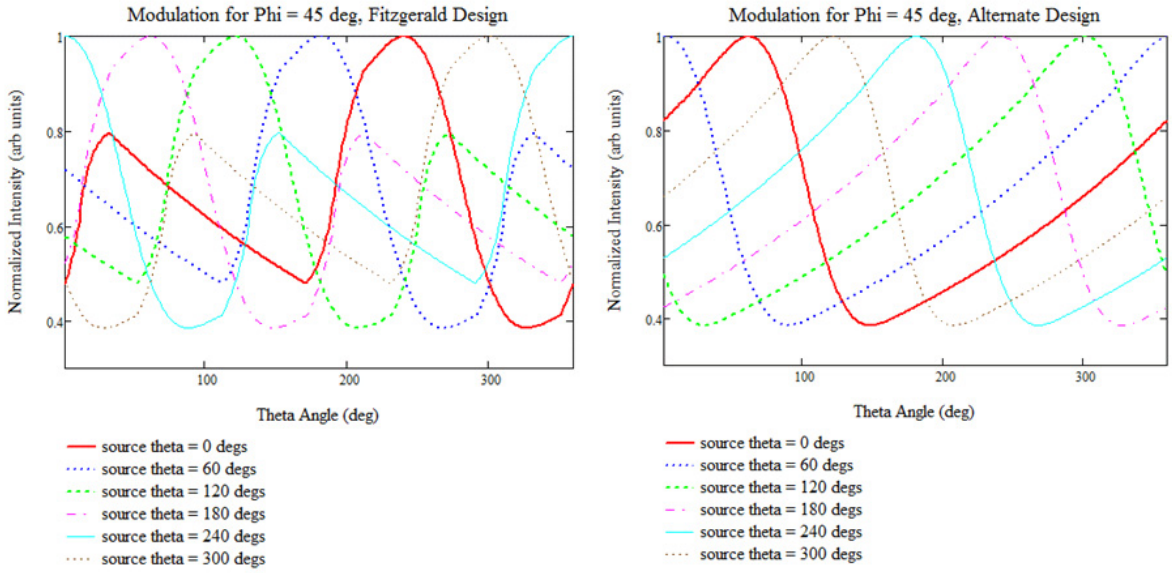

Figure 19. Comparison of both RSM designs with FitzGerald's on the (left) and smooth alternate on the (right) for a unique φ = 45° angle and various θ coordinate positions.

Comparisons of both the FitzGerald and alternate smooth RSM design for a source located at θ = 0° and φ viewing angle positions of 22.5°, 45°, 67.5°, 90°, 112.5°, 135° and 157.5° are also shown in Figure 20. In these cases, a predictable, smooth pattern is observed in the smooth alternate design case, whereas the modulation pattern from the FitzGerald design does not vary in a smooth way. It was quickly shown, by using this advanced model, that the smooth filling matrix design created ghost images (degeneracies) of other possible source directions due to only having one peak and trough throughout the entire rotation, whereas the FitzGerald design possibilities appeared rather distinct. This will be detailed more in Chapter III.

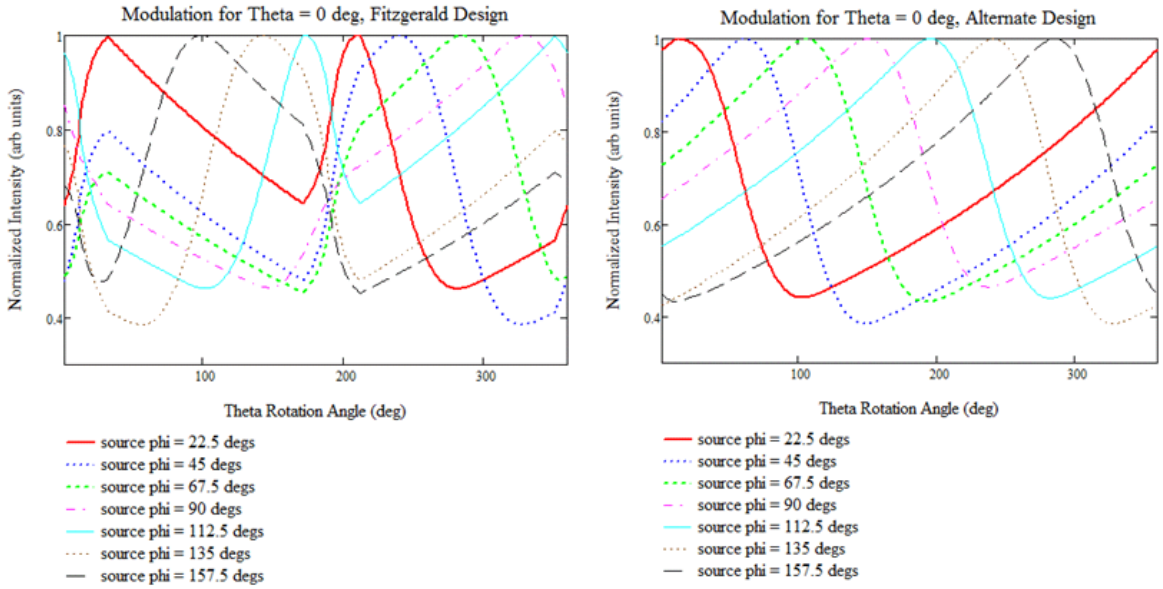

Figure 20. Comparison of both RSM designs for a unique θ = 0° angle and various φ coordinate positions.

The average modulation curve height of the FitzGerald design, differenced from the normalized peak height was also investigated using the advanced model over a range of possible RSM diameters. Two of these products for a 15" and 10" diameter RSM are show in Figure 21, where values were constructed according to Equation 12.

$$Difference(\varphi_i) = 1 - \frac{\left(\sum_{\theta=0}^{359} ModValue(\varphi_i, \theta)\right)}{360} \tag{12}$$

As expected, it was observed that the relative distance between the modulation curve peak and trough changed when the size of the RSM was varied, so this knowledge was used to decide on the production size of the large RSM. The averages were generated using the seven φ positions centered at θ = 0, as seen below in Figure 21 for a given RSM diameter. This was done to compare how RSM size will affect the modulation results, which in turn gives an indication of the fraction of FEP photons expected to scatter-out of the solid angle subtending the active area.

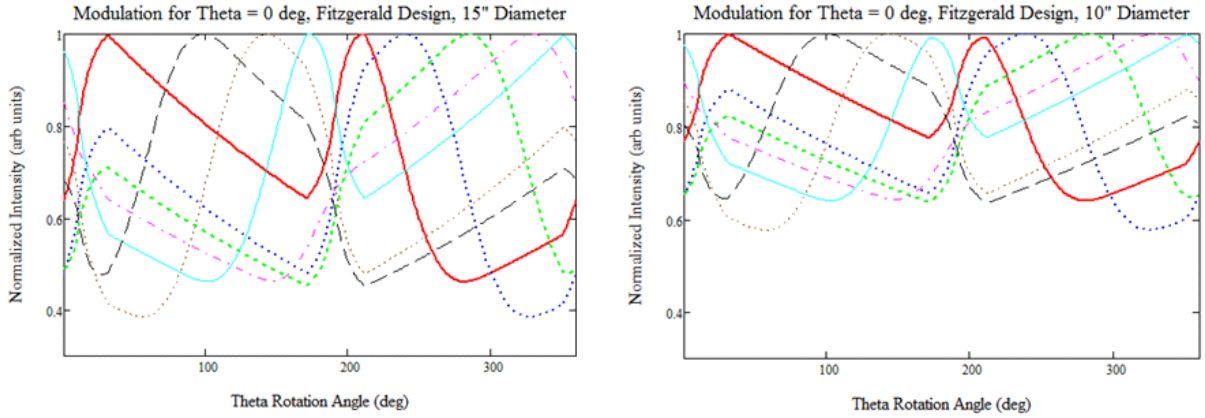

Figure 21. The relative amplitude variations of the modulation curve were observed to vary significantly with a change in RSM diameter.

For final RSM production size determination, comparison of these averages of the FitzGerald designs over a range of possible diameters was accomplished. It was determined that any final diameter greater than 15” would be sufficient to meet an arbitrary minimum criterion for the trough to be, on average, 20% of the maximum (i.e. maximum of 80% line-of-sight FEPs scattered out). This was considered to be a manufacturing constraint, as another 10% increase in efficiency of FEPs scattering-out came with a material and size cost of nearly doubling the RSM design diameter. These relative efficiency results are shown in Figure 22.

Initially, a cylindrical extrusion of 7” in radius and 14” in height of HDPE was purchased for machining into the large RSM because of the large price gap between that of the 8” radius stock, which presented a cost and acquisition time constraint. However, a tooling path for the

AFIT Model Shop 5-axis mill could not be determined by its software due to the complex nature of the RSM's outer surface shape. Therefore, 3D additive manufacturing was developed and used for the final design production with a maximum radius of 7" (slightly smaller than that of FitzGerald's original paper design of 7.48" [1]).

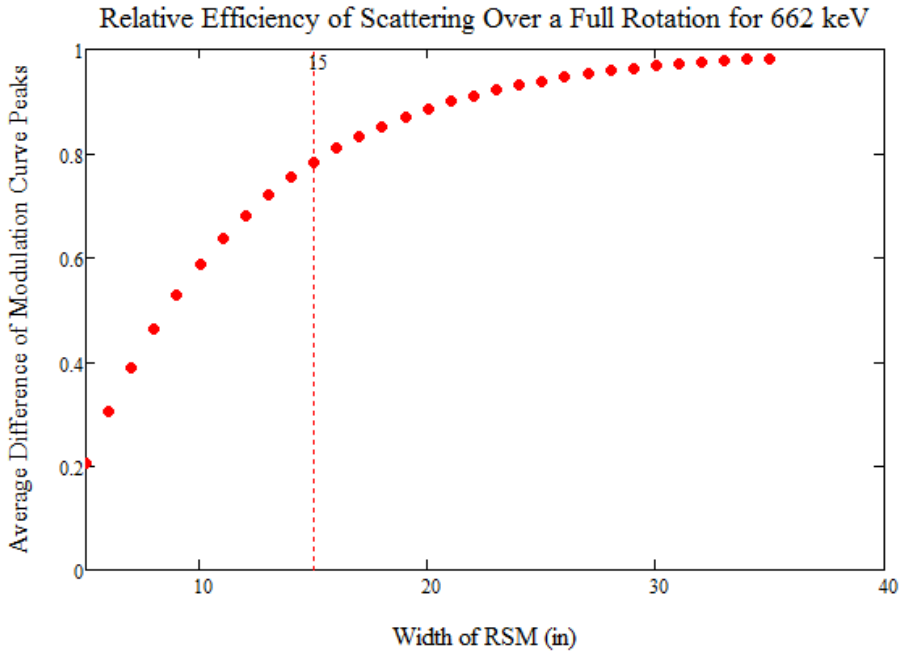

Figure 22. Comparison of total attenuation efficiency over a range of possible RSM diameters.

2.5 2nd Alternate RSM Design Modeling

Due to the perceived degeneracies in the modulation curves of the smooth design (right-hand side of Figure 20), a 2nd alternate design was numerically constructed. It was formed by adding another discontinuity to the FitzGerald design filling matrix, resulting in a more complicated RSM outer surface, but used the same rules of total material length over a complete rotation consistent with the FitzGerald class of RSM designs. Both designs investigated in this work, their filling matrices, and further treatment of the FitzGerald class RSM design theory are covered in Chapter III.

When modulation curves were generated for the 2nd alternate design case, they usually had three peaks, as opposed to two for the FitzGerald design. It was theorized this extra peak may provide for better library matching to the experimental results, since early work using the advanced model with random noise incorporated showed some ghost imaging (degeneracies) when conducting the DRM library matching using the FitzGerald's design. Therefore, the 2nd alternate design was also CAD drafted in SolidWorks based on this modeling work.

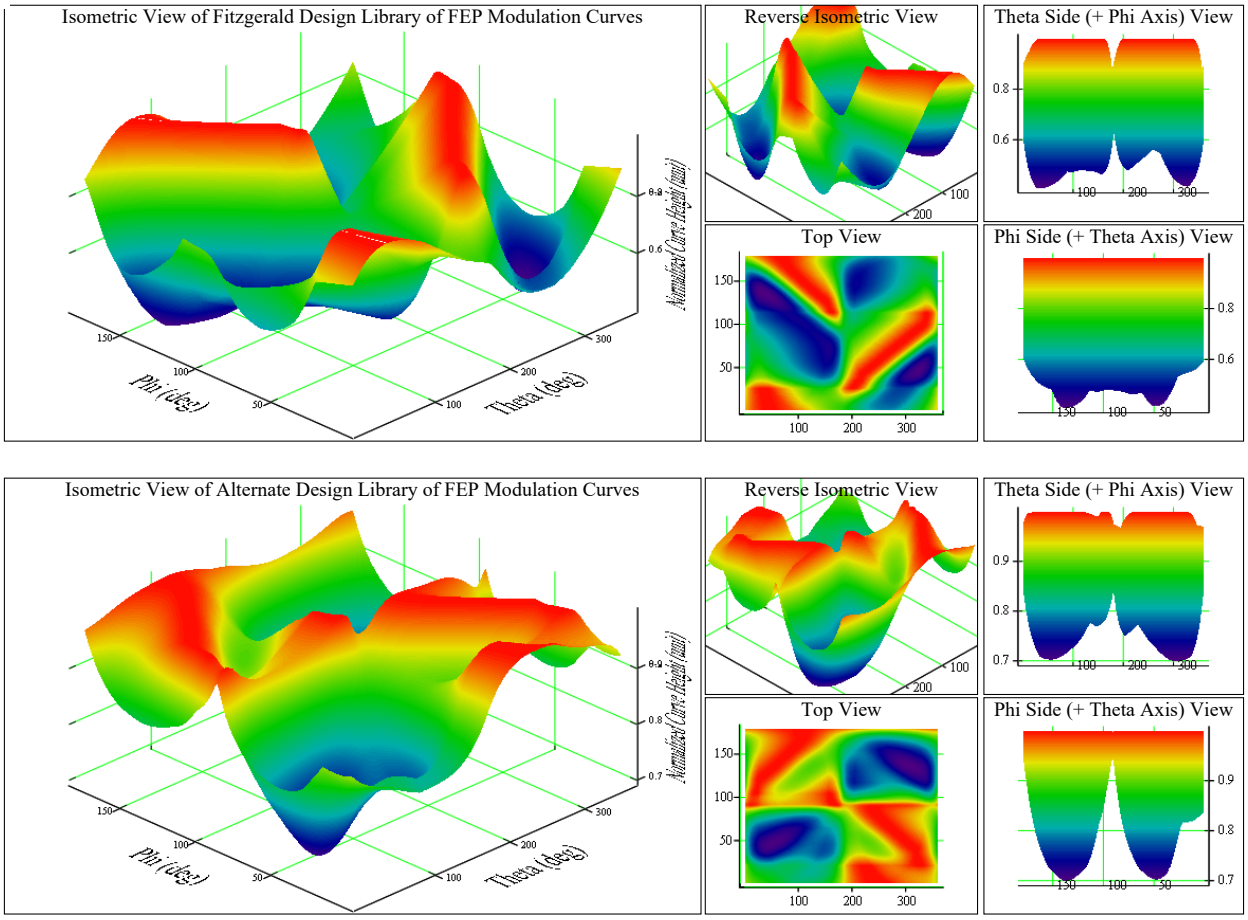

Figure 23. Comparison of both production designs' library of modulation curves over the range of possible φ and θ source angular positions. FitzGerald design is top, while the results of the alternate design is bottom.

A visual mapping of the DRMs for the scatter-out FEP modulation curves of both the FitzGerald design and the 2nd alternative design (henceforth referred to as the alternate design), are seen in Figure 23 for comparison. The FEP scatter-out model libraries for the planned small

versions of the RSMs were also slightly modified for use with the $LaBr_3$ detector, which is discussed next.

2.6 Other Modeling Considerations

In experiments using the smaller $LaBr_3$ scintillator, the dimensions and geometry of the crystal are that of an extruded cube (10x10x50 mm), dissimilar to the cylindrical natural of the 3"x3" NaI(Tl) detector. So, the library generation program was modified to keep the solid angle (Ω) of the θ component of the model static, while varying the φ spread from 1 Ω to 5Ω for $\varphi = 1° – 90°$ and from 5Ω back to 1Ω for $\varphi = 91° – 179°$, by incorporating a simple amplitude shifted $\text{Cos}(\varphi)$ factor into the φ weighting function of the model. Results of the original experimentally fitting library and the WF "adjusted" library for the $LaBr_3$ detector geometry are presented in Chapter V, along with the implications of this modification.

In addition, before the final build versions of the two RSM's filing matrices was decided upon, a computationally study of the library modulation curves with 10% random noise added was conducted for both, using MathCAD's built in, normal distribution, random number generator. This was done to simulate the anticipated experimental data and associated noise. The FitzGerald's design had better direction matching (i.e. lowest average distance of the predicted angular position away from the true direction when multiple randomized curves were compared). His design also had better "clustering" characteristics when displaying the first 500 rank ordered matches (Figure 24), whereas the theoretical "smooth" filling matrix design and the alternate design manufactured for this work (and described in Chapter III) showed regions of degeneracy sooner (Figure 30). These degeneracies are characterized by the "next" closest match comparison presenting in a different quadrant of the polar plot used for display after a certain point, and then usually alternating between distinct regions compared to the actual source position cluster.

Therefore, it was ultimately hypothesized that the experimental results of the FitzGerald design would show better overall performance. This indeed was proved during the experimental work and showed the more intricate alternate design was inferior when using the experimental scattergrams generated by bracketing the FEP of interest. The alternate design did show some promise however when utilizing the Compton portion of the spectra for direction determination. So, it is likely that utilizing a more complex RSM design when looking at the Compton scatter-in portion of the recorded spectra may be useful.

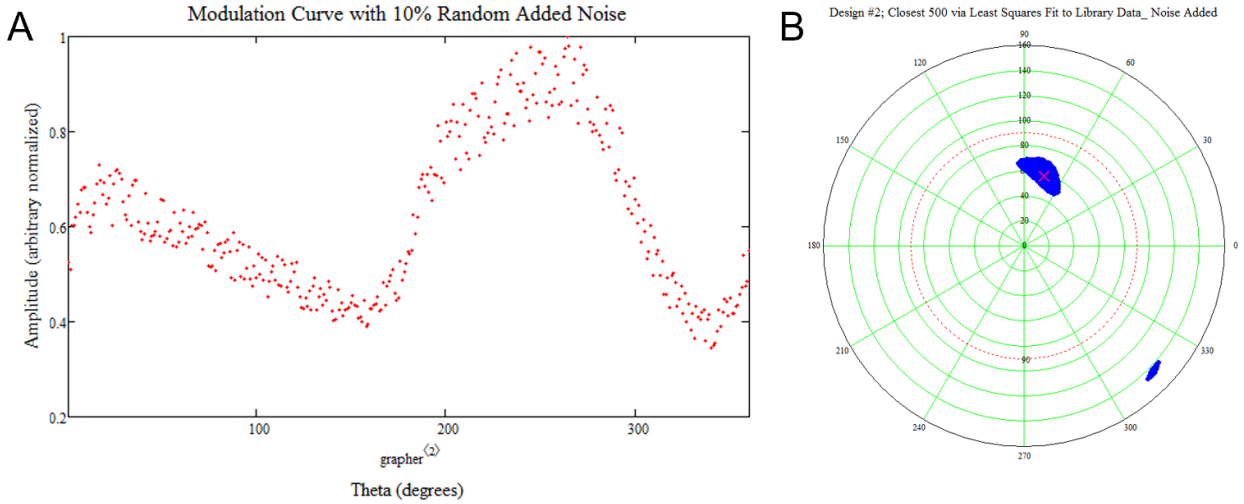

Figure 24. (A) Advanced modulation curve model with 10% random noise added; (B) 500 closest library matches looking for potential false positive (ghost) symmetry image predictions of the FitzGerald Design.

2.7 Final FEP Scatter-out Library Computational Results

Final modeling work to increase the accuracy of the advanced model in matching the original FitzGerald MCNP® results, around the turning points of the generated curves, was conducted. When experimental results became available, parameters $index_{\varphi}$, $index_{\theta}$ (and therefore WF_{φ} and WF_{θ}), ε, and α and β were investigated over a range of values for the $\varphi = 45°$ viewing angle, in steps of ± 0.01 for each variable around the previously established baseline, resulting in 112,896 comparison files that were then checked for goodness of fit against the initial experimental result. The FEP scattergram of the $\varphi = 45°$ data set is showed in Chapter V on Figure 66.

This force fitting of the final parameter values was used to generate a new experimentally calibrated, advanced model library over all viewing angles. A comparison of the before (qualitatively fit to FitzGerald's MCNP® work) and after (experimentally calibrated library), and how well they matched the experimental data are shown in Chapter V for the large FitzGerald design RSM in Table 3. It is noted here and shown in the results, that this new, experimentally fitted library had similar position matching results at almost every source view angle, φ, compared to the commercial standard MCNP® and GEANT codes used in generation of the DRM libraries of Logan's work [2]. The success of the experimentally fitted library shows that in the future, an efficient analytical algorithm can be substituted for the direction determination, instead of the brute force DRM search routine.

2.8 Development of the Compton Scatter-in Library

While the development of the advanced model for the FEP scatter-out library was a relatively straight forward process, the addition of a Compton scatter-in DRM, which leverages position information contained within the Compton portion of the spectra was slightly more complicated. Normally, the convoluted spectra information of the Compton continuum produces little useful information [44] without significant work to unfold its contributions. Therefore, a significant portion of this work was designed to show that direction information can be extracted from this portion of the spectra when using the RSM (i.e. by considering it as a whole, without complicated energy "slice"/discretization inspection).

Whereas the only assumption in developing the FEP scatter-out library was that line-of-sight gammas would Compton scatter out of the way of the detector when passing through the active region defined by Ω in accordance with Equation (8), the scatter-in library construction had four primary mechanisms hypothesized to contribute to the DRC at each viewing angle. First, the

source FEP was still allowed to scatter-out of the path of the detector and then fail to interact further to produce a recorded signal. Second, the gamma was still allowed to proceed unfettered and produce an FEP record in the spectra. This however would be filtered out of the scattergram by only considering the portion of the spectra with energies below that of the FEP record (i.e. the Compton continuum) when energy binning to create the modulation curve. Third, a line-of-sight gamma would Compton scatter, lose some energy and then deposit within the detector in the Compton continuum energy range. And finally, fourth, Compton scatter from non-line-of-sight gammas would interact, and scatter into and be recorded by the detector. In this way, the information about the source direction is referred to as existing within these scatter-in interactions, if the information of the down-scattered, but not scatter-out of the path of the detector could be eliminated. A graphic example of these considered interactions is seen in Figure 25. As with the scatter-out library, any gamma reaching the detector is assumed to fully deposit its energy.

Since the advanced model was not ideally designed to account for these scatter-in events (i.e. bounds of the φ & θ considered for weighting could not be opened to exclude the active region), the baseline for the Compton scatter-in library was constructed by taking the inverse of the experimentally calibrated FEP library results in the active regions (i.e. interior to Ω). Realizing that the relative amplitude contribution of the active area might be drastically different than the results of the experiment for the Compton information scattered-in from outside the active area (i.e. exterior to Ω), heavy reliance on scaling this library (even after normalization) was planned to account for the actual scattergram amplitudes.

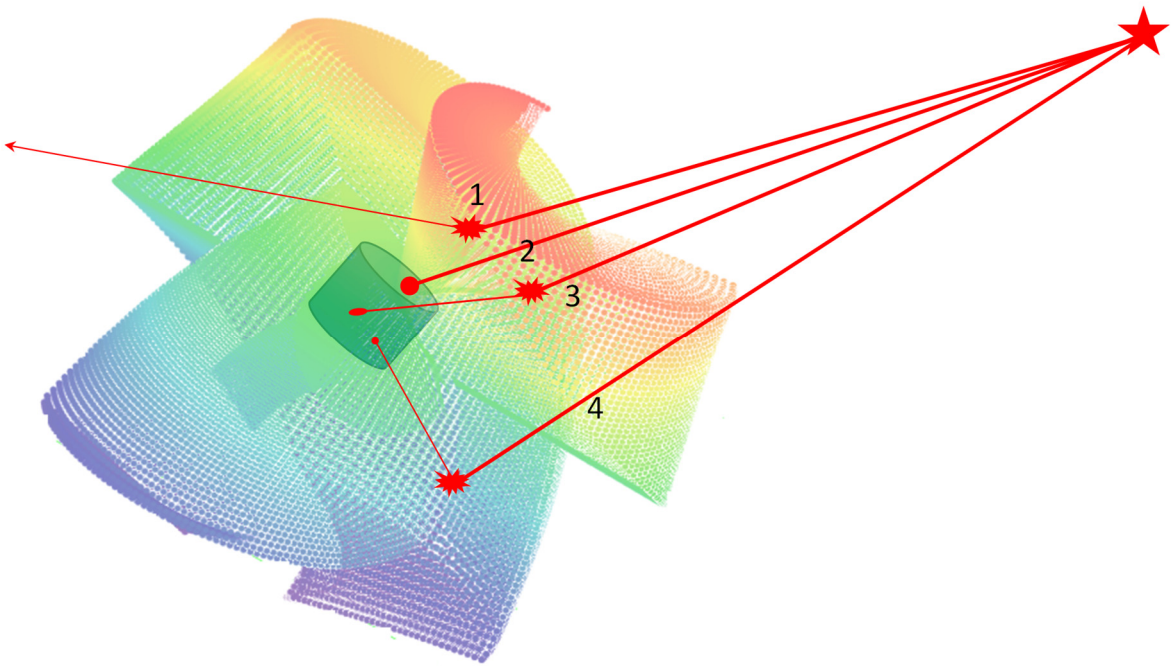

Figure 25. Primary interactions for the Compton scatter-in library development. 1) Source gammas from the active region scatter-out of the path of the detector; 2) FEP gamma proceed through the active region; 3) FEP gammas down-scatter in energy in the active region and are recorded by the detector; 4) FEP gammas from the source down-scatter in energy outside the active region and are scattered to interact with the detector.

The first example of a limitation in this model is the need to successfully eliminate the Compton down-scattered gammas that interacted within the active area and were recorded by the detector. The baseline inverted FEP library was therefore differenced from the experimental results of the scattergrams created by using the Compton continuum portion of the spectra at the primary 18 viewing angles ($\varphi = 5° – 175°$, in increments of 10°), and this information was saved in a temporary array of files. The results were then linearly interpolated to fill the intervening φ space, point-by-point over the 360° θ rotation of the RSM, to construct another temporary array with 1° resolution. This permitted the final look-up library DRM to be compatible with the standard search algorithm developed for this work. Next, the baseline FEP and this temporary array were convolved in such a way as to give each a relative weighting between 5% and 95% to each. The resultant 20 temporary libraries were then used in conjunction with the experimental results to find which weighting scheme produced the best direction determination (i.e. least angular

distance from true source direction). A split of 25% to 75% of the down-scattered active region (temporary array) to the scattered-in (FEP inverse) baseline was found to produce the closest match. A normalized DRM was then constructed for both the FitzGerald design and the alternate using this method. Of note, the modulation curve amplitudes did not match the Compton continuum experimental scattergrams as expected, but they did produce sufficiently good matching results when scaled, as will be discussed in Chapter IV. Results of the Compton scatter-in library development are seen below in Figure 26. As with the FEP scatter-out library development, two addition libraries were also constructed for comparison of the small RSM builds and the $LaBr_3$ detectors when using the Compton portion of the spectra. These are referred to as the "modified" libraries, as opposed to "original" in the Chapter V results.

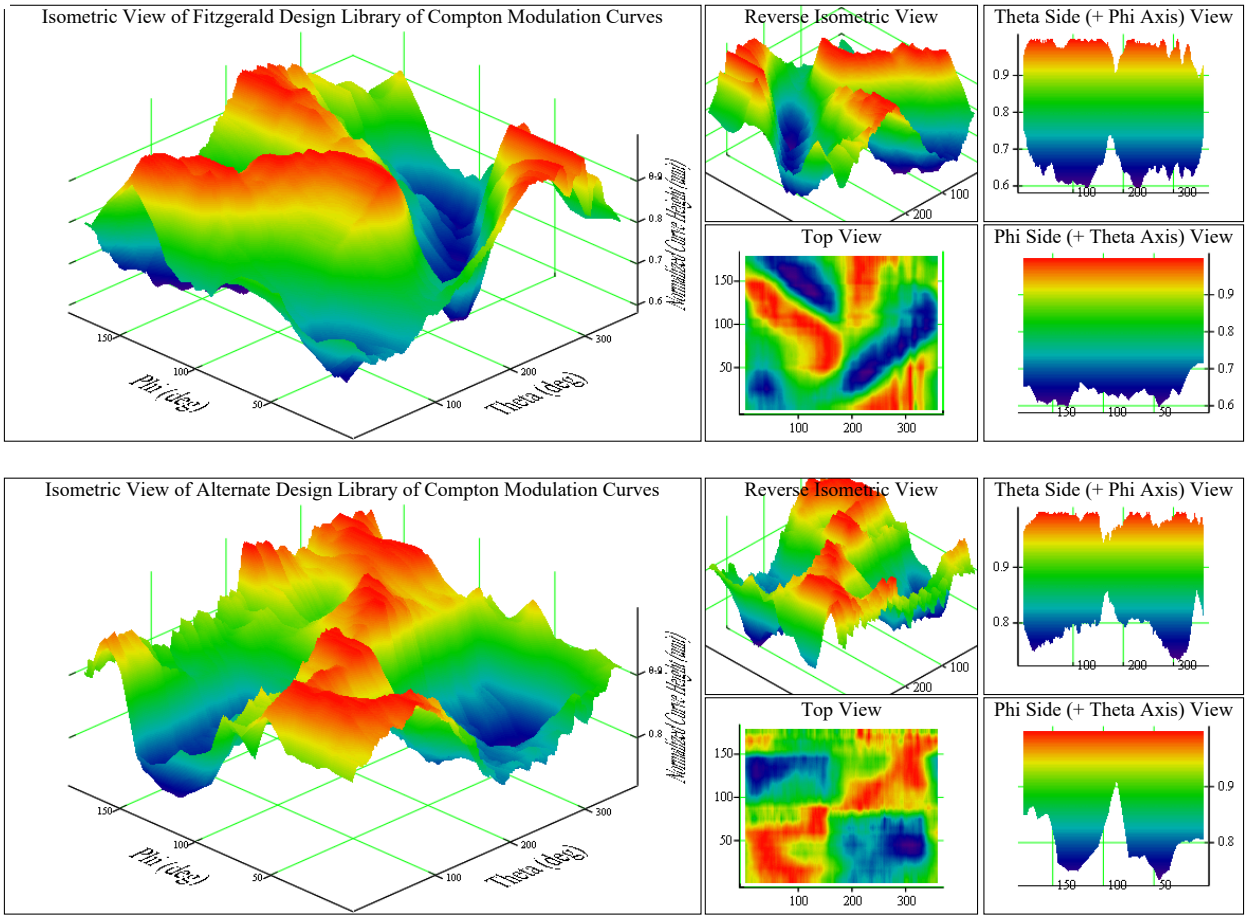

Figure 26. Comparison of both production design's library of modulation curves over the range of possible φ and θ source angular positions.

These scatter-in libraries proved especially useful in determining the direction of the source using the Compton continuum when the large, FitzGerald design RSM was used in conjunction with the phoswich detector. Here, the phoswich detector is used to suppress Compton scatter from the mounting structure behind the mask that shows up in the spectra. After filtering the results to only include the front NaI(Tl) scintillator and not the rear CsI(Tl) "guard slab" the angular position prediction of the source improved compared to the non-phoswich configuration. This was especially evident at the rearward viewing angles (i.e. $\varphi > 90°$), and shows that the laboratory environment was a significant contributor to the recorded Compton continuum. This is addressed in the phoswich section of Chapter V, but introduced here for completeness, as the requirement to use experimental data in its production is a limitation of the model.

The other Monte Carlo modeling efforts at AFIT of the expected RSM spectra all depart from experimental results below ~200 keV [45]. They were not able to account for the significant Compton backscatter from detection and control equipment behind the RSM assembly. The phoswich detector has the capability to effectively suppress this extraneous signal, as shown later when using a rope source to augment the expected backscatter signal, so its inclusion into this RSM characterization work is important. These extraneous contributions to the Compton continuum portion of the spectra provide no useful source direction information, and they in fact dilute the actual direction information. By removing most of the dilutive contribution using the phoswich, the remaining Compton scatter signal is useful in identifying the source direction.

Finally, energy measurements below this nominal ~200 keV limit are also greatly influenced by the inclusion of low-energy gamma and x-ray background sources. So even with the use of a phoswich detector, this may make using the Compton continuum portion of the spectra below ~200 keV of little use for source direction determination when using the RSM.

III. RSM Design Theory and System Build

3.1 Introduction

Design of the FitzGerald class RSMs is fundamentally constrained. FitzGerald's criteria ensured that for any particular viewing angle ($\varphi = 0° – 180°$) that the amount of scatter material between the source and the detector varies, and that this length is unique compared to all other φ possibilities for all points over a full rotation ($\theta = 0° – 359°$) [1]. This was briefly addressed in Chapter II, but more detail will be added here. The modified right-cylindrical coordinate system shown in Figure 27 is useful when visualizing the development of the FitzGerald [1] named "filling matrix". Many RSM shapes based on the filling matrix rules discussed later, sizes, materials, potential detectors, and methods of operations, such as static vs. continuously rotating, were considered.

The data acquisition equipment and set-up were selected for ease of use, availability and compatibility of equipment, limited modification of the raw PMT output signal, energy windowing considerations, and the recorded data set size/storage requirements. Some loss of information in the true scintillator rise- and fall-time due to waveform compression and chosen sampling rate was expected and deemed acceptable. Due to the high number of gamma interactions initially recorded, it was determined that triggering for acquisition at a threshold energy of 40 keV, and down sampling to 80 points for the entire output waveform was reasonable. The sampling rate for these 80 points was 100 MHz (or conversely in 10 ns spaced intervals).

3.2 RSM Coordinate System

There are a number of possible ways to construct a scattering mask [36], but only one technique [1] ensures each potential source placement has a different length of scattering material

between it and the detector for every particular viewing angle (φ) over a complete revolution (θ), and that the average path length over a full rotation is the same. For this work, a series of nested cylinders to outline the shape of a NaI(Tl) 3"x3" detector, each assigned an unique identification number, were used to determine the outermost dimension of the RSM surface at each allowed angular position (φ,θ).

Phi (φ) is designated as the angle measured off the positive z-axis (polar angle), which is also the longitudinal axis of the detector RSM system. The theta (θ) measurement angle is defined as being azimuthal (lying in the x-y plane). This is the Spherical Coordinate System used in Mathematics, except in the RSM case, the distance from the origin, *r*, is determined by which outer surface cylinder is specified. The potential, discrete source placement positions were limited in this investigation to 64,440 (179x360) positions. φ = 0° and 180° were neglected to facilitate with construction of the filling matrix and therefore the outer surface point cloud generation. Viewing angles of φ = 0° – 15° and φ = 155° – 175° were not expected to produce usable modulation curve results, due to the relative lack of material change over the width of the detector over a full rotation when forward looking, while the detector, integrated PMT, and associated electronics placement interfere with the assumptions of the advanced model in the rearward looking cases.

By filling a square matrix, defined as φ for columns and θ for rows, with unique values of the cylinder number (across both the rows and columns) for every possible position combination, an unique amount of scatter material can be engineered to fall in-line between the source and detector for a fixed viewing angle, *φ*, over a complete rotation in θ. As was previously described, by having a different amount of scattering material between every possible stationary source placement and the detector over a full rotation, a different amount of source attenuation will occur on average, for each point over the rotation. Further, the shape of the expected modulation curve

will not be repeated over any other viewing or rotation angle if each matrix surface point is properly valued.

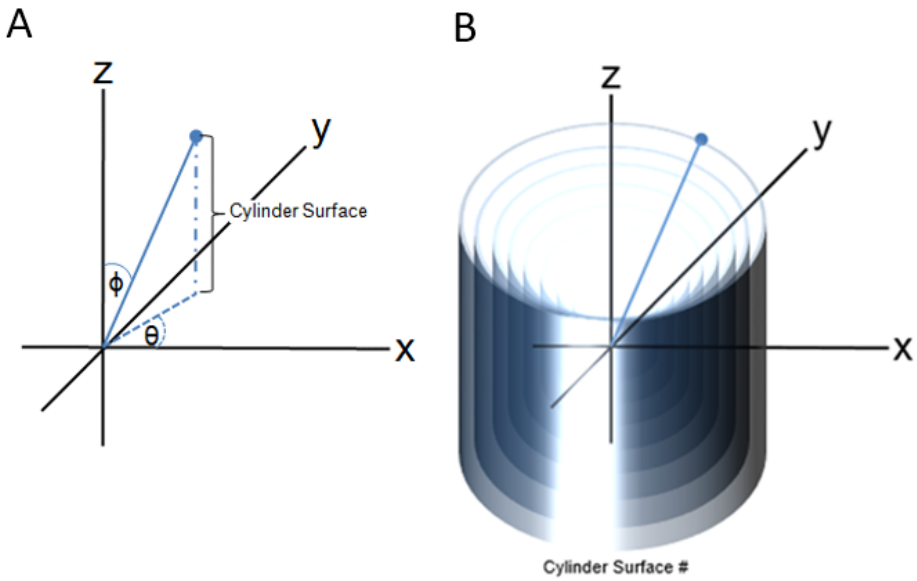

Figure 27. The coordinate systems used to define the geometry of the surface point locations of the RSM.

In this way, the filling of the cylinder surface matrix can vary in a smooth way for each defined row or column, but at least one discontinuity in this filling will be seen when transitioning between 1 and N_{max} (the outermost cylinder surface). The modulation curves for each defined angular position should then not have any overlapping or repeated values, given that the same cylinder is never chosen twice in a given row of φ (i.e. the surface numbers are not repeated in the filling matrix over the range of θ). And, for any given θ, the cylinder surface numbers should also not be repeated. This in essence gives the filling matrix the property of having the same average value when any individual row or column is summed, which was also recognized by FitzGerald [1]. As well, this served as a rudimentary check of the validity of the square matrix after it was populated.

While the integer value of the filling matrix corresponds to a particular nested cylinder (with 1 being the closest surface to the detector and N_{max}, based on the dimensions of the filling

matrix, being the farthest), the actual distances to the surface points are found by dividing the difference of the maximum RSM radius and the innermost cylindrical shell by the number of columns of the matrix and multiplying by the matrix value at the particular (φ,θ) direction. The innermost shell location was determined by taking into account the distance from the center of the detector crystal to its edge and allowing for 1/16" of μ-metal encasement. Another 1/8" for the planned aluminum support tube structure was also added to the side wall of the cylinder, but not for the top or bottom dimensions. These calculated lengths are therefore the material present between the source and outermost surface of the detector/support casing.

It should also be noted, that while cylinders were used to characterize the outer surface of the RSM in this work, because of the finite size and shape of the detector crystal, it may be interesting to produce a spherically based geometry for future RSM designs. As the ratio of the size of the RSM to detector increases, the detector looks more and more like a point compared to the RSM (as the size of the RSM increases or the size of the detector decreases). This may be advantageous to the integration of a Bonner sphere for future neutron detection work.

3.3 FitzGerald's Paper Proposed Design and Operation

An example of the modeling work done to replicate the proposed design from FitzGerald's paper [1] is shown in Figure 28. The filling matrix in this case is a 20x20 array, for display purposes only, of the method by which it was conceived and filled by FitzGerald. Notice the changes in the filling order after 10 columns, giving 2 distinct halves. This was the induced discontinuity in the RSM shape previously mentioned (along with the natural transition from 1 to N_{max} or vice-versa). Regions between these boundary points are then defined by a smooth linear transition as either φ or θ changes.

Ultimately, a 180x180 square matrix was used for the point cloud generation used in defining the outer surface of the RSM in this work. Results of the point cloud were then exported into SolidWorks. This effectively means that each possible φ value from 1° to 180° was directly addressed for a specific cylinder value, whereas the θ values were addressed between 0° and 358°. Since the θ values varied by units of 2°, care was taken to assure appropriate smoothing and interpolation measures were taken in SolidWorks during the stitching and solid object generation process. This also cut the time for creating a solid object into a quarter of what it would have been for a 360x360 matrix, as each point had to be selected and associated with its nearest neighbor manually. Using a square matrix was desirable (if not necessary for the alternate design) to ensure appropriately created symmetric discontinuities for modulation curve uniqueness. The final φ = 0° point was manually added to the point cloud and fell on the z-axis at the maximum height of the RSM. This allowed for the final step in creating the solid object from the stitched surfaces in SolidWorks to be completed.

A compilation graphic which shows the basic RSM coordinate system used and the filling matrix format for the FitzGerald design is seen in Figure 28. The outer surface point cloud generation results used for SolidWorks construction and an introductory look at plotting the source direction prediction results is also shown. It can be considered in conjunction with Figure 30 to compare the three filling matrix variations that were considered for production.

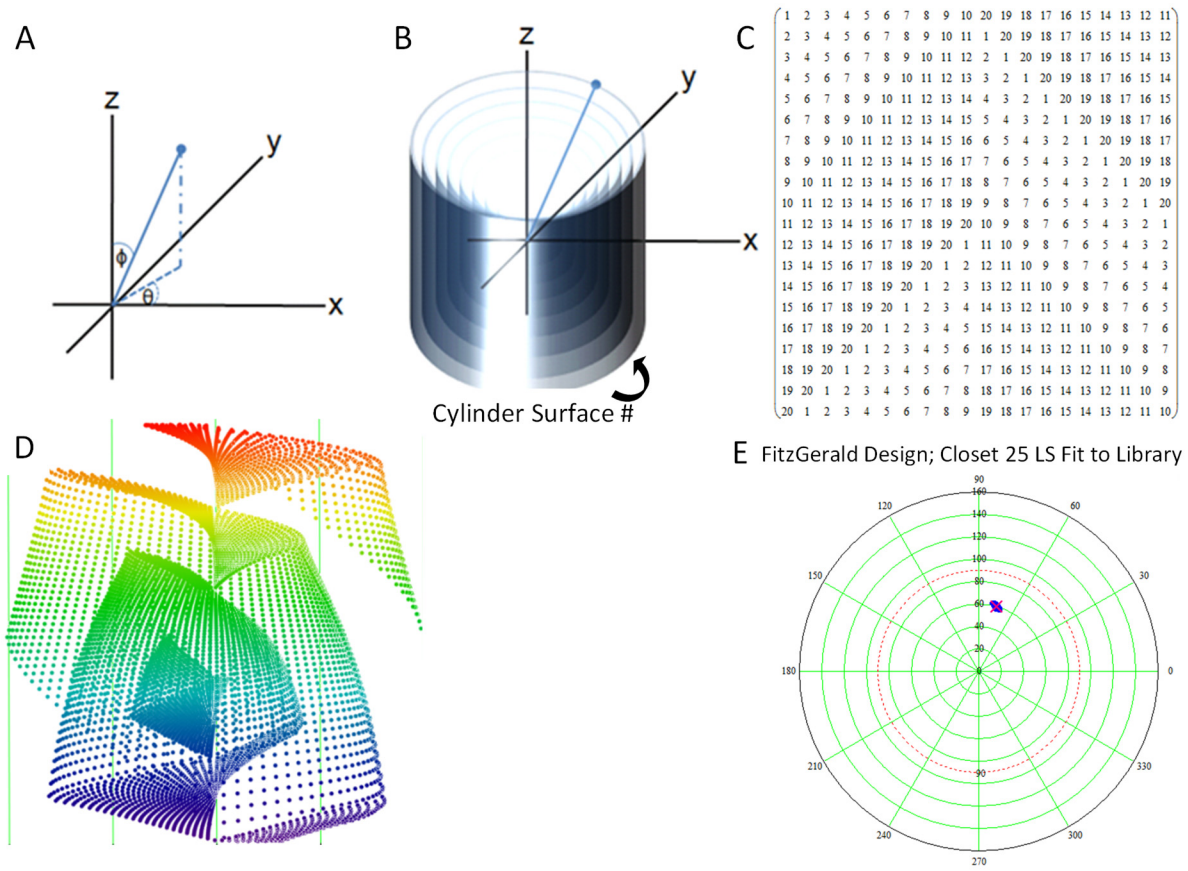

Figure 28. (A) and (B): Coordinate systems used to define the RSM; (C) and (D): Example of filling matrix strategy and point cloud generated for FitzGerald's design; (E): Clustering of "closest" library matches in pilot display when testing the DRM search algorithm;

Kowash's [6] RMC equipment served as the foundation of this RSM effort. His data acquisition computer, RMC mounting hardware and source support/translation peripherals from his Dissertation [6] were loaned to AFIT by Professor Wehe from the University of Michigan. This investigation however eventually replaced the RMC masks and collimator, with the RSM made of lightweight, low-Z, acrylic scatter material set about the detector. This low-Z scatter material is different than the high-Z attenuation by absorption material(s) used in Kowash's work, as it functions to scatter the source gammas out of the path of the detector, to down-scatter them in energy before recording instead of them being acted on primarily through absorption, or to scatter rays that would have otherwise not interacted into the path of the detector. FitzGerald's novel RSM idea also positions the detector at the center of the encompassing scatter material and

results in a significantly increased FOV compared to other RM or RMC systems which operate using a highly collimated view of the source being investigated. The notional RSM system, from FitzGerald, is shown below in Figure 29.

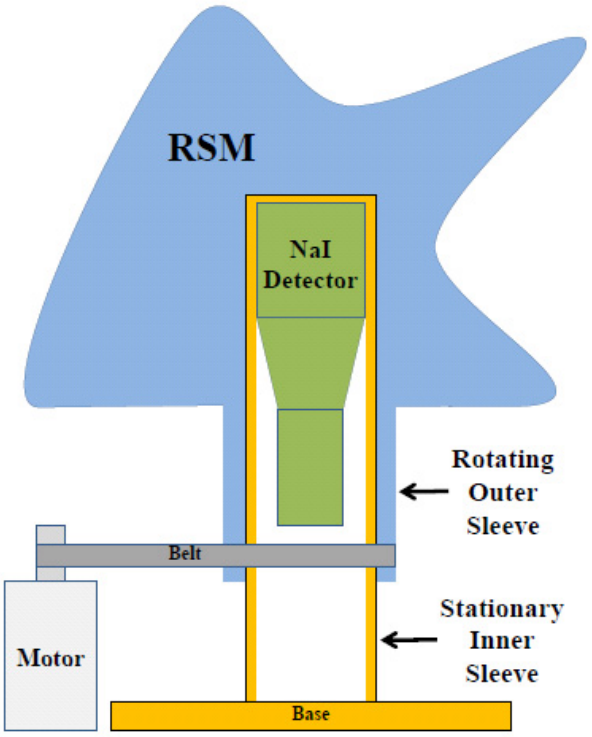

Figure 29. RSM set-up as envisioned in FitzGerald's paper. Reprinted with permission of the author.

Because of the RSM's specific surface design, unique modulation functions due to scattering of the FEP of the source gammas out of the path of the detector, or down-scattered in energy and redirected into the detector from other mask interactions (and recorded in the Compton continuum) was expected. Two or more unique experimental scattergrams can then be constructed for each spectra recorded. By binning the total counts of the gamma energy range of interest in the spectra (i.e. FEP, Compton continuum, etc,) and associating the rotation angle of the mask at acquisition of the recorded deposition, the scattergram is constructed. Comparison of the experimental scattergram results for any particular source placement can then be made to the computational generated DRM libraries of expected results.

In theory, the FitzGerald RSM design should be able to determine source directions over nearly 4π steradian angles as its FOV. In practice however, the experimentally recorded scattergrams did have some limitations due to engineering constraints as discussed. Still though, the RSM's greatly extended FOV (i.e. $\varphi = 15° - 145°$ over all θ), when compared to other gamma imagers currently used, like the coded aperture, RM, and RMC technologies, which are limited to tens of degrees due to the solid angle subtended by the collimator placed between the source and detector, makes FitzGerald's contribution a significant advancement.

3.4 All Alternate Designs Considered

In Chapter II, alternate designs were created for potential manufacturing, to compare FitzGerald's design to some other baseline. The "smooth" design, designated now as the 1st alternate, was introduced in Figure 12. The 2nd alternate design, which included more counting discontinuities in the filling matrix than the FitzGerald design is shown side-by-side the 1st alternate in Figure 30.

An inspection of the filling matrices in Figure 30 (A) and (B) shows that the summation and unique, discrete integer rules of matrix filling are maintained across both the rows and columns. However, no induced discontinuities are introduced in (A), only the natural one is present. The closet matching comparison modeling work showed 4 regions where the modulation curves were too similar and produced some degeneracies for the closest 500 matches criteria used, so the idea of building this smooth shape was abandoned as previously reported on. By contrast, the filling matrix of (B) shows four distinct quadrants, with a matching false-positive possibility on par with that of the FitzGerald design (Figure 24). The filling matrix of this design was essentially a repeat of the FitzGerald induced discontinuity onto the columns, but with an added discontinuity after half the rows. Incidentally, this design maintained an anti-symmetry when a

cross-sectional cut of the point cloud was viewed, whereas the 1st alternate smooth design was symmetric. This example is visualized in Figure 31. The symmetric (1st alternate) vs. anti-symmetric (2nd alternate) visualization turns out to be particularly effective in predicting which designs will exhibit degeneracies and indicates that symmetric designs should avoided. Of note though, filling matrices with symmetry still obey the summation and averaging criteria. The degeneracies occur because the same shape modulation curve will be produced for a forward-looking viewing angle φ_i and also its mirror angle φ_{180-i}, as measured off of the z-axis (albeit with a shift in θ). Therefore, library matching would likely alternate between correct and false-positive directions when measurement error is introduced.

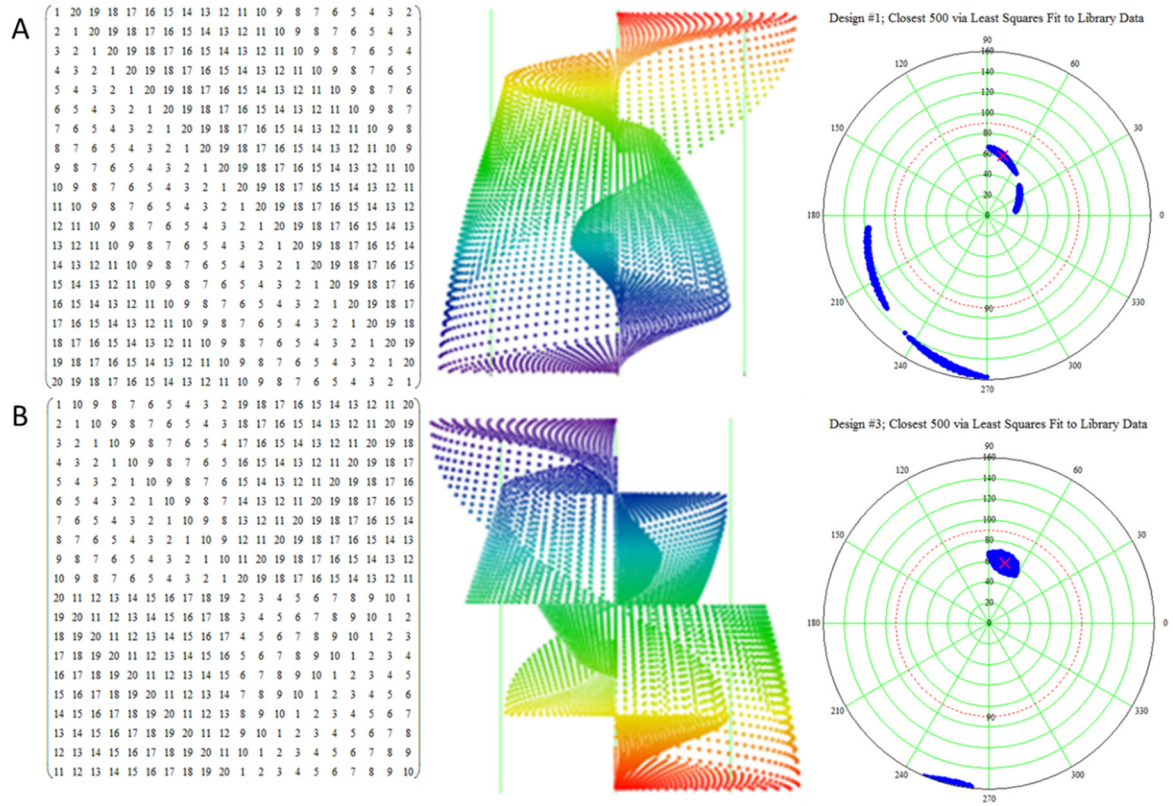

Figure 30. (A) and (B): Other filing matrices considered, their point clouds and theoretical matching results.

To maintain anti-symmetry of the next matrix considered, the 3rd alternate design would have to break the four distinct regions of the 2nd alternate (matrix (B) in Figure 30) into eight sub-regions, either after a quarter and then three-quarters of the rows. This would have been possible

with a 360x360 matrix (but comes at a SolidWorks CAD construction cost of quadrupling the size of the point cloud). The iteration after this, or 4th alternate design, could have been made by breaking the 8 distinct regions of the 3rd alternate into 16, after a quarter and three-quarters of the columns (i.e. the opposite of whichever direction was chosen for the 3rd alternate). In this case, for the divisibility necessary to evenly distribute the sub-regions in a square matrix, the filling matrix could then have been returned to the preferred 180x180 size.

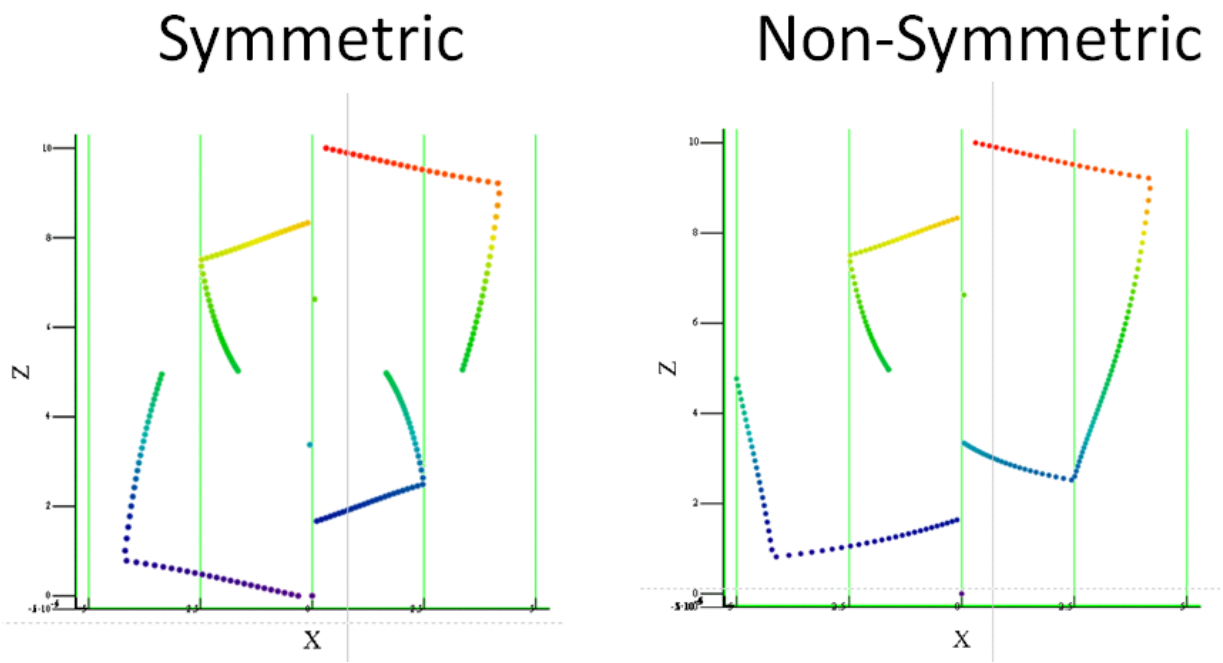

Figure 31. Cross-cut view of the point-cloud plane showing the difference in symmetric (smooth design) vs non-symmetric (alternate design) filling matrices. FitzGerald summation rules were maintained in both cases, but the symmetric case would lead to multiple degeneracies in the modulation curves.

Further explanation to understand how the same average value under summation was maintained for both rows and columns in the filling matrix, in addition to the symmetric vs. non-symmetric argument, for the FitzGerald and alternate design RSMs is given next. Cylinder surface numbers were not introduced haphazardly into the matrix for the FitzGerald class of designs. Instead, care was taken to fully understand the 3D spatial nature of the surface numbers. For the FitzGerald design, the filling matrix incorporated an induced discontinuity in the chosen numbering pattern. Halfway through the construction of the matrix, the pattern for filling the

columns was increased by exactly half the number of rows (while continuing to use the same increment logic to fill the rest of the column). As a result, an induced discontinuity was formed that corresponded to 90° degrees in φ because the shift occurred after half the number of columns. This rearrangement of the φ viewing angle RSM material also caused the natural discontinuity (N_{max} to 1) to present at both 0° and 180° degrees in θ, one for the upper half (φ = 0 – 89) and one for the lower half (φ = 90 – 179) respectively. For the alternate design, this same method was incorporated regarding filling of the matrix rows when reaching the halfway point. This caused material discontinuities to occur at 45°, 90°, and 135° in φ and 0°, 90°, 180°, and 270° in θ.

3.5 RSM Point Cloud Generation and SolidWorks CAD Construction

The filling matrices were designed to determine on which imagined cylindrical surface the material of the RSM would terminate. For the outermost surface, a value of 14" (radius of 7") between the maximum and minimum point in each coordinate plane was chosen because this corresponded to an ~80% relative efficiency seen in Figure 22, was compatible with the size of the HDPE stock rod acquired, and was close to FitzGerald's [1] original vision. Once defined, a surface location point cloud for every (φ, θ) position was calculated. These points were converted to a standard Cartesian coordinate system through transformations of the RSM's modified spherical coordinate system, to facilitate with SolidWorks importation. The data file consisting of the RSM surface points was then parsed per θ angle and all the φ locations were connected by line segments to create an importable .dxf file of slices centered around the z-axis. The reading in of point data, parsing, and conversion to .dxf files was supported by the AFIT Aeronautics Department contractor, Mr. Phil Smith. After explanation of the problems faced with correctly importing the .txt data into SolidWorks, he wrote a single-use program in C++, converted to an .exe and graciously supplied instructions.

Using the .dxf slices as defined closed perimeters, SolidWorks was then used to successfully add surfaces to these planes. Subsequently, these adjacent surfaces and their turning points, defined as ≥ 45°, where used to define the loft that was performed between the slices to create an outer surface between the two. After constructing the necessary 180 slices of the SolidWorks design and forming their corresponding solid, the original .dxf planes were deleted. This allowed for the solids to then be joined together as one. A void to accommodate the placement of the detector within the RSM was then manually subtracted from the solid, in such a way that the center of the detector crystal would be placed at the origin/center of the RSM.

The following figures show the progression of the build using MathCAD to generate the point cloud, the .dxf generator to define the slices, the wedges as they were stitched/lofted together in SolidWorks, and finally multiple views of the FitzGerald design and the alternate for the reader to familiarize themselves with the multifaceted geometric nature of these RSM productions.

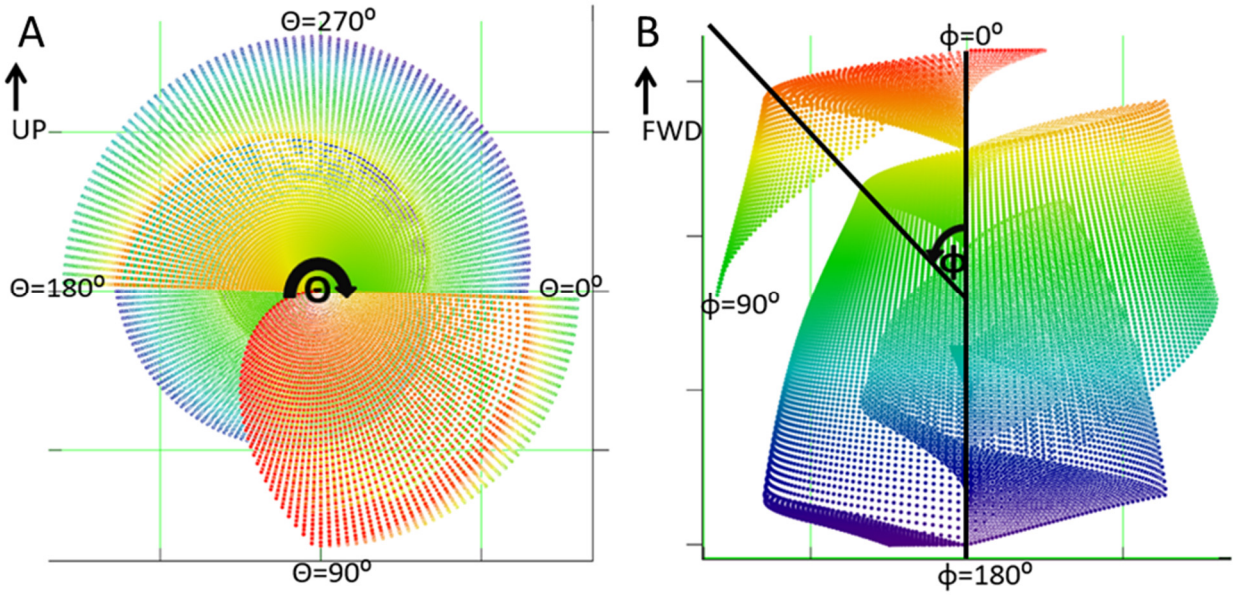

Figure 32. (A) Front and (B) side view of FitzGerald design RSM surface points with coordinate system defined.

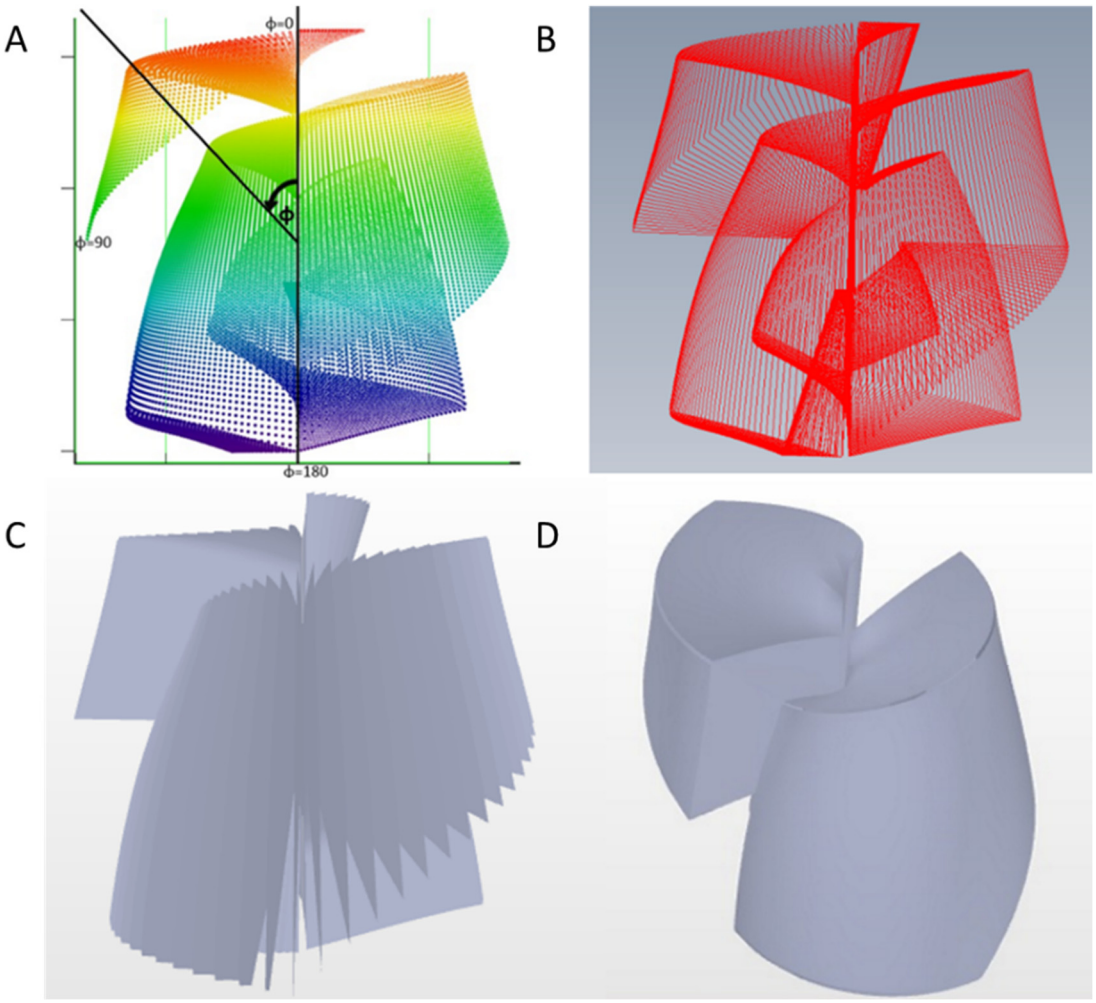

Figure 33. Stages of development of the Large RSM CAD model: (A) Initial point cloud generation of surface points; (B) DXF wireframes constructed for importation into SolidWorks; (C) Filled in theta planes; (D) Solid model.

On average, it took about 80 hours per design to navigate the necessary dot-to-dot connections needed by SolidWorks to finally be able to interpret what it was looking at, and then generate the solid for production. Future RSM designs will need to mitigate this delay with improved, automated, 3rd party intermediate software if SolidWorks specific CAD files are needed for production. Otherwise, some other finite element modeling software, such as ABAQUS/CAE might be used [46].

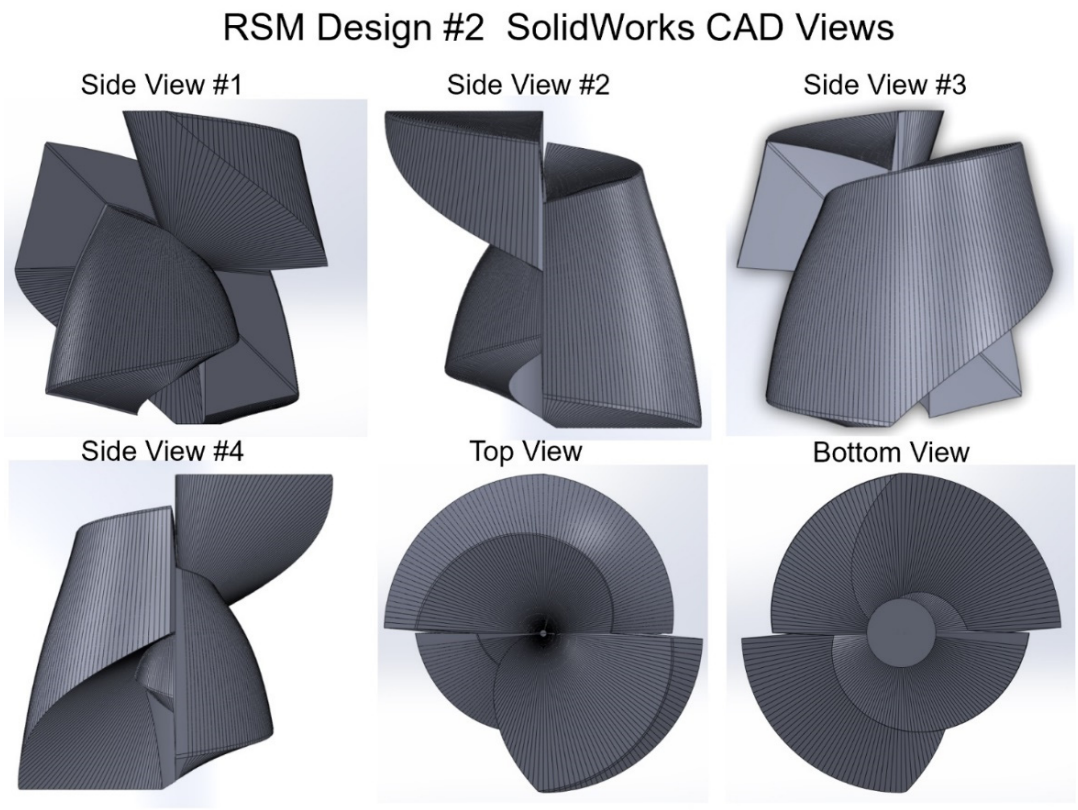

Figure 34. Final SolidWorks CAD results for the FitzGerald design.

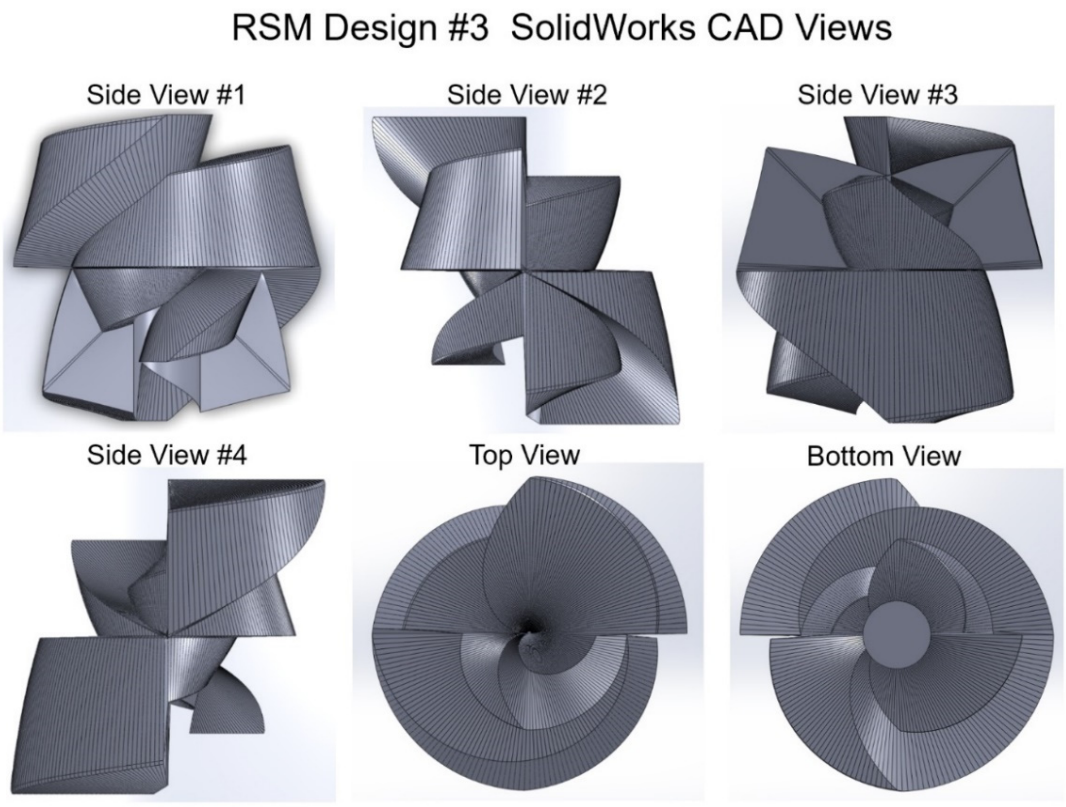

Figure 35. Final SolidWorks CAD results for the alternate design.

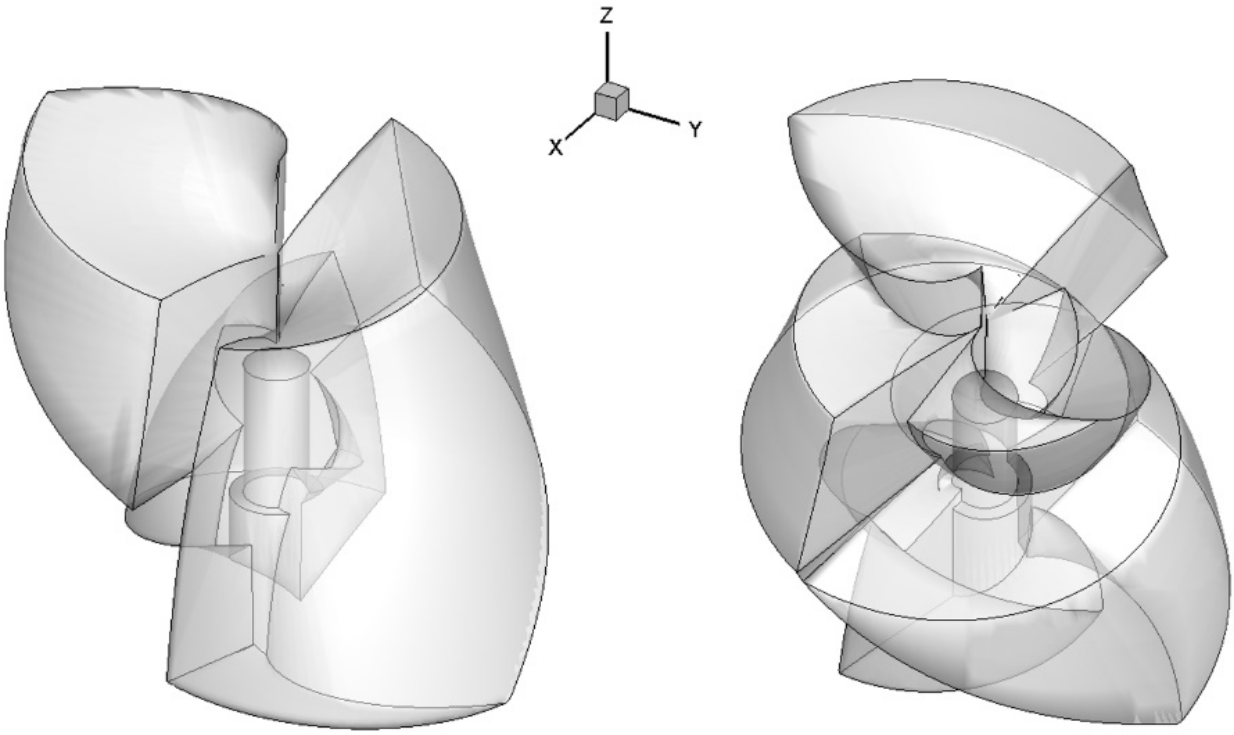

Figure 36. FitzGerald (left) and alternate (right) RSM designs compared side-by-side.

3.6 RSM Additive Manufacturing

After much trial and effort, the AFIT Model and Manufacturing machine shop determined the software for their 5-axis mill could not correctly generate a tooling path to accommodate the unusual and complex outer surface geometry of the FitzGerald RSM design. Many methods for overcoming this difficulty were tried, including breaking the RSM SolidWorks file into halves and quarters. The HDPE stock would then be seen as individual pieces, which would have to be manually repositioned during the 5-axis mill machining process. None of these were successful however, and the plan to machine the RSM from a contiguous piece of HDPE was abandoned.

Additive manufacturing (3D printing) options were then explored. The AFIT Aeronautics Department had a StrataSys Objet composite printer available for use. With the 16-micron thick layering capability of this printer, it was determined to be a good substitute for the manufacturing of the RSM. The additively manufactured sections were subsequently printed from an acrylic like

proprietary material named VeroClear from Stratasys [47]. The material is advertised by the manufacturer as a substitute/mechanical equivalent of polymethyl methacrylate (PMMA), or colloquially: Plexiglas®. Of note, the computational models were developed using HDPE ($(C_2H_4)_n$) as the scatter material, not acrylic ($(C_5O_2H_8)_n$). Because of the similar average atomic number, the total mass attenuation coefficient for these materials at 662 keV are within <6% of each other, so the ratio of the peaks and troughs of the scattergrams were expected to be in good agreement with the numeric model but not exact. The small difference was compensated for later, by forcing a fit between the scattergram and DRM, before each curve was compared for source direction determination.

The final RSM SolidWorks CAD was modified slightly before additive manufacturing to facilitate in the final assembly. The solid was broken up into 8 pieces, along the octants of the Cartesian x-, y-, and z-planes due to size limitations of the StrataSys Objet. Plugs and holes were added to ensure the exact alignment and gluing assembly of the pieces for final construction. Because of the size of the individual pieces of the large RSM (having at least one dimension of 7.5" with the addition of the alignment plug), and the limited capacity of the StrataSys printer, production of the large, FitzGerald design RSM was carried out over three separate printing sessions. This printing time totaled approximately 240 hours and consumed 72 pounds of the acrylic print structure material, as well as an additional 45 pounds of base support material (which would be later washed off with a high-pressure nozzle). On the other hand, the small RSMs of the FitzGerald design and the chosen alternate were additively printed on a half scale to match the size to that of the $LaBr_3$ detector. Being a maximum of 7" across (3.5" radius), both could be printed at one time. This is shown in Figure 38. The total cost for all printing was approximately $17,000 in acrylic 3D printer structure and flexible/washable base support material.

Before assembly of the large RSM individual pieces, each was carefully inspected and polished to smooth the surfaces. Slight layer overlap defects due to the material lay down process were eliminated to ensure proper alignment/fit upon final assembly. The alignment plugs and holes tended to have residual support structure material still present in corner areas, even after the pressure washing, so this was a necessary step. The RSM was then assembled by supergluing the pieces together and using rubber bands to secure the structure until the Gorilla Impact-tough® gel superglue could set. Impact-tough® was chosen because of its addition of rubberizing agents that allows for some flexibility in the super glue (i.e. it won't shatter/cleave like traditional super glue under lateral loading). The process steps for printing and assembly of the Large RSM and two smaller RSMs is visually chronicled in the following figures.

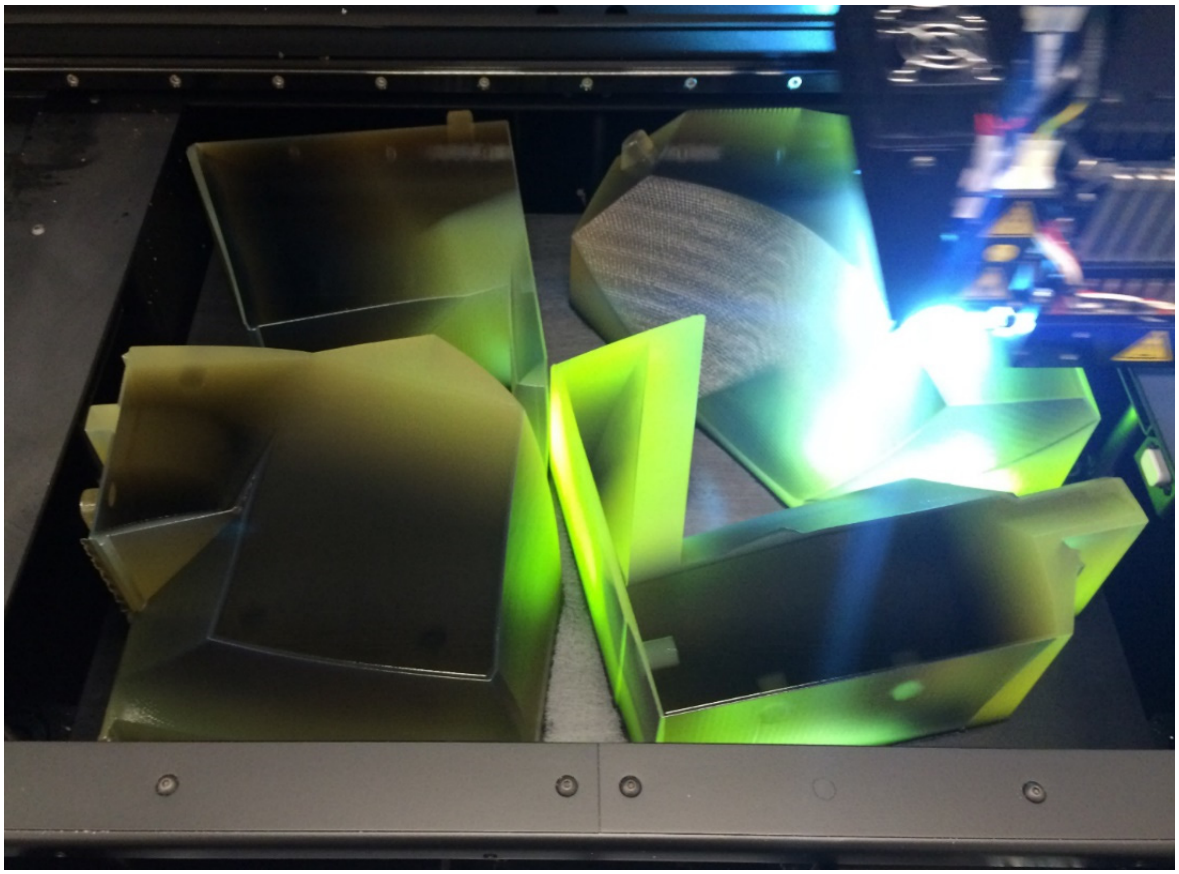

Figure 37. Closeup view of 3D printing, showing support and build material, along with holes and pegs designed into the SolidWorks CAD drawing to facilitate easy assembly.

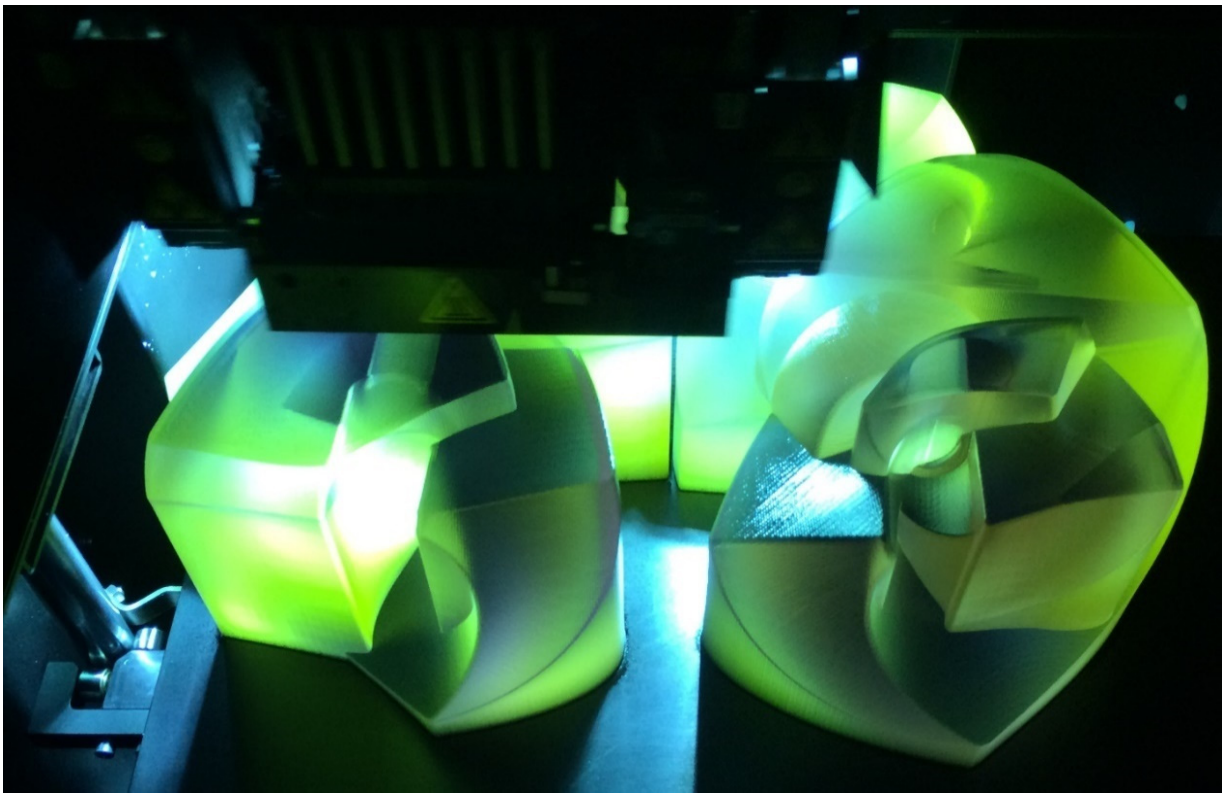

Figure 38. Printing the small FitzGerald and alternate design RSMs for the LaBr detector.

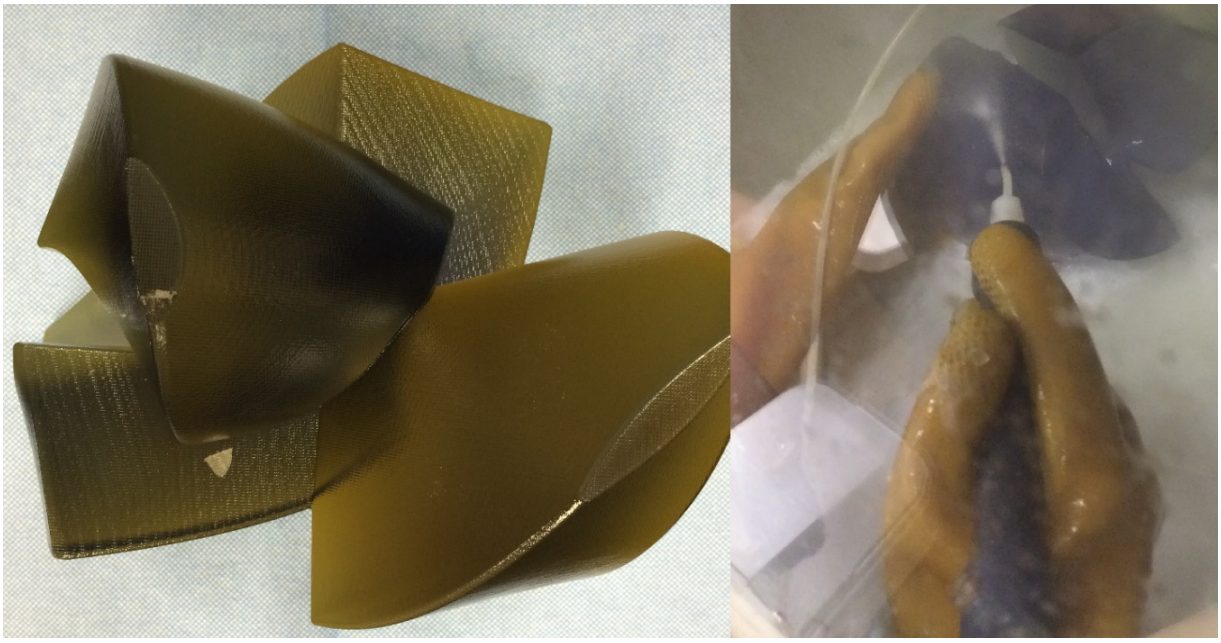

Figure 39. Small FitzGerald RSM design after 3D printing before and after pressure washing rubberized support material from the acrylic structure. Notice the fine-tipped, flexible nozzle for detailed washing/cleaning of the corners and detector cut-out.

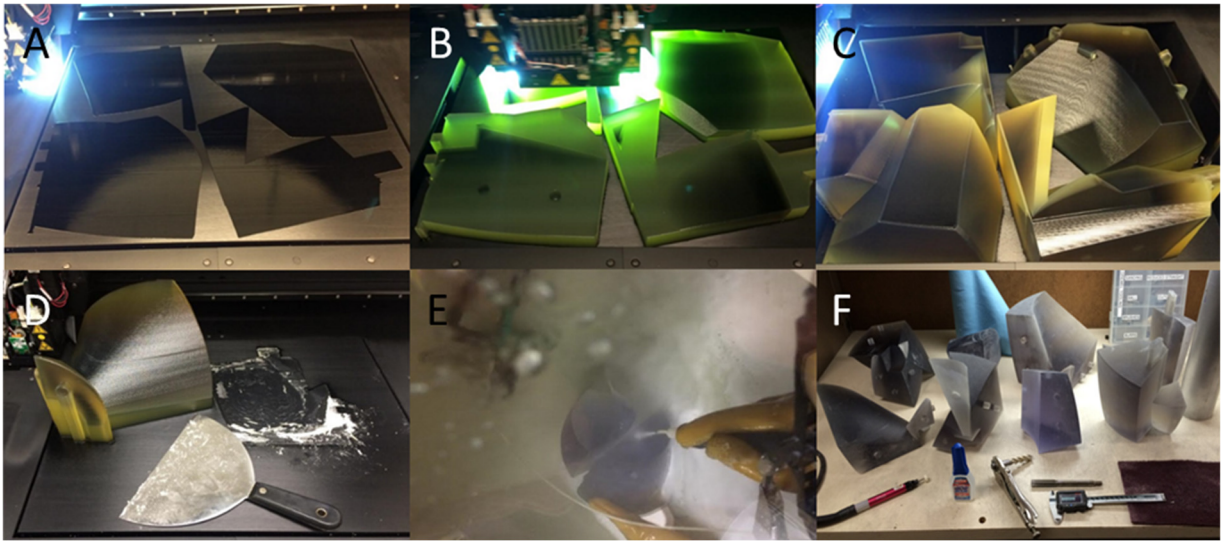

Figure 40. 3D printing and assembly of the Large RSM. (A), (B), and (C): Printing in progress; (D): Removal from the build tray; (E): Pressure washing; (F): Final polishing/fit testing before superglue assembly.

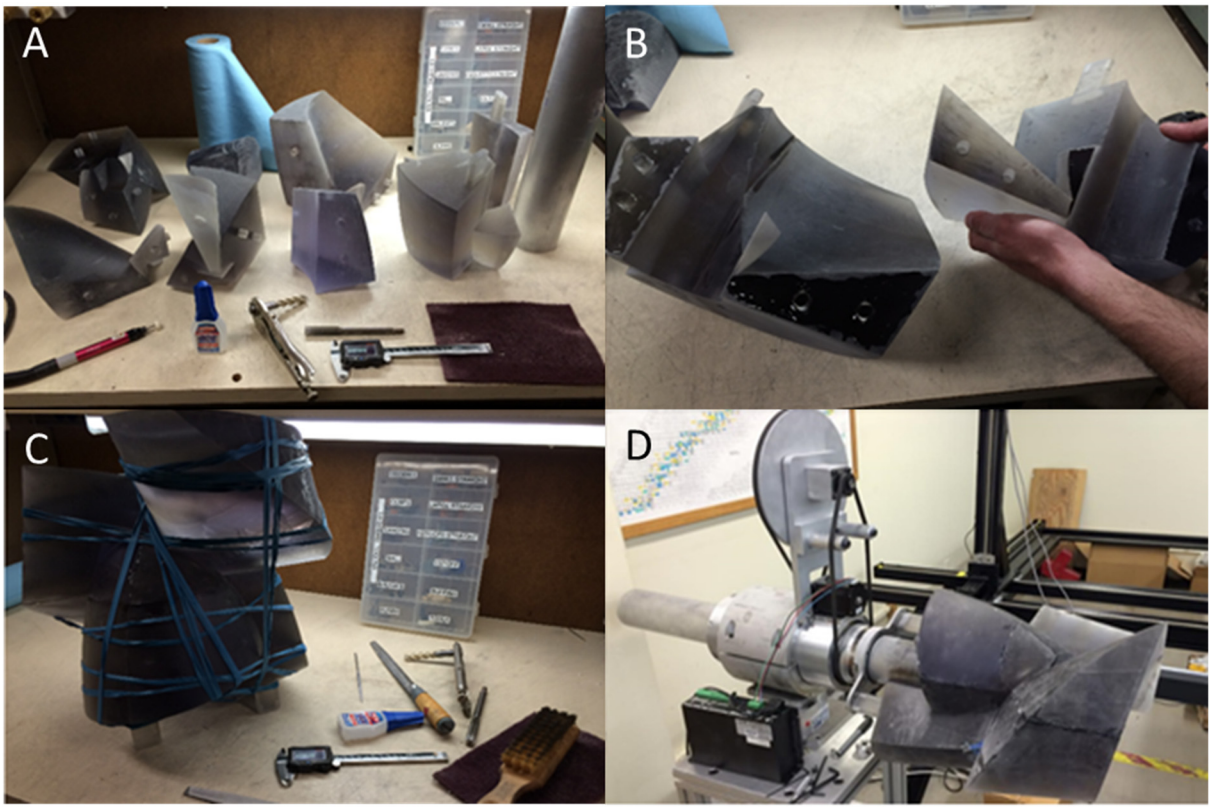

Figure 41. Assembly of the Large RSM. (A): Fit check and final polishing; (B): Super glue applied; (C): Completed assembly and rubber band secured for 24-hr cure; (D): Installed on rotational rig with stepper-motor torque multiplication addition.

3.7 RSM Mounting

The large and small RSMs mounted to their support structures, with nominal source location highlighted as a red star, are seen in Figure 42. The seams where the 3-D printed acrylic parts were glued together are visible (before further polishing) on the large RSM. Also seen are the equipment modifications, with the addition of a high-torque stepper motor, torque multiplication gearing, larger support tube, and pivot mount for changing the viewing angle, φ, that were made. These upgrades were necessary to support and rotate the approximately 70 pounds large RSM. In these views, the 3D translation-stage Velmex equipment used to position the source is visible, as well as the adapter collar and new stepper-motor control unit.

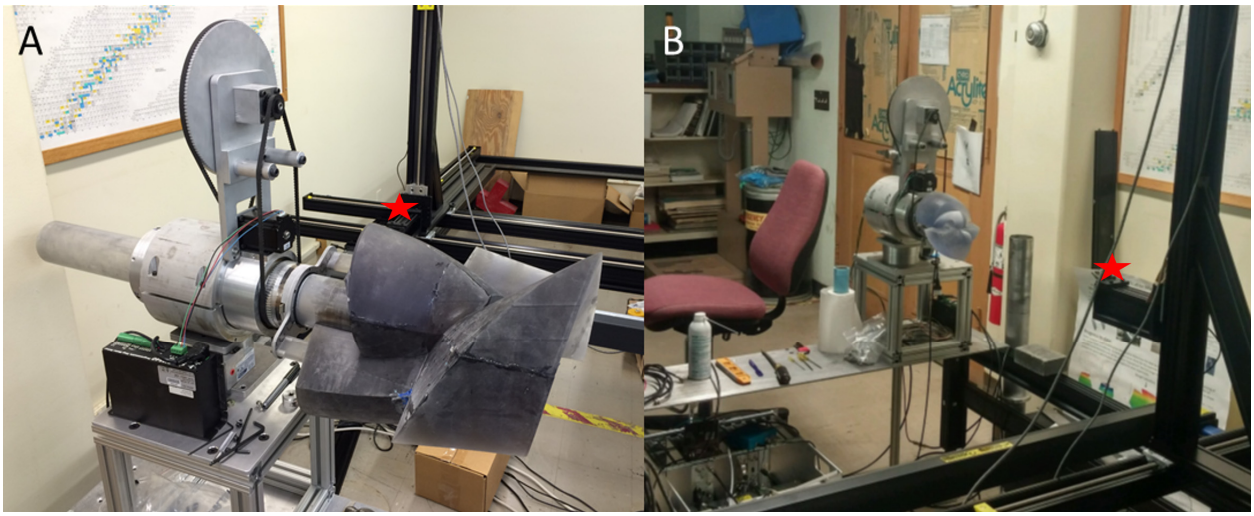

Figure 42. (A): The large FitzGerald design RSM mounted to its support structure; (B): The miniaturized RSM after support structure interchange. Nominal source placement is marked by a red star.

Concurrent with the printing of the RSM, the rotating and support components of the detector assembly rig were upgraded to allow for the known addition rotational mass and moment of inertia of the full-size RSM compared to previous usage. This included not only upgrading the torque capabilities as mentioned, but also adapting the encoder ring with a mating collar and manufacturing new internal supports on which to mount the aluminum support tube to account for large mass and off-center center-of-gravity of the large assembly.

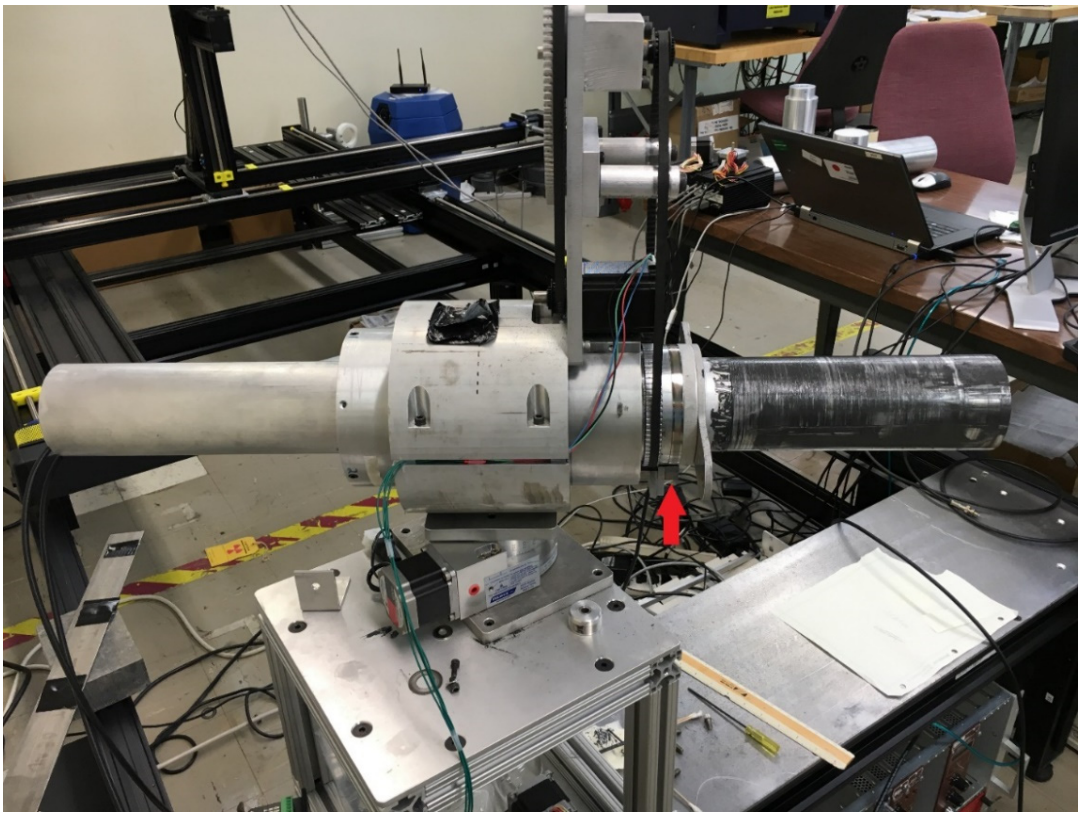

Figure 43. A side-view of the mount/support structure with lubrication applied. The red arrow is pointing to the Renishaw holographic encoder ring reader. The ring itself can be noticed by its shiny contrast.

The detector is positioned internal to the support tube and placed into the support tube before the RSM is secured in place. The 3”x3” scintillator and PMT combination detector is loaded into the front of the aluminum support tube in the large RSM case, with the high-voltage and signal cables being routed through the remainder of the tube and out the back side. The fitment of the detector within the support tube was very tight, so it was determined additional structure to keep it from sliding back into the tube would not be necessary. Extra care (and personnel) was taken to push, not tap and potentially break, the $3k detector into position. With the detector in place, the support tube and interior sliding surfaces of the RSM were lubricated with a combination of white Lithium grease and powdered graphite. It was expected that the graphite would, over time, fill in any rough patches present on the sliding surface of the already polished support tube, while the Lithium would provide the needed interstitial layer of friction-reducing material to allow

a smooth and jerk-free rotation of the RSM. The RSM was then mated to its support collar, of which the Renishaw encoder ring was a part of. The encoder ring reader was mounted and aligned to a non-rotating portion of the mount.

A side-view of the RSM and detector mount before addition of the RSM is seen in Figure 43. Notice the power and signal co-axial wires routed out of the back of the support tube. The torque multiplication gears, and drive motor are evident, as well as the propeller like structure that was used to connect the RSM to the drive mount. The encoder ring reader has been highlighted by a red arrow to point out its location beneath the Renishaw holographical optical encoder ring. This ring and reader were cleaned thoroughly before each experimental run using an Ethanol solution and utilizing cotton-tip wipes. The Velmex translation stages are in the background of Figure 43. Figure 44 shows the final rig assembly for the small RSM, which dually used the $LaBr_3$ detector its support tube and no lubrication was required.

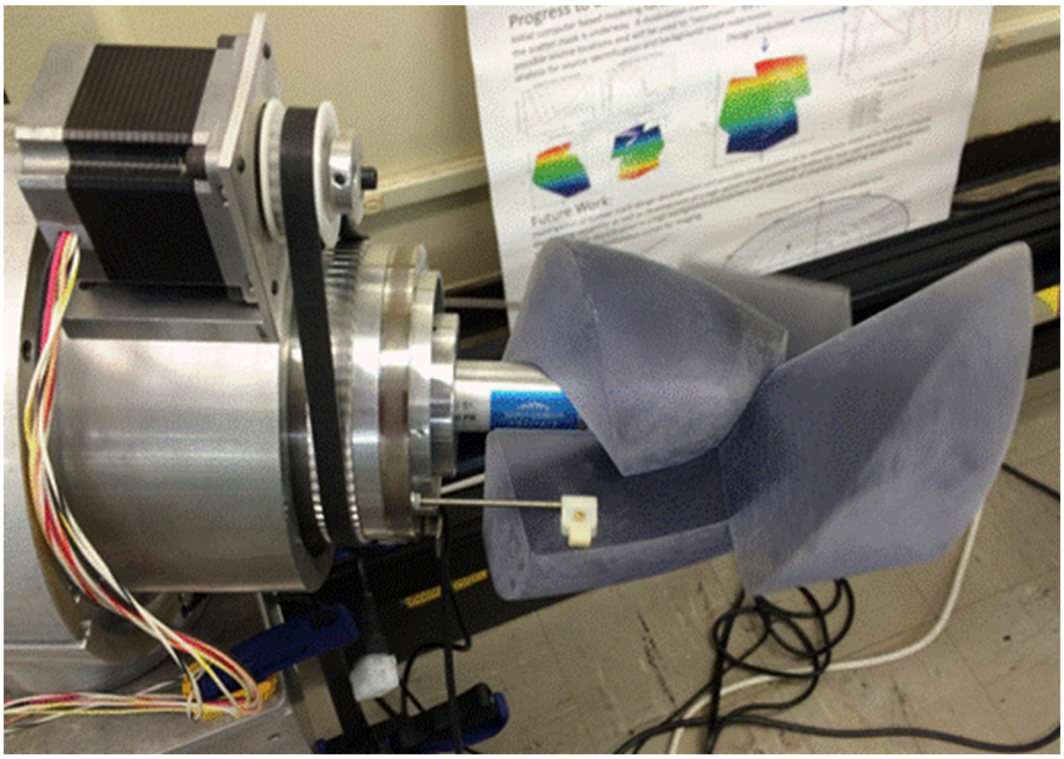

Figure 44. Sideview of small FitzGerald design RSM installed on mount with encoder ring and $LaBr_3$ detector visible. The small RSM was light enough, that it was its own RSM support.

IV. Experimental Equipment and Data Processing

4.1 Introduction

This chapter describes the size variants of the RSMs utilized, their detectors, other acquisition hardware used, the hardware settings, sources used, calibration, typical spectra collected and data post-processing techniques. Post-processing techniques include waveform peak identification, waveform rise- and fall-time determination for filtering NaI(Tl) or CsI(Tl) crystal events in the phoswich detector, formation of the modulation curves from energy bin bracketing and RSM rotation angle, normalization and MAC matching to the DRM lookup library, and the distance metric by which the performance/resolution of the entire system can be assessed.

Especially noteworthy is the usefulness of the "matching" methodology. It was found that the RSM systems used here, of two different sizes and detector shapes, and various activities and distances, could be modeled by just one set (FEP & Compton continuum) of DRM library modulation curves for each design. Rise- and fall-time calculations of the individual waveforms captured also proved useful in characterizing the dead-time of the system due to pile-up events, which were subsequently eliminated from the data sets when found.

4.2 Expected Contribution of the Compton Portion of the Spectra

To determine if information from any gammas scattered into the path of the detector by the material of the RSM (which would have otherwise not interacted), resulting in an addition to Compton portion of the spectra would be useful in enhancing the RSM source direction determination capability, a preliminary experiment was conducted to determine what measurable affect the scatter material might have on the spectrum of a source. A standard 3"x3" NaI(Tl) St. Gobain point-source detector was used for this portion of the project.

The setup and results of this steppingstone using the Cs-137 #1 test source are shown below in Figure 45 and Figure 46. The experiment was conducted with a distance of 20" between the isotopically emitting source and the detector. Spectrum data was taken for 2 hours, to reduce counting statistics uncertainty. Next, an 18" long rod of HDPE, with a 3" diameter was placed between the source and the detector, and the spectrum was again recorded for 2 hours. The rod was placed at a 10° angle to the centers of the source and detector to allow for a maximum of scattering interactions (i.e. maximum amount of material between the source and detector) to occur and be recorded. It was determined that some off-axis gammas scattered back into the detector over this short range through considering total counts recorded in the Compton continuum.

Figure 45. Initial investigation into HDPE scatter of the Cs-137 #1 source. Spectra data was recorded with and without the HDPE in place.

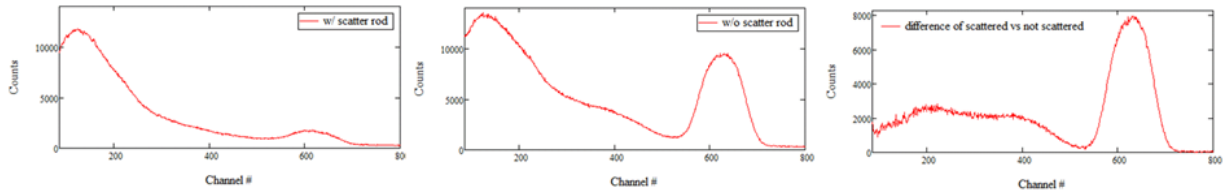

Figure 46. Initial results of scatter only imaging investigation. (Left) The spectra with the scatter rod. (Middle) Without the scatter rod. (Right) Difference of the left and right spectra. Note that the difference graphic shows a slight bump in the down-scattered contributions happen between the Compton edge and the channel 200 (roughly 148 keV), as expected according to Equation (5).

FEP attenuation caused by the addition of the HDPE scatter rod was as expected and reduced the number of counts into the detector over the time period. As well, smoothing of the transitional energies between the base of the FEP and the Compton edge, caused by scatter within

the detector itself and surrounding laboratory environment, is seen in the scatter rod spectra. These results are seen in Figure 46.

More care might have been taken to eliminate close by laboratory sources of down-scatter, but the contribution was taken to be a constant. Therefore, the difference of the two recorded spectra, with and without the HDPE in place, represents the scattering trends and shows that there is evidence for a scatter contribution in the spectra from the addition of the rod. This set-up was also used as the initial investigation into whether dead time in the source/detector configuration would be an issue, as the majority of the rest of the experiments were planned to use this source.

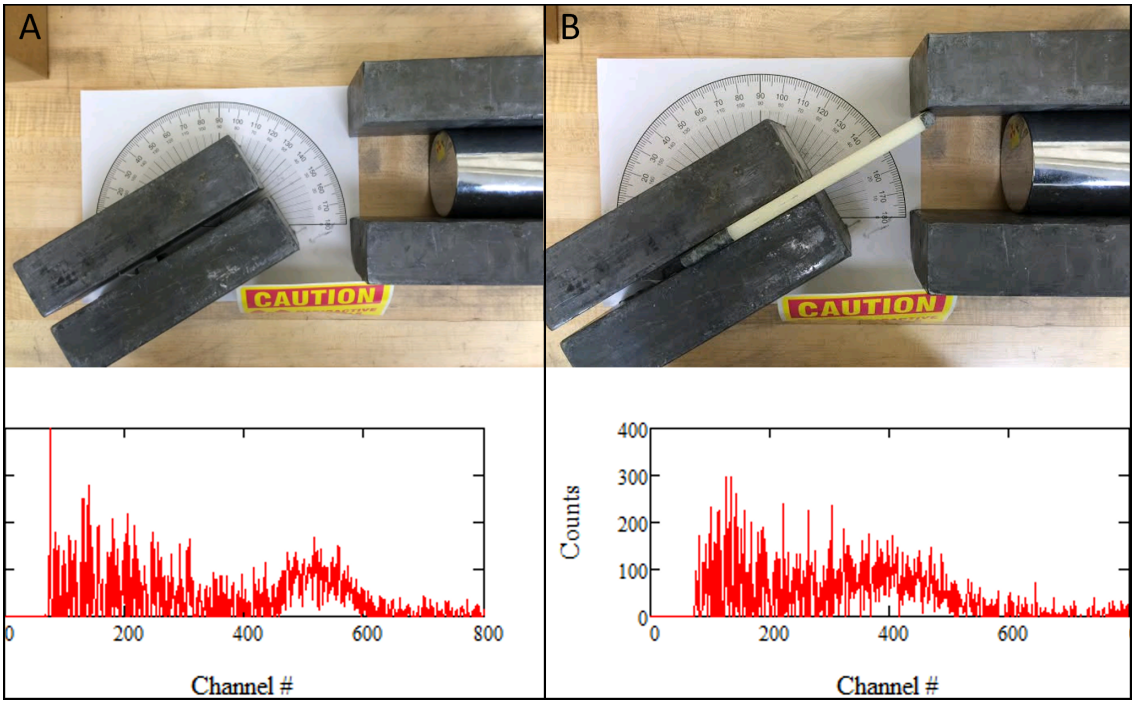

Figure 47. Example of initial work to ensure a noticeable scattering was observed in both count and energy shift with a small (i.e. much less than a scatter length) piece of HDPE. The (left) panel shows the source and detector without a direct line-of-sight due to the addition of the Lead bricks as collimators. The (right) panel shows a small HDPE kitchen cutting board placed in-line with the source. The recording time of this experiment should have been extended for better counting statistics.

The built-in dead time analysis function of ORTEC's GammaVision [48] showed the dead time for both of these configurations was less than 1.8% of the total time. For the rest of the RSM experimental data, the distance between the source and the detector was planned to be greater than

the scenario chosen here, so while this first test showed that system dead time would not be a major issue, it did show that the post-processing of the waveforms from the proposed RSM should be analyzed for pile-up and could not be neglected. This preliminary experiment was the first step in investigating the possibility of acquiring a scattered signal to see if the RSM system had merit using the Compton continuum information for source direction determination. As well, other concurrent experimentation showed a significant amount of scattering and energy shifting, even over distances shorter than a typical scatter-length for acrylic, as seen in Figure 47. Therefore, a decision to finalize the experimental setup and data processing algorithms was made based on this preliminary investigation.

4.3 Laboratory Operations

The Concept of Operations (CONOPS) for individual waveform discrimination and capture followed the following steps: 1) After passing the pre-amplified signal through a Delay Line Amplifier (DLA) (to compress the temporal axis of the PMT waveform) an 80 point sample size was recorded; 2) The waveform data was temporarily stored in the acquisition computer's memory buffer, while the LabView acquisition software checked to see if the threshold criteria had been met; and 3) When met, the stored data was associated with the angle of rotation of the RSM and appended to a .txt file, otherwise it was discarded.

Because an ORTEC DLA was used, it was also necessary to include the ORTEC pre-amplifier. This is because the two were designed to work in concert, as the preamp output is the DLA input. The capacitance of the preamp was set to as low as possible (45 pF), reducing its shaping effect on the captured waveform. Thus, representative rise- and fall-time information could still be calculated and used. This was especially important for the phoswich detector and the Pulse Shape Analysis (PSA) that accompanied its use.

The LabView based acquisition/recording to .txt files was chosen over GammaVision and allowed for more freedom in post-processing, as encoder data of the rotational position of the RSM was not easily integrated into the GammaVision software for capture.

4.4 RSM Configurations and Acquisition Hardware

Along with the two RSM designs and sizes, three different detectors were utilized in this work. For the large FitzGerald design RSM, both the SCIONIX 3”x3” NaI (Tl) type 76B76/3M-E1-NEG and SCIONIX 3”x3” NaI(Tl)/CsI(Tl) phoswich type 76B30Ph46/3M-E1-Cs-X-NEG detectors [49] were used. Both of the 3”x3” detectors were operated at -520 V as specified by the SCIONIX test sheet instructions with an ORTEC 556 High-Voltage Power Supply. The phoswich was configured as 46 mm of CsI(Tl) scintillator optically coupled to the PMT, which served as a guard slab of material for an optically coupled 30 mm slab of NaI(Tl) scintillator in front of it. The thicker guard layer of CsI(Tl) helps to identify any originally higher than source energy backscatter events that may end up looking like the FEP under investigation through a Compton event, in the support structure or PMT electronics of the detector. It is also used to filter, through PSA, almost all Compton scatter events from the source that occurred in the RSM mount hardware/PMT and distinguish them from RSM scattered-in events which deposited in the front slab. For the smaller RSMs, a Saint-Gobain BrilLanCe® ($LaBr_3(Ce)$) [50] scintillator was used. The dimensions of the crystal were that of an extruded cube (10x10x50 mm) configuration of unknown axial orientation within the encasement. This detector operated at +900 V, and has a superior energy resolution compared to the NaI(Tl). Even though the crystal is smaller, the FEP counts are in a narrower energy range. This reduces the relative influence of background counts and results in a higher SNR than might be seen otherwise.

The output of these detectors was routed through an ORTEC Preamplifier (Model 113), with its capacitance selector switch set to the available minimum of 45 pF. A preamplifier was not technically needed in this case and was in fact undesirable because of its slight distortion effect on the outputted waveform. However, an ORTEC 460 Delay-Line Amplifier (DLA) was also used to compress the outputted waveforms and delay its sending to the Analog-to-Digital Converter (ADC). The input for this DLA was designed to only come from the preamp. The length of the pulse and the available sample rate of the National Instruments LabView acquisition software regarding the NIMbox NDA8 DAC necessitated this addition. The DLA effectively compressed the waveform temporally and allowed for successful sampling of the waveform by the software. Sampling was set at 80 evenly spaced points of 10 ns width (or alternately a 100 MHz sampling rate). While both the rise- and fall-time characteristics of the pulse were affected by the DLA, the PSA used in conjunction with the phoswich was able to distinguish distinct average rise times for both scintillation materials. This sampling rate proved adequate for discretization and the total storage space necessary to characterize each individual gamma event. A random sampling of events using a peripherally attached oscilloscope set to single-shot acquisition and the LabView trigger set to record only one interaction above the source threshold proved this for the 662 keV FEP of Cs-137. The built-in analysis function of the oscilloscope for waveform rise- and fall-times was within 5% of the calculated values after the discretized waveform was reconstructed using the calculated the rise- and fall-times in conjunction with Equation (13) . This sampling also limited the file data storage size per set to a reasonable amount, given the 1TB drive being used at the time. As it was, using the most active Cs-137 #1 source, the laboratory spacing between the source and RSM, and the time length of the usual acquisition (24 hours), data sets for the large RSM configuration were on average about 4 GB (over 4.5M waveforms). Gain on the DLA was

set to the available minimums and the pulse integration time was set to 0.04 μs for the 3"x3" detectors and 0.25 μs for the $LaBr_3$ detector. The switch position change also scaled the output of the $LaBr_3$ waveform to fit entirely into the 800 ns sampling time width. Now, the developed MathCAD reduction code software for post-processing the data sets could be used in both cases. Of note, the polarity switch on the DLA was set to "pos" for the 3"x3" detectors and flipped to "neg" for the $LaBr_3$ detector. This was to keep the captured waveform upright due to the operating voltages of the detectors, which also proved useful for the data reduction software coding. The DLA output was split into three separate signal outputs for comparisons and initial experiment debugging. Along with sending to the NIMbox ADC for the sampling and the oscilloscope, the output was also sent to an ORTEC 926 ADCAM MCB for capture by ORTEC's industry standard MAESTRO GammaVision [48] software on another laptop computer. Data from all three tools proved useful in adjusting the system to operate and record within the desire parameters, and to also verify the correct functioning of the LabView acquisition captures and writing of the data files. Therefore, a high-confidence level in the LabView program developed to capture and record both the generated waveform and the rotational position data of the RSM system was established.

The RSM angular position was recorded using a Renishaw RESR R20-115 Optical Encoder Ring, mounted to the base support of the RSM and optically read. The position information was then made available to the LabView acquisition program as a coincident, secondary data stream. Upon waveform threshold trigger, it was subsequently queried and saved.

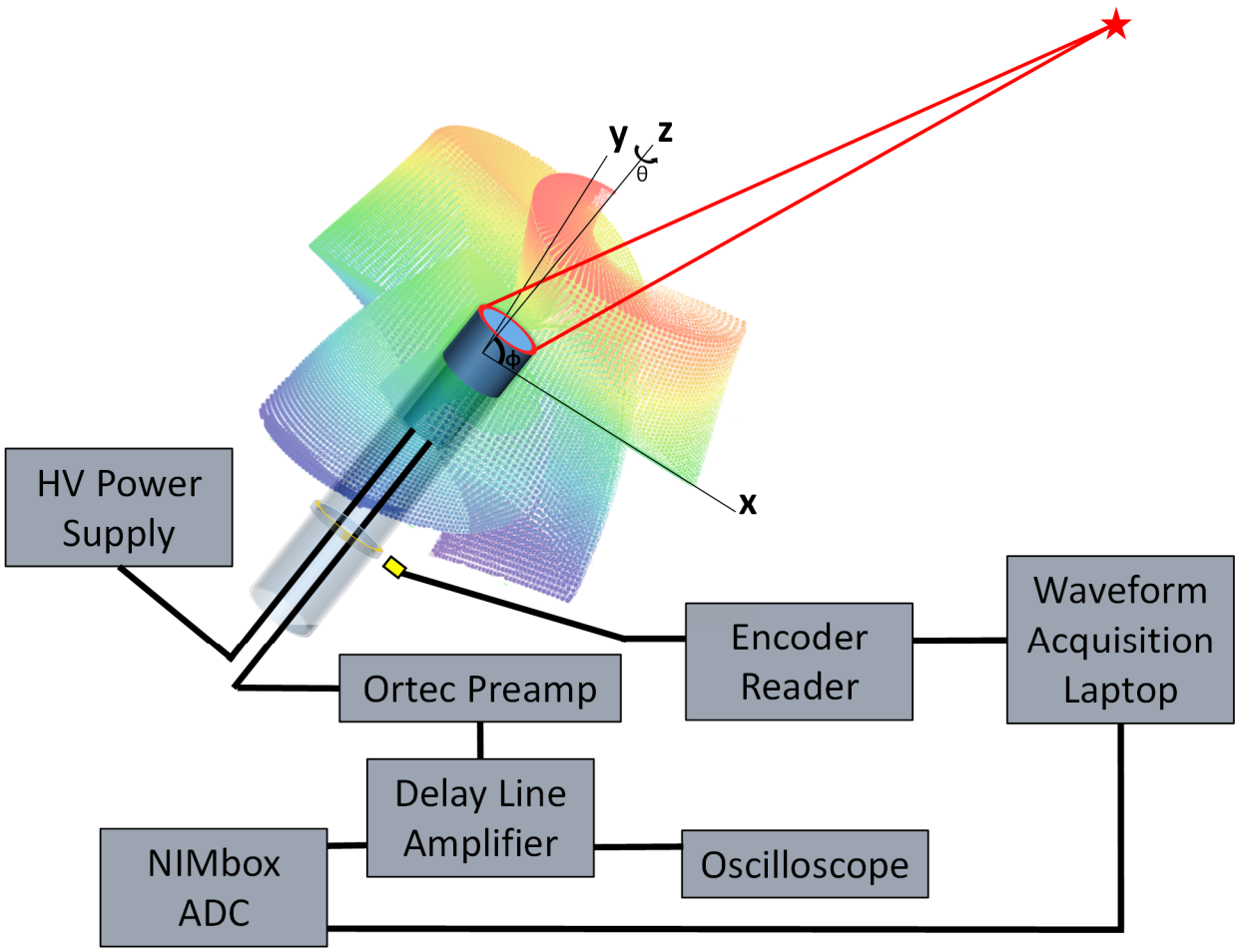

Figure 48. The typical RSM lab equipment set-up. Superimposed on the figure are the axis sets used to characterize position. The cut-away shows the placement of the detector/PMT combination internal to the RSM. The detector crystal center was made to coincide with the RSM's coordinate system origin.

The typical laboratory setup for the RSM described herein is shown in Figure 48. Prior to each collection effort, a cursory check of the previous data set was accomplished to ensure that all equipment was still in good working order and outputting data in the expected format. This was especially important with regard to the Renishaw encoder ring that was recycled from Kowash's work. It proved to be very fickle and required many minor adjustments. Some reacquisitions of entire data sets due to its failure to accurately capture the RSM rotation angle information were made. More on this in Chapter V when work to fit the partial experimental scattergrams to the modulation curves libraries is presented.

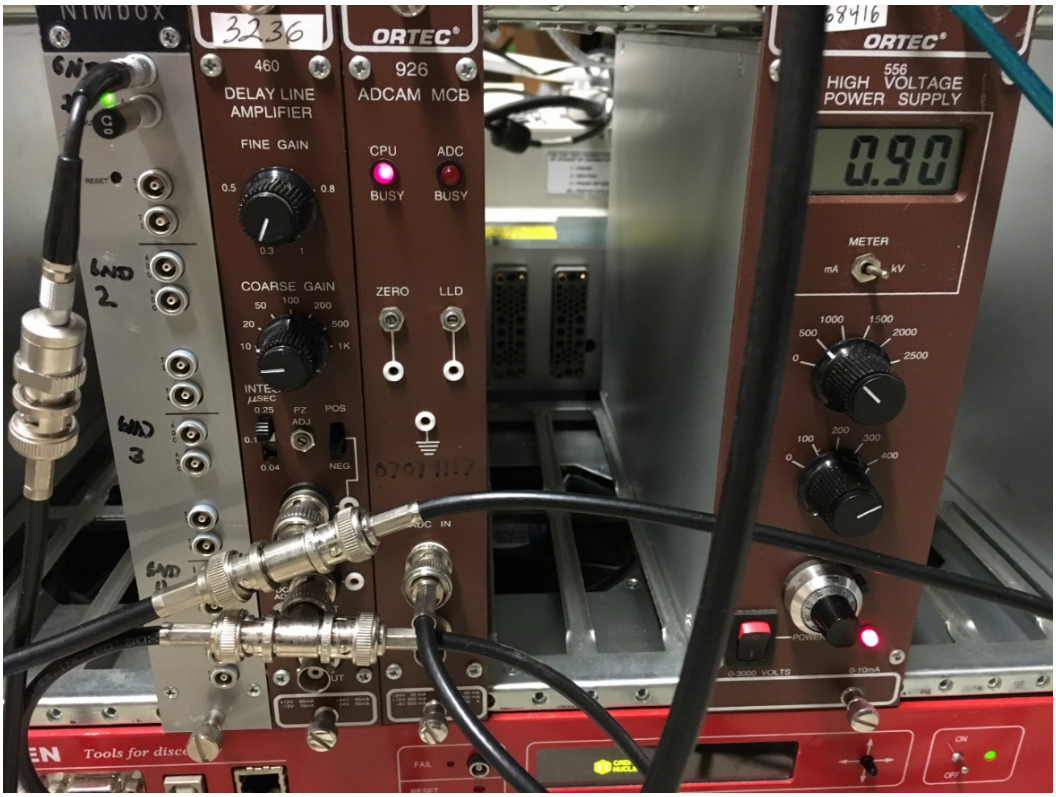

Figure 49. Power supply and waveform collection electronics.

The power supply and collection electronics used to acquire the waveform pulses from the detector(s) and send them through the DLA to the collector systems are shown in Figure 49. It should also be noted here that the laboratory wall plug power exhibited some frequency and voltage variations. Therefore, the entire RSM system and acquisition set-up had an intermediate power conditioner to reduce wall plug grounding noise.

4.5 Phoswich Detector Incorporation

A further enhancement besides the standard 3”x3” NaI(Tl) detector used in this work for RSM characterization is the first demonstration of the benefit achieved by substitution of a phoswich (phosphor/sandwich) type NaI(Tl)/CsI(Tl) scintillator detector [51] for backscatter suppression for some of the data sets.

A phoswich detector was used along with PSA and Pulse-Shape Discrimination (PSD) to reduce the influence of back-scattered gammas into the recorded spectra from the detector PMT and associated electronics, and the rotational machinery/mount behind the RSM. By having a thinner layer of NaI(Tl) material, backed by a thicker "guard" layer of CsI(Tl) and by using PSA on the waveforms produced by scintillation light emitted during an ionizing event, it was determined if a detected gamma ray interacted with just the NaI(Tl) or CsI(Tl) portion of the crystal, or deposited its energy partially in both. Because of the difference in lifetime of the fluorescence response of the two scintillator materials, it is possible to ID/discard an event that deposited energy in one or the other layers, or events that deposited in both scintillator materials simultaneously, depending on what type of filtering is desired. For this work, PSA is used to retain only those interactions that resulted in complete absorption within the front NaI(Tl) crystal, and filter the resultant spectra of the rest. This was shown to significantly reduce the effects of the recorded lower-energy down scatter off of the RSM electronics and mount (i.e. increase in the SNR) and is presented in the results of Chapter V. However, this comes at the expense of a longer counting/dwell times for establishing a scattergram with reasonable counting statics fidelity but is offset by the accuracy gains when utilizing the Compton portion of the spectra for source direction identification. For this work, due to the limited availability of a high-activity Cs-137 source to subsequently produce many backscatter events in the mounting hardware of the RSM, a low-energy Co-57 (122 keV) rope source was placed onto the RSM rotational support structure behind the mount as a "simulator". It is shown that the gamma interactions from this source are mostly captured by the CsI(Tl) guard slab material on the backside of the NaI(Tl), and can be suppressed computationally when post-processing the captured scintillator waveforms to build the scattergrams. Also of note here, the phoswich detectors in this work are unique in that they are

advertised as being designed (due to scintillator doping levels in each crystal) specifically to have similar total light output at any distinct gamma energy. Therefore, the subsequent signal to the PMT will be the same for similar energy gammas, so Compton scattering in one and subsequent absorption in the other should still product the same light intensity peak (total gamma energy) and would be recorded as a single event (but with a slightly altered waveform shape).

The initial calibration and characterization results for the phoswich used in this work are shown in Figure 50. The top half of the figure shows the physical configuration. The bottom left-hand scatter-plot is that of the NaI(Tl) characteristic rise-time, and the middle plot is that of only the CsI(Tl) crystal. The total phoswich reactions are shown in the third, right-hand plot. Notice that by bracketing the search parameters of this final graph, to exclude any interactions outside of the -0.08 to -0.10 time constant range, the primary interaction band of the CsI(Tl) crystal and subsequently recorded depositions can be discarded. This in-turn does clean up the lower energy portions of the spectra which included a significant source back-scatter contribution from the RSM mount and Co-57 simulator. While the characteristic decay time of the CsI(Tl) is longer than the NaI(Tl), the fall-time equivalent of Figure 50 did not show an identifiable banding structure. This is due to the intervening signal shaping electronics affecting the waveform shape before sampling. A significant RC time constant was selected when integrating the waveform to reduce noise. Because of this, the decay time difference is convolved into the leading edge of the integrated pulses. So, while the decay time of both crystals is fast compared to their rise times [11], it was expected that the fall time of the integrated signal would only contains information about the electronics used (which is constant), and not about the bi-modal phoswich crystal signals. Therefore, the differentiation of which crystal was interacted within the detector was carried out using only the rise-time information for this work.

According to the previous, it was possible to effectively eliminate any signal that fell within the energy window under investigation but showed through PSA that the waveform signal was generated in the CsI(Tl) guard layer. This is shown in the phoswich results of Chapter V, where a comparison of the filtered vs. unfiltered spectra (and subsequent improvement to the source direction prediction) is made. Phoswich detectors are specifically designed to allow for directional identification of lower-energy, scattered gamma rays in a high-energy background environment. They are therefore a key component in determining if the low-cost, RSM system under investigation is a viable competitor to the higher-resolution, higher-cost HPGe Compton-camera type systems when utilized to determine what source direction information is contained in the Compton spectrum.

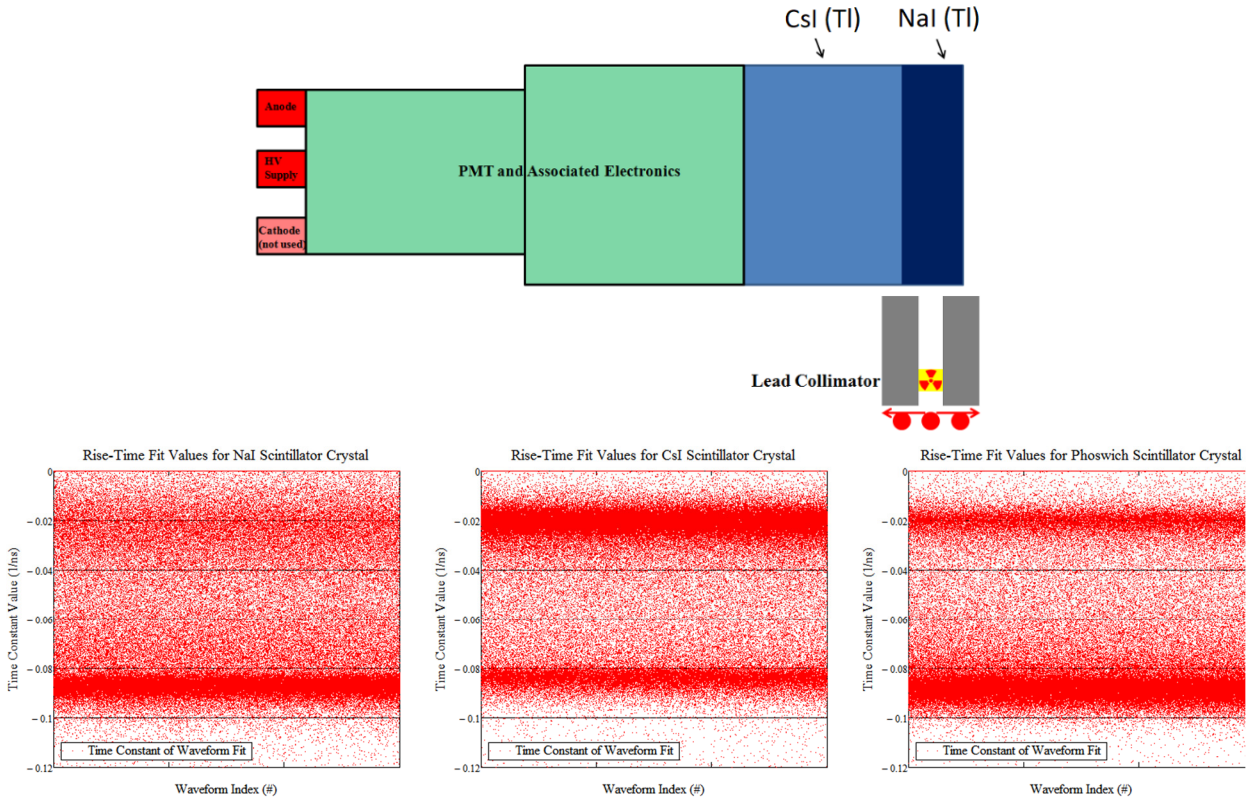

Figure 50. Phoswich design and calibration set-up used to isolate individual crystals, along with scatter plot examples of the regularity of the time-constants found when fitting waveforms of either the NaI(Tl), CsI(Tl) or both. By excluding interactions that happen outside of the main banding of the NaI(Tl) crystal, the total spectra can be significantly modified as seen in Chapter V.

Finally, there may also be utility when using the CsI(Tl) guard slab back-scattered data, instead of using it as a filter, to characterize the source direction. This type of work in relation to the RSM system is left for future investigation, but Compton backscatter imaging has been previously used by Evans [52] at AFIT for single-sided noninvasive inspection and may be adaptable to the RSM to further enhance the source direction determination.

4.6 Sources and Calibration

A range of gamma energies from multiple sources were utilized in this work. They are listed below in Table 1. The primary work reported on here focuses on the Cs-137 662 keV line. An objective of this work was to show successful RSM operation and characterization over the ~40 keV to 1.4 MeV energy range. This range includes the Lead (Pb) characteristic x-ray K to L shell electron transition all the way to the Na-24 deexcitation line (1.38 MeV) seen in the cooling operations of some reactors. While investigation of RSM performance with sources further into the MeV range was desired they were not available. As well, as configured, the acquisition electronics had a saturation point of approximately 1.3 MeV for the final acquisition set-up used. Data in the sub-200 keV range was greatly affected by the natural background noise of the lab, and so was difficult to collect without a significant increase to the data sets' final file sizes. Further, only the one multinuclide source used had energies above the Cs-137 (662 keV) line of the sources available at the time, but activity in this regime was low. While all three detectors could measure the Y-88 and Co-60 emission lines at 0.898 MeV and 1.173 MeV respectively of the multinuclide source, the FEPs were not distinguishable for the activity, spacing of the source, detector efficiency, and RSM interaction point spread function. Therefore, these lines did not lead to an accurate matching of the experimental scattergrams to the computational DRM library matching files, which is shown later in Chapter V.

Table 1. Sources used in this work.

Multi-Nuclide Source Details							
Peak Number	Gamma Energy (keV)	Half-Life (in days)		Original Activity (μCi)	Source Activity at NaI Detector Calibration (μCi)	Original Gammas per sec (#/sec)	Gammas per sec at NaI Detector Calibration (#/sec)
1	60	157850		0.0300	0.0299	399	399
2	88	463		0.2987	0.2499	401	336
3	122	272		0.0099	0.0073	312	230
4	159	120		0.0141	0.0071	440	221
5	320	28		0.3355	0.0171	1224	62
6	392	115		0.0497	0.0243	1194	583
7	514	65		0.0642	0.0180	2337	655
8	662	11020		0.0427	0.0424	1345	1335
9	898	107		0.1008	0.0465	3506	1618
10	1173	1926		0.0532	0.0509	1964	1882
11*	1333	1926		0.0532	0.0509	1966	1884
12*	1836	107		0.1008	0.0465	3707	1710
*Energies not considered in work, as they were past the saturation point (upper threshold bound) for the ADC to record							
Am-241 Source Details							
Am-241	60	157850		0.1951	0.1838	7219	6799
Ba-133 Source Details							
Ba-133	80	3839		108.3000	95.9422	4007100	3549863
Co-57 Rope Source Details							
Co-57	122	270		300.0000	62.6638	11100000	2318560
Cs-137 #1 Source Details							
Cs-137	662	157850		1045.0000	1042.2046	38665000	38561570
Cs-137 #2 Source Details							
Cs-137	662	157850		10.0000	9.7245	370000	359806

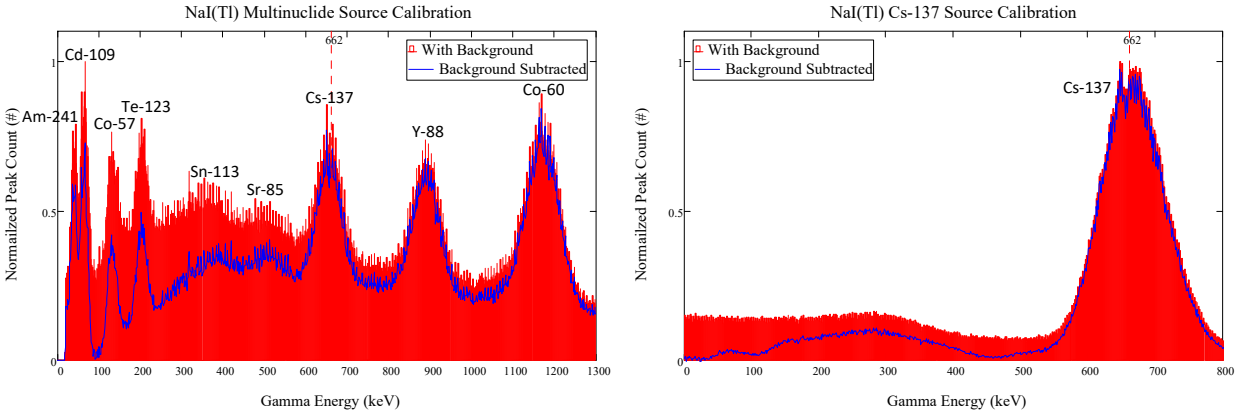

Figure 51. Calibration energy spectra for both the multinuclide and Cs-137 sources on the NaI(Tl) detector used in this work.

The results of the calibration of the NaI(Tl) detector for both the multinuclide source and the strong Cs-137 #1 source are shown in Figure 51. The scintillator/PMT linear least squares fit of response for the energies is also shown in Figure 52.

It is worthwhile to point out that while an exact calibration of any detector prior to use is desirable, especially when trying to identify a particular source material ID, strict tolerances are not necessary in the case of RSM field operations and laboratory tolerances can be loosened. As will be discussed later, when searching for an unlocated radioactive source any FEP (or its associated Compton continuum) of interest which happens to distinguish itself from the noise floor, can be quickly determined through automated search algorithms. The counts in these energy ranges then simply need to be associated with the RSM rotation angle (θ) information at capture and binned to generate the scattergrams. Assuming a single source is present in the field-of-view, the post-processing can be done on the spot. Multiple sources of the same energy but different locations can also be found, but this requires more computationally intensive techniques or new analytic solutions. As envisioned, RSM operations would be automated in a "set-it, forget-it" mode, and once enough information for source direction determination was made, the data would be passed on appropriately. As well, data could be sent back to a centralized processing location, where the analysis could be done. This would be useful if data on an area's natural background (or previously cataloged search incident) was databased properly. New hot spots could be identified through a coherent change detection method. In these ways, field operations could be done in a simple and safe way, while taking advantage of the portability advantages of the RSM.

Characterization of the SCIONIX 3"x3" NaI(Tl) detector with and without background correction for both the multinuclide source and Cs-137 #1 source used is shown in Figure 51. Notice the nuanced split peak of the Cs-137 calibration. This is an interesting artifact and seemed to persist throughout all data sets examined in this work. It is possibly due to an unidentified ADC equipment issue. It should also be noted that peak shifting of approximately ~10 – 15 keV in either

direction was occasionally observed in this work (even with the steps taken to condition the wall plug power of the laboratory).

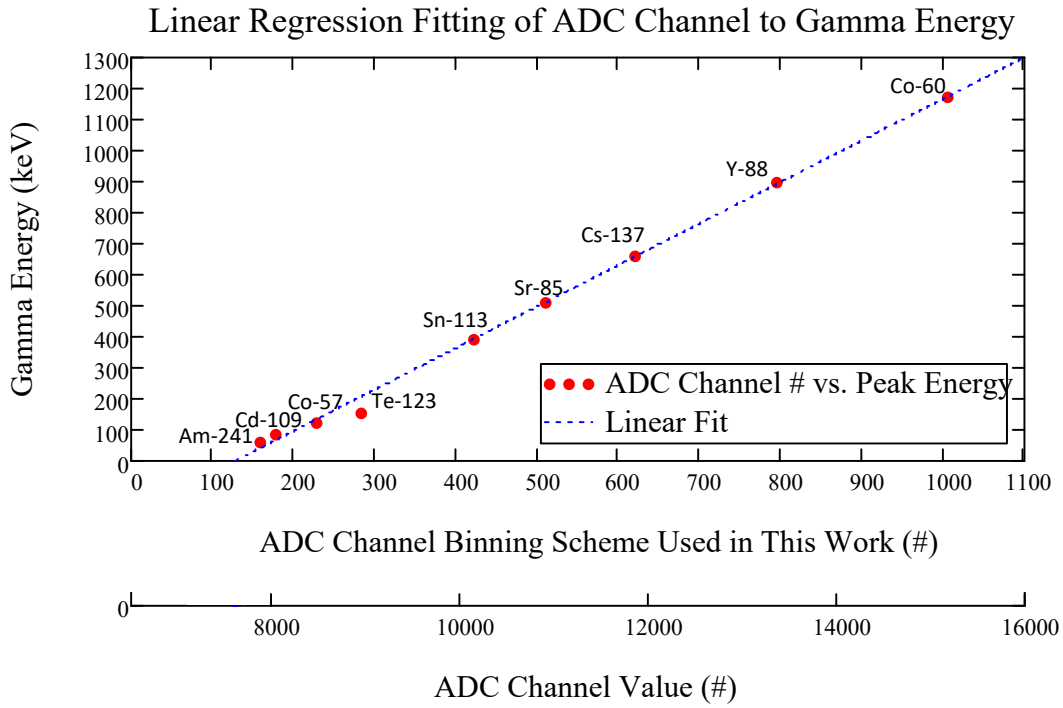

Figure 52. Energy response fitting of the NaI(Tl) detector comparing ADC channel value, the binning scheme used in this work, and the actual peak energies.

The linear response of the SCIONIX detectors to the range of energies investigated is shown in Figure 52. This figure also shows two different energy correlations for the ADC channel and ADC channel binning used in this work. The binning scheme used here nominally lines up with that of the energy in keV, however, it is not exact. For the rest of this work, the spectrum data is reported as a value between 0 and 1098. This "bin" number only aligns to the actual energy of the gamma in an approximate way of 1 keV change per bin. The reason for this is that in most cases, the trigger height/discrimination level of the LabView collection software was set to be channel 6,500 of the possible 16,382 reporting channels of the NIMbox ADC. The actual saturation point of the NIMbox was a report value of 16,383, but any waveforms that reached this value were disregarded, as the incoming waveform peak may have been much higher. This eliminated a potentially confusing peak on the high end of the spectrum in the graphical reporting.

Starting at the threshold value, every 9 energy reporting channels were grouped together, for a total of 1,098 energy bins. This was the smallest evenly divisible number of the difference between the saturation and threshold ADC channels. Since it was about equivalent to 1 keV, it was used for the numerical binning scheme. Binning at some point is necessary for counting the total number of interactions of interest, of a particular energy range, and associating them with the RSM rotation angle. Incident count vs. rotation angle is the definition of the experimental scattergram, to be compared with the DRM. The 9 channels per bin scheme and not the actual energy was chosen for computational convenience when post-processing and was used in the case of all 3 detectors. However, the $LaBr_3$ detector bin values do not nominally line up with the actual incident gamma energy depositions, and therefore, no attempt at making comparisons across the two detector sizes and their resultant spectra should be made. Certain FEPs have been labeled in Chapter V and in the Appendices where applicable, to avoid bin number vs. actual energy confusion.

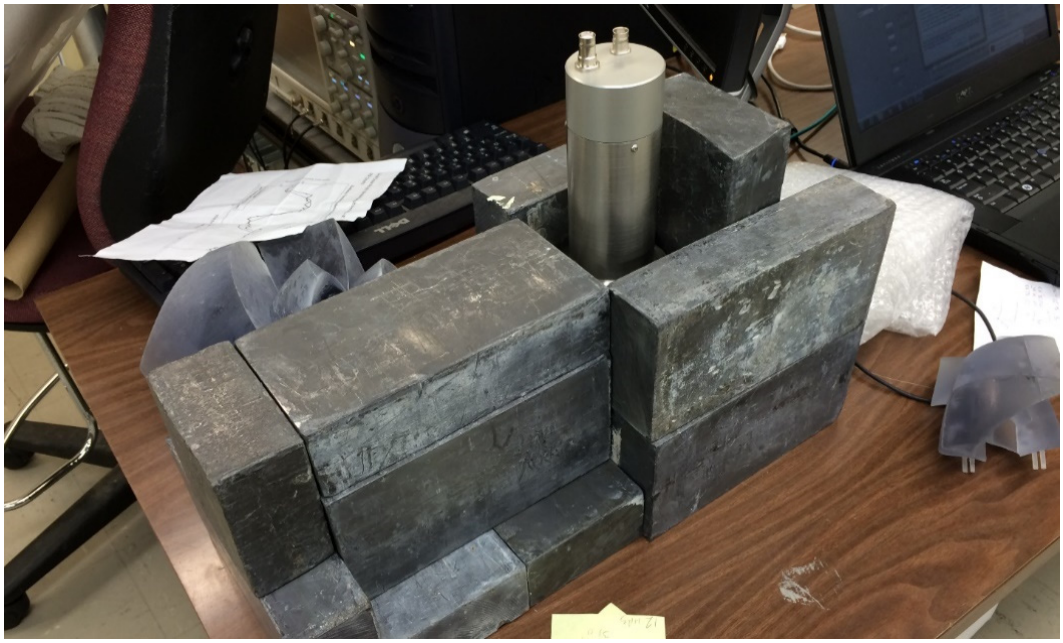

Figure 53. Lead collimator set-up used for characterizing the detectors prior to insertion into the RSM. Notice the tiny, desk model of the FitzGerald design. It was printed as a "Show and Tell" demo before the large RSM construction began, and for validation/fitment of the CAD design efforts.

Figure 53 shows the lead collimator configuration used to calibrate all 3 detectors. Care was taken to reconfigure and carefully align the internal phoswich detector crystals when characterizing the differences between the NaI(Tl) and CsI(Tl) rise- and fall-times.

4.7 Data Collection Routine

The RSM system was tested for correct operation by starting the rotation (~2° per second for the large RSM, or ~70° per second for the smaller RSMs), observing that the encoder reader output was performing nominally, and placing the Cs-137 #1 source at φ = 45° (and about 3 feet from the detector center). φ = 45° was the viewing angle predicted to produce the scattergram with the best peak-to-valley ratio. The laboratory geometry and coordinate system are seen in Figure 54. Signal from the detector PMT was then observed on an oscilloscope and in GammaVision. Operation of the system was consistent with expectations, and the previous characterization(s) done on the detector(s). Concurrently, the LabView acquisition program was initiated. The function and reporting of the encoder position reader information was also validated before long experimental collections were done, as the reader proved to occasionally need adjustment.

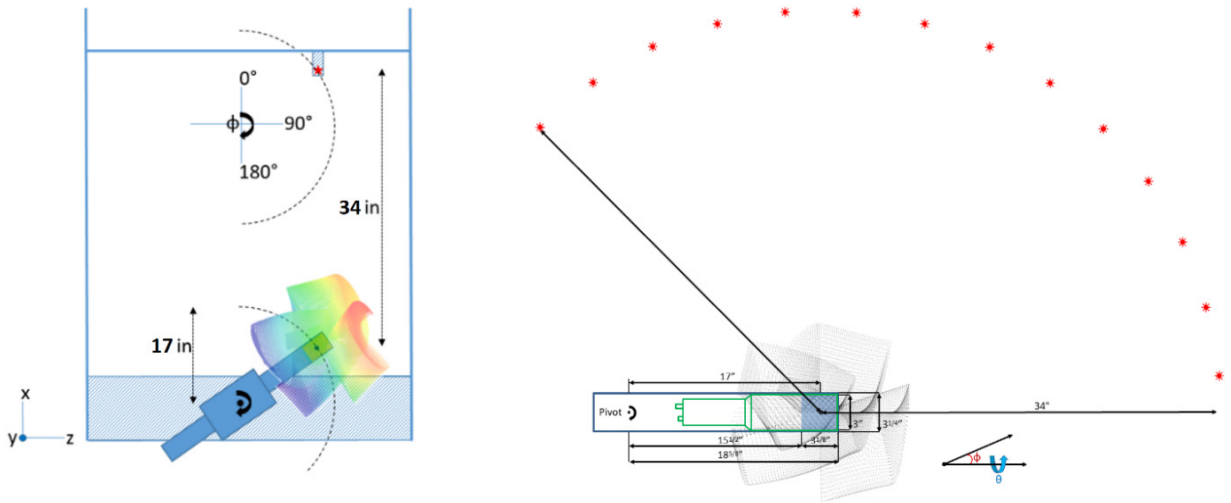

Figure 54. Overhead view of the final RSM lab configuration and source holder geometries, from the lab (left) and RSM (right) reference frames.

Having built confidence in the in-house developed LabView acquisition program, data sets at various φ viewing angles were then collected. Figure 54 shows two top-down views of the final laboratory geometry for the large RSM, in both the lab reference frame and the RSM reference frame. Viewing angles, φ, between 5° and 135° in increments of 10° are shown in the right-hand side RSM reference frame visualization.

As the φ viewing angle was changed, the source translation stages were also adjusted to keep the source distance-to-the-center of the detector crystal consistent at 34". This was the maximum spacing possible due to mechanical limitations of the Velmex translations stages and the pivoting of the RSM when changing φ from 5° to 175° in 10° increments. This resulted in an almost a 2.5:1 ratio of source distance to maximum RSM dimension, and so would still be considered a near field condition. The height of the source was held constant at the height of the detector center.

4.8 Data Reduction and Processing

Sampled waveform data from the ADC and encoder ring reader of the experimental setup was flowed into LabView for recording onto the laptop in separate .txt files upon trigger and processed according to the steps flow-charted in Figure 55. Therefore, the encoder ring position data was not associated with the waveform capture data until post-processing. This is due to the 80 points per capture of the waveform as compared to the 1 point for the encoder. As well, handling the data merge in this way sped up the rate at which the LabView laptop could reset and wait for another trigger event.

On average, the raw .txt files contained about ~4.5M waveforms/encoder positions (or 360M lines for the waveforms data file), resulting in total file sizes of approximately 4 GB for the waveforms and 75 MB for the encoder per test. The minimum possible spacing for the NIMbox

ADC temporal resolution was 5 ns (200 MHz sampling), but the initial 24-hr data collection runs created total file sizes in excess of 8 GB. For the planned collection strategy, this exceeded the limits of the external hard drive used to store/archive the complete set of experimental data. By decreasing the sampling rate of the waveform to 100 MHz, each data set size was cut in half. This loss of fidelity was determined to be acceptable, as the initial waveform reconstruction work was also done at this rate and found to be within 5% as previously reported.

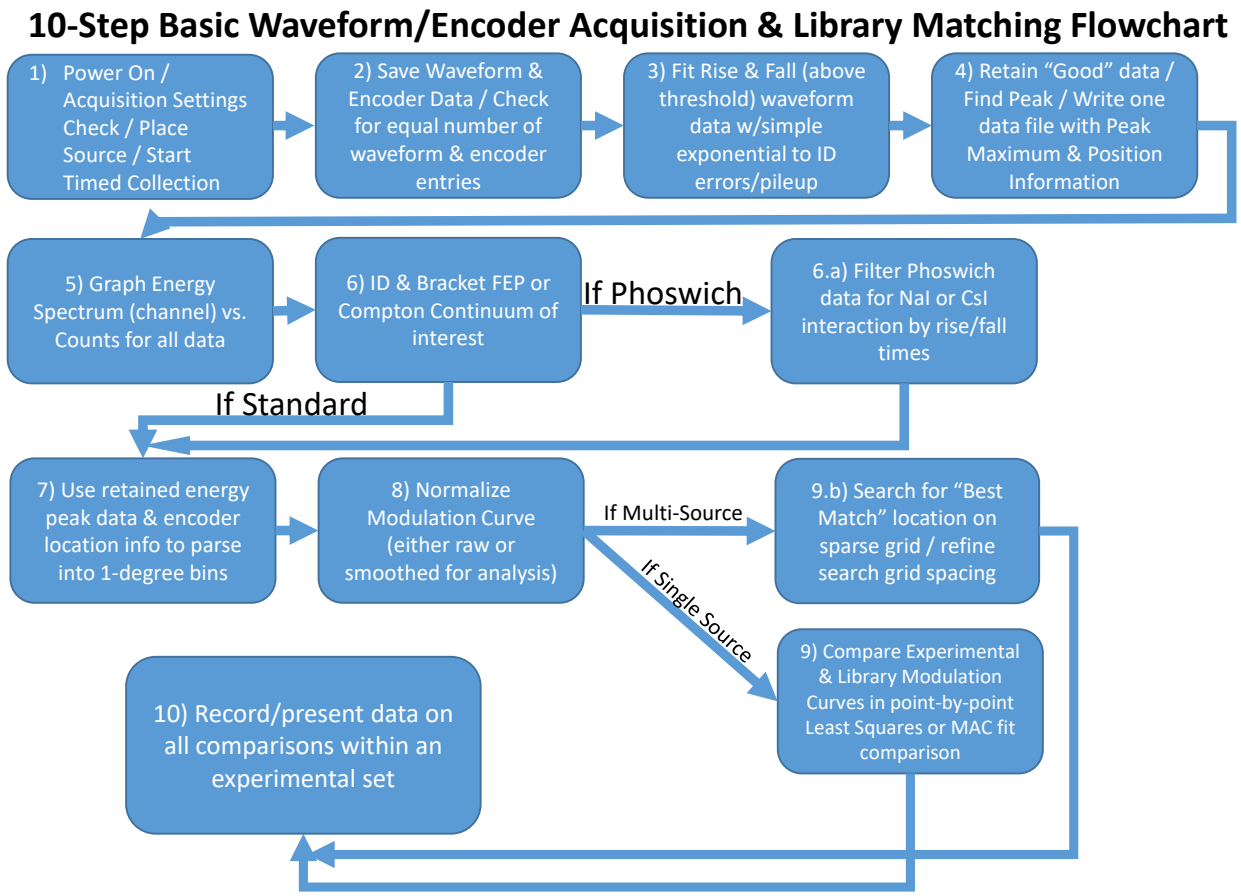

Figure 55. Steps for collection and processing of RSM data.

The encoder was read the moment the trigger activated. Both the sampled waveform values and the encoder value were stored in two separate internal buffers within the LabView acquisition program until it had reached 50 encoder entries (i.e. 4,000 waveform points). The buffers were then written to the separate text files on the acquisition laptop. Upon completion of

the 24 hour data collection period for the large RSM or 12 hours for the smaller builds, the waveform data file was post-processed to find the individual waveform peaks of the pulse, which corresponds to the deposited gamma energy. Rise- and fall-times of the individual waveforms were also calculated and saved. The singular energy value was then associated with its encoder position information in a separate file for energy and position binning. Examples of these data files used to build the scattergrams are presented in Appendix A.1, along with their associated φ viewing angle for both bracketing of the FEP and Compton continuum regions. Electronic versions of the data files and the SolidWorks models are available for research use. Contact information is noted in the Appendix.

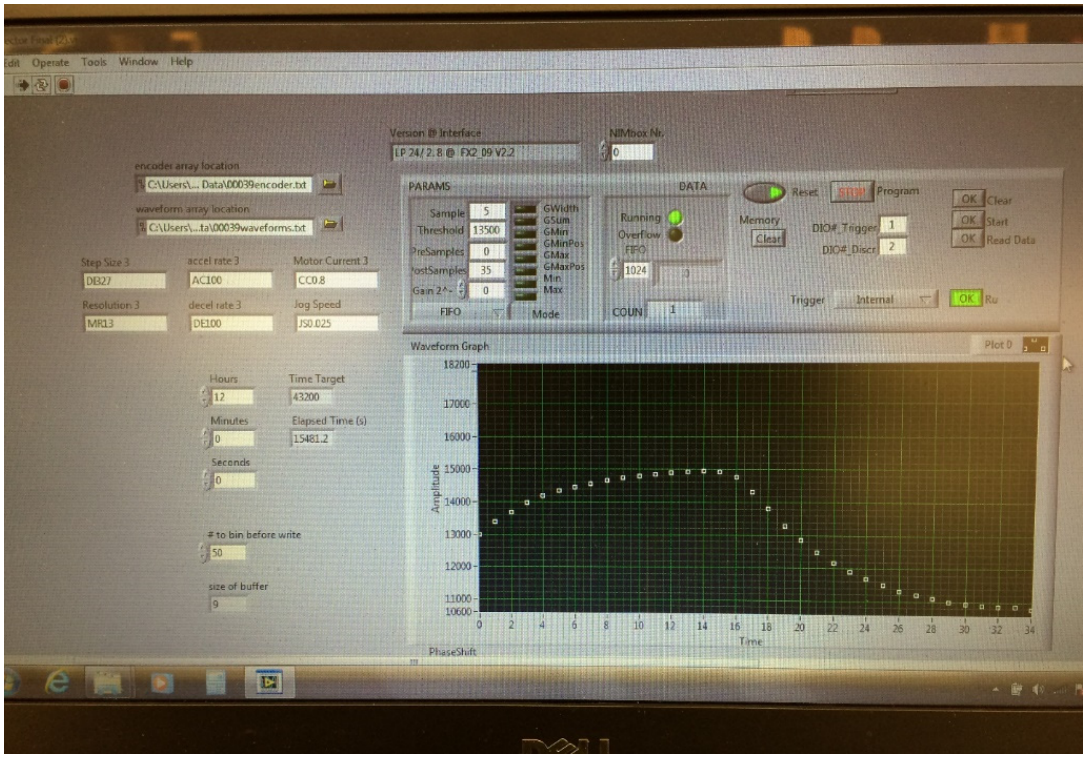

Figure 56. LabView acquisition control screen (encoder/waveform save locations, rotational stepper motor speed control, time of collection effort, buffer size for write files, sampling threshold, data point spacing, number of pre- and post- threshold data points to record, and single shot check for electronics function).

To import and process the millions of lines in the generated .txt data files, they were split into manageable sizes of approximately 25 MB using a freeware program called GSplit. This freeware proved quite useful, as it was the only one found that could count individual lines of a

text file and accurately subdivide the large .txt file consistently for importation and peak waveform value/position data association. All other split programs investigated specified a final file size, but they were not consistent with the exact number of lines split into each smaller file. This was vitally important, as the down-select had to be exactly 80:1 for the imported waveform data to be correctly associated the RSM positional in the merge of the two.

A generic exponential rise- and fall-fit was then conducted on the portions of the waveform before and after the peak respectively, as seen in Figure 57. To do these fits each set of points were binned separately and only points above the threshold value were retained. The subsets were then analyzed for an appropriate number of points (determined to be at minimum of 4) to conduct the generalized exponential fitting function. If both subsets passed this test the points were then fit according to the simple exponential function of Equation (13).

$$a(1 - e^{bx}) + c \tag{13}$$

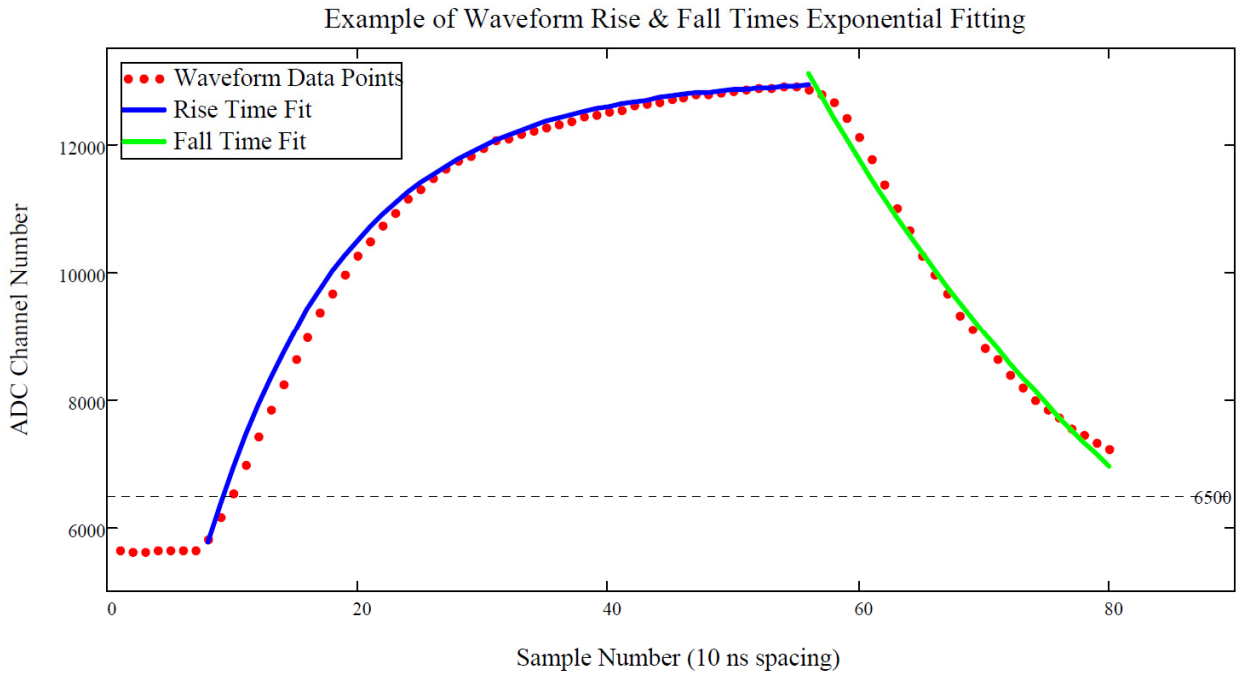

Figure 57. Example of fitting the rise and fall data of an individual waveform to eliminate instances of "pile-up" and to also enable sorting for the phoswich detector data.

In Equation (13) *a* is amplitude, *b* could fit as either a positive or negative time constant, and *c* was the linear off-set/shift of the threshold or peak, respective to a rise (+) or fall (-) time constant. *b* is the important value saved for later rise- and fall-time categorizing. Both the rise- and fall-times, *b*, could be effectively fit using this generalized functional form, while the baseline, and amplitude components showed opposite behavior according to the two data subgroups as expected. As a bonus, if the generalized function failed to converge to a fitting solution, the waveform could be eliminated from the data set as a whole, because this probably indicated a "pile-up" situation in the detector. With more than one gamma arriving during any waveform pulse acquisition, the potential for a skewed recorded pulse peak height, and therefore incorrect, noisier spectra would result and not be indicative of the true source energy. On average, only 0.2% of the data was eliminated in this manner (< 10,000 throw-a-ways per set in a 24 hour, ~4.5M recorded waveforms run; or 90 seconds of total acquisition time). Figure 58 was generated to show an example of this. It shows an example of waveform capture that only contained a single gamma/scintillator interaction (left), and well as examples of pile-up in the data sets that failed to converge to a fit (middle and right) for comparison. The middle pane shows another incoming gamma deposited while the light output response of the detector was still climbing, while the righthand pane shows another deposition during the fall time.

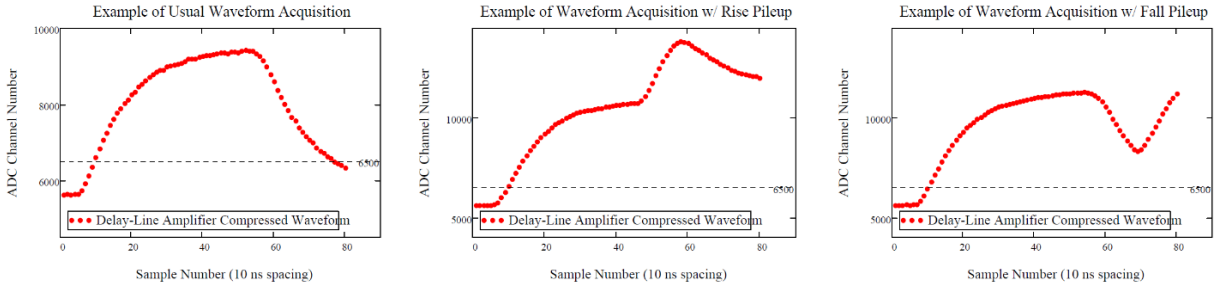

Figure 58. Example of the collection threshold, and before and after threshold sampling points. Rejection of waveforms affected by "pile-up" (middle and right panes) is showed for another gamma interacting during the rise time (middle pane) and for one interacting during the fall time (right pane).

In the case of phoswich detector usage, the individual waveform rise- and fall-times could then be used to further reduce the data set to discriminate areas of interest regarding which scintillator interacted and produced light. By filtering *b* for the usual rise- and fall-time value range of the discrete NaI(Tl) or CsI(Tl) scintillator, known from calibration, determination of which crystal the gamma interacted with was made. This is previously shown in Figure 50.

For the rest of the data post-processing, the software then linked the data set peak, rise-, and fall-values, with the .txt file value of the Renishaw holographic encoder ring at acquisition. This piece of hardware was mounted to the same aluminum collar that held the RSM in place and provided for its attachment to the drive motor. The ring contained 72,000 discrete lines for positional information measurement (0 – 71,999); therefore, groups of 200 lines (i.e. 1 degree) were binned together. Now knowing the angular position data and its association with individual waveform captures, the entire energy spectra could be sorted and binned for ease of use. Each event was recorded as a count in a matrix of 1,098x360 (energy x position) array. In this manner, the entirety of the ~4.5M interactions contained within each data set could later be displayed on a peak normalized count basis compared to the orientation angle of the RSM, once the energy range of interest was identified. These energy range bounds of the spectrum, either FEP(s) or the Compton continuum, are defined by the user. By polling only the matrix energy bins values between the bounds of interest an experimental scattergram, which plots the normalized number of counts within the selected energy window to the angular position of the RSM, is quickly generated. Subsequently, these scattergrams can be smoothed for a noisy encoder data condition or further filtered if encoder position data is found to be missing at some angles of rotation. A typical result of the large, FitzGerald RSM design with the NaI(Tl) 3”x3” detector is shown in

Figure 59, along with the three smoothing options built into the processing code. The smoothing is a nearest-neighbor average by points.

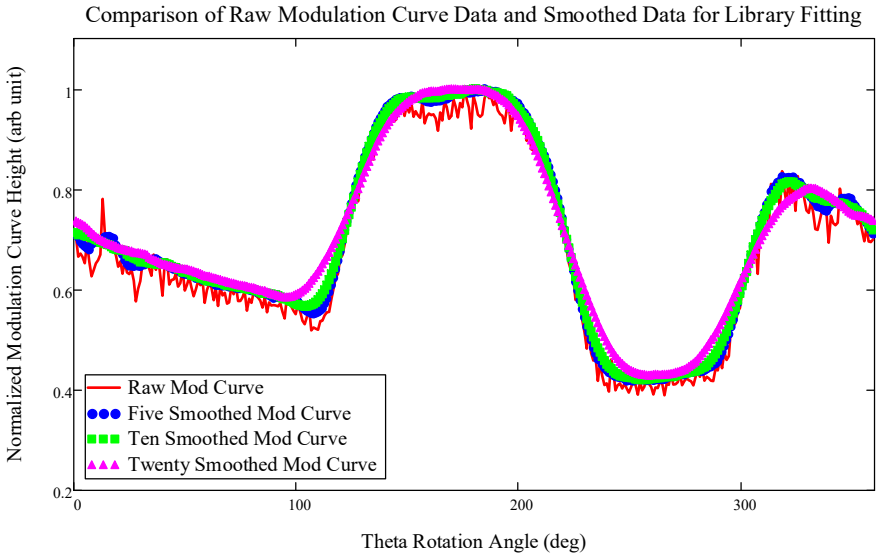

Figure 59. Example of smoothing of modulation curve data to facilitate in library position matching.

Direction determination data was in general computed by comparing the experimentally generated scattergrams to the scaled library of modulation curves through both a LS and MAC method. MAC methods have been used previously to characterize RSM experimental and library matching results [5] [2]. The generalized form of the MAC computation is shown in Equation (14).

$$MAC = \frac{(|Exp^T * LibAdjusted|)^2}{(Exp^T * Exp) * (LibAdjusted^T * LibAdjusted)} \tag{14}$$

Here *Exp* is the experimentally obtained scattergram. *LibAdjusted* is the particular library DRC of the total DRM, at a given (φ,θ) position as the matching algorithm cycles through all possibilities of source placement, with modified amplitudes to best fit the scattergram. This modification will be addressed imminently. MAC comparisons are a statistical indicator, fundamentally based on a least squares form of linear regression. They are sensitive to large differences in overall shape, while relatively insensitive to smaller differences [53] between the

RSM experimental and library curves. This means that MAC values will increase rapidly at first, from some minimum value associated with curves that are the most dissimilar and then slowly converge to 1.0 as the curve shapes become identical. The LS method on the other hand is simply a summation of the square of the differences between two similar points (i.e. same x-axis value, in this case the measured θ rotation angle) of both the experimental and library modulation curves. Therefore, the LS values start at 0 for identical curves and only grow larger for more dissimilar curves. Both MAC and LS should however present a similar order when appropriately ordering the resultant 64,440 matching results. As previously stated, to be able to compare the accuracy and resolution metrics of performance for the predicted source direction of both methods, it is necessary to calculate the geometric distance between the known source and the predicted angular position. For this work, the distance between the known true source position and the LS and MAC predictions is calculated in terms of the spherical φ and θ units coordinate system according to Equation (17). This allows for a comparison of which method was better at predicting the true source direction. It was often observed in this work, that the LS method made a better prediction of the source direction over the intermediate "good" φ viewing angles of 15° – 145°, while it appears that the MAC method had better results in the extreme "viewing angles" of φ (i.e. 5° and 155° – 175°) for the angular positions selected for investigation here. There are some exceptions to this, especially when looking at the data generated by the small RSMs with the $LaBr_3$ detector. This will be shown in Chapter V.

As just alluded to, a final normalization and amplitude manipulation step for comparison of the DRM library files to the experimental results is made before either the LS or MAC comparisons. To accomplish this, each normalized scattergram was shifted so that its average amplitude value coincided with a y-axis value of zero. The average amplitude value of the

individual DRCs for each position in the library were also shifted in this manner. Using Equations (15) and (16), where *Exp* is the experimentally obtained scattergram and *Lib* is the library DRC of the DRM at a given (φ,θ) angular position the library files are acted upon to modify their amplitudes for a best fit of the advanced model generated prediction to the experimental data. Shifting is necessary to artificially place all points below the average into the negative half of the axis, as Equation (15) always has a positive result. In this way, and in conjunction with, *c*, the determined scaling function can be applied across all points of the curve to shift the peaks and the troughs of the library modulation curve into a best fit with the scattergram by creating a new temporary library file, *Lib′*, for comparison. Since the value of *c* is always positive, had the curves been exclusively valued in the positive upper half of the y-axis, the value of the adjustment could only increase the value of the individual points of the modulation curve. By taking these extra steps, the positive fitting value of *c* was seen to increase significantly, and the resultant new library curves did have a better fit to the scattergram. This was verified by using the MAC value method according to Equation (14).

$$c = \frac{Exp^T Lib}{Lib^T Lib} \tag{15}$$

$$Lib' = cLib \tag{16}$$

The verification was made by comparing both the MAC value of the *Lib′* array (shifted by the new average back to the positive portion of the axis with the major peak renormalized to an amplitude value of 1.0) to that of the original. This was done because the resultant MAC value was found to be a y-axis value dependent metric (i.e. the same relative curves produced different MAC results based on both the position and the scale of the y-axis position). This dependency may explain some of the discrepancies between the work of Logan [34] and Condon [3], which essentially used the same source data sets for the large, FitzGerald design RSM but found

drastically different MAC values when comparing experimental data to their MCNP® and GEANT generated DRMs. Each used the same large RSM SolidWorks CAD file developed here. Results of the method of scaling, using Equations (15) and (16), are shown in Figure 60.

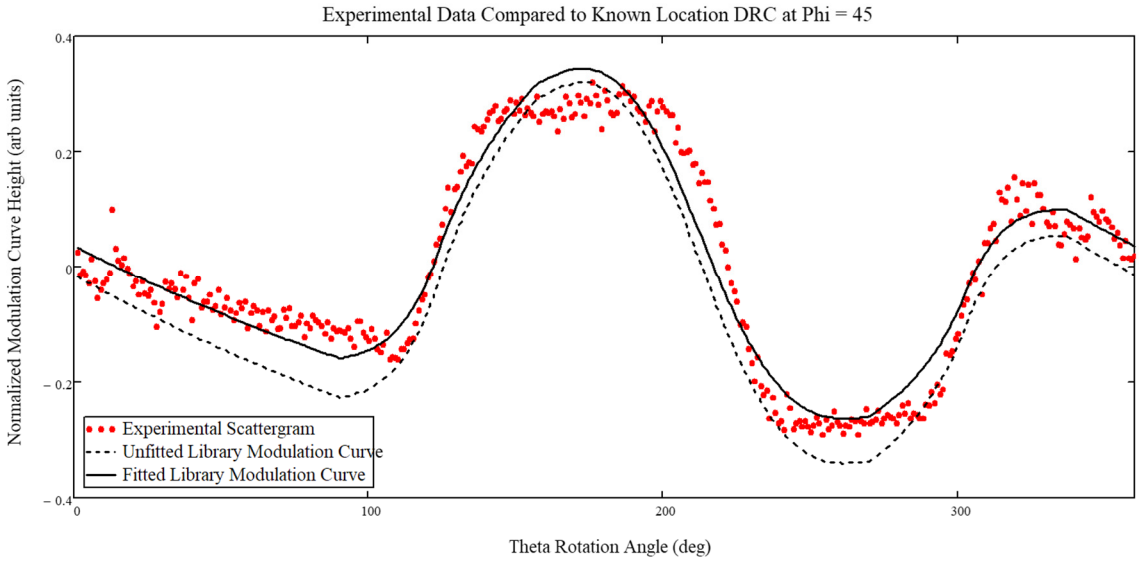

Figure 60. Comparison of the experimental scattergram and the known source direction modulation curve for φ = 45°, and the library curve fitted over all the points of the scattergram.

A comparison of the results in this work are compared to Logan's in Chapter V. Her best (highest) MAC values occurred consistently around the 0.99 range, whereas Codon's used a different normalization method for his comparison, with subsequent MAC values ranging from 0.63 to 0.84. So, while MAC values are instructive, a further step was taken in this work to ensure accurate comparison of the results between the differently sized RSMs and the multiple detectors used (and the other RSM work previously published). By adding an angular distance metric, *s*, according to Equation (17), the geometric length in degrees of separation between the predicted angular direction and that of the known, true source placement is quantified. This same method can be used independently on either the viewing angle, φ, or the theta rotation angle, θ, differences from true as a direct method of characterizing the resolution of the RSM and is presented later.

$$s = \sqrt{(\varphi_{actual} - \varphi_{experimental})^2 + (\theta_{actual} - \theta_{experimental})^2} \tag{17}$$

The reader will notice that some of the work presented here does not use this method of scaling the library modulation curve, but rather a force fitting and stretching of the curve to the highest and lowest data points across the entire rotation is used. That is, the individual modulation curve (DRC) in the library DRM file had its peak and lowest trough adjusted to the maximum and minimum of the experimentally produced and normalized scattergram. This was accomplished through forcing the averages of all the points of the experimental and library modulation curve to converge to within 1% of each other and stretching the library curve toward the maximum or minimum depending on if the points were above or below the average in a linear fashion. Points of the library file in a range above the experimental average were interpolated toward the maximum point. The varying minimum was also handled this way, with the value of points falling below the average reduced or increased in a linear fashion until the least point of the library matched the least experimentally record value. The problem with this method was that obviously outlying points in the scattergram due to encoder errors significantly skewed the resultant fit in some cases. Therefore, the method described above was implemented, but time constraints kept it from being used ubiquitously throughout the results.

It should also be noted here that the amplitude adjustments to the library DRC described above are a requirement. If the experimental data scattergram is altered to better fit the library (which should never be done, but was investigated during the software development), both the LS point-by-point difference summation and MAC methods of curve comparison (and ultimately the direction prediction) very often failed to produce an s value anywhere close to the actual source direction. The model predicts that the library modulation curves are very flat from $\varphi = 1° – 15°$, $\varphi = 155° – 179°$, and around $\varphi = 90°$ and their overall average is close to 1 based on the geometries constructed and tested. When normalized, only small variation exists between the maximum and

minimum(s), this is because of the shape of the RSMs. When subsequent comparisons were made over the entire DRM file, both the LS and MAC methods tended toward inaccurate predictions around all possible θ angles in the viewing angles, φ, of 1° and 180°. This is due to the minimization of the LS differences and maximization of the MAC method value (i.e. MAC values greater than .9999) at these "flat" modulation curve positions. However, by adjusting the library to fit the experimental data, all incorrect direction predictions in these flat regions were eliminated.

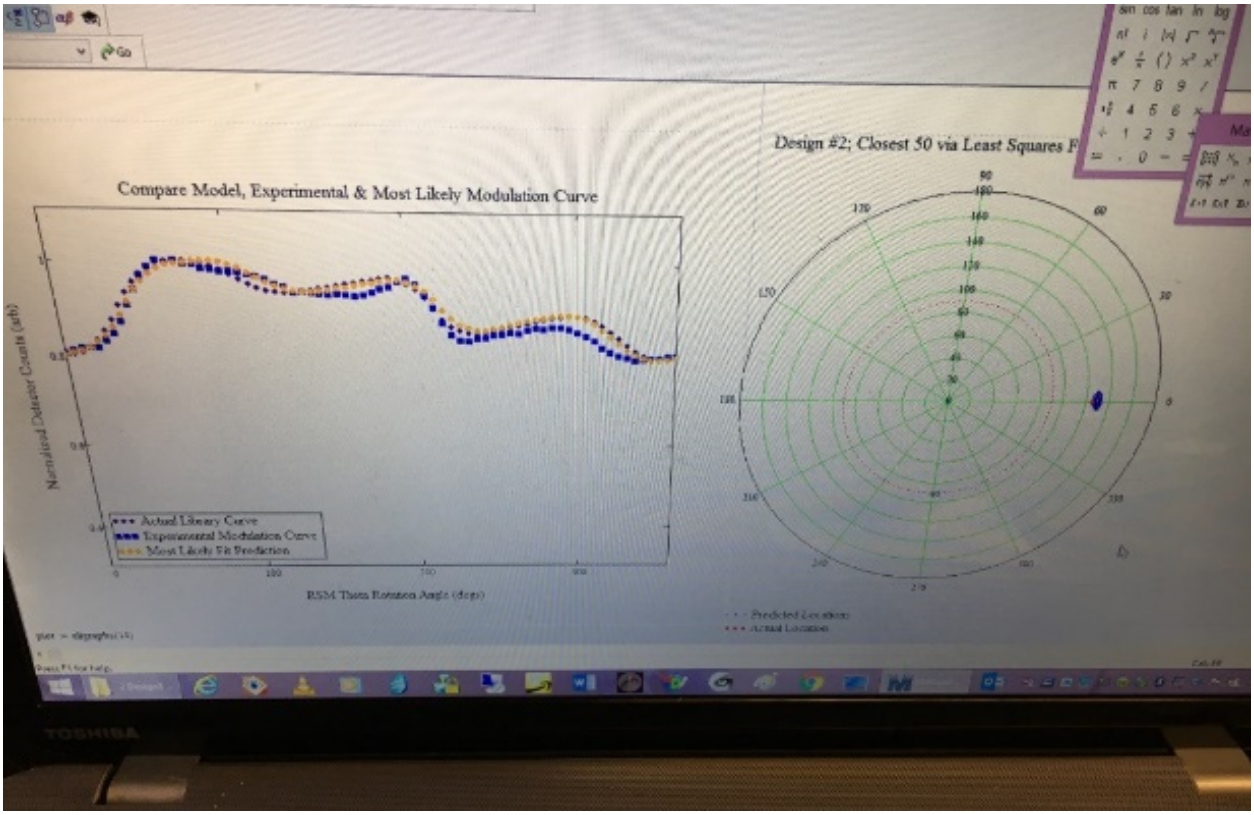

Figure 61. Initial attempts at matching the modulation curve library. Amplitude adjustments were made to account for experimental attenuation vs computational RSM size and construction material, and comparison was made to the DRM file over all 64,440 allowed source placements. On the right-hand side, but hard to see, is the actual, known source angular position, surrounded by the first 50 matches of the value ordered MAC results array.

Initial work to graphically display the results when post-processing the scattergram data and source direction determination work are shown in Figure 61. The process described above generates the most probable position of the source in the (φ,θ) coordinate system of the RSM when the 64,440 comparisons of the DRM and individual scattergram are numerically rank ordered. The

LS was sorted by minimum to maximum value, whereas the MAC array was sorted from a maximum of 1 to 0. The 5,000 points with the closest match to the experimental data were then saved for later display if desired, to show both the consistency of the comparison algorithm and to be able to visualize the areas of degeneracy. The first point in either the LS or MAC stacked arrays was defined as the highest probability source direction. This one "closest match" point's distance, *s*, is calculated from Equation (17). This was the ideal method for comparing the different scales of the LS and MAC methods to each other, for showing which method was most successful on a case-by-case basis regarding source direction prediction.

Further, plotting of the closest subsequent ~250 points (0.5% of available source positions) also proved useful in the graphics display. On occasion, the closest point (or even the first 100 or 200) were clustered in an area not associated with the source, due to an RSM degeneracy. This was especially apparent when developing the direction prediction algorithm which used the Compton continuum scatter-in library as the comparator of scattergrams which had encoder inconsistency issues.

So, the accuracy results, presented next in Chapter V should only be interpreted in the context of a "best" direction prediction result (i.e. one *s* value, from the source direction prediction to the actual angular placement), but with the next closest LS and MAC results graphically displayed to help the reader in interpretation of the data. This is especially useful when the DRM comparisons fail to provide an accurate prediction.

4.9 Scatter-in and Compton Libraries Degeneracies

Finally, a last numerical investigation was conducted to compare the developed DRMs to themselves to look for regions of degeneracy in the chosen RSM designs, this gave insight to and expectations of the experimental results, which are presented in Chapter V. Figure 62 shows the

comparison of the FitzGerald design over the entire 64,440 individual DRCs in the DRM. The diagonal line is associated with matching the reference modulation curve to itself, while points present elsewhere indicate close similarity of two modulation curves (i.e. high MAC value) within the other possible DRCs of the library. The equation for determining the MAC value was defined earlier as Equation (17).

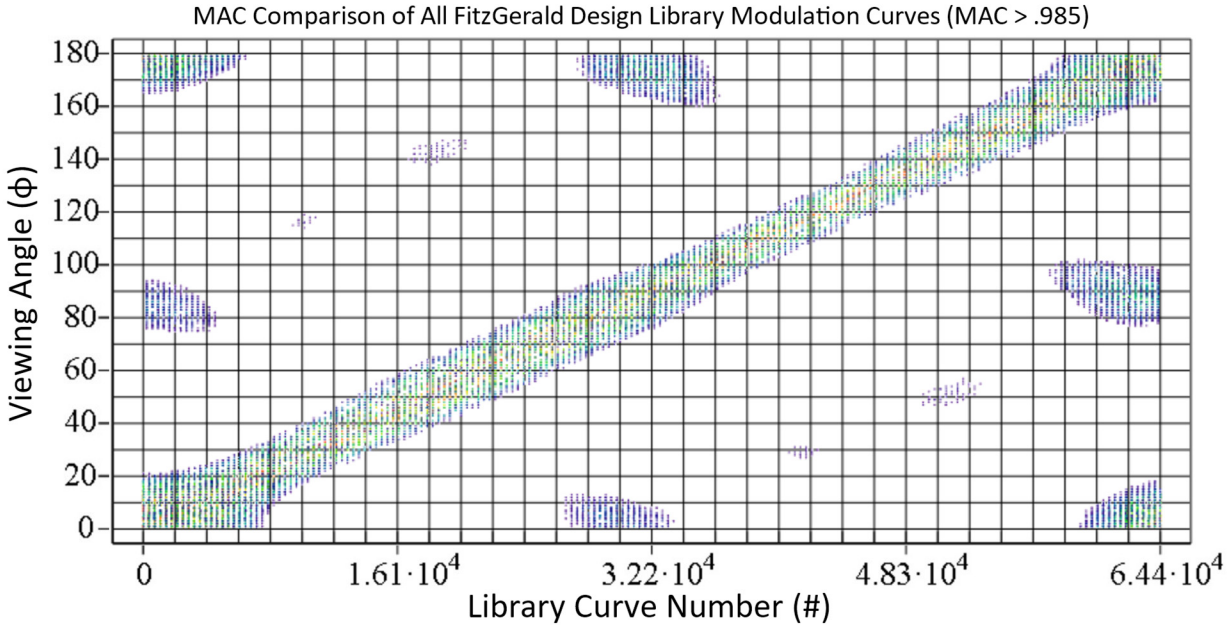

Figure 62. Structure is seen, and therefore degeneracies or potential ghost imaging problems are expected, especially if noise is a factor in the experimental scattergrams. The diagonal is a comparison of the modulation curve to itself (i.e. μ = 1).

Perhaps a better way of displaying the results of the degeneracy investigation is shown in Figure 63 and Figure 64 below. If the left-hand side of the figure is the actual angular position of the source, we can see that regions exist in opposite octants of the design where the expected modulation curves are very similar and could thus lead to false position identification.

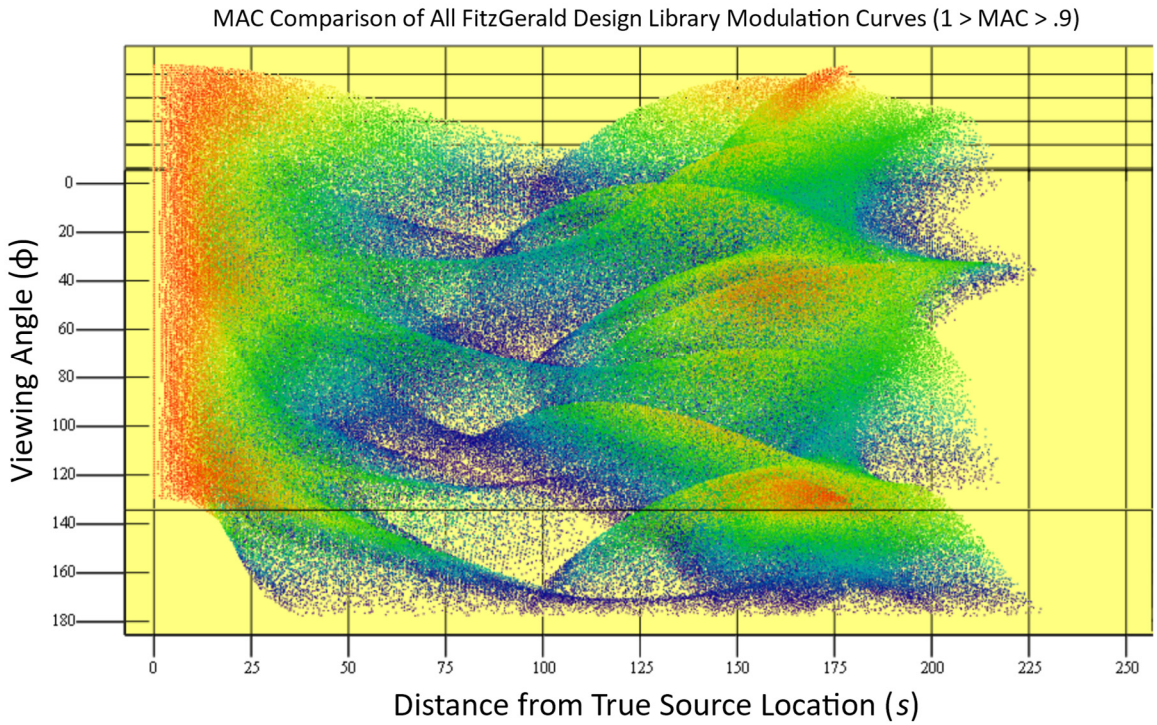

Figure 63. Fitzgerald RSM design MAC map of the comparison of a particular viewing angle baseline modulation curve to all others within the DRM. Structure is seen in terms of distance from the true source and corresponds to degeneracies in the design.

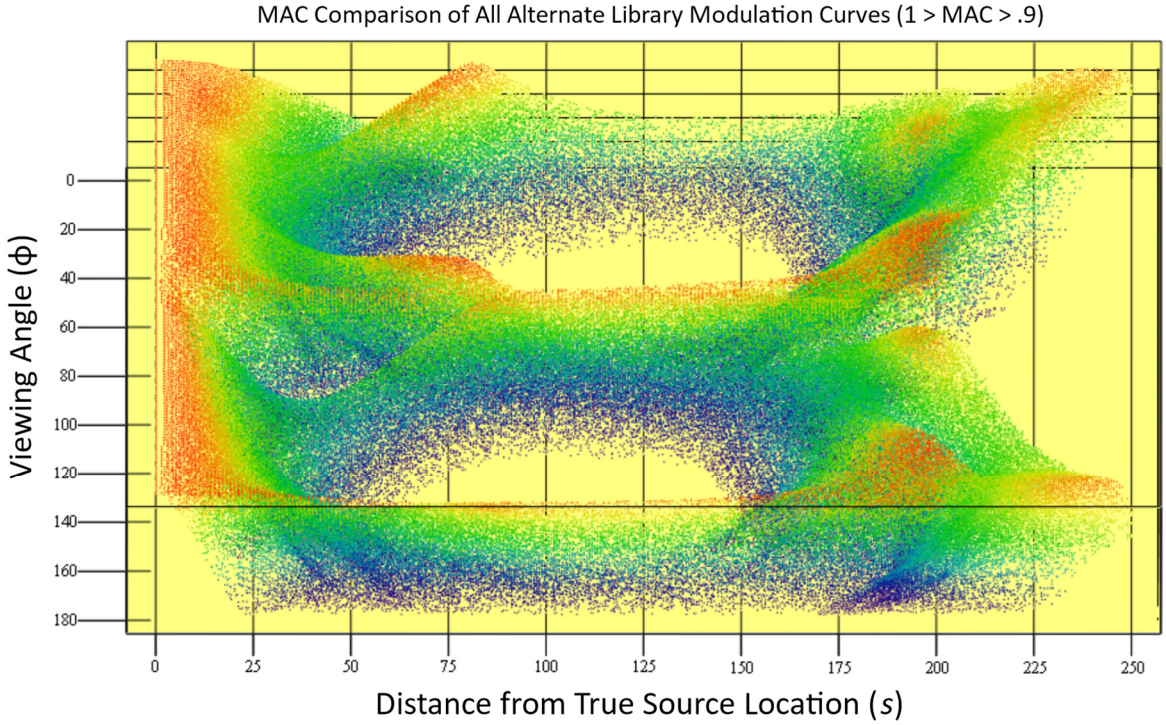

Figure 64. Alternate RSM design MAC map of the comparison of a particular viewing angle baseline modulation curve to all others within the DRM. Structure is seen in terms of distance from the true source and corresponds to degeneracies in the design.

V. Results, Analysis, and Conclusions

5.1 Introduction

As a foreword to these results and as addressed in the Literature Review of Chapter I, at the time these data were taken (2016) all the results were novel and first-of-their-kind. However, this work was not finished while in-residence at AFIT. In the intervening time until this publication, many of the results were repeated and extended, and they were reported in the literature by follow-on AFIT students. The efforts to recover partial data sets after encoder ring fault, the phoswich inclusion to the large RSM, the gridded position search routine of the same energy, two source location deconvolution, and the miniaturization, test, and characterizations of the small RSMs remain as the novel results presented here. These results are therefore grouped together at the end of this Chapter and specified in the Original Contributions section of Chapter VI. These are in addition to the development of the analytic modeling and fitting method and the large RSM assembly as already described.

For the primary data sets, the large RSM was setup to take a total of 18 data points, accounting for viewing angles (φ) between 5° and 175° in increments of 10°. Both the Cs-137 #1 and the multinuclide source were used separately at the incremental source placement positions. These 36 primary data sets were taken with the standard 3”x3” NaI(Tl) and start the Results review. Various other source direction determination investigations were then conducted with sources at the same or different locations and are reported on. And finally, the phoswich detector was integrated into the large RSM system not only utilizing the primary Cs-137 #1 source but also including a Co-57 rope source wrapped around the backend of the support tube to augment and simulate backscatter.

For the small RSMs, a total of 72 data sets were recorded over the two designs, using the Cs-137 #1 and multinuclide sources separately. The sources were placed in the same 18 angular direction positions used in the large RSM data collection for consistency of the investigation.

The totality of the data taking effort is shown in Table 2. One can see that a combination of both the large and small RSMs, along with the various detectors utilizing several sources, source positions, and conditions (elevated background) were measured in the data taking schema for this first RSM baseline investigation. Collection effort time for the large RSM was set at 24 hours per data set, while the smaller RSMs with the $LaBr_3$ detector were 12 hours in length.

Table 2. Totality of collection effort.

	RSM Data Collection Effort					TOTAL: 120 Days
	Large Mask			Small Mask		
	Fitzgerald's Design Standard NaI*			Toy Size Fitzgerald Design LaBr**	Toy Size Alternate Design LaBr**	
	Cs-137	Multinuclide	Cs-137/Am-241	Ba-133/Cs-137	Ba-133/Cs-137	Totals:
10 degree spacing over range of Phi:	18 points	18 Points		18 Points/18 Points	18 Points/18 Points	72 days
Additional for MCNP Comparison:	2 points	2 points				4 days
35,45,55 & 125,135,145 degrees w/elevated background:	6 points	6 points				12 days
Distributed 2-point source investigation:	1 point	1 point				2 days
Hide and Seek:			2 points			2 days
Total:	27 days	27 days	2 days	18 Days	18 Days	92 days
	Fitzgerald's Design NaI/CsI Phoswich*					
	Cs-137	Multinuclide	Cs-137/Am-241			
35,45,55 & 125,135,145 degrees:	6 points	6 points				12 days
35,45,55 & 125,135,145 degrees w/elevated background:	6 points	6 points				12 days
Distributed 2-point source investigation:	1 point	1 point				2 days
Hide and Seek:			2 points			2 days
Total:	13 days	13 days	2 days			28 days
	* 24 hours collection			** 12 hour collection		

5.2 Proof-of-Concept

For the original, first of its kind Proof-of-Concept work, a relatively small (6”x6”x6”) RSM of FitzGerald’s design was 3D printed out of a mix of available photon activated/UV cured, material from one of the older 3D machines at the AFIT Modeling and Machine Shop. This was done after the completion of the computational model and further justified the initial expense associated in procuring the original HDPE cylindrical bulk material planned for manufacturing. The material and scattering properties of this composite mix are unknown. Since CHO polymers have similar average atomic numbers, the density-normalized scattering cross-sections are

expected to be nearly the same even though the density for polymer materials varies in a narrow range around 1 g/cm^3 [45].

While the computational models created up to that point appeared to justify the attenuation-by-scatter theory of the FEP as the primary interaction, an actual hardware demonstration to verify such was desired. FitzGerald's MCNP® model and the advanced model developed here seemed to indicate that the RSM should function as desired, but the amount of scatter and therefore depth of the experimental scattergram troughs compared to the normalized peak value was truly unknown for this proof-of-concept build. This small-scale attempt was designed to lessen the total investment risk.

The proof-of-concept RSM, in conjunction with the small, Saint-Gobain $LaBr_3$ detector was mounted to a reinforced cardboard backing and hand rotated in 10° increments, for a total of 36 scattergram data points as shown in Figure 65. The Cs-137 source #1, characterized in Table 1, was placed at the viewing angle $\varphi = 45°$ at a distance of approximately 1 meter. Gamma interactions and counting data statistics, such as detector deadtime, were recorded via ORTEC's GammaVision software package. The dwell time for each point was 5 minutes. As noted previously, the RSM design is intrinsically based on the shape of the scintillator crystal that is planned to be used within it. In this case, it was recognized that the extruded cube shape of the $LaBr_3$ detector was not compatible with the design. However, it was expected that the system would produce an approximate scattergram for validation. The preliminary results are shown in Figure 65.

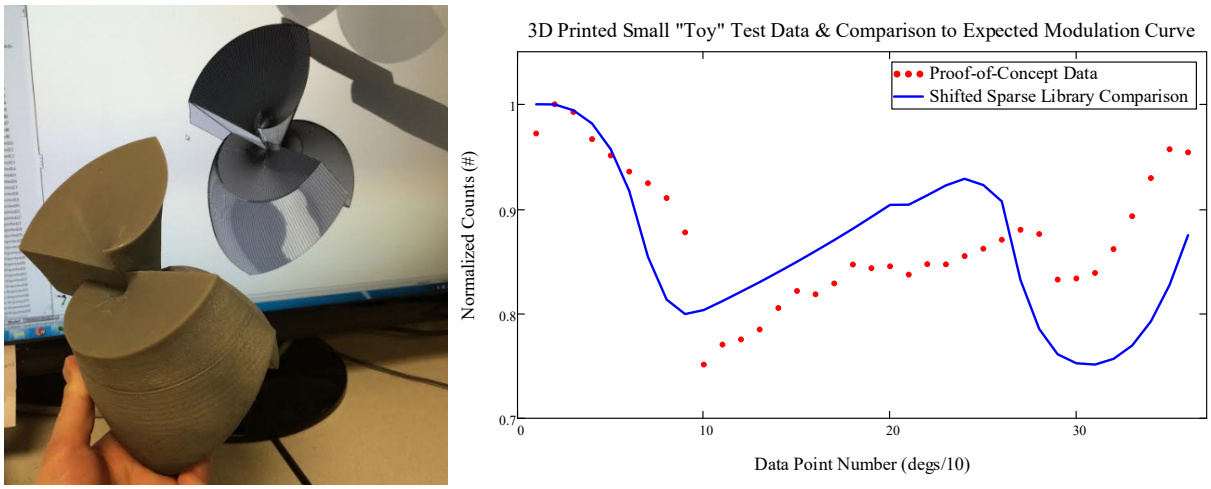

Figure 65. Initial "toy test" data comparison to analytic, computational library.

The library modulation curve has been linearly stretched to ensure the maximum and minimum line up with the corresponding experimental values. While the general shapes are in agreement, one can easily see that the matching of the scattergram to library fit needed further refinement. But, given the relatively successful shape matching, as seen, even while using a size/shape detector and material for which the library was not calculated to match, it was decided to move forward with procurement of the large HDPE stock. While this investment was eventually overcome by tooling path/milling technical difficulties, as previously described, the success of this small-scale, proof-of-concept was enough evidence to justify further investment.

5.3 Large RSM with Cs-137 Source (Data Sets 1-18)

Introduction

The first set of data acquired on the large, FitzGerald design RSM used the Cs-137 #1 source listed in Table 1. Each viewing angle, φ, was recorded for a 24 hour period and produced .txt files of the waveform captures in excess of 4 GB (or about 4.5 million individual waveforms), while the theta, θ, rotation rate was held constant at about ~2° per second.

The energy spectra for all data collected over the period was used to visually identify and manually bracket the Cs-137 #1 source FEP energy range. As well, the Compton continuum range

was defined as all the recorded interactions less energetic than that of the lower bound of the FEP. A final scattergram was also constructed by opening the entire energy range considered to include all of the 1098 available bins. This resulted in the creation of three separate scattergrams for comparison to the DRMs. The FEP binning scattergrams showed excellent source direction predictions when using the attenuation by scatter-out DRM developed in Chapter II, and the results were used to characterize the resolution of the system. The entire energy range was expected to give adequate direction prediction results, as the total area under the peak of the FEP is the majority of the recorded data and it did. As well, source gammas that down-scattered in the active region but did not scatter out of the way of interaction of the detector, would result in the Compton portion of the spectra retaining scattergram information similar to the shape expected according to the scatter-out library. The scatter-in library, used in conjunction with the Compton continuum energy binning generally showed less accuracy and resolution than the scatter-out FEP results. Nevertheless, it did show many locations in good agreement, and so is the first (and only RSM system to date) to have used this portion of the spectra for source direction prediction.

Results

An example of the energy spectrum of the total collection, the manual bracketing of the energy ranges of interest, and the three resulting scattergrams are shown in Figure 66. This figure also contains an example of the results of the DRM position library match, after amplitude fit adjustments were made to the original library file, as described in Chapter IV. This adjustment accounts for the actual size and material of the final RSM experimental build, compared to the computationally generated models. This fit is governed by the implementation of Equations (15) and (16), as described in Chapter IV. Both the LS and MAC methods of determining the most probable source direction were used and results are visualized in Figure 67. The black dot indicates

the known source placement, while the subsequent small white dots for the MAC heat maps and the color-coded dots for the operator style display show the next closest position predictions. These additions are used to inform the reader of the relative closeness of the degeneracies present in the RSM design. In this case, they start to appear within 5% of the total 64,440 potential source direction curves as the DRM is polled.

Notice in Figure 66 that there are in some cases, considerable distance between the normalized number of counts (y-axis) between certain rotation angles θ. This noisiness between adjacent points of the modulation curves is due to binning of the peak waveform values and the encoder rotational angle data taken at the time of acquisition. It was not expected based on the numeric model for the total counts in the bin (on the order of 20,000 per bin degree) and for the 72,000-line encoder ring resolution. Originally, it was hypothesized that this was due to errors in the encoder reader preferentially favoring some angles, possibly due to inconsistent RSM rotational velocity. The lopsidedness (off-axis moment of inertia) of the RSM's mass distribution, and the limits of performance of the torque multiplication system (which did sometimes exhibit sticking or jerking vibrations when the lubrication used between the support tube structure and the acrylic RSM was not adequately maintained) were thought to cause inconsistencies in the operation of the encoder reader. However, a 48 hour data set, with approximately twice the counting showed a 50% reduction in the previously described noise of the scattergram, so the encoder was accepted as properly functioning. Therefore, to try and facilitate a better match to the computational model lookup DRC of the known source placement, a simple smoothing by averaging the nearest neighbors to every degree of rotation was conducted. Nearest-neighbor points of 5, 10, and 20 points on either side of the raw data were averaged to investigate. The resulting scattergrams were then renormalized and compared against three separate DRMs, each

of which incorporated the same averaging methods of 5, 10, and 20 nearest neighbors. Smoothing qualitatively looked to give better visually agreement between the scattergrams and library DRC curves, but the resultant distance to true placement, did not show significant quantitative improvement. This is seen in the averages and standard deviations at the bottom of Table 3.

While only the raw scattergram data and best match DRC and the source prediction results are pictorially presented in Figure 66 and Figure 67 respectively, the three smoothing algorithms were used on all three energy regions of interest in the Cs-137 #1 source recorded spectra. As an addition to the advanced model developed in Chapter II, addition modeling efforts in conjunction with these first experimental data were undertaken to improve the source direction prediction accuracy of both DRMs, as previously described. Therefore, the results presented throughout are that of the experimentally calibrated libraries.

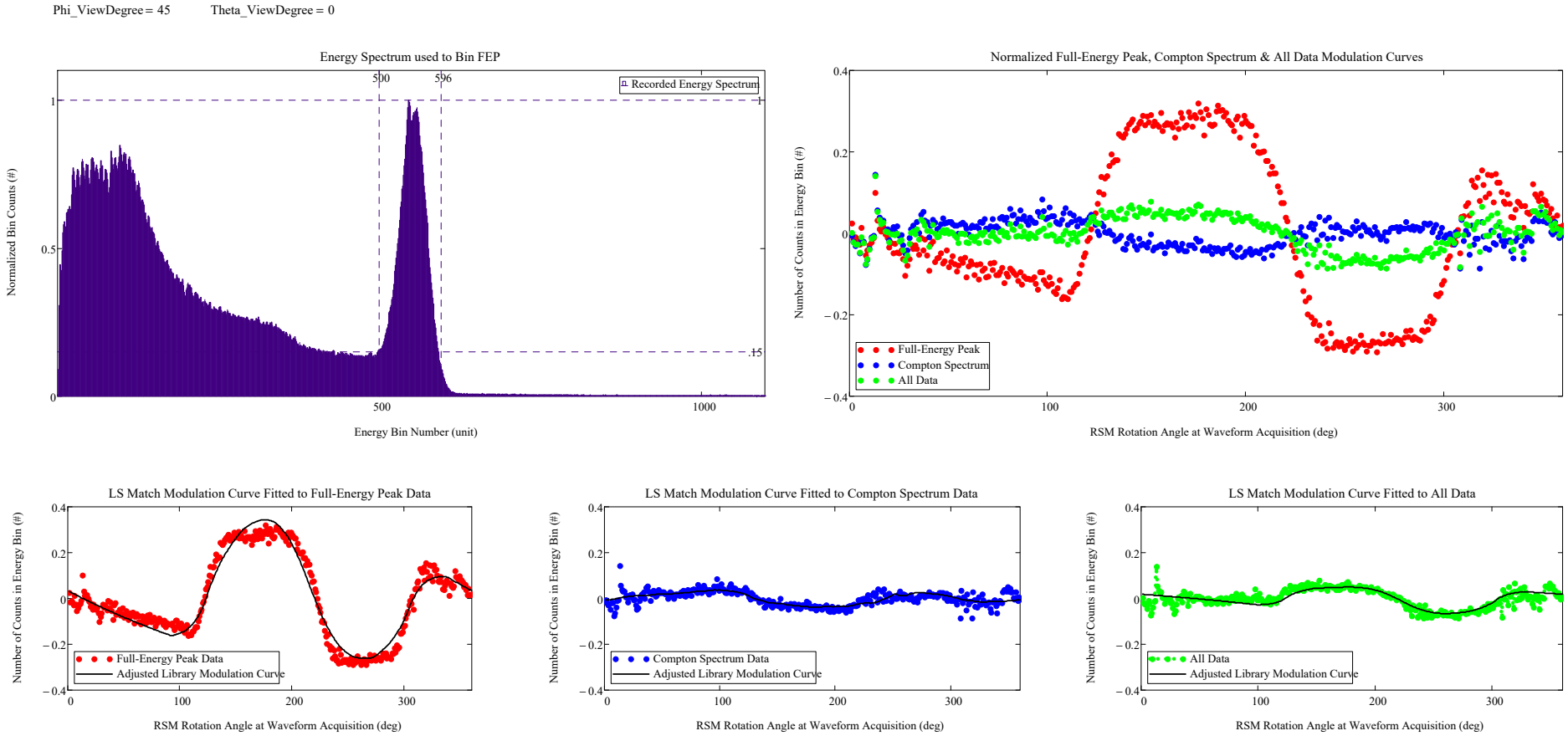

Figure 66. Example of large RSM, FitzGerald design Cs-137 #1 source recorded data at a viewing angle of φ = 45°. The total energy spectra recorded, and well as the FEP and Compton portions used for binning are marked. The resultant raw scattergrams and their library position match modulation curves are shown.

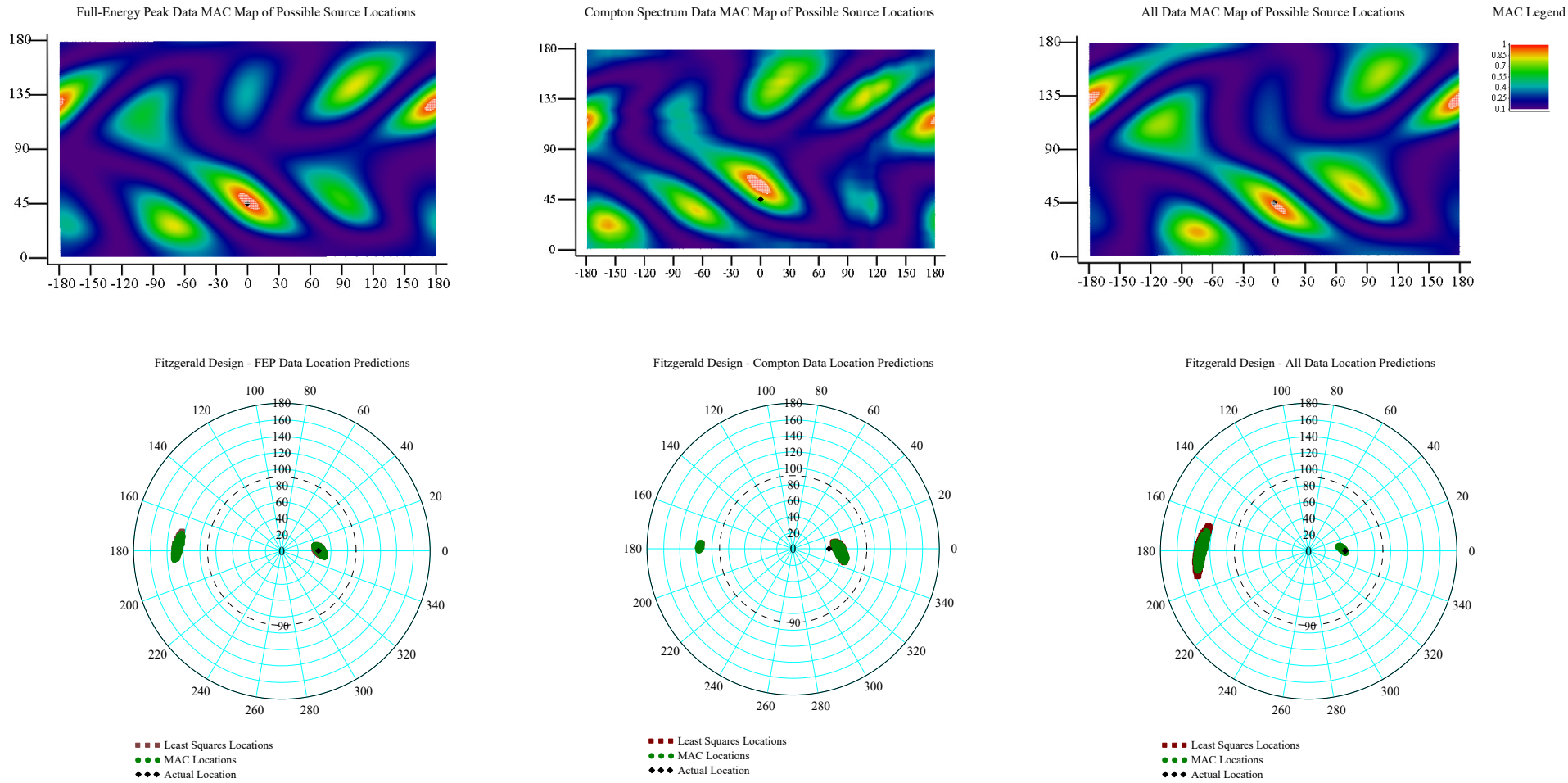

Figure 67. Example of large RSM, FitzGerald design Cs-137 #1 source point source direction prediction displays at φ = 45°. MAC result heat maps of the scattergram to library comparisons. The black dot indicates the known source direction, while the subsequent overlaid white dots (seen in the high MAC value regions) on the heat maps (top) and color-coded dots for the operator style display (bottom) show the next closest predictions. Normally, the LS and MAC results overlap in the polar plots, but in some cases they are distinct.

In addition to these new experimentally calibrated DRMs, Logan's GEANT and MCNP® generated libraries of modulation curves for the FEP portion of the spectra were compared to the entirety of the experimental data for the large RSM. This was seen as a good test/verification of the experimentally calibrated advanced model, since the viewing angle data sets were the same and she used the SolidWorks model developed here. However, her models used a binning scheme in θ of 5° increments. Therefore, for direct comparison, interpolation of every four points between the RSM rotational angles defined by her models was accomplished. With her libraries slightly modified by linear interpolation, the developed MathCAD routine of this work compared her DRM library results. It should be pointed out that her GEANT libraries added structures to replicate the RSM support structure, detector, and other laboratory structures in an effort to more closely match the real environment. Her MCNP® work, like the models developed here, assumed only the source, mask, and detector to exist isolation. In addition, both models used variance reduction (i.e. non-isotopically emitting source, to further speed up the simulation process). As well, her models did not use as many incident particles (approximately 400,000) [34] for modulation curve generation, compared to the ~4.5 million that constitute these experimental results. Based on the relative success of her models, shown in Table 3, it is suspected that the experimental results presented here are oversampled, and that good predictions could have been made with much smaller data sets. This will be addressed later. For now, the results of the interpolation of her models are shown in Figure 68.

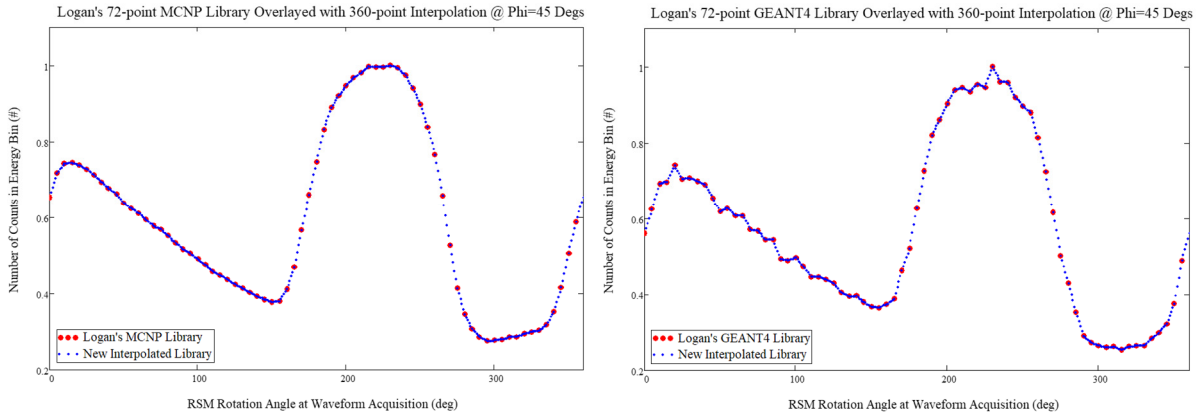

Figure 68. Logan's modulation curve library work and interpolation to move from 72 to 360 values over a full rotation of the RSM. The MCNP® generation (left) compared to the "noisier" looking GEANT (right).

With the addition of Logan's two DRMs, comparison of the smoothing methods across all four models (original, experimentally calibrated, Logan's MCNP, and GEANT), of the FEP results for each of the 18 viewing angles was made. Each of the 288 results presented in Table 3, are calculated distances from the MAC predicted source direction to the known, true placement in accordance with the, *s*, distance metric of Equation (17). They are presented in columns of four groups, to separate the smoothing methods tried. Within the grouping, four additional columns are used to display the results of the individual models. Notice that the four models used in this comparison were also generated as smoothed versions of themselves for the smoothed scattergram comparisons. Therefore, at each viewing angle, a total of 16 different DRMs were polled over all allowed source positions, with the highest resultant MAC value being used in conjunction with its associated φ and θ position values to find the error/distance between the source and prediction. Of critical note, the fitting of each library file to the scattergram before MAC calculation, and subsequent distance evaluation did not use the scaling method characterized by Equations (15) and (16). Rather, the initial max/min stretching method was used in these cases, as previously described. This is why comparable distance metric points for Table 3 and Table 4 do not match exactly with regard this works FEP scatter-out DRM library.

Table 3. Large RSM, NaI(Tl), Cs-137 #1 Source - Raw experimental and smoothed FEP scattergrams best MAC value DRM comparison DRM libraries. Lowest distance value, *s*, per smoothing method per row is shaded in green, while the highest is shaded in red.

		"Best" Fit Distance (s): Large RSM w/ NaI - Original, Experimentally Fit, and Logan's MCNP and GEANT Smoothing Comparison															
		No Smoothing				5-Point Smoothing				10-Point Smoothing				20-Point Smoothing			
Data Set #	View Deg	Org Fit Lib	Exp Fit Lib	Logan's MCNP	Logan's GEANT	Org Fit Lib	Exp Fit Lib	Logan's MCNP	Logan's GEANT	Org Fit Lib	Exp Fit Lib	Logan's MCNP	Logan's GEANT	Org Fit Lib	Exp Fit Lib	Logan's MCNP	Logan's GEANT
1	5	15.6	207.5	21.5	11.0	206.7	209.5	21.5	11.0	176.6	176.9	24.0	17.0	176.6	176.9	24.0	19.0
2	15	3.6	4.1	16.0	10.0	3.6	3.6	16.0	10.0	3.6	3.6	16.0	10.0	3.6	3.6	16.0	10.0
3	25	4.5	3.2	11.0	6.0	3.2	2.0	11.0	6.0	3.2	2.0	11.0	5.0	2.0	2.0	11.0	5.0
4	35	1.4	1.4	9.0	4.0	1.4	2.0	9.0	5.0	1.4	2.0	9.0	4.0	1.4	2.0	9.0	4.0
5	45	2.0	1.4	9.0	4.0	2.0	1.4	9.0	4.0	2.0	1.4	9.0	4.0	1.4	1.4	9.0	4.0
6	55	1.4	2.0	8.0	3.0	2.0	2.0	8.0	3.0	2.0	2.0	8.0	3.0	1.4	1.4	8.0	3.0
7	65	3.0	3.2	8.0	3.0	2.2	2.0	8.0	3.0	2.2	2.0	8.0	3.0	3.0	2.0	8.0	4.0
8	75	2.2	2.0	8.0	4.0	2.2	2.0	8.0	3.0	2.2	2.2	8.0	3.0	2.0	2.8	7.0	3.0
9	85	2.2	2.2	9.0	3.0	2.2	2.2	9.0	4.0	2.2	2.8	8.0	4.0	3.2	4.2	8.0	3.0
10	95	5.7	3.2	8.0	3.0	4.2	3.2	8.0	3.0	4.2	3.2	7.0	3.0	5.0	3.2	7.0	2.0
11	105	6.4	5.0	9.0	15.6	6.4	6.4	9.0	3.0	6.4	6.4	9.0	15.6	7.8	7.8	20.6	15.6
12	115	4.5	2.2	6.0	1.0	2.2	1.0	6.0	1.0	2.2	1.0	6.0	1.0	2.2	1.0	6.0	1.0
13	125	7.1	7.2	16.0	11.0	7.1	7.2	16.0	11.0	7.8	7.2	16.0	11.0	7.8	7.6	17.0	11.0
14	135	7.1	7.2	12.2	10.2	7.1	7.2	12.2	10.2	7.1	7.2	12.2	10.2	7.2	7.2	12.2	10.2
15	145	7.8	7.8	15.0	9.0	7.8	7.8	15.0	9.0	7.8	7.8	15.0	9.0	7.8	7.8	15.0	9.0
16	155	9.5	9.5	6.0	1.0	9.5	8.2	6.0	1.0	9.5	9.8	6.0	1.0	9.8	9.8	6.0	1.0
17	165	21.0	20.0	14.1	11.2	20.0	19.0	14.1	11.2	20.0	20.0	14.1	11.2	20.0	20.0	13.5	10.8
18	175	289.6	102.6	21.0	291.7	284.8	282.8	284.3	292.5	285.2	282.1	283.6	287.6	285.2	282.1	283.6	290.0
Average		21.9 ± 65.1	21.8 ± 50.5	11.5 ± 4.6	22.3 ± 65.5	31.9 ± 76.8	31.6 ± 76.9	26.1 ± 62.7	21.7 ± 65.8	30.3 ± 73.3	30.0 ± 72.8	26.1 ± 62.6	22.4 ± 64.5	30.4 ± 73.3	30.2 ± 72.8	26.7 ± 62.5	22.5 ± 65.1
"Good" Viewing Angles Avg		4.2 ± 2.2	3.7 ± 2.2	10.3 ± 3.1	6.2 ± 4.1	3.8 ± 2.2	3.6 ± 2.4	10.3 ± 3.1	5.4 ± 3.2	3.9 ± 2.3	3.6 ± 2.3	10.2 ± 3.2	6.1 ± 4.1	4.0 ± 2.5	3.9 ± 2.5	11.0 ± 4.3	6.1 ± 4.2

* "Good" Viewing Angles are 15° - 145°

Table 3 has been color coded to show the best match (smallest *s* value) distance across each row per smoothing method. The shortest distance between the actual, known source position and the prediction is shown in green, the farthest in red, and intermediate values are light blue. Distances can be considered good matches if the total distance is less than or equal to 2.0. This should be the upper limit of an ideal RSM/detector combination, for library files at every φ and θ in 1° (angular resolution) increments if the DRM model is correct and uncertainty in the scattergrams is low. The color coding clearly shows that both the original advanced model and the experimentally calibrated advanced model work well. Logan's MCNP® and GEANT models also give solid predictions, particularly GEANT, which certainly modeled the φ = 155°, 165°, and 175° viewing angles better than the models developed here, as it accounted for material removal required for the detector placement. Careful inspection of the averaged values and standard deviations reported in each column show no real benefit to using smoothed scattergrams however (and their associated smoothed DRM library for direction determination). The 5-point smoothing routine produced slightly better results than the unmodified raw comparisons; but overall, the improvements attributed to the smoothing methods for the experimental fit advanced model were not significant compared to the unsmoothed data (i.e. < 0.1 change in the distance metric).

Based on the smoothing comparison results, and since this was first-of-its-kind data, it was decided that the raw data sets should be reported as a baseline. Smoothing was therefore abandoned for the rest of the experimental and the experimentally calibrated advanced model was used for all subsequent data set comparisons. This does, however, leave room for future analysis of the data sets and comparison of various smoothing methods and models. It is worthwhile to note, that while only the MAC comparison method results are shown here, the LS method results also performed well. In some cases, outperforming the MAC method, so benefit would certainly be found through a rigorous, computationally based RSM model design and results simulation study.

As well, since Logan's GEANT developed DRM was also found to have superior prediction characteristics compared to her MCNP® model when compared to the experimental scattergrams, the observed smoothness versus irregularity differences between the two models, as seen in Figure 68, is very interesting. The GEANT and experimental results seem to indicate that ideal smooth scattergrams should not be expected in a real-world environment due to complex background, scattering interactions. Her MCNP® and GEANT transport models used "identical volumes, materials, and sources" [33] however, so one would expect a better agreement between the two. The cause of the differences is unknown and so should be further numerically investigated. Additionally, better predictions from both of Logan's libraries might have occurred if a higher number of gamma interactions were used during simulation and if she calculated the expected modulation curves using a 1° binning scheme. These would come at a significant processing time expense however, as each modulation curve for a particular viewing angle already took approximately 6 hours to generate [34]. These questions could be answered through further complex modeling efforts using both the GEANT and MCNP® industry standard codes.

However, a quick, simple approach using the modeling work developed here could also be done in a more expeditious and computationally optimized way. It is noted that the limits of the experimentally calibrated advance model did "max out" the upper search limit for two of the adjustable parameters during development. This indicates that even though it has the best overall performance to date [2] [3] for these data sets in particular (and the Fitzgerald design specifically), the advanced model and the experimentally calibrated library model could still be improved.

Results of the initial large, FitzGerald RSM for all three defined energy regions of the spectra are presented in Table 4 comparing both the MAC and LS determination methods used. The total spectra comparisons show that some source direction determination might be made under certain circumstances without any bracketing of the spectra when used in conjunction with the FEP scatter-out DRM, but it is inaccurate. Therefore, the total spectra comparison is not presented for the rest of this work after being reported on here. These results show that source direction determination works well using the FEP scatter-out but less so for the Compton continuum scatter-in DRMs, especially over $\varphi = 35° – 145°$, defined as the good viewing angles. Further, the high-valued distances are in most cases not as disastrous as they appear. The reader is encouraged to review Appendix A.1. Here, they will find that in many of the high cases, the value is based on scattergram/library DRM comparison matching to an expected degenerate area of the RSM. This is expected to improve through further model development and reduction of the persevered noisiness/uncertainty in the scattergrams with further experimental improvements. In most cases though, the additional display of the next 50 closest matches (or < 0.1% of total), shows that the actual source direction may still be obtainable, if the degenerate region can be identified and removed. Finally, an exact experimental scattergram/DRM library match to the true, known

source placement would be $s = 0.0$. This was not observed in any of the data sets, so it was thought the RSM system might have had a slight, systematic misalignment and this was investigated.

Table 4. Large RSM, NaI(Tl), Cs-137 #1 Source - Raw Experimental Mod Curves, Library Closest Fit "Distance" to Actual Position for LS and MAC Methods for the Cs-137 FEP and Compton continuum from spectra.

		LS Best Match Distance from Actual			MAC Best Match Distance from Actual		
Data Set #	View Deg	Bracketed FEP	Compton Continuum	ALL Spectra Data	Bracketed FEP	Compton Continuum	ALL Spectra Data
1	5	227.903000	132.004000	183.576000	226.632000	117.154000	117.273000
2	15	228.037000	139.119000	64.413000	226.374000	141.778000	69.527000
3	25	218.577000	126.210000	63.600000	218.577000	115.000000	65.803000
4	35	2.000000	121.017000	70.838000	3.000000	85.586000	69.080000
5	45	1.414000	13.000000	199.489000	2.236000	14.318000	198.588000
6	55	2.000000	13.928000	70.831000	2.236000	14.560000	191.838000
7	65	4.123000	9.000000	166.469000	2.236000	11.180000	165.076000
8	75	3.000000	6.000000	175.966000	2.236000	6.083000	173.217000
9	85	2.236000	5.099000	88.051000	2.000000	2.828000	91.022000
10	95	3.162000	179.338000	71.176000	3.606000	176.409000	71.694000
11	105	6.403000	180.878000	20.518000	6.403000	178.059000	17.029000
12	115	1.000000	182.003000	13.454000	1.414000	182.964000	11.402000
13	125	7.211000	14.000000	12.042000	7.810000	188.162000	11.000000
14	135	7.810000	13.153000	11.045000	7.810000	13.038000	10.198000
15	145	7.810000	11.180000	12.649000	8.485000	89.454000	11.705000
16	155	219.477000	141.152000	155.322000	219.477000	140.456000	152.552000
17	165	223.403000	114.000000	157.867000	222.423000	115.000000	155.000000
18	175	40.000000	96.167000	107.019000	44.045000	93.606000	107.005000
Average:		66.98 ± 97	83.18 ± 68	91.35 ± 64	67.06 ± 97	93.65 ± 66	93.83 ± 65
"Good" Viewing Angles: 35°-145°		4.01 ± 2	62.38 ± 73	76.04 ± 62	4.12 ± 76	80.22 ± 73	85.15 ± 69

Large RSM Alignment and Uncertainty Analysis

Due to the results shown, it is strongly suspected that the RSM system angular calibration was systematically misaligned by about 3° in either φ, θ, or both. To determine if any systematic error in the alignment of the experiment existed, Table 6 was developed. When determining the overall error of the RSM's library match to the experimentally derived modulation curve, it is recognized that there are a variety of ways to introduce uncertainty into the measurement.

Since the scattergram itself is composed of the count of source FEPs (or energy regime of interest) and the relative rotation angle, θ, it should in fact have error bars associated with its display. However, the total number of waveforms captured that meet the energy window criterion was normally on the order of tens of thousands for any given 1° binning of the rotation angle. After normalization to the highest bin count value, the calculated error based on counting statistics, is small and on the order of 10^{-1} of the arbitrary units of the normalized display and are not normally

displayed when presenting the graphical results. There is also some uncertainty in bracketing the energy regions, and in the determination of the down-sampled waveform "peak" energy (on the order of ~5%). Finally, uncertainty in the rotation angle is also exceedingly small, since the Renishaw encoder ring has 72,000 discreet values, making each 1° bin 200 holographic lines wide. No attempt was made at estimating this horizontal bin uncertainty value.

If misalignment is present, it is still possible to compare the experimentally fitted advanced model library DRM for the actual placed source position and the scattergram results. One would expect however that as misalignment grows, the agreement of these two curves will decrease. However, it gives good insight into the accuracy of the developed models and if misalignment is present, based on adding the counting uncertainty to the scattergrams and seeing if the library points fall inside the bounds. This is shown for both the FEP and Compton continuum portions of the spectra below, at $\varphi = 115°$, in Figure 69. While the representative plot shows the error bars on the scattergram as a value of 2σ, Table 5 shows the tallied results of overlap between the uncertainty bounds of the scattergram and the library curve at 1, 2, and 3σ. All results from this investigation for the different viewing angles are presented in Appendix A.1.2.

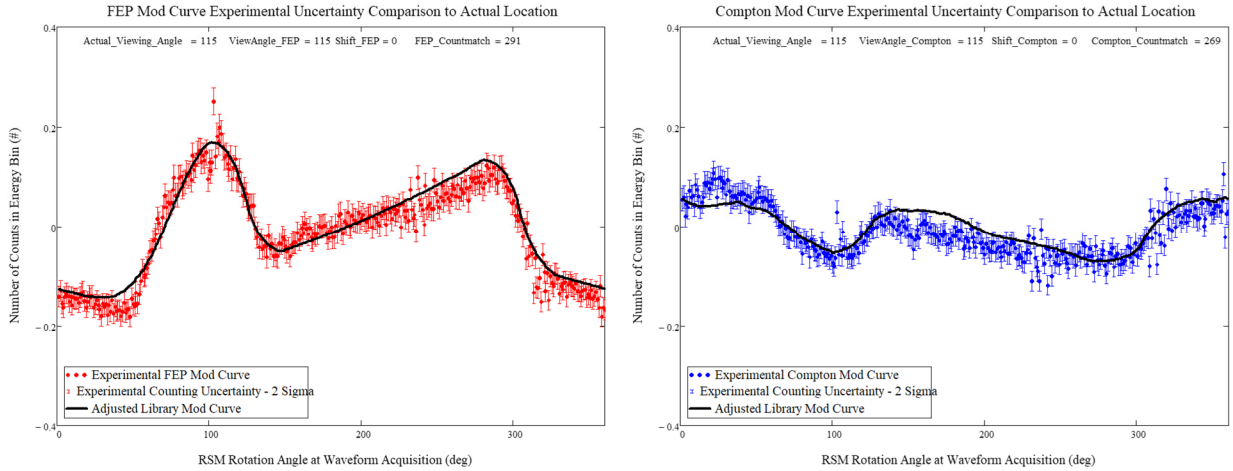

Figure 69. Left: Comparison of the advanced model to the experimental scattergram with counting uncertainty included to the actual, placed position of the source DRC for the FEP region of the energy spectrum. Right: Comparison of the Compton continuum energy range experimental scattergram to the known source placement DRC.

Table 5. Uncertainty results associated with adding counting error to the scattergram and determining how many of the 360 points of the library modulation curve fall within these bounds for the actual source placement.

Source Actual Location Comparison to Library of the DRM Modulation Curves

1 SIGMA		FEP Mod Curve		Compton Mod Curve	
Set #	View Angle	In Bounds #	%	In Bounds #	%
1	5	116	32.2	242	67.2
2	15	127	35.3	225	62.5
3	25	183	50.8	206	57.2
4	35	180	50.0	176	48.9
5	45	146	40.6	205	56.9
6	55	151	41.9	216	60.0
7	65	158	43.9	229	63.6
8	75	189	52.5	230	63.9
9	85	221	61.4	245	68.1
10	95	203	56.4	236	65.6
11	105	179	49.7	220	61.1
12	115	217	60.3	196	54.4
13	125	188	52.2	168	46.7
14	135	184	51.1	208	57.8
15	145	162	45.0	221	61.4
16	155	176	48.9	197	54.7
17	165	160	44.4	210	58.3
18	175	262	72.8	232	64.4
Avg Overall		177.9 ± 33.8	49.4 ± 9.4	214.6 ± 20.6	59.6 ± 5.7
Avg "Good" view angles 35°-145°		155.6 ± 23.3	43.2 ± 6.5	182.1 ± 22.3	50.6 ± 6.2

2 SIGMA		FEP Mod Curve		Compton Mod Curve	
Set #	View Angle	In Bounds #	%	In Bounds #	%
1	5	199	55.3	281	78.1
2	15	209	58.1	292	81.1
3	25	260	72.2	281	78.1
4	35	229	63.6	262	72.8
5	45	213	59.2	260	72.2
6	55	220	61.1	270	75.0
7	65	239	66.4	288	80.0
8	75	261	72.5	292	81.1
9	85	282	78.3	309	85.8
10	95	287	79.7	304	84.4
11	105	259	71.9	295	81.9
12	115	291	80.8	269	74.7
13	125	231	64.2	250	69.4
14	135	226	62.8	270	75.0
15	145	198	55.0	282	78.3
16	155	238	66.1	256	71.1
17	165	212	58.9	280	77.8
18	175	321	89.2	287	79.7
Avg Overall		243.1 ± 34.1	67.5 ± 9.5	279.3 ± 15.9	77.6 ± 4.4
Avg "Good" view angles 35°-145°		209.7 ± 29.4	58.3 ± 8.2	239.4 ± 17.8	66.5 ± 4.9

3 SIGMA		FEP Mod Curve		Compton Mod Curve	
Set #	View Angle	In Bounds #	%	In Bounds #	%
1	5	275	76.4	310	86.1
2	15	268	74.4	319	88.6
3	25	299	83.1	321	89.2
4	35	288	80.0	308	85.6
5	45	259	71.9	298	82.8
6	55	275	76.4	307	85.3
7	65	288	80.0	317	88.1
8	75	310	86.1	326	90.6
9	85	325	90.3	343	95.3
10	95	332	92.2	343	95.3
11	105	316	87.8	333	92.5
12	115	331	91.9	312	86.7
13	125	263	73.1	302	83.9
14	135	248	68.9	314	87.2
15	145	229	63.6	315	87.5
16	155	281	78.1	298	82.8
17	165	252	70.0	316	87.8
18	175	347	96.4	323	89.7
Avg Overall		288.1 ± 32.2	80.0 ± 8.9	316.9 ± 12.8	88.0 ± 3.6
Avg "Good" view angles 35°-145°		247.4 ± 33.1	68.7 ± 9.2	272.7 ± 14.4	75.8 ± 4.0

Table 5 shows that the models do not follow the expected 3-sigma rule for a normal distribution as given by 68-95-99.7%. Rather, for the good viewing angles of the RSM, $\varphi = 35° – 145°$, they are ~50-68-80% for the FEP scatter-out model and ~60-78-88% for the Compton continuum scatter-in model. This result is interesting, taken in conjunction with the distances data presented in Table 4, it shows that while the scatter-in Compton continuum model developed matches the experimental scattergrams better than the scatter-out FEP model, it is not as accurate at source direction prediction. This could be due to the slightly greater noise associated with the generally lower counts of the Compton portion of the spectra after normalization. It could also indicate that the source direction prediction using these scatter-in gammas from other areas of the RSM is more sensitive to the degeneracies associated with the RSM geometry.

However, a judgment about the system performance (accuracy) and the resolution (precision) can still be made, using the distance metric and also by considering the individual φ and θ components of that distance. In this way, the misalignment error and uncertainty in both φ and θ can be estimated. Whether the error propagated through the system based on RSM misalignment, source positioning faults, encoder ring jitter, detector placement (and potential slippage), waveform down-sampling, post-processing and imaging matching code errors, the overall performance of the large RSM in this work can be directly estimated with the distance metric. The distances previously presented retained information on and took into account the direction (i.e. greater than or less than) of the predicted source direction compared to the known source placement in terms of their components. Table 6 shows that using both the LS and MAC methods independently, the average of the components, φ and θ, of the distance between predicted and true position can be easily found. The uncertainty in this average is then found by finding the standard deviation of each column. The average is an estimate of the misalignment (accuracy), while the standard deviation presents the resolution/uncertainty (precision) in the direction prediction. Table 7 repeats this method, but uses just the singularly valued distance metric, *s*, of Equation (17) over the 18 primary viewing angles. Both are of use in that the actual physical distance spacing of θ is much smaller at the poles in spherical coordinates, while the φ physical spacing remains constant throughout. Meaning that the found θ misalignment and resolution could be greatly affected when using a 1° incremented modulation curve library as is done in this work and averaging in values found near the poles. However, due to the similarity of the library curves between the adjacent points and the overall noise seen in the scattergrams at these poles, direct comparisons between the two tables is not easy to make. This is why the data presented as the estimates is based on the average of viewing angles φ = 35° – 145°. Changing the distance metric

to actual arc length on the sphere, instead of a Pythagorean based φ and θ difference may have benefit for future work and comparisons in addition to the needed library improvements.

Using the FEP data results, a slight misalignment when determining θ = 0 is indicated, but good accuracy is found in the φ alignment. The continued combination in quadrature of the φ and θ precision terms of Table 6 indicate a system resolution lower bound on the order of ~4°, which in turn translates into the distance resolution of ~2.5 units (but this is highly dependent on how the individual φ and θ differences from true are distributed, and so may be more weighted to/indicative of the perceived θ alignment shift) of Table 7. These findings are on the order of similar calculations by Logan et al. [33] and Egner et al. [37] when using this RSM or a similar setup. When considering the Compton scatter-in library results of the tables, the data shows that an accurate source direction determination cannot yet be made by this method. However, some of the source placement predictions are within a few degrees (or of reasonable distance) to true, so using this portion of the spectra with a better developed scatter-in reference library in future experiment is warranted. It does appear directionality information can be extracted, but that degeneracies in the RSM design need to be evaluated further.

Table 6. Accuracy and Resolution of the large RSM estimation using both the developed libraries and both the LS and MAC methods, on the components of the predicted source angular position in φ and θ.

FEP Closest Match Comparison

Set #	ViewAngle	Least Squares Method		MAC Method	
		Phi (Δ°)	Theta (Δ°)	Phi (Δ°)	Theta (Δ°)
1	5	-168	-154	-169	-151
2	15	-145	-176	-146	-173
3	25	-124	-180	-124	-180
4	35	0	2	0	3
5	45	-1	1	-1	2
6	55	-2	0	-2	1
7	65	-4	-1	-2	1
8	75	-3	0	-2	1
9	85	-2	-1	-2	0
10	95	-3	1	-3	2
11	105	-4	5	-4	5
12	115	-1	0	-1	1
13	125	6	4	6	5
14	135	6	5	6	5
15	145	6	5	6	6
16	155	127	179	127	-179
17	165	135	-178	136	-176
18	175	0	-40	2	-44
Average over ALL Viewing Angles:		-9.83 ± 73.56	-29.3 ± 87.25	-9.61 ± 73.93	-48.4 ± 77.48
Average (Δ°) of "Good" Viewing Angles 35° - 145°:		-0.17 ± 3.738	1.75 ± 2.278	0.083 ± 3.546	2.667 ± 1.972

Average ϕ Accuracy/Misalignment =	-0.04 °	Average θ Accuracy/Misalignment =	2.21 °
Average ϕ Precision/Resolution =	3.64 °	Average θ Precision/Resolution =	2.12 °
System Resolution = (using Scatter-out DRM)	4.2 °		

Compton Closest Match Comparison

Set #	ViewAngle	Least Squares Method		MAC Method	
		Phi (Δ°)	Theta (Δ°)	Phi (Δ°)	Theta (Δ°)
1	5	-80	105	-6	117
2	15	-65	123	-65	126
3	25	-100	77	0	115
4	35	-89	82	-10	-85
5	45	-13	0	-14	-3
6	55	-13	-5	-14	-4
7	65	-9	0	-11	-2
8	75	-6	0	-6	1
9	85	-1	5	-2	2
10	95	11	-179	12	-176
11	105	26	-179	27	-176
12	115	50	175	50	176
13	125	14	0	58	179
14	135	13	-2	13	1
15	145	11	-2	9	89
16	155	50	-132	48	-132
17	165	0	114	0	115
18	175	92	28	89	29
Average (Δ°) over ALL Viewing Angles:		-6.06 ± 48.93	11.67 ± 94.96	9.889 ± 33.64	20.67 ± 107.2
Average (Δ°) of "Good" Viewing Angles 35° - 145°:		-0.5 ± 31.83	-8.75 ± 91.55	9.333 ± 23.44	0.167 ± 108.1

Average ϕ Accuracy/Misalignment =	4.42 °	Average θ Accuracy/Misalignment =	-4.29 °
Average ϕ Precision/Resolution =	27.64 °	Average θ Precision/Resolution =	99.81 °
System Resolution = (using Scatter-in DRM)	103.6 °		

Table 7. Accuracy and Resolution of the large RSM estimation using both the developed libraries and both the LS and MAC methods, on the calculated distance, *s*, of the predicted angular position.

FEP Closest Distance (*s*) Comparison			
Set #	ViewAngle	LS Method	MAC Method
1	5	227.903	226.632
2	15	228.037	226.374
3	25	218.577	218.577
4	35	2	3
5	45	1.414	2.236
6	55	2	2.236
7	65	4.123	2.236
8	75	3	2.236
9	85	2.236	2
10	95	3.162	3.606
11	105	6.403	6.403
12	115	1	1.414
13	125	7.211	7.81
14	135	7.81	7.81
15	145	7.81	8.485
16	155	219.477	219.477
17	165	223.403	222.423
18	175	40	44.045
Average (*s*) over ALL Viewing Angles:		66.98 ± 97.4448	67.06 ± 96.9857
Average (*s*) of "Good" Viewing Angles 35° - 145°:		4.014 ± 2.47708	4.123 ± 2.5663
Average Distance Accuracy/Misalignment =			4.07
Average Distance Precision/Resolution =			2.52

Compton Closest Distance (*s*) Comparison			
Set #	ViewAngle	LS Method	MAC Method
1	5	132.004	117.154
2	15	139.119	141.778
3	25	126.21	115
4	35	121.017	85.586
5	45	13	14.318
6	55	13.928	14.56
7	65	9	11.18
8	75	6	6.083
9	85	5.099	2.828
10	95	179.338	176.409
11	105	180.878	178.059
12	115	182.003	182.964
13	125	14	188.162
14	135	13.153	13.038
15	145	11.18	89.454
16	155	141.152	140.456
17	165	114	115
18	175	96.167	93.606
Average over ALL Viewing Angles:		83.18 ± 68.3063	93.65 ± 66.1237
Average (*s*) of "Good" Viewing Angles 35° - 145°:		62.38 ± 74.6935	80.22 ± 76.6848
Average Distance Accuracy/Misalignment =			71.30
Average Distance Precision/Resolution =			75.69

Large RSM "Parsed" Data Set (Oversampling)

For the primary Cs-137 data set, it was noticed that the total acquisition length (24 hours) and therefore total waveform capture may have been too long. Parsing of the ~4.5M waveform data set of the $\varphi = 45°$ viewing angle into ~500k increments was done to find out how the distance metric value might change with a shorter capture period. This work found that the acquisition time had in fact exceeded the point of diminishing return. The data was found to converge on the same solution for the source angular position after the first ~1.5M waveform captures (about 8 hours) of the full set. Therefore, the data was oversampled by approximately a factor of 3 in this work for the large RSM. This also indicates that the multinuclide work of the large RSM configuration may be oversampled. Table 8 shows the full results from this parsing work, and the full set of associated graphics can be found in Appendix A.1.1.

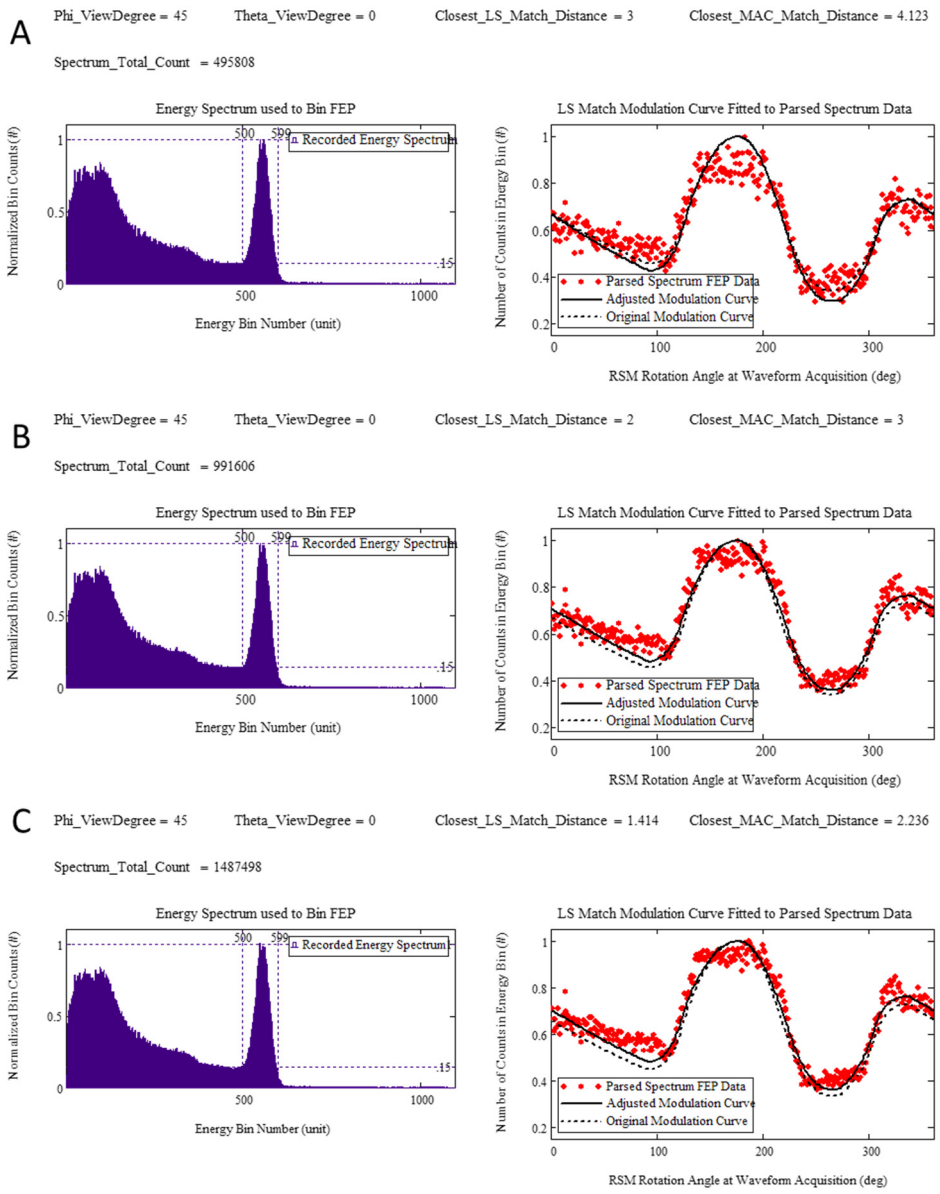

Figure 70. Parsed data from the primary Cs-137 φ = 45° showing convergence to the full set after only ~1.5M waveform captures.

Table 8. Parsed data comparison results.

Data Set #	View Deg	# of Waveforms	Least Squares Best Fit	MAC Best Fit
5	45	~500K	**3.000**	**4.123**
5	45	~1.0M	**2.000**	**3.000**
5	45	~1.5M	**1.414**	**2.236**
5	45	~2.0M	**1.414**	**2.236**
5	45	~2.5M	**1.414**	**2.236**
5	45	~3.0M	**1.414**	**2.236**
5	45	~3.5M	**1.414**	**2.236**
5	45	~4.0M	**1.414**	**2.236**
Average:			1.686	2.567

5.4 Large RSM with Multinuclide Source (Data Sets 30-47)

Further experimentation with the large RSM and NaI(Tl) detector combination, using a multinuclide source present was carried out. This work was planned to further extend the range of gamma energies considered, in order to verify RSM operations at energies other than 662 keV. Because of the range of activities in the constituents of the multinuclide source, an investigation into the point at which an FEP is obscured by the background of the scene was planned. Unfortunately, just about every data set and FEP met this criterion. Except for the set taken at $\varphi = 45°$, the results of which are seen in Figure 71, all had a combined energy spectrum that did not show clear peaks for bracketing the FEP energy windows to form the scattergrams.

The known energy window(s) from calibration were nonetheless still used to bracket where the FEPs should have been. It was hoped that some of the resultant scattergram information would be adequate to predict the source direction. In general, calculating an *s* angular distance of less than 4.0 was considered a successful prediction, as determined by Table 7. However, only 3 distances fell into this category, across all the viewing angles recorded, and only then by artificially considering the uncertainty of the RSM as found for the Cs-137 investigation. Two cases occurred at $\varphi = 45°$, and 1 at $\varphi = 35°$, for the Y-88 (898 keV) and Co-60 (1.173 MeV) FEPs respectively, for both the LS and MAC methods. In the other data sets spectra, some of the FEPs did seem distinguishable, but this was not proved out by the distance metric. All distance measurement results for three distinguishable FEPs and the Compton continuum (defined in these cases as below the Cs-137 FEP range) can be seen in Table 9 for both the LS and MAC methods. Some clustering of the next closest match points, as given for visualization around the true, known position did occur. These are seen in the various visual examples of the polar plots and heatmaps associated with a particular data set across both the FEP and the Compton continuum ranges. While none of

the tabulated distance metric results of Table 9 appear convincing, with the noisiness of the multinuclide scattergrams and degeneracies of the RSM considered, the reader is encouraged to review the full graphical results. In a few of the cases, the source direction is determinable. All multinuclide results are found in Appendix A.2.

None of the data sets presented in this work used any background subtraction methods to reduce noise of the recorded energy spectrum. This was done intentionally. In the search for a real-world, lost or diverted source, scene background information would probably not be known. So, finding any potential weakly radioactive sources compared to background would require at least a barely distinguishable FEP in the raw spectra for the operator to bracket and investigate. In this work, it is observed that that distinguishing limit is remarkably close to the activities of the Y-88 and Co-60 constituents of the multinuclide source and the detector/distance and RSM size used. Notice in Figure 71 that the Cs-137 or Co-60 (FEPs 1 and 3) look like they should be more distinguishable than the Y-88 FEP, and therefore probably give a better prediction. In both cases, by cross-referencing Table 9, this appears to not be the case. In the case of the Co-60 peak, while it appears the FEP is more distinguishable when the energy spectrum is zoomed in, the total number of counts in this energy region is too low to reduce the background uncertainty and results in a noisy, variable scattergram which affected how well the source position was predicted using the DRM. The SNR of these mentioned peaks might serve as a good starting point for future investigation into peak distinguishability. Further laboratory background characterization using this RSM mount and machinery has been accomplished by Condon [3]. His work used a Trapezoidal subtraction method, and what are essentially a repeat of the multinuclide data sets presented here. A significant amount of the energy spectra noise was removed, which allowed the smaller FEPs to be distinguishable, and better direction predictions to occur than are reported here.

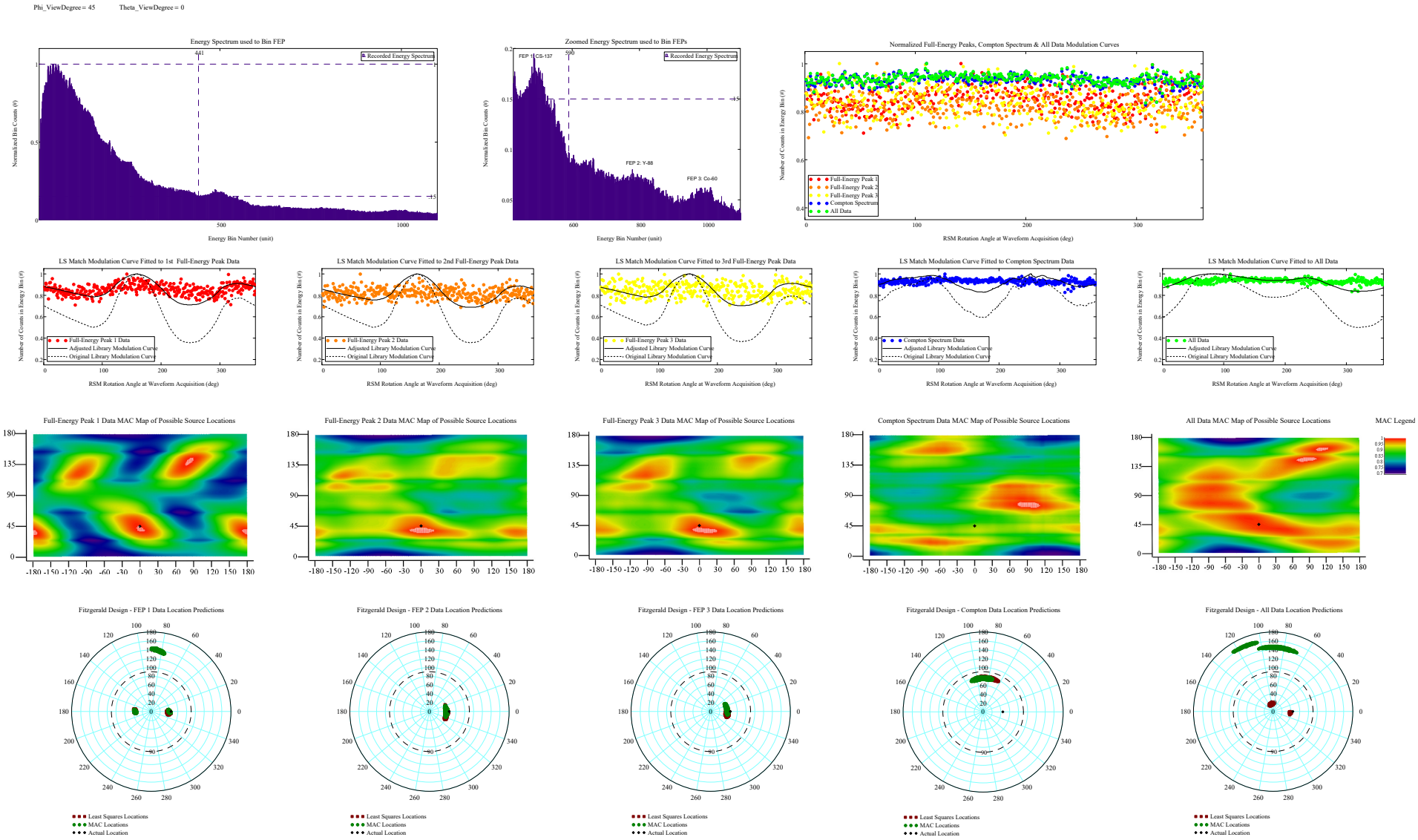

Figure 71. Example of large, FitzGerald RSM design multinuclide source data collected and processed for source direction prediction at φ = 45°. The entire energy spectra captured, as well as a "zoomed" area are shown, along with the scattergrams generated. Heat maps and polar plots are consistent with the previously shown figures (i.e. true source position is shown as a black dot, while other points serve to visualize the closest 50 DRM matches for comparison).

Table 9. Large RSM, NaI(Tl), Multinuclide Source – Predicted source placement distances, *s*, to the known source placement position for both the LS and MAC Methods using the various FEPs or Compton continuum.

		Least Squares Best Match Distance from Actual				Modal Assurance Criteria Best Match Distance from Actual			
Data Set #	View Deg	1st FEP: Cs-137	2nd FEP: Y-88	3rd FEP: Co-60	Compton Continuum	1st FEP: Cs-137	2nd FEP: Y-88	3rd FEP: Co-60	Compton Continuum
30	5	180.8340	88.7694	102.4600	101.8330	183.1750	75.1532	79.6241	96.3330
31	15	48.0416	69.9214	26.4008	89.1070	185.0000	81.0432	25.6320	96.6750
32	25	178.8990	73.9797	133.3750	94.5780	174.9430	55.7853	47.1275	110.4630
33	35	172.0470	61.1310	5.3852	98.4120	173.0460	51.1566	9.8489	106.4050
34	45	7.2111	6.0000	12.0416	99.9300	179.1790	6.0000	6.3246	103.4460
35	55	172.4090	91.2140	121.0830	127.4130	175.5140	78.1601	16.4924	101.2030
36	65	48.8365	104.4030	36.7696	127.9880	23.0217	68.1542	27.2029	72.1110
37	75	79.2591	36.2215	112.8940	118.8280	77.8267	36.1248	76.1577	165.3870
38	85	78.8162	52.8394	101.7100	17.2050	83.4865	62.2896	85.4459	169.1690
39	95	64.0078	91.2140	71.8401	23.0220	66.8880	100.1250	71.2180	23.6010
40	105	75.1532	70.2282	76.6616	31.7800	72.9178	74.7061	79.8812	33.1060
41	115	77.8781	98.4124	101.3160	43.4630	78.5875	100.6580	100.0050	44.0110
42	125	78.3390	139.9460	90.5539	55.0360	79.4292	106.0190	69.6419	55.4620
43	135	80.4984	120.9340	123.0650	67.5350	88.2383	118.8280	113.7410	65.7420
44	145	73.2462	125.3990	131.6050	71.8400	68.7677	124.8680	127.5810	74.8470
45	155	68.0074	150.7480	132.0040	82.2800	66.8506	153.6810	131.5290	81.2530
46	165	66.2193	150.3330	132.5030	90.6090	64.7611	148.7180	135.9300	92.1790
47	175	71.8471	146.1100	147.4620	101.0000	57.5587	169.2570	144.2220	101.2030
Average:		90.086	93.211	92.174	80.103	105.511	89.485	74.867	88.478
"Good" Viewing Angle Avg:		88.189	81.560	81.764	76.153	109.060	75.994	61.164	87.259

5.5 Hide and Seek

As a test of the large RSM system's ability (and the MathCAD computational code) to correctly match libraries off the rotational axis (with respect to $\theta = 0°$) the Cs-137 #1 and Am-241 sources were moved off the Velmex translation stage source holder to an alternate location near the RSM on two separate occasions. Results are shown in Figure 72. The angular position in φ and θ was not measured until after the data set had been acquired and the predicted direction known. This was an interesting validation of the off-axis flexibility of the search code. The reader will recognize that the φ viewing angle is very "shallow" in these tests and that was not intentional. At the time, it was not recognized that the "flatness" of the library modulation curves at these shallow angles could be a problem when comparing to the scattergram in this region. However, the prediction appears to have worked well ($s = 4.0$ and $s = 2.2$) for the Am-241 and Cs-137 sources respectively using the MAC method. The viewing angle, φ, is 18° and so would be expected to have a greater distance in matching (similar to the shallow viewing angles of 15° and 25° listed in Table 4), it appears to not be unduly affected. This is attributed to the closeness of the sources (24") to the detector over a 24-hr acquisition run when compared to the standard distance and the higher SNR of the FEP. Use of the Compton scatter-in DRM was not evaluated for these cases.

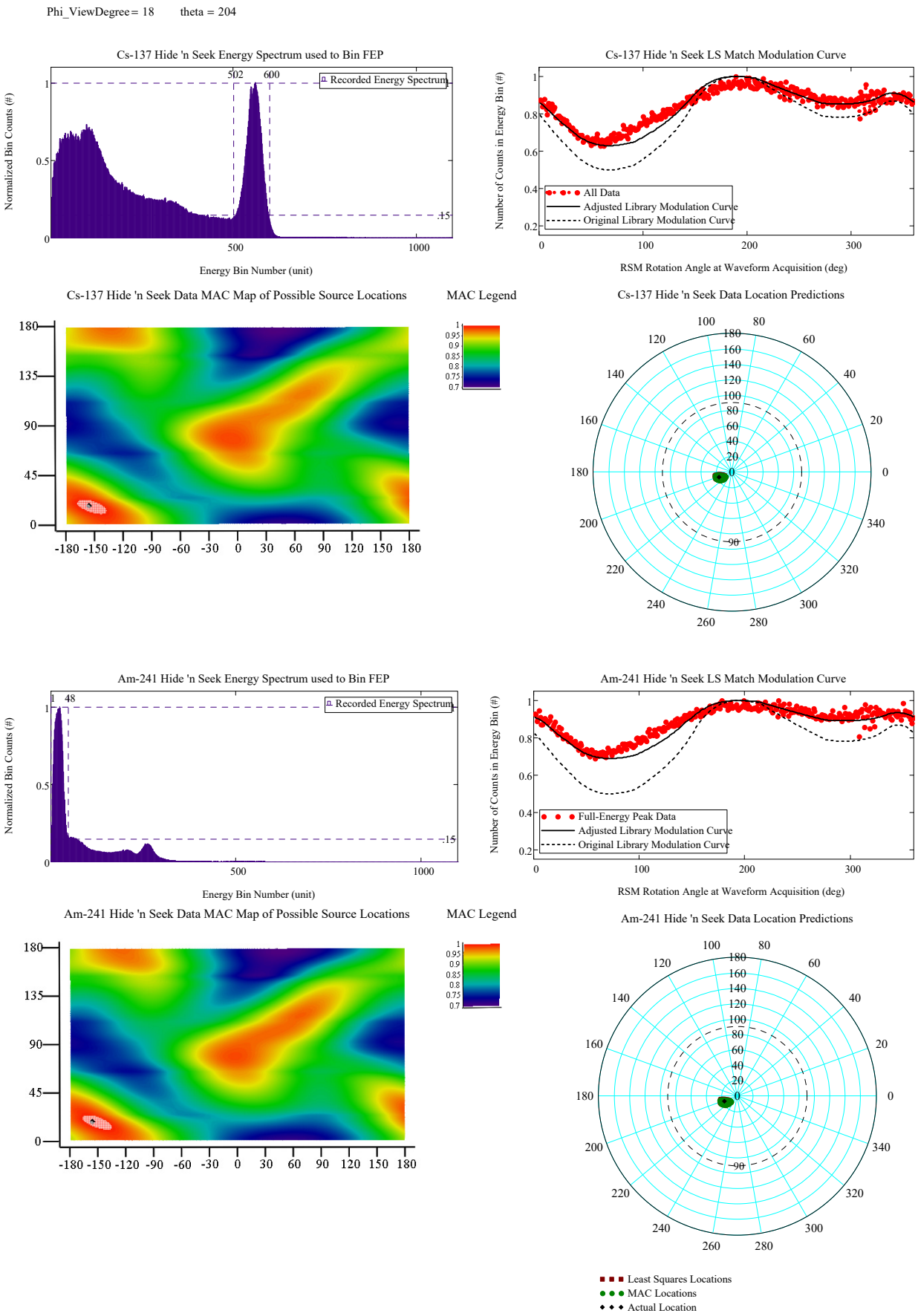

Figure 72. Large RSM, NaI(Tl), Cs-137 #1 Source – Hide & Seek directions for the Cs-137 and Am-241 results.

5.6 Large RSM with Am-241 and Multinuclide Sources at Different Locations

In a similar fashion to the preceding section, two sources of different energies were placed at the [{45,000}, {152,090}] positions, respectively, but this time the placement was simultaneous. The source at the primary {45,000} position was the Am-241 of Table 1, while the multinuclide source was placed at the secondary position {152,090}. Because the FEPs from the multinuclide source could not be distinguished in the spectra, the entire energy region above the upper-bound of the Am-241 FEP was used in generation of its associated FEP scattergram (knowing that the entire spectrum scattergram results often tended to follow the FEP results, as already showed for data sets 1-18). These two scattergrams were subsequently matched to the scatter-out FEP DRM. The best predicted angular directions were found to be {47,017} and {162,087}, respectively. This is an s = 17.83 distance-units when using a 4-dimension Euclidian space and greater than what was expected. Subsequent review of the author's laboratory notes found that the intended source for placement at the primary location was the Ba-133 source of Table 1. This was an inadvertent mistake and skewed the expected results. Since Am-241 was also incorporated in the multinuclide source, it appears that the predicted source directions moved toward each other in θ_1 and θ_2, while causing the predicted φ_1 and φ_2 angles to be higher than expected. However, this φ shift could also be attributed to misalignment as discussed earlier. Condon [3] later showed that two and three sources of different energies and locations were distinguishable by this system. It's noted that these scenarios, which do not involve convolution of the DRM are easily tackled using the RSM system since bounding of the FEP in the spectra is the first step in building the scattergram. This is of course assuming the individual source FEPs do not overlap and are distinguishable/resolvable based on the resolution and efficiency of the detector.

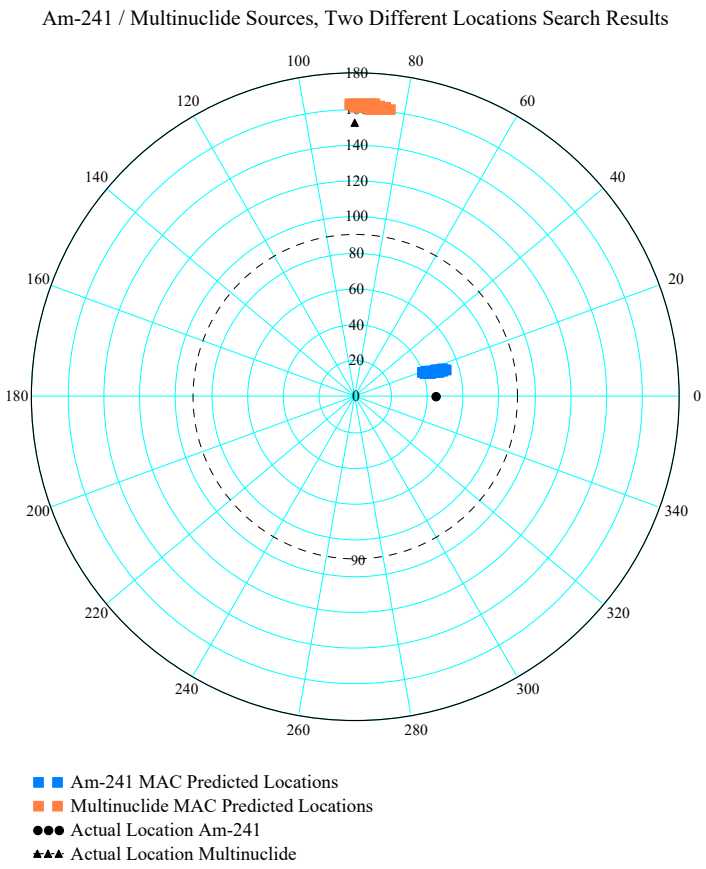

Figure 73. Different energies, two source locations. The actual directions of the sources are plotted, along with the prediction results which are shown along with the next 25 closest valued MAC comparisons.

5.7 Zeroed or Missing Encoder Data (Data Sets 57-61 and 64-69)

Introduction to the Rest of the Data Collected on the Large RSM

After the primary 36 data sets of the large RSM were acquired and it was observed that the multinuclide data set only had a few "good" matching results, due to FEP distinguishability from the laboratory background, additional data sets (from the expected best performing viewing angles) were taken. These angles, φ= 45° and 135°, correspond to the filling matrix positions where the maximum difference between the lowest trough of the modulation curve and the normalized peak occurs (i.e. maximum scattering and therefore gamma attenuation due to the geometry of the RSM). Data sets for the angles directly adjacent to these max performance positions (φ = 35°, 55°, 125° and 155°) were also repeated for both the Cs-137 #1 and multinuclide sources over the 24-hour acquisition period. The intention was to combine these data sets with the previously acquired to show an overall reduction in scattergram and to increase the SNR of the spectra (for the multinuclide cases especially). In addition to these 12 sets, a similar set of the best performing source placements and their adjacent viewing angles, but with a distributed Co-57 "rope" source (to simulate/enhance the lower-energy backscatter that was expected from the PMT and support structure) attached to the back of the RSM structure tube were also captured to be used in conjunction with the phoswich detector results for comparison. Finally, data sets using the Cs-137 #1 source, with placements as modeled by FitzGerald's [1] were also taken at φ = 72° and φ = 126° during this time for validation of his MCNP® model.

Unexpected Encoder Reader Failure

However, unexpected results/errors from the encoder data were discovered instead, as is seen in the 11 sets chosen for reporting here. All these sets showed significant errors in the encoder data, and so caused the computational effort to veer into a quest for data recovery, and to find an

explanation of what happened across these three distinctly different sets. Over certain regions of the rotation, it appeared that the encoder data, when binning was inaccurate (recorded no information at certain angles, showed the same value between subsequent interrogations even though the rotation was known to still in fact be progressing, or the expected normalize amplitude of the modulation curve was significantly different than expected). Only when the magnetic reset (mounted to the rotating ring) passed the reader would the expected behavior be restored for a time. Since these data sets were taken after the author left the program, it was not immediately recognized that the encoder electronic eye reader needed a slight adjustment to perform in an acceptable manner.

Multiple computational efforts to recover and use the parts of the scattergram data that was "believable" and subsequently predict the source direction with a partial set were undertaken. The first method of recovery identified in which region(s) of rotation the data was simply missing. These areas, once defined, had their energy bin(s) numerically zeroed. The modulation curves were then normalized as usual. This abbreviated data scattergram was then compared to the DRM libraries, by both the LS and MAC methods, over all positions not zeroed. Care was taken to never use the zeroed regions in the comparisons when shifting θ through the possible source positions of the DRM. This method did not produce any clarifying results, and the predicted source directions did not correspond to the known position as well as one might expect for simply "dropped" data.

Therefore, further comparison with the previously acquired same viewing angle data sets (and their successfully direction predictions) was done. Analysis indicated that the resultant modulation curves of these affected sets were not only missing data in certain regions, but that the remaining data, after what looked like encoder recovery was spatially compressed. That is, the

encoder position reporting not advancing in increments as fast as it should have. However, reset to normal operation occurred after the magnetic reset, and was seen as a significant discontinuity of the original (raw experimental data) scattergram at $\theta = 0°$, an example of this is seen in Figure 74. Knowing that the amplitude value of the scattergram, right after magnetic reset was most-likely correct, helped in determining at what value of rotation the data diverged from nominal for the angular positions leading up to 359°. In total, it was found that the encoder was missing its advancement command intermittently over what appeared to be about the last half of RSM rotation in most cases. It was assumed that the first "bad" location in the rotation (where it appears the data divergences from the expected behavior of the ultra-high precision bin counting) is an encoder read error due to alignment. In other words, the RSM system rotation was still in progress, but the encoder position reporting software was not updating correctly. Therefore, an interpolation between points is used in this region, until what looked to be normal operation resumed. Whereas the final region (before magnetic reset) completely dropped out in data (characterized by very low, or no counts per bin) and work was done to replaces the missing region by "stretching" the intermediate data. This stretch occurred between the position immediately after the last interpolated value to 359° in a linear manner and is shown in the bottom half of Figure 74.

Working on these assumptions, that most of the full rotation was actually captured in the data set, but it was compressed proved valuable. In this way, the scattergrams were adjusted before DRM comparison and showed better success in source direction prediction. A sample of these issues and results is seen in Figure 74, where a viewing angle of $\varphi = 35°$ is shown. As can be seen in Table 10, the best results across this investigation were primarily found when interpolating the first region of error (instead of zeroing) to the angular position where it appeared that correct

operating was restored, and then applying a stretching technique to the remaining data. The reader is directed to Appendix A.3 where the full graphical results for these sets are located.

As seen in Table 10, in some cases satisfactory source direction predictions are made. A few of the predictions even fell into the expected "good match" category ($s \leq 2.0$), when accounting for the uncertainty of the system, by either the LS or MAC methods. However, it was not clear that one matching method (LS, MAC, Zeroed or Stretched combinations) over another was actually favored. On a few occasions, the direct zeroing method worked better, but just slightly, compared to the stretching method. So, while generalizations can be made, the data set is clearly too limited to determine a superior methodology. Data set #69 did not have the inaccurate encoder data present, but was lumped in with this group of data, because it was the only one from the "background" set that did not and so is included here for completeness.

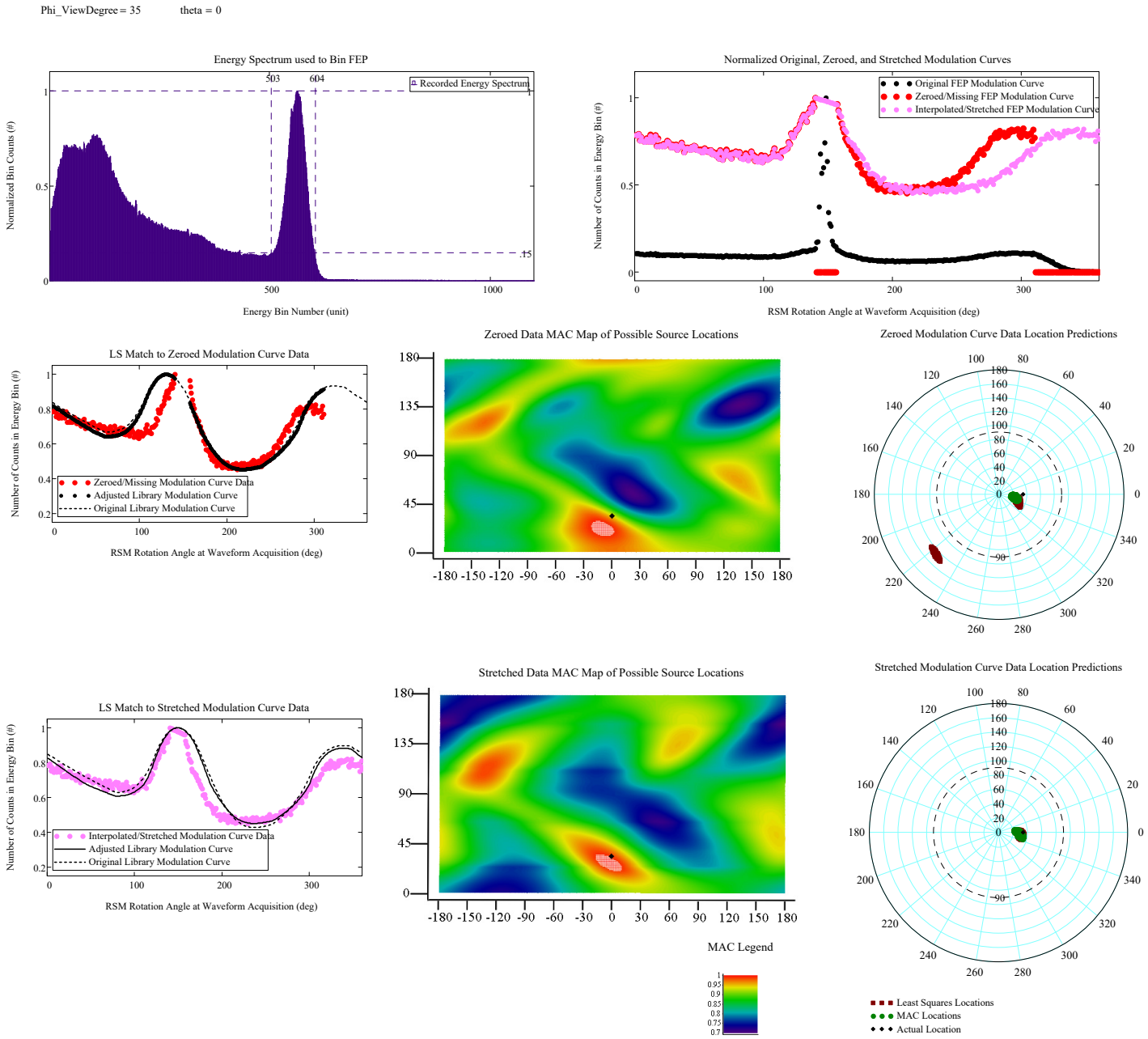

Figure 74. Example of Large RSM FitzGerald Design Cs-137 #1 Source – Data sets with encoder errors. The usual spectrum and unsmoothed scattergram data is shown. As well, the "Zeroed" and "Stretched" methods and their resulting MAC heat map and operator display polar plots are shown. Imaging in this case is at φ = 35°.

Table 10. Large RSM, NaI(Tl), Cs-137 #1 Source – Data sets #57-61 and #64-69, Distance to the known source placement for LS and MAC Methods of the "encoder error" data examined.

		Least Squares Best Match Distance from Actual		MAC Best Match Distance from Actual			
Data Set #	View Deg	Zeroed/Missing Data	Stretched Data	Zeroed/Missing Data	Stretched Data	Best Fit	Notes:
57	125	**160.515**	**10.296**	**162.635**	**155.795**	**Least Squares, Stretched**	Duplicate of data set #13
58	135	**152.201**	**151.644**	**157.410**	**151.644**	**Tie, Stretched**	Duplicate of data set #14
59	145	**150.456**	**28.178**	**152.594**	**151.727**	**Least Squares, Stretched**	Duplicate of data set #15
60	72	**73.756**	**22.672**	**163.933**	**21.260**	**MAC, Stretched**	MCNP Comparison Set ($\phi = 2\pi/5$)
61	126	**160.590**	**15.652**	**161.276**	**151.380**	**Least Squares, Stretched**	MCNP Comparison Set ($\phi = 7\pi/10$)
64	35	**18.385**	**5.099**	**15.620**	**7.280**	**Least Squares, Stretched**	Rope Source Background
65	45	**5.831**	**6.708**	**6.083**	**6.708**	**Least Squares, Zeroed**	Rope Source Background
66	55	**11.180**	**4.472**	**16.125**	**4.123**	**MAC, Stretched**	Rope Source Background
67	125	**1.414**	**6.708**	**1.000**	**10.770**	**MAC, Zeroed**	Rope Source Background
68	135	**5.385**	**7.616**	**5.385**	**8.544**	**Tie, Zeroed**	Rope Source Background
69*	145	**5.099**		**5.000**		**MAC**	Rope Source Background

*Part of the "elevated background" rope source investigation; however, only data set in group without missing data in modulation curve.

Issues that caused the encoder value to "stick" over a significant portion of the rotation and then recover (but only intermittently) and then to "miss" approximately a half of its advancement commands could be due to mechanical strain on the system, based on the off-center moment-of-inertia of the RSM and a warping of the holographic ring. Also, a dirty reader or ring situation (due to the graphite/Lithium lubrication mix used on the support tube), or advancement sticking/jitters over the high torque loading periods of the rotation could be at fault for slightly misaligning the reader head over time, as this error was not observed in the first 36 primary data sets. Having the magnetic reset mounted to the ring was instrumental in allowing for a periodic reset and restoration of the correct data flow, as proved by the recovered results, so the encoder error may have been internal to its control hardware. It should also be noted that the manipulation of the scattergrams was not easily accomplished in an automatic way. The nature of the errors could only be located, and appropriate bin limits set for regions of interpolation or stretching, through a trial-and-error approach. It took extensive familiarization with normal scattergram results of the large RSM to eventually and correctly identify the bin limits used in the recovery effort. As well, it's noted that each data sets exhibited unique failure points. That is, the rotation angle at failure was not consistent. So, no comparison between the individual set results of Table 10 should be made.

Figure 75 shows the rear-view of the RSM experimental configuration, with the Cs-137 #1 source clearly visible in the background on the Velmex translational stage, and the Co-57 rope source occasionally used to induce low-energy noise into the energy spectrum is set in the foreground. The position of the RSM relative to the source is consistent with a source/detector aspect angle of $\varphi = 65°$ as defined by this experiment's coordinate system.

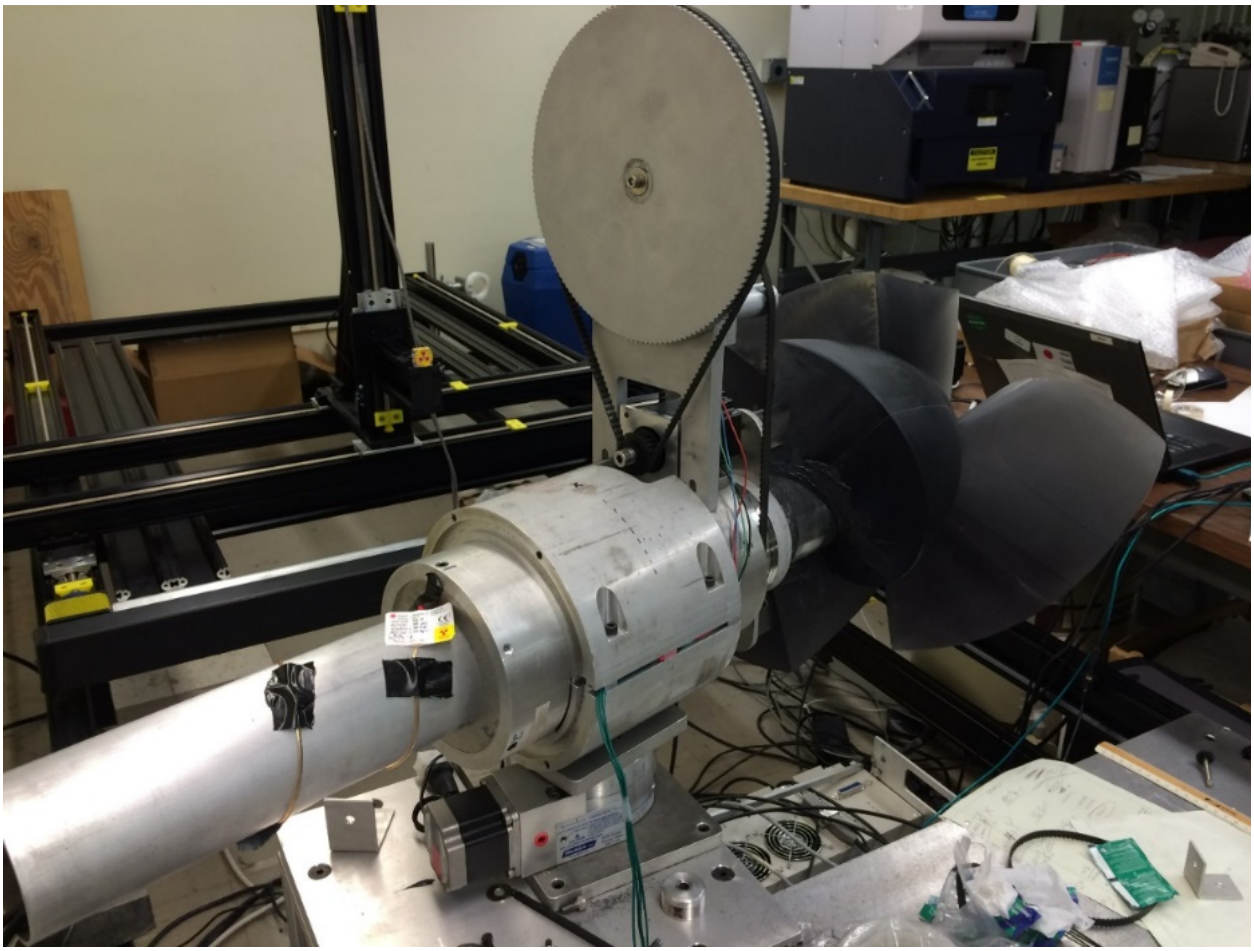

Figure 75. Rear view of the RSM experimental configuration, showing the Co-57 "rope source" used to enhance the low-energy area of the spectrum, this was especially useful in helping to determine which waveform filtering method worked best when used in conjunction with the phoswich detector.

5.8 Large RSM with NaI(Tl)/CsI(Tl) Phoswich Detector (Data Sets P07-P18)

Phoswich Introduction

Once the large RSM with the standard 3"x3" NaI(Tl) detector configuration data collection was finished, the phoswich detector was installed and operation of the system fixed and verified during a cross-country visit to the lab by the author. Ms. Logan graciously proceeded to acquire the remaining planned data sets for both the Cs-137 #1 and multinuclide sources, limited to the best performance angles. The multinuclide data sets (P01-P06 and P17-P22) were not analyzed based on the relative lower activity of the multinuclide, and the shown inability to match experimental data to the computational library, as previously described in this work. Finally, the last 4 (P15, P16, P17 and P18) Cs-137 #1 source data sets, with the added Co-57 rope source backscatter enhancement, showed the same encoder reader error as discussed in the last section, but were analyzed and included here using the same methods.

Since the original MathCAD data parsing and reduction program had an exponentially fit capability built into it for pile-up rejection, the rise- and fall-times of the captured waveform and a sorting by these parameters could be quickly accomplished for the phoswich detector experimental results. The fall-time data appeared to not be interesting or show any banding as introduced in Figure 50, so just the rise-time data was sorted by the probable scintillator crystal of interaction. Two separate exponential fitting functions were tried to characterize this rise-time when post-processing the data, the first has already been presented in Equation (13). The 2nd was formed by simply adding another exponential component as shown in Equation (18).

$$a_1(1 - e^{b_1 x}) + a_2(1 - e^{b_2 x}) + c \tag{18}$$

Since the purpose of the phoswich was to see if backscatter from the detector electronics and mounting structure could be successfully captured by interaction with the CsI(Tl)) guard slab material, a comparison to determine which fitting method, the single-exponential or a double-exponential function, performed the best in the reduction of lower-energy interactions in the recorded spectra. It is interesting to note that in a vast majority of the cases, the double-exponential fitting form failed to converge to a solution and was therefore eliminated from the set. Therefore, the total available remaining recorded gamma interactions used to build the scattergrams was quite low. In these cases, the shallow slope of the rise-time of the lower-energy gammas were not handled well by the MathCAD genfit function, defined to be Equation (18).

Figure 76 shows an example of the filtered results (NaI(Tl) or CsI(Tl)) for the two timing fit functions applied. Here the purple spectra are the combination of all experimental data peak heights after the particular rise-time fitting function is applied. The top-left and top-right panes are results of the single-exponential fitting, while the bottom-left and bottom-right show the double-exponential fitting. As can be seen by inspection of Figure 76, the data that only retained the CsI(Tl) guard slab waveforms (top-left and bottom-left panes), shows that the low-energy noise relative to the FEP height (which has been adjusted on the black line spectra overlay for comparison) after filtering is exacerbated. The NaI(Tl) only data overlays (top-right and bottom-right panes) shows good elimination of the energy region expected to contain any backscatter. All plots in Figure 76 have had their filtered data overlay adjusted to keep the Cs-137 FEP of the same magnitude as the unfiltered for comparison. While the single-exponential fitting method was ultimately chosen for continued analysis because of its higher total count/size of the phoswich data sets, it appears as though the two-exponential fitting method automatically filtered the low-energy regime of interest (~ 40 – 80 keV) as seen in the bottom-left and bottom-right panes of Figure 76

of the CsI(Tl) interaction, and so might be useful in future work. This determination can be made by looking at the filtering/suppression of energies below ~80 keV when only the NaI(Tl) data is plotted (bottom-right pane). This is hypothesized to be due to the shallow slopes of the CsI(Tl) waveform rise time compared to the NaI(Tl) material response. Figure 76 also shows the minor difference in total light production (and subsequent PMT multiplication) of the CsI(Tl) slab, as a slight shift to the left (lower energy) of the FEP location (top-left and bottom-left panes). This is notable, as the light output at a certain energy is advertised as being the same for both slabs.

In summation then, these results gave good confidence that the rear slab, CsI(Tl) guard layer of material did effectively shield the front NaI(Tl) slab from both the expected backscatter and the introduced Co-57 rope source gammas. Contrasting then the low total count results of the double-exponential fit routine results, the method ultimately chosen for filtering of the phoswich spectra was that of the single-exponential fit, filtered to only retain the NaI(Tl) interactions in accordance with expectations.

Phoswich Results

Table 11 and Figure 72 show the summation of the distance metric results for both the LS and MAC comparison methodologies and an example of the graphical data for $\varphi = 45°$, respectively. Notice that the final four data sets exhibited the same encoder error as previously described and showed up at the end of the order of acquisition. When discovered, Ms. Logan investigated and found the RSM to be rotating smoothly (lacking noticeable jerking), and not lacking in lubrication. As well, the encoder ring and its reader head were found to be clean and in constant contact (green light condition) over the full rotation. Therefore, it does seem that the errors in knowing the rotational position of the RSM did not come about solely through the reader/ring alignment slippage over time, but rather was due to a combination of mechanical

strain/warping on the holographic encoder ring by the system over certain regions of the rotation and contributed to incorrect interpretation of the advancement information by the reader. A full display of these phoswich inclusion results are in Appendix A.4.

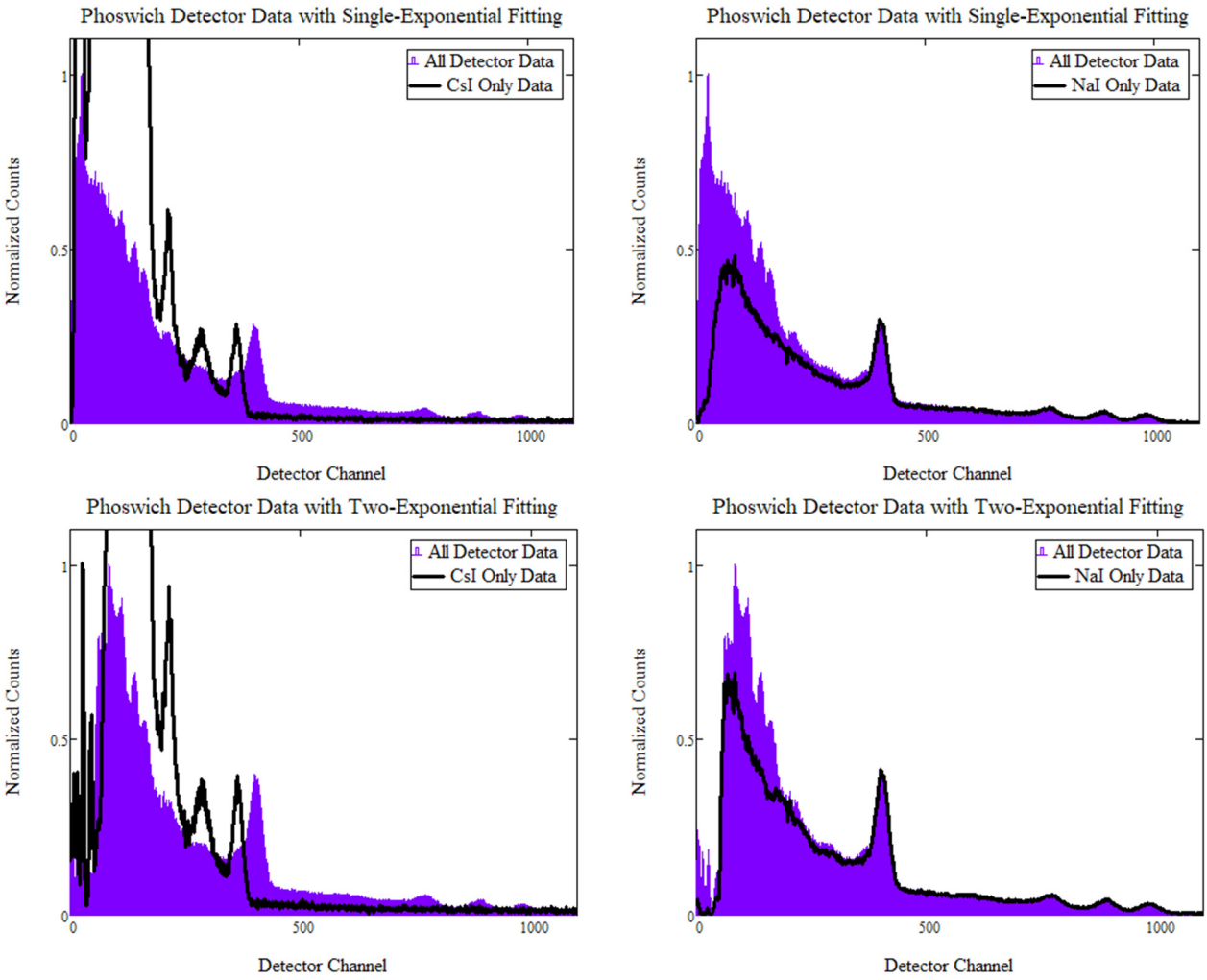

Figure 76. Examples of the phoswich spectrum (original in purple) and its modified associate (in black) when fitting experimental waveforms to either a 1- or 2-term exponential function (top and bottom respectively). Filtering for the phoswich scintillator of interest, CsI(Tl) "guard slab" is on the left and the NaI(Tl) is shown on the right half. In each case, the resultant (filtered) spectra have been scaled to the original spectra. This shows CsI only filtering produces much more relative low-energy noise, while NaI filtering reduces this backscatter as expected.

Table 11. Large RSM, Phoswich, Cs-137 #1 Source – Data Sets #P07-P18, Distance to the actual source placement using both the LS and MAC Methods.

			Least Squares Best Match Distance from Actual							
Elevated Background?	Data Set #	View Deg	Raw Phoswich FEP Data		Raw Phoswich Compton Data		Background Filtered Phoswich FEP Data		Background Filtered Phoswich Compton Data	
Normal Background	P07	35	7.6160		118.1059		7.6160		9.4868	
	P08	45	7.2800		114.2322		7.2800		12.7279	
	P09	55	7.6160		138.6218		7.6160		30.8869	
	P10	125	7.6160		89.1067		6.3250		171.8400	
	P11	135	5.0000		111.8302		5.0000		109.8362	
	P12	145	4.1230		122.9837		4.1230		93.5361	
Co-57 Rope Source Elevated Background	P13	35	7.6160		114.4945		7.6160		10.4403	
	P14	45	9.0000		151.5586		9.0000		164.4012	
			Zeroed Data	Stretched Data	Zeroed Data	Stretched Data	Zeroed Data	Stretched Data	Zeroed Data	Stretched Data
	*P15	55	18.1108	176.5899	44.0114	68.0955	18.1108	176.5899	42.1545	65.5134
	*P16	125	124.5552	57.2014	174.4279	142.2146	124.5552	58.0086	73.5935	30.1496
	*P17	135	7.0711	22.8035	147.7633	163.4656	7.0711	22.8035	81.9390	31.1127
	*P18	145	1.0000	30.0167	134.0933	191.0314	1.4142	26.9258	70.4557	66.2873

*Part of the elevated background phoswich investigation; Encoder ring failure present for a majority of the sets.

			MAC Best Match Distance from Actual							
Elevated Background?	Data Set #	View Deg	Raw Phoswich FEP Data		Raw Phoswich Compton Data		Background Filtered Phoswich FEP Data		Background Filtered Phoswich Compton Data	
Normal Background	P07	35	7.6160		101.5529		7.6160		11.7047	
	P08	45	8.5440		104.0000		8.5440		15.0000	
	P09	55	9.2200		144.2775		9.2200		22.8254	
	P10	125	8.6020		89.2693		8.6020		158.4456	
	P11	135	5.8310		99.8499		5.8310		173.6923	
	P12	145	6.0830		108.2959		6.0830		107.4663	
Co-57 Rope Source Elevated Background	P13	35	7.8100		118.1059		7.8100		12.3693	
	P14	45	9.0550		101.2373		9.0550		15.0000	
			Zeroed Data	Stretched Data	Zeroed Data	Stretched Data	Zeroed Data	Stretched Data	Zeroed Data	Stretched Data
	*P15	55	29.0689	172.6963	196.9772	113.0398	29.0689	172.6963	199.6021	64.6607
	*P16	125	125.6423	58.5235	174.2642	142.9021	125.6423	58.5235	102.8251	30.0832
	*P17	135	10.6301	36.6197	47.1699	174.1838	10.6301	36.6197	123.3694	29.2062
	*P18	145	9.4340	29.1548	54.1202	202.8916	9.4340	29.1548	68.1175	92.5905

*Part of the elevated background phoswich investigation; Encoder ring failure present for a majority of the sets.

As expected, the FEP scatter-in library performed well when using the phoswich detector, with both the unfiltered and filtered spectra. Since no other higher-energy source (than the Cs-137 used) was located in the laboratory at the time, little potential down-scattering into the CsI(Tl) portion of the detector needed to be filtered by the rise-time algorithm when using the FEP bin. However, the direction prediction greatly improved between the unfiltered and filtered spectras in the case of using the Compton continuum portion of the energy spectrum and in concert with the Compton scatter-in DRM. This is especially noticeable at the forward-looking viewing angles. Less improvement was observed in the rearward looking viewing angles of the RSM and is possibly due to the DRMs developed here not considering the RSM material displaced by detector placement, as already theorized. It's also interesting to note that the "zeroing" of the partial scattergrams led to better direction predictions in the FEP data. The opposite is true of the Compton continuum data, in these cases, better accuracy was observed using the stretch method.

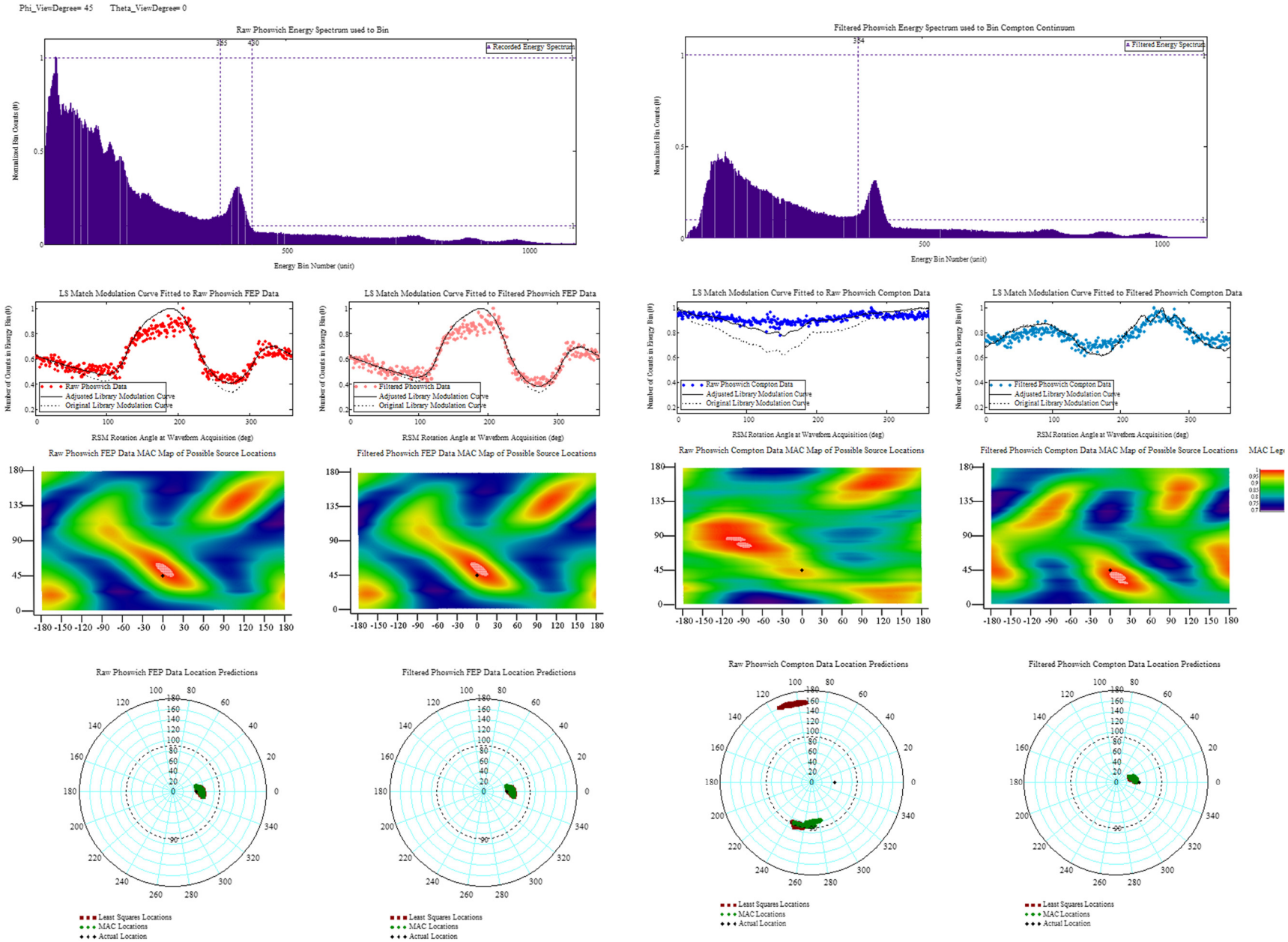

Figure 77. Example of Large RSM FitzGerald Design Cs-137 #1 Source with Phoswich Detector Results – FEP library results are similar for the unfiltered/filtered results as expected; however, improvement in source direction determination is seen (far-right column) when the Compton scatter-in DRM is used with the filtered spectra. The phoswich filtered the low-energy scatter recorded in the Compton continuum of the spectra.

5.9 Large RSM with two Cs-137 Sources at Different Locations

Introduction

As a further test of the large RSM system, it was desired to see if two sources of the same energy, placed at two distinct locations, could be deconvolved from the resulting modulation curve and individual source directions accurately predicted. This is a significant milestone, as it would indicate the flexibility of the system for multiple sources search and be an indicator of potential imaging applications regarding an extended source by the RSM system. The following method of deconvolving two sources shows, while computationally expensive, showed good results and allows for the possibility that an RSM system can be used in a coherent change detection manner as well. If the background scene is sufficiently characterized in advance (background subtraction) or it is known that two or more sources of the same energy are present, it can be used to identify the separate components through post-processing and deconvolving the recorded scattergram.

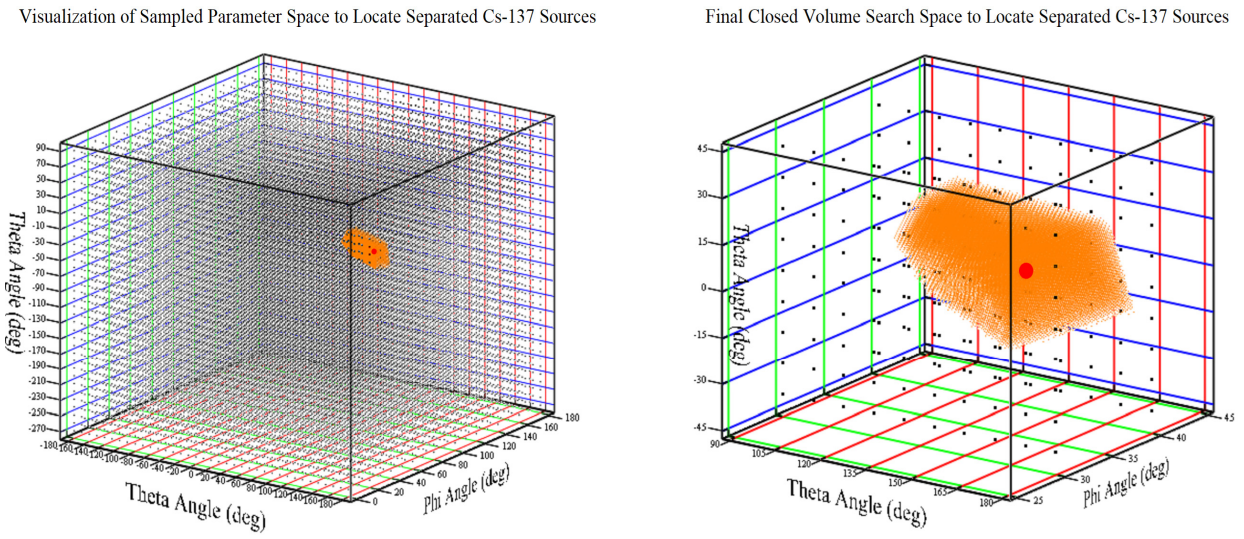

Figure 78. 3D visualization of 4D space for finding (through an initial sparse grid search) and solving the same energy, two different source locations problem. The left-hand panel shows the total sparse grid of 10° spacing in both θ and φ over all possible placements. The right-hand panel shows a "zoomed" in view to the volume where a finer griding (1°) has been implemented. Notice that the sparse gridding can still be seen. The sources' positions are represented by a single pink dot, which contains the multiple angular direction information and can be interpreted to find both source directions.

Method and Results

For this work, a new modulation curve library was constructed to account for the convolution of two sources, from each possible φ and θ position (i.e. each viewing angle, φ_1 and φ_2, and all possible shifting in θ_1 and θ_2 over a full rotation). This convolved DRM was designed, and sources placed, to only consider the φ viewing angle possibilities between 10° and 160°. Initial φ and θ spacing increments of 10° were used (e.g. $\theta_1,\theta_2 = 0°, 10°, \ldots, 350°$ and $\varphi_1,\varphi_2 = 10°, 20°, \ldots, 160°$). An example of this gridded space is shown in Figure 78. The convolution program also allowed for varying contributions of the parent sources (Cs-137_1 and Cs-137_2) to the modulation curve in 10% weighting increments, for a total of 9 intensity combinations (i.e. $10\%\{\varphi_1,\theta_1\} + 90\%\{\varphi_2,\theta_2\}$, or $20\%\{\varphi_1,\theta_1\} + 80\%\{\varphi_2,\theta_2\}$, etc…) at each position. This resulted in 2,985,984 (or $16^2 36^2 9$) separate comparison files, which then had to be compared to the experimentally generated modulation curve. This comparison resulted in a MAC method prediction of:

$$MAC_{LargeGrid} = \text{Cs-}137_1\% \{\varphi_1,\theta_1\} + \text{Cs-}137_2\% \{\varphi_2,\theta_2\} = 80\%\{050,000\} + 20\%\{150,090\}$$

A second, more finely grided set of library lookup files encompassing the closest 10° on either side of this sparse grid prediction (in increments of 1°, for a range of 21 positions in each of the φ_1, φ_2, θ_1, θ_2 variables) was subsequently generated, and resulted in 1,750,329 (or $21^4 9$) files for final comparison. The reason that the entire grid was not generated for all positions was one of computational expense. Had the ~40B possible sets (or $180^2 360^2 9$) been generated and stored for comparison it would have taken approximately 12,000 times as long (or about 230 years) on the laptop used to generate the library files. This does show the need for using high-performance computing (HPC) or alternate imaging methods for any reasonable real-world scenario. Some of these alternate methods have already been explored by Oleson [40], in subsequent RSM design iterations in 2019.

The second, finer grid search space shown in Figure 78 (cluster in orange, with the actual source position information point marked by a pink dot), combined the two viewing degrees (φ_1 and φ_2) into an artificial one axis for display purposes. This was for visualization of the closed, patterned search-space only. The actual parameter search was over four degrees of freedom. Displaying Figure 78 in this method was only done to give the RSM operator a visual sense of being able to use the sparse grid initial results to bound/defined the extent of the finer grid before the secondary DRM library generation.

Searching within this new finer gridded DRM, the MAC method determination of the convolved modulation curves to the experimentally recorded scattergram was found to be:

$$MAC_{SmallGrid} = [80\%\{051,003\} + 20\%\{148,092\}].$$

The actual positions and expected contribution of the sources was [90%{045,000}, 10%{152,090}] and so the total distance measured from the known sources to the calculated positions is s = 8.06 distance-units when using a 4-dimension Euclidian space. This is approximately double the distances/resolution previously reported on for the Large RSM with a single source, that resulted in a good library match, and was therefore considered a success. However, of note, the calculated and expected contribution of the sources was expected to be closer to 7.5% and 92.5% when the activities, distances and relationship to detector geometry were considered. This is in fact the reason the search library was setup in a manner to allow the contributions of each to vary in 10% increments, and so it is a bit surprising that the best match was for a 20% to 80% contribution case. It is assumed the noise present in the scattergram, as well as the method of fitting the DRM files (in this case, the original max/min stretching method) contributed to this slight error/anomaly.

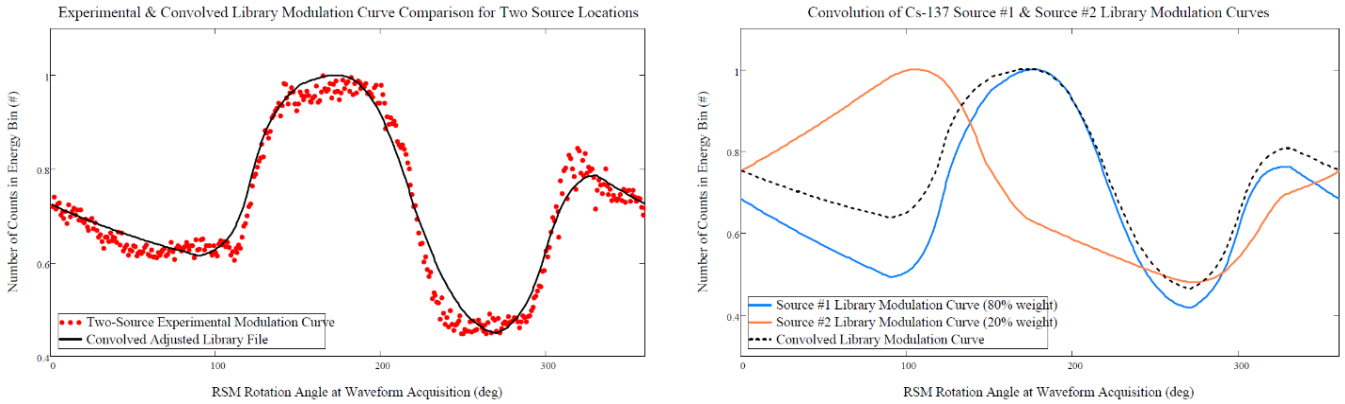

Figure 79. Convolution and weighting of individual source direction DRM modulation curves to test against experimental data. The left-hand panel shows the final fitting of two convolved modulation curves to the experimental data. The right-hand panel breaks out the individual modulation curves convolved.

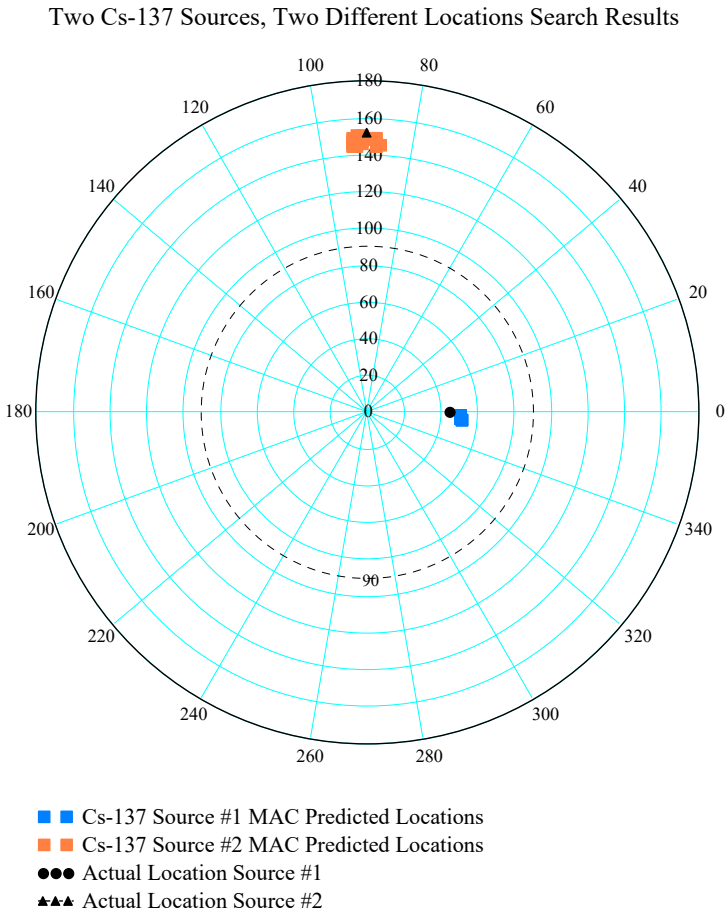

Figure 80. Same energy, two source location actual directions and prediction results are shown, along with the first 25 closest-matching points to show consistency of the numerical matching routine.

The direction prediction result of the MAC method comparison of experimental scattergram and finer gridded DRM modulation curve search are displayed in the combined θ_1,θ_2 axis format in Figure 78 as a pink dot. The polar plot operator display, with an additional next 25 highest MAC valued position to show the clustering of the matching routine are shown in Figure 80 for each source. Condon [3] later used this large RSM system to take similar same energy, two location data. His deconvolution method varied slightly in library resolution as he used the experimental modulations curves generated over the 18 ($\varphi = 5° – 175°$) usual viewing angles and binned θ in 5° increments. Further, Condon's weighting scheme varied in 1% increments. However, similar results and resolution to the data presented were obtained.

5.10 Small FitzGerald/Alternate Comparison (Data Sets SF1-15 and SA1-15)

Introduction

To test the scalability of the large RSM to the more manageable size needed for UAV mounting and portability, and to compare FitzGerald's RSM design to the alternate developed here, smaller RSMs of each design were additively manufactured as described in Chapter 3. In addition, a smaller detector for these miniature builds was needed. Hence the use of the smaller (but of higher-resolution and more responsive) $LaBr_3$ scintillator [50] to improve FEP identification from the background was made. $LaBr_3$ offers significantly better resolution (< 3% at 662 keV compared to ~7% for the NaI(Tl)) and they are able to identify FEPs 2-3 times faster when used with the same identification software [54].

Four final data compilation (2 designs and 2 sources) were taken with the small models and the $LaBr_3$ detector for investigation and comparison. The same angular positions and orientations ($\varphi = 0° – 175°$ in 10° increments) already used for the primary, large RSM were repeated. The full graphical results of these 18 positions for each small RSM and using a Ba-133 (low energy) and Cs-137 #2 (high energy) source are shown in Appendices B.1 and B.2.

Results and Comparison

The combined results of the FitzGerald design small RSM for both sources used are shown in Table 12, while Table 13 shows the alternate results. Both the FEP scatter-out DRM and the Compton continuum scatter-in DRM libraries were used, along with the fitting method of scattergrams to individual DRCs within the libraries as defined by Equations (15) and (16). As well, the distance comparison metric, *s*, is the same as used throughout and resulted from both the LS and MAC direction prediction methods. Finally, entirely new computational work was done to generate a new DRM for both the FEP scatter-out and Compton continuum scatter-in source

position libraries. This was done to take into account the extended $LaBr_3$ extruded cube the shape, in comparison to the 3"x"3 cylindrical shape of the NaI(Tl), on which the outer surface geometry of both RSM designs was based, as described in Chapter 2. These new DRMs are henceforth referred to as the "adjusted" libraries.

Table 12. Small RSM (FitzGerald Design), $LaBr_3$, Cs-137 (top) and Ba-133 (bottom) Sources - Mod Curves #SF1-15; Distance to the known position for both to Original and Modified Library using the LS and MAC Methods for FEP and Compton continuum.

		Original Library Best Match Distance				LaBr Detector Shape Adjusted Library Best Match Distance			
		Bracketed Full-Energy Peak		Compton Continuum		Bracketed Full-Energy Peak		Compton Continuum	
Data Set #	View Deg	Least Squares	MAC	Least Squares	MAC	Least Squares	MAC	Least Squares	MAC
SF1	5	232.768	233.452	133.843	132.280	226.716	227.379	169.594	170.473
SF2	15	218.344	219.100	0.000	2.236	218.160	219.659	89.443	87.824
SF3	25	212.269	213.663	1.414	1.000	213.663	213.663	80.006	80.000
SF4	35	205.292	203.421	4.123	5.099	5.000	205.653	130.000	121.000
SF5	45	196.825	197.307	174.771	175.582	197.730	196.888	80.100	80.056
SF6	55	188.162	190.055	5.099	6.000	189.108	5.099	90.022	90.050
SF7	65	183.134	182.428	3.606	4.472	183.848	183.848	81.006	82.006
SF8	75	176.148	174.195	174.943	175.932	177.685	176.706	98.000	104.000
SF9	85	178.070	178.070	7.280	7.071	176.045	178.045	39.115	31.048
SF10	95	175.642	175.559	10.630	8.062	177.553	176.556	193.329	189.615
SF11	105	178.084	176.309	12.207	12.806	178.885	177.902	184.394	183.439
SF12	115	183.807	183.807	61.855	62.682	185.162	184.765	178.373	177.553
SF13	125	2.236	1.414	193.023	190.276	1.000	2.236	179.179	178.180
SF14	135	1.000	0.000	197.677	196.787	1.000	0.000	178.025	178.025
SF15	145	210.839	211.684	85.147	84.291	211.376	212.219	87.092	88.051
Average:		141.3 ± 68.0	141.1 ± 68.4	59.2 ± 78.0	59.1 ± 77.5	130.2 ± 78.5	131.1 ± 79.1	103.2 ± 49.5	102.3 ± 49.8
"Good" Viewing Angles: 35°-145°		134.2 ± 70.2	133.9 ± 70.4	66.5 ± 80.0	66.4 ± 79.7	120.3 ± 80.3	121.4 ± 81.1	108.5 ± 51.2	107.4 ± 51.4

		Original Library Best Match Distance				LaBr Detector Shape Adjusted Library Best Match Distance			
		Bracketed Full-Energy Peak		Compton Continuum		Bracketed Full-Energy Peak		Compton Continuum	
Data Set #	View Deg	Least Squares	MAC	Least Squares	MAC	Least Squares	MAC	Least Squares	MAC
SF1	5	118.870	171.817	2.828	5.000	165.245	106.066	97.124	95.603
SF2	15	165.206	222.081	14.765	13.416	166.148	223.826	179.981	180.936
SF3	25	15.297	14.318	17.263	20.025	17.029	15.033	107.117	107.075
SF4	35	199.459	15.033	197.740	198.093	14.142	15.033	105.171	106.118
SF5	45	188.322	191.838	194.077	194.077	19.000	17.720	104.000	106.005
SF6	55	24.739	24.331	184.383	186.271	26.019	24.083	103.019	102.000
SF7	65	28.178	28.443	166.904	171.210	26.000	26.306	156.109	155.724
SF8	75	25.495	26.476	30.017	175.000	21.095	22.091	201.837	199.060
SF9	85	40.706	42.048	25.000	25.000	143.544	140.236	196.064	196.064
SF10	95	30.414	31.016	182.390	183.371	32.249	32.016	185.324	183.927
SF11	105	27.000	25.000	186.550	185.586	28.071	26.019	180.624	181.604
SF12	115	20.025	19.026	189.763	190.707	20.100	19.026	177.913	179.011
SF13	125	197.669	195.880	194.743	195.151	197.669	196.774	177.138	178.138
SF14	135	203.571	203.226	201.259	201.718	204.941	204.941	77.006	76.026
SF15	145	212.758	212.219	175.559	87.367	210.839	212.758	86.023	87.092
Average:		83.2 ± 81.2	79.0 ± 86.3	109.1 ± 80.4	112.9 ± 76.7	71.8 ± 79.4	71.2 ± 82.5	118.6 ± 43.9	118.6 ± 43.8
"Good" Viewing Angles: 35°-145°		85.6 ± 85.2	72.5 ± 82.6	137.7 ± 60.3	142.4 ± 51.5	67.4 ± 79.9	66.9 ± 80.0	125.0 ± 44.8	125.1 ± 44.5

A close inspection of the column averages and comparison of both portions of Table 12 does not seem to indicate an overall general trend regarding whether the Cs-137 (higher-energy) or the Ba-133 (lower-energy) experiments had better source angular direction prediction results. As well, it appears the adjusted library did not contribute to better accuracy performance in source

direction determination. However, results of the alternate design, presented in Table 13, do in general have smaller distance metric values.

Table 13. Small RSM (Alternate Design), $LaBr_3$, Cs-137 (top) and Ba-133 (bottom) Sources - Mod Curves #SA1-18; Distance to the known position for both to Original and Modified Library using the LS and MAC Methods for FEP and Compton continuum.

		Original Library Best Match Distance				LaBr Detector Shape Adjusted Library Best Match Distance			
		Bracketed Full-Energy Peak		Compton Continuum		Bracketed Full-Energy Peak		Compton Continuum	
Data Set #	View Deg	Least Squares	MAC	Least Squares	MAC	Least Squares	MAC	Least Squares	MAC
SA1	5	197.874	172.290	168.012	169.047	26.019	26.019	203.335	23.022
SA2	15	5.000	15.264	153.551	153.639	10.198	7.616	200.960	201.358
SA3	25	9.849	9.220	36.222	216.601	4.243	3.606	26.926	15.133
SA4	35	12.042	14.036	106.794	107.056	6.000	104.005	10.296	9.220
SA5	45	181.218	181.218	91.411	90.609	14.036	14.142	106.042	106.042
SA6	55	180.878	179.747	14.866	15.232	16.125	16.279	207.685	206.828
SA7	65	19.026	20.224	50.120	50.606	178.631	16.125	15.033	15.524
SA8	75	35.128	179.627	32.558	34.828	179.627	178.631	14.000	35.511
SA9	85	26.420	25.080	29.614	30.594	172.653	68.731	157.848	160.627
SA10	95	75.240	76.059	22.472	26.249	11.180	10.440	175.419	175.824
SA11	105	18.111	18.028	34.655	178.639	74.000	11.045	190.895	191.760
SA12	115	78.058	77.026	57.723	58.694	9.000	9.055	60.299	60.671
SA13	125	76.026	75.027	79.076	78.918	14.142	14.318	20.224	16.763
SA14	135	77.000	77.026	101.435	101.435	78.006	12.166	11.180	11.662
SA15	145	79.006	79.025	112.178	112.178	76.007	77.026	73.171	67.186
SA16	155	192.938	82.024	132.004	132.699	78.026	80.025	134.373	134.629
SA17	165	74.813	74.330	164.842	164.842	164.368	164.985	160.465	161.186
SA18	175	199.905	90.355	171.686	171.828	169.956	134.826	104.484	87.281
Average:		85.5 ± 70.2	80.3 ± 59.1	86.6 ± 53.1	105.2 ± 59.6	71.2 ± 68.2	52.7 ± 56.4	104.0 ± 74.1	93.3 ± 72.2
"Good" Viewing Angles: 35°-145°		71.5 ± 55.3	83.5 ± 61.1	61.1 ± 34.0	73.8 ± 45.2	69.1 ± 67.6	44.3 ± 51.0	86.8 ± 74.2	88.1 ± 73.3

		Original Library Best Match Distance				LaBr Detector Shape Adjusted Library Best Match Distance			
		Bracketed Full-Energy Peak		Compton Continuum		Bracketed Full-Energy Peak		Compton Continuum	
Data Set #	View Deg	Least Squares	MAC	Least Squares	MAC	Least Squares	MAC	Least Squares	MAC
SA1	5	173.531	173.666	172.012	169.027	23.022	22.091	163.086	203.907
SA2	15	89.275	2.828	148.408	148.486	7.000	6.000	205.039	98.020
SA3	25	9.000	10.000	214.960	217.341	3.162	94.000	6.083	5.385
SA4	35	97.046	14.318	99.725	102.956	6.083	6.325	11.180	10.770
SA5	45	181.838	17.117	90.934	89.627	18.028	18.111	104.019	106.042
SA6	55	181.000	181.177	10.296	11.662	24.021	24.083	100.005	17.263
SA7	65	143.126	140.730	160.823	161.805	180.347	180.347	20.100	20.224
SA8	75	193.693	193.693	33.121	34.000	57.940	56.648	88.238	39.217
SA9	85	185.302	188.958	72.339	72.691	23.707	24.042	73.926	191.888
SA10	95	69.029	69.007	61.188	61.984	21.000	21.000	26.000	27.313
SA11	105	69.065	70.007	45.706	46.872	16.000	17.029	50.160	51.245
SA12	115	72.000	72.007	60.166	60.877	15.033	15.033	27.659	30.806
SA13	125	72.007	71.028	83.546	77.466	16.031	18.111	20.616	20.881
SA14	135	76.007	75.027	101.435	101.789	15.033	15.133	10.440	11.180
SA15	145	80.006	80.025	112.969	113.159	77.026	74.027	82.037	136.565
SA16	155	63.781	82.024	173.142	171.187	145.798	162.484	211.152	209.468
SA17	165	129.321	129.321	165.052	161.012	143.388	102.956	73.007	125.603
SA18	175	137.000	137.768	77.104	76.164	176.876	176.006	118.870	151.172
Average:		112.3 ± 52.8	94.9 ± 61.8	104.6 ± 54.8	104.3 ± 54.4	53.9 ± 60.6	57.4 ± 58.8	77.3 ± 62.8	80.9 ± 70.6
"Good" Viewing Angles: 35°-145°		118.3 ± 51.3	97.8 ± 60.3	77.7 ± 38.3	77.9 ± 38.2	39.2 ± 46.8	39.2 ± 46.4	51.2 ± 34.6	55.3 ± 55.7

It is noted though, that save for just a few occasions across the data sets, these results are not on par with what was observed using the large RSM in general. The reader is directed to the final Appendices of B.1 and B.2 for a full display of the graphical results. On investigation there,

it is obvious that most of the large distance values are the result from degeneracy matching in the scattergram/DRM comparison. Further plotting of the next closest 50 best fit MAC values (< 0.1% of the allowable positions) shows better agreement with the actual source direction. As well, the scattergrams overall have good structure, and the fitting of the individual DRCs of the DRM follow the structure well. So, while the directionality predictions for these small designs is not on the level of the large RSM, due to the similarity of LS and MAC results in most cases, it's theorized that degeneracies of the designs (when used with the off-design dimensions of the $LaBr_3$) appeared to be more prevalent for this miniaturization goal test.

Table 14. Comparison of the small FitzGerald (left) and alternate (right) design RSMs. The best distance from each LS or MAC column of Table 12 and Table 13 are retained.

		Fitzgerald Design FEP		Fitzgerald Design Compton	
Data Set #	View Deg	Original Library Distance	LaBr Detector Adjusted Library Distance	Original Library Distance	LaBr Detector Adjusted Library Distance
SF1	5	118.87	106.07	2.83	95.60
SF2	15	165.21	166.15	0.00	87.82
SF3	25	14.32	15.03	1.00	80.00
SF4	35	15.03	5.00	4.12	105.17
SF5	45	188.32	17.72	174.77	80.06
SF6	55	24.33	5.10	5.10	90.02
SF7	65	28.18	26.00	3.61	81.01
SF8	75	25.50	21.10	30.02	98.00
SF9	85	40.71	140.24	7.07	31.05
SF10	95	30.41	32.02	8.06	183.93
SF11	105	25.00	26.02	12.21	180.62
SF12	115	19.03	19.03	61.86	177.55
SF13	125	1.41	1.00	190.28	177.14
SF14	135	0.00	0.00	196.79	76.03
SF15	145	210.84	210.84	84.29	86.02
Average:		60.5 ± 70	52.8 ± 66	52.1 ± 72	108.7 ± 46
"Good" Viewing Angles: 35°-145°		50.7 ± 68	42.0 ± 62	64.8 ± 75	113.9 ± 50

		Alternate Design FEP		Alternate Design Compton	
Data Set #	View Deg	Original Library Distance	LaBr Detector Adjusted Library Distance	Original Library Distance	LaBr Detector Adjusted Library Distance
SA1	5	172.29	22.09	168.01	23.02
SA2	15	2.83	6.00	148.41	98.02
SA3	25	9.00	3.16	36.22	5.39
SA4	35	12.04	6.00	99.73	9.22
SA5	45	17.12	14.04	89.63	104.02
SA6	55	179.75	16.13	10.30	17.26
SA7	65	19.03	16.13	50.12	15.03
SA8	75	35.13	56.65	32.56	14.00
SA9	85	25.08	23.71	29.61	73.93
SA10	95	69.01	10.44	22.47	26.00
SA11	105	18.03	11.05	34.66	50.16
SA12	115	72.00	9.00	57.72	27.66
SA13	125	71.03	14.14	77.47	16.76
SA14	135	75.03	12.17	101.44	10.44
SA15	145	79.01	74.03	112.18	67.19
SA16	155	63.78	78.03	132.00	134.37
SA17	165	74.33	102.96	161.01	73.01
SA18	175	90.36	134.83	76.16	87.28
Average:		60.3 ± 50	33.9 ± 38	80.0 ± 48	47.4 ± 39
"Good" Viewing Angles: 35°-145°		56.0 ± 45	22.0 ± 20	59.8 ± 34	36.0 ± 29

For further comparison of these results, and to try and shed light on the overall performance comparison between the two designs, Table 12 and Table 13 are collapsed by combining the LS and MAC methods columns, and retaining the best distance value over both methods. Distinction of primary and adjusted DRMs is maintained. These results are seen in Table 14. Notice that the FitzGerald design is missing the rearward looking viewing angles of φ = 155°, 165°, and 175°. While lab notes indicate these viewing angles were measured, they were not transferred to/recorded in the final data compilation archive by error. It is probably of little consequence

however, as these angles in general do not produce good results. In fact, in future versions of the RSM, it is suggested that it be used in an upright, vertical configuration, as opposed to the horizontal configuration presented in this work. This would maximize the useable FOV for use in ground-based applications.

In Table 14, it appears that the best direction prediction results were obtained for the FitzGerald design when using the original scatter-in based DRM and the Compton continuum portion of the spectra. The alternate design shows opposite behavior, as the best prediction results occurred using the FEP portion of the spectra with the scatter-out based DRM and that the adjusted library produced these positions. This split was not expected, as the intent was to show much better performance of the adjusted library over both designs. It does show however, that consideration of using the FEP scatter-out DRM versus the Compton continuum scatter-in DRM as the primary source direction prediction method may be RSM design dependent.

Table 15. Comparison of the small FitzGerald and alternate design RSMs. (Left) Best distance from DRM library columns of Table 14, sorted by FEP or Compton continuum results and subdivided into design options. (Right) Each row is further collapsed by retaining the best distance value of either the FEP or Compton continuum columns from the left pane.

	Bracketed FEP		Compton Continuum	
View Deg	Fitzgerald Design	Alternate Design	Fitzgerald Design	Alternate Design
5	106.066	22.091	2.828	23.022
15	165.206	2.828	0.000	98.020
25	14.318	3.162	1.000	5.385
35	5.000	6.000	4.123	9.220
45	17.720	14.036	80.056	89.627
55	5.099	16.125	5.099	10.296
65	26.000	16.125	3.606	15.033
75	21.095	35.128	30.017	14.000
85	40.706	23.707	7.071	29.614
95	30.414	10.440	8.062	22.472
105	25.000	11.045	12.207	34.655
115	19.026	9.000	61.855	27.659
125	1.000	14.142	177.138	16.763
135	0.000	12.166	76.026	10.440
145	210.839	74.027	84.291	67.186
Average:	45.8 ± 62	18.0 ± 17	36.9 ± 49	31.6 ± 28
"Good" Viewing Angles: 35°-145°	33.5 ± 55	20.2 ± 18	45.8 ± 50	28.9 ± 24

	BEST Match Values Overall	
View Deg	Fitzgerald Design	Alternate Design
5	2.828	22.091
15	0.000	2.828
25	1.000	3.162
35	4.123	6.000
45	17.720	14.036
55	5.099	10.296
65	3.606	15.033
75	21.095	14.000
85	7.071	23.707
95	8.062	10.440
105	12.207	11.045
115	19.026	9.000
125	1.000	14.142
135	0.000	10.440
145	84.291	67.186
Average:	12.5 ± 20	15.6 ± 15
"Good" Viewing Angles: 35°-145°	15.3 ± 22	17.1 ± 16

Table 15 makes a final comparison of the FitzGerald and alternate RSM designs. The left-hand pane shows the alternate design performed better using the FEP portion of the spectra, while

the FitzGerald design performed better using the Compton continuum portion. So, both libraries and designs have their advantages. The right pane, which retains the smallest distance metric is a further reduction across both the FEP scatter-out and Compton scatter-in DRMs of the left pane and is displayed per design. It shows similar performance between the two designs overall. However, the alternate design may be more useful in the rearward-looking viewing angles, whereas the FitzGerald might perform better in the forward-looking viewing angles, as seen in the color coding.

While this is a qualitative interpretation, it may be that the additional induced discontinuity of the alternate design made better use of the available Compton scatter information, and that the adjusted library modification accounted for the RSM mounting structure and detector PMT/electronics on the back half of the viewing angles in a better way. Follow-on work by Holland [5] does show a class of highly discontinuous RSM designs, modeled and built by Egner [37] that showed very good results. So that might be the case and would add to the value of this work.

5.11 After Action Report

Upon disassembly of the large RSM/Phoswich detector configuration, to change the equipment configuration to that of the small RSM, several interesting discoveries were made. In Figure 81, notice that the phoswich detector has "backed-off" approximately 1.5" from its original position. It should be flush with the end of the RSM support tube. This was probably caused by a slightly non-level condition in the aluminum support tube and the small vibrations caused by the occasional "sticking" of the RSM acrylic surface to the tube (ever though care was taken to regularly lubricate the interface). However, it is also possible that the power and signal co-axial wires, that were connected to the back of the detector and routed out the back of the tube, were

accidentally stressed at some point during the data sets collection period. Consequently, this may invalidate or affect the accuracy of some of that large RSM data.

As well, the support structure for mounting the RSM to the motorized mount was designed to minimize the amount of "extra" scatter material between the source and detector when approaching $\varphi = 180°$. While no mechanical issues presented themself during operation, the acrylic based material of the RSM broke upon removal of an adapter support screw during disassembly. This indicates that the structure was being driven right at its material limit and any future designs of this size and weight should incorporate a more robust support design, to ensure that any potential breakage is averted and the RSM does not need to be taken out of operation or rebuilt. The addition of this extra material would not be disastrous to imaging as the rearward viewing angles ($\varphi = 155° - 175°$) are shown to not perform well. However, as discussed previously, this probably due to the placement of the detector and mounting hardware, which in this case are not modeled by the DRMs developed. Future designs and experimentation should include higher-fidelity, more robust simulation when developing their DRMs, which in turn may improve the RSM FOV.

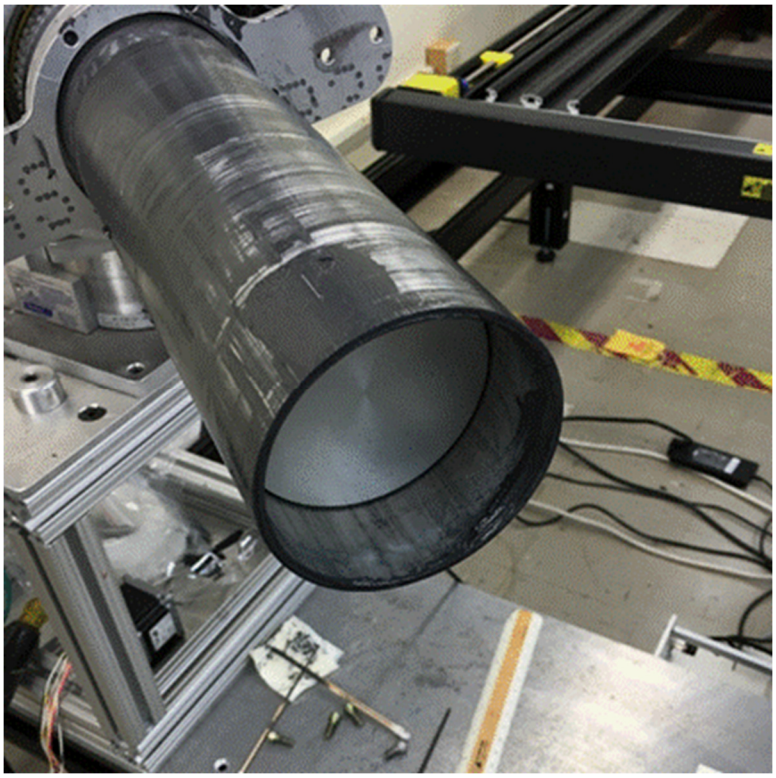

Figure 81. Detector and support tube after large RSM removal showing the phoswich had backed-off through vibrating or had the power and signal cables stressed at some point.

Figure 82. Damage to the RSM support structure is seen on the support leg after removal of the adapter supporting screws.

VI. Summary, Contributions, and Continuing Efforts

6.1 Summation

This work demonstrates the first instantiation of the FitzGerald design [1] RSM and its use as a proof-of-concept system at AFIT to spur further research efforts of a wide FOV, two-dimensional gamma point-source locator using a single, non-cooled scintillators. As well, it is the first attempt at including a phoswich type detector in RSM operation. Two different sizes and two distinct designs of additively manufactured RSMs from an acrylic, low-Z base material, were used in conjunction with three types of inexpensive scintillators. It also documents the very first build of a system of this kind, which was productively employed to create a new class of RSM imaging technology.

The geometric design of the RSMs followed the "filling matrix" rules set forth by FitzGerald [1], such that for any given "viewing angle" (φ) of the radioactive gamma source, a unique length of scatter material is introduced between the source and the internally placed detector at every rotational angle (θ) of the RSM. Rotation angle of the system, at gamma detection was recorded using a Renishaw holographic encoder ring. The recorded waveform peaks were later binned by energy region (in both the FEP and Compton continuum portions of the recorded spectra) and associated with the RSM rotational position, to create experimentally generated scattergrams. These results were then compared to a library of computationally generated curves in order to predict the radiation source direction. Uniqueness (degeneracies) of the two designs developed is explored, to show the limitation in source direction prediction of the FitzGerald class of RSM designs. A total of four different design considerations were investigated, and results of the two manufactured designs are presented here.

Two simple models, using Compton scattering of the source gammas out of the path of the detector by the RSM material for the recorded spectra FEP, and using Compton scatter into the recorded Compton continuum portion of the spectra of non-line-of-sight gamma/detector paths through RSM material interactions were developed and experimentally calibrated. This simplified code runs significantly faster than the original or subsequently developed MCNP® or GEANT codes used in RSM modeling efforts but is comparable in its results. This provides a baseline in validating the mechanisms of primary interaction within RSM systems. Simple LS comparison and MAC direction prediction algorithms where then used to match the experimental scattergram data to the DRM library files.

The FOV was found to be limited in the forward-looking viewing angles up to 15°, due to the lack of relative change in RSM structure material in this region when compared to the size of the detector used (i.e. flat scattergrams with little structure). Additionally, a small exclusion region behind the detector, from $\varphi = 145° – 180°$, was found to be outside the FOV, due to the detectors internal RSM placement and the associated electronics, support, and rotational drive components of the system over this range.

Experiments were conducted for strong Am-241, Ba-133, and Cs-137 sources, as well as various weaker peaks of a multinuclide source. The final energy range investigated was from 80 keV to 1.1 MeV.

The ability of the computational algorithms to correctly determine source position are quantified and discussed in this Chapter for 130 data sets. Acceptable source direction predictions were obtained, with an average resolution of the large RSM build determined to be ~4° when using the FEP attenuation by scatter-out based library. The phoswich detector incorporation was shown to suppress the anomalous back-scatter contribution to the Compton continuum below 200 keV.

When used with the large RSM and in conjunction with PSA, the source direction prediction improved. This novel incorporation of a phoswich detector in a RSM has not been reported on previously.

Overall RSM design considerations, two original SolidWorks CAD drawings, and the 3D printing construction of the RSMs are catalogued in this work, as are the laboratory equipment set-up, data acquisition system, postprocessing of the recorded waveform data, and final graphical data and results. It is shown that the source direction can be determined over a ~3π steradians total viewing area in the general proximity (i.e. near field conditions for this RSM set-up). This is an improvement on the allowed viewing angle area, as compared with previous RMC imaging efforts work by Kowash [6], which also used point source detectors for 2D location determination, while still maintaining comparable resolution. However, in contrast, his work was able to image extended sources. Further efforts are needed with the RSM to move beyond point source direction determination and into a true imaging and location finding system. The groundwork for this has been done by Olesen [39].

Two source energies at the same location were shown to be distinguishable, as was a separated same energy source at two distinct locations. The use of miniaturized RSM components was also tested and reported on.

Some data sets showed encoder ring errors and efforts were made to recover and make comparisons with these partial scattergrams.

6.2 Original Contributions of This Work

Along with the original SolidWorks design files of the FitzGerald design RSM and an alternate, developed from the filling matrices' theoretical rules as set down by FitzGerald, this

work shows the original "proof-of-concept" work which advanced the confidence of the developed computational modeling work. In turn, this led to the first investment in RSM technology by AFIT. Additionally, this is the only work to date to utilize the Compton continuum portion of the spectra for point source direction prediction. All of these are unique to this project, serve as a baseline, and are the steppingstones from FitzGerald's original concept paper to the subsequent, more advanced RSM design work conducted to date.

Finally, the models developed here and the fitting technique of modifying the DRM reference libraries to experimental scattergrams amplitudes, showed that potential source placements can be simply and robustly modeled over a wide range of viewing angles, and different RSM materials/sizes without extensive Monte Carlo type simulations for the different configuration. The accuracy comparisons of these models were on par with the industry standard MCNP® and GEANT commercial programs. Thus, allows for quick prototyping of future designs and in only requiring a few reference DRMs during RSM operation, as opposed to multiple DRMs for specific material, detector characteristics, or energy ranges to be necessarily generated and referenced.

A summary of the unique points in this work are as follows:

1) Creation/Production of the two distinct FitzGerald class RSM CAD designs and filling matrices are not contained in any other publications, although further alternative RSM designs have been produced and 3D printed, by both Olesen and Egner [35] [37] after this work, but before this publication.
2) The simple, attenuation by scatter-out computational code used to generate the DRM used in conjunction with the bracketed source FEP, and the Compton scatter-in DRM developed to utilize the Compton continuum information in Chapter II and their

subsequent fitting to experimental results to identify the source direction is comparable in performance to the developed MCNP® and GEANT codes. It is however significantly faster (600x) for DRM construction than both commercial codes.

3) The first instance of additive manufacturing (3D printing) used in the production of RSMs.
4) Extensive modification of previously used RMC experimental data acquisition equipment [6], which has subsequently been used and reported on by others [3].
5) Acquired first of its kind RSM data with three different detectors and two different RSM sizes:

    a. Single-location, and single energy (Cs-137) data, later shared with Logan [2].
    b. Validation that the Compton continuum data can be used when determining the source direction with the data from (a), but that it is not as accurate. This in itself is significant, as it indicates attenuation appears more important than scatter for getting an accurate direction prediction, but that further modeling work is needed [26].
    c. Multinuclide source data (two or more sources at the same location), however other multinuclide data with better background characterization was later taken by Condon [3].
    d. Two same energy sources at different locations data (gridded "hunter" program showed proof-of-concept for more advanced computational efforts to be made with an initial sparse to finer mesh grid search). Search routine was similar to Condon's [3], but with better spatial discretization. Further advanced imaging methods have been explored by Olesen [40], but the work here and Condon's supported this

development of the next generation of RSMs, and emphasized the need for true extended source imaging investigation.

e. RSM/phoswich detector combination data set and back-scatter suppression work using waveform PSA is shown to be viable.
f. Missing/Faulted encoder data can be partially recovered, and remaining portions of the scattergrams can be successfully compared to the DRM libraries.
g. Experimental comparison and performance characterization of two unique "miniaturized" RSM designs for potential UAV applications.

6.3 Motivation for Continued RSM Wide-Area Search Development

Introduction

Currently, first responders [55] in the United States are more than likely to use Geiger counters mounted to 10-foot poles, to identify radiation hazards in any area they may be entering than any other method. Of course, first, they must know to look for something potentially radioactive, and then to ensure the safety of others, they must walk around and measure locations/objects one-by-one to determine safety, putting themselves at risk. For disaster response or for averting/mitigating any future RDD or RED events, an RSM system, set-up in the middle of a suspected hot zone, then allowed to autonomously collect data for a time, could give these responders a better picture of hazards.

Further, baseline background data is just not measured in most areas of the United States. A distributed network of inexpensive/robust automated RSMs, along with other types of sensors (such as cell phone integrated gamma and neutron detectors [56]), could be used in a data fusion method to characterize the background radiological signature of cities, as well as quickly identifying any point-of-interest anomalies that might arise. Since future versions of the RSM are

predicted to be able to take a nearly 4π radian image of the area, identification of extended radiological sources through a permanently mounted RSM can occur more quickly than using other methods, such as walking a grid (slow), sensors mounted on a vehicle (limited by terrain and access roads), or an UAV search (which would require a landing/take-off location, have dwell time considerations, and be limited to high-activity sources based on its transit time over the area of concern). The use of permanently mounted RSMs could lead to the rapid identification of any significant changes to the background using a coherent change detection technique, and potentially save in search time costs since it does not rely on multiple personnel/operators and the grid-pattern search normally associated with point-source detectors.

In high-density urban areas, the fusion of cell phone tracking [29] and an array of RSMs or other permanently mounted, long-term, background spectrum collecting devices could be used to quickly identify a new source. Considering that a well characterized background not only reduced the number of false-positive alarms, an array of sensors helps to increase the statistical significance of any detected events that fall above the background is useful. While a national network for the security and safety of the public regarding errant nuclear material, through cell phone tracking may face some legal challenges, an RSM network, permanently mounted and integrated into a city's infrastructure, would fill the gap in capability. Precedent already exists for a network of these type of sensors, as is the case for the EPA's RadNet sensors. However, they only offer point-source of collection information, either through air sampling or omni-direction Geiger counters. A system of RSMs, to effectively take 4π radian gamma "pictures" of the area may be more effective. They offer the ability to characterize background, rapidly pin-point hotspots based on any new or unexpected fallout, would avoid any public privacy concerns of

government data collection, and could easily be integrated as part of the Civil Defense of the United States.

The groundwork for fusion tracking is already being laid with the technology adaptations being made to handle the current COVID-19 crisis. Apple recently introduced an "Exposure Notification" opt-in to its iPhone operating system, which allows users to be notified in case of "close proximity" of an infected person, based on data compiled by local Public Health Authorities. Perhaps something similar could be used to allow users to opt-in to send their cell phone data to a national nuclear material tracking database. As well, work on small, distributed sensors and tracking networks is underway, in an effort to detect terrorist activity before a critical event happens. DARPA physicist Dr. Tang [57] has been working on miniaturizing thallium-activated CsI(Tl) scintillators for gamma detection and identification. He is also incorporating chemical and biological detection components into the unit. In fact, the technology is advancing to the point where the energy of the gamma source, chemical structure of the compound, or biology of the pathogen can be processed and determined on the device itself. This helps with not only network bandwidth intrusion, but also the reporting of false positives due to medical isotopes used for imaging or treatment in our modern society, or standard industrial chemicals used in cleaning or manufacturing. The device, Sigma, as currently used, can be carried by law enforcement personnel, fire fighters, and first responders. Sigma is BlueTooth connected to the users' phone and the sensors send real-time data to a central network. Using this "Crowdsourcing Dragnet" to bring together the device data, a dynamically changing, real-time location identification of potential threats is developed and visualized. A distinct advantage of having mobile sensors, is that their area density changes as crowds of people gather. For instant, a stadium, minimally occupied in a preceding 24 hour period (and well characterized by a fixed sensor suite, or airborne

survey [30]) all of a sudden has a dense array of sensors to record and pin-point any anomalies from the background.

Monitoring does happen in the United States and some European countries before large public events like Inaugurations and sporting contests, but it does not happen on a continual basis for most locations and requires a specialized team and equipment, such as the Aerial Measuring System (AMS) team that is maintained and managed at the Remote Sensing Laboratory of the Nevada National Security Site (NNSS). These teams usually consist of both fixed-wing and rotary based assets, as well as ground mobile units. Having an RSM system permanently mounted at an event sight/location of consistent use may augment the team's other assets and provided them with a site history/natural radiological background update between times of survey [30].

Finally, RSM miniaturization, in conjunction with any ground- or ship-based background collectors, could help monitor shipments that have a long-transit time, like international shipping, before a potentially hazardous shipping container is allowed to approach the coastline. Over 35 million shipping containers enter the United States every year. New cargo ships are being designed with a capacity to exceed 20,000 containers per ship. DHS already divides up the responsibility for the monitoring and detection of radioactive material shipped into the United States between the Coast Guard, the Office of the Transportation Secretary, Federal Emergency Management Agency (FEMA), Customs and Border Patrol (CBP), and the Domestic Nuclear Detection Office (DNDO) [58]. Over 400 large-scale detectors Radiation Portal Monitors (or RPMs) are already deployed at the largest 22 U.S. ports. It's clear that the workload is significant and is only going to increase in the future.

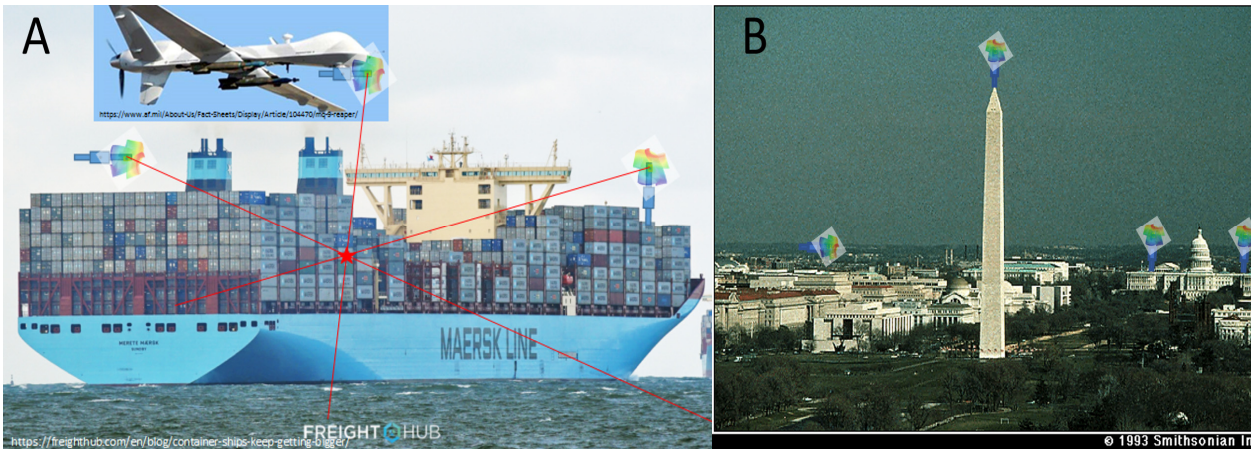

Figure 83. Distributed RSM networks for (A) determining source location or (B) establishing robust scene background characterization.

Current Radiological Detection Efforts and Emerging Threats

In 2005, the DNDO was broken out of the Department of Homeland Security's (DHS) Science and Technology Directorate. Specifically, they were charged with tackling the problem of identifying radioactive material coming through the United States' Ports-of-Entry (either land border crossings or seaports) or by scanning/clearing shipping containers at their country port-of-origin prior to shipping [59]. A little over 7 years later and with many millions of dollars invested, their Advance Spectroscopic Portal (ASP) program was canceled when the estimated cost ballooned from $2B to $3B, not to mention the numerous technological and logical issues facing it. These included such issues as false alarm rates, due to products like kitty litter clay, bananas, and tiles which contain natural occurring radioactive nuclides. In fact, naturally occurring K-40 (bananas) and Pu-239 cannot be distinguished from each other (even though the decay method and energies are quite different) because of the type of plastic scintillator materials currently used at our border crossings. To further complicate the matter, some people can have a trace radiological signature based on medical procedures or even spending too long in certain locations (a person can become more radiative by spending time in the granite mountains for New Hampshire, than the equivalent amount of time aboard a nuclear submarine!) [60]. As well, the deployment and

operation/maintenance of DNDO's equipment in both domestic and foreign ports is also a logistical and diplomatic hurdle. Despite the ASP acquisition program failure, lessons learned include the fact that there is not a "one-size-fits-all" solution to the problem. DHS has recognized the fact that a combination of mobile and agile technologies, along with the portal entry devices already in use, is the best solution. As well, even with the cancelation of the ASP program, they are still planning on spending approximately $2B per decade in order to address the issue of radioactive security. This leaves a wide berth for programs like the RSM (or a networked array of RSMs), along with other novel, cheap, robust, and deployable devices to fill the gap left by its cancellation.

Legislative bills, in both the United States House of Representatives and the Senate, requiring 100% inspection of cargo containers have faced significant opposition; and rightfully so, from a number of shipping and transportation groups. Implementing the requirement without the capability/capacity may force warehouses to keep stock in inventory much longer than necessary. This would clog supply lines, raise prices, complicate logistics and in general negatively impact world trade and the flow of good. Further, not only do the bills lack a precise definition of exactly what scanning means, it's not clear that the implementation of 100% would bring about an increase in safety and security [20]. The RSM presents a good option to alleviate some of these issues, while contributing to a multi-layered, rick-based approach to security. DHS has recognized that it can't use a one-size-fits-all solution and should adapt to the resources and technologies at hand, as well as the legitimate logistical and economic issues. In fact, through a balanced approach, with a multi-layer system and location scanning/surveillance, it could be possible to strike a balance with efficiency and security. The RSM offers a means to quickly distribute a significant number of cheap and reliable sensors to add data in a layered approach.

Not only does the United States need to spend resources at home, but also abroad. However, this is becoming more and more difficult. As an example, post 9-11, the Authorized and Appropriated budget for port security was in excessive of $400M. By 2013, it had fallen to just $94M [58]. So, the question of where, when, and to what magnitude monitoring is required will not disappear anytime soon, and the U.S. will need to decide if the expenditure is worth it? Granted, the risk is low, but one radiological incident is one too many and can never be undone.

A nightmare scenario for Homeland Security agents is the smuggling of Special Nuclear Material, whether the intent is to detonate as a nuclear weapon, or to be used simply as an exposure or dispersal device across our border from another country. The Ports-of-Entry offer a logical chokepoint for pin-pointing radiological material, but simply inspecting each item has turned out to be expensive, time consuming and technically frustrating. Neutron detectors are more expensive than gamma scintillators based on the materials used, and neutrons (used to either bombard a suspect material for identification or originating from the suspect material) are easy to shield with Hydrogen rich supplies, such as food, clothing, and fuel (wood, charcoal and liquid fuels). High-power x-rays may get around some of the issues when interrogating shielded material, and also offer the advantage of being able to identify all sorts of other materials (such as checking for conventional explosives or residues) but require arrays of expensive high-purity germanium detectors. However, the cost, and thermal management requirements of a system of this sort are prejudicial. It might be more cost-effective to outfit the actual cargo ship (or truck) carrying the container with an RSM system. As well, getting sufficient (but affordable) systems in place now, would enhance DHS's ability to ensure that other areas, such as Nuclear Reactor sites, spent fuel rod storage areas, fuel refineries and power distribution centers are adequately protected [61].

Dabiq, an ISIS propaganda magazine, raise the "hypothetical" scenario of the Islamic State purchasing a functional nuclear weapon from the Pakistanis back in May 2015. Fortunately, it appears that ISIS is currently in decline, but at the time this "hypothetical" threat was very plausible. The caliphate had billions of dollars in U.S. currency that it had seized from banks within its area of control, it would only be a matter of finding a sympathizer within the Pakistani government to support their plan. As far-fetched as it may sound now, this really does bring up a non-zero probability of a terrorist state quickly obtaining a nuclear weapon, especially considering the current rise of the Taliban in Afghanistan. Also, it should be noted that there are no political or moral issues standing in their way for its immediate use, as is evidenced by rhetoric [62].

6.4 Future Proposed Hybrid RSM/RMC System

Further development and validation of the parameterized Beer-Lambert's Law FEP attenuation by scatter-out or addition by Compton scatter-in based DRMs developed here should be investigated, as is the case with Holland's current line of research [42]. Initial work already shows good promise compared to time-consuming commercial code and when validated by experimental results could replace MCNP® or GEANT for prototyping and design comparison purposes. Further imaging techniques, using a high-speed image processing routine for near real-time scene generation and multisource/extended source identification and actual 2D imaging (not just point-source direction determination) in a high-background environment should be developed, as is the case with Olesen's ongoing research [40]. Miniaturization of the RSM was shown to be feasible and further work using faster acquisition capture electronics and correctly shaped detector crystals should be accomplished.

Due to the FOV of the current RSM designs and relatively poor-performing forward-looking solid angle of 15°, possible incorporation/hybridization of an attenuation by absorption

material, such as the Tungsten slit masks from Kowash's work, would enhance the forward-looking capabilities of a RSM and should be undertaken. Kowash's work showed a solid angle FOV for viewing in front of his RMC of about 17° [6], while this work found the RSM to be of limited use in this range. Furthermore, RSM systems will probably always be limited in their resolution of closely spaced source objects due to the scintillator detector volume compared to the scatter mask material dimensions in the forward-looking orientation. It would be interesting in future instantiations of the RSM to incorporate RMC like slit masks into the production of the RSM. It would not significantly affect the RSM performance over the rest of its viewing area and could most likely be used to increase resolution of two closely spaced sources after a general "hot spot" area had been identified by the RSM. Building a hybrid RSM/RMC as envisioned above would consist of little integration effort but offers the potential for significantly enhanced source discrimination. It was recognized early on in this work, that investigation of further RSM designs and development, with the incorporation of a slitted/patterned high-Z, attenuation material (possibly in the additive manufacturing process) to mimic an RMC or coded-aperture like system could improve the forward-looking capabilities of the RSM. Although not generally thought of as a scatterer, it may be of benefit to also incorporate a thin layer of Tungsten into the design to offset any size constraint posed by the mass of acrylic used in this work. Since the Z_{eff} of the two materials is similar, especially when looking for higher energy gamma sources where incoherent scattering outpaces photoelectric absorption after about 500 keV in Tungsten [15], the system could be engineered to a resultant smaller size while maintaining the performance characteristics. Gridded/patterned attenuation material may also enhance the side-viewing angles performance and assist in image reconstruction. Current proof-of-concept work, which has proven especially useful for neutron detection/imaging applications, is the Sandia National Laboratory TEI-2D system [63].

Similar to the RSM it uses a single, internally placed detector with a coded aperture made of HDPE material. The hollow, coded cylinder aperture is then rotated, with time/rotation information retained for later source image reconstruction.

From an aerial CONOPS perspective, any source identified would likely first be seen in the side viewing angles of the RSM. At this point, the UAV operator would need to reorient the RSM to take advantage of the resolution of the RMC hybrid integration. This is what the "Operator Display" in Figure 84 is meant to help with for airborne RSM detection systems. This notional flat panel display is composed of a 0^{o} to 360^{o} gridded view in θ, with the forward facing 2π radians of the φ viewing angle falling within the red dashed line. Outside of the dashed line, the operator would have to realize that the source is behind them in the rearward facing 2π radians of coverage. Then they would just simply center the indicated source position by rolling left or right and pulling back on the stick. The inherent separation distance from the ground to a UAV-based system would also maintain the desirable "far field" conditions for optimal RMC modulation curve formation and image processing.

However, any UAV-based RSM system will also require a mechanism to point-and-track the sensor, to maintain the appropriate viewing angle configuration while maintaining stable flight conditions. In conjunction, algorithms to "lock" the source search space to a stable reference frame, relative to the motion of the aircraft through the area will be needed for post-processing the data. These transformations are easily done utilizing differential GPS to track the UAV location and orientation angle of the RSM in flight and will be necessary for versatile use. These methodologies should be developed by the AFIT Physics and Nuclear Engineering Department in partnership with AFIT's Aeronautics Department for flight test.

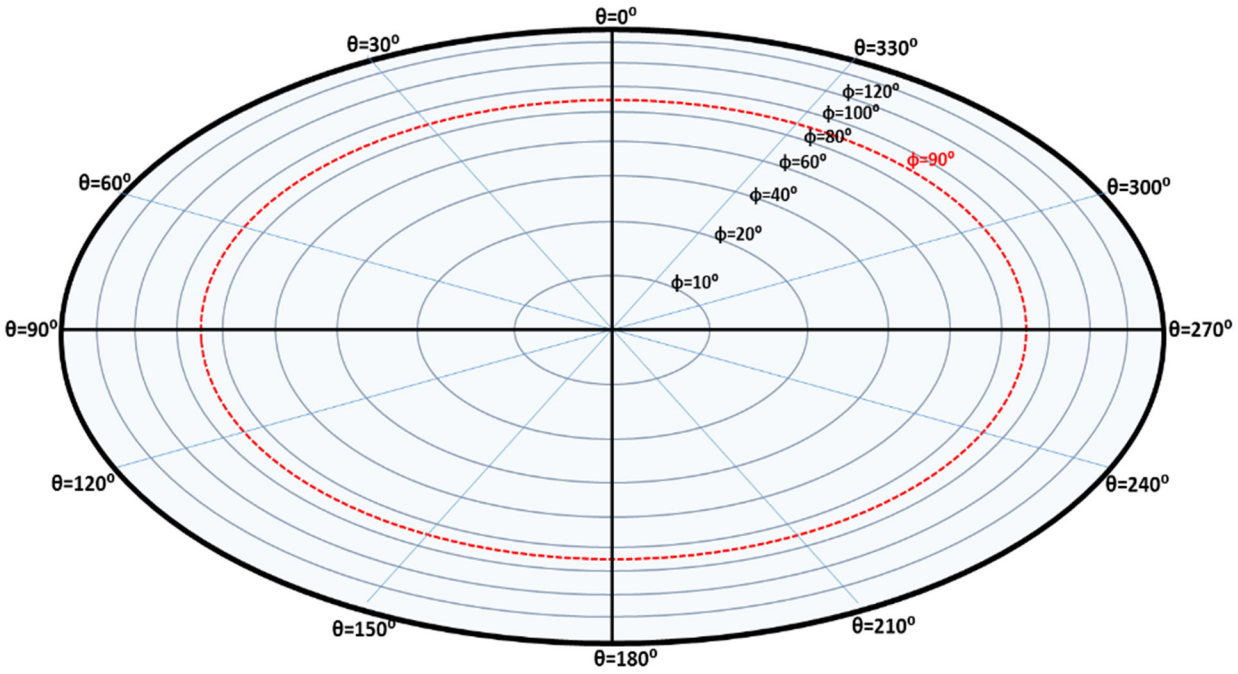

Figure 84. Notional Operator Display for flying to and centering a detected radiation source.

VII. Bibliography

[1] J. Fitzgerald, "A Rotating Scatter Mask for Inexpensive Gamma-Ray Imaging in Orphan Source Search: Simulation Results, DRAFT 4," *IEEE Transactions on Nuclear Science,* Unpublished.

[2] J. V. Logan, *Master's Thesis - Rotating Scatter Mask for Gamma Source Inaging,* Wright-Patterson AFB, OH: Air Force Institute of Technology, 2017.

[3] Z. T. Condon, *Masters Thesis - Multisource Direction Identification Using a Rotating Scatter Mask,* Wright-Patterson AFB, OH: Air Force Institute of Technology, 2018.

[4] K. Vetter, L. Mihailescu, K. Nelson, J. Valentine and D. Wright, "Gamma-ray Imaging Methods UCRL-TR-225239," DOE, Lawrence Livermore National Laboratory, Pleasanton CA, 2006.

[5] D. Holland, J. Bevins, L. Burggraf, B. O'Day and R. Olesen, "Rotating Scatter Mask for Directional Radiation Detection and Imaging". U.S. Patent and Trademark Office Patent 17/007063, 17 12 2020.

[6] B. R. Kowash, *PhD Dissertation - A Rotating Modulation Imager for the Orphan Source Search Problem,* DTIC, 2008.

[7] K. S. Krane, Introductory Nuclear Physics, Oregon State University: John Wiley & Sons, 1988.

[8] National Institute for Standards U.S. Department of Commerce, "XCOM: Photon Cross-Sections Database," Physical Measurements Laboratory, Nov 2010. [Online]. Available: https://www.nist.gov/pml/xcom-photon-cross-sections-database. [Accessed Sep 2021].

[9] LD Didactic, "Compton Effect (spectrum)," LD Didactic, 2021. [Online]. Available: https://www.ld-didactic.de/software/524221en/Content/Appendix/ComptonSpectrum.htm. [Accessed 25 07 2021].

[10] NIST, "XCOM: Photon Cross-Section Database," 2015. [Online]. Available: https://www.nist.gov/pml/xcom-photon-cross-sections-database. [Accessed 2015].

[11] G. F. Knoll, Radiation Detection and Measurement, Ann Arbor, Michigan: John Wiley & Sons, 2010.

[12] Y. Yamashita, M. Kimura, M. Kitahara, T. Hamaguchi, I. Kanno, M. Ohtaka, M. Hashimoto, K. Ara and H. Onabe, "Measurement of effective atomic numbers using energy-resolved computed tomography," *Journal of Nuclear Science and Technology,* vol. 51, no. 10, pp. 1256-1263, 2014.

[13] optics.org, "NaI Iodide Crystal," optics.org, 06 07 2020. [Online]. Available: https://optics.org/products/P000023046. [Accessed 25 07 2021].

[14] J. H. Hubbell, "Radiation Physics," in *Encyclopedia of Physical Science and Technology (Third Edition)*, Elsevier Science Ltd., 2003, pp. 561-580.

[15] N. I. o. S. a. Technology, "XCOM," Physical Measurements Laboratory, [Online]. Available: https://physics.nist.gov/PhysRefData/Xcom/html/xcom1.html. [Accessed 01 06 2015].

[16] O. D. o. Crystallography, "Mass Attenuation Coefficient," International Union of Crystallography, 8 05 2018. [Online]. Available: https://dictionary.iucr.org/Mass_attenuation_coefficient. [Accessed 25 07 2021].

[17] T. E. Peterson and L. R. Furenlid, "SPECT detectors: the Anger Camera and beyond," *Phys Med Biol,* no. Sep 2011, pp. R145-R182, 2011.

[18] J. G. FitzGerald, A Programmable Liquid Collimator for Both Coded Aperture Adaptive Imaging and Multiplexed Compton Scatter Tomography, vol. 1026, Wright-Patterson AFB: AFIT - Theses and Dissertations, 2012.

[19] B. Budden, G. Case and M. Cherry, "Image Reconstruction with a Labr3-Based Rotational Modulator," *Nuclear Instruments & Methods in Physics Research Section a, vol. 652, no. 1,* pp. 610-614, 2011.

[20] A. Natter, "Shippers Screening Security," JOC Regulation & Policy, 08 July 2007. [Online]. Available: https://www.joc.com/regulation-policy/shippers-screening-security_20070708.html.

[21] M. Kagaya, H. Katagiri, R. Enomoto, R. Hanafusa, M. Hosokawa, Y. Itoh, H. Muraishi, K. Nakayama, K. Satoh, T. Takeda, M. Tanaka, T. Uchida, T. Watanabe, S. Yanagita, T. Yoshida and K. Umehara, "Development of a Low-Cost-High-Sensitivity Compton Camera Using Csi (Tl) Scintillators (Γi)," *Nuclear Instruments & Methods in Physics Research Section a, vol. 804,* pp. 25-32, 2015.

[22] J. B. Martin, N. Dogan, J. E. Gormley, G. F. Knoll, M. O'Donnell and D. K. Wehe, "Imaging Multi-energy Gamma-ray Fields with a Compton Scatter Camera," *IEEE Transactions on Nuclear Science,* vol. 41, no. 4, pp. 1019-1025, August 1994.

[23] J. B. Martin, L. W. Burggraf and M. C. Roggemann, "Demonstration of Energy-coded Compton Scatter Tomography with Fan Beams for One-sided Inspection," *Nuclear Instruments & Methods in Physics Research Section A (Accelerators, Spectrometers, Detectors and Associated Equipment),* vol. 480, no. 2-3, pp. 797-806, 2002.

[24] B. L. Evans, J. B. Martin, L. W. Burggraf and M. C. Roggeman, "Nondestructive Inspection Using Compton Scatter Tomography," *IEEE Transactions on Nuclear Science,* vol. 45, 1998.

[25] Y. Shirakawa, "Developments of Directional Detectors with Nai(Tl)/BGO Scintillators," *Nuclear Instruments & Methods in Physics Research Section B, vol. 213, no. 1-4,* pp. 255-259, 2004.

[26] D. E. Holland, *Email Correspondence/Corrections on the Final RSM Efforts of this Dissertation,* Wright-Patterson AFB: AFIT/ENP, 2022.

[27] J. Rodgers, "Chernobyl's Red Forest mapped by drones as scientists discover radioactive hotspots," Fox News, 08 May 2019. [Online]. Available: https://www.foxnews.com/science/chernobyl-red-forest-mapped-drones-radioactive-hotspots.

[28] C. R. Yard, "Lost Radiation Sources: Raising Public Awareness about the Hazards Associated with Industrial," *Journal of Environmental Health, vol. 58, no. 10,* pp. 6-18, 1996.

[29] E. Fischbach and J. Jenkins, "Radiation Detection: There's an App for That," *Bulletin of the Atomic Scientists, vol. 68, no. 2,* pp. 63-69, March 2012.

[30] N. N. S. S. Remote Sensing Laboratory, *Tour Presentation,* Nellis AFB, NV, 2018.

[31] E. Kulisch, "U.S. lawmakers say with new technology, it's time to inspect all inbound containers," American Shipper, 18 August 2016. [Online]. Available: http://www.westarusa.com/u-s-lawmakers-say-new-technology-time-inspect-inbound-containers/.

[32] United Nations, "Other Peacekeeping-Related Matters," *UN Chronicle, vol. 39, no. 3,* p. 74, September-November 2002.

[33] J. V. Logan, D. E. Holland, L. W. Burggraf, J. A. Clinton and B. E. O'Day, "Monte Carlo and Experimental Analysis of a Novel Directional Rotating Scatter Mask Gamma Detection System," *Nuclear Instrumenation and Methods in Physics Research A,* 2019.

[34] J. Logan, *Email Correspondence,* 2021.

[35] R. Oleson, B. O'Day, D. Holland, L. Burggraf and J. Bevins, "Characterization of Novel Rotating Scatter Mask Designs for Gamma Direction Indentification," *Nuclear Instrumentation and Methods in Physics Research A,* 2018.

[36] R. J. Olesen, Masters Thesis - Optimization and Parameter Characterization for Rotating Scatter Mask Designs, Wright-Patterson AFB, OH: Air Force Institute of Technology, 2018.

[37] B. V. Egner, D. E. Holland, L. W. Burggraf and J. E. Bevins, "Development of a Modular Mixed-Radiation Directional Rotating Scatter Mask Detection System," *Nuclear Instrumention and Methods in Physics Research A,* 2020.

[38] L. W. Burggraf and et al., "An Effecient, Dual-Particle Directional Detection System using a Rotating Scatter Mask". U.S. Patent and Trademark Office Patent 62/816,451, 11 March 2019.

[39] R. J. Olesen, Dissertation: Low-Information Radiation Imaging using Rotating Scatter Mask Systems and Neural Network Algorithms, Wright-Patterson AFB, OH: Air Force Institute of Technology, 2020.

[40] R. J. Oleson, D. E. Holland, E. Brubaker, J. Cole and J. Bevins, "Advanced Radiation Imaging Algorithms with Rotating Scatter Masks," *Sandia National Laboratories White Paper,* no. 6448C, 2019.

[41] L. W. Buggraf, "Rotating Scatter Mask Design Classes for Directional Radiation Detection and Imaging". U.S. Patent and Trademark Office Patent 62/816,435, 11 March 2019.

[42] D. E. Holland, R. J. Olesen and J. E. Bevins, "Multi-objective genetic algorithm optimization of a directionally sensitive radiation detection system using a surrogate transport model," *Engineering Applications of Artificial Intelligence,* 16 06 2021.

[43] A. Rohatgi, "WebPlotDigitizer," [Online]. Available: https://automeris.io/WebPlotDigitizer/. [Accessed Dec 2015].

[44] U. S. N. R. Commission, "Basic Health Physics - Gamma Spectrum Features," 04 02 2011. [Online]. Available: https://www.nrc.gov/docs/ML1122/ML11229A703.pdf. [Accessed 25 07 2021].

[45] L. W. Burggraf, *Feedback Notes and Comments,* Wright-Patterson AFB: AFIT, 2022.

[46] D. Systemes, "COMPLETE SOLUTION FOR ABAQUS FINITE ELEMENT MODELING, VISUALIZATION, AND PROCESS AUTOMATION," ABAQUS/CAE, [Online]. Available: https://www.3ds.com/products-services/simulia/products/abaqus/abaquscae/. [Accessed 25 07 2021].

[47] "Veroclear Information Homepage," StrataSys, [Online]. Available: https://www.stratasys.com/materials/search/veroclear. [Accessed 01 2021].

[48] "ORTEC's Software Applications Page," ORTEC, [Online]. Available: https://www.ortec-online.com/products/application-software/gammavision. [Accessed 01 2021].

[49] SCIONIX, "Nomenclature & Type Numbering," SCIONIX HOLLAND, 2015. [Online]. Available: https://scionix.nl/nomenclature-type-numbering/. [Accessed 2021].

[50] "BrilLanCe Scintillators," St. Gobain, 01 2009. [Online]. Available: https://www.crystals.saint-

gobain.com/sites/imdf.crystals.com/files/documents/brillance-scintillators-performance-summary.pdf. [Accessed 03 01 2021].

[51] "Scintillator Crystals Properties Sheet," Scionix, [Online]. Available: https://scionix.nl/scintillation-crystals/#tab-id-4. [Accessed 01 2021].

[52] B. L. Evans, Fan-Beam Multiplexed Compton Scatter Tomography for Single-Sided Noninvasive Inspection, Wright-Patterson AFB: DTIC, 1999.

[53] M. Pastor, M. Binda and T. Harcarik, "Modal Assurance Criterion," *SciVerse ScienceDirect,* vol. Procedia Engineering 48, pp. 543 - 548, 2012.

[54] B. D. Milbrath, B. J. Choate, J. E. Fast, W. K. Hensley, R. T. Kouzes and J. E. Schweppe, "Comparison of LaBr3:Ce and NaI(Tl) Scintillators for Radio-Isotope Identifcation Devices," Pacific Northwest National Laboratory, U.S. Department of Energy, Richland, Washington, 2006.

[55] S. White, Interviewee, *First Responder, Fire Station Chief.* [Interview]. 2016.

[56] B. Li, Y. Zhu, Z. Wang, C. Li, Z.-R. Peng and L. Ge, "Use of Multi-Rotor Unmanned Aerial Vehicles for Radioactive Source Search," *Remote Sensing, vol. 10, no. 5,* pp. 728-741, 2018.

[57] D. Dubno, "Tiny Device Can Detect Nuclear Armageddon," *Popular Mechanics,* p. 18, May 2019.

[58] J. Bondareff and P. O'Neill, "Maritime Publications," BlankRome, July 2013. [Online]. Available: https://www.blankrome.com/publications/are-our-ports-safe-hodgepodge-maritime-security-laws-come-question.

[59] S. Magnuson, "DHS' Nuclear Detection Efforts Continue on Smaller Scale," *National Defense, no. 706,* pp. 14-15, September 2012.

[60] J. McHale, "DHS Turns to High Tech to Control Borders," *Military & Aerospace Electronics, vol. 16, no. 7,* pp. 22-26, July 2005.

[61] C. Biever, "Improved X-Ray Vision to Stop the Nuke Smugglers," *New Scientist, vol. 188, no. 2522,* pp. 30-31, September 2012.

[62] R. S. Litwak, "Recalibrating Deterrence to Prevent Nuclear Terrorism," *Washington Quarterly, vol. 40, no. 1,* pp. 55-70, January 2017.

[63] P. Marleau, "Feasibility Demonstration of Two Dimensional Time-Encoded Fast Neutron Imaging Using a Single Detector Pixel," Office of Scientific and Technical Information, Sandia National Laboratories, [Online]. Available: https://www.osti.gov/servlets/purl/1331945. [Accessed 25 07 2021].

[64] N. I. o. S. a. Technology, "NIST Standard Reference Database," Physical Measurements Laboratory, [Online]. Available: https://physics.nist.gov/PhysRefData/XrayMassCoef/chap2.html. [Accessed 25 07 2021].

[65] A. P. Society, "Arthur Holly Compton Laboratory of Physics, Washington University, St. Louis," History Outreach, 2021. [Online]. Available: https://www.aps.org/programs/outreach/history/historicsites/compton.cfm. [Accessed 25 07 2021].

[66] N. I. o. S. a. Technology, "X-Ray Mass Attenuation Coefficients," NIST, [Online]. Available: https://physics.nist.gov/PhysRefData/XrayMassCoef/chap2.html. [Accessed 25 07 2021].

[67] J. V. Logan, D. E. Holland, L. W. Burggraf, J. A. Clinton and B. E. O'Day III, "Monte Carlo and experimental analysis of a novel directional rotating scatter mask gamma detection system," *Nuclear Instruments and Methods in Physics ,* vol. 947, no. Research Section A: Accelerators, Spectrometers, Detectors and Associated Equipment, 2019.

VIII. Appendices

Full, unprocessed (or post-processed) experimental data sets, the computational DRM libraries, and the SolidWorks CAD files are available electronically upon request. Please contact the author at: ChrisCharles117@gmail.com.

Appendix A.1: Large FitzGerald Design RSM Data, NaI Detector, Cs-137 Single Source; Experimentally Derived Library Matching Results

View Angle φ = 5° : Spectrum, Modulation Curve Data (No Smoothing), Library Curve, MAC and Least Squares Direction Predict

Phi_ViewDegree = 5 Theta_ViewDegree = 0

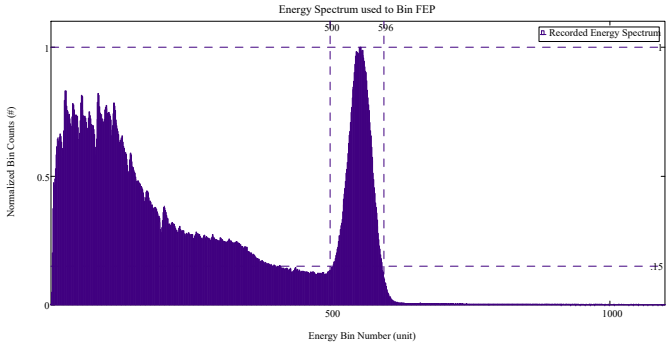

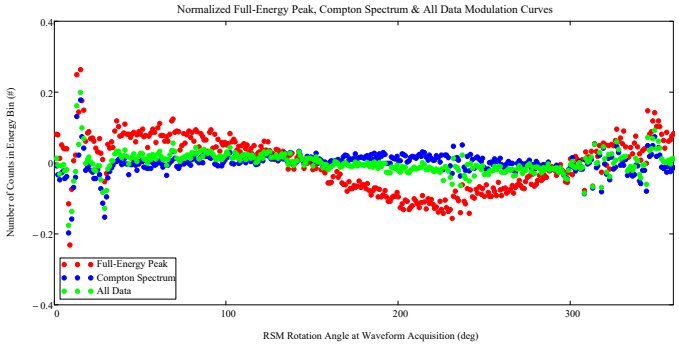

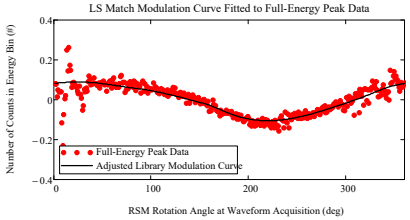

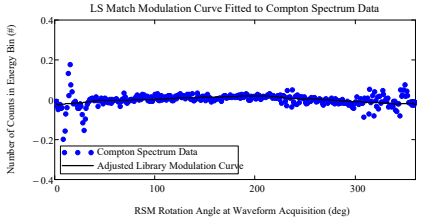

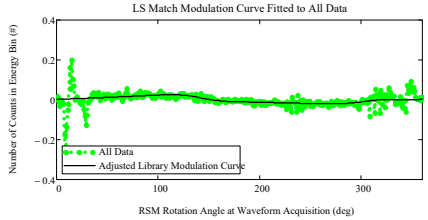

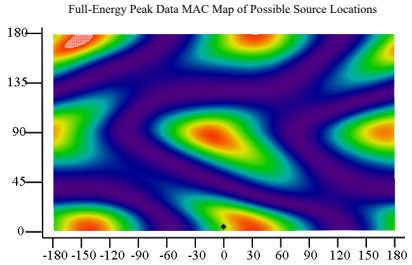

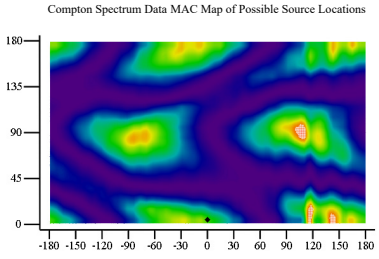

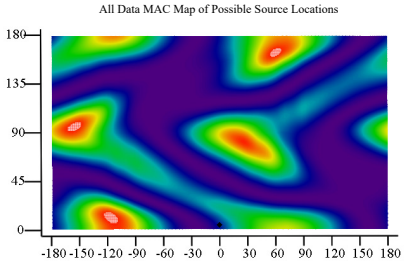

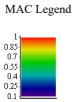

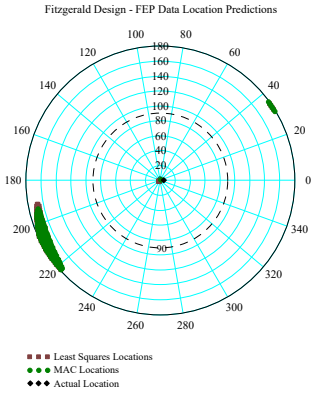

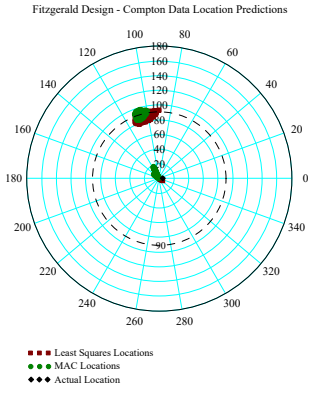

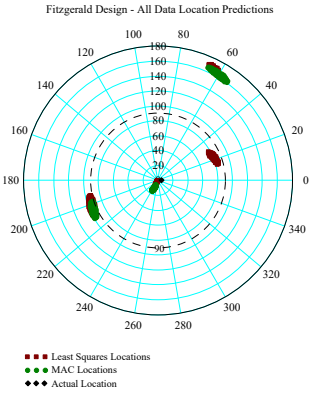

FEP Counting of Waveforms, Binned by RSM Rotation Angle; Used to Generate the Modulation Curve (ϕ = 5°)

RSM Rotation Angle	Number of Waveforms Recorded	RSM Rotation Angle	Number of Waveforms Recorded	RSM Rotation Angle	Number of Waveforms Recorded	RSM Rotation Angle	Number of Waveforms Recorded	RSM Rotation Angle	Number of Waveforms Recorded	RSM Rotation Angle	Number of Waveforms Recorded	RSM Rotation Angle	Number of Waveforms Recorded	RSM Rotation Angle	Number of Waveforms Recorded	Total Number of Waveforms in FEP
1	3194	46	3214	91	3241	136	2808	181	2595	226	2323	271	2627	316	2951	1034411
2	3186	47	3110	92	3043	137	2965	182	2648	227	2471	272	2604	317	3071	
3	2931	48	3185	93	3192	138	2983	183	2574	228	2385	273	2593	318	2779	
4	3072	49	3225	94	3057	139	2814	184	2527	229	2341	274	2670	319	3098	
5	3039	50	3192	95	3140	140	2876	185	2571	230	2363	275	2718	320	3082	
6	3034	51	3249	96	3009	141	2939	186	2600	231	2270	276	2737	321	2855	
7	3037	52	3166	97	3104	142	2973	187	2601	232	2508	277	2646	322	3071	
8	2429	53	3181	98	3073	143	2932	188	2502	233	2564	278	2757	323	2811	
9	1976	54	3049	99	3102	144	2921	189	2589	234	2489	279	2625	324	3080	
10	2591	55	3171	100	3077	145	2818	190	2506	235	2459	280	2644	325	3069	
11	2901	56	3209	101	3090	146	2889	191	2527	236	2332	281	2688	326	3127	
12	2961	57	3247	102	3202	147	2874	192	2571	237	2636	282	2739	327	3250	
13	3848	58	3213	103	3109	148	2918	193	2505	238	2454	283	2685	328	3115	
14	3439	59	3106	104	3137	149	2889	194	2456	239	2424	284	2706	329	3153	
15	3902	60	3264	105	3113	150	2803	195	2457	240	2596	285	2744	330	3091	
16	3560	61	3313	106	3017	151	2834	196	2493	241	2326	286	2720	331	3227	
17	3459	62	3181	107	3062	152	2816	197	2510	242	2580	287	2802	332	3057	
18	3115	63	3182	108	2997	153	2876	198	2511	243	2505	288	2791	333	2934	
19	3205	64	3117	109	3066	154	2880	199	2555	244	2491	289	2840	334	2943	
20	3225	65	3163	110	3092	155	2804	200	2507	245	2591	290	2828	335	3050	
21	3146	66	3115	111	3035	156	2803	201	2388	246	2544	291	2789	336	2975	
22	3154	67	3197	112	3075	157	2768	202	2430	247	2615	292	2739	337	3098	
23	3119	68	3337	113	2990	158	2845	203	2366	248	2535	293	2788	338	3171	
24	3042	69	3358	114	3037	159	2654	204	2469	249	2592	294	2861	339	3054	
25	3001	70	3214	115	2977	160	2660	205	2457	250	2513	295	2801	340	2975	
26	3147	71	3226	116	3067	161	2664	206	2365	251	2639	296	2780	341	2908	
27	2988	72	3219	117	2945	162	2730	207	2383	252	2554	297	2672	342	3013	
28	2913	73	3023	118	2982	163	2878	208	2408	253	2512	298	2667	343	3035	
29	2670	74	3067	119	2999	164	2786	209	2481	254	2511	299	2770	344	2876	
30	2762	75	3198	120	3064	165	2720	210	2453	255	2603	300	2919	345	3453	
31	3085	76	3099	121	3018	166	2758	211	2428	256	2570	301	2750	346	3197	
32	3040	77	3189	122	3117	167	2659	212	2384	257	2521	302	2870	347	3223	
33	3111	78	3229	123	3019	168	2645	213	2441	258	2664	303	2949	348	3343	
34	3050	79	3156	124	3111	169	2637	214	2517	259	2582	304	2916	349	3433	
35	3227	80	3217	125	3014	170	2566	215	2448	260	2516	305	2815	350	3279	
36	3338	81	3118	126	2987	171	2670	216	2369	261	2597	306	2845	351	3340	
37	3280	82	3241	127	2977	172	2598	217	2485	262	2599	307	2914	352	3275	
38	3170	83	3219	128	2917	173	2596	218	2434	263	2545	308	2571	353	3194	
39	3179	84	3053	129	3026	174	2628	219	2473	264	2567	309	3002	354	3125	
40	3210	85	3201	130	3021	175	2611	220	2421	265	2587	310	2945	355	3042	
41	3305	86	3166	131	2983	176	2624	221	2376	266	2631	311	2944	356	3215	
42	3197	87	3130	132	2942	177	2678	222	2391	267	2546	312	3007	357	3118	
43	3195	88	3133	133	3009	178	2611	223	2334	268	2611	313	2623	358	3128	
44	3157	89	3004	134	2970	179	2636	224	2454	269	2638	314	3086	359	3172	
45	3196	90	3212	135	2934	180	2634	225	2364	270	2683	315	3004	360	3203	

Compton Counting of Waveforms, Binned by RSM Rotation Angle; Used to Generate the Modulation Curve (ϕ = 5°)

RSM Rotation Angle	Number of Waveforms Recorded	RSM Rotation Angle	Number of Waveforms Recorded	RSM Rotation Angle	Number of Waveforms Recorded	RSM Rotation Angle	Number of Waveforms Recorded	RSM Rotation Angle	Number of Waveforms Recorded	RSM Rotation Angle	Number of Waveforms Recorded	RSM Rotation Angle	Number of Waveforms Recorded	RSM Rotation Angle	Number of Waveforms Recorded	Total Number of Waveforms in FEP
1	9921	46	10120	91	10190	136	10040	181	10260	226	9806	271	10040	316	9929	3606018
2	9623	47	9946	92	10240	137	10380	182	10280	227	10290	272	9817	317	10300	
3	9452	48	9767	93	9988	138	9993	183	10170	228	10290	273	9992	318	9036	
4	9699	49	9988	94	9976	139	9990	184	10330	229	10210	274	9928	319	10540	
5	9761	50	10130	95	9928	140	10070	185	10150	230	9931	275	10050	320	9988	
6	9501	51	10070	96	10220	141	10080	186	10370	231	9676	276	10120	321	9643	
7	9564	52	9897	97	9929	142	10440	187	10230	232	10610	277	9868	322	10200	
8	7622	53	9865	98	10040	143	10300	188	10170	233	10190	278	9974	323	9458	
9	6340	54	9846	99	10130	144	10130	189	10340	234	10220	279	9801	324	10230	
10	8106	55	10060	100	10350	145	10000	190	10260	235	10120	280	10090	325	9819	
11	9180	56	9836	101	10230	146	10030	191	10390	236	9577	281	10020	326	9897	
12	9548	57	10040	102	10390	147	10260	192	10320	237	10650	282	9929	327	10610	
13	11640	58	9959	103	10010	148	10200	193	10020	238	9892	283	9785	328	10380	
14	10290	59	9973	104	9994	149	10240	194	10010	239	9781	284	9976	329	9957	
15	12190	60	10050	105	10250	150	9973	195	10020	240	10250	285	9817	330	10080	
16	10940	61	10110	106	10280	151	10210	196	10240	241	9764	286	9975	331	9958	
17	10530	62	10020	107	10010	152	10370	197	10200	242	10330	287	10060	332	10140	
18	9787	63	9888	108	10050	153	10040	198	10170	243	10160	288	9823	333	9596	
19	9863	64	9945	109	10140	154	10160	199	10260	244	9845	289	9825	334	9683	
20	9951	65	9614	110	10220	155	10130	200	10100	245	10210	290	9844	335	9692	
21	9774	66	9941	111	10030	156	9907	201	10110	246	10230	291	9835	336	9580	
22	9709	67	10050	112	10220	157	10050	202	10350	247	10140	292	9952	337	9623	
23	9504	68	10100	113	10280	158	9996	203	10320	248	10080	293	9703	338	9950	
24	9499	69	10440	114	10080	159	9968	204	10270	249	10200	294	9860	339	9939	
25	9791	70	10200	115	10300	160	10060	205	10050	250	9859	295	9742	340	9408	
26	9622	71	9901	116	10080	161	10090	206	10110	251	9792	296	9624	341	9322	
27	9138	72	9838	117	9966	162	10090	207	10220	252	9823	297	9545	342	9788	
28	8637	73	9950	118	9996	163	10100	208	10260	253	10050	298	9499	343	9787	
29	8173	74	10020	119	10110	164	10120	209	10230	254	10070	299	9796	344	9049	
30	8873	75	9994	120	10230	165	10150	210	10180	255	9958	300	9914	345	10620	
31	9511	76	10040	121	10100	166	9958	211	10250	256	10180	301	10220	346	10260	
32	9737	77	10070	122	10280	167	10100	212	10320	257	10080	302	9881	347	10310	
33	9873	78	10030	123	10320	168	10240	213	10270	258	10110	303	9746	348	10640	
34	9946	79	9955	124	10290	169	10300	214	10410	259	10180	304	9853	349	10940	
35	10070	80	10150	125	10390	170	10270	215	10380	260	9964	305	10080	350	10250	
36	10090	81	10190	126	10180	171	10120	216	10230	261	9895	306	9812	351	10560	
37	10140	82	10340	127	10180	172	10180	217	10130	262	9921	307	9816	352	10290	
38	10110	83	10110	128	10270	173	10150	218	10290	263	10000	308	8975	353	9878	
39	9965	84	10030	129	10230	174	10200	219	10200	264	10080	309	10120	354	9835	
40	10010	85	10240	130	10110	175	10340	220	10120	265	10020	310	9990	355	9892	
41	10200	86	10040	131	10220	176	10180	221	10130	266	10020	311	10030	356	9721	
42	9997	87	10380	132	10350	177	10200	222	10270	267	9778	312	10140	357	9903	
43	9628	88	10260	133	10170	178	10240	223	10210	268	9718	313	9170	358	9726	
44	9971	89	10320	134	10360	179	10210	224	10060	269	10020	314	10660	359	9913	
45	9977	90	10220	135	10090	180	10180	225	10310	270	10110	315	9871	360	9862	

View Angle φ = 15° : Spectrum, Modulation Curve Data (No Smoothing), Library Curve, MAC and Least Squares Direction Predictions

Phi_ViewDegree = 15 Theta_ViewDegree = 0

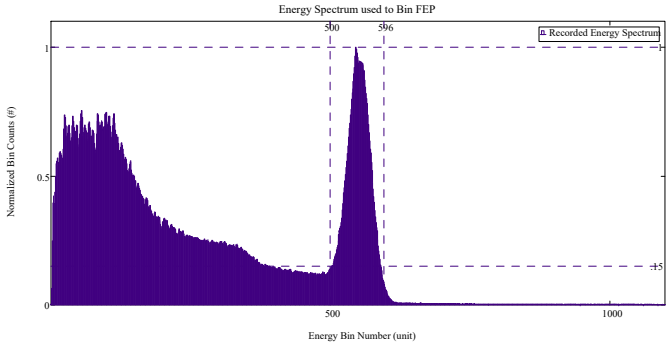

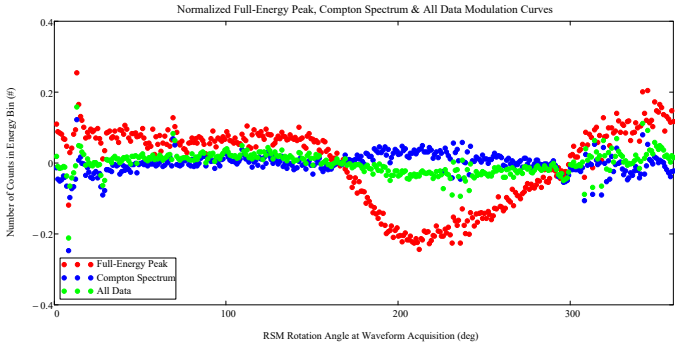

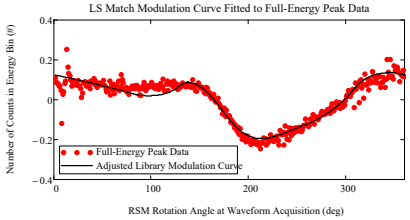

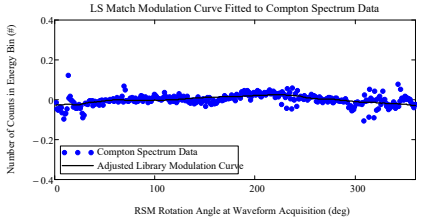

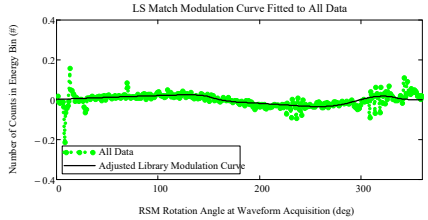

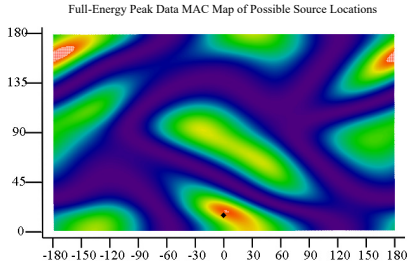

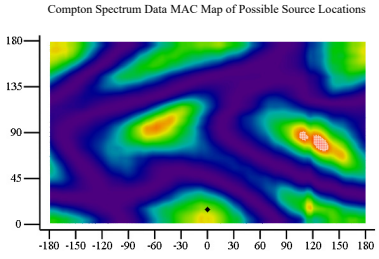

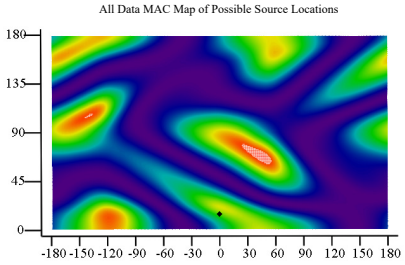

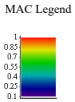

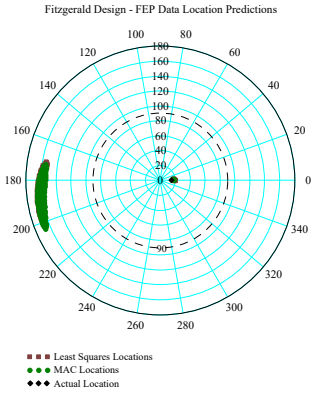

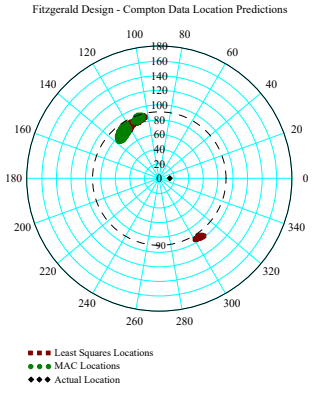

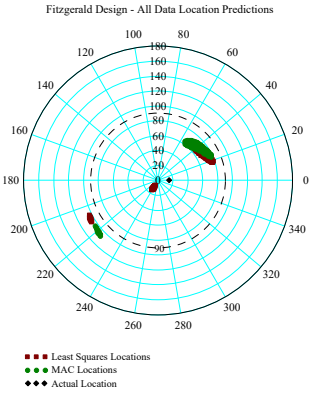

FEP Counting of Waveforms, Binned by RSM Rotation Angle; Used to Generate the Modulation Curve (ϕ = 15°)

RSM Rotation Angle	Number of Waveforms Recorded	RSM Rotation Angle	Number of Waveforms Recorded	RSM Rotation Angle	Number of Waveforms Recorded	RSM Rotation Angle	Number of Waveforms Recorded	RSM Rotation Angle	Number of Waveforms Recorded	RSM Rotation Angle	Number of Waveforms Recorded	RSM Rotation Angle	Number of Waveforms Recorded	RSM Rotation Angle	Number of Waveforms Recorded	Total Number of Waveforms in FEP
1	3224	46	3125	91	3071	136	3067	181	2387	226	2036	271	2433	316	3032	1011350
2	3147	47	3133	92	3150	137	3115	182	2443	227	2107	272	2483	317	3109	
3	3135	48	3092	93	3044	138	3076	183	2406	228	2071	273	2508	318	2842	
4	3118	49	3096	94	2983	139	3066	184	2356	229	2127	274	2553	319	3296	
5	3069	50	3112	95	3078	140	3084	185	2285	230	2048	275	2595	320	3093	
6	3067	51	3180	96	3067	141	3051	186	2338	231	1962	276	2532	321	3101	
7	2990	52	3080	97	3046	142	3193	187	2268	232	2237	277	2586	322	3188	
8	2365	53	3015	98	3089	143	3064	188	2220	233	2198	278	2555	323	3001	
9	2921	54	2970	99	3067	144	3081	189	2291	234	2149	279	2545	324	3189	
10	2970	55	3023	100	3144	145	2988	190	2163	235	2200	280	2580	325	3135	
11	3116	56	2989	101	3107	146	2974	191	2275	236	1960	281	2626	326	3155	
12	3169	57	3174	102	3051	147	3097	192	2150	237	2321	282	2619	327	3344	
13	3773	58	2902	103	3048	148	3129	193	2062	238	2151	283	2553	328	3260	
14	3433	59	3089	104	3023	149	3074	194	2084	239	2063	284	2660	329	3141	
15	3308	60	3013	105	3079	150	3064	195	2095	240	2195	285	2741	330	3228	
16	3267	61	3106	106	3035	151	3041	196	2142	241	2058	286	2612	331	3213	
17	3196	62	2934	107	3011	152	3052	197	2022	242	2284	287	2605	332	3130	
18	3077	63	3024	108	3020	153	3032	198	2097	243	2228	288	2646	333	3257	
19	3141	64	3096	109	3122	154	2953	199	2122	244	2141	289	2744	334	3258	
20	3093	65	3011	110	3071	155	2925	200	2036	245	2270	290	2770	335	3051	
21	3173	66	3167	111	3054	156	3053	201	2044	246	2181	291	2728	336	3130	
22	3149	67	2993	112	3206	157	3037	202	1973	247	2274	292	2672	337	3139	
23	3157	68	3056	113	2983	158	2938	203	2041	248	2286	293	2763	338	3239	
24	3081	69	3292	114	2973	159	2959	204	2065	249	2225	294	2650	339	3189	
25	3178	70	3198	115	3111	160	2891	205	1991	250	2280	295	2728	340	3047	
26	3069	71	3137	116	3169	161	2848	206	1991	251	2223	296	2682	341	3206	
27	3023	72	3023	117	2983	162	2860	207	2032	252	2294	297	2721	342	3572	
28	2857	73	3006	118	3123	163	2865	208	1971	253	2261	298	2718	343	3339	
29	2942	74	3048	119	3104	164	2920	209	1961	254	2208	299	2795	344	3265	
30	3130	75	2962	120	3149	165	2808	210	2007	255	2252	300	2887	345	3581	
31	3141	76	2959	121	3097	166	2779	211	1967	256	2329	301	2902	346	3243	
32	3151	77	2922	122	3066	167	2814	212	1893	257	2322	302	2992	347	3265	
33	3076	78	3024	123	3170	168	2850	213	2007	258	2449	303	2880	348	3199	
34	3091	79	3029	124	3117	169	2747	214	1994	259	2354	304	2877	349	3462	
35	3150	80	3077	125	3113	170	2714	215	2086	260	2345	305	2946	350	3371	
36	3076	81	3031	126	3113	171	2664	216	2073	261	2303	306	2955	351	3354	
37	3030	82	3073	127	3008	172	2664	217	2083	262	2328	307	3013	352	3436	
38	3169	83	3028	128	3028	173	2551	218	1955	263	2444	308	2664	353	3401	
39	3157	84	3090	129	3062	174	2606	219	1986	264	2421	309	3137	354	3329	
40	3122	85	3080	130	3101	175	2657	220	2043	265	2398	310	3008	355	3152	
41	3213	86	3053	131	3069	176	2494	221	2032	266	2536	311	3116	356	3308	
42	3174	87	3011	132	3137	177	2616	222	2145	267	2359	312	3088	357	3280	
43	3080	88	2911	133	3096	178	2516	223	2089	268	2501	313	2761	358	3248	
44	3045	89	2888	134	3090	179	2515	224	2083	269	2468	314	3169	359	3368	
45	3126	90	3020	135	3061	180	2506	225	2033	270	2459	315	3192	360	3253	

Compton Counting of Waveforms, Binned by RSM Rotation Angle; Used to Generate the Modulation Curve (ϕ = 15°)

RSM Rotation Angle	Number of Waveforms Recorded	RSM Rotation Angle	Number of Waveforms Recorded	RSM Rotation Angle	Number of Waveforms Recorded	RSM Rotation Angle	Number of Waveforms Recorded	RSM Rotation Angle	Number of Waveforms Recorded	RSM Rotation Angle	Number of Waveforms Recorded	RSM Rotation Angle	Number of Waveforms Recorded	RSM Rotation Angle	Number of Waveforms Recorded	Total Number of Waveforms in FEP
1	9436	46	9545	91	9635	136	9553	181	9878	226	9325	271	9644	316	9529	3446890
2	9079	47	9572	92	9659	137	9582	182	9865	227	10030	272	9464	317	9586	
3	9020	48	9291	93	9421	138	9523	183	9787	228	9922	273	9725	318	8600	
4	9075	49	9526	94	9674	139	9380	184	9796	229	9817	274	9725	319	10060	
5	9183	50	9582	95	9603	140	9428	185	9674	230	9710	275	9552	320	9573	
6	9144	51	9591	96	9488	141	9445	186	10020	231	9120	276	9666	321	9010	
7	8875	52	9533	97	9685	142	9631	187	9958	232	10200	277	9448	322	9645	
8	6888	53	9538	98	9705	143	9733	188	9915	233	9902	278	9423	323	9089	
9	8518	54	9499	99	9890	144	9508	189	10080	234	9995	279	9559	324	9788	
10	8802	55	9598	100	9862	145	9542	190	9897	235	9646	280	9668	325	9321	
11	8854	56	9560	101	9770	146	9403	191	9983	236	9079	281	9665	326	9527	
12	9094	57	9559	102	9672	147	9590	192	10080	237	10230	282	9547	327	10050	
13	10930	58	9657	103	9641	148	9655	193	9834	238	9616	283	9545	328	9575	
14	9679	59	9492	104	9633	149	9524	194	9995	239	9589	284	9499	329	9613	
15	9778	60	9545	105	9605	150	9245	195	9590	240	9929	285	9553	330	9407	
16	9582	61	9610	106	9559	151	9515	196	9754	241	9216	286	9560	331	9223	
17	9557	62	9721	107	9626	152	9701	197	9881	242	10110	287	9488	332	9348	
18	9208	63	9476	108	9705	153	9603	198	10010	243	9655	288	9466	333	9061	
19	9445	64	9508	109	10000	154	9728	199	9949	244	9635	289	9573	334	9125	
20	9293	65	9644	110	9821	155	9409	200	9846	245	9775	290	9646	335	9285	
21	9139	66	9595	111	9705	156	9330	201	9873	246	9733	291	9507	336	9213	
22	9111	67	9766	112	9718	157	9419	202	10090	247	9683	292	9446	337	9347	
23	9254	68	9487	113	9614	158	9560	203	9965	248	9623	293	9169	338	9472	
24	9324	69	10330	114	9747	159	9372	204	10030	249	9826	294	9197	339	9366	
25	9130	70	10140	115	9462	160	9447	205	9787	250	9710	295	9250	340	9122	
26	9270	71	9545	116	9608	161	9398	206	9758	251	9715	296	8988	341	9243	
27	8862	72	9524	117	9669	162	9495	207	9889	252	9582	297	9007	342	10450	
28	8591	73	9501	118	9520	163	9530	208	9890	253	9699	298	9040	343	9243	
29	8731	74	9540	119	9768	164	9642	209	9989	254	9687	299	9207	344	9495	
30	9386	75	9674	120	9704	165	9614	210	9863	255	9792	300	9446	345	10170	
31	9379	76	9661	121	9448	166	9595	211	9937	256	9889	301	9379	346	9690	
32	9351	77	9699	122	9757	167	9535	212	10000	257	9763	302	9454	347	9634	
33	9321	78	9529	123	9565	168	9592	213	10020	258	9817	303	9388	348	9564	
34	9511	79	9504	124	9920	169	9819	214	10120	259	9785	304	9378	349	9770	
35	9533	80	9695	125	9785	170	9612	215	9932	260	9755	305	9393	350	9734	
36	9504	81	9484	126	9684	171	9697	216	9925	261	9513	306	9319	351	9598	
37	9527	82	9597	127	9565	172	9669	217	9919	262	9479	307	9434	352	9669	
38	9247	83	9506	128	9800	173	9646	218	10060	263	9668	308	8420	353	9631	
39	9321	84	9581	129	9652	174	9668	219	9980	264	9734	309	9849	354	9599	
40	9497	85	9723	130	9552	175	9688	220	9724	265	9553	310	9519	355	9484	
41	9361	86	9804	131	9624	176	9837	221	9840	266	9649	311	9570	356	9379	
42	9464	87	9786	132	9792	177	9717	222	9922	267	9448	312	9542	357	9287	
43	9387	88	9488	133	9469	178	9782	223	9749	268	9582	313	8621	358	9170	
44	9298	89	9683	134	9571	179	9632	224	9970	269	9542	314	10170	359	9323	
45	9536	90	9764	135	9417	180	9557	225	9883	270	9623	315	9666	360	9340	

View Angle φ = 25° : Spectrum, Modulation Curve Data (No Smoothing), Library Curve, MAC and Least Squares Direction Predictions

Phi_ViewDegree = 25 Theta_ViewDegree = 0

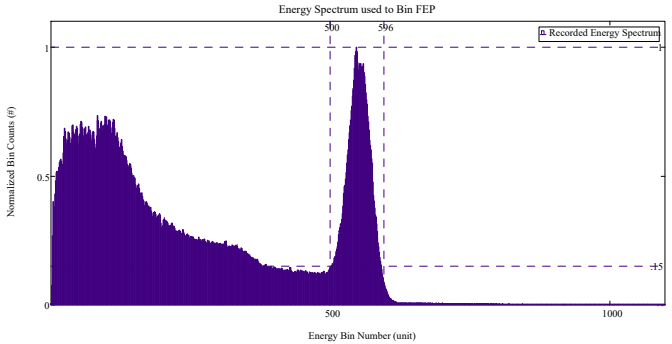

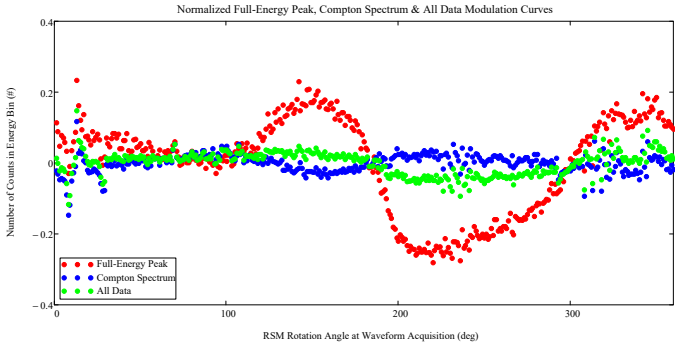

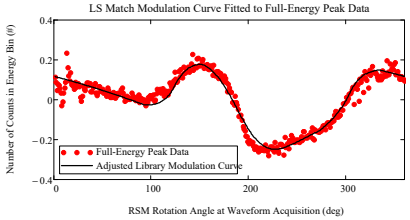

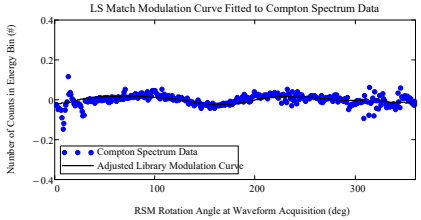

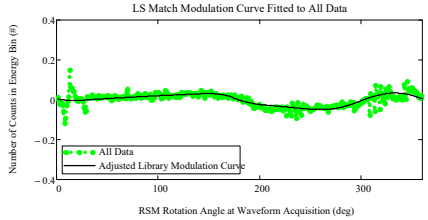

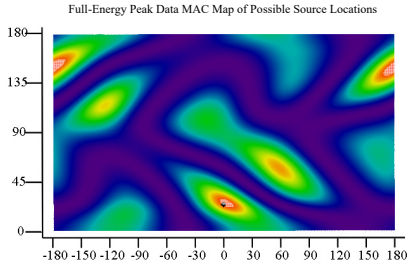

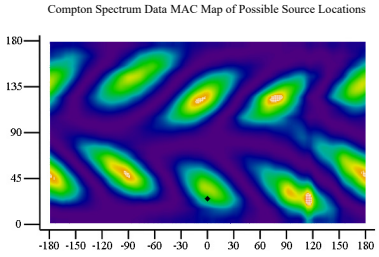

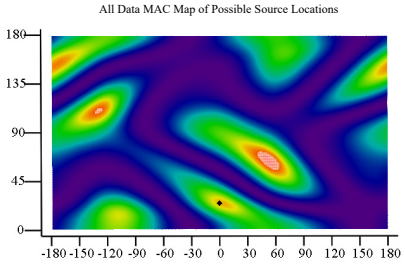

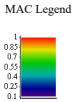

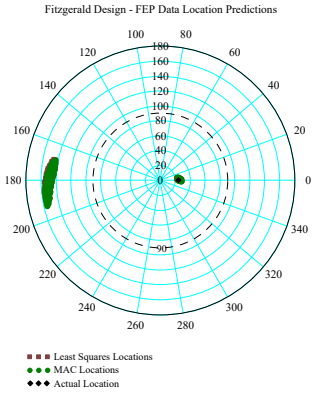

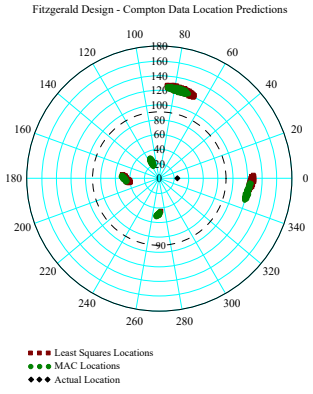

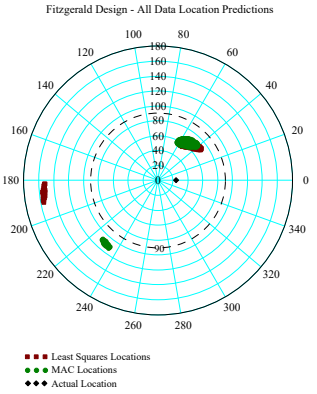

FEP Counting of Waveforms, Binned by RSM Rotation Angle; Used to Generate the Modulation Curve (ϕ = 25°)

RSM Rotation Angle	Number of Waveforms Recorded	RSM Rotation Angle	Number of Waveforms Recorded	RSM Rotation Angle	Number of Waveforms Recorded	RSM Rotation Angle	Number of Waveforms Recorded	RSM Rotation Angle	Number of Waveforms Recorded	RSM Rotation Angle	Number of Waveforms Recorded	RSM Rotation Angle	Number of Waveforms Recorded	RSM Rotation Angle	Number of Waveforms Recorded	Total Number of Waveforms in FEP
1	3154	46	2978	91	2753	136	3293	181	2896	226	1807	271	2177	316	3116	987433
2	3063	47	2985	92	2721	137	3306	182	2876	227	1980	272	2165	317	3160	
3	2916	48	2900	93	2739	138	3339	183	2695	228	1850	273	2194	318	2874	
4	3024	49	2917	94	2640	139	3248	184	2703	229	1894	274	2182	319	3251	
5	3000	50	2939	95	2710	140	3284	185	2654	230	1834	275	2228	320	3140	
6	2953	51	2873	96	2700	141	3388	186	2809	231	1787	276	2273	321	3092	
7	2864	52	2873	97	2788	142	3566	187	2697	232	1952	277	2273	322	3220	
8	2641	53	2890	98	2767	143	3275	188	2655	233	1949	278	2288	323	2959	
9	2714	54	2813	99	2817	144	3343	189	2570	234	1941	279	2205	324	3276	
10	2872	55	2954	100	2762	145	3335	190	2443	235	1915	280	2314	325	3186	
11	2958	56	2908	101	2824	146	3326	191	2453	236	1757	281	2338	326	3246	
12	3059	57	2865	102	2830	147	3485	192	2472	237	2075	282	2336	327	3342	
13	3579	58	2791	103	2716	148	3490	193	2384	238	1886	283	2253	328	3244	
14	3327	59	2793	104	2738	149	3359	194	2265	239	1910	284	2339	329	3232	
15	3178	60	2821	105	2858	150	3359	195	2224	240	1956	285	2350	330	3230	
16	3082	61	2876	106	2938	151	3373	196	2189	241	1867	286	2376	331	3211	
17	3237	62	2785	107	2892	152	3434	197	2099	242	2013	287	2370	332	3157	
18	3012	63	2782	108	2894	153	3472	198	2081	243	1996	288	2474	333	3102	
19	3016	64	2858	109	2939	154	3311	199	1989	244	2101	289	2537	334	3108	
20	2979	65	2826	110	2865	155	3359	200	1954	245	2062	290	2438	335	3178	
21	2931	66	2871	111	2897	156	3366	201	2018	246	2013	291	2531	336	3112	
22	3062	67	2857	112	2946	157	3381	202	1998	247	1981	292	2438	337	3269	
23	2975	68	2870	113	2816	158	3294	203	1957	248	1996	293	2457	338	3155	
24	3003	69	2923	114	2846	159	3285	204	1978	249	2030	294	2472	339	3179	
25	3036	70	2957	115	2906	160	3335	205	1912	250	1989	295	2575	340	3221	
26	2982	71	2866	116	2887	161	3353	206	1852	251	2024	296	2557	341	3169	
27	2788	72	2805	117	2837	162	3295	207	1907	252	1976	297	2677	342	3447	
28	2722	73	2723	118	2897	163	3191	208	1878	253	2000	298	2671	343	3241	
29	2807	74	2738	119	3045	164	3372	209	1874	254	2082	299	2684	344	3202	
30	2998	75	2806	120	3009	165	3235	210	1816	255	2014	300	2787	345	3396	
31	2940	76	2792	121	2972	166	3180	211	1834	256	2173	301	2717	346	3263	
32	2912	77	2750	122	3002	167	3254	212	1884	257	2172	302	2770	347	3309	
33	2992	78	2752	123	3087	168	3256	213	1847	258	2058	303	2848	348	3283	
34	3046	79	2782	124	3239	169	3125	214	1845	259	2087	304	2859	349	3380	
35	3045	80	2866	125	3118	170	3216	215	1871	260	2062	305	2873	350	3410	
36	3001	81	2814	126	3058	171	3216	216	1839	261	2101	306	2923	351	3200	
37	3034	82	2774	127	3087	172	3176	217	1938	262	2103	307	2967	352	3248	
38	2893	83	2774	128	3251	173	3103	218	1840	263	2084	308	2668	353	3251	
39	2890	84	2737	129	3157	174	3077	219	1818	264	2161	309	2967	354	3180	
40	2975	85	2752	130	3290	175	3171	220	1739	265	2241	310	3013	355	3122	
41	2976	86	2797	131	3187	176	3130	221	1864	266	2048	311	2934	356	3123	
42	3041	87	2834	132	3145	177	3063	222	1904	267	2022	312	3019	357	3166	
43	2872	88	2692	133	3332	178	2889	223	1890	268	2208	313	2717	358	3131	
44	2822	89	2781	134	3219	179	3029	224	1901	269	2184	314	3118	359	3106	
45	2864	90	2753	135	3227	180	2959	225	1847	270	2170	315	3066	360	3086	

Compton Counting of Waveforms, Binned by RSM Rotation Angle; Used to Generate the Modulation Curve (ϕ = 25°)

RSM Rotation Angle	Number of Waveforms Recorded	RSM Rotation Angle	Number of Waveforms Recorded	RSM Rotation Angle	Number of Waveforms Recorded	RSM Rotation Angle	Number of Waveforms Recorded	RSM Rotation Angle	Number of Waveforms Recorded	RSM Rotation Angle	Number of Waveforms Recorded	RSM Rotation Angle	Number of Waveforms Recorded	RSM Rotation Angle	Number of Waveforms Recorded	Total Number of Waveforms in FEP
1	9073	46	9342	91	9503	136	9133	181	9332	226	9133	271	9388	316	9189	3349535
2	8993	47	9287	92	9735	137	9199	182	9425	227	9570	272	9382	317	9392	
3	8812	48	9399	93	9297	138	9055	183	9210	228	9601	273	9426	318	8474	
4	8858	49	9305	94	9421	139	9013	184	9223	229	9496	274	9481	319	9737	
5	8808	50	9448	95	9590	140	9057	185	9297	230	9283	275	9481	320	9270	
6	8767	51	9379	96	9508	141	9125	186	9374	231	9165	276	9354	321	8882	
7	8370	52	9430	97	9822	142	9155	187	9475	232	9874	277	9233	322	9281	
8	7764	53	9213	98	9771	143	9319	188	9208	233	9630	278	9360	323	8824	
9	8051	54	9175	99	9776	144	9156	189	9596	234	9531	279	9561	324	9525	
10	8775	55	9318	100	9821	145	8959	190	9354	235	9387	280	9392	325	9043	
11	9022	56	9226	101	9686	146	8863	191	9470	236	8988	281	9577	326	9214	
12	9206	57	9477	102	9601	147	9054	192	9444	237	9754	282	9212	327	9633	
13	10560	58	9431	103	9465	148	9060	193	9226	238	9274	283	9307	328	9388	
14	9598	59	9454	104	9489	149	9064	194	9218	239	9305	284	9391	329	9280	
15	9701	60	9437	105	9385	150	9032	195	9224	240	9550	285	9288	330	9035	
16	9594	61	9253	106	9531	151	9039	196	9439	241	9103	286	9351	331	8914	
17	9388	62	9427	107	9861	152	9179	197	9479	242	9739	287	9317	332	9113	
18	9316	63	9464	108	9565	153	8988	198	9528	243	9494	288	9222	333	9061	
19	9095	64	9446	109	9607	154	9083	199	9738	244	9338	289	9387	334	8938	
20	9015	65	9329	110	9329	155	8883	200	9570	245	9584	290	9283	335	8976	
21	9047	66	9357	111	9488	156	8997	201	9574	246	9564	291	9169	336	8984	
22	9061	67	9486	112	9384	157	9126	202	9607	247	9480	292	9453	337	8987	
23	9135	68	9322	113	9523	158	8967	203	9500	248	9377	293	8809	338	9092	
24	9096	69	9699	114	9509	159	8877	204	9575	249	9355	294	8948	339	9005	
25	9020	70	9862	115	9401	160	9022	205	9399	250	9253	295	9023	340	8817	
26	8938	71	9465	116	9364	161	8996	206	9495	251	9346	296	9067	341	9031	
27	8707	72	9410	117	9538	162	8999	207	9473	252	9406	297	9031	342	9660	
28	8480	73	9415	118	9307	163	9050	208	9491	253	9412	298	9056	343	9199	
29	8487	74	9440	119	9355	164	9006	209	9564	254	9379	299	9123	344	8915	
30	9263	75	9423	120	9384	165	9043	210	9480	255	9507	300	9086	345	9953	
31	9232	76	9537	121	9271	166	9082	211	9574	256	9524	301	9264	346	9483	
32	9297	77	9549	122	9343	167	9043	212	9379	257	9509	302	9147	347	9396	
33	9217	78	9443	123	9484	168	9130	213	9534	258	9447	303	9237	348	9412	
34	9256	79	9588	124	9310	169	9035	214	9597	259	9524	304	9284	349	9537	
35	9379	80	9645	125	9405	170	9054	215	9679	260	9479	305	9173	350	9494	
36	9235	81	9484	126	9454	171	9151	216	9555	261	9398	306	9230	351	9368	
37	9268	82	9618	127	9356	172	9100	217	9634	262	9394	307	9205	352	9491	
38	9310	83	9413	128	9339	173	9146	218	9534	263	9376	308	8316	353	9271	
39	9246	84	9497	129	9330	174	9040	219	9699	264	9336	309	9544	354	9410	
40	9138	85	9519	130	9284	175	9224	220	9645	265	9220	310	9286	355	9377	
41	9381	86	9679	131	9326	176	9123	221	9500	266	9537	311	9243	356	9125	
42	9277	87	9678	132	9391	177	9070	222	9662	267	9176	312	9195	357	9139	
43	9279	88	9525	133	9090	178	9199	223	9416	268	9250	313	8494	358	9034	
44	9402	89	9455	134	9101	179	9192	224	9525	269	9317	314	9963	359	9239	
45	9443	90	9567	135	9250	180	9197	225	9523	270	9434	315	9138	360	9116	

View Angle φ = 35° : Spectrum, Modulation Curve Data (No Smoothing), Library Curve, MAC and Least Squares Direction Predictions

Phi_ViewDegree = 35 Theta_ViewDegree = 0

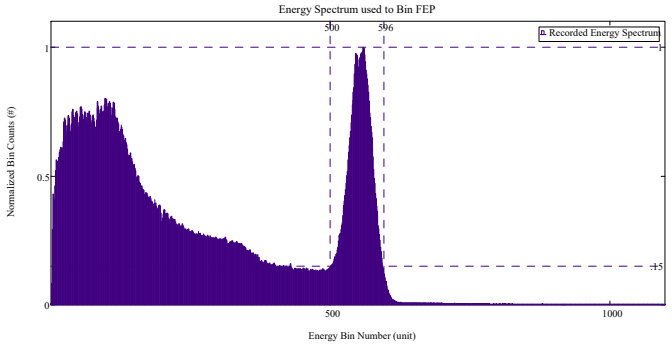

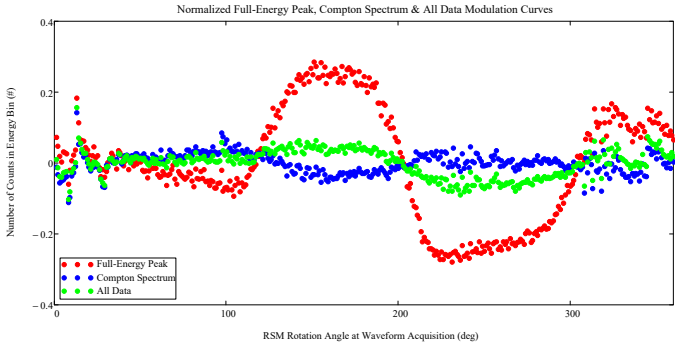

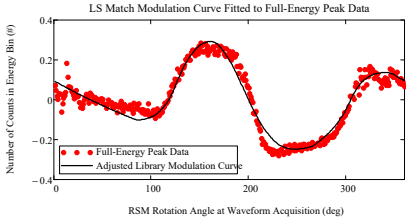

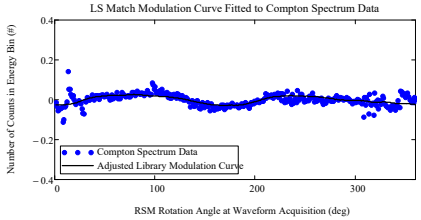

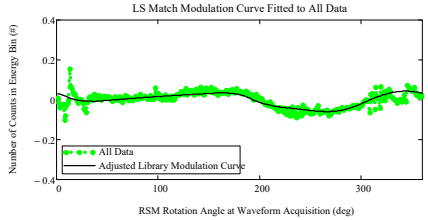

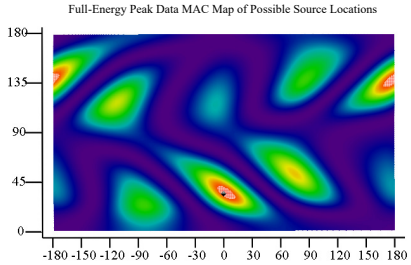

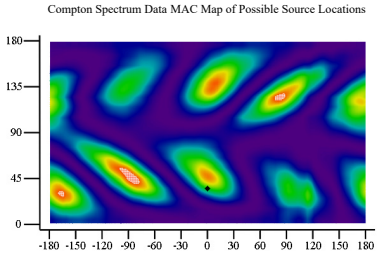

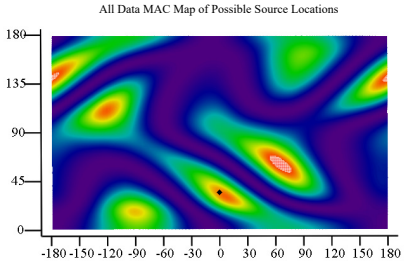

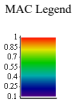

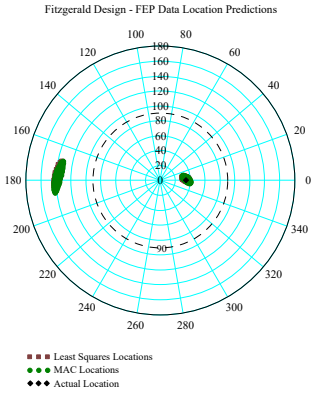

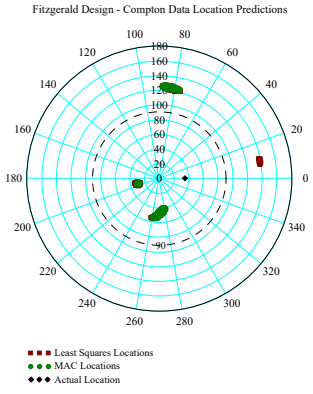

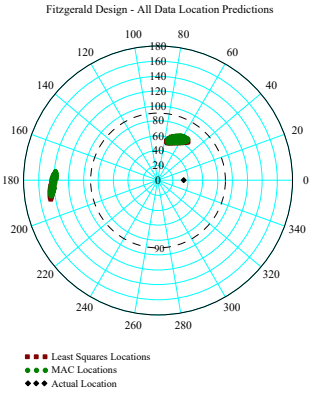

FEP Counting of Waveforms, Binned by RSM Rotation Angle; Used to Generate the Modulation Curve (ϕ = 35°)

RSM Rotation Angle	Number of Waveforms Recorded	RSM Rotation Angle	Number of Waveforms Recorded	RSM Rotation Angle	Number of Waveforms Recorded	RSM Rotation Angle	Number of Waveforms Recorded	RSM Rotation Angle	Number of Waveforms Recorded	RSM Rotation Angle	Number of Waveforms Recorded	RSM Rotation Angle	Number of Waveforms Recorded	RSM Rotation Angle	Number of Waveforms Recorded	Total Number of Waveforms in FEP
1	2929	46	2635	91	2480	136	3399	181	3480	226	1649	271	1861	316	3041	957327
2	2840	47	2667	92	2469	137	3479	182	3405	227	1703	272	1843	317	3076	
3	2732	48	2650	93	2401	138	3469	183	3554	228	1693	273	1808	318	2884	
4	2670	49	2677	94	2400	139	3402	184	3467	229	1679	274	1922	319	3229	
5	2776	50	2672	95	2447	140	3403	185	3487	230	1702	275	1946	320	3086	
6	2769	51	2589	96	2453	141	3545	186	3460	231	1624	276	1929	321	2942	
7	2760	52	2575	97	2583	142	3592	187	3506	232	1719	277	1826	322	3225	
8	2437	53	2582	98	2369	143	3533	188	3291	233	1736	278	1848	323	3092	
9	2585	54	2507	99	2401	144	3560	189	3290	234	1702	279	1922	324	3281	
10	2689	55	2578	100	2404	145	3489	190	3160	235	1679	280	1938	325	3150	
11	2745	56	2656	101	2377	146	3589	191	3292	236	1644	281	1904	326	3243	
12	2800	57	2603	102	2473	147	3601	192	3269	237	1795	282	1969	327	3223	
13	3342	58	2613	103	2379	148	3518	193	3071	238	1679	283	1963	328	3176	
14	3086	59	2608	104	2314	149	3658	194	3096	239	1686	284	1979	329	3060	
15	2903	60	2542	105	2429	150	3588	195	3023	240	1718	285	2002	330	3170	
16	2898	61	2515	106	2497	151	3723	196	3147	241	1663	286	1967	331	3129	
17	2890	62	2518	107	2455	152	3679	197	3029	242	1817	287	1976	332	3146	
18	2827	63	2572	108	2358	153	3556	198	2933	243	1730	288	2050	333	3055	
19	2798	64	2537	109	2450	154	3559	199	2891	244	1733	289	2037	334	3020	
20	2747	65	2425	110	2415	155	3716	200	2885	245	1761	290	2054	335	3006	
21	2679	66	2532	111	2433	156	3586	201	2774	246	1719	291	2123	336	2883	
22	2742	67	2545	112	2511	157	3669	202	2721	247	1837	292	2128	337	2967	
23	2834	68	2592	113	2531	158	3497	203	2662	248	1717	293	2207	338	3024	
24	2722	69	2637	114	2599	159	3585	204	2608	249	1788	294	2172	339	3001	
25	2736	70	2494	115	2590	160	3572	205	2415	250	1732	295	2300	340	3069	
26	2616	71	2438	116	2621	161	3600	206	2401	251	1795	296	2239	341	2931	
27	2517	72	2573	117	2645	162	3599	207	2445	252	1819	297	2328	342	3048	
28	2596	73	2547	118	2785	163	3648	208	2269	253	1759	298	2426	343	2990	
29	2511	74	2526	119	2732	164	3601	209	2209	254	1718	299	2361	344	2928	
30	2574	75	2506	120	2810	165	3507	210	2195	255	1818	300	2420	345	3239	
31	2664	76	2494	121	2920	166	3550	211	2114	256	1826	301	2441	346	3120	
32	2706	77	2514	122	2955	167	3677	212	2079	257	1837	302	2481	347	3210	
33	2766	78	2566	123	2925	168	3503	213	1943	258	1758	303	2537	348	3086	
34	2742	79	2554	124	3046	169	3572	214	1833	259	1782	304	2733	349	3090	
35	2680	80	2475	125	2987	170	3645	215	1879	260	1746	305	2717	350	3158	
36	2602	81	2411	126	3039	171	3666	216	1843	261	1836	306	2736	351	3081	
37	2795	82	2599	127	3237	172	3645	217	1828	262	1809	307	2717	352	3182	
38	2769	83	2497	128	3033	173	3598	218	1762	263	1836	308	2670	353	3018	
39	2738	84	2492	129	3166	174	3615	219	1761	264	1765	309	2911	354	3042	
40	2634	85	2572	130	3213	175	3507	220	1747	265	1868	310	2973	355	2967	
41	2682	86	2502	131	3140	176	3475	221	1696	266	1813	311	2957	356	3056	
42	2709	87	2591	132	3289	177	3622	222	1733	267	1819	312	2904	357	2951	
43	2596	88	2465	133	3266	178	3500	223	1694	268	1792	313	2754	358	2998	
44	2676	89	2470	134	3309	179	3484	224	1647	269	1826	314	3229	359	2952	
45	2675	90	2425	135	3410	180	3567	225	1727	270	1838	315	3090	360	2902	

Compton Counting of Waveforms, Binned by RSM Rotation Angle; Used to Generate the Modulation Curve (ϕ = 35°)

RSM Rotation Angle	Number of Waveforms Recorded	RSM Rotation Angle	Number of Waveforms Recorded	RSM Rotation Angle	Number of Waveforms Recorded	RSM Rotation Angle	Number of Waveforms Recorded	RSM Rotation Angle	Number of Waveforms Recorded	RSM Rotation Angle	Number of Waveforms Recorded	RSM Rotation Angle	Number of Waveforms Recorded	RSM Rotation Angle	Number of Waveforms Recorded	Total Number of Waveforms in FEP
1	9227	46	9551	91	9701	136	9274	181	9073	226	9328	271	9320	316	9078	3366309
2	8994	47	9636	92	9863	137	9304	182	9089	227	9698	272	9375	317	9183	
3	8749	48	9645	93	9693	138	9100	183	8948	228	9663	273	9447	318	8503	
4	8799	49	9534	94	9680	139	9015	184	8928	229	9227	274	9315	319	9732	
5	8851	50	9564	95	9618	140	9033	185	9015	230	9386	275	9401	320	9249	
6	8904	51	9580	96	9673	141	9276	186	9150	231	9254	276	9295	321	9022	
7	8938	52	9650	97	10290	142	9302	187	9079	232	9826	277	9362	322	9348	
8	8148	53	9524	98	10180	143	9196	188	9010	233	9336	278	9295	323	8883	
9	8294	54	9499	99	9954	144	8884	189	9140	234	9460	279	9455	324	9332	
10	8961	55	9364	100	10070	145	8854	190	9216	235	9260	280	9443	325	9123	
11	9056	56	9402	101	9740	146	9036	191	9140	236	9103	281	9583	326	9215	
12	9249	57	9632	102	9809	147	9224	192	9064	237	9648	282	9388	327	9560	
13	10910	58	9411	103	9725	148	9192	193	8984	238	9193	283	9352	328	9439	
14	9943	59	9555	104	9693	149	8925	194	8889	239	9345	284	9459	329	9150	
15	9953	60	9491	105	9869	150	8995	195	9084	240	9410	285	9492	330	9028	
16	9676	61	9478	106	9716	151	9007	196	9228	241	9219	286	9432	331	9019	
17	9539	62	9760	107	9936	152	9227	197	9186	242	9854	287	9472	332	8923	
18	9602	63	9413	108	9672	153	8995	198	9151	243	9414	288	9344	333	8927	
19	9369	64	9440	109	9738	154	9117	199	9282	244	9366	289	9380	334	8933	
20	9235	65	9418	110	9664	155	8770	200	9197	245	9659	290	9406	335	8790	
21	9123	66	9578	111	9648	156	9160	201	9298	246	9650	291	9485	336	9047	
22	9213	67	9769	112	9777	157	8996	202	9367	247	9514	292	9385	337	8956	
23	9229	68	9656	113	9500	158	8839	203	9242	248	9409	293	9403	338	9033	
24	9321	69	9637	114	9673	159	8780	204	9197	249	9264	294	9291	339	9028	
25	9225	70	9574	115	9442	160	8921	205	9270	250	9267	295	9329	340	8809	
26	9145	71	9537	116	9446	161	8926	206	9292	251	9302	296	9250	341	9074	
27	8871	72	9561	117	9625	162	8872	207	9310	252	9313	297	9146	342	9328	
28	8634	73	9592	118	9584	163	8892	208	9273	253	9319	298	9200	343	8955	
29	8605	74	9512	119	9657	164	8885	209	9434	254	9570	299	9279	344	8951	
30	9288	75	9508	120	9584	165	8971	210	9703	255	9448	300	9203	345	9822	
31	9242	76	9578	121	9458	166	9067	211	9449	256	9605	301	9244	346	9806	
32	9476	77	9765	122	9682	167	9001	212	9627	257	9739	302	9396	347	9624	
33	9463	78	9758	123	9660	168	9063	213	9569	258	9483	303	9337	348	9700	
34	9365	79	9687	124	9505	169	8816	214	9608	259	9258	304	9242	349	9679	
35	9350	80	9578	125	9409	170	9031	215	9536	260	9421	305	9297	350	9479	
36	9472	81	9714	126	9461	171	8945	216	9642	261	9271	306	9160	351	9711	
37	9628	82	9850	127	9594	172	9076	217	9476	262	9323	307	9237	352	9735	
38	9609	83	9729	128	9338	173	9005	218	9448	263	9364	308	8430	353	9531	
39	9336	84	9705	129	9375	174	9089	219	9673	264	9432	309	9504	354	9334	
40	9452	85	9650	130	9359	175	8970	220	9605	265	9382	310	9066	355	9352	
41	9591	86	9736	131	9505	176	9072	221	9576	266	9458	311	9492	356	9219	
42	9608	87	9723	132	9412	177	9195	222	9718	267	9212	312	9312	357	9364	
43	9558	88	9714	133	9330	178	9072	223	9485	268	9124	313	8572	358	9202	
44	9373	89	9578	134	9245	179	9036	224	9547	269	9291	314	9666	359	9486	
45	9592	90	9684	135	8957	180	9040	225	9708	270	9181	315	9116	360	9392	

View Angle φ = 45° : Spectrum, Modulation Curve Data (No Smoothing), Library Curve, MAC and Least Squares Direction Predictions

Phi_ViewDegree = 45 Theta_ViewDegree = 0

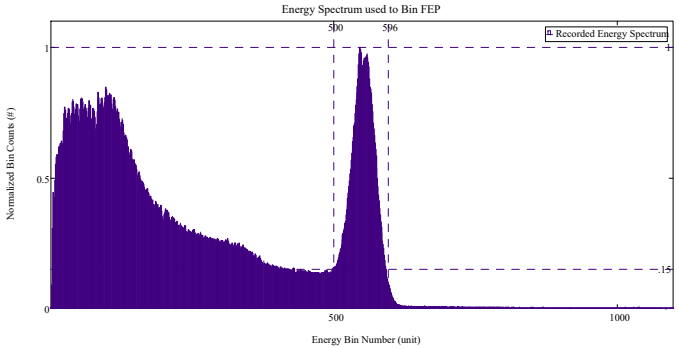

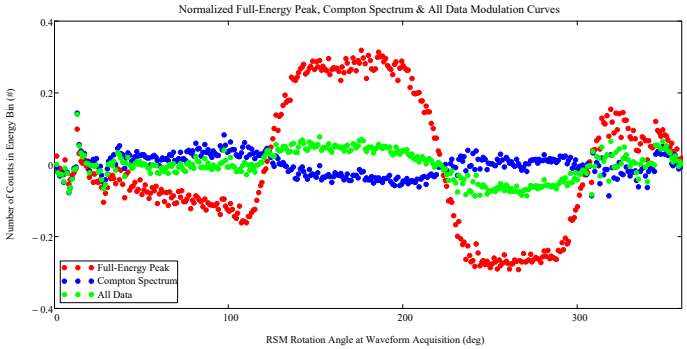

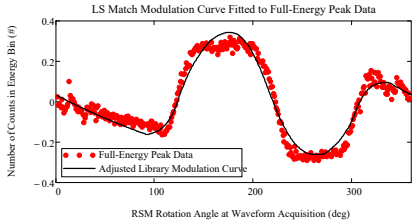

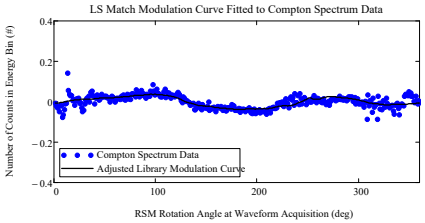

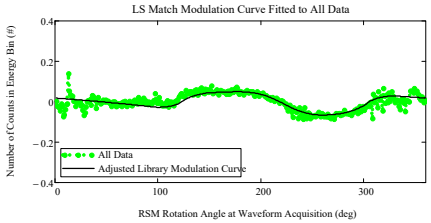

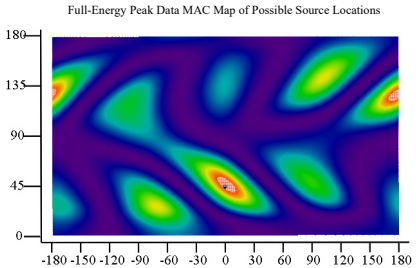

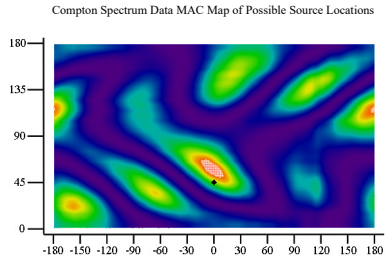

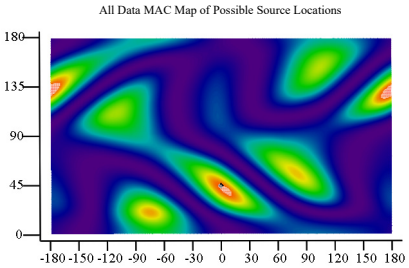

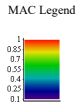

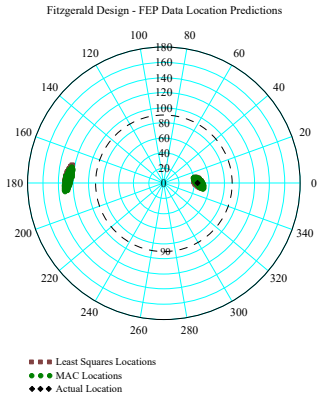

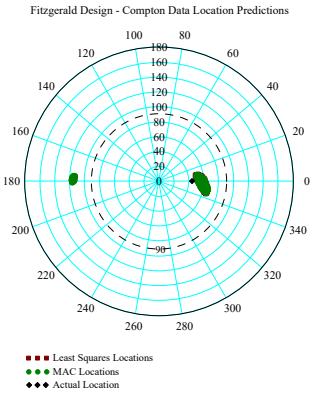

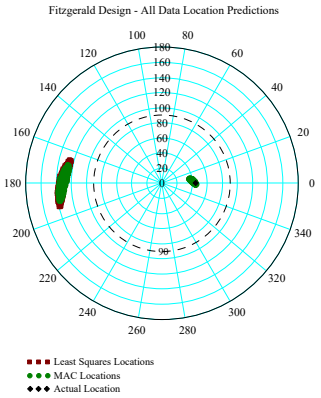

FEP Counting of Waveforms, Binned by RSM Rotation Angle; Used to Generate the Modulation Curve (ϕ = 45°)

RSM Rotation Angle	Number of Waveforms Recorded	RSM Rotation Angle	Number of Waveforms Recorded	RSM Rotation Angle	Number of Waveforms Recorded	RSM Rotation Angle	Number of Waveforms Recorded	RSM Rotation Angle	Number of Waveforms Recorded	RSM Rotation Angle	Number of Waveforms Recorded	RSM Rotation Angle	Number of Waveforms Recorded	RSM Rotation Angle	Number of Waveforms Recorded	Total Number of Waveforms in FEP
1	2634	46	2357	91	2122	136	3451	181	3624	226	2164	271	1538	316	2965	914197
2	2486	47	2263	92	2116	137	3433	182	3543	227	2182	272	1553	317	3052	
3	2509	48	2289	93	2140	138	3422	183	3527	228	2150	273	1615	318	2841	
4	2485	49	2388	94	2079	139	3451	184	3543	229	2012	274	1529	319	3123	
5	2437	50	2234	95	2026	140	3497	185	3663	230	1922	275	1560	320	2984	
6	2592	51	2279	96	2187	141	3538	186	3716	231	1802	276	1582	321	2875	
7	2450	52	2334	97	2189	142	3559	187	3666	232	1955	277	1566	322	3082	
8	2340	53	2258	98	2114	143	3584	188	3671	233	1771	278	1559	323	2909	
9	2389	54	2192	99	2081	144	3490	189	3615	234	1713	279	1528	324	3074	
10	2436	55	2244	100	2058	145	3505	190	3648	235	1737	280	1586	325	2827	
11	2460	56	2308	101	2137	146	3550	191	3574	236	1562	281	1644	326	3086	
12	2502	57	2274	102	2077	147	3564	192	3547	237	1698	282	1592	327	3007	
13	2916	58	2318	103	2009	148	3622	193	3535	238	1601	283	1655	328	3009	
14	2657	59	2142	104	1984	149	3533	194	3479	239	1531	284	1564	329	2919	
15	2582	60	2237	105	2038	150	3611	195	3586	240	1544	285	1593	330	2830	
16	2557	61	2285	106	2114	151	3559	196	3614	241	1483	286	1581	331	2812	
17	2600	62	2257	107	1938	152	3628	197	3423	242	1721	287	1564	332	2898	
18	2534	63	2162	108	1959	153	3527	198	3547	243	1628	288	1560	333	2810	
19	2497	64	2250	109	1950	154	3569	199	3618	244	1491	289	1651	334	2691	
20	2412	65	2119	110	1942	155	3538	200	3576	245	1529	290	1640	335	2685	
21	2451	66	2258	111	2007	156	3520	201	3546	246	1543	291	1730	336	2757	
22	2360	67	2198	112	2009	157	3645	202	3528	247	1506	292	1657	337	2835	
23	2449	68	2218	113	2049	158	3478	203	3527	248	1542	293	1777	338	2818	
24	2369	69	2137	114	2072	159	3532	204	3348	249	1506	294	1718	339	2796	
25	2356	70	2146	115	2076	160	3551	205	3440	250	1474	295	1747	340	2590	
26	2388	71	2263	116	2170	161	3540	206	3286	251	1514	296	1976	341	2790	
27	2308	72	2207	117	2253	162	3546	207	3277	252	1569	297	1969	342	2736	
28	2154	73	2273	118	2328	163	3515	208	3287	253	1530	298	1991	343	2720	
29	2247	74	2157	119	2359	164	3423	209	3293	254	1459	299	2074	344	2739	
30	2304	75	2157	120	2473	165	3560	210	3207	255	1555	300	2104	345	2992	
31	2441	76	2183	121	2497	166	3500	211	3209	256	1491	301	2223	346	2898	
32	2401	77	2228	122	2579	167	3646	212	3086	257	1519	302	2296	347	2870	
33	2432	78	2085	123	2688	168	3598	213	3155	258	1604	303	2330	348	2840	
34	2400	79	2173	124	2728	169	3512	214	3091	259	1540	304	2437	349	2907	
35	2344	80	2143	125	2814	170	3533	215	3094	260	1518	305	2499	350	2853	
36	2501	81	2222	126	2920	171	3655	216	2971	261	1461	306	2459	351	2839	
37	2389	82	2198	127	3057	172	3606	217	2920	262	1513	307	2576	352	2802	
38	2483	83	2182	128	2898	173	3522	218	2818	263	1509	308	2358	353	2728	
39	2336	84	2160	129	3045	174	3630	219	2822	264	1553	309	2696	354	2766	
40	2196	85	2108	130	3066	175	3597	220	2688	265	1542	310	2700	355	2680	
41	2438	86	2184	131	3157	176	3736	221	2651	266	1455	311	2795	356	2601	
42	2467	87	2073	132	3267	177	3653	222	2536	267	1543	312	2822	357	2708	
43	2279	88	2145	133	3194	178	3596	223	2436	268	1533	313	2708	358	2600	
44	2313	89	2123	134	3216	179	3438	224	2380	269	1621	314	3027	359	2595	
45	2317	90	2126	135	3210	180	3683	225	2319	270	1534	315	2981	360	2615	

Compton Counting of Waveforms, Binned by RSM Rotation Angle; Used to Generate the Modulation Curve (ϕ = 45°)

RSM Rotation Angle	Number of Waveforms Recorded	RSM Rotation Angle	Number of Waveforms Recorded	RSM Rotation Angle	Number of Waveforms Recorded	RSM Rotation Angle	Number of Waveforms Recorded	RSM Rotation Angle	Number of Waveforms Recorded	RSM Rotation Angle	Number of Waveforms Recorded	RSM Rotation Angle	Number of Waveforms Recorded	RSM Rotation Angle	Number of Waveforms Recorded	Total Number of Waveforms in FEP
1	9308	46	9617	91	9800	136	9232	181	8924	226	9136	271	9176	316	9224	3371895
2	9149	47	9770	92	9722	137	9311	182	9019	227	9409	272	9413	317	9222	
3	9041	48	9631	93	9664	138	8955	183	8819	228	9540	273	9498	318	8436	
4	9075	49	9660	94	9664	139	8942	184	8968	229	9314	274	9523	319	9684	
5	8840	50	9686	95	9944	140	9093	185	8901	230	9279	275	9513	320	9295	
6	9200	51	9683	96	9840	141	9242	186	8967	231	9055	276	9543	321	8970	
7	9148	52	9613	97	10290	142	9307	187	8899	232	9539	277	9432	322	9307	
8	8525	53	9580	98	9974	143	9167	188	8835	233	9643	278	9551	323	8942	
9	8671	54	9578	99	9764	144	9029	189	8963	234	9486	279	9503	324	9449	
10	8948	55	9362	100	9789	145	8939	190	8952	235	9621	280	9510	325	9122	
11	9266	56	9616	101	10060	146	9229	191	8974	236	9200	281	9686	326	9076	
12	9305	57	9662	102	9827	147	9054	192	9048	237	9812	282	9522	327	9591	
13	10940	58	9594	103	9829	148	9094	193	8862	238	9322	283	9490	328	9300	
14	10000	59	9497	104	9674	149	9058	194	8775	239	9345	284	9562	329	9179	
15	9799	60	9350	105	9632	150	9004	195	8739	240	9719	285	9469	330	9037	
16	9697	61	9515	106	9630	151	9137	196	8934	241	9228	286	9546	331	9174	
17	9715	62	9574	107	9738	152	9353	197	8992	242	9802	287	9523	332	9144	
18	9449	63	9535	108	9907	153	8915	198	8741	243	9539	288	9439	333	9184	
19	9489	64	9571	109	10050	154	8991	199	8784	244	9247	289	9507	334	8896	
20	9193	65	9500	110	9608	155	8998	200	8886	245	9519	290	9634	335	8700	
21	9444	66	9688	111	9904	156	9042	201	8882	246	9604	291	9627	336	9177	
22	9535	67	9650	112	9688	157	9072	202	8962	247	9540	292	9600	337	9275	
23	9423	68	9760	113	9857	158	9008	203	8791	248	9237	293	9649	338	9285	
24	9561	69	9509	114	9718	159	8835	204	8860	249	9423	294	9411	339	9032	
25	9304	70	9477	115	9566	160	9016	205	8889	250	9409	295	9496	340	8677	
26	9320	71	9559	116	9763	161	9124	206	8852	251	9409	296	9608	341	9167	
27	9050	72	9766	117	9668	162	9070	207	8845	252	9374	297	9273	342	9265	
28	8843	73	9551	118	9707	163	9053	208	8929	253	9355	298	9388	343	9243	
29	8923	74	9552	119	9655	164	9106	209	8707	254	9549	299	9528	344	9162	
30	9258	75	9511	120	9734	165	9020	210	8943	255	9438	300	9247	345	9691	
31	9487	76	9786	121	9809	166	8908	211	8992	256	9703	301	9326	346	9785	
32	9591	77	9816	122	9871	167	8974	212	9024	257	9516	302	9259	347	9744	
33	9477	78	9740	123	9794	168	9089	213	8789	258	9317	303	9375	348	9704	
34	9674	79	9790	124	9594	169	8890	214	8999	259	9592	304	9263	349	9928	
35	9381	80	9646	125	9431	170	8900	215	9047	260	9534	305	9078	350	9704	
36	9880	81	10040	126	9336	171	9045	216	9087	261	9434	306	9405	351	9838	
37	9949	82	9855	127	9646	172	9060	217	9026	262	9472	307	9326	352	9666	
38	9716	83	9866	128	9567	173	9046	218	9009	263	9378	308	8422	353	9668	
39	9688	84	9640	129	9406	174	8985	219	9070	264	9324	309	9737	354	9400	
40	9277	85	9752	130	9388	175	9235	220	9306	265	9533	310	9162	355	9348	
41	9589	86	9997	131	9452	176	9149	221	9303	266	9406	311	9438	356	9670	
42	9747	87	9759	132	9350	177	9165	222	9325	267	9333	312	9344	357	9399	
43	9660	88	9834	133	9331	178	8924	223	9268	268	9212	313	8803	358	9258	
44	9476	89	9690	134	9180	179	8974	224	9378	269	9290	314	9584	359	9445	
45	9506	90	9592	135	9212	180	8911	225	9205	270	9409	315	9072	360	9334	

View Angle φ = 55° : Spectrum, Modulation Curve Data (No Smoothing), Library Curve, MAC and Least Squares Direction Predictions

Phi_ViewDegree = 55 Theta_ViewDegree = 0

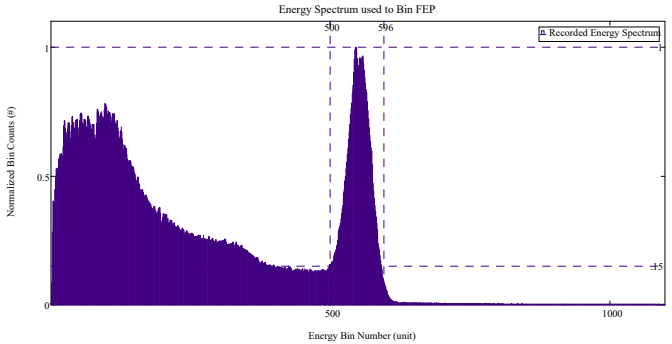

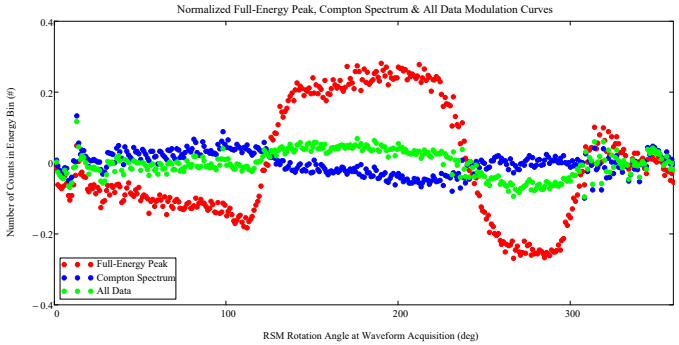

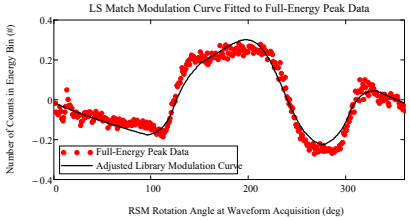

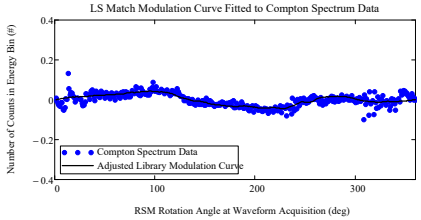

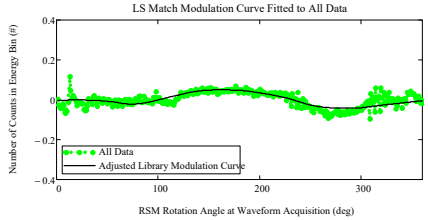

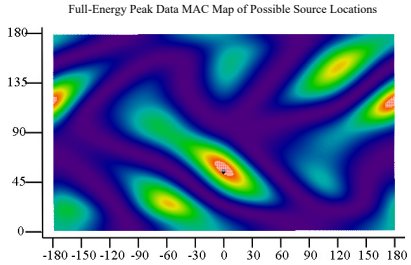

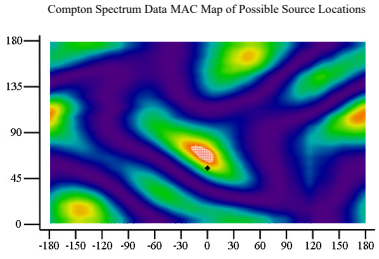

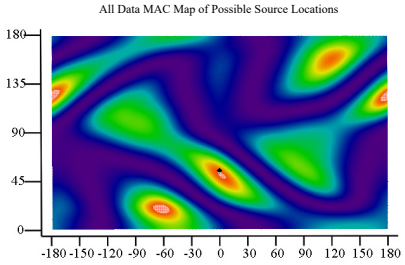

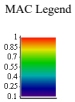

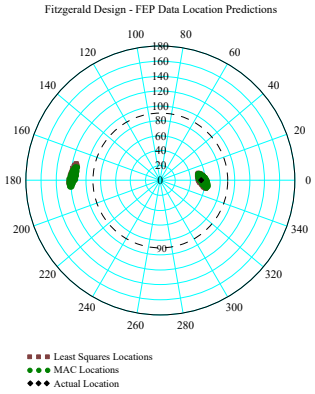

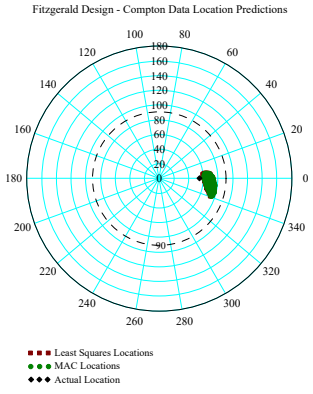

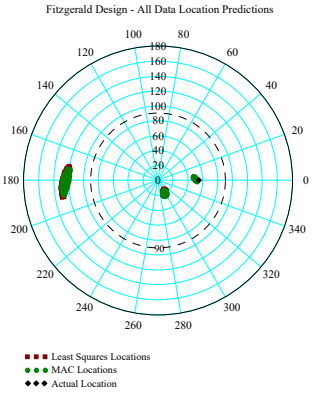

FEP Counting of Waveforms, Binned by RSM Rotation Angle; Used to Generate the Modulation Curve (ϕ = 55°)

RSM Rotation Angle	Number of Waveforms Recorded	RSM Rotation Angle	Number of Waveforms Recorded	RSM Rotation Angle	Number of Waveforms Recorded	RSM Rotation Angle	Number of Waveforms Recorded	RSM Rotation Angle	Number of Waveforms Recorded	RSM Rotation Angle	Number of Waveforms Recorded	RSM Rotation Angle	Number of Waveforms Recorded	RSM Rotation Angle	Number of Waveforms Recorded	Total Number of Waveforms in FEP
1	2600	46	2313	91	2262	136	3307	181	3499	226	3252	271	1695	316	2865	955861
2	2428	47	2381	92	2224	137	3356	182	3607	227	3343	272	1722	317	2951	
3	2412	48	2336	93	2147	138	3386	183	3478	228	3273	273	1840	318	2670	
4	2390	49	2404	94	2139	139	3308	184	3507	229	3268	274	1721	319	3026	
5	2416	50	2265	95	2249	140	3421	185	3528	230	3258	275	1796	320	2891	
6	2524	51	2303	96	2135	141	3492	186	3592	231	3046	276	1811	321	2782	
7	2445	52	2327	97	2149	142	3418	187	3612	232	3351	277	1699	322	2987	
8	2319	53	2311	98	2237	143	3462	188	3550	233	3145	278	1760	323	2740	
9	2270	54	2288	99	2220	144	3433	189	3512	234	3060	279	1713	324	2935	
10	2321	55	2136	100	2104	145	3363	190	3697	235	3038	280	1719	325	2827	
11	2433	56	2261	101	2154	146	3423	191	3623	236	2860	281	1713	326	2857	
12	2532	57	2281	102	2184	147	3409	192	3569	237	3079	282	1754	327	2934	
13	2841	58	2208	103	2118	148	3439	193	3656	238	2884	283	1739	328	2862	
14	2672	59	2258	104	2057	149	3380	194	3471	239	2710	284	1714	329	2770	
15	2545	60	2274	105	2025	150	3544	195	3597	240	2673	285	1671	330	2768	
16	2561	61	2327	106	2061	151	3386	196	3544	241	2583	286	1726	331	2801	
17	2518	62	2270	107	2099	152	3474	197	3533	242	2669	287	1706	332	2735	
18	2508	63	2207	108	2112	153	3382	198	3547	243	2540	288	1693	333	2632	
19	2383	64	2307	109	2044	154	3454	199	3545	244	2445	289	1748	334	2598	
20	2355	65	2123	110	1994	155	3426	200	3657	245	2502	290	1733	335	2634	
21	2421	66	2262	111	2090	156	3345	201	3644	246	2342	291	1734	336	2699	
22	2388	67	2301	112	1979	157	3521	202	3647	247	2321	292	1745	337	2763	
23	2432	68	2203	113	2045	158	3308	203	3617	248	2199	293	1805	338	2645	
24	2338	69	2188	114	2072	159	3383	204	3631	249	2157	294	1753	339	2762	
25	2402	70	2256	115	2103	160	3375	205	3529	250	2150	295	1847	340	2666	
26	2373	71	2278	116	2164	161	3431	206	3598	251	2075	296	1872	341	2680	
27	2190	72	2251	117	2219	162	3526	207	3561	252	2111	297	2041	342	2710	
28	2252	73	2186	118	2256	163	3473	208	3584	253	1937	298	2008	343	2600	
29	2267	74	2177	119	2310	164	3438	209	3567	254	2022	299	2117	344	2547	
30	2372	75	2171	120	2419	165	3454	210	3538	255	1998	300	2088	345	2698	
31	2426	76	2192	121	2580	166	3520	211	3569	256	1921	301	2179	346	2769	
32	2328	77	2233	122	2580	167	3436	212	3688	257	1901	302	2290	347	2699	
33	2424	78	2243	123	2646	168	3406	213	3503	258	1920	303	2261	348	2715	
34	2404	79	2185	124	2635	169	3449	214	3547	259	1849	304	2323	349	2685	
35	2350	80	2184	125	2721	170	3662	215	3641	260	1810	305	2419	350	2671	
36	2432	81	2211	126	2923	171	3482	216	3519	261	1836	306	2535	351	2719	
37	2436	82	2294	127	2902	172	3541	217	3570	262	1732	307	2572	352	2729	
38	2414	83	2197	128	2972	173	3496	218	3553	263	1808	308	2433	353	2668	
39	2249	84	2236	129	2967	174	3437	219	3405	264	1795	309	2825	354	2596	
40	2267	85	2280	130	3055	175	3612	220	3524	265	1801	310	2668	355	2529	
41	2328	86	2240	131	3249	176	3674	221	3525	266	1842	311	2795	356	2583	
42	2400	87	2237	132	3189	177	3615	222	3562	267	1663	312	2822	357	2567	
43	2448	88	2205	133	3140	178	3414	223	3538	268	1749	313	2646	358	2478	
44	2345	89	2165	134	3195	179	3524	224	3506	269	1790	314	3034	359	2551	
45	2329	90	2186	135	3229	180	3639	225	3375	270	1733	315	2809	360	2460	

Compton Counting of Waveforms, Binned by RSM Rotation Angle; Used to Generate the Modulation Curve (ϕ = 55°)

RSM Rotation Angle	Number of Waveforms Recorded	RSM Rotation Angle	Number of Waveforms Recorded	RSM Rotation Angle	Number of Waveforms Recorded	RSM Rotation Angle	Number of Waveforms Recorded	RSM Rotation Angle	Number of Waveforms Recorded	RSM Rotation Angle	Number of Waveforms Recorded	RSM Rotation Angle	Number of Waveforms Recorded	RSM Rotation Angle	Number of Waveforms Recorded	Total Number of Waveforms in FEP
1	9312	46	9692	91	9581	136	9120	181	9045	226	8548	271	9200	316	9075	3315755
2	9142	47	9556	92	9497	137	9230	182	8922	227	8847	272	9207	317	9184	
3	9002	48	9577	93	9520	138	9009	183	8917	228	8836	273	9154	318	8421	
4	8944	49	9490	94	9480	139	8995	184	8817	229	8812	274	9285	319	9650	
5	8887	50	9327	95	9776	140	8938	185	8825	230	8767	275	9349	320	9081	
6	9087	51	9621	96	9654	141	9057	186	9098	231	8371	276	9429	321	8769	
7	9060	52	9562	97	9879	142	9154	187	9000	232	8932	277	9149	322	9370	
8	8694	53	9476	98	10160	143	9198	188	8762	233	8844	278	9377	323	8792	
9	8682	54	9359	99	9781	144	8988	189	8783	234	8736	279	9103	324	9246	
10	8791	55	9285	100	9676	145	9015	190	8863	235	8902	280	9162	325	8901	
11	9278	56	9572	101	9907	146	8986	191	8869	236	8479	281	9313	326	9232	
12	9248	57	9579	102	9665	147	9162	192	8917	237	9297	282	9322	327	9443	
13	10630	58	9401	103	9633	148	9187	193	8681	238	8770	283	9155	328	9106	
14	9820	59	9424	104	9614	149	8932	194	8633	239	8626	284	9172	329	9084	
15	9483	60	9195	105	9637	150	8938	195	8755	240	9146	285	9304	330	8944	
16	9611	61	9565	106	9781	151	9296	196	8844	241	8737	286	9469	331	9165	
17	9596	62	9553	107	9711	152	9176	197	8904	242	9240	287	9408	332	9113	
18	9414	63	9453	108	9674	153	9016	198	8570	243	9158	288	9218	333	9156	
19	9351	64	9393	109	9534	154	8960	199	8831	244	8893	289	9307	334	8680	
20	9113	65	9323	110	9678	155	9167	200	8901	245	9276	290	9294	335	8871	
21	9294	66	9604	111	9641	156	9109	201	8776	246	9181	291	9418	336	9286	
22	9314	67	9592	112	9763	157	9036	202	8827	247	9085	292	9282	337	9046	
23	9316	68	9656	113	9590	158	8937	203	8655	248	9296	293	9225	338	9259	
24	9281	69	9444	114	9534	159	8863	204	8715	249	9256	294	9354	339	9021	
25	9255	70	9341	115	9462	160	8955	205	8739	250	9203	295	9226	340	8663	
26	9254	71	9654	116	9523	161	8981	206	8621	251	9038	296	9436	341	9175	
27	9025	72	9608	117	9708	162	8932	207	8617	252	9086	297	9228	342	9226	
28	8893	73	9385	118	9684	163	8956	208	8620	253	9095	298	9190	343	9274	
29	8952	74	9483	119	9626	164	9041	209	8755	254	9287	299	9235	344	9123	
30	9105	75	9387	120	9562	165	8945	210	8665	255	9279	300	9090	345	9686	
31	9539	76	9535	121	9566	166	9005	211	8735	256	9380	301	9283	346	9479	
32	9509	77	9732	122	9830	167	9105	212	8625	257	9425	302	9126	347	9593	
33	9491	78	9611	123	9642	168	9078	213	8516	258	9446	303	9167	348	9724	
34	9482	79	9545	124	9546	169	8980	214	8621	259	9228	304	9330	349	9694	
35	9231	80	9643	125	9408	170	8880	215	8734	260	9354	305	9128	350	9558	
36	9670	81	9924	126	9403	171	8989	216	8716	261	9287	306	9251	351	9584	
37	9743	82	9840	127	9391	172	9034	217	8692	262	9292	307	9232	352	9485	
38	9553	83	9539	128	9366	173	8960	218	8579	263	9180	308	8169	353	9384	
39	9362	84	9465	129	9186	174	9065	219	8679	264	9014	309	9491	354	9195	
40	9175	85	9462	130	9292	175	8964	220	8825	265	9338	310	8973	355	9339	
41	9695	86	9865	131	9175	176	9122	221	8756	266	9202	311	9291	356	9545	
42	9573	87	9719	132	9293	177	8894	222	8651	267	8926	312	9149	357	9397	
43	9455	88	9562	133	9278	178	9166	223	8682	268	9144	313	8415	358	9199	
44	9372	89	9577	134	9041	179	8811	224	8697	269	9033	314	9661	359	9327	
45	9332	90	9507	135	9052	180	8796	225	8912	270	9019	315	9020	360	9198	

View Angle φ = 65° : Spectrum, Modulation Curve Data (No Smoothing), Library Curve, MAC and Least Squares Direction Predictions

Phi_ViewDegree = 65 Theta_ViewDegree = 0

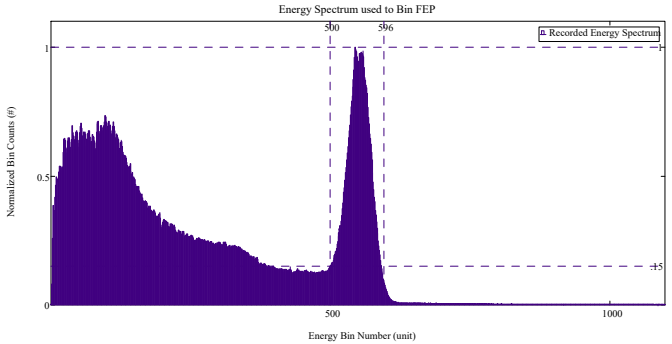

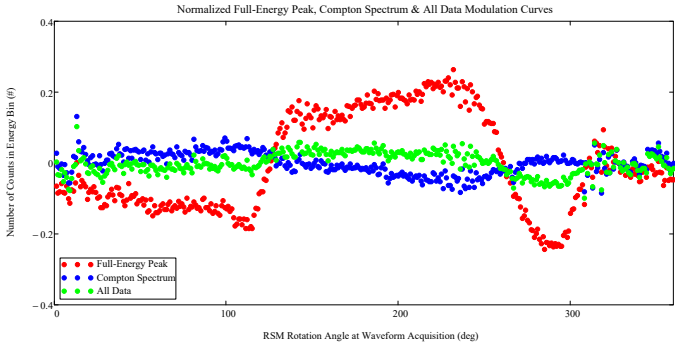

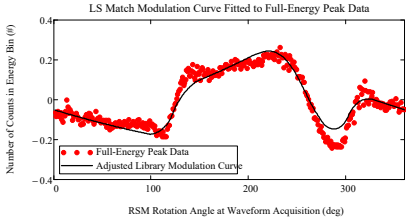

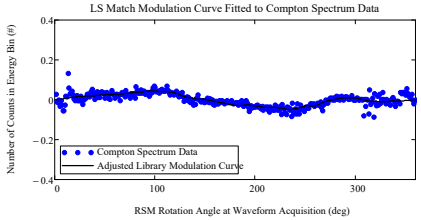

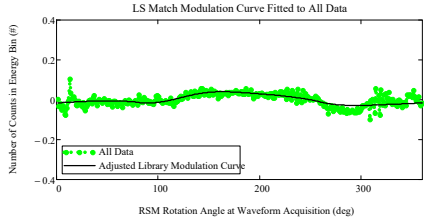

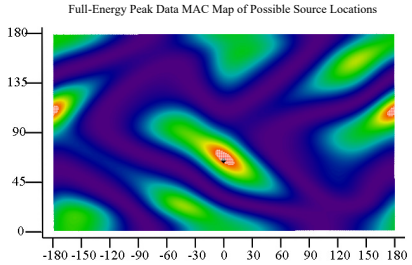

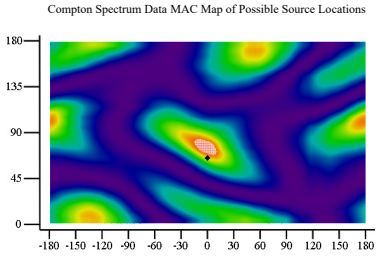

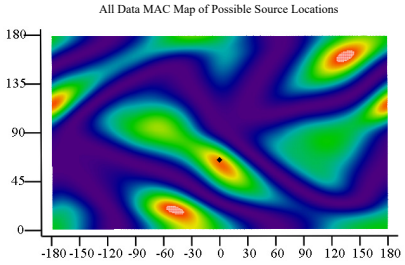

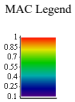

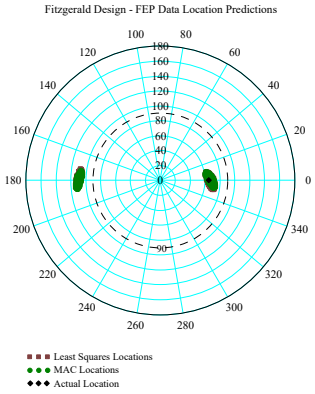

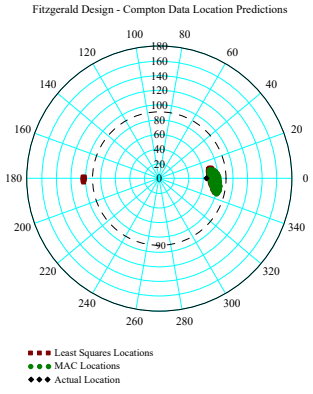

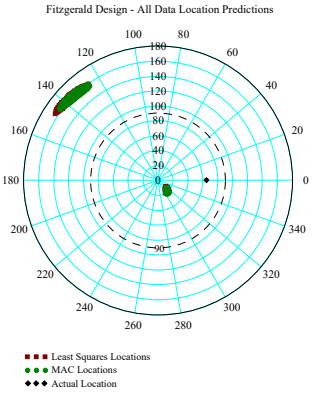

FEP Counting of Waveforms, Binned by RSM Rotation Angle; Used to Generate the Modulation Curve (ϕ = 65°)

RSM Rotation Angle	Number of Waveforms Recorded	RSM Rotation Angle	Number of Waveforms Recorded	RSM Rotation Angle	Number of Waveforms Recorded	RSM Rotation Angle	Number of Waveforms Recorded	RSM Rotation Angle	Number of Waveforms Recorded	RSM Rotation Angle	Number of Waveforms Recorded	RSM Rotation Angle	Number of Waveforms Recorded	RSM Rotation Angle	Number of Waveforms Recorded	Total Number of Waveforms in FEP
1	2556	46	2445	91	2366	136	3365	181	3447	226	3568	271	2332	316	2912	1007501
2	2480	47	2473	92	2263	137	3348	182	3534	227	3681	272	2207	317	2987	
3	2495	48	2366	93	2281	138	3403	183	3443	228	3682	273	2237	318	2705	
4	2583	49	2400	94	2346	139	3260	184	3438	229	3716	274	2293	319	3162	
5	2484	50	2399	95	2259	140	3262	185	3390	230	3638	275	2186	320	2978	
6	2480	51	2415	96	2239	141	3354	186	3573	231	3531	276	2162	321	2769	
7	2555	52	2348	97	2342	142	3472	187	3486	232	3804	277	2084	322	2954	
8	2419	53	2407	98	2400	143	3328	188	3546	233	3665	278	2080	323	2721	
9	2374	54	2278	99	2326	144	3222	189	3471	234	3606	279	2003	324	2960	
10	2515	55	2290	100	2311	145	3167	190	3480	235	3610	280	2044	325	2814	
11	2497	56	2413	101	2338	146	3283	191	3475	236	3409	281	2091	326	2875	
12	2587	57	2233	102	2279	147	3439	192	3389	237	3672	282	1983	327	2938	
13	2804	58	2342	103	2308	148	3312	193	3499	238	3620	283	1933	328	2800	
14	2669	59	2270	104	2217	149	3291	194	3452	239	3459	284	2009	329	2704	
15	2545	60	2266	105	2126	150	3178	195	3478	240	3600	285	1878	330	2727	
16	2614	61	2292	106	2147	151	3370	196	3530	241	3369	286	1951	331	2805	
17	2581	62	2343	107	2204	152	3416	197	3536	242	3640	287	1942	332	2672	
18	2550	63	2365	108	2201	153	3382	198	3403	243	3568	288	1915	333	2764	
19	2412	64	2303	109	2142	154	3266	199	3527	244	3436	289	1943	334	2692	
20	2483	65	2302	110	2201	155	3311	200	3560	245	3505	290	1899	335	2650	
21	2518	66	2357	111	2102	156	3288	201	3496	246	3522	291	1937	336	2735	
22	2493	67	2385	112	2197	157	3319	202	3497	247	3422	292	1906	337	2680	
23	2547	68	2292	113	2099	158	3374	203	3488	248	3388	293	1929	338	2728	
24	2485	69	2326	114	2116	159	3169	204	3471	249	3383	294	1906	339	2667	
25	2425	70	2343	115	2101	160	3304	205	3438	250	3217	295	1906	340	2605	
26	2436	71	2319	116	2242	161	3293	206	3529	251	3249	296	2024	341	2607	
27	2326	72	2389	117	2315	162	3235	207	3479	252	3244	297	2055	342	2702	
28	2323	73	2340	118	2310	163	3354	208	3485	253	3235	298	2004	343	2716	
29	2354	74	2365	119	2471	164	3270	209	3475	254	3226	299	2075	344	2650	
30	2343	75	2329	120	2494	165	3310	210	3570	255	3228	300	2262	345	2759	
31	2436	76	2277	121	2495	166	3266	211	3540	256	3135	301	2301	346	2751	
32	2467	77	2427	122	2629	167	3312	212	3563	257	3134	302	2312	347	2772	
33	2520	78	2306	123	2614	168	3276	213	3466	258	2941	303	2429	348	2732	
34	2461	79	2340	124	2715	169	3254	214	3541	259	2900	304	2451	349	2676	
35	2396	80	2327	125	2736	170	3417	215	3655	260	2869	305	2521	350	2697	
36	2543	81	2386	126	2828	171	3409	216	3620	261	2807	306	2519	351	2820	
37	2531	82	2349	127	2910	172	3300	217	3672	262	2714	307	2570	352	2706	
38	2468	83	2313	128	2965	173	3389	218	3649	263	2654	308	2358	353	2697	
39	2455	84	2324	129	3000	174	3420	219	3671	264	2716	309	2759	354	2564	
40	2391	85	2289	130	3123	175	3424	220	3603	265	2590	310	2775	355	2614	
41	2343	86	2413	131	3174	176	3475	221	3647	266	2643	311	2851	356	2748	
42	2406	87	2423	132	3233	177	3475	222	3626	267	2444	312	2749	357	2618	
43	2578	88	2322	133	3079	178	3429	223	3667	268	2463	313	2649	358	2626	
44	2425	89	2325	134	3124	179	3387	224	3612	269	2423	314	3037	359	2620	
45	2454	90	2290	135	3186	180	3400	225	3624	270	2418	315	3013	360	2622	

Compton Counting of Waveforms, Binned by RSM Rotation Angle; Used to Generate the Modulation Curve (ϕ = 65°)

RSM Rotation Angle	Number of Waveforms Recorded	RSM Rotation Angle	Number of Waveforms Recorded	RSM Rotation Angle	Number of Waveforms Recorded	RSM Rotation Angle	Number of Waveforms Recorded	RSM Rotation Angle	Number of Waveforms Recorded	RSM Rotation Angle	Number of Waveforms Recorded	RSM Rotation Angle	Number of Waveforms Recorded	RSM Rotation Angle	Number of Waveforms Recorded	Total Number of Waveforms in FEP
1	9424	46	9515	91	9474	136	9148	181	8999	226	8370	271	9101	316	8986	3284225
2	9025	47	9545	92	9456	137	9073	182	8919	227	8905	272	8964	317	9237	
3	8979	48	9507	93	9511	138	8865	183	8868	228	8685	273	9125	318	8238	
4	9113	49	9455	94	9339	139	8893	184	9003	229	8460	274	9119	319	9447	
5	8775	50	9228	95	9399	140	8883	185	8906	230	8468	275	9228	320	8965	
6	9093	51	9475	96	9544	141	9182	186	9083	231	8353	276	9232	321	8808	
7	8850	52	9508	97	9515	142	9227	187	8989	232	8745	277	9138	322	9311	
8	8544	53	9212	98	9768	143	9380	188	8788	233	8715	278	9237	323	8844	
9	8542	54	9409	99	9868	144	9131	189	8808	234	8600	279	9109	324	9407	
10	8858	55	9165	100	9788	145	9088	190	8993	235	8668	280	9252	325	8951	
11	9327	56	9453	101	9565	146	9013	191	9105	236	8259	281	9319	326	9166	
12	9286	57	9617	102	9575	147	9076	192	8953	237	8945	282	9153	327	9526	
13	10510	58	9446	103	9563	148	9099	193	8711	238	8441	283	9276	328	9150	
14	9753	59	9405	104	9492	149	8973	194	8535	239	8372	284	9119	329	9075	
15	9472	60	9232	105	9633	150	9034	195	8663	240	8661	285	9163	330	8936	
16	9455	61	9419	106	9653	151	9119	196	8814	241	8401	286	9328	331	9160	
17	9593	62	9418	107	9676	152	9220	197	8711	242	8906	287	9207	332	9042	
18	9377	63	9329	108	9599	153	9037	198	8753	243	8589	288	9136	333	9027	
19	9202	64	9376	109	9613	154	8997	199	8772	244	8401	289	9211	334	8888	
20	9087	65	9101	110	9582	155	9193	200	8752	245	8843	290	9291	335	8864	
21	9298	66	9412	111	9608	156	9130	201	8813	246	8632	291	9296	336	9172	
22	9347	67	9525	112	9847	157	9111	202	8868	247	8693	292	9262	337	9254	
23	9086	68	9409	113	9610	158	8881	203	8754	248	8642	293	9157	338	9144	
24	9096	69	9393	114	9503	159	8857	204	8793	249	8523	294	9178	339	9004	
25	9075	70	9297	115	9396	160	8941	205	8705	250	8731	295	9192	340	8805	
26	9339	71	9608	116	9537	161	9061	206	8647	251	8742	296	9371	341	9067	
27	9082	72	9439	117	9452	162	8931	207	8795	252	8677	297	9225	342	9053	
28	8904	73	9384	118	9502	163	8936	208	8592	253	8703	298	9120	343	9029	
29	9115	74	9346	119	9379	164	9074	209	8702	254	8833	299	9120	344	8935	
30	9211	75	9222	120	9474	165	8995	210	8756	255	8930	300	9135	345	9540	
31	9226	76	9472	121	9590	166	9052	211	8711	256	8920	301	9235	346	9444	
32	9408	77	9450	122	9530	167	9097	212	8759	257	8887	302	9219	347	9521	
33	9419	78	9445	123	9364	168	8997	213	8599	258	8931	303	9120	348	9519	
34	9356	79	9376	124	9292	169	8922	214	8489	259	8804	304	9112	349	9504	
35	9302	80	9219	125	9466	170	9012	215	8755	260	8893	305	9140	350	9406	
36	9552	81	9831	126	9335	171	8988	216	8644	261	8898	306	9156	351	9723	
37	9693	82	9613	127	9525	172	9101	217	8613	262	8964	307	9139	352	9484	
38	9411	83	9504	128	9288	173	8978	218	8580	263	8848	308	8272	353	9322	
39	9365	84	9483	129	9047	174	8991	219	8585	264	8869	309	9151	354	9292	
40	9156	85	9491	130	9164	175	8990	220	8849	265	9023	310	8775	355	9218	
41	9537	86	9656	131	9125	176	9075	221	8798	266	8719	311	9143	356	9419	
42	9563	87	9483	132	9277	177	8996	222	8594	267	8553	312	9109	357	9122	
43	9264	88	9589	133	9266	178	8939	223	8699	268	8856	313	8395	358	8917	
44	9490	89	9575	134	9041	179	8968	224	8585	269	8933	314	9672	359	9061	
45	9273	90	9424	135	8979	180	8948	225	8804	270	9127	315	8881	360	9121	

View Angle φ = 75° : Spectrum, Modulation Curve Data (No Smoothing), Library Curve, MAC and Least Squares Direction Predictions

Phi_ViewDegree = 75 Theta_ViewDegree = 0

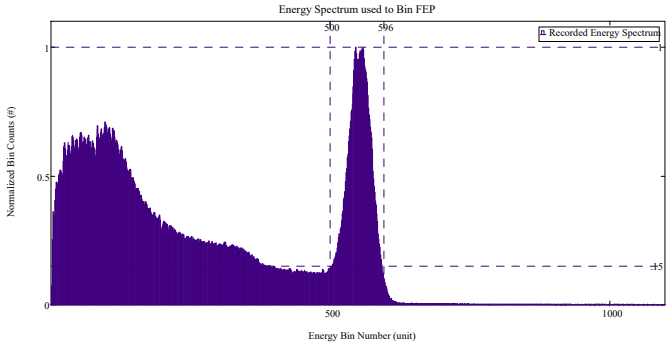

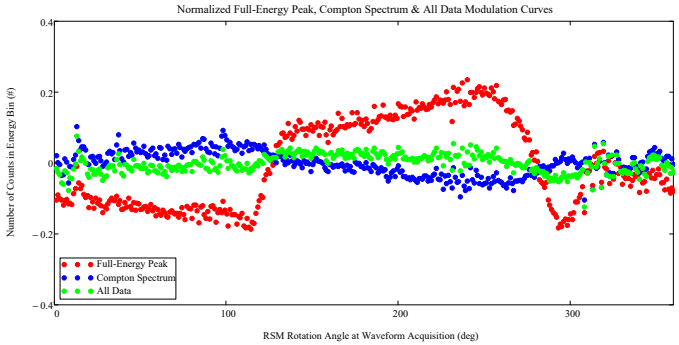

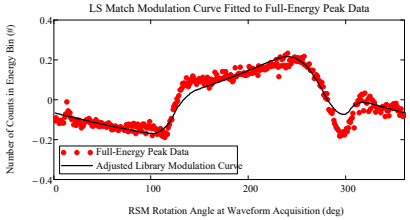

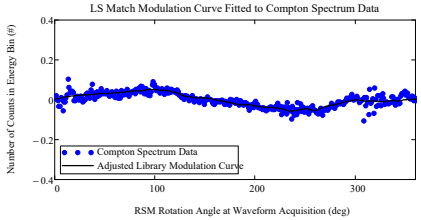

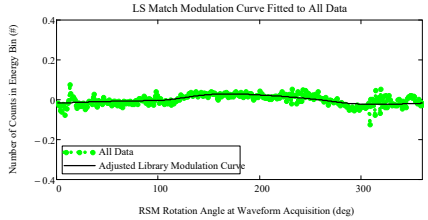

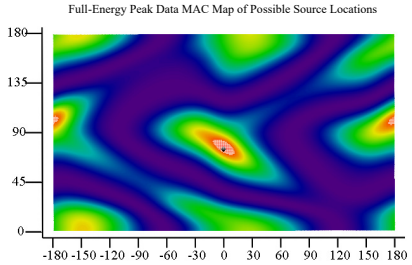

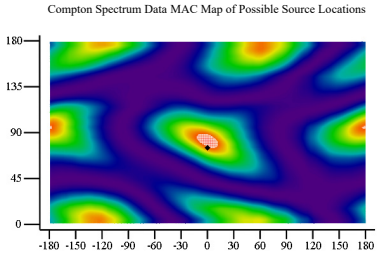

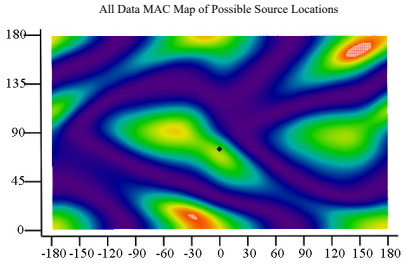

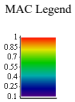

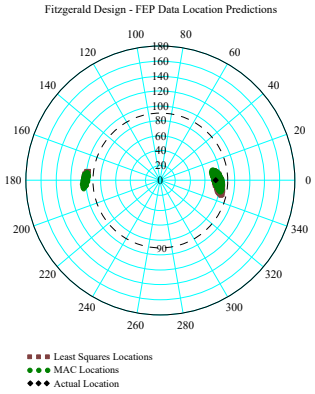

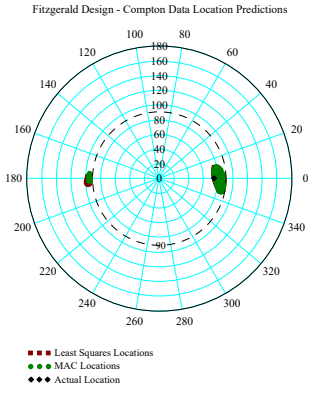

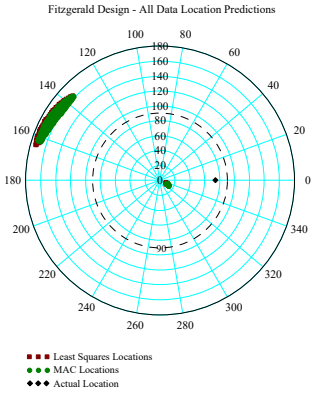

FEP Counting of Waveforms, Binned by RSM Rotation Angle; Used to Generate the Modulation Curve (ϕ = 75°)

RSM Rotation Angle	Number of Waveforms Recorded	RSM Rotation Angle	Number of Waveforms Recorded	RSM Rotation Angle	Number of Waveforms Recorded	RSM Rotation Angle	Number of Waveforms Recorded	RSM Rotation Angle	Number of Waveforms Recorded	RSM Rotation Angle	Number of Waveforms Recorded	RSM Rotation Angle	Number of Waveforms Recorded	RSM Rotation Angle	Number of Waveforms Recorded	Total Number of Waveforms in FEP
1	2512	46	2488	91	2443	136	3333	181	3385	226	3554	271	3307	316	3015	1046670
2	2571	47	2403	92	2450	137	3236	182	3337	227	3588	272	3264	317	3021	
3	2525	48	2477	93	2418	138	3166	183	3254	228	3676	273	3181	318	2701	
4	2516	49	2471	94	2273	139	3206	184	3284	229	3592	274	3158	319	3039	
5	2461	50	2415	95	2376	140	3299	185	3358	230	3536	275	3241	320	2870	
6	2506	51	2416	96	2412	141	3254	186	3519	231	3358	276	3157	321	2846	
7	2523	52	2439	97	2379	142	3367	187	3350	232	3725	277	2998	322	2936	
8	2470	53	2444	98	2502	143	3346	188	3373	233	3557	278	3026	323	2692	
9	2477	54	2392	99	2405	144	3274	189	3407	234	3679	279	2938	324	2985	
10	2467	55	2428	100	2361	145	3274	190	3418	235	3701	280	3028	325	2737	
11	2584	56	2467	101	2232	146	3207	191	3531	236	3576	281	2925	326	2911	
12	2638	57	2399	102	2410	147	3278	192	3401	237	3767	282	2731	327	2902	
13	2875	58	2435	103	2359	148	3270	193	3404	238	3527	283	2705	328	2799	
14	2698	59	2343	104	2358	149	3321	194	3386	239	3567	284	2680	329	2865	
15	2638	60	2412	105	2356	150	3254	195	3421	240	3802	285	2648	330	2681	
16	2669	61	2364	106	2254	151	3296	196	3383	241	3542	286	2705	331	2773	
17	2573	62	2348	107	2334	152	3293	197	3375	242	3669	287	2516	332	2747	
18	2538	63	2408	108	2321	153	3339	198	3424	243	3668	288	2456	333	2748	
19	2559	64	2380	109	2370	154	3204	199	3387	244	3613	289	2412	334	2742	
20	2434	65	2336	110	2238	155	3304	200	3547	245	3665	290	2376	335	2663	
21	2539	66	2332	111	2215	156	3296	201	3521	246	3711	291	2355	336	2721	
22	2496	67	2383	112	2316	157	3346	202	3509	247	3730	292	2327	337	2782	
23	2423	68	2397	113	2220	158	3212	203	3411	248	3666	293	2215	338	2762	
24	2533	69	2377	114	2201	159	3134	204	3511	249	3641	294	2256	339	2776	
25	2482	70	2364	115	2276	160	3270	205	3432	250	3713	295	2229	340	2594	
26	2516	71	2368	116	2260	161	3310	206	3436	251	3661	296	2284	341	2817	
27	2450	72	2332	117	2371	162	3210	207	3490	252	3646	297	2308	342	2700	
28	2380	73	2369	118	2439	163	3250	208	3470	253	3634	298	2243	343	2708	
29	2441	74	2435	119	2505	164	3267	209	3381	254	3714	299	2304	344	2610	
30	2416	75	2357	120	2561	165	3443	210	3564	255	3675	300	2367	345	2783	
31	2476	76	2306	121	2538	166	3302	211	3478	256	3601	301	2304	346	2797	
32	2504	77	2444	122	2732	167	3392	212	3506	257	3741	302	2376	347	2752	
33	2537	78	2425	123	2785	168	3300	213	3497	258	3572	303	2494	348	2830	
34	2513	79	2418	124	2840	169	3288	214	3545	259	3558	304	2491	349	2747	
35	2510	80	2316	125	2796	170	3320	215	3511	260	3539	305	2543	350	2785	
36	2552	81	2459	126	2932	171	3305	216	3484	261	3585	306	2573	351	2845	
37	2467	82	2458	127	2884	172	3323	217	3491	262	3592	307	2657	352	2786	
38	2504	83	2396	128	2989	173	3449	218	3539	263	3470	308	2379	353	2699	
39	2414	84	2268	129	3099	174	3321	219	3514	264	3475	309	2822	354	2707	
40	2417	85	2437	130	3102	175	3337	220	3560	265	3458	310	2823	355	2620	
41	2487	86	2454	131	3131	176	3449	221	3588	266	3473	311	2824	356	2739	
42	2441	87	2358	132	3224	177	3382	222	3619	267	3316	312	2895	357	2627	
43	2536	88	2315	133	3231	178	3325	223	3544	268	3329	313	2668	358	2589	
44	2443	89	2389	134	3184	179	3370	224	3587	269	3387	314	2984	359	2644	
45	2412	90	2307	135	3201	180	3302	225	3580	270	3365	315	2907	360	2612	

Compton Counting of Waveforms, Binned by RSM Rotation Angle; Used to Generate the Modulation Curve (ϕ = 75°)

RSM Rotation Angle	Number of Waveforms Recorded	RSM Rotation Angle	Number of Waveforms Recorded	RSM Rotation Angle	Number of Waveforms Recorded	RSM Rotation Angle	Number of Waveforms Recorded	RSM Rotation Angle	Number of Waveforms Recorded	RSM Rotation Angle	Number of Waveforms Recorded	RSM Rotation Angle	Number of Waveforms Recorded	RSM Rotation Angle	Number of Waveforms Recorded	Total Number of Waveforms in FEP
1	9330	46	9697	91	9703	136	9141	181	9135	226	8366	271	8629	316	9014	3282274
2	9135	47	9553	92	9601	137	9349	182	8991	227	8758	272	8590	317	9176	
3	9084	48	9450	93	9388	138	9198	183	8964	228	8545	273	8679	318	8427	
4	8779	49	9493	94	9590	139	9023	184	8875	229	8777	274	8761	319	9718	
5	8797	50	9425	95	9339	140	9093	185	9090	230	8584	275	8772	320	9138	
6	9236	51	9442	96	9547	141	9186	186	9036	231	8401	276	8941	321	8783	
7	9146	52	9608	97	9891	142	9159	187	8993	232	8983	277	8770	322	9348	
8	8557	53	9393	98	10060	143	9102	188	8848	233	8724	278	8795	323	8849	
9	9032	54	9296	99	9923	144	8996	189	8880	234	8574	279	8709	324	9340	
10	9009	55	9328	100	9782	145	9198	190	8991	235	8582	280	8847	325	8822	
11	9230	56	9500	101	9613	146	9120	191	8903	236	8158	281	8852	326	9111	
12	9360	57	9549	102	9720	147	9153	192	8930	237	8780	282	9021	327	9436	
13	10170	58	9330	103	9613	148	9106	193	8743	238	8468	283	8983	328	9221	
14	9766	59	9394	104	9569	149	8880	194	8615	239	8330	284	9036	329	8887	
15	9520	60	9255	105	9481	150	9079	195	8723	240	8618	285	8908	330	8959	
16	9584	61	9569	106	9512	151	9175	196	8848	241	8383	286	8968	331	9006	
17	9583	62	9550	107	9684	152	9267	197	8897	242	8988	287	9004	332	8998	
18	9502	63	9230	108	9646	153	9185	198	8743	243	8638	288	8907	333	8931	
19	9097	64	9357	109	9401	154	9165	199	8961	244	8551	289	9050	334	8982	
20	9075	65	9216	110	9595	155	9162	200	9041	245	8918	290	9036	335	8978	
21	9294	66	9614	111	9627	156	9109	201	8865	246	8781	291	9220	336	9286	
22	9320	67	9528	112	9732	157	8990	202	8905	247	8542	292	9116	337	9278	
23	9198	68	9380	113	9481	158	8913	203	8743	248	8725	293	9136	338	9053	
24	9111	69	9513	114	9666	159	8889	204	8732	249	8491	294	9164	339	8932	
25	9302	70	9534	115	9511	160	9079	205	8690	250	8533	295	9282	340	8848	
26	9309	71	9410	116	9669	161	9087	206	8707	251	8552	296	9400	341	9141	
27	9195	72	9656	117	9632	162	9008	207	8645	252	8688	297	9231	342	9151	
28	9028	73	9566	118	9528	163	9045	208	8717	253	8413	298	9120	343	8925	
29	9085	74	9295	119	9617	164	9070	209	8670	254	8528	299	9250	344	8946	
30	9149	75	9520	120	9544	165	9031	210	8608	255	8734	300	9191	345	9312	
31	9408	76	9461	121	9485	166	9058	211	8579	256	8592	301	9301	346	9438	
32	9457	77	9526	122	9647	167	9104	212	8681	257	8840	302	9216	347	9454	
33	9393	78	9571	123	9522	168	9034	213	8682	258	8629	303	9129	348	9497	
34	9421	79	9584	124	9391	169	8901	214	8667	259	8586	304	8995	349	9580	
35	9228	80	9428	125	9349	170	9064	215	8761	260	8571	305	9050	350	9386	
36	9644	81	9658	126	9249	171	8927	216	8752	261	8480	306	9122	351	9412	
37	9935	82	9647	127	9350	172	9032	217	8618	262	8506	307	9147	352	9457	
38	9478	83	9654	128	9245	173	8880	218	8702	263	8407	308	8059	353	9261	
39	9248	84	9722	129	9141	174	8863	219	8628	264	8552	309	9244	354	9195	
40	9156	85	9546	130	9343	175	9161	220	8766	265	8699	310	8842	355	9183	
41	9507	86	9832	131	9318	176	9096	221	8815	266	8533	311	9254	356	9309	
42	9524	87	9800	132	9326	177	9109	222	8964	267	8343	312	9025	357	9309	
43	9314	88	9535	133	9215	178	9033	223	8671	268	8613	313	8365	358	9070	
44	9432	89	9450	134	9077	179	9027	224	8641	269	8603	314	9670	359	9246	
45	9362	90	9425	135	9200	180	8968	225	8810	270	8625	315	8969	360	9089	

View Angle φ = 85° : Spectrum, Modulation Curve Data (No Smoothing), Library Curve, MAC and Least Squares Direction Predictions

Phi_ViewDegree = 85 Theta_ViewDegree = 0

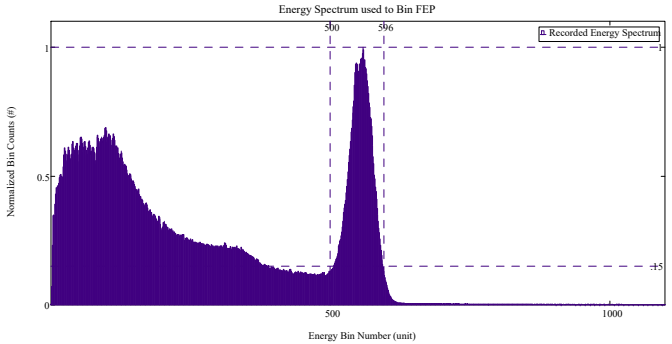

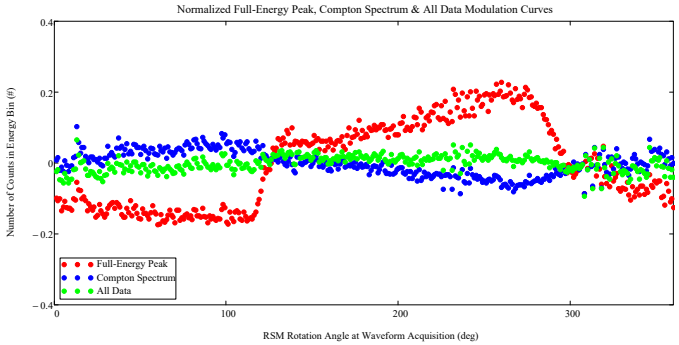

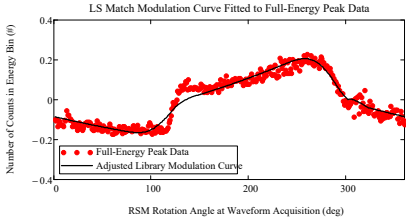

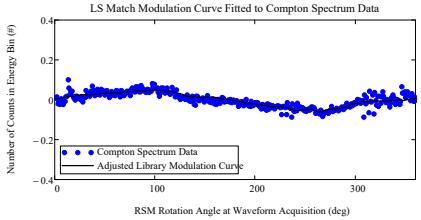

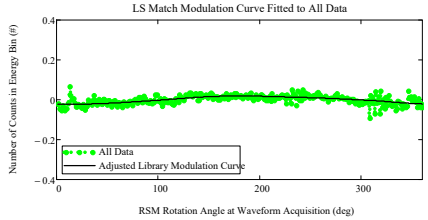

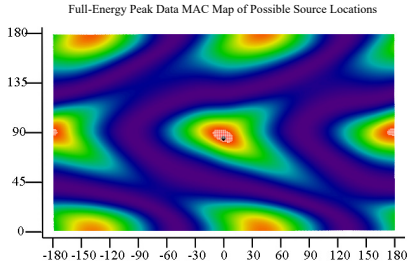

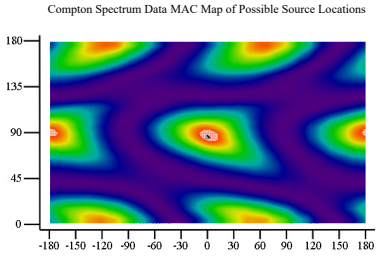

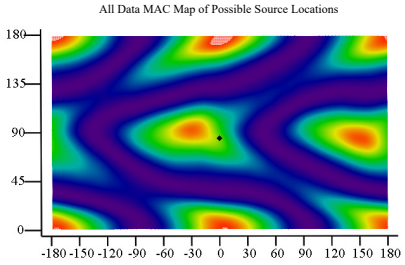

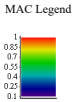

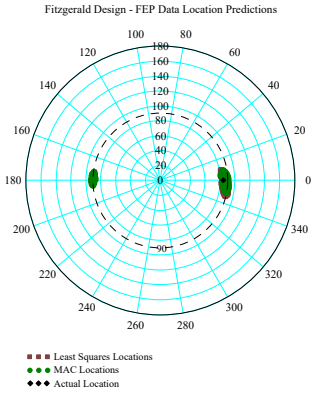

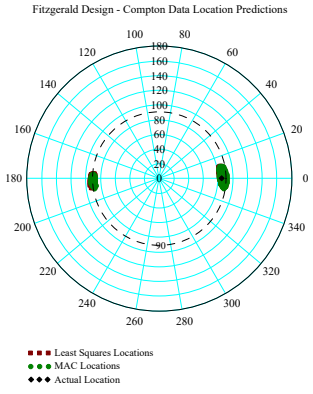

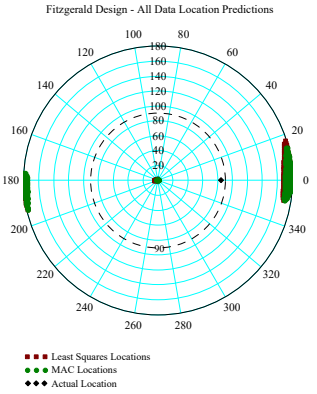

FEP Counting of Waveforms, Binned by RSM Rotation Angle; Used to Generate the Modulation Curve (ϕ = 85°)

RSM Rotation Angle	Number of Waveforms Recorded	RSM Rotation Angle	Number of Waveforms Recorded	RSM Rotation Angle	Number of Waveforms Recorded	RSM Rotation Angle	Number of Waveforms Recorded	RSM Rotation Angle	Number of Waveforms Recorded	RSM Rotation Angle	Number of Waveforms Recorded	RSM Rotation Angle	Number of Waveforms Recorded	RSM Rotation Angle	Number of Waveforms Recorded	Total Number of Waveforms in FEP
1	2602	46	2490	91	2369	136	3305	181	3295	226	3469	271	3682	316	3032	1072004
2	2570	47	2513	92	2398	137	3179	182	3264	227	3653	272	3587	317	2919	
3	2589	48	2435	93	2371	138	3366	183	3367	228	3447	273	3732	318	2753	
4	2462	49	2381	94	2357	139	3188	184	3333	229	3409	274	3808	319	3165	
5	2499	50	2373	95	2380	140	3216	185	3340	230	3537	275	3780	320	2831	
6	2562	51	2480	96	2370	141	3214	186	3392	231	3432	276	3692	321	2754	
7	2498	52	2434	97	2477	142	3199	187	3340	232	3783	277	3701	322	2853	
8	2487	53	2431	98	2532	143	3180	188	3371	233	3727	278	3610	323	2721	
9	2486	54	2404	99	2496	144	3220	189	3364	234	3585	279	3595	324	2953	
10	2468	55	2369	100	2339	145	3214	190	3397	235	3664	280	3635	325	2786	
11	2591	56	2440	101	2317	146	3211	191	3399	236	3478	281	3577	326	2824	
12	2579	57	2515	102	2448	147	3191	192	3333	237	3742	282	3585	327	2866	
13	2769	58	2447	103	2375	148	3168	193	3343	238	3550	283	3585	328	2702	
14	2687	59	2427	104	2344	149	3183	194	3258	239	3494	284	3511	329	2676	
15	2684	60	2310	105	2448	150	3196	195	3349	240	3702	285	3459	330	2707	
16	2591	61	2316	106	2462	151	3281	196	3354	241	3494	286	3451	331	2699	
17	2613	62	2417	107	2442	152	3224	197	3387	242	3758	287	3395	332	2695	
18	2573	63	2353	108	2372	153	3248	198	3287	243	3576	288	3307	333	2772	
19	2463	64	2339	109	2358	154	3126	199	3287	244	3496	289	3335	334	2632	
20	2536	65	2365	110	2444	155	3217	200	3289	245	3764	290	3295	335	2579	
21	2499	66	2414	111	2397	156	3216	201	3409	246	3669	291	3137	336	2725	
22	2465	67	2466	112	2351	157	3119	202	3421	247	3709	292	3242	337	2611	
23	2499	68	2415	113	2372	158	3216	203	3486	248	3600	293	3158	338	2669	
24	2390	69	2391	114	2383	159	3160	204	3335	249	3621	294	3086	339	2697	
25	2413	70	2328	115	2373	160	3241	205	3374	250	3724	295	3089	340	2635	
26	2533	71	2467	116	2412	161	3208	206	3347	251	3733	296	3106	341	2732	
27	2463	72	2467	117	2444	162	3125	207	3336	252	3544	297	2952	342	2727	
28	2423	73	2357	118	2536	163	3183	208	3378	253	3723	298	2877	343	2641	
29	2395	74	2383	119	2583	164	3221	209	3478	254	3666	299	2964	344	2697	
30	2424	75	2372	120	2674	165	3229	210	3473	255	3738	300	2942	345	2663	
31	2488	76	2415	121	2806	166	3221	211	3398	256	3712	301	2874	346	2856	
32	2526	77	2423	122	2932	167	3267	212	3575	257	3840	302	2825	347	2739	
33	2542	78	2387	123	2871	168	3165	213	3535	258	3728	303	2858	348	2718	
34	2552	79	2407	124	2909	169	3126	214	3344	259	3765	304	2897	349	2782	
35	2487	80	2363	125	2906	170	3284	215	3391	260	3860	305	2959	350	2766	
36	2549	81	2477	126	2978	171	3366	216	3477	261	3704	306	2935	351	2787	
37	2532	82	2470	127	3145	172	3197	217	3497	262	3709	307	2965	352	2782	
38	2502	83	2407	128	3109	173	3260	218	3439	263	3717	308	2646	353	2606	
39	2420	84	2403	129	3144	174	3267	219	3539	264	3833	309	3000	354	2619	
40	2392	85	2394	130	3247	175	3345	220	3527	265	3746	310	2925	355	2522	
41	2390	86	2488	131	3234	176	3295	221	3605	266	3664	311	3024	356	2754	
42	2488	87	2402	132	3178	177	3446	222	3621	267	3640	312	3036	357	2672	
43	2440	88	2395	133	3255	178	3247	223	3477	268	3789	313	2708	358	2554	
44	2572	89	2328	134	3199	179	3334	224	3451	269	3673	314	3079	359	2590	
45	2403	90	2408	135	3339	180	3262	225	3604	270	3706	315	2838	360	2494	

Compton Counting of Waveforms, Binned by RSM Rotation Angle; Used to Generate the Modulation Curve (ϕ = 85°)

RSM Rotation Angle	Number of Waveforms Recorded	RSM Rotation Angle	Number of Waveforms Recorded	RSM Rotation Angle	Number of Waveforms Recorded	RSM Rotation Angle	Number of Waveforms Recorded	RSM Rotation Angle	Number of Waveforms Recorded	RSM Rotation Angle	Number of Waveforms Recorded	RSM Rotation Angle	Number of Waveforms Recorded	RSM Rotation Angle	Number of Waveforms Recorded	Total Number of Waveforms in FEP
1	9408	46	9872	91	9710	136	9373	181	9275	226	8542	271	8681	316	9202	3351394
2	9468	47	9846	92	9857	137	9499	182	9222	227	8951	272	8685	317	9567	
3	9106	48	9774	93	9769	138	9277	183	8972	228	8984	273	8620	318	8594	
4	9206	49	9777	94	9705	139	9094	184	9105	229	8984	274	8764	319	9715	
5	9077	50	9575	95	9841	140	9031	185	9209	230	8917	275	8744	320	9275	
6	9376	51	9753	96	9773	141	9501	186	9227	231	8546	276	8964	321	9056	
7	9260	52	9815	97	10180	142	9497	187	9209	232	9175	277	8719	322	9494	
8	9077	53	9683	98	10040	143	9312	188	9024	233	8944	278	8755	323	8993	
9	9220	54	9447	99	10150	144	9270	189	9119	234	8898	279	8793	324	9501	
10	9239	55	9610	100	9890	145	9327	190	9256	235	8879	280	8802	325	9143	
11	9485	56	9753	101	9933	146	9343	191	9355	236	8411	281	8869	326	9462	
12	9511	57	9735	102	9926	147	9424	192	9082	237	9125	282	8785	327	9736	
13	10380	58	9579	103	9721	148	9394	193	9010	238	8766	283	8753	328	9502	
14	9923	59	9560	104	9512	149	9218	194	9004	239	8732	284	8849	329	9298	
15	9615	60	9550	105	9632	150	9309	195	8993	240	9005	285	8837	330	9164	
16	9776	61	9817	106	9922	151	9403	196	9254	241	8742	286	8955	331	9343	
17	9773	62	9676	107	9853	152	9528	197	8998	242	9161	287	8921	332	9309	
18	9514	63	9647	108	9943	153	9404	198	9036	243	8971	288	8806	333	9145	
19	9402	64	9760	109	9758	154	9221	199	9131	244	8879	289	8985	334	8956	
20	9321	65	9465	110	9683	155	9271	200	9169	245	8954	290	8914	335	9146	
21	9493	66	9797	111	9878	156	9191	201	9177	246	8845	291	9155	336	9456	
22	9495	67	9644	112	9934	157	9391	202	9178	247	8917	292	9029	337	9564	
23	9414	68	9619	113	9739	158	9291	203	9040	248	8852	293	8987	338	9431	
24	9418	69	9551	114	9657	159	9103	204	8992	249	8757	294	8949	339	9290	
25	9342	70	9627	115	9620	160	9137	205	9060	250	8799	295	9084	340	9069	
26	9460	71	9718	116	9658	161	9081	206	8860	251	8730	296	9099	341	9340	
27	9269	72	9760	117	9953	162	9331	207	9068	252	8822	297	9008	342	9305	
28	9227	73	9732	118	9787	163	9278	208	8871	253	8838	298	9071	343	9279	
29	9466	74	9686	119	9741	164	9314	209	8969	254	8792	299	9175	344	9082	
30	9455	75	9544	120	9461	165	9145	210	9049	255	8827	300	9105	345	9230	
31	9807	76	9839	121	9821	166	9299	211	8786	256	8948	301	9147	346	10020	
32	9545	77	9948	122	9578	167	9427	212	9120	257	8935	302	9340	347	9665	
33	9629	78	9865	123	9534	168	9393	213	8817	258	8898	303	9236	348	9673	
34	9557	79	9736	124	9439	169	9204	214	8887	259	8833	304	9297	349	9726	
35	9497	80	9746	125	9353	170	9241	215	9047	260	8602	305	9132	350	9439	
36	9761	81	9988	126	9444	171	9259	216	8917	261	8685	306	9203	351	9644	
37	10050	82	10000	127	9457	172	9230	217	8999	262	8692	307	9285	352	9750	
38	9756	83	9893	128	9419	173	9318	218	8963	263	8649	308	8415	353	9574	
39	9811	84	9752	129	9422	174	9202	219	8859	264	8591	309	9574	354	9541	
40	9553	85	9741	130	9347	175	9352	220	8917	265	8774	310	9124	355	9264	
41	9712	86	10070	131	9484	176	9167	221	8979	266	8701	311	9426	356	9649	
42	9875	87	9951	132	9565	177	9247	222	9006	267	8467	312	9208	357	9443	
43	9594	88	9877	133	9367	178	9300	223	8994	268	8564	313	8636	358	9232	
44	9656	89	9822	134	9267	179	9198	224	8986	269	8657	314	9780	359	9482	
45	9589	90	9748	135	9231	180	9219	225	8923	270	8684	315	9245	360	9311	

View Angle φ = 95° : Spectrum, Modulation Curve Data (No Smoothing), Library Curve, MAC and Least Squares Direction Predictions

Phi_ViewDegree = 95 Theta_ViewDegree = 0

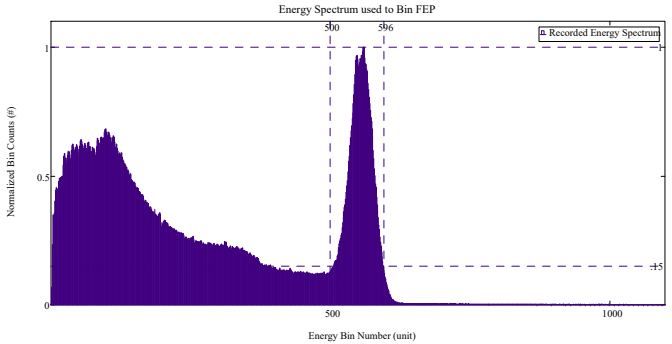

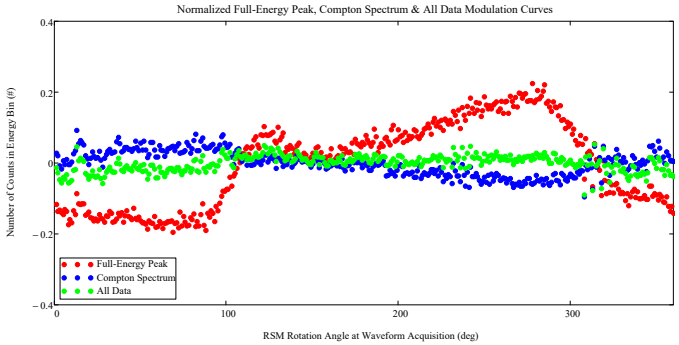

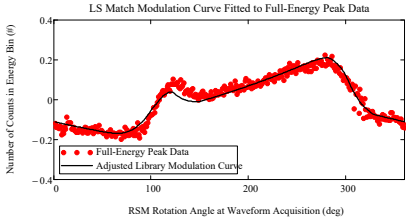

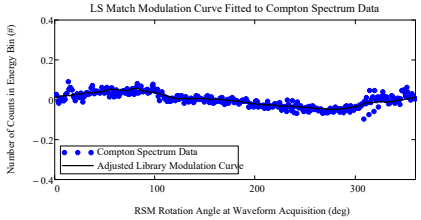

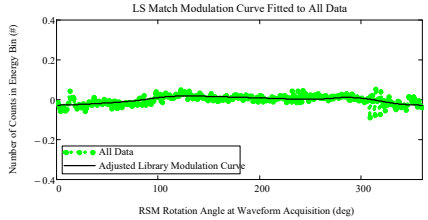

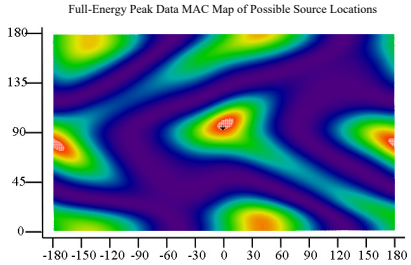

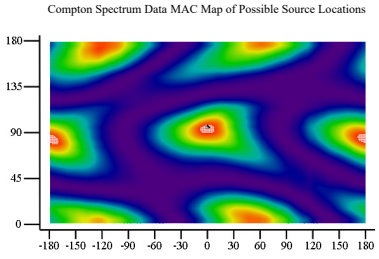

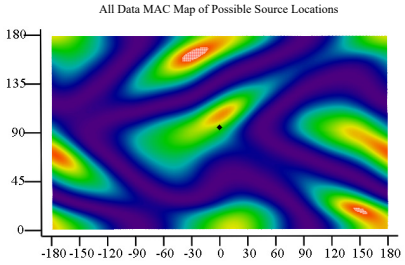

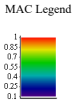

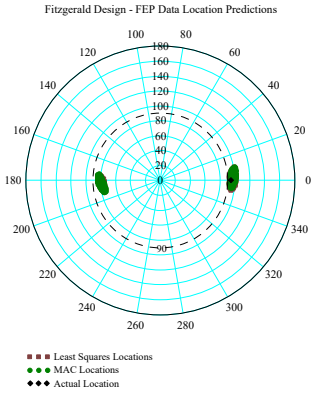

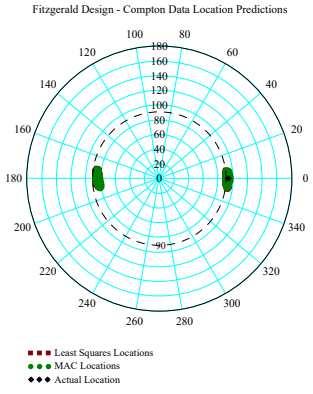

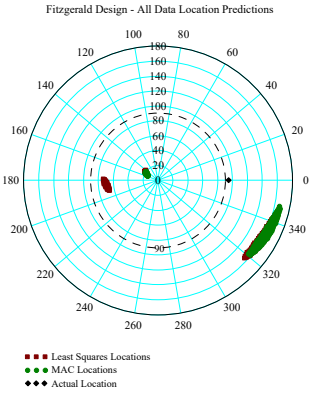

FEP Counting of Waveforms, Binned by RSM Rotation Angle; Used to Generate the Modulation Curve (ϕ = 95°)

RSM Rotation Angle	Number of Waveforms Recorded	RSM Rotation Angle	Number of Waveforms Recorded	RSM Rotation Angle	Number of Waveforms Recorded	RSM Rotation Angle	Number of Waveforms Recorded	RSM Rotation Angle	Number of Waveforms Recorded	RSM Rotation Angle	Number of Waveforms Recorded	RSM Rotation Angle	Number of Waveforms Recorded	RSM Rotation Angle	Number of Waveforms Recorded	Total Number of Waveforms in FEP
1	2545	46	2506	91	2481	136	3149	181	3301	226	3353	271	3753	316	2951	1078390
2	2471	47	2396	92	2453	137	3192	182	3253	227	3481	272	3706	317	2919	
3	2483	48	2382	93	2364	138	3161	183	3213	228	3456	273	3747	318	2645	
4	2458	49	2412	94	2528	139	3090	184	3182	229	3424	274	3754	319	3024	
5	2439	50	2366	95	2477	140	3142	185	3222	230	3468	275	3669	320	2807	
6	2492	51	2349	96	2560	141	3192	186	3368	231	3422	276	3678	321	2665	
7	2472	52	2344	97	2634	142	3216	187	3283	232	3558	277	3679	322	2795	
8	2323	53	2332	98	2694	143	3069	188	3111	233	3520	278	3864	323	2675	
9	2383	54	2280	99	2694	144	3062	189	3168	234	3448	279	3661	324	2758	
10	2349	55	2368	100	2712	145	3106	190	3206	235	3577	280	3683	325	2673	
11	2475	56	2344	101	2712	146	3088	191	3183	236	3377	281	3786	326	2762	
12	2436	57	2342	102	2846	147	3040	192	3264	237	3601	282	3696	327	2777	
13	2663	58	2419	103	2747	148	2994	193	3277	238	3517	283	3729	328	2710	
14	2555	59	2296	104	2859	149	3058	194	3229	239	3464	284	3784	329	2665	
15	2545	60	2307	105	2887	150	3108	195	3195	240	3617	285	3848	330	2679	
16	2551	61	2363	106	2943	151	3058	196	3361	241	3540	286	3654	331	2665	
17	2553	62	2341	107	3053	152	3159	197	3411	242	3706	287	3671	332	2589	
18	2427	63	2288	108	3001	153	3173	198	3239	243	3599	288	3610	333	2662	
19	2445	64	2340	109	3097	154	3061	199	3254	244	3538	289	3558	334	2533	
20	2465	65	2344	110	3100	155	3111	200	3358	245	3658	290	3662	335	2630	
21	2404	66	2363	111	3157	156	3050	201	3287	246	3574	291	3607	336	2682	
22	2394	67	2364	112	3175	157	3042	202	3296	247	3653	292	3603	337	2710	
23	2367	68	2371	113	3090	158	3064	203	3221	248	3509	293	3515	338	2625	
24	2389	69	2240	114	3164	159	3006	204	3331	249	3569	294	3624	339	2688	
25	2371	70	2339	115	3176	160	3077	205	3241	250	3721	295	3465	340	2612	
26	2435	71	2347	116	3249	161	3153	206	3291	251	3631	296	3474	341	2611	
27	2393	72	2289	117	3288	162	3019	207	3263	252	3590	297	3374	342	2617	
28	2391	73	2466	118	3194	163	3036	208	3286	253	3622	298	3443	343	2645	
29	2357	74	2309	119	3164	164	3063	209	3364	254	3592	299	3395	344	2601	
30	2420	75	2415	120	3306	165	3076	210	3345	255	3631	300	3422	345	2600	
31	2413	76	2354	121	3298	166	3174	211	3287	256	3644	301	3316	346	2746	
32	2468	77	2310	122	3395	167	3154	212	3267	257	3664	302	3371	347	2747	
33	2452	78	2321	123	3304	168	3089	213	3298	258	3558	303	3243	348	2636	
34	2356	79	2399	124	3302	169	3152	214	3322	259	3587	304	3193	349	2666	
35	2359	80	2379	125	3303	170	3121	215	3371	260	3672	305	3212	350	2651	
36	2386	81	2442	126	3318	171	3116	216	3380	261	3542	306	3297	351	2597	
37	2448	82	2303	127	3336	172	3122	217	3420	262	3664	307	3203	352	2657	
38	2421	83	2363	128	3239	173	3218	218	3382	263	3674	308	2826	353	2628	
39	2458	84	2314	129	3213	174	3092	219	3312	264	3543	309	3268	354	2574	
40	2351	85	2436	130	3391	175	3260	220	3447	265	3725	310	3108	355	2565	
41	2422	86	2556	131	3250	176	3206	221	3488	266	3670	311	3124	356	2632	
42	2476	87	2317	132	3282	177	3193	222	3403	267	3614	312	3089	357	2529	
43	2417	88	2261	133	3328	178	3173	223	3441	268	3715	313	2738	358	2469	
44	2404	89	2453	134	3113	179	3222	224	3391	269	3607	314	3209	359	2529	
45	2381	90	2407	135	3166	180	3205	225	3467	270	3764	315	3035	360	2450	

Compton Counting of Waveforms, Binned by RSM Rotation Angle; Used to Generate the Modulation Curve (ϕ = 95°)

RSM Rotation Angle	Number of Waveforms Recorded	RSM Rotation Angle	Number of Waveforms Recorded	RSM Rotation Angle	Number of Waveforms Recorded	RSM Rotation Angle	Number of Waveforms Recorded	RSM Rotation Angle	Number of Waveforms Recorded	RSM Rotation Angle	Number of Waveforms Recorded	RSM Rotation Angle	Number of Waveforms Recorded	RSM Rotation Angle	Number of Waveforms Recorded	Total Number of Waveforms in FEP
1	9603	46	9729	91	9808	136	9401	181	9264	226	8770	271	8646	316	9323	3349091
2	9522	47	9950	92	9852	137	9378	182	9239	227	8956	272	8651	317	9468	
3	9232	48	9757	93	9647	138	9185	183	9109	228	8868	273	8773	318	8727	
4	9136	49	9667	94	9701	139	9288	184	9096	229	8979	274	8722	319	9805	
5	9368	50	9882	95	9733	140	9318	185	9220	230	8916	275	8864	320	9403	
6	9265	51	9685	96	9839	141	9547	186	9252	231	8709	276	8860	321	9281	
7	9412	52	9950	97	10060	142	9405	187	9296	232	9296	277	8712	322	9462	
8	9269	53	9693	98	10120	143	9494	188	9247	233	9076	278	8697	323	8952	
9	9261	54	9468	99	9896	144	9342	189	9265	234	8937	279	8738	324	9422	
10	9346	55	9565	100	9763	145	9358	190	9321	235	8940	280	8952	325	9291	
11	9583	56	9910	101	9770	146	9381	191	9377	236	8764	281	8815	326	9488	
12	9669	57	9906	102	9856	147	9333	192	9243	237	9275	282	8799	327	9714	
13	10250	58	9696	103	9494	148	9306	193	8931	238	8948	283	8842	328	9532	
14	9864	59	9479	104	9265	149	9194	194	8961	239	8648	284	8686	329	9351	
15	9969	60	9491	105	9597	150	9287	195	9093	240	9047	285	8834	330	9321	
16	9915	61	9809	106	9693	151	9453	196	9002	241	8607	286	8856	331	9464	
17	9829	62	9683	107	9725	152	9545	197	9025	242	9197	287	8713	332	9337	
18	9517	63	9669	108	9535	153	9351	198	8931	243	8917	288	8660	333	9103	
19	9429	64	9503	109	9366	154	9170	199	9093	244	8917	289	8745	334	9135	
20	9269	65	9627	110	9457	155	9394	200	9222	245	9016	290	8966	335	9230	
21	9456	66	9730	111	9434	156	9457	201	9275	246	8918	291	9019	336	9530	
22	9637	67	9751	112	9253	157	9280	202	9220	247	8806	292	8807	337	9451	
23	9505	68	9773	113	9414	158	9142	203	8936	248	8702	293	8791	338	9266	
24	9446	69	9802	114	9249	159	9184	204	9018	249	8768	294	8673	339	9146	
25	9460	70	9671	115	9246	160	9301	205	9020	250	8897	295	9014	340	9324	
26	9645	71	9806	116	9273	161	9237	206	8983	251	8746	296	8960	341	9253	
27	9389	72	9876	117	9414	162	9286	207	9014	252	8947	297	8835	342	9390	
28	9201	73	9589	118	9335	163	9286	208	9040	253	8697	298	8794	343	9282	
29	9454	74	9607	119	9359	164	9236	209	8896	254	8983	299	8906	344	9071	
30	9559	75	9624	120	9265	165	9409	210	8903	255	8794	300	8985	345	9371	
31	9659	76	9678	121	9387	166	9220	211	9080	256	8907	301	8935	346	9798	
32	9707	77	9900	122	9540	167	9426	212	9232	257	9009	302	8884	347	9776	
33	9595	78	9817	123	9537	168	9169	213	8869	258	8952	303	8878	348	9822	
34	9621	79	9588	124	9344	169	9077	214	8955	259	8806	304	9045	349	9647	
35	9639	80	9720	125	9429	170	9227	215	9021	260	8834	305	8990	350	9494	
36	9928	81	9966	126	9527	171	9250	216	8986	261	8879	306	9093	351	9940	
37	10050	82	10150	127	9444	172	9327	217	8954	262	8858	307	9088	352	9737	
38	9870	83	9673	128	9379	173	9127	218	9012	263	8739	308	8324	353	9439	
39	9629	84	9678	129	9154	174	9330	219	9122	264	8820	309	9252	354	9493	
40	9665	85	9949	130	9451	175	9368	220	9118	265	8860	310	9112	355	9299	
41	9760	86	10030	131	9456	176	9315	221	9007	266	8723	311	9440	356	9625	
42	9768	87	9801	132	9351	177	9437	222	9095	267	8607	312	9172	357	9520	
43	9699	88	9735	133	9215	178	9306	223	8933	268	8698	313	8558	358	9403	
44	9698	89	9748	134	9266	179	9183	224	9184	269	8689	314	9795	359	9368	
45	9648	90	9756	135	9265	180	9317	225	9041	270	8754	315	9189	360	9366	

View Angle φ = 105° : Spectrum, Modulation Curve Data (No Smoothing), Library Curve, MAC and Least Squares Direction Predictions

Phi_ViewDegree = 105 Theta_ViewDegree = 0

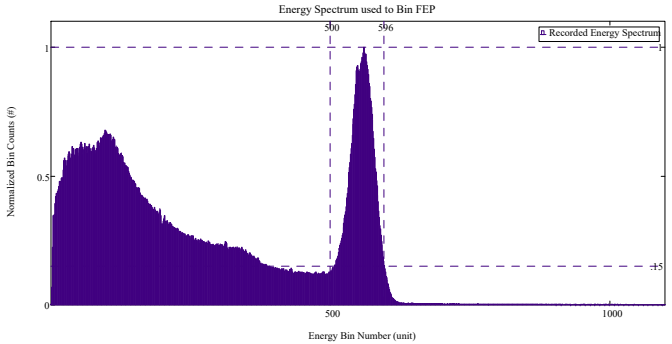

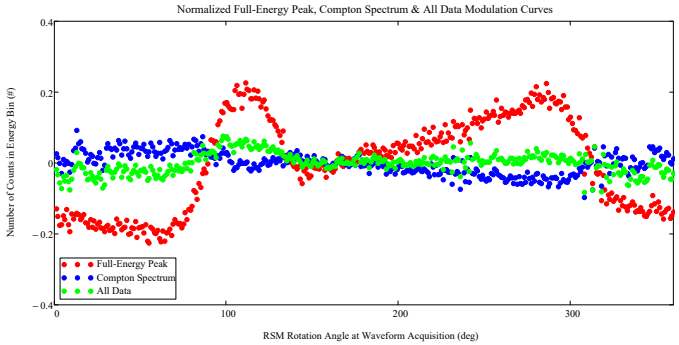

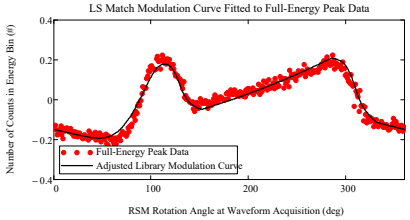

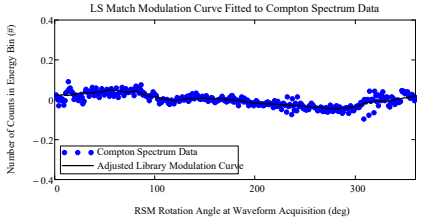

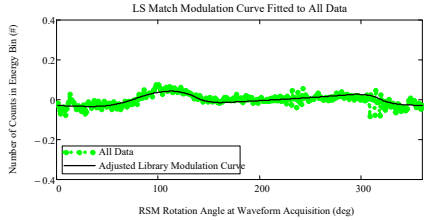

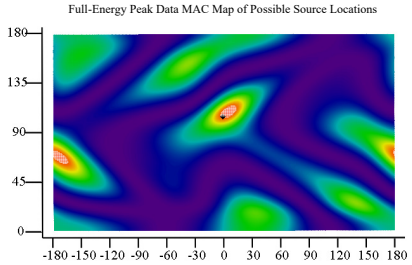

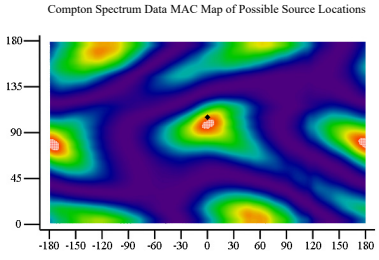

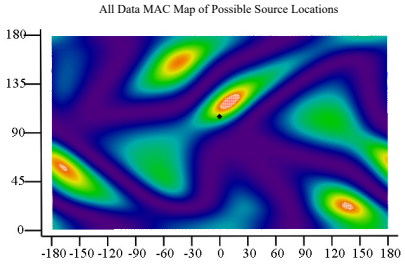

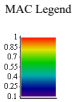

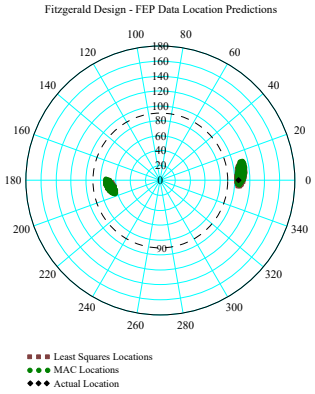

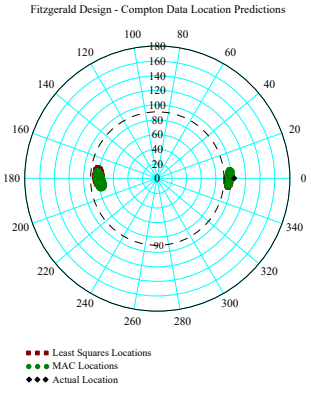

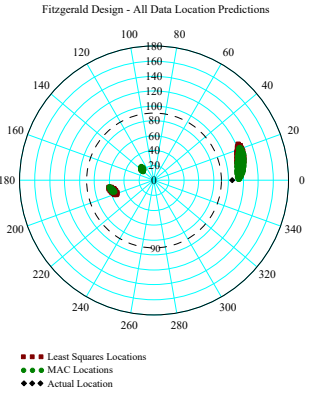

FEP Counting of Waveforms, Binned by RSM Rotation Angle; Used to Generate the Modulation Curve (ϕ = 105°)

RSM Rotation Angle	Number of Waveforms Recorded	RSM Rotation Angle	Number of Waveforms Recorded	RSM Rotation Angle	Number of Waveforms Recorded	RSM Rotation Angle	Number of Waveforms Recorded	RSM Rotation Angle	Number of Waveforms Recorded	RSM Rotation Angle	Number of Waveforms Recorded	RSM Rotation Angle	Number of Waveforms Recorded	RSM Rotation Angle	Number of Waveforms Recorded	Total Number of Waveforms in FEP
1	2479	46	2266	91	3221	136	2985	181	3170	226	3194	271	3508	316	2850	1069020
2	2392	47	2340	92	3219	137	2988	182	3103	227	3386	272	3591	317	2864	
3	2298	48	2166	93	3189	138	2971	183	3080	228	3208	273	3576	318	2562	
4	2306	49	2273	94	3203	139	2936	184	3083	229	3296	274	3655	319	2836	
5	2398	50	2280	95	3390	140	2938	185	3165	230	3250	275	3659	320	2684	
6	2361	51	2283	96	3432	141	2910	186	3140	231	3242	276	3631	321	2528	
7	2469	52	2217	97	3533	142	2936	187	3091	232	3419	277	3730	322	2624	
8	2302	53	2306	98	3519	143	2801	188	3060	233	3369	278	3590	323	2579	
9	2230	54	2123	99	3619	144	2750	189	3094	234	3381	279	3717	324	2644	
10	2418	55	2105	100	3627	145	2889	190	3042	235	3369	280	3797	325	2559	
11	2368	56	2276	101	3592	146	2918	191	3133	236	3203	281	3665	326	2582	
12	2413	57	2253	102	3568	147	2853	192	3116	237	3388	282	3713	327	2604	
13	2430	58	2217	103	3553	148	2812	193	3050	238	3281	283	3638	328	2461	
14	2412	59	2206	104	3555	149	2829	194	3045	239	3328	284	3680	329	2562	
15	2362	60	2241	105	3760	150	2989	195	3093	240	3351	285	3661	330	2511	
16	2383	61	2152	106	3810	151	2923	196	3031	241	3231	286	3832	331	2597	
17	2416	62	2120	107	3716	152	2913	197	3160	242	3546	287	3737	332	2495	
18	2324	63	2238	108	3726	153	2938	198	3086	243	3403	288	3567	333	2452	
19	2321	64	2127	109	3563	154	2909	199	3187	244	3459	289	3670	334	2506	
20	2280	65	2212	110	3720	155	2963	200	3185	245	3447	290	3682	335	2519	
21	2356	66	2223	111	3841	156	2951	201	3132	246	3399	291	3619	336	2551	
22	2274	67	2259	112	3772	157	2891	202	3112	247	3465	292	3615	337	2518	
23	2342	68	2191	113	3760	158	2816	203	3161	248	3353	293	3641	338	2444	
24	2257	69	2314	114	3672	159	2927	204	3205	249	3426	294	3632	339	2455	
25	2312	70	2362	115	3668	160	2915	205	3080	250	3451	295	3555	340	2450	
26	2331	71	2322	116	3768	161	2893	206	3154	251	3525	296	3702	341	2490	
27	2272	72	2308	117	3675	162	2871	207	3156	252	3455	297	3579	342	2446	
28	2260	73	2318	118	3751	163	2906	208	3156	253	3481	298	3580	343	2398	
29	2228	74	2270	119	3670	164	2995	209	3130	254	3488	299	3445	344	2396	
30	2286	75	2310	120	3577	165	3069	210	3272	255	3532	300	3469	345	2421	
31	2297	76	2435	121	3635	166	2977	211	3084	256	3491	301	3399	346	2450	
32	2240	77	2358	122	3653	167	2948	212	3179	257	3658	302	3334	347	2509	
33	2250	78	2471	123	3562	168	2938	213	3128	258	3418	303	3325	348	2617	
34	2267	79	2459	124	3485	169	3021	214	3237	259	3480	304	3291	349	2528	
35	2205	80	2504	125	3437	170	3003	215	3339	260	3565	305	3463	350	2449	
36	2366	81	2677	126	3446	171	3025	216	3193	261	3490	306	3263	351	2552	
37	2308	82	2655	127	3436	172	3005	217	3203	262	3524	307	3242	352	2488	
38	2319	83	2580	128	3386	173	2989	218	3306	263	3517	308	2853	353	2419	
39	2251	84	2753	129	3369	174	2975	219	3166	264	3473	309	3271	354	2368	
40	2271	85	2709	130	3318	175	2972	220	3358	265	3508	310	3136	355	2443	
41	2280	86	2858	131	3268	176	2983	221	3233	266	3543	311	3077	356	2469	
42	2351	87	2910	132	3194	177	3095	222	3200	267	3508	312	3035	357	2484	
43	2202	88	2864	133	3321	178	3120	223	3210	268	3513	313	2751	358	2372	
44	2211	89	2961	134	3022	179	2990	224	3255	269	3534	314	3147	359	2403	
45	2271	90	3086	135	3059	180	3077	225	3302	270	3548	315	2864	360	2443	

Compton Counting of Waveforms, Binned by RSM Rotation Angle; Used to Generate the Modulation Curve (ϕ = 105°)

RSM Rotation Angle	Number of Waveforms Recorded	RSM Rotation Angle	Number of Waveforms Recorded	RSM Rotation Angle	Number of Waveforms Recorded	RSM Rotation Angle	Number of Waveforms Recorded	RSM Rotation Angle	Number of Waveforms Recorded	RSM Rotation Angle	Number of Waveforms Recorded	RSM Rotation Angle	Number of Waveforms Recorded	RSM Rotation Angle	Number of Waveforms Recorded	Total Number of Waveforms in FEP
1	9641	46	9839	91	9547	136	9550	181	9313	226	8884	271	8783	316	9411	3371241
2	9528	47	9956	92	9545	137	9679	182	9351	227	9171	272	8753	317	9382	
3	9360	48	9838	93	9510	138	9543	183	9063	228	9185	273	8951	318	8704	
4	9075	49	9623	94	9326	139	9430	184	9292	229	9113	274	8804	319	9839	
5	9469	50	9801	95	9582	140	9637	185	9350	230	9114	275	9112	320	9590	
6	9332	51	9780	96	9514	141	9724	186	9515	231	8756	276	8925	321	9299	
7	9422	52	9923	97	9659	142	9524	187	9387	232	9528	277	8783	322	9629	
8	9363	53	9719	98	9800	143	9602	188	9260	233	9046	278	8968	323	9065	
9	9104	54	9566	99	9655	144	9435	189	9460	234	9131	279	8840	324	9546	
10	9335	55	9694	100	9672	145	9406	190	9370	235	9069	280	9053	325	9342	
11	9733	56	9946	101	9608	146	9423	191	9272	236	8611	281	9067	326	9671	
12	9803	57	9839	102	9422	147	9564	192	9379	237	9433	282	8815	327	9781	
13	10310	58	9699	103	9389	148	9457	193	9060	238	9080	283	8784	328	9504	
14	9930	59	9573	104	9168	149	9384	194	9270	239	8830	284	8994	329	9316	
15	9982	60	9656	105	9236	150	9417	195	9121	240	9195	285	8917	330	9485	
16	9795	61	9973	106	9243	151	9586	196	9237	241	8804	286	8901	331	9539	
17	9775	62	9653	107	9326	152	9446	197	9215	242	9535	287	8686	332	9509	
18	9657	63	9494	108	9436	153	9307	198	9055	243	9068	288	8775	333	9072	
19	9400	64	9722	109	9359	154	9364	199	9183	244	9050	289	8945	334	8999	
20	9482	65	9753	110	9364	155	9364	200	9260	245	9201	290	8941	335	9228	
21	9631	66	9820	111	9368	156	9487	201	9331	246	9145	291	8967	336	9540	
22	9565	67	10020	112	9393	157	9477	202	9275	247	8974	292	8923	337	9472	
23	9371	68	9934	113	9205	158	9328	203	9090	248	8900	293	8685	338	9232	
24	9345	69	9590	114	9140	159	9254	204	9105	249	9013	294	8802	339	9139	
25	9526	70	9745	115	9200	160	9226	205	9159	250	8906	295	9061	340	9255	
26	9671	71	9943	116	9349	161	9298	206	9139	251	8848	296	8879	341	9370	
27	9503	72	9763	117	9228	162	9367	207	9183	252	8918	297	8835	342	9379	
28	9168	73	9833	118	9229	163	9319	208	9083	253	8886	298	8818	343	9226	
29	9310	74	9762	119	9154	164	9382	209	9101	254	9079	299	8892	344	9277	
30	9801	75	9828	120	9320	165	9415	210	9156	255	9035	300	9012	345	9313	
31	9937	76	9911	121	9362	166	9382	211	9222	256	9199	301	9032	346	9841	
32	9812	77	9799	122	9492	167	9571	212	9263	257	9151	302	9055	347	9792	
33	9766	78	9913	123	9436	168	9411	213	9139	258	9038	303	8959	348	9835	
34	9549	79	9604	124	9302	169	9326	214	9123	259	8988	304	9007	349	9677	
35	9813	80	9844	125	9335	170	9391	215	9208	260	8956	305	9223	350	9758	
36	9757	81	10070	126	9421	171	9272	216	9142	261	8936	306	9120	351	9753	
37	10020	82	10040	127	9539	172	9333	217	9095	262	8816	307	9260	352	9798	
38	9939	83	9880	128	9460	173	9344	218	8969	263	8837	308	8372	353	9563	
39	9598	84	9715	129	9378	174	9491	219	9343	264	8901	309	9389	354	9475	
40	9783	85	9933	130	9498	175	9316	220	9246	265	8997	310	9250	355	9561	
41	10000	86	10140	131	9440	176	9593	221	9028	266	8938	311	9341	356	9675	
42	9780	87	9776	132	9556	177	9610	222	9313	267	8776	312	9404	357	9608	
43	9606	88	9614	133	9292	178	9267	223	9035	268	8942	313	8588	358	9391	
44	9505	89	9709	134	9592	179	9463	224	9051	269	8763	314	9808	359	9346	
45	9700	90	9621	135	9384	180	9282	225	9150	270	8980	315	9299	360	9501	

View Angle φ = 115° : Spectrum, Modulation Curve Data (No Smoothing), Library Curve, MAC and Least Squares Direction Predictions

Phi_ViewDegree = 115 Theta_ViewDegree = 0

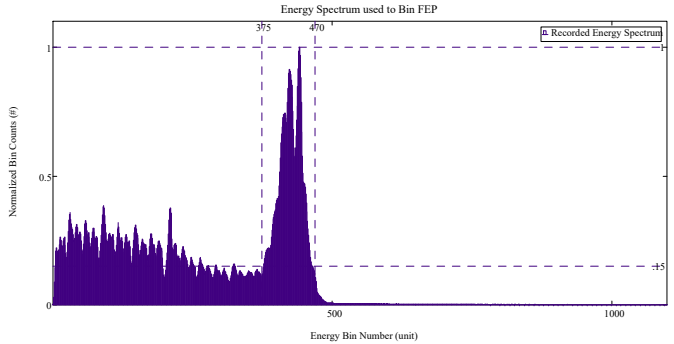

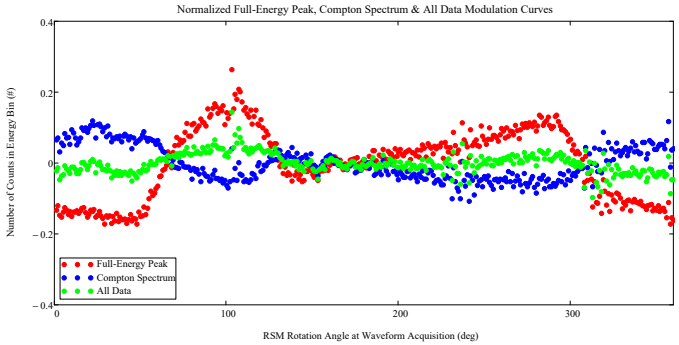

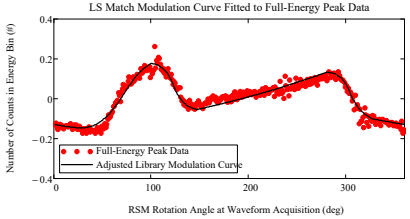

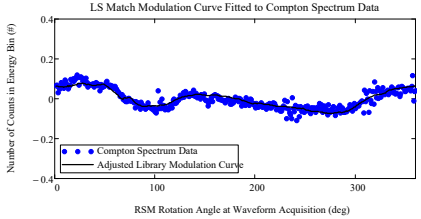

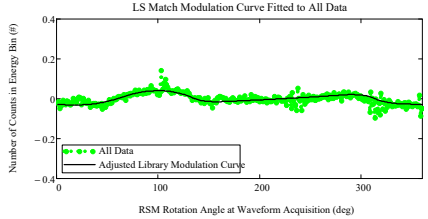

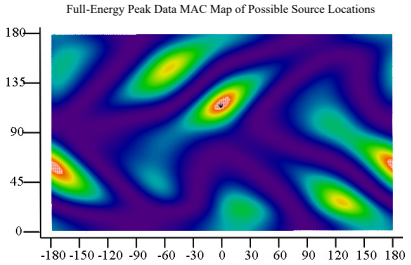

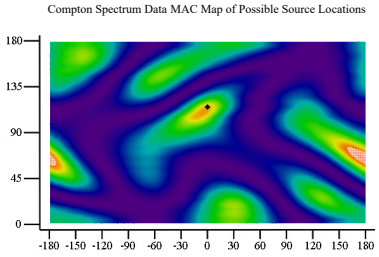

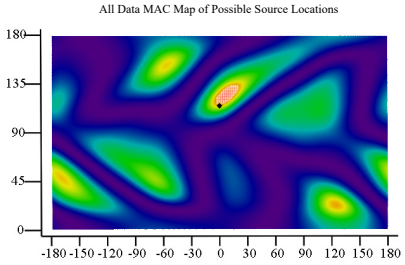

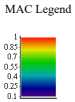

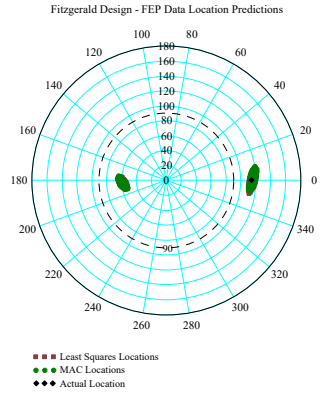

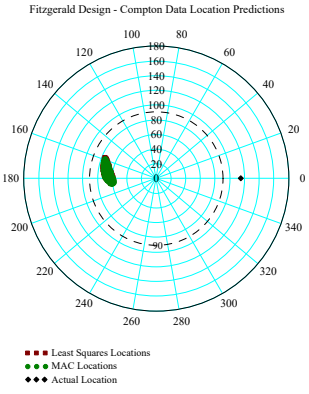

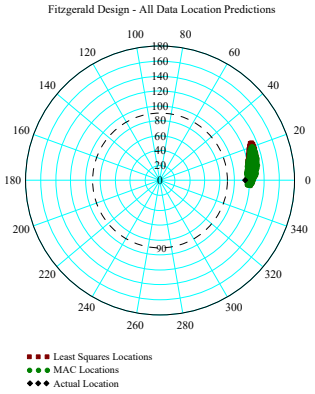

FEP Counting of Waveforms, Binned by RSM Rotation Angle; Used to Generate the Modulation Curve (ϕ = 115°)

RSM Rotation Angle	Number of Waveforms Recorded	RSM Rotation Angle	Number of Waveforms Recorded	RSM Rotation Angle	Number of Waveforms Recorded	RSM Rotation Angle	Number of Waveforms Recorded	RSM Rotation Angle	Number of Waveforms Recorded	RSM Rotation Angle	Number of Waveforms Recorded	RSM Rotation Angle	Number of Waveforms Recorded	RSM Rotation Angle	Number of Waveforms Recorded	Total Number of Waveforms in FEP
1	3370	46	3231	91	4867	136	3953	181	4035	226	4177	271	4631	316	3479	1476413
2	3436	47	3230	92	4970	137	3924	182	4034	227	4432	272	4721	317	3585	
3	3289	48	3149	93	5038	138	3821	183	4207	228	4361	273	4669	318	3313	
4	3254	49	3339	94	5001	139	4074	184	4091	229	4280	274	4727	319	3846	
5	3334	50	3269	95	4890	140	3914	185	4301	230	4351	275	4667	320	3664	
6	3401	51	3278	96	4961	141	3967	186	4304	231	4247	276	4738	321	3446	
7	3368	52	3418	97	4922	142	3848	187	4137	232	4593	277	4693	322	3626	
8	3298	53	3298	98	5003	143	3918	188	4087	233	4375	278	4682	323	3343	
9	3344	54	3400	99	4703	144	3813	189	4229	234	4258	279	4751	324	3604	
10	3270	55	3543	100	4892	145	3828	190	4206	235	4312	280	4612	325	3528	
11	3335	56	3659	101	4806	146	3982	191	4320	236	4120	281	4687	326	3491	
12	3338	57	3595	102	4890	147	3967	192	4173	237	4734	282	4860	327	3637	
13	3352	58	3630	103	5569	148	4053	193	4161	238	4470	283	4831	328	3617	
14	3319	59	3704	104	4959	149	3987	194	4289	239	4421	284	4699	329	3556	
15	3359	60	3740	105	5188	150	3927	195	4248	240	4361	285	4740	330	3386	
16	3394	61	3889	106	5110	151	3881	196	4250	241	4191	286	4768	331	3489	
17	3407	62	3904	107	5266	152	3925	197	4203	242	4629	287	4826	332	3448	
18	3322	63	3995	108	5226	153	3833	198	4331	243	4381	288	4699	333	3517	
19	3251	64	4013	109	5068	154	3960	199	4211	244	4426	289	4649	334	3529	
20	3298	65	4070	110	4938	155	3989	200	4278	245	4465	290	4675	335	3353	
21	3370	66	4283	111	4973	156	3984	201	4320	246	4381	291	4841	336	3497	
22	3341	67	4208	112	4873	157	3995	202	4240	247	4371	292	4854	337	3532	
23	3378	68	4033	113	4831	158	4094	203	4218	248	4690	293	4754	338	3497	
24	3258	69	4271	114	4937	159	3991	204	4273	249	4530	294	4691	339	3485	
25	3283	70	4382	115	4717	160	4068	205	4287	250	4471	295	4633	340	3461	
26	3348	71	4504	116	4836	161	4140	206	4308	251	4401	296	4625	341	3507	
27	3278	72	4386	117	4941	162	4099	207	4160	252	4483	297	4598	342	3433	
28	3236	73	4466	118	4717	163	4198	208	4267	253	4655	298	4559	343	3429	
29	3149	74	4433	119	4696	164	4150	209	4260	254	4478	299	4445	344	3371	
30	3279	75	4461	120	4787	165	4086	210	4223	255	4538	300	4480	345	3433	
31	3252	76	4592	121	4658	166	4153	211	4307	256	4537	301	4308	346	3441	
32	3273	77	4728	122	4508	167	4037	212	4200	257	4509	302	4394	347	3450	
33	3154	78	4529	123	4604	168	3998	213	4307	258	4446	303	4252	348	3357	
34	3270	79	4524	124	4544	169	4093	214	4389	259	4545	304	4295	349	3395	
35	3195	80	4708	125	4416	170	4059	215	4335	260	4648	305	4252	350	3364	
36	3320	81	4725	126	4365	171	4084	216	4201	261	4608	306	4053	351	3435	
37	3187	82	4605	127	4395	172	4155	217	4411	262	4501	307	4161	352	3347	
38	3259	83	4647	128	4413	173	4160	218	4374	263	4661	308	3800	353	3382	
39	3212	84	4686	129	4414	174	4168	219	4344	264	4525	309	4215	354	3395	
40	3216	85	4793	130	4151	175	4169	220	4252	265	4608	310	3837	355	3341	
41	3223	86	4752	131	4051	176	4187	221	4369	266	4600	311	3945	356	3244	
42	3155	87	4742	132	4089	177	4090	222	4331	267	4552	312	3849	357	3489	
43	3216	88	4692	133	3947	178	4017	223	4366	268	4695	313	3411	358	3146	
44	3299	89	4957	134	4038	179	4121	224	4358	269	4621	314	3810	359	3245	
45	3193	90	4827	135	3911	180	4154	225	4418	270	4486	315	3487	360	3205	

Compton Counting of Waveforms, Binned by RSM Rotation Angle; Used to Generate the Modulation Curve (ϕ = 115°)

RSM Rotation Angle	Number of Waveforms Recorded	RSM Rotation Angle	Number of Waveforms Recorded	RSM Rotation Angle	Number of Waveforms Recorded	RSM Rotation Angle	Number of Waveforms Recorded	RSM Rotation Angle	Number of Waveforms Recorded	RSM Rotation Angle	Number of Waveforms Recorded	RSM Rotation Angle	Number of Waveforms Recorded	RSM Rotation Angle	Number of Waveforms Recorded	Total Number of Waveforms in FEP
1	7243	46	7284	91	6382	136	6965	181	6682	226	6269	271	6275	316	6565	2425198
2	7281	47	7176	92	6486	137	6884	182	6750	227	6408	272	6120	317	7031	
3	6985	48	7196	93	6585	138	7077	183	6628	228	6462	273	6517	318	6531	
4	7172	49	7222	94	6409	139	6853	184	6769	229	6676	274	6295	319	7402	
5	7119	50	7263	95	6414	140	6835	185	6740	230	6405	275	6226	320	7016	
6	7376	51	7357	96	6362	141	6960	186	6472	231	5976	276	6312	321	6796	
7	7282	52	7426	97	6397	142	6778	187	6512	232	6640	277	6389	322	7183	
8	7303	53	7282	98	6317	143	6838	188	6642	233	6339	278	6447	323	6771	
9	7152	54	7208	99	6368	144	6862	189	6586	234	6200	279	6216	324	7046	
10	7464	55	7272	100	6257	145	6725	190	6492	235	6133	280	6095	325	6821	
11	7387	56	7257	101	6208	146	6914	191	6796	236	5973	281	6284	326	6987	
12	7285	57	7222	102	6338	147	6835	192	6653	237	6783	282	6408	327	7168	
13	7130	58	7217	103	7053	148	6804	193	6571	238	6371	283	6392	328	7014	
14	7202	59	7151	104	6381	149	6935	194	6494	239	6248	284	6482	329	6898	
15	7283	60	7225	105	6627	150	6681	195	6731	240	6490	285	6196	330	6969	
16	7498	61	7135	106	6371	151	6694	196	6720	241	5918	286	6359	331	7029	
17	7452	62	7068	107	6744	152	6648	197	6565	242	6457	287	6396	332	7076	
18	7502	63	6993	108	6505	153	6464	198	6573	243	6363	288	6229	333	6896	
19	7406	64	6972	109	6471	154	6616	199	6485	244	6059	289	6228	334	6993	
20	7490	65	6842	110	6335	155	6678	200	6388	245	6452	290	6304	335	7070	
21	7556	66	6848	111	6388	156	6780	201	6557	246	6261	291	6250	336	7205	
22	7650	67	6902	112	6350	157	6638	202	6490	247	6357	292	6301	337	6981	
23	7563	68	6703	113	6330	158	6853	203	6431	248	6380	293	6362	338	7115	
24	7283	69	6810	114	6381	159	6885	204	6439	249	6233	294	6512	339	6990	
25	7573	70	6660	115	6514	160	6918	205	6560	250	6443	295	6342	340	6936	
26	7578	71	6646	116	6489	161	6862	206	6579	251	6399	296	6488	341	6954	
27	7527	72	6634	117	6405	162	6868	207	6428	252	6458	297	6268	342	7185	
28	7420	73	6761	118	6687	163	6731	208	6474	253	6323	298	6381	343	7191	
29	7499	74	6752	119	6746	164	6816	209	6499	254	6262	299	6568	344	6836	
30	7317	75	6668	120	6561	165	6701	210	6425	255	6172	300	6364	345	6940	
31	7544	76	6656	121	6589	166	6719	211	6346	256	6387	301	6478	346	7229	
32	7361	77	6659	122	6692	167	6693	212	6511	257	6390	302	6520	347	7188	
33	7206	78	6648	123	6681	168	6686	213	6440	258	6341	303	6470	348	7161	
34	7289	79	6582	124	6744	169	6650	214	6574	259	6389	304	6562	349	7040	
35	7272	80	6395	125	6874	170	6599	215	6396	260	6215	305	6616	350	7032	
36	7305	81	6631	126	6790	171	6700	216	6396	261	6377	306	6661	351	7102	
37	7269	82	6562	127	6804	172	6683	217	6532	262	6426	307	6634	352	7147	
38	7323	83	6595	128	6986	173	6758	218	6583	263	6339	308	6204	353	7145	
39	7204	84	6502	129	6817	174	6716	219	6567	264	6565	309	7078	354	7139	
40	7318	85	6344	130	7028	175	6535	220	6483	265	6347	310	6645	355	7055	
41	7360	86	6627	131	7008	176	6554	221	6319	266	6512	311	6945	356	7222	
42	7330	87	6514	132	6895	177	6633	222	6369	267	6231	312	6733	357	7634	
43	7244	88	6462	133	6851	178	6581	223	6382	268	6355	313	6235	358	6656	
44	7306	89	6444	134	6843	179	6678	224	6336	269	6469	314	7061	359	7025	
45	7053	90	6350	135	6928	180	6820	225	6273	270	6361	315	6692	360	7057	

View Angle φ = 125° : Spectrum, Modulation Curve Data (No Smoothing), Library Curve, MAC and Least Squares Direction Predictions

Phi_ViewDegree = 125 Theta_ViewDegree = 0

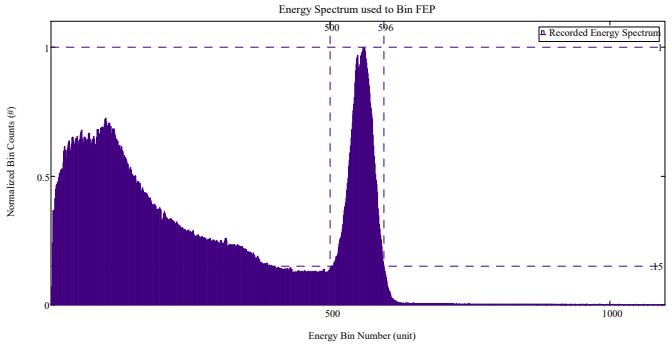

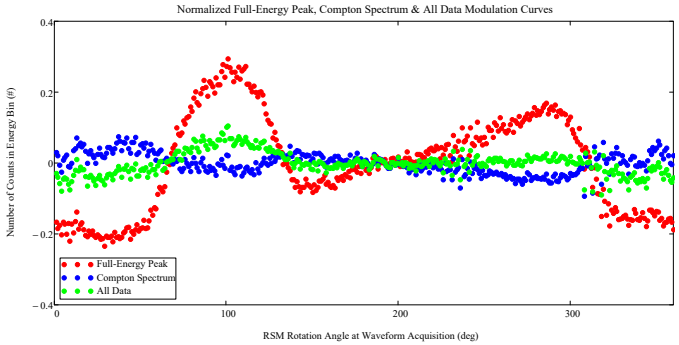

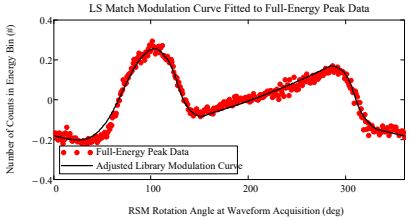

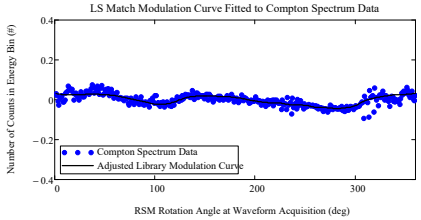

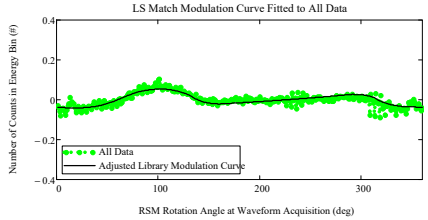

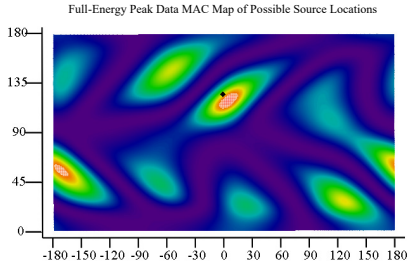

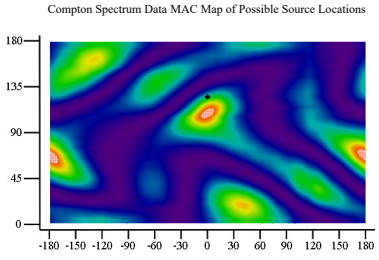

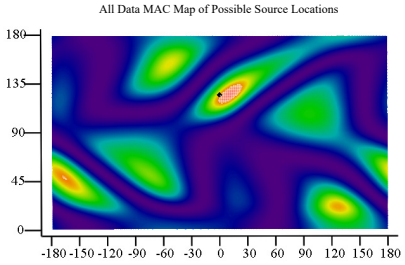

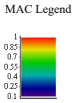

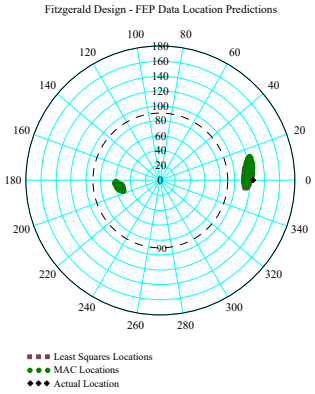

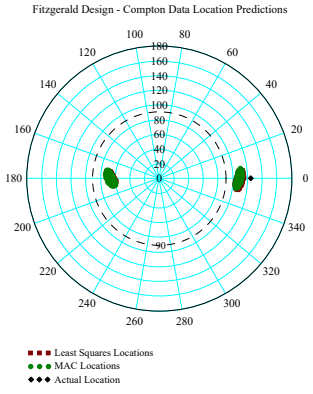

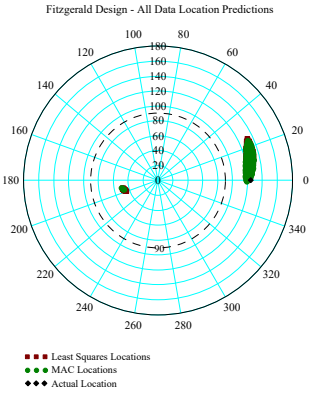

FEP Counting of Waveforms, Binned by RSM Rotation Angle; Used to Generate the Modulation Curve (ϕ = 125°)

RSM Rotation Angle	Number of Waveforms Recorded	RSM Rotation Angle	Number of Waveforms Recorded	RSM Rotation Angle	Number of Waveforms Recorded	RSM Rotation Angle	Number of Waveforms Recorded	RSM Rotation Angle	Number of Waveforms Recorded	RSM Rotation Angle	Number of Waveforms Recorded	RSM Rotation Angle	Number of Waveforms Recorded	RSM Rotation Angle	Number of Waveforms Recorded	Total Number of Waveforms in FEP
1	2437	46	2287	91	4209	136	3131	181	3099	226	3295	271	3666	316	2803	1148731
2	2362	47	2343	92	4166	137	3093	182	3123	227	3369	272	3714	317	2792	
3	2395	48	2405	93	4092	138	2979	183	3058	228	3422	273	3746	318	2510	
4	2281	49	2322	94	4285	139	2980	184	3133	229	3430	274	3781	319	2856	
5	2437	50	2355	95	4193	140	2883	185	3257	230	3290	275	3822	320	2709	
6	2416	51	2369	96	4195	141	2954	186	3212	231	3211	276	3745	321	2532	
7	2282	52	2460	97	4361	142	2895	187	3276	232	3549	277	3801	322	2672	
8	2422	53	2360	98	4448	143	2828	188	3122	233	3401	278	3830	323	2391	
9	2195	54	2363	99	4292	144	2884	189	3206	234	3348	279	3905	324	2594	
10	2415	55	2453	100	4429	145	2882	190	3195	235	3474	280	3807	325	2551	
11	2298	56	2590	101	4527	146	2992	191	3199	236	3274	281	3859	326	2622	
12	2450	57	2526	102	4410	147	2926	192	3238	237	3646	282	3812	327	2577	
13	2572	58	2626	103	4352	148	2909	193	3180	238	3468	283	3854	328	2472	
14	2347	59	2611	104	4235	149	2881	194	3172	239	3479	284	3905	329	2477	
15	2404	60	2794	105	4354	150	2818	195	3190	240	3539	285	3938	330	2484	
16	2428	61	2887	106	4293	151	2919	196	3244	241	3290	286	3962	331	2508	
17	2344	62	2858	107	4419	152	2842	197	3252	242	3644	287	3819	332	2526	
18	2267	63	2825	108	4266	153	2884	198	3181	243	3443	288	3876	333	2476	
19	2256	64	2895	109	4370	154	2962	199	3217	244	3421	289	3914	334	2396	
20	2326	65	3076	110	4392	155	2968	200	3270	245	3526	290	3867	335	2468	
21	2289	66	3188	111	4428	156	2988	201	3148	246	3713	291	3938	336	2463	
22	2329	67	3176	112	4198	157	3034	202	3218	247	3480	292	3787	337	2601	
23	2273	68	3324	113	4203	158	2921	203	3174	248	3514	293	3853	338	2554	
24	2249	69	3384	114	4155	159	2951	204	3255	249	3426	294	3863	339	2470	
25	2276	70	3426	115	4108	160	2897	205	3333	250	3522	295	3823	340	2466	
26	2250	71	3644	116	4177	161	2886	206	3256	251	3438	296	3832	341	2498	
27	2224	72	3559	117	4093	162	2904	207	3218	252	3653	297	3816	342	2559	
28	2227	73	3544	118	4041	163	2878	208	3207	253	3613	298	3685	343	2484	
29	2132	74	3578	119	4097	164	3009	209	3197	254	3609	299	3738	344	2382	
30	2264	75	3729	120	4104	165	2972	210	3210	255	3522	300	3778	345	2459	
31	2243	76	3694	121	4060	166	3009	211	3305	256	3709	301	3620	346	2595	
32	2247	77	3773	122	3947	167	3020	212	3307	257	3679	302	3574	347	2592	
33	2259	78	3790	123	3822	168	2975	213	3299	258	3607	303	3517	348	2562	
34	2192	79	3909	124	3742	169	3049	214	3251	259	3773	304	3468	349	2520	
35	2312	80	3853	125	3701	170	3023	215	3265	260	3635	305	3636	350	2578	
36	2245	81	4022	126	3692	171	3088	216	3340	261	3683	306	3429	351	2566	
37	2253	82	4106	127	3515	172	3007	217	3309	262	3594	307	3357	352	2467	
38	2232	83	3970	128	3587	173	3108	218	3369	263	3580	308	3122	353	2487	
39	2242	84	3935	129	3491	174	3150	219	3388	264	3614	309	3395	354	2388	
40	2298	85	4077	130	3415	175	3107	220	3350	265	3686	310	3333	355	2427	
41	2319	86	4147	131	3400	176	3074	221	3351	266	3750	311	3268	356	2438	
42	2370	87	4253	132	3331	177	3153	222	3410	267	3588	312	3127	357	2480	
43	2377	88	4163	133	3173	178	3062	223	3380	268	3736	313	2887	358	2486	
44	2223	89	4046	134	3190	179	3153	224	3250	269	3698	314	3137	359	2438	
45	2319	90	4232	135	3188	180	3200	225	3396	270	3787	315	2990	360	2342	

Compton Counting of Waveforms, Binned by RSM Rotation Angle; Used to Generate the Modulation Curve (ϕ = 125°)

RSM Rotation Angle	Number of Waveforms Recorded	RSM Rotation Angle	Number of Waveforms Recorded	RSM Rotation Angle	Number of Waveforms Recorded	RSM Rotation Angle	Number of Waveforms Recorded	RSM Rotation Angle	Number of Waveforms Recorded	RSM Rotation Angle	Number of Waveforms Recorded	RSM Rotation Angle	Number of Waveforms Recorded	RSM Rotation Angle	Number of Waveforms Recorded	Total Number of Waveforms in FEP
1	10770	46	11090	91	10200	136	10690	181	10530	226	9894	271	9854	316	10590	3752513
2	10670	47	11250	92	10260	137	10970	182	10450	227	10420	272	9762	317	10680	
3	10360	48	10700	93	10180	138	10640	183	10270	228	10150	273	9934	318	9756	
4	10140	49	10780	94	10030	139	10450	184	10340	229	10210	274	9890	319	11090	
5	10520	50	11000	95	10400	140	10760	185	10410	230	10220	275	10130	320	10560	
6	10600	51	11040	96	10370	141	10830	186	10700	231	9896	276	10060	321	10430	
7	10680	52	10900	97	10540	142	10810	187	10520	232	10570	277	9890	322	10560	
8	10310	53	11060	98	10370	143	10550	188	10400	233	10140	278	9966	323	10090	
9	10300	54	10660	99	10250	144	10700	189	10570	234	10220	279	9969	324	10720	
10	10420	55	10810	100	10690	145	10680	190	10540	235	10280	280	10000	325	10580	
11	10830	56	11020	101	10670	146	10650	191	10510	236	9643	281	9936	326	10740	
12	10880	57	10840	102	10210	147	10680	192	10420	237	10540	282	9936	327	10930	
13	11230	58	10740	103	10300	148	10660	193	10340	238	10000	283	9917	328	10730	
14	10980	59	10530	104	10140	149	10490	194	10260	239	10060	284	9988	329	10420	
15	11080	60	10730	105	10060	150	10570	195	10260	240	10250	285	9917	330	10670	
16	10950	61	10800	106	10290	151	10740	196	10430	241	9928	286	10080	331	10510	
17	11030	62	10850	107	10300	152	10730	197	10390	242	10470	287	9868	332	10440	
18	10810	63	10490	108	10320	153	10410	198	10360	243	10090	288	9803	333	10360	
19	10420	64	10500	109	10030	154	10750	199	10380	244	10270	289	9791	334	10080	
20	10730	65	10580	110	10130	155	10680	200	10590	245	10380	290	10000	335	10550	
21	10830	66	10500	111	10260	156	10600	201	10400	246	10220	291	10070	336	10650	
22	10680	67	10530	112	10310	157	10420	202	10430	247	10110	292	9865	337	10620	
23	10610	68	10470	113	10180	158	10310	203	10310	248	9937	293	9850	338	10340	
24	10420	69	10400	114	10110	159	10470	204	10380	249	10190	294	9967	339	10320	
25	10700	70	10550	115	10220	160	10540	205	10280	250	10050	295	10060	340	10450	
26	10900	71	10480	116	10050	161	10570	206	10120	251	10020	296	10030	341	10350	
27	10710	72	10550	117	10440	162	10510	207	10340	252	10050	297	10010	342	10420	
28	10620	73	10250	118	10230	163	10650	208	10220	253	10180	298	9895	343	10360	
29	10600	74	10150	119	10120	164	10420	209	10330	254	10140	299	9942	344	10190	
30	10750	75	10270	120	10370	165	10650	210	10060	255	10080	300	10110	345	10500	
31	10930	76	10550	121	10440	166	10540	211	10240	256	10110	301	10040	346	10820	
32	10920	77	10430	122	10600	167	10510	212	10420	257	10150	302	10060	347	10700	
33	10870	78	10330	123	10420	168	10420	213	10180	258	10070	303	10060	348	10920	
34	10750	79	10170	124	10370	169	10510	214	10240	259	10070	304	10120	349	10830	
35	10890	80	10430	125	10580	170	10530	215	10400	260	10100	305	10220	350	10910	
36	11080	81	10610	126	10430	171	10480	216	10290	261	9996	306	10300	351	11120	
37	11270	82	10420	127	10660	172	10690	217	10440	262	10070	307	10270	352	11010	
38	11130	83	10280	128	10480	173	10410	218	10110	263	9923	308	9369	353	10710	
39	10820	84	10170	129	10580	174	10490	219	10420	264	9976	309	10650	354	10560	
40	11100	85	10450	130	10730	175	10590	220	10290	265	9995	310	10340	355	10830	
41	11060	86	10590	131	10630	176	10750	221	10430	266	9925	311	10400	356	10910	
42	11230	87	10320	132	10700	177	10540	222	10320	267	9943	312	10290	357	10660	
43	10890	88	10180	133	10710	178	10560	223	10240	268	9774	313	9473	358	10410	
44	10750	89	10140	134	10600	179	10320	224	10270	269	9923	314	10950	359	10380	
45	11090	90	10330	135	10570	180	10490	225	10230	270	9922	315	10570	360	10670	

View Angle φ = 135° : Spectrum, Modulation Curve Data (No Smoothing), Library Curve, MAC and Least Squares Direction Predictions

Phi_ViewDegree = 135 Theta_ViewDegree = 0

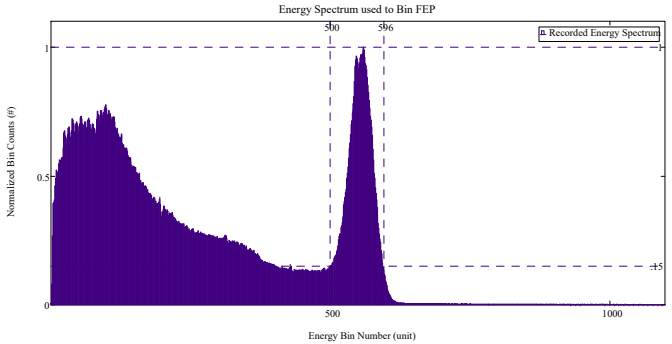

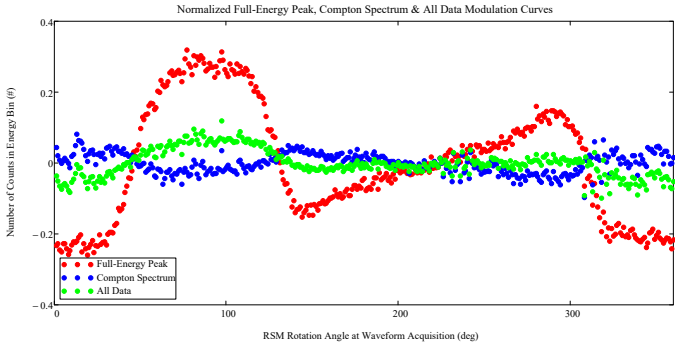

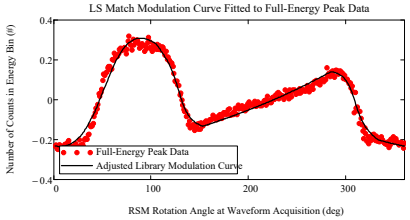

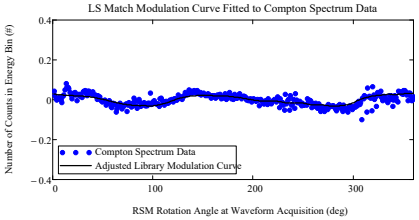

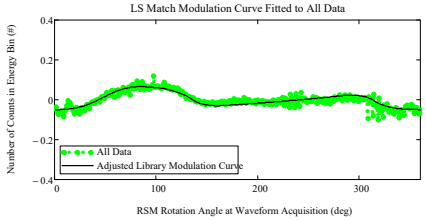

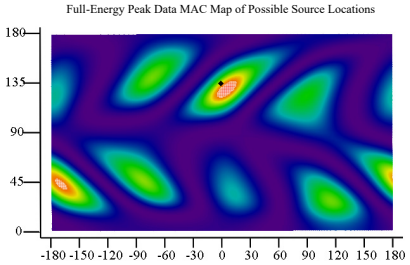

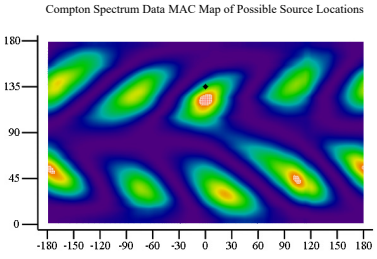

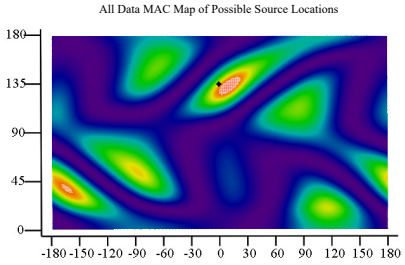

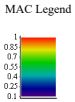

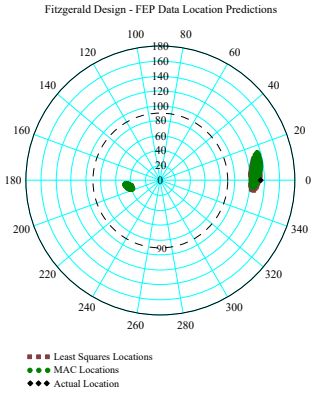

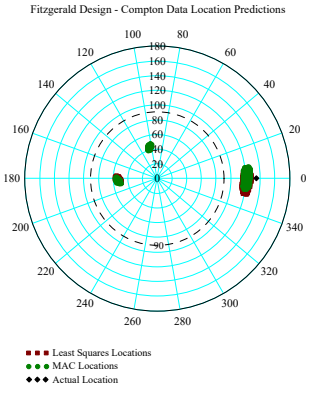

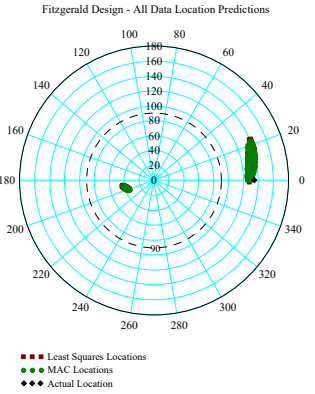

FEP Counting of Waveforms, Binned by RSM Rotation Angle; Used to Generate the Modulation Curve (ϕ = 135°)

RSM Rotation Angle	Number of Waveforms Recorded	RSM Rotation Angle	Number of Waveforms Recorded	RSM Rotation Angle	Number of Waveforms Recorded	RSM Rotation Angle	Number of Waveforms Recorded	RSM Rotation Angle	Number of Waveforms Recorded	RSM Rotation Angle	Number of Waveforms Recorded	RSM Rotation Angle	Number of Waveforms Recorded	RSM Rotation Angle	Number of Waveforms Recorded	Total Number of Waveforms in FEP
1	1764	46	2805	91	3753	136	2352	181	2380	226	2688	271	3004	316	2193	964588
2	1786	47	2756	92	3752	137	2378	182	2395	227	2765	272	3023	317	2072	
3	1715	48	2829	93	3639	138	2197	183	2412	228	2749	273	2981	318	1916	
4	1697	49	2887	94	3756	139	2263	184	2391	229	2800	274	3066	319	2134	
5	1788	50	3068	95	3689	140	2132	185	2453	230	2830	275	3078	320	2017	
6	1787	51	3190	96	3818	141	2162	186	2520	231	2708	276	3077	321	1865	
7	1726	52	3164	97	3916	142	2172	187	2516	232	2795	277	3042	322	1958	
8	1667	53	3219	98	3827	143	2192	188	2389	233	2756	278	3089	323	1814	
9	1706	54	3231	99	3719	144	2079	189	2577	234	2769	279	3085	324	1957	
10	1771	55	3322	100	3679	145	2127	190	2499	235	2749	280	3312	325	1873	
11	1809	56	3348	101	3643	146	2161	191	2518	236	2695	281	3173	326	1894	
12	1799	57	3340	102	3784	147	2205	192	2533	237	2878	282	3211	327	1988	
13	1816	58	3281	103	3723	148	2104	193	2567	238	2756	283	3142	328	2008	
14	1857	59	3299	104	3705	149	2214	194	2488	239	2780	284	3232	329	1904	
15	1881	60	3483	105	3675	150	2103	195	2522	240	2835	285	3195	330	1879	
16	1696	61	3468	106	3785	151	2224	196	2464	241	2702	286	3255	331	1966	
17	1783	62	3602	107	3679	152	2200	197	2559	242	2878	287	3156	332	1866	
18	1729	63	3554	108	3754	153	2160	198	2504	243	2811	288	3124	333	1886	
19	1660	64	3531	109	3700	154	2228	199	2599	244	2747	289	3262	334	1854	
20	1745	65	3543	110	3673	155	2239	200	2636	245	2883	290	3265	335	1933	
21	1781	66	3589	111	3737	156	2266	201	2572	246	2861	291	3252	336	1948	
22	1818	67	3685	112	3716	157	2227	202	2596	247	2876	292	3198	337	1886	
23	1688	68	3704	113	3650	158	2234	203	2597	248	2797	293	3234	338	1852	
24	1766	69	3658	114	3568	159	2261	204	2597	249	2832	294	3253	339	1830	
25	1758	70	3665	115	3644	160	2291	205	2570	250	2836	295	3232	340	1810	
26	1885	71	3692	116	3483	161	2290	206	2652	251	2813	296	3209	341	1807	
27	1776	72	3716	117	3531	162	2307	207	2551	252	2907	297	3110	342	1836	
28	1796	73	3681	118	3465	163	2383	208	2561	253	2817	298	3167	343	1858	
29	1805	74	3589	119	3425	164	2334	209	2647	254	2838	299	3089	344	1745	
30	1769	75	3687	120	3423	165	2308	210	2600	255	2895	300	3085	345	1795	
31	1891	76	3839	121	3404	166	2344	211	2571	256	2863	301	3096	346	1903	
32	1910	77	3943	122	3343	167	2291	212	2601	257	2872	302	3044	347	1917	
33	1909	78	3784	123	3199	168	2308	213	2571	258	2855	303	3005	348	1949	
34	1902	79	3751	124	3055	169	2365	214	2614	259	2904	304	3015	349	1838	
35	1986	80	3665	125	3041	170	2392	215	2602	260	2972	305	2913	350	1874	
36	2009	81	3875	126	3051	171	2322	216	2672	261	2911	306	2961	351	1915	
37	2183	82	3774	127	2980	172	2318	217	2675	262	2842	307	2848	352	1852	
38	2151	83	3862	128	2969	173	2393	218	2584	263	2912	308	2428	353	1829	
39	2169	84	3824	129	2779	174	2435	219	2753	264	2923	309	2831	354	1794	
40	2222	85	3873	130	2820	175	2433	220	2624	265	2970	310	2511	355	1819	
41	2355	86	3848	131	2685	176	2391	221	2665	266	2892	311	2536	356	1846	
42	2426	87	3792	132	2580	177	2428	222	2627	267	3038	312	2466	357	1845	
43	2517	88	3708	133	2493	178	2402	223	2634	268	3020	313	2218	358	1807	
44	2508	89	3731	134	2448	179	2492	224	2734	269	3063	314	2457	359	1729	
45	2593	90	3792	135	2455	180	2507	225	2716	270	3026	315	2321	360	1830	

Compton Counting of Waveforms, Binned by RSM Rotation Angle; Used to Generate the Modulation Curve (ϕ = 135°)

RSM Rotation Angle	Number of Waveforms Recorded	RSM Rotation Angle	Number of Waveforms Recorded	RSM Rotation Angle	Number of Waveforms Recorded	RSM Rotation Angle	Number of Waveforms Recorded	RSM Rotation Angle	Number of Waveforms Recorded	RSM Rotation Angle	Number of Waveforms Recorded	RSM Rotation Angle	Number of Waveforms Recorded	RSM Rotation Angle	Number of Waveforms Recorded	Total Number of Waveforms in FEP
1	9862	46	9534	91	9272	136	9919	181	9701	226	9027	271	8809	316	9611	3387637
2	9627	47	9569	92	9105	137	9797	182	9583	227	9469	272	9053	317	9502	
3	9508	48	9386	93	9124	138	9855	183	9513	228	9261	273	9030	318	8860	
4	9410	49	9322	94	9110	139	9773	184	9496	229	9281	274	8922	319	10090	
5	9479	50	9340	95	9256	140	9833	185	9668	230	9143	275	9197	320	9656	
6	9548	51	9386	96	9232	141	9898	186	9731	231	8881	276	9063	321	9442	
7	9487	52	9407	97	9778	142	9852	187	9620	232	9702	277	9090	322	9585	
8	9401	53	9161	98	9167	143	9760	188	9489	233	9212	278	9076	323	9091	
9	9281	54	9206	99	9225	144	9892	189	9572	234	9366	279	9108	324	9801	
10	9604	55	9243	100	9299	145	9723	190	9610	235	9429	280	9113	325	9672	
11	9672	56	9392	101	9364	146	9725	191	9604	236	8885	281	9018	326	9774	
12	9924	57	9281	102	9242	147	9797	192	9562	237	9653	282	8917	327	9853	
13	10250	58	9042	103	9217	148	9673	193	9406	238	9139	283	8854	328	9535	
14	10060	59	9011	104	9169	149	9699	194	9472	239	9191	284	9079	329	9390	
15	10060	60	9245	105	9199	150	9780	195	9379	240	9438	285	9133	330	9594	
16	9990	61	9218	106	9094	151	9697	196	9456	241	8975	286	9191	331	9564	
17	9814	62	9180	107	9473	152	9652	197	9462	242	9724	287	9009	332	9410	
18	9631	63	8804	108	9508	153	9675	198	9317	243	9403	288	8953	333	9439	
19	9460	64	8967	109	9369	154	9622	199	9430	244	9278	289	8827	334	9278	
20	9683	65	9162	110	9256	155	9751	200	9466	245	9292	290	9166	335	9375	
21	9778	66	9162	111	9135	156	9664	201	9409	246	9353	291	8996	336	9628	
22	9788	67	9234	112	9317	157	9609	202	9396	247	9226	292	8960	337	9637	
23	9658	68	9050	113	9338	158	9519	203	9345	248	9101	293	8881	338	9442	
24	9382	69	8939	114	9249	159	9624	204	9438	249	9241	294	8780	339	9069	
25	9670	70	9126	115	9234	160	9560	205	9416	250	9158	295	9033	340	9396	
26	9701	71	9100	116	9315	161	9635	206	9126	251	9165	296	9100	341	9642	
27	9603	72	9194	117	9398	162	9506	207	9429	252	9187	297	9112	342	9529	
28	9702	73	9226	118	9391	163	9559	208	9398	253	9166	298	9031	343	9392	
29	9538	74	8809	119	9447	164	9666	209	9312	254	9483	299	8929	344	9317	
30	9844	75	9160	120	9303	165	9611	210	9226	255	9337	300	9082	345	9872	
31	9869	76	9270	121	9483	166	9676	211	9204	256	9422	301	9037	346	9808	
32	9905	77	9162	122	9485	167	9694	212	9388	257	9379	302	9060	347	9819	
33	9758	78	9045	123	9420	168	9474	213	9250	258	9018	303	9218	348	9736	
34	9639	79	9089	124	9395	169	9515	214	9185	259	9247	304	9101	349	9694	
35	9855	80	9293	125	9671	170	9572	215	9483	260	9177	305	9359	350	9893	
36	9878	81	9497	126	9524	171	9575	216	9278	261	9089	306	9184	351	9903	
37	9763	82	9385	127	9500	172	9738	217	9260	262	9256	307	9285	352	9847	
38	9761	83	9102	128	9562	173	9448	218	9227	263	9119	308	8416	353	9659	
39	9697	84	8971	129	9452	174	9565	219	9353	264	9000	309	9500	354	9383	
40	9829	85	9354	130	9576	175	9641	220	9388	265	9208	310	9490	355	9759	
41	9672	86	9456	131	9622	176	9806	221	9456	266	9074	311	9647	356	9758	
42	9683	87	9280	132	9800	177	9590	222	9392	267	8830	312	9570	357	9609	
43	9611	88	9079	133	9666	178	9485	223	9315	268	9088	313	8785	358	9391	
44	9430	89	9163	134	9713	179	9606	224	9565	269	8994	314	10040	359	9411	
45	9653	90	9205	135	9715	180	9429	225	9416	270	8979	315	9565	360	9579	

View Angle φ = 145° : Spectrum, Modulation Curve Data (No Smoothing), Library Curve, MAC and Least Squares Direction Predictions

Phi_ViewDegree = 145 Theta_ViewDegree = 0

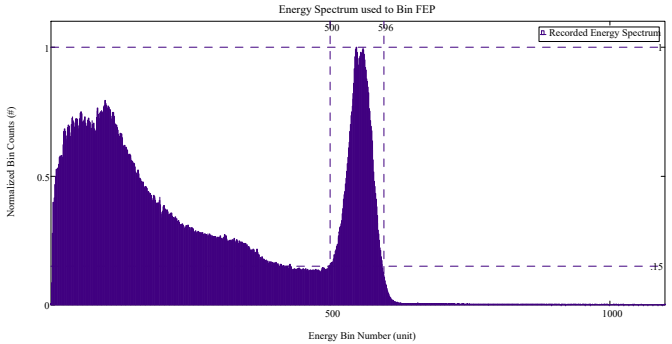

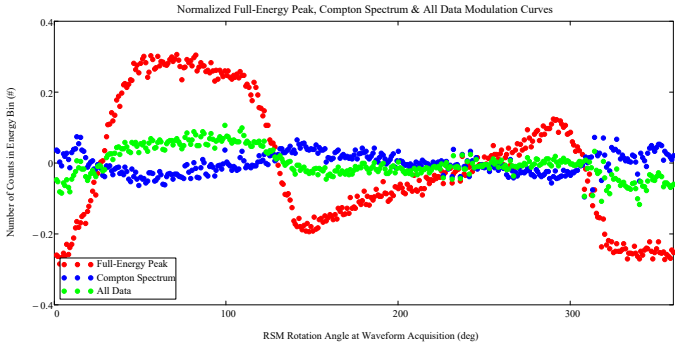

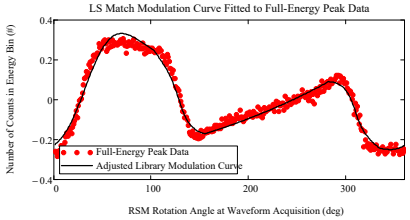

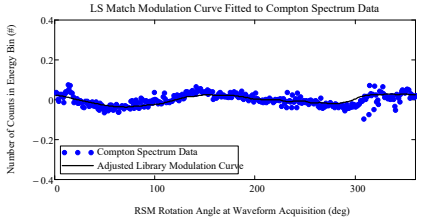

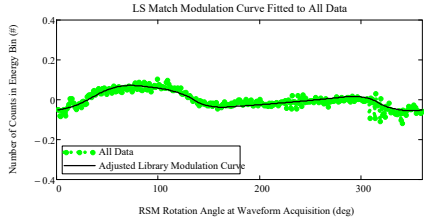

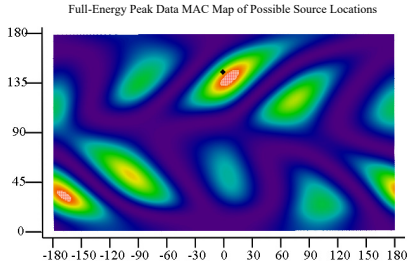

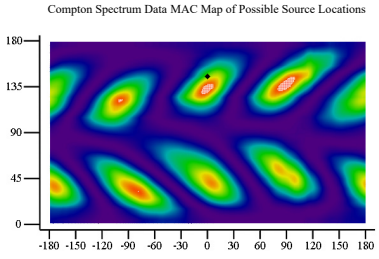

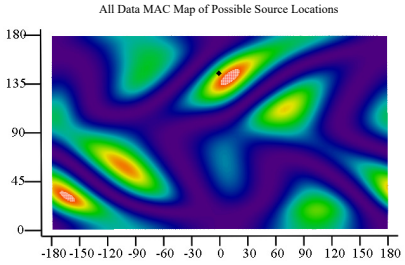

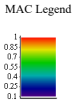

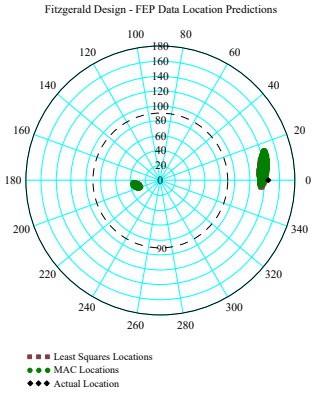

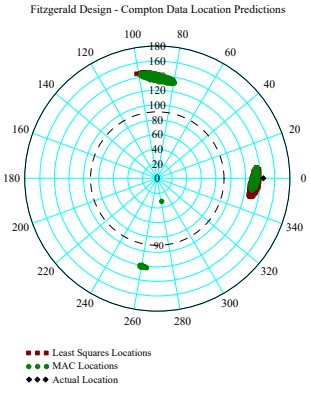

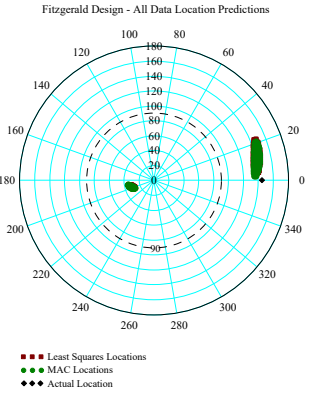

FEP Counting of Waveforms, Binned by RSM Rotation Angle; Used to Generate the Modulation Curve (ϕ = 145°)

RSM Rotation Angle	Number of Waveforms Recorded	RSM Rotation Angle	Number of Waveforms Recorded	RSM Rotation Angle	Number of Waveforms Recorded	RSM Rotation Angle	Number of Waveforms Recorded	RSM Rotation Angle	Number of Waveforms Recorded	RSM Rotation Angle	Number of Waveforms Recorded	RSM Rotation Angle	Number of Waveforms Recorded	RSM Rotation Angle	Number of Waveforms Recorded	Total Number of Waveforms in FEP
1	1690	46	3793	91	3800	136	2359	181	2243	226	2474	271	2899	316	2107	969963
2	1672	47	3719	92	3709	137	2295	182	2331	227	2589	272	2843	317	2101	
3	1591	48	3767	93	3594	138	2207	183	2233	228	2667	273	2948	318	1777	
4	1658	49	3689	94	3717	139	2063	184	2322	229	2652	274	2858	319	2083	
5	1706	50	3792	95	3617	140	2025	185	2292	230	2641	275	3063	320	1917	
6	1677	51	3837	96	3715	141	2000	186	2326	231	2477	276	2974	321	1802	
7	1806	52	3869	97	3682	142	2091	187	2408	232	2579	277	2873	322	1845	
8	1696	53	3794	98	3645	143	1999	188	2345	233	2601	278	2934	323	1761	
9	1775	54	3640	99	3705	144	1963	189	2332	234	2627	279	3011	324	1836	
10	1808	55	3696	100	3657	145	2012	190	2332	235	2635	280	3043	325	1715	
11	1873	56	3872	101	3704	146	1951	191	2496	236	2498	281	3053	326	1728	
12	1985	57	3829	102	3640	147	2034	192	2365	237	2769	282	2941	327	1813	
13	2058	58	3730	103	3620	148	1944	193	2361	238	2576	283	3005	328	1732	
14	1994	59	3744	104	3659	149	2002	194	2278	239	2563	284	3104	329	1727	
15	2042	60	3865	105	3641	150	1949	195	2297	240	2701	285	3015	330	1753	
16	2114	61	3761	106	3674	151	2106	196	2370	241	2656	286	3077	331	1815	
17	2135	62	3812	107	3628	152	1976	197	2341	242	2697	287	3078	332	1760	
18	2037	63	3802	108	3701	153	1989	198	2440	243	2606	288	3073	333	1650	
19	2164	64	3778	109	3661	154	2075	199	2431	244	2649	289	3121	334	1706	
20	2220	65	3769	110	3658	155	2093	200	2414	245	2651	290	3180	335	1710	
21	2286	66	3792	111	3544	156	2052	201	2464	246	2760	291	3164	336	1704	
22	2386	67	3833	112	3560	157	2121	202	2427	247	2681	292	3173	337	1785	
23	2484	68	3861	113	3530	158	2061	203	2377	248	2658	293	3032	338	1712	
24	2347	69	3808	114	3444	159	2095	204	2363	249	2681	294	3159	339	1677	
25	2582	70	3841	115	3383	160	2132	205	2468	250	2765	295	3126	340	1648	
26	2686	71	3885	116	3580	161	2118	206	2414	251	2686	296	3089	341	1729	
27	2708	72	3826	117	3530	162	2075	207	2428	252	2750	297	3114	342	1687	
28	2722	73	3758	118	3441	163	2134	208	2386	253	2751	298	3015	343	1746	
29	2834	74	3610	119	3305	164	2084	209	2562	254	2781	299	3023	344	1762	
30	2989	75	3743	120	3296	165	2199	210	2403	255	2886	300	3032	345	1756	
31	3117	76	3751	121	3216	166	2166	211	2389	256	2794	301	2933	346	1834	
32	3124	77	3830	122	3271	167	2207	212	2505	257	2794	302	2893	347	1729	
33	3250	78	3794	123	3112	168	2134	213	2416	258	2741	303	2826	348	1649	
34	3158	79	3816	124	3114	169	2142	214	2346	259	2798	304	2872	349	1714	
35	3220	80	3760	125	2950	170	2202	215	2419	260	2842	305	2836	350	1758	
36	3391	81	3851	126	2914	171	2145	216	2542	261	2682	306	2711	351	1834	
37	3429	82	3884	127	2918	172	2319	217	2519	262	2757	307	2790	352	1715	
38	3318	83	3708	128	2876	173	2204	218	2472	263	2790	308	2407	353	1706	
39	3462	84	3750	129	2775	174	2215	219	2514	264	2858	309	2634	354	1723	
40	3556	85	3794	130	2671	175	2199	220	2506	265	2674	310	2503	355	1638	
41	3566	86	3766	131	2583	176	2334	221	2564	266	2810	311	2575	356	1693	
42	3529	87	3766	132	2478	177	2268	222	2531	267	2625	312	2348	357	1673	
43	3559	88	3699	133	2462	178	2242	223	2550	268	2840	313	2231	358	1655	
44	3608	89	3711	134	2352	179	2285	224	2540	269	2912	314	2402	359	1746	
45	3603	90	3689	135	2344	180	2390	225	2613	270	2785	315	2143	360	1713	

Compton Counting of Waveforms, Binned by RSM Rotation Angle; Used to Generate the Modulation Curve (ϕ = 145°)

RSM Rotation Angle	Number of Waveforms Recorded	RSM Rotation Angle	Number of Waveforms Recorded	RSM Rotation Angle	Number of Waveforms Recorded	RSM Rotation Angle	Number of Waveforms Recorded	RSM Rotation Angle	Number of Waveforms Recorded	RSM Rotation Angle	Number of Waveforms Recorded	RSM Rotation Angle	Number of Waveforms Recorded	RSM Rotation Angle	Number of Waveforms Recorded	Total Number of Waveforms in FEP
1	9774	46	9011	91	9351	136	9792	181	9738	226	9048	271	9106	316	9598	3378503
2	9722	47	9128	92	9278	137	9881	182	9571	227	9414	272	9139	317	9680	
3	9425	48	8930	93	9019	138	9690	183	9519	228	9447	273	9109	318	8887	
4	9316	49	8753	94	9185	139	9758	184	9579	229	9227	274	9158	319	10100	
5	9660	50	8984	95	9308	140	9675	185	9672	230	9322	275	9240	320	9628	
6	9576	51	8926	96	9336	141	10050	186	9823	231	9013	276	9174	321	9273	
7	9666	52	8952	97	9227	142	9927	187	9467	232	9775	277	9052	322	9372	
8	9500	53	8824	98	9371	143	9824	188	9429	233	9329	278	9061	323	9174	
9	9258	54	8886	99	9773	144	9939	189	9550	234	9342	279	9013	324	9840	
10	9696	55	9115	100	9412	145	9970	190	9677	235	9282	280	9197	325	9768	
11	9791	56	9114	101	9370	146	9847	191	9616	236	9003	281	9155	326	9787	
12	9804	57	9092	102	9308	147	9779	192	9517	237	9641	282	9055	327	10080	
13	10150	58	8881	103	9189	148	9760	193	9363	238	9286	283	9013	328	9717	
14	9947	59	8896	104	9291	149	9794	194	9422	239	9300	284	9048	329	9510	
15	10130	60	8962	105	9254	150	9784	195	9494	240	9457	285	9081	330	9620	
16	9773	61	9158	106	9177	151	9784	196	9591	241	9004	286	9141	331	9553	
17	9727	62	9051	107	9227	152	9914	197	9650	242	9732	287	9142	332	9457	
18	9551	63	8781	108	9556	153	9670	198	9276	243	9464	288	8958	333	9505	
19	9270	64	8766	109	9725	154	9835	199	9461	244	9252	289	8830	334	9443	
20	9346	65	8998	110	9457	155	9761	200	9732	245	9552	290	9011	335	9418	
21	9424	66	9078	111	9264	156	9758	201	9460	246	9225	291	9174	336	9624	
22	9451	67	9092	112	9336	157	9804	202	9442	247	9291	292	8952	337	9578	
23	9228	68	9062	113	9291	158	9420	203	9390	248	9347	293	8961	338	9429	
24	9224	69	8937	114	9257	159	9540	204	9329	249	9272	294	9001	339	9076	
25	9357	70	9080	115	9328	160	9535	205	9343	250	9258	295	9020	340	8882	
26	9320	71	9072	116	9317	161	9492	206	9294	251	9344	296	9187	341	9671	
27	9246	72	9027	117	9305	162	9531	207	9371	252	9253	297	9019	342	9540	
28	9043	73	9012	118	9412	163	9690	208	9253	253	9144	298	9154	343	9466	
29	9000	74	8982	119	9596	164	9732	209	9318	254	9341	299	9118	344	9297	
30	9309	75	8941	120	9439	165	9767	210	9424	255	9369	300	9038	345	9682	
31	9271	76	9307	121	9483	166	9537	211	9262	256	9254	301	9130	346	9826	
32	9308	77	9355	122	9639	167	9604	212	9389	257	9327	302	9107	347	9887	
33	9176	78	9137	123	9393	168	9643	213	9310	258	9178	303	9175	348	9823	
34	9063	79	8957	124	9341	169	9551	214	9484	259	9326	304	9187	349	9724	
35	9215	80	9186	125	9597	170	9589	215	9415	260	9355	305	9346	350	9834	
36	9263	81	9394	126	9618	171	9530	216	9388	261	9248	306	9319	351	9932	
37	9278	82	9246	127	9672	172	9558	217	9362	262	9258	307	9337	352	9932	
38	9091	83	8993	128	9450	173	9503	218	9243	263	9050	308	8423	353	9889	
39	9122	84	8962	129	9491	174	9621	219	9312	264	8992	309	9562	354	9481	
40	9056	85	9258	130	9630	175	9771	220	9422	265	9494	310	9405	355	9722	
41	9273	86	9497	131	9804	176	9520	221	9378	266	9159	311	9550	356	9658	
42	9152	87	9404	132	9793	177	9651	222	9385	267	8967	312	9566	357	9619	
43	8927	88	9073	133	9690	178	9680	223	9413	268	9134	313	8630	358	9547	
44	8855	89	9029	134	9692	179	9818	224	9345	269	9023	314	10140	359	9500	
45	9227	90	9299	135	9744	180	9700	225	9452	270	9233	315	9692	360	9611	

View Angle φ = 155° : Spectrum, Modulation Curve Data (No Smoothing), Library Curve, MAC and Least Squares Direction Predictions

Phi_ViewDegree = 155 Theta_ViewDegree = 0

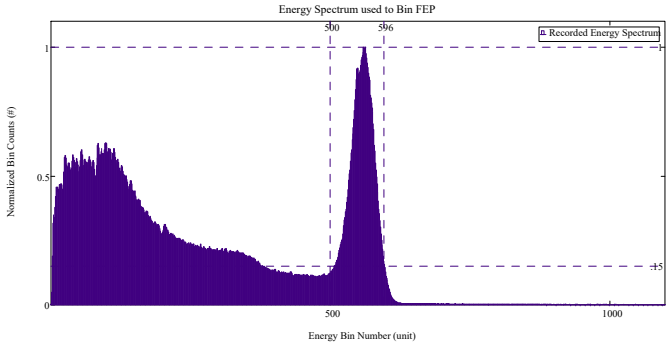

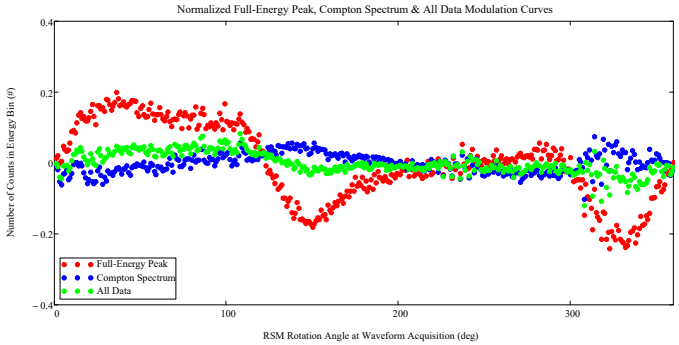

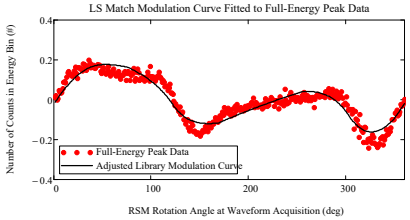

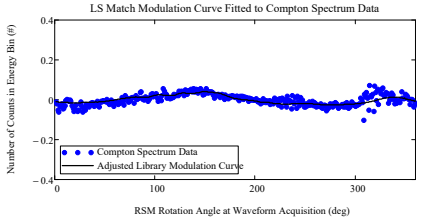

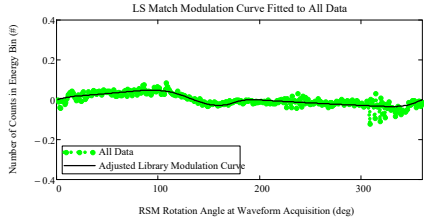

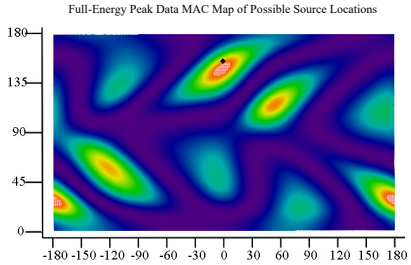

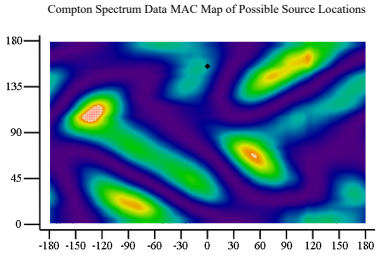

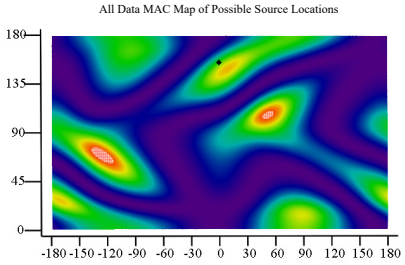

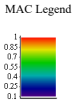

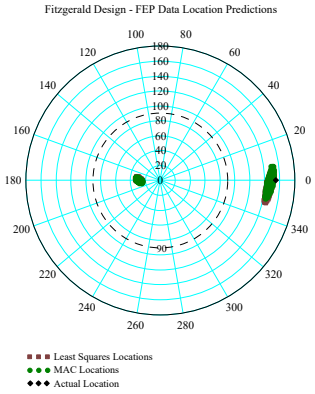

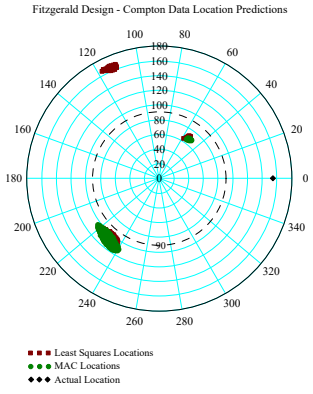

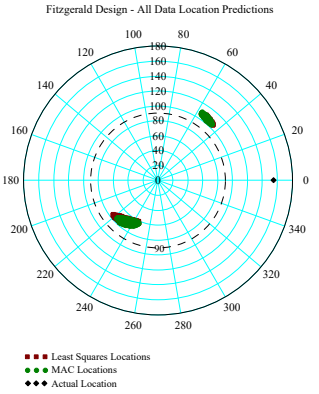

FEP Counting of Waveforms, Binned by RSM Rotation Angle; Used to Generate the Modulation Curve (ϕ = 155°)

RSM Rotation Angle	Number of Waveforms Recorded	RSM Rotation Angle	Number of Waveforms Recorded	RSM Rotation Angle	Number of Waveforms Recorded	RSM Rotation Angle	Number of Waveforms Recorded	RSM Rotation Angle	Number of Waveforms Recorded	RSM Rotation Angle	Number of Waveforms Recorded	RSM Rotation Angle	Number of Waveforms Recorded	RSM Rotation Angle	Number of Waveforms Recorded	Total Number of Waveforms in FEP
1	3397	46	4074	91	3814	136	2889	181	3130	226	3204	271	3455	316	2705	1201910
2	3426	47	4066	92	3786	137	2926	182	3005	227	3320	272	3410	317	2667	
3	3335	48	3938	93	3740	138	2755	183	3052	228	3304	273	3408	318	2445	
4	3360	49	3893	94	3817	139	2686	184	3147	229	3331	274	3424	319	2766	
5	3542	50	3987	95	3781	140	2752	185	3034	230	3284	275	3429	320	2749	
6	3505	51	4015	96	3928	141	2873	186	3205	231	3156	276	3415	321	2445	
7	3480	52	3912	97	3852	142	2811	187	3110	232	3401	277	3437	322	2522	
8	3494	53	3886	98	3731	143	2672	188	3242	233	3264	278	3391	323	2332	
9	3581	54	3889	99	4040	144	2685	189	3172	234	3303	279	3506	324	2536	
10	3709	55	3969	100	3828	145	2662	190	3160	235	3305	280	3506	325	2474	
11	3726	56	4046	101	3826	146	2627	191	3127	236	3219	281	3492	326	2438	
12	3697	57	3919	102	3788	147	2650	192	3183	237	3562	282	3578	327	2605	
13	3819	58	3845	103	3814	148	2651	193	3141	238	3333	283	3390	328	2551	
14	3905	59	3916	104	3735	149	2620	194	3122	239	3256	284	3485	329	2443	
15	3934	60	3913	105	3812	150	2584	195	3113	240	3270	285	3497	330	2414	
16	3871	61	3993	106	3800	151	2623	196	3206	241	3286	286	3565	331	2399	
17	3887	62	3913	107	3858	152	2662	197	3195	242	3425	287	3439	332	2347	
18	3841	63	3863	108	3917	153	2700	198	3166	243	3503	288	3380	333	2371	
19	3838	64	3838	109	3820	154	2677	199	3216	244	3346	289	3428	334	2426	
20	3874	65	3894	110	3791	155	2787	200	3213	245	3369	290	3519	335	2528	
21	3950	66	3940	111	3706	156	2722	201	3205	246	3420	291	3488	336	2544	
22	4031	67	3830	112	3751	157	2734	202	3259	247	3364	292	3368	337	2575	
23	3893	68	3771	113	3711	158	2676	203	3280	248	3312	293	3386	338	2401	
24	3796	69	3853	114	3619	159	2845	204	3254	249	3372	294	3437	339	2498	
25	4014	70	3862	115	3628	160	2789	205	3377	250	3387	295	3513	340	2573	
26	4019	71	3852	116	3620	161	2757	206	3184	251	3348	296	3374	341	2711	
27	3983	72	3911	117	3534	162	2819	207	3289	252	3364	297	3239	342	2604	
28	3994	73	3941	118	3593	163	2878	208	3262	253	3304	298	3252	343	2622	
29	3949	74	3749	119	3674	164	2841	209	3189	254	3341	299	3269	344	2719	
30	4091	75	3899	120	3487	165	2893	210	3220	255	3429	300	3403	345	2678	
31	4083	76	3932	121	3484	166	2968	211	3219	256	3368	301	3234	346	2751	
32	4036	77	3895	122	3461	167	2919	212	3229	257	3496	302	3125	347	2926	
33	3967	78	3753	123	3310	168	2870	213	3193	258	3337	303	3136	348	2929	
34	4010	79	3862	124	3225	169	2952	214	3159	259	3388	304	3145	349	2933	
35	4057	80	3904	125	3259	170	3008	215	3258	260	3428	305	3146	350	3064	
36	4177	81	3902	126	3212	171	2941	216	3187	261	3328	306	3045	351	3071	
37	4102	82	3999	127	3164	172	3014	217	3360	262	3379	307	3146	352	3121	
38	4021	83	3740	128	3097	173	3085	218	3325	263	3389	308	2725	353	3002	
39	4029	84	3788	129	3190	174	3014	219	3206	264	3329	309	3094	354	3035	
40	4062	85	3928	130	3032	175	3175	220	3230	265	3386	310	2942	355	3086	
41	4018	86	3984	131	3056	176	3068	221	3323	266	3392	311	2917	356	3242	
42	4005	87	3913	132	3085	177	3105	222	3330	267	3183	312	2809	357	3207	
43	4030	88	3751	133	2925	178	3078	223	3391	268	3352	313	2556	358	3233	
44	4050	89	3785	134	2927	179	3172	224	3346	269	3415	314	3033	359	3274	
45	4075	90	3774	135	2835	180	3043	225	3333	270	3441	315	2754	360	3347	

Compton Counting of Waveforms, Binned by RSM Rotation Angle; Used to Generate the Modulation Curve (ϕ = 155°)

RSM Rotation Angle	Number of Waveforms Recorded	RSM Rotation Angle	Number of Waveforms Recorded	RSM Rotation Angle	Number of Waveforms Recorded	RSM Rotation Angle	Number of Waveforms Recorded	RSM Rotation Angle	Number of Waveforms Recorded	RSM Rotation Angle	Number of Waveforms Recorded	RSM Rotation Angle	Number of Waveforms Recorded	RSM Rotation Angle	Number of Waveforms Recorded	Total Number of Waveforms in FEP
1	9556	46	9576	91	9750	136	10210	181	9837	226	9263	271	9079	316	9801	3471012
2	9447	47	9546	92	9754	137	10060	182	9826	227	9727	272	9181	317	9925	
3	9096	48	9621	93	9566	138	10230	183	9683	228	9642	273	9237	318	9035	
4	9013	49	9590	94	9677	139	10090	184	9598	229	9633	274	9263	319	10350	
5	9317	50	9584	95	9766	140	10080	185	9833	230	9471	275	9437	320	10040	
6	9347	51	9542	96	9930	141	10200	186	9781	231	9278	276	9414	321	9594	
7	9430	52	9688	97	9973	142	10160	187	9832	232	9852	277	9291	322	10200	
8	9163	53	9518	98	9807	143	9989	188	9665	233	9624	278	9438	323	9416	
9	9219	54	9424	99	9870	144	10170	189	9808	234	9625	279	9369	324	10150	
10	9349	55	9506	100	9927	145	10220	190	9775	235	9556	280	9502	325	9960	
11	9612	56	9643	101	9967	146	10070	191	9788	236	9169	281	9442	326	10190	
12	9661	57	9586	102	9749	147	10100	192	9727	237	9875	282	9293	327	10270	
13	9655	58	9398	103	9562	148	9894	193	9567	238	9557	283	9222	328	9921	
14	9562	59	9313	104	9666	149	9940	194	9751	239	9457	284	9326	329	9855	
15	9634	60	9547	105	9729	150	10080	195	9633	240	9764	285	9314	330	10030	
16	9575	61	9505	106	9596	151	10240	196	9720	241	9205	286	9368	331	9958	
17	9355	62	9533	107	9857	152	10100	197	9631	242	9839	287	9418	332	9958	
18	9211	63	9415	108	10240	153	9990	198	9648	243	9584	288	9268	333	9463	
19	9037	64	9464	109	10100	154	10070	199	9632	244	9356	289	9443	334	9657	
20	9153	65	9482	110	9975	155	10050	200	9640	245	9763	290	9282	335	9785	
21	9381	66	9622	111	9934	156	10060	201	9705	246	9535	291	9504	336	10010	
22	9100	67	9788	112	9742	157	10040	202	9579	247	9655	292	9276	337	9893	
23	9039	68	9587	113	9765	158	9922	203	9544	248	9440	293	9198	338	9677	
24	9105	69	9386	114	9780	159	9757	204	9625	249	9290	294	9267	339	9459	
25	9418	70	9877	115	9718	160	9928	205	9457	250	9278	295	9400	340	9682	
26	9536	71	9778	116	9755	161	9860	206	9535	251	9442	296	9528	341	9487	
27	9286	72	9728	117	9769	162	9881	207	9525	252	9328	297	9482	342	9564	
28	9026	73	9555	118	9760	163	9924	208	9710	253	9372	298	9372	343	9531	
29	9228	74	9553	119	9929	164	9837	209	9569	254	9552	299	9405	344	9504	
30	9126	75	9610	120	9860	165	9785	210	9497	255	9388	300	9312	345	9662	
31	9418	76	9734	121	9857	166	9914	211	9599	256	9461	301	9378	346	10060	
32	9338	77	9763	122	9954	167	9945	212	9555	257	9586	302	9386	347	9735	
33	9361	78	9776	123	9873	168	9862	213	9531	258	9352	303	9412	348	9705	
34	9287	79	9487	124	10100	169	9675	214	9611	259	9519	304	9434	349	9742	
35	9393	80	9729	125	9989	170	9919	215	9422	260	9433	305	9752	350	9928	
36	9490	81	9880	126	10120	171	9830	216	9590	261	9263	306	9688	351	9875	
37	9519	82	9671	127	10020	172	9797	217	9588	262	9361	307	9516	352	9795	
38	9456	83	9727	128	10000	173	9723	218	9452	263	9320	308	8583	353	9671	
39	9323	84	9742	129	9881	174	9850	219	9745	264	9347	309	9925	354	9414	
40	9482	85	10040	130	10160	175	9789	220	9682	265	9458	310	9803	355	9661	
41	9480	86	10060	131	10140	176	9831	221	9686	266	9257	311	10030	356	9662	
42	9575	87	9742	132	9937	177	9886	222	9577	267	9226	312	9733	357	9648	
43	9356	88	9669	133	10120	178	9820	223	9383	268	9358	313	9103	358	9280	
44	9290	89	9635	134	10130	179	9837	224	9700	269	9379	314	10420	359	9377	
45	9505	90	9809	135	10100	180	9764	225	9607	270	9353	315	9861	360	9463	

View Angle φ = 165° : Spectrum, Modulation Curve Data (No Smoothing), Library Curve, MAC and Least Squares Direction Predictions

Phi_ViewDegree = 165 Theta_ViewDegree = 0

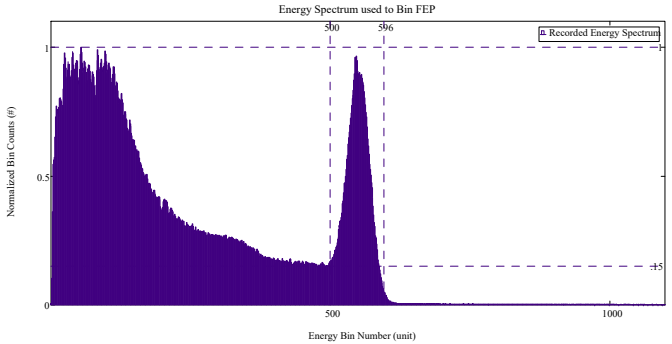

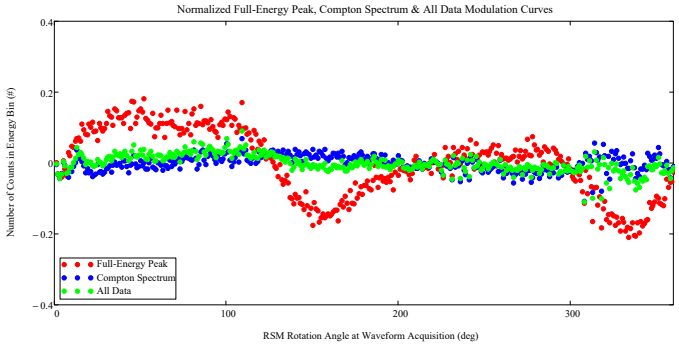

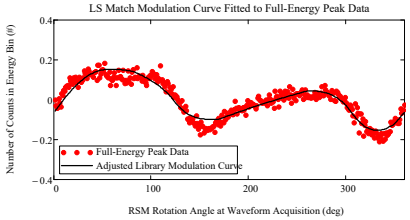

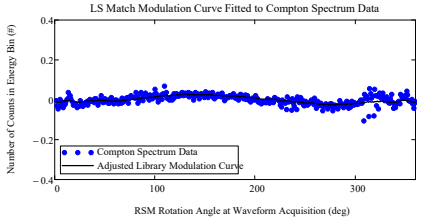

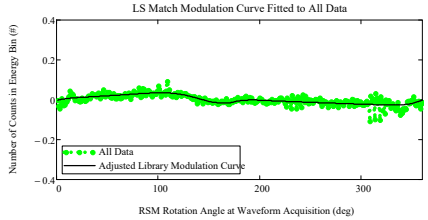

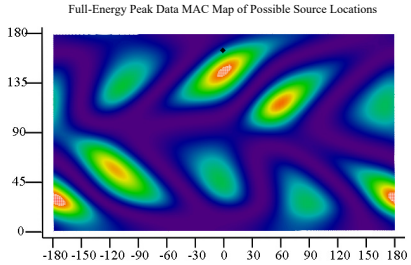

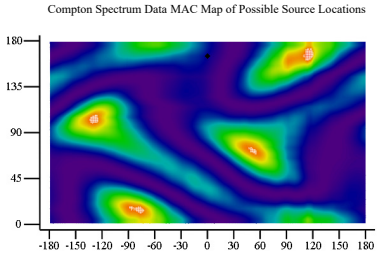

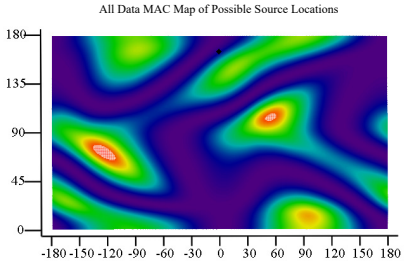

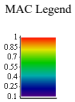

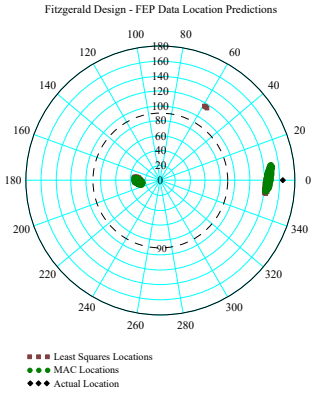

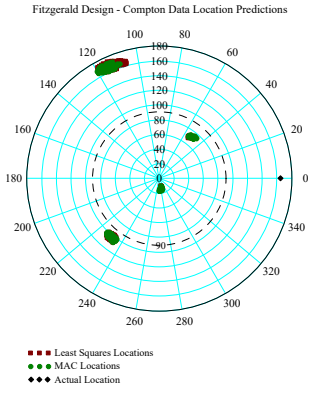

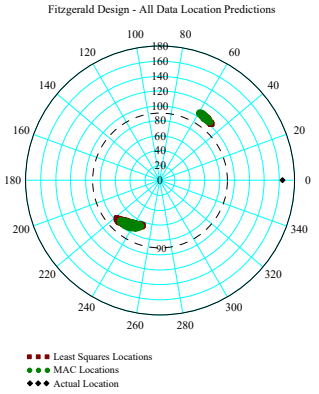

FEP Counting of Waveforms, Binned by RSM Rotation Angle; Used to Generate the Modulation Curve (ϕ = 165°)

RSM Rotation Angle	Number of Waveforms Recorded	RSM Rotation Angle	Number of Waveforms Recorded	RSM Rotation Angle	Number of Waveforms Recorded	RSM Rotation Angle	Number of Waveforms Recorded	RSM Rotation Angle	Number of Waveforms Recorded	RSM Rotation Angle	Number of Waveforms Recorded	RSM Rotation Angle	Number of Waveforms Recorded	RSM Rotation Angle	Number of Waveforms Recorded	Total Number of Waveforms in FEP
1	2135	46	2584	91	2456	136	1989	181	1970	226	2026	271	2224	316	1826	767674
2	2055	47	2426	92	2402	137	1882	182	2002	227	2248	272	2164	317	1887	
3	2025	48	2474	93	2369	138	1873	183	1946	228	2162	273	2184	318	1659	
4	2031	49	2519	94	2360	139	1835	184	1938	229	2184	274	2222	319	1799	
5	2151	50	2533	95	2322	140	1903	185	2008	230	2139	275	2310	320	1854	
6	2089	51	2509	96	2416	141	1875	186	2120	231	2040	276	2194	321	1720	
7	2038	52	2609	97	2433	142	1881	187	2028	232	2251	277	2187	322	1754	
8	2213	53	2461	98	2413	143	1837	188	1954	233	2201	278	2326	323	1695	
9	2190	54	2448	99	2457	144	1828	189	2025	234	2159	279	2269	324	1759	
10	2259	55	2432	100	2453	145	1793	190	2036	235	2219	280	2232	325	1744	
11	2251	56	2423	101	2509	146	1923	191	2003	236	2129	281	2233	326	1675	
12	2297	57	2500	102	2478	147	1822	192	2020	237	2249	282	2193	327	1736	
13	2316	58	2326	103	2411	148	1753	193	1992	238	2195	283	2211	328	1693	
14	2319	59	2394	104	2466	149	1802	194	2029	239	2169	284	2141	329	1636	
15	2294	60	2392	105	2460	150	1674	195	1997	240	2240	285	2255	330	1726	
16	2423	61	2428	106	2361	151	1843	196	2044	241	2158	286	2235	331	1698	
17	2378	62	2487	107	2413	152	1795	197	1937	242	2307	287	2221	332	1632	
18	2349	63	2425	108	2390	153	1785	198	2066	243	2199	288	2126	333	1662	
19	2340	64	2323	109	2579	154	1699	199	2128	244	2092	289	2119	334	1586	
20	2419	65	2425	110	2388	155	1731	200	2045	245	2275	290	2245	335	1651	
21	2399	66	2522	111	2394	156	1759	201	2090	246	2160	291	2228	336	1695	
22	2434	67	2432	112	2345	157	1731	202	2100	247	2195	292	2208	337	1603	
23	2364	68	2438	113	2356	158	1748	203	2083	248	2124	293	2162	338	1595	
24	2369	69	2414	114	2304	159	1761	204	2076	249	2217	294	2184	339	1694	
25	2299	70	2401	115	2243	160	1744	205	2073	250	2212	295	2147	340	1618	
26	2427	71	2524	116	2375	161	1756	206	2050	251	2216	296	2127	341	1704	
27	2392	72	2388	117	2347	162	1772	207	2013	252	2193	297	2107	342	1672	
28	2368	73	2344	118	2234	163	1786	208	2057	253	2220	298	2123	343	1689	
29	2387	74	2388	119	2294	164	1788	209	2158	254	2243	299	2165	344	1714	
30	2424	75	2357	120	2270	165	1709	210	2183	255	2266	300	2092	345	1719	
31	2516	76	2514	121	2213	166	1831	211	2136	256	2140	301	2034	346	1844	
32	2483	77	2378	122	2303	167	1858	212	2125	257	2207	302	2016	347	1802	
33	2474	78	2424	123	2167	168	1809	213	2119	258	2261	303	2001	348	1818	
34	2413	79	2343	124	2202	169	1889	214	2092	259	2167	304	2063	349	1847	
35	2535	80	2494	125	2188	170	1839	215	2100	260	2199	305	2050	350	1890	
36	2517	81	2531	126	2170	171	1793	216	2103	261	2163	306	2005	351	1878	
37	2466	82	2413	127	2140	172	1933	217	2095	262	2168	307	1925	352	1841	
38	2470	83	2429	128	2108	173	1841	218	2133	263	2171	308	1837	353	1830	
39	2466	84	2425	129	2096	174	1833	219	2057	264	2156	309	2081	354	1822	
40	2428	85	2553	130	2034	175	1986	220	2139	265	2166	310	1910	355	1873	
41	2485	86	2418	131	2122	176	1874	221	2198	266	2177	311	2032	356	2018	
42	2499	87	2443	132	2013	177	1909	222	2141	267	2185	312	1962	357	1955	
43	2507	88	2444	133	1978	178	1958	223	2092	268	2231	313	1702	358	1992	
44	2387	89	2431	134	2005	179	1906	224	2124	269	2142	314	1951	359	1998	
45	2589	90	2383	135	2046	180	1970	225	2109	270	2182	315	1954	360	2069	

Compton Counting of Waveforms, Binned by RSM Rotation Angle; Used to Generate the Modulation Curve (ϕ = 165°)

RSM Rotation Angle	Number of Waveforms Recorded	RSM Rotation Angle	Number of Waveforms Recorded	RSM Rotation Angle	Number of Waveforms Recorded	RSM Rotation Angle	Number of Waveforms Recorded	RSM Rotation Angle	Number of Waveforms Recorded	RSM Rotation Angle	Number of Waveforms Recorded	RSM Rotation Angle	Number of Waveforms Recorded	RSM Rotation Angle	Number of Waveforms Recorded	Total Number of Waveforms in FEP
1	9748	46	10010	91	10040	136	10130	181	9917	226	9422	271	9475	316	9877	3522007
2	9472	47	9761	92	10000	137	10030	182	9988	227	9777	272	9313	317	9979	
3	9324	48	9653	93	9900	138	9794	183	9792	228	9706	273	9552	318	8959	
4	9489	49	9697	94	9785	139	9953	184	9924	229	9689	274	9456	319	10350	
5	9828	50	9862	95	10040	140	10190	185	10070	230	9630	275	9584	320	10020	
6	9732	51	9705	96	9897	141	10040	186	10070	231	9291	276	9581	321	9478	
7	9480	52	9796	97	9843	142	10120	187	9935	232	9955	277	9215	322	9986	
8	9372	53	9620	98	9911	143	10020	188	9864	233	9669	278	9349	323	9305	
9	9559	54	9618	99	10070	144	9843	189	9896	234	9782	279	9519	324	10150	
10	9539	55	9801	100	10360	145	10070	190	10050	235	9717	280	9492	325	9896	
11	9688	56	9926	101	10110	146	10120	191	9803	236	9236	281	9486	326	10060	
12	9804	57	9677	102	9884	147	10090	192	10020	237	9852	282	9331	327	10170	
13	10180	58	9634	103	9690	148	10040	193	9794	238	9569	283	9465	328	9940	
14	9928	59	9591	104	9819	149	9928	194	9795	239	9444	284	9736	329	9752	
15	10010	60	9799	105	9947	150	10200	195	9697	240	9788	285	9588	330	9788	
16	9842	61	9777	106	10040	151	9973	196	9752	241	9288	286	9592	331	9963	
17	9717	62	9727	107	9813	152	10030	197	9876	242	9943	287	9554	332	9783	
18	9501	63	9581	108	10120	153	9932	198	9844	243	9830	288	9394	333	9637	
19	9631	64	9726	109	10520	154	10140	199	9773	244	9658	289	9593	334	9629	
20	9507	65	9713	110	10060	155	10100	200	10010	245	9904	290	9504	335	9861	
21	9546	66	9630	111	10170	156	10020	201	9877	246	9678	291	9705	336	10070	
22	9396	67	9881	112	9875	157	10190	202	9857	247	9776	292	9675	337	9654	
23	9434	68	9696	113	9845	158	9932	203	9669	248	9532	293	9349	338	9335	
24	9458	69	9826	114	9791	159	9857	204	9649	249	9496	294	9424	339	9488	
25	9746	70	9763	115	9925	160	9963	205	9712	250	9700	295	9424	340	9393	
26	9515	71	9837	116	9944	161	9949	206	9579	251	9638	296	9728	341	9619	
27	9541	72	9907	117	9788	162	10080	207	9668	252	9524	297	9551	342	9609	
28	9456	73	9623	118	9847	163	10070	208	9660	253	9577	298	9517	343	9720	
29	9516	74	9839	119	10120	164	9978	209	9679	254	9633	299	9638	344	9596	
30	9637	75	9935	120	9959	165	10090	210	9635	255	9696	300	9546	345	10080	
31	9637	76	10010	121	10120	166	9955	211	9634	256	9774	301	9551	346	9991	
32	9711	77	9952	122	10100	167	10150	212	9853	257	9700	302	9573	347	9876	
33	9527	78	9927	123	9989	168	9982	213	9679	258	9539	303	9583	348	9890	
34	9725	79	9905	124	10050	169	9748	214	9607	259	9875	304	9696	349	10030	
35	9815	80	9884	125	10030	170	9800	215	9776	260	9568	305	9796	350	9926	
36	9719	81	10170	126	10160	171	9955	216	9745	261	9352	306	9607	351	10250	
37	9738	82	9940	127	10170	172	9938	217	9752	262	9706	307	9790	352	10060	
38	9775	83	9622	128	10020	173	9917	218	9664	263	9485	308	8665	353	9748	
39	9664	84	9752	129	10090	174	10010	219	9920	264	9574	309	10090	354	9713	
40	9856	85	10130	130	10140	175	9976	220	9899	265	9621	310	9888	355	9753	
41	9866	86	10180	131	10050	176	9944	221	9829	266	9477	311	9998	356	9832	
42	9695	87	9884	132	10040	177	10060	222	9828	267	9205	312	9851	357	9591	
43	9501	88	9754	133	10170	178	10120	223	9780	268	9442	313	8918	358	9356	
44	9726	89	9992	134	9962	179	10020	224	9731	269	9525	314	10390	359	9613	
45	9773	90	10160	135	10070	180	9882	225	9529	270	9582	315	10100	360	9693	

View Angle φ = 175° : Spectrum, Modulation Curve Data (No Smoothing), Library Curve, MAC and Least Squares Direction Predictions

Phi_ViewDegree = 175 Theta_ViewDegree = 0

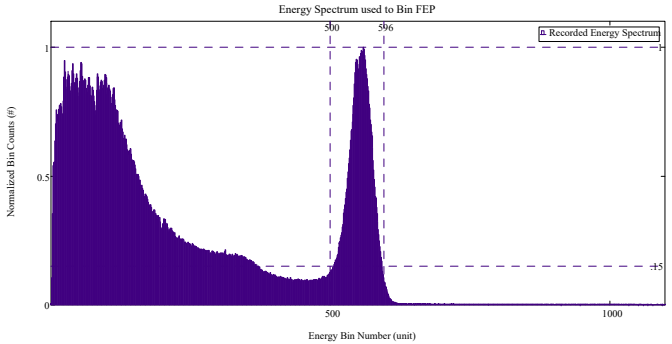

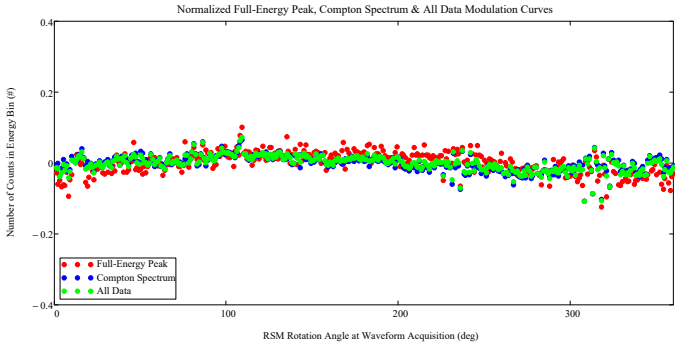

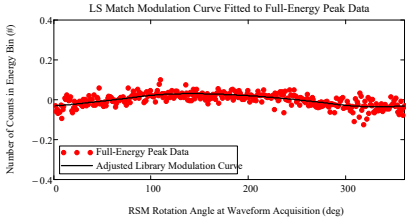

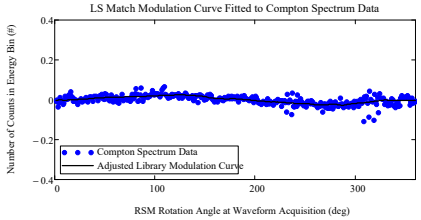

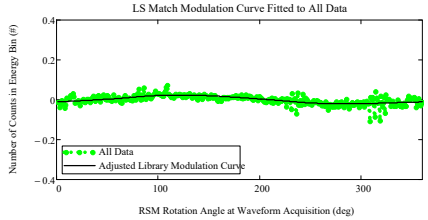

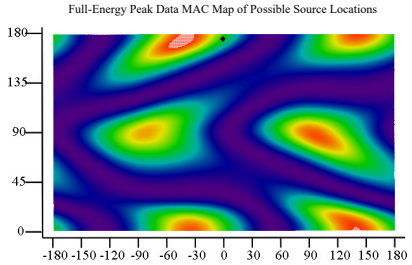

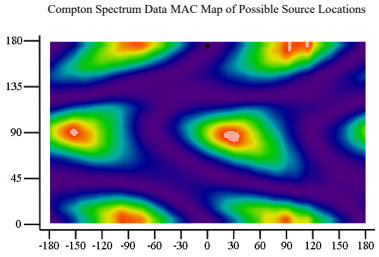

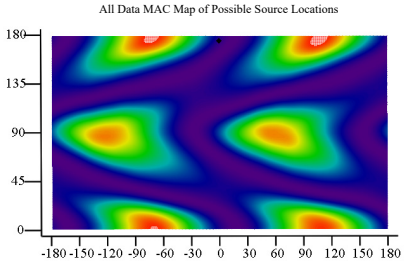

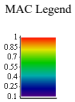

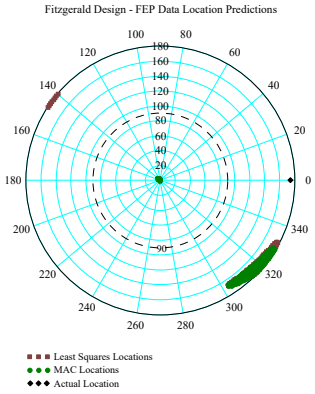

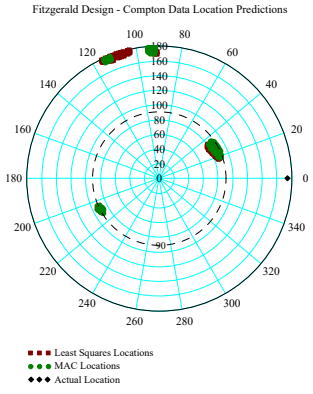

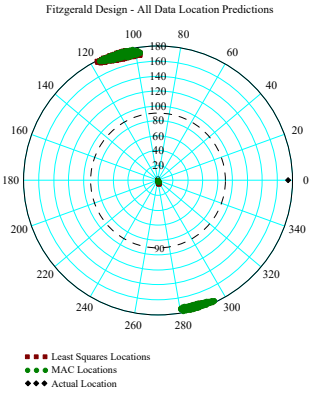

FEP Counting of Waveforms, Binned by RSM Rotation Angle; Used to Generate the Modulation Curve (ϕ = 175°)

RSM Rotation Angle	Number of Waveforms Recorded	RSM Rotation Angle	Number of Waveforms Recorded	RSM Rotation Angle	Number of Waveforms Recorded	RSM Rotation Angle	Number of Waveforms Recorded	RSM Rotation Angle	Number of Waveforms Recorded	RSM Rotation Angle	Number of Waveforms Recorded	RSM Rotation Angle	Number of Waveforms Recorded	RSM Rotation Angle	Number of Waveforms Recorded	Total Number of Waveforms in FEP
1	2435	46	2678	91	2594	136	2605	181	2559	226	2374	271	2400	316	2369	903874
2	2347	47	2460	92	2472	137	2513	182	2652	227	2610	272	2471	317	2418	
3	2376	48	2478	93	2494	138	2582	183	2661	228	2546	273	2416	318	2165	
4	2325	49	2456	94	2501	139	2504	184	2512	229	2604	274	2480	319	2494	
5	2342	50	2465	95	2625	140	2621	185	2545	230	2501	275	2424	320	2425	
6	2338	51	2424	96	2566	141	2500	186	2636	231	2513	276	2430	321	2246	
7	2442	52	2484	97	2591	142	2578	187	2585	232	2628	277	2478	322	2546	
8	2249	53	2435	98	2622	143	2660	188	2587	233	2582	278	2465	323	2321	
9	2380	54	2487	99	2645	144	2529	189	2547	234	2623	279	2488	324	2519	
10	2423	55	2540	100	2569	145	2613	190	2645	235	2586	280	2491	325	2446	
11	2536	56	2568	101	2561	146	2658	191	2612	236	2330	281	2432	326	2431	
12	2523	57	2558	102	2554	147	2583	192	2573	237	2637	282	2414	327	2521	
13	2582	58	2558	103	2569	148	2580	193	2519	238	2520	283	2341	328	2339	
14	2537	59	2533	104	2488	149	2561	194	2554	239	2513	284	2457	329	2334	
15	2499	60	2492	105	2605	150	2530	195	2517	240	2534	285	2460	330	2366	
16	2512	61	2499	106	2641	151	2595	196	2557	241	2500	286	2452	331	2456	
17	2553	62	2512	107	2575	152	2607	197	2550	242	2649	287	2453	332	2390	
18	2359	63	2417	108	2730	153	2596	198	2596	243	2586	288	2332	333	2364	
19	2331	64	2455	109	2798	154	2540	199	2642	244	2439	289	2441	334	2373	
20	2402	65	2501	110	2593	155	2511	200	2544	245	2575	290	2541	335	2422	
21	2495	66	2519	111	2604	156	2575	201	2488	246	2649	291	2420	336	2456	
22	2448	67	2502	112	2547	157	2597	202	2586	247	2577	292	2432	337	2348	
23	2380	68	2548	113	2601	158	2454	203	2576	248	2564	293	2520	338	2374	
24	2468	69	2544	114	2588	159	2520	204	2558	249	2480	294	2492	339	2383	
25	2465	70	2516	115	2494	160	2551	205	2513	250	2538	295	2526	340	2451	
26	2491	71	2558	116	2538	161	2577	206	2534	251	2518	296	2548	341	2407	
27	2481	72	2488	117	2616	162	2541	207	2500	252	2439	297	2394	342	2390	
28	2436	73	2486	118	2613	163	2593	208	2577	253	2545	298	2408	343	2393	
29	2426	74	2439	119	2548	164	2571	209	2638	254	2538	299	2412	344	2387	
30	2524	75	2508	120	2576	165	2569	210	2578	255	2524	300	2412	345	2420	
31	2443	76	2681	121	2647	166	2520	211	2584	256	2523	301	2497	346	2559	
32	2518	77	2541	122	2566	167	2612	212	2571	257	2496	302	2438	347	2451	
33	2432	78	2479	123	2538	168	2674	213	2480	258	2477	303	2406	348	2459	
34	2493	79	2554	124	2564	169	2468	214	2578	259	2527	304	2364	349	2500	
35	2451	80	2569	125	2637	170	2622	215	2655	260	2590	305	2396	350	2419	
36	2575	81	2637	126	2634	171	2591	216	2578	261	2430	306	2422	351	2536	
37	2522	82	2572	127	2581	172	2560	217	2574	262	2517	307	2336	352	2441	
38	2503	83	2539	128	2592	173	2540	218	2554	263	2489	308	2211	353	2345	
39	2516	84	2582	129	2551	174	2624	219	2546	264	2442	309	2528	354	2308	
40	2443	85	2558	130	2548	175	2604	220	2573	265	2546	310	2424	355	2391	
41	2585	86	2658	131	2612	176	2603	221	2553	266	2522	311	2483	356	2496	
42	2443	87	2536	132	2575	177	2589	222	2556	267	2443	312	2448	357	2358	
43	2461	88	2614	133	2549	178	2535	223	2534	268	2469	313	2269	358	2297	
44	2548	89	2593	134	2564	179	2592	224	2572	269	2414	314	2609	359	2405	
45	2525	90	2587	135	2720	180	2599	225	2571	270	2461	315	2561	360	2431	

Compton Counting of Waveforms, Binned by RSM Rotation Angle; Used to Generate the Modulation Curve (ϕ = 175°)

RSM Rotation Angle	Number of Waveforms Recorded	RSM Rotation Angle	Number of Waveforms Recorded	RSM Rotation Angle	Number of Waveforms Recorded	RSM Rotation Angle	Number of Waveforms Recorded	RSM Rotation Angle	Number of Waveforms Recorded	RSM Rotation Angle	Number of Waveforms Recorded	RSM Rotation Angle	Number of Waveforms Recorded	RSM Rotation Angle	Number of Waveforms Recorded	Total Number of Waveforms in FEP
1	9096	46	9302	91	9363	136	9328	181	9248	226	8859	271	8819	316	9109	3301193
2	9178	47	9456	92	9324	137	9382	182	9361	227	9132	272	8759	317	9088	
3	8821	48	9228	93	9280	138	9142	183	9081	228	9066	273	9014	318	8179	
4	9022	49	9208	94	9388	139	9176	184	9283	229	9128	274	8759	319	9451	
5	9283	50	9496	95	9366	140	9382	185	9249	230	9051	275	9123	320	9092	
6	9090	51	9450	96	9458	141	9355	186	9354	231	8585	276	8977	321	8965	
7	9153	52	9225	97	9643	142	9399	187	9261	232	9457	277	8749	322	9301	
8	8941	53	9278	98	9455	143	9049	188	9214	233	9056	278	8827	323	8548	
9	9003	54	9134	99	9417	144	9410	189	9380	234	9155	279	9052	324	9473	
10	9360	55	9151	100	9483	145	9430	190	9253	235	9107	280	9065	325	9254	
11	9240	56	9433	101	9493	146	9280	191	9240	236	8453	281	8892	326	9224	
12	9189	57	9251	102	9468	147	9365	192	9211	237	9508	282	8883	327	9214	
13	9237	58	9090	103	9416	148	9279	193	9174	238	8870	283	8863	328	9262	
14	9421	59	9202	104	9443	149	9174	194	9132	239	8831	284	8965	329	8951	
15	9418	60	9261	105	9332	150	9267	195	9228	240	9099	285	9262	330	9014	
16	9567	61	9336	106	9461	151	9205	196	9191	241	8854	286	8984	331	9122	
17	9321	62	9076	107	9665	152	9407	197	9319	242	9411	287	8898	332	8886	
18	9105	63	9133	108	9769	153	9281	198	9044	243	9100	288	8788	333	8969	
19	9223	64	9027	109	9810	154	9279	199	9253	244	8969	289	8977	334	8916	
20	9117	65	9202	110	9438	155	9437	200	9350	245	9228	290	8851	335	9020	
21	9165	66	9287	111	9419	156	9402	201	9295	246	9076	291	9076	336	9228	
22	9101	67	9439	112	9356	157	9186	202	9156	247	9025	292	8923	337	9169	
23	8944	68	9135	113	9253	158	9157	203	9047	248	8896	293	8817	338	8903	
24	9147	69	9198	114	9339	159	9068	204	9012	249	8978	294	8957	339	8904	
25	9143	70	9212	115	9302	160	9175	205	9039	250	8944	295	8991	340	8803	
26	9244	71	9234	116	9410	161	9118	206	8962	251	8813	296	9021	341	9005	
27	9090	72	9174	117	9436	162	9074	207	9033	252	9118	297	8989	342	9087	
28	9100	73	9204	118	9357	163	9187	208	9109	253	9093	298	8785	343	8873	
29	9209	74	9173	119	9425	164	9264	209	9049	254	9005	299	9104	344	8876	
30	9197	75	9118	120	9414	165	9277	210	9062	255	8982	300	9037	345	9261	
31	9282	76	9301	121	9417	166	9238	211	8947	256	9128	301	8904	346	9378	
32	9106	77	9437	122	9396	167	9156	212	9221	257	9084	302	9111	347	9264	
33	9082	78	9232	123	9481	168	9150	213	8992	258	8967	303	8843	348	9283	
34	9238	79	9292	124	9272	169	9301	214	8973	259	8948	304	9077	349	9303	
35	9340	80	9484	125	9354	170	9231	215	9098	260	8948	305	9206	350	9333	
36	9340	81	9719	126	9379	171	9229	216	9057	261	8896	306	9011	351	9270	
37	9307	82	9436	127	9275	172	9260	217	9025	262	8806	307	9117	352	9401	
38	9112	83	9103	128	9389	173	9354	218	8929	263	8883	308	8125	353	9300	
39	9366	84	9134	129	9360	174	9226	219	9080	264	8843	309	9311	354	8910	
40	9335	85	9430	130	9510	175	9290	220	9109	265	9033	310	9232	355	9061	
41	9352	86	9767	131	9496	176	9355	221	9040	266	8896	311	9368	356	9267	
42	9273	87	9331	132	9373	177	9232	222	9207	267	8571	312	9000	357	9025	
43	9136	88	9099	133	9278	178	9261	223	9171	268	8884	313	8330	358	9043	
44	9302	89	9249	134	9278	179	9312	224	9154	269	8992	314	9612	359	9045	
45	9391	90	9437	135	9300	180	9223	225	9149	270	8809	315	9190	360	9095	

Appendix A.1.1: Large FitzGerald Design RSM Data, NaI Detector, Cs-137 Single Source; Experimentally Derived Library Matching Results Modulation Comparison for Parsed Data View Angle φ = 45

Parsed Data Set Results for ϕ = 45°: ~500K Total Waveform Captures

Phi_ViewDegree = 45 Theta_ViewDegree = 0 Closest_LS_Match_Distance = 3 Closest_MAC_Match_Distance = 4.123

Spectrum_Total_Count = 495808

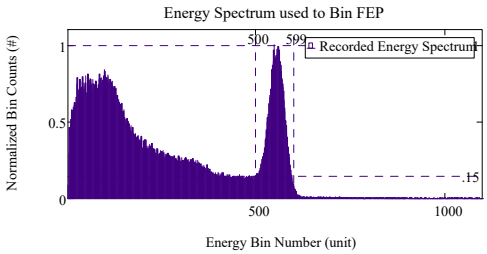

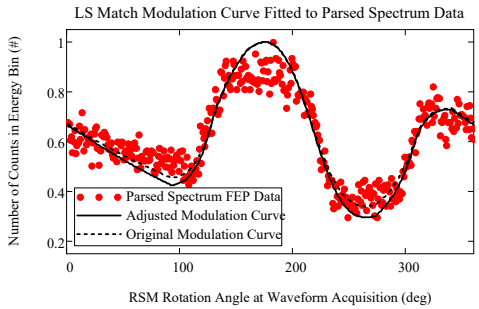

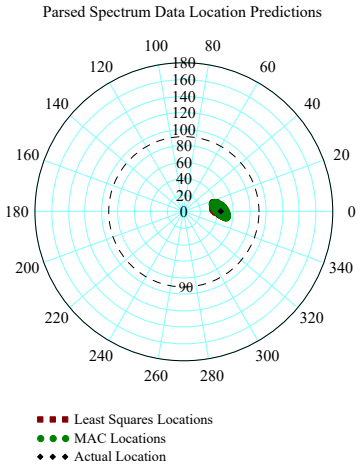

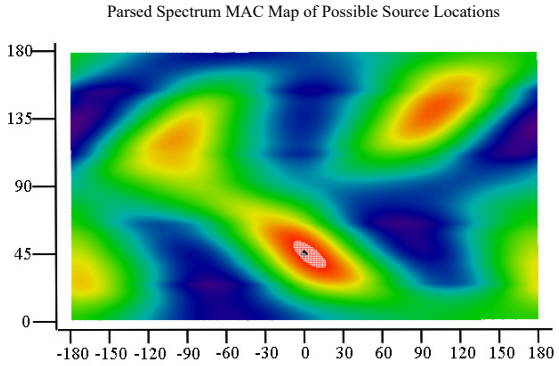

Parsed Data Set Results for ϕ = 45°: ~1.0M Total Waveform Captures

Phi_ViewDegree = 45 Theta_ViewDegree = 0 Closest_LS_Match_Distance = 2 Closest_MAC_Match_Distance = 3

Spectrum_Total_Count = 991606

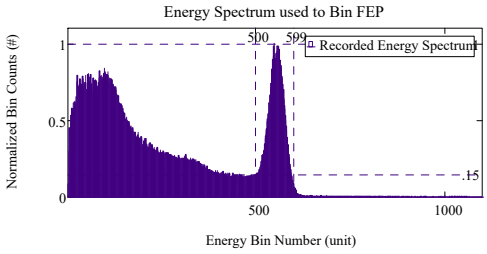

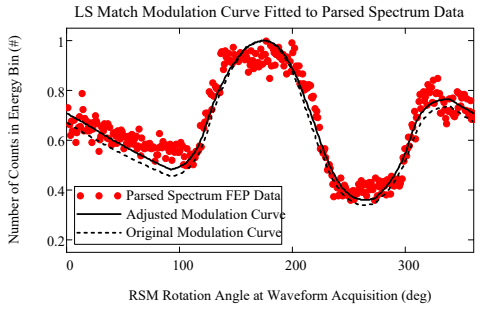

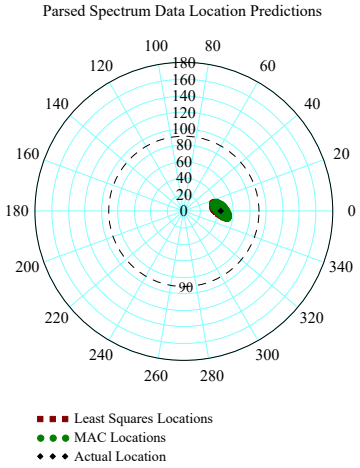

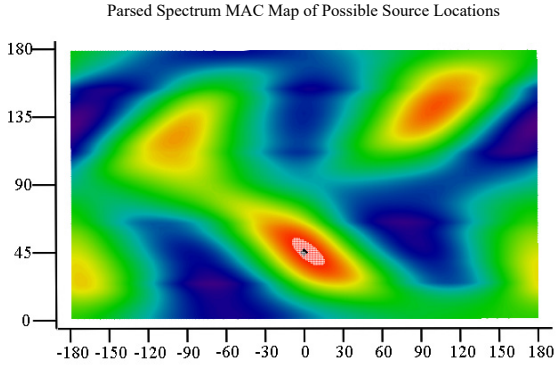

Parsed Data Set Results for ϕ = 45°: ~1.5M Total Waveform Captures

Phi_ViewDegree = 45 Theta_ViewDegree = 0 Closest_LS_Match_Distance = 1.414 Closest_MAC_Match_Distance = 2.236

Spectrum_Total_Count = 1487498

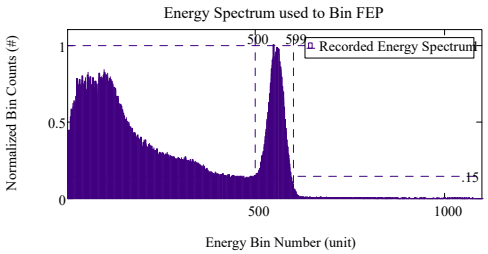

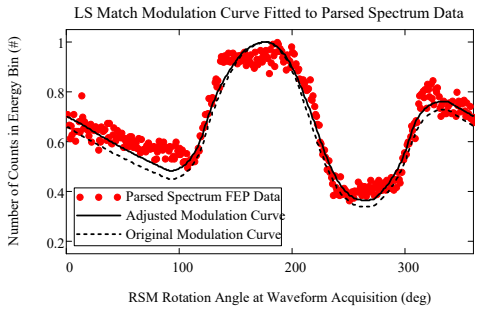

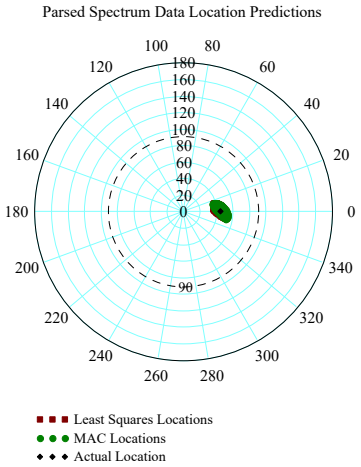

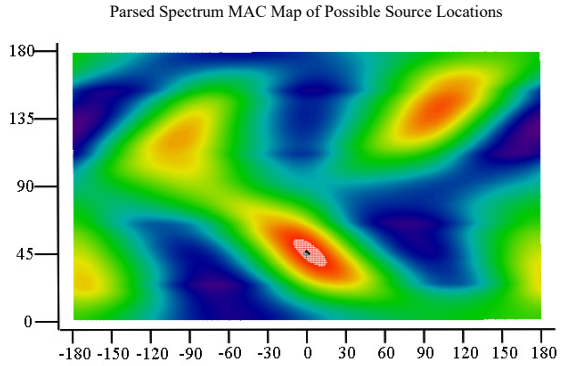

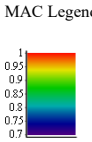

Parsed Data Set Results for ϕ = 45°: ~2.0M Total Waveform Captures

Phi_ViewDegree = 45 Theta_ViewDegree = 0 Closest_LS_Match_Distance = 1.414 Closest_MAC_Match_Distance = 2.236

Spectrum_Total_Count = 1983215

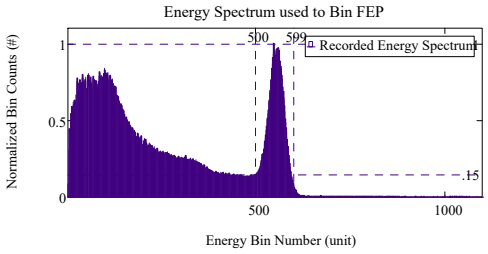

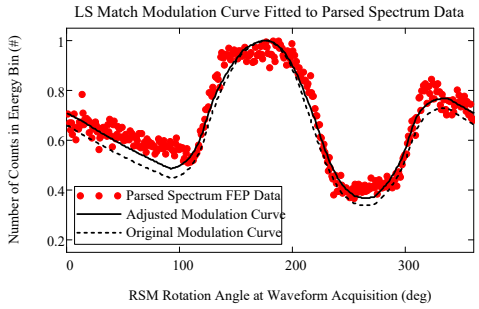

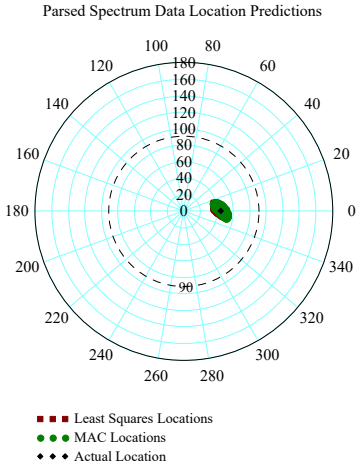

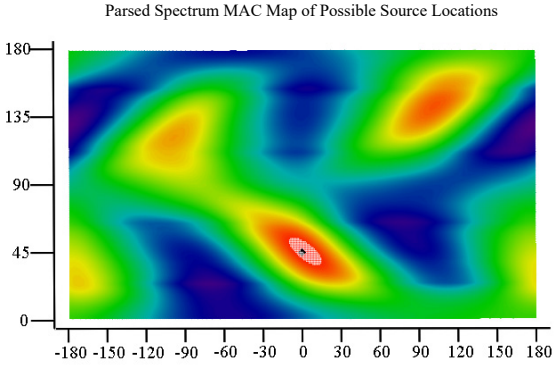

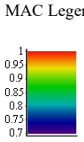

Parsed Data Set Results for ϕ = 45°: ~2.5M Total Waveform Captures

Phi_ViewDegree = 45 Theta_ViewDegree = 0 Closest_LS_Match_Distance = 1.414 Closest_MAC_Match_Distance = 2.236

Spectrum_Total_Count = 2479164

Energy Spectrum used to Bin FEP

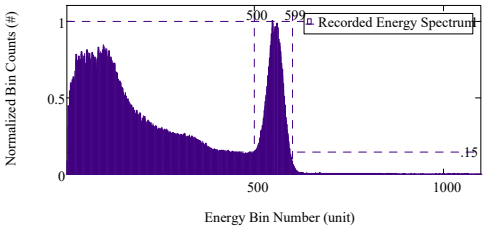

LS Match Modulation Curve Fitted to Parsed Spectrum Data

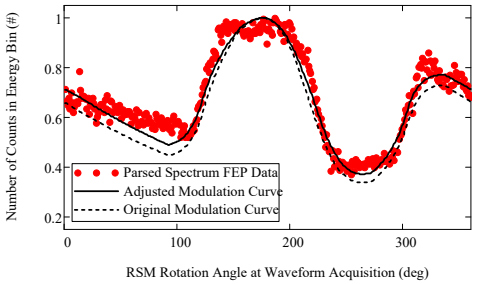

Parsed Spectrum Data Location Predictions

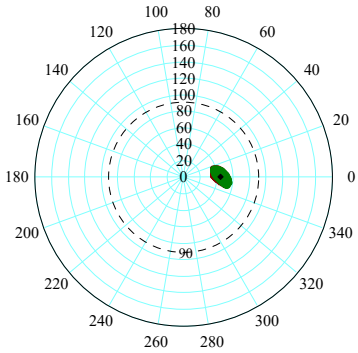

Parsed Spectrum MAC Map of Possible Source Locations

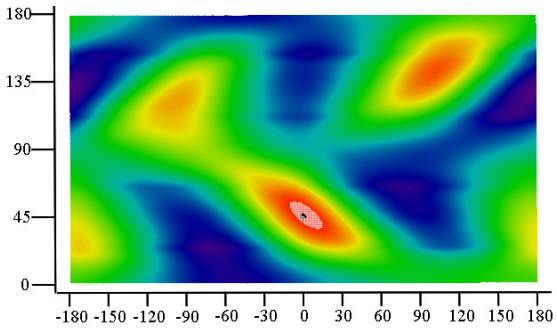

MAC Legend

Parsed Data Set Results for ϕ = 45°: ~3.0M Total Waveform Captures

Phi_ViewDegree = 45 Theta_ViewDegree = 0 Closest_LS_Match_Distance = 1.414 Closest_MAC_Match_Distance = 2.236

Spectrum_Total_Count = 2974966

Energy Spectrum used to Bin FEP

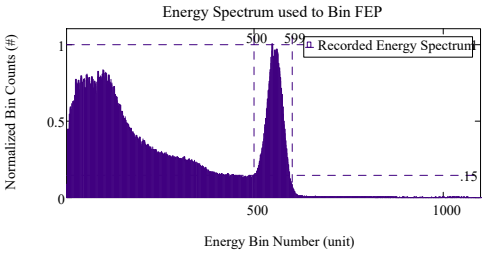

LS Match Modulation Curve Fitted to Parsed Spectrum Data

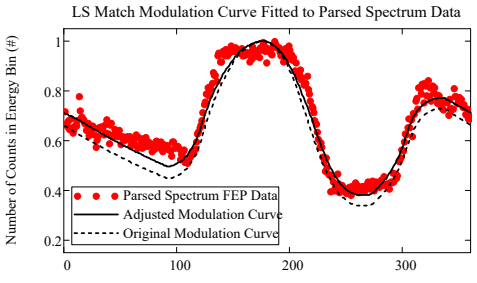

Parsed Spectrum Data Location Predictions

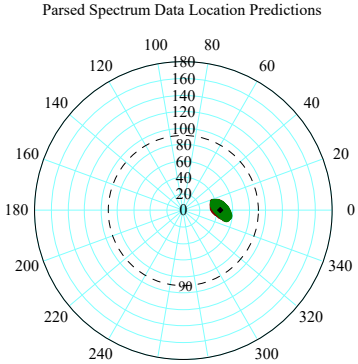

Parsed Spectrum MAC Map of Possible Source Locations

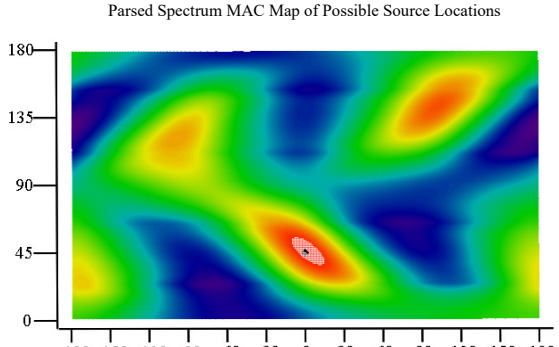

MAC Legend

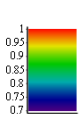

Parsed Data Set Results for ϕ = 45°: ~3.5M Total Waveform Captures

Phi_ViewDegree = 45 Theta_ViewDegree = 0 Closest_LS_Match_Distance = 1.414 Closest_MAC_Match_Distance = 2.236

Spectrum_Total_Count = 3470723

Energy Spectrum used to Bin FEP

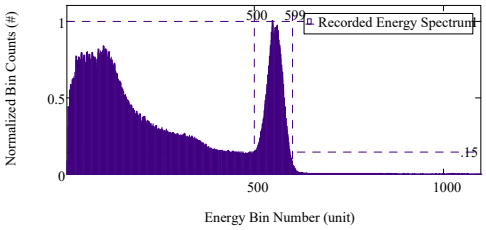

LS Match Modulation Curve Fitted to Parsed Spectrum Data

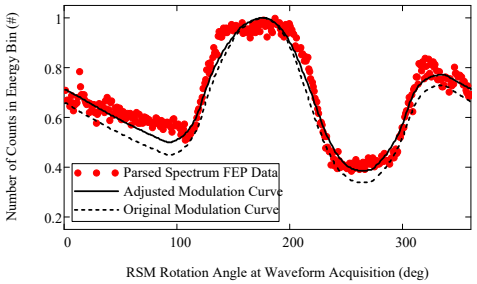

Parsed Spectrum Data Location Predictions

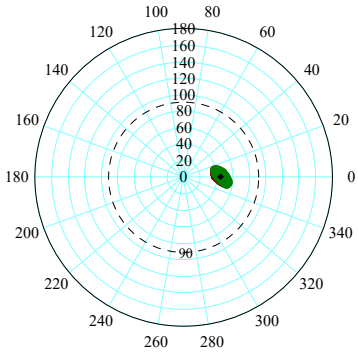

Parsed Spectrum MAC Map of Possible Source Locations

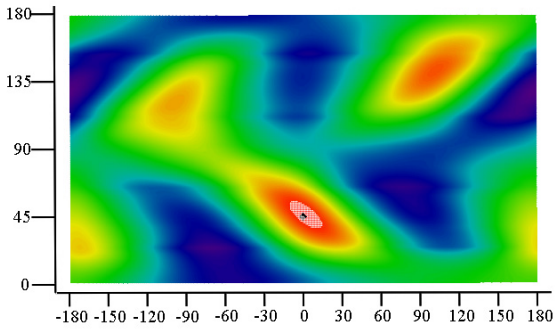

MAC Legend

Parsed Data Set Results for ϕ = 45°: ~4.0M Total Waveform Captures

Phi_ViewDegree = 45 Theta_ViewDegree = 0 Closest_LS_Match_Distance = 1.414 Closest_MAC_Match_Distance = 2.236

Spectrum_Total_Count = 3966608

Energy Spectrum used to Bin FEP

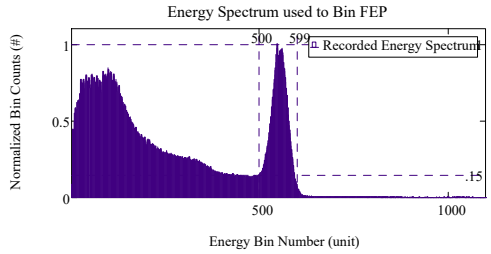

LS Match Modulation Curve Fitted to Parsed Spectrum Data

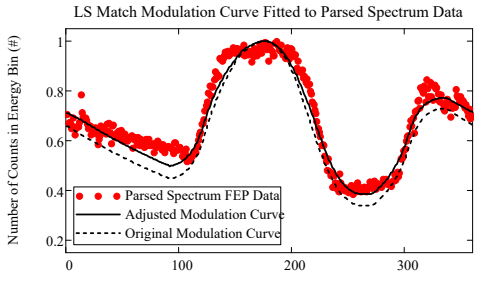

Parsed Spectrum Data Location Predictions

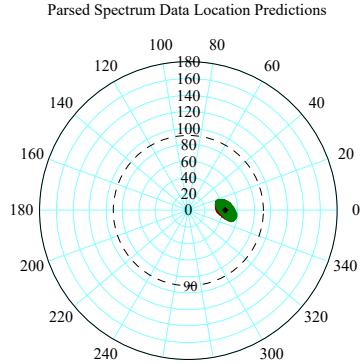

Parsed Spectrum MAC Map of Possible Source Locations

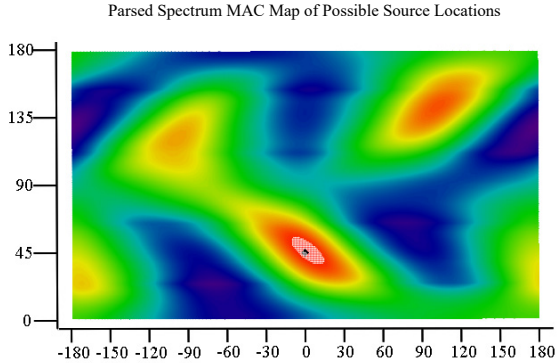

MAC Legend

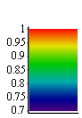

Appendix A.1.2: Large FitzGerald Design RSM Data, NaI Detector, Cs-137 Single Source; Experimental Uncertainty and Best Library Matching Results

Viewing Angle

ϕ = 5°

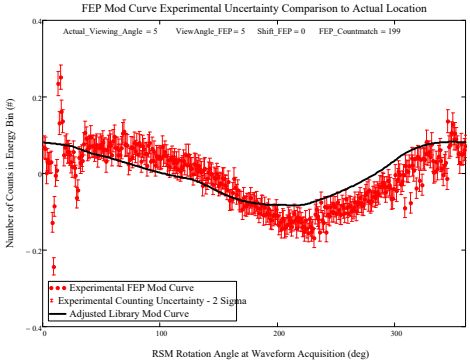

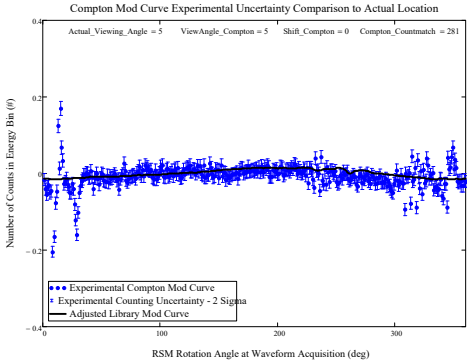

ϕ = 15°

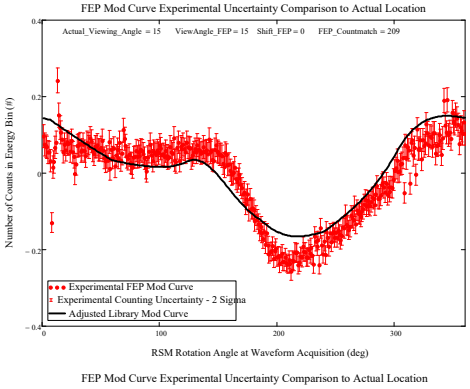

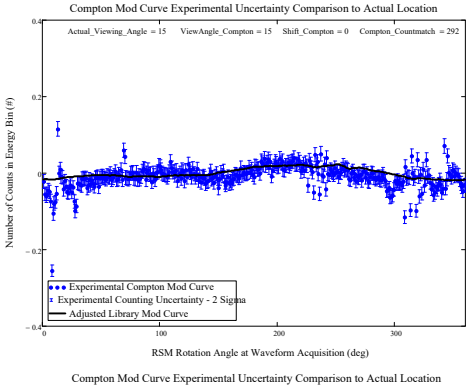

ϕ = 25°

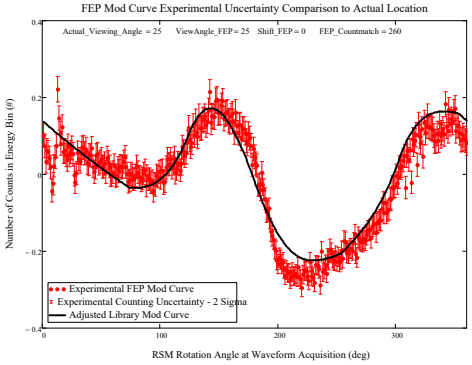

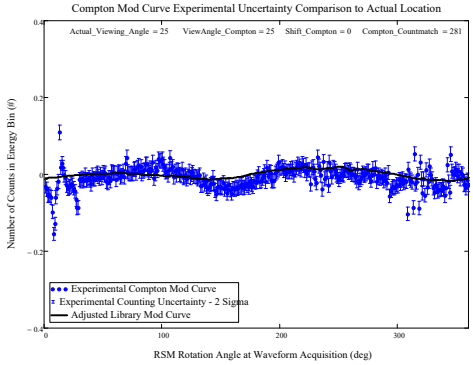

ϕ = 35°

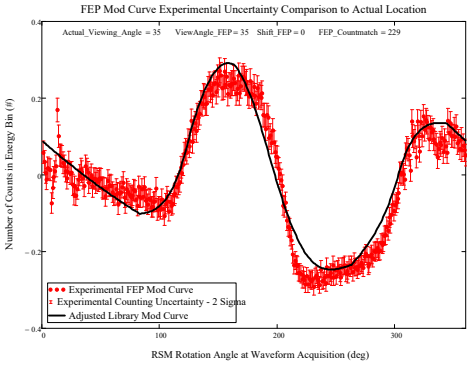

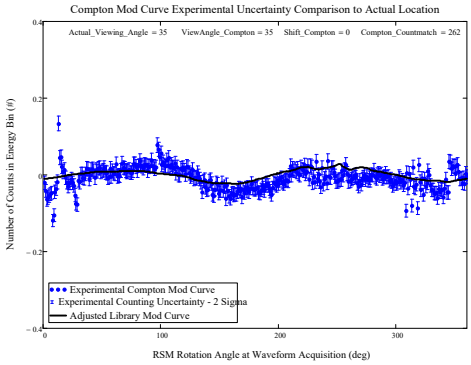

Viewing Angle

ϕ = 45°

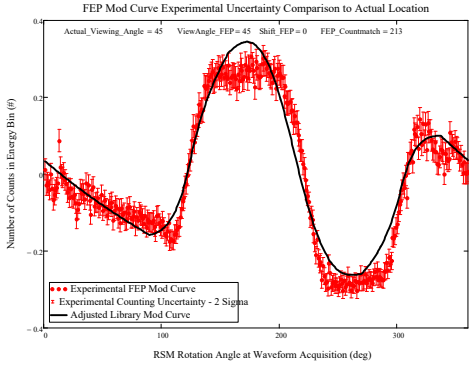

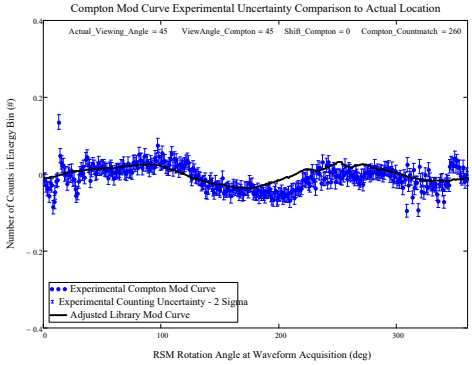

ϕ = 55°

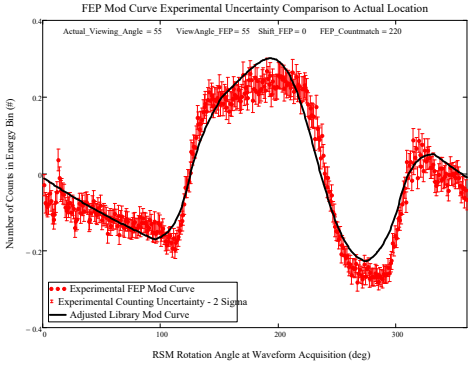

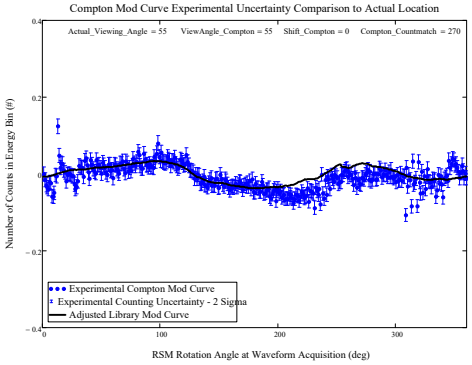

ϕ = 65°

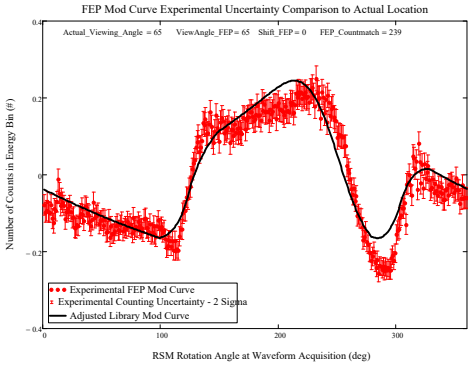

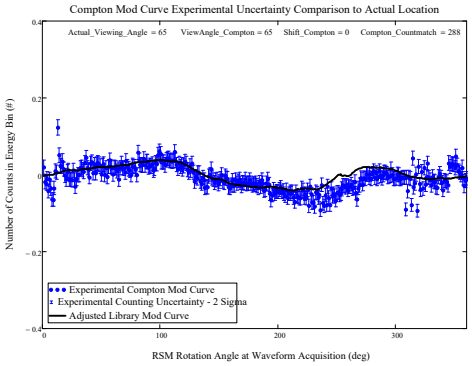

ϕ = 75°

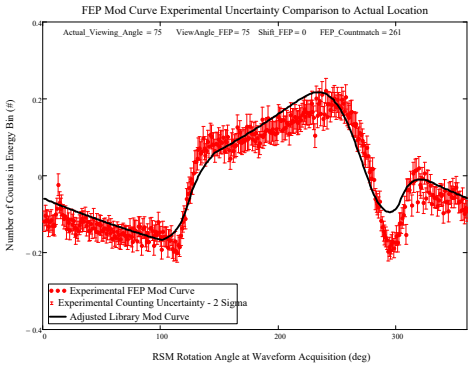

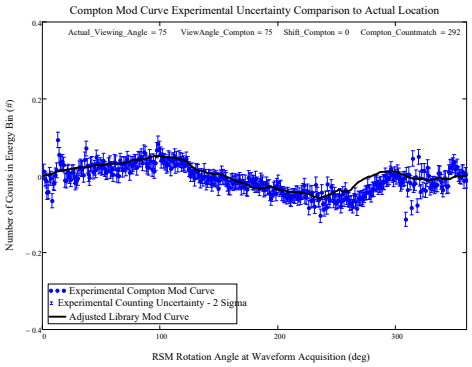

Viewing Angle

ϕ = 85°

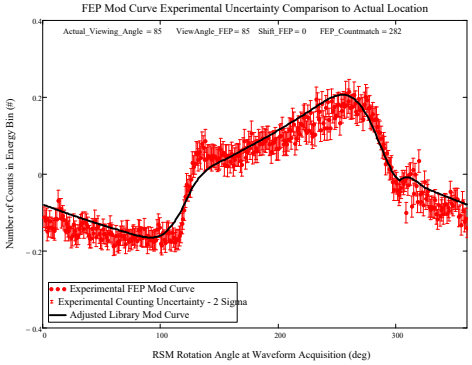

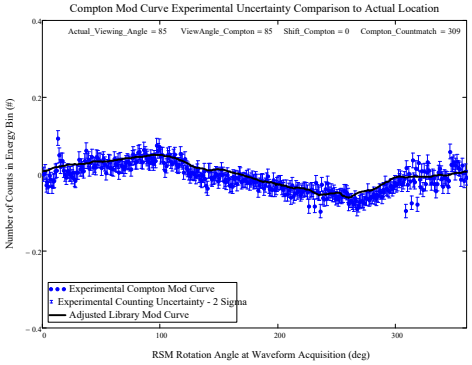

ϕ = 95°

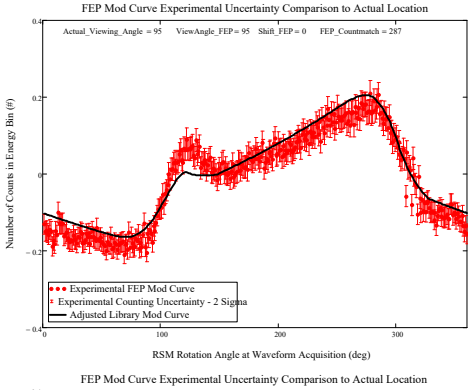

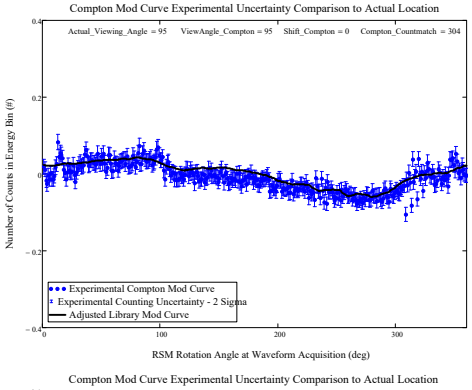

ϕ = 105°

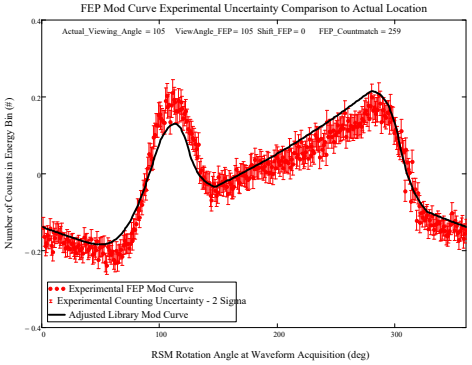

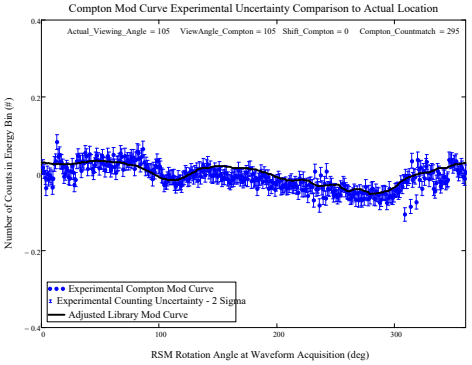

ϕ = 115°

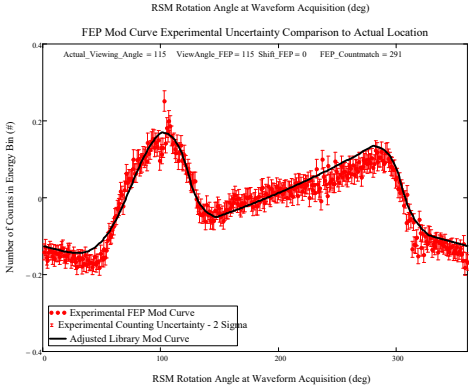

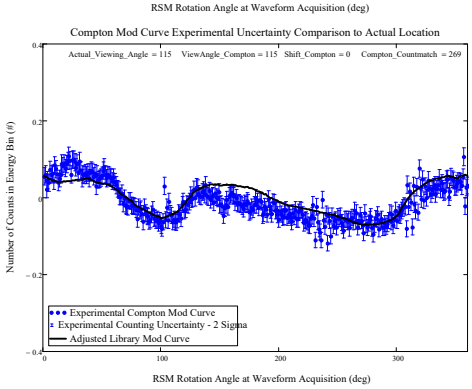

Viewing Angle

ϕ = 125°

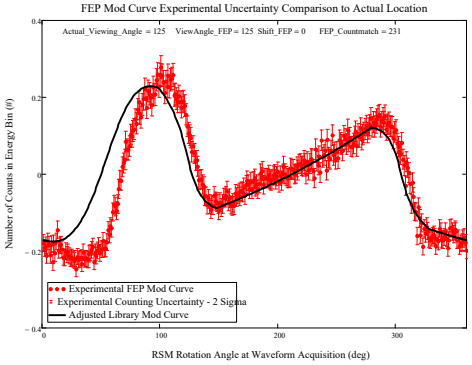

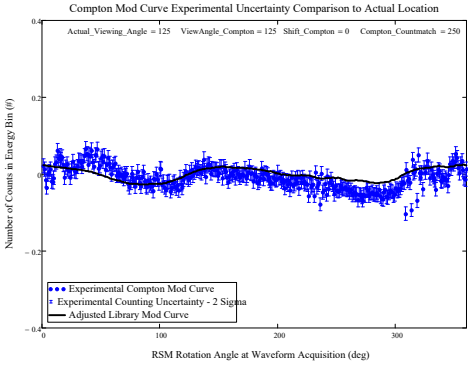

ϕ = 135°

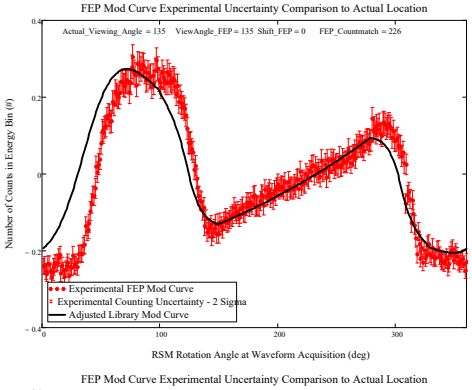

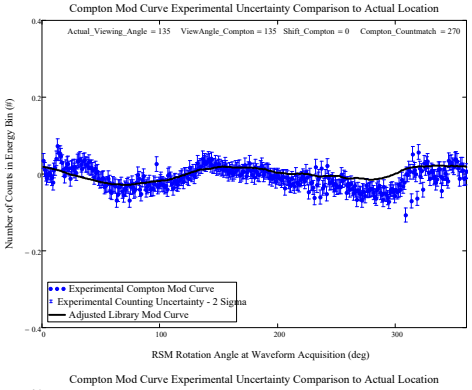

ϕ = 145°

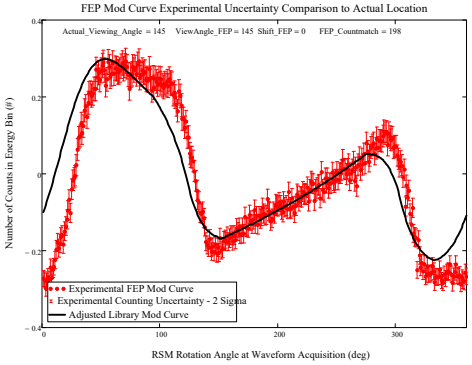

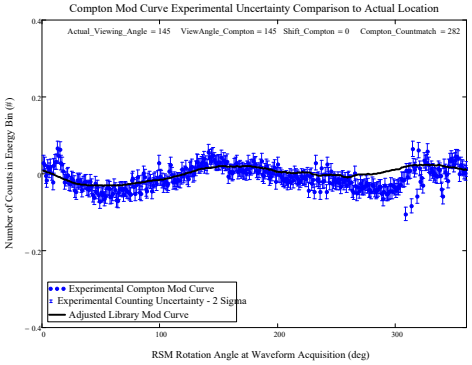

ϕ = 155°

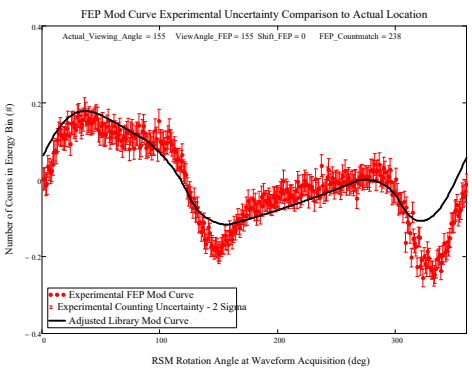

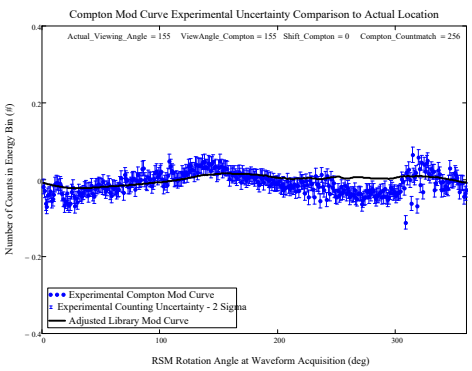

Viewing Angle

ϕ = 165°

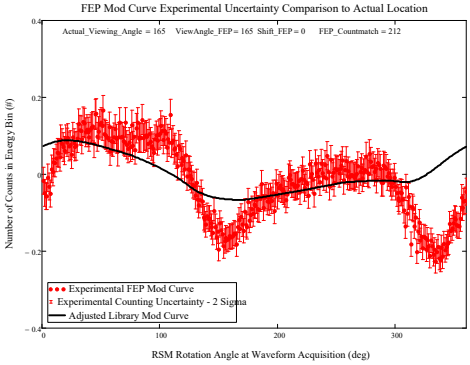

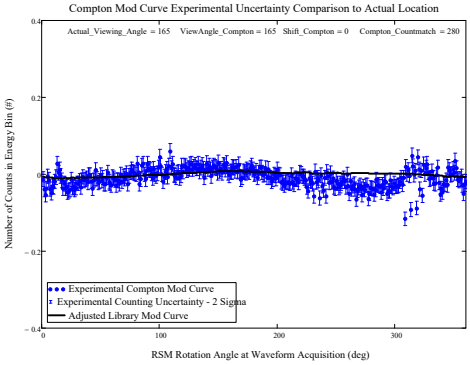

ϕ = 175°

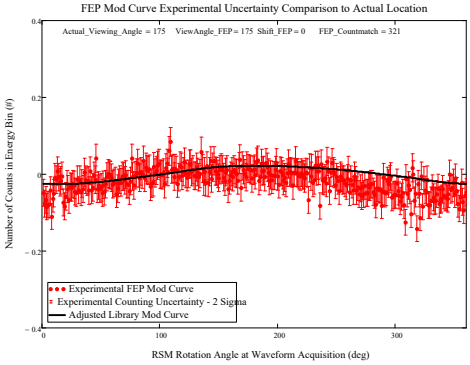

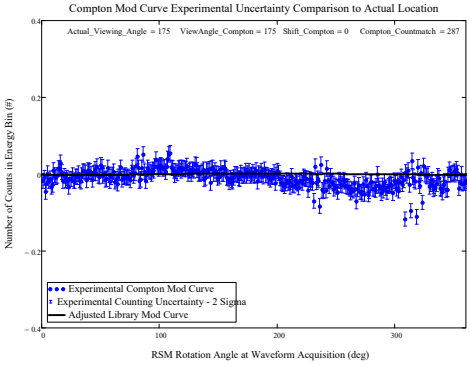

Appendix A.1.3: Large FitzGerald Design RSM Data, NaI Detector, Cs-137 Single Source; Experimentally Derived Library Matching Results Modulation Curve Smoothing Comparison for View Angle φ = 45

View Angle φ = 45° : Spectrum, Modulation Curve Data (No Smoothing), Library Curve, MAC and Least Squares Direction Predictions

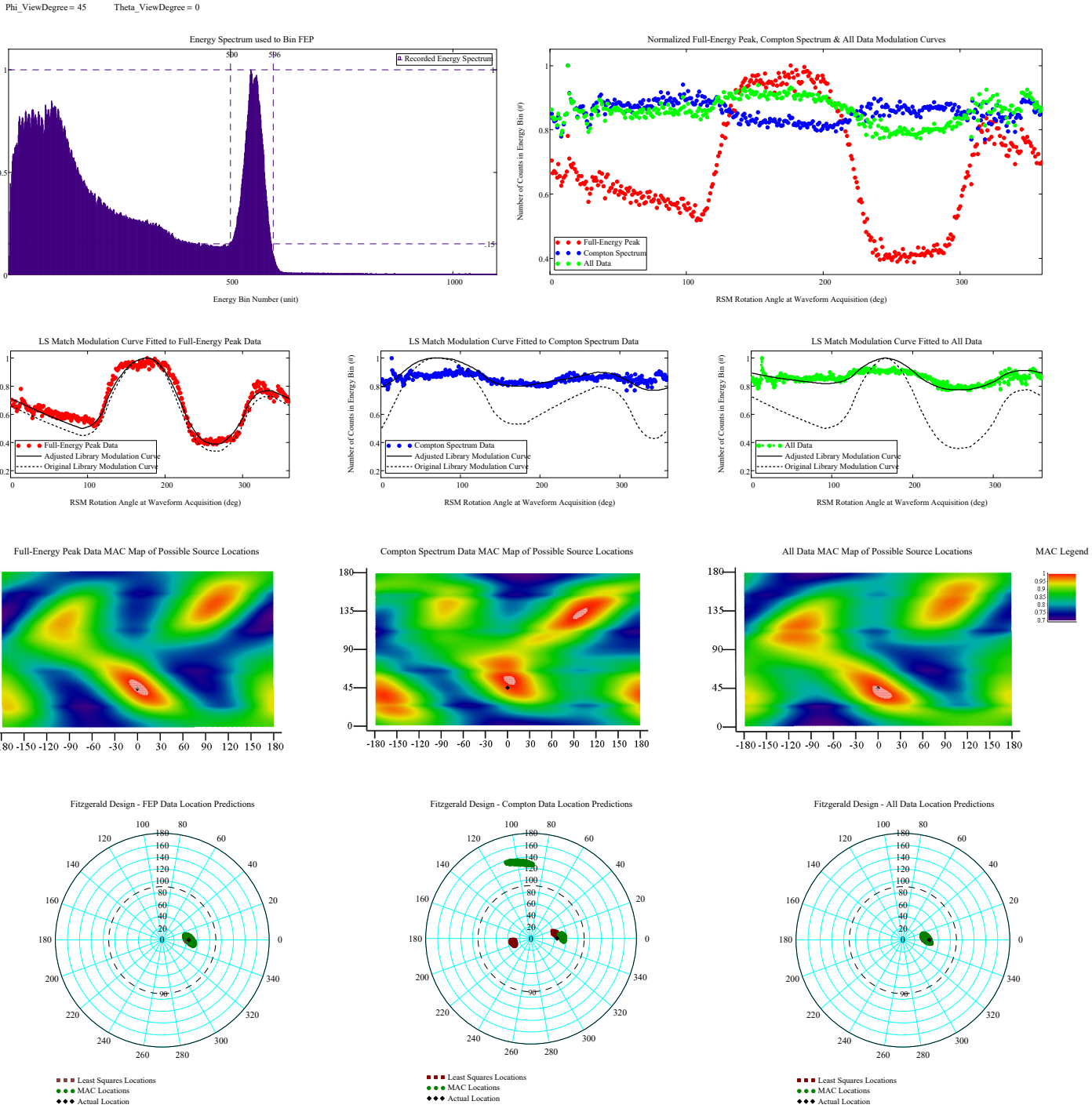

View Angle φ = 45° : Spectrum, Modulation Curve Data (5 Smoothing), Library Curve, MAC and Least Squares Direction Predictions

Phi_ViewDegree = 45 Theta_ViewDegree = 0

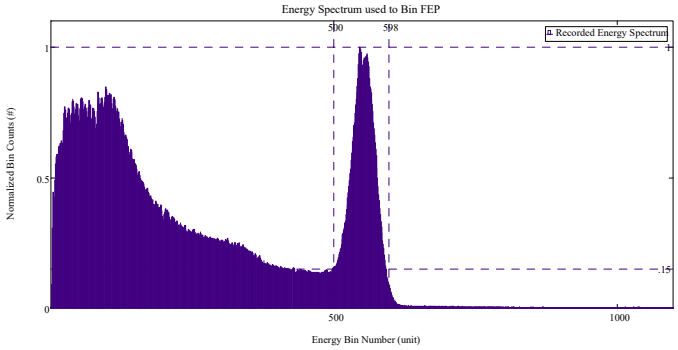

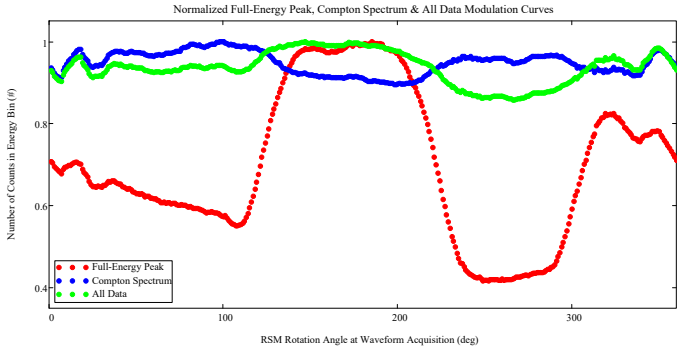

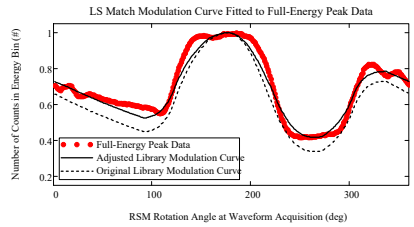

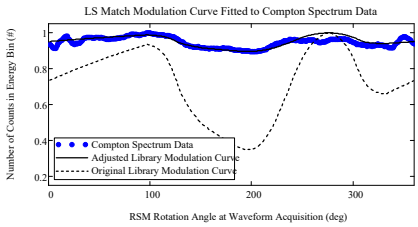

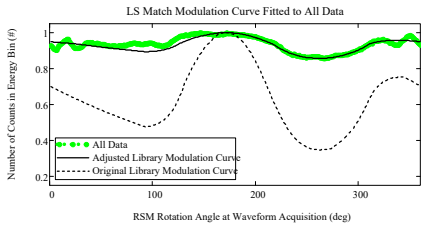

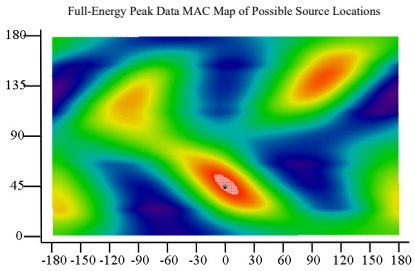

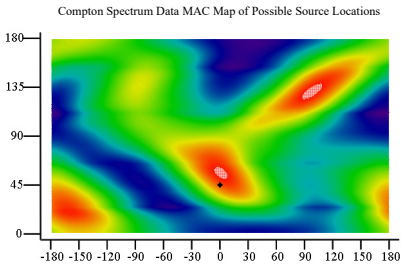

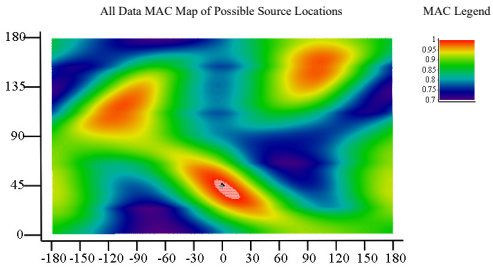

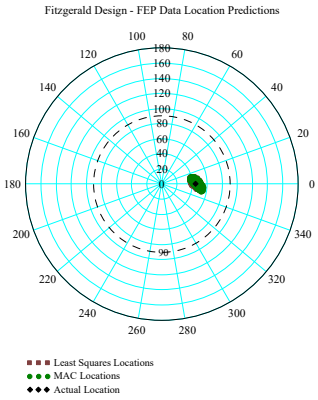

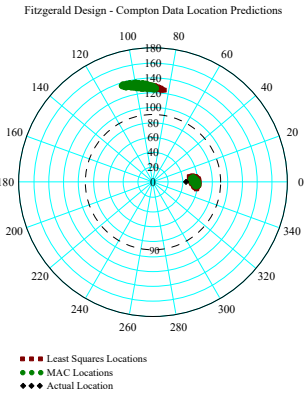

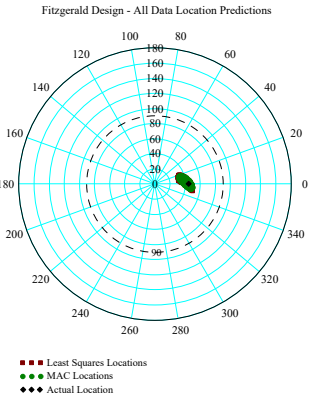

View Angle φ = 45° : Spectrum, Modulation Curve Data (10 Smoothing), Library Curve, MAC and Least Squares Direction Predictions

Phi_ViewDegree = 45 Theta_ViewDegree = 0

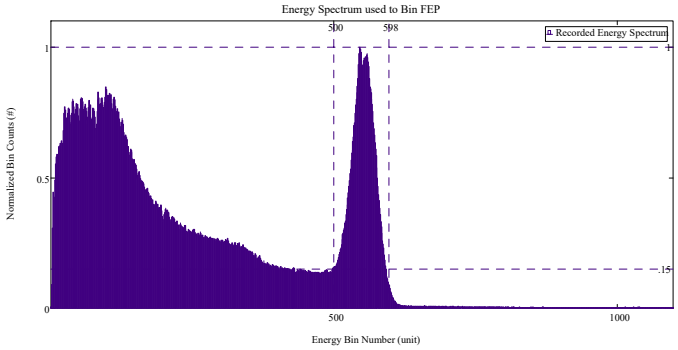

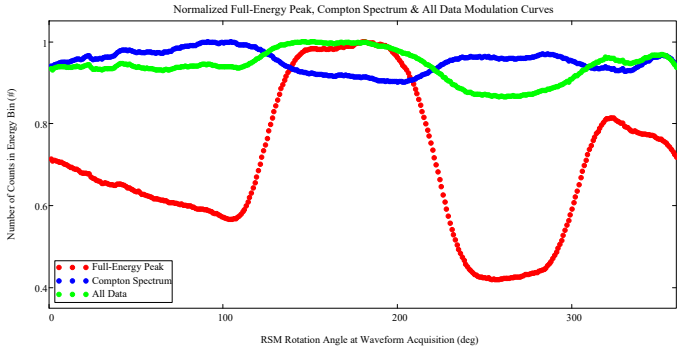

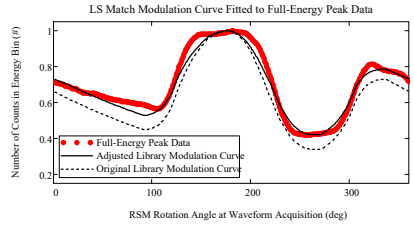

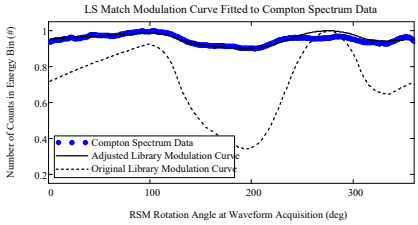

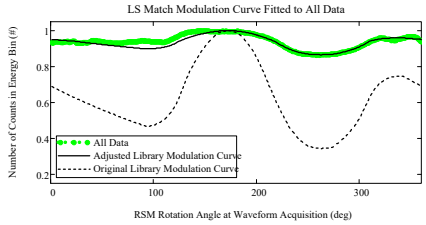

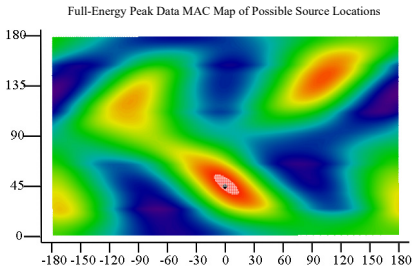

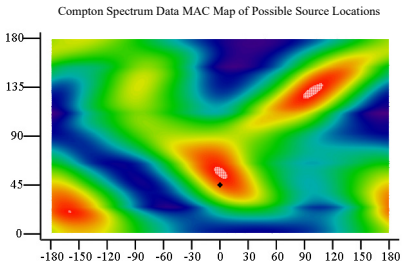

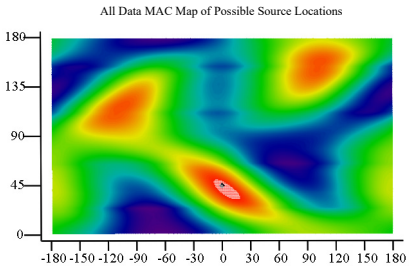

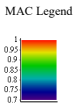

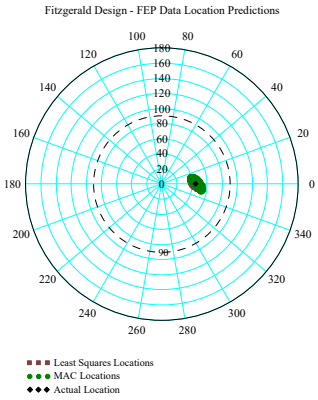

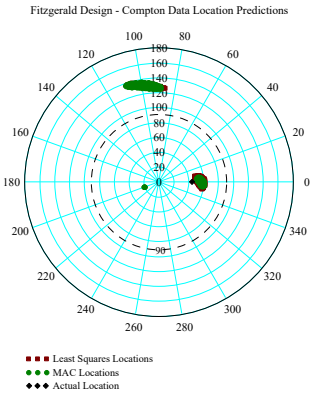

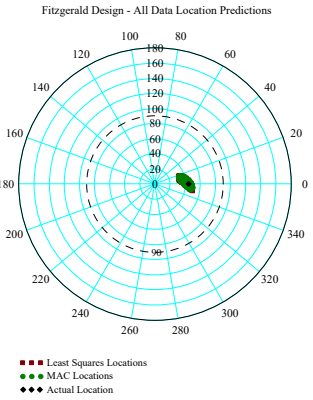

View Angle φ = 45° : Spectrum, Modulation Curve Data (20 Smoothing), Library Curve, MAC and Least Squares Direction Predictions

Phi_ViewDegree = 45 Theta_ViewDegree = 0

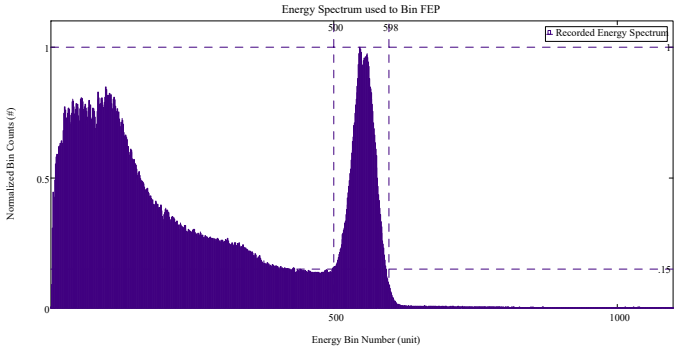

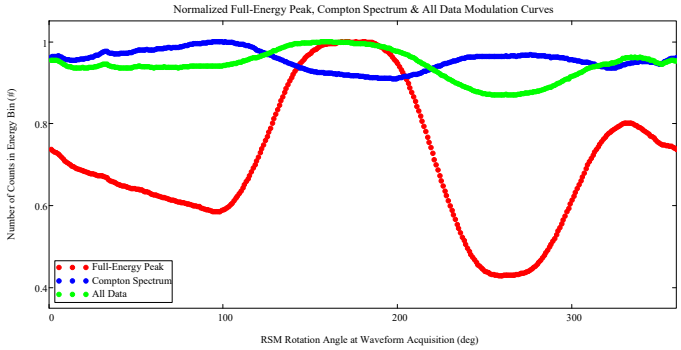

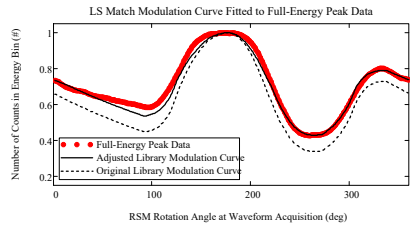

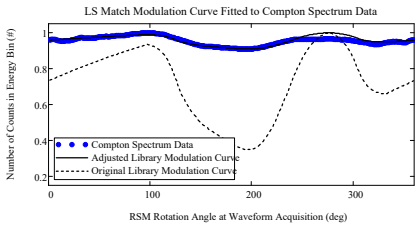

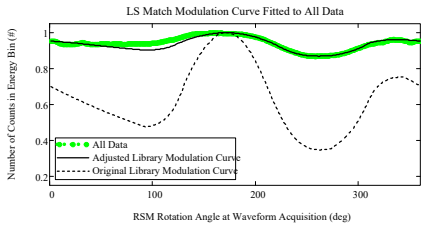

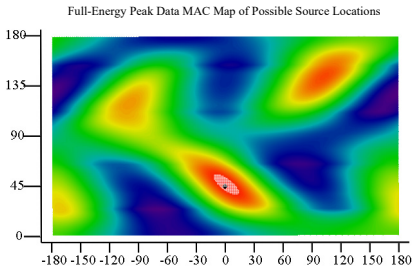

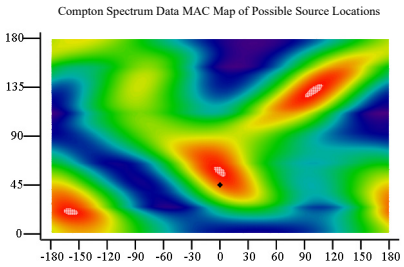

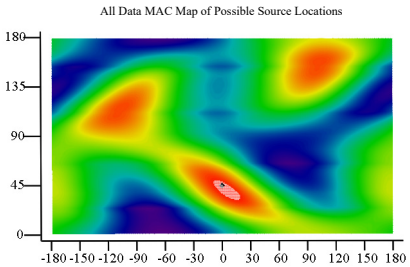

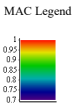

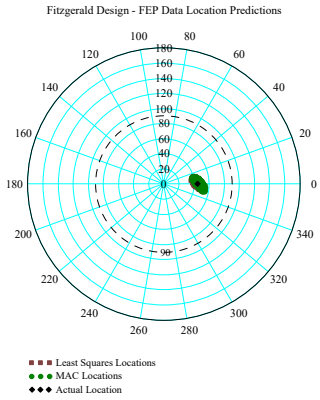

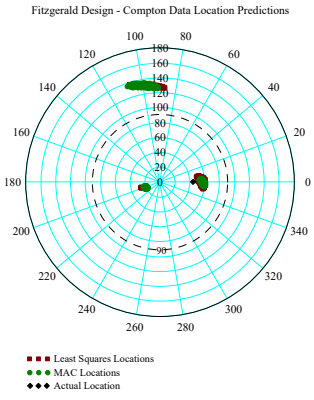

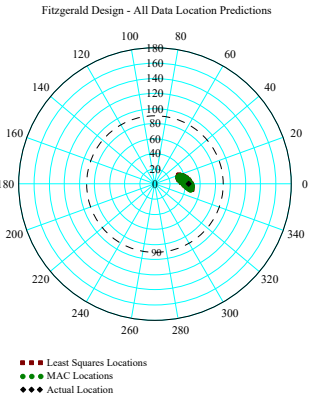

Appendix A.2: Large FitzGerald Design RSM Data, NaI Detector, Multinuclide Source; Experimentally Derived Library Matching Results

View Angle φ = 5° : Spectrum, Modulation Curve Data (No Smoothing), Library Curve, MAC and Least Squares Direction Predictions

Phi_ViewDegree = 5 Theta_ViewDegree = 0

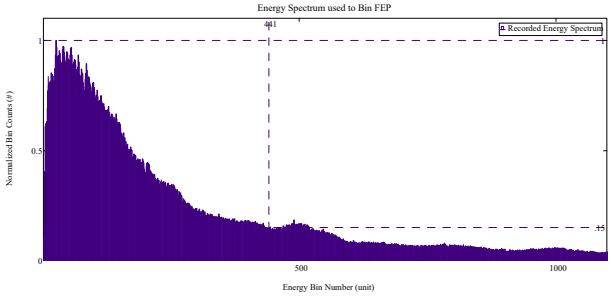

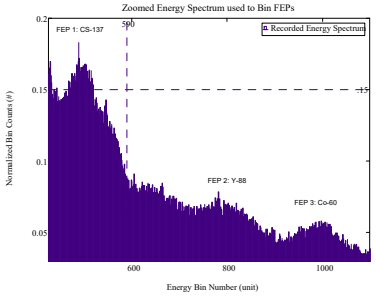

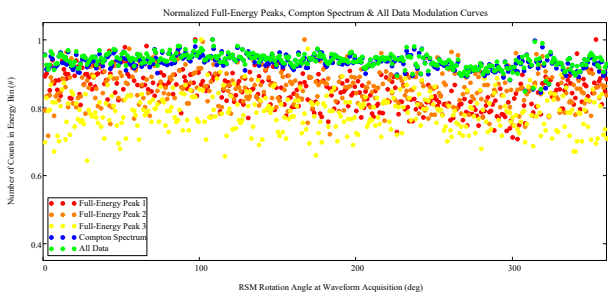

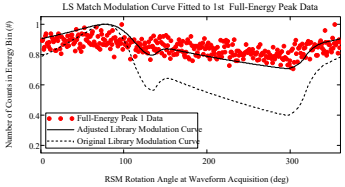

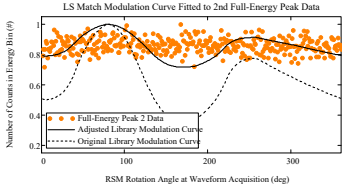

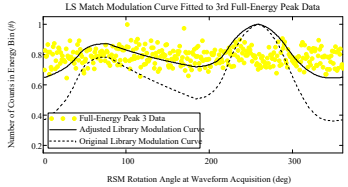

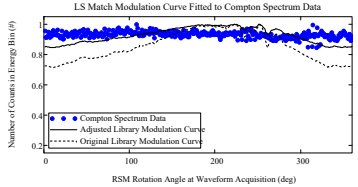

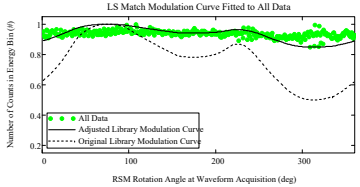

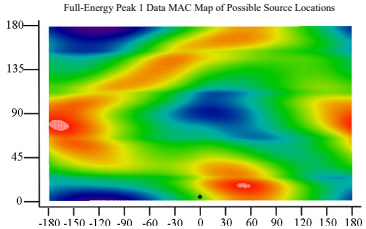

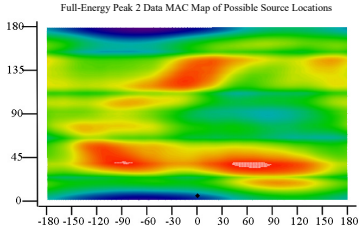

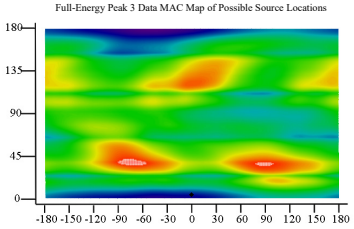

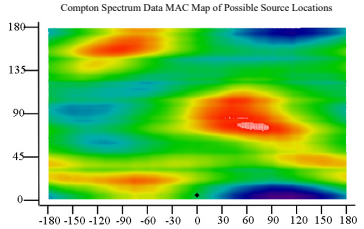

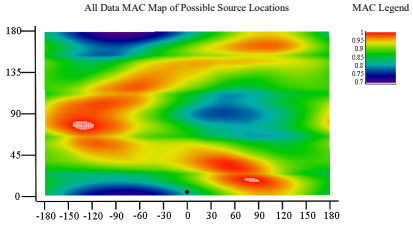

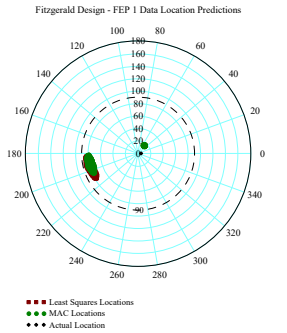

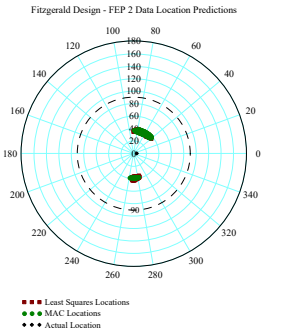

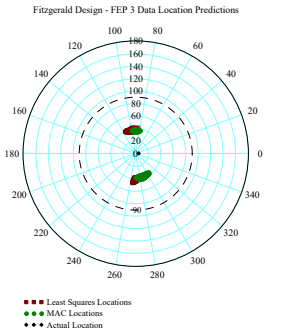

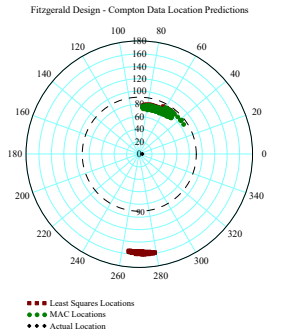

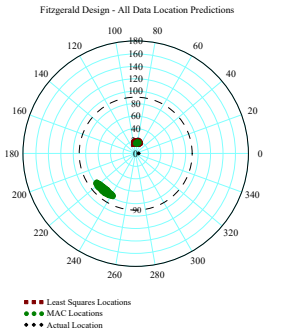

View Angle φ = 15° : Spectrum, Modulation Curve Data (No Smoothing), Library Curve, MAC and Least Squares Direction Predictions

Phi_ViewDegree = 15 Theta_ViewDegree = 0

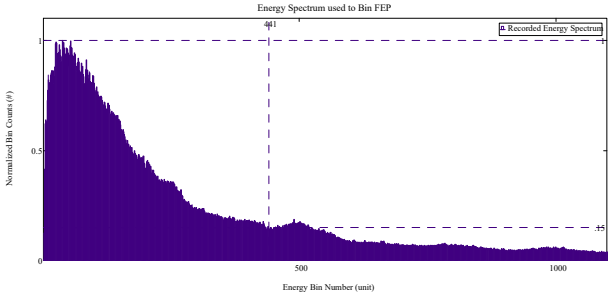

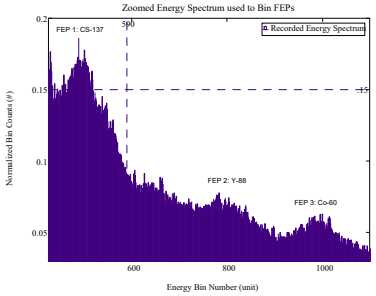

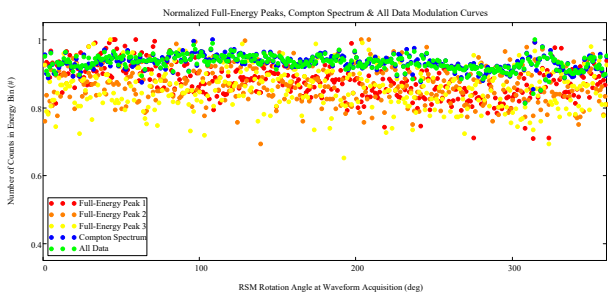

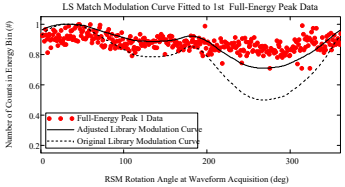

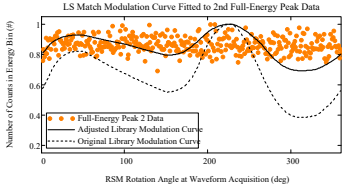

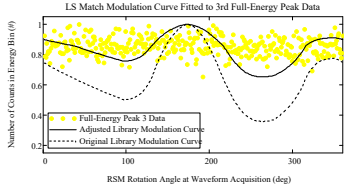

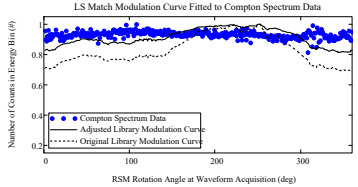

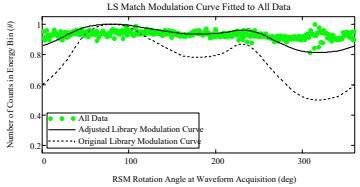

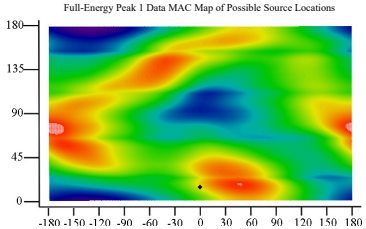

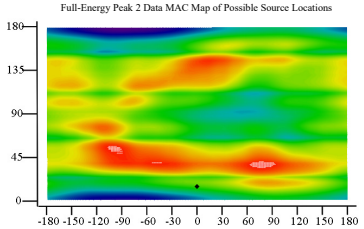

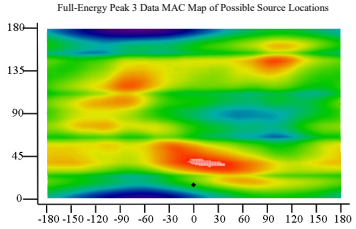

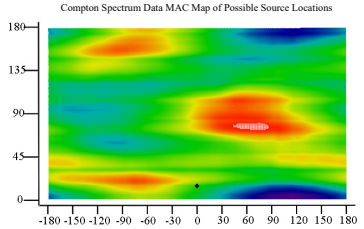

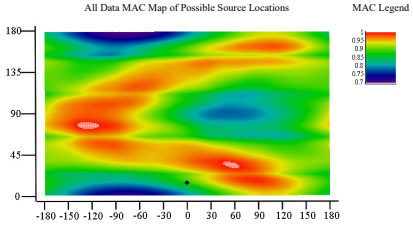

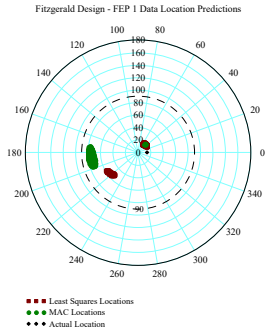

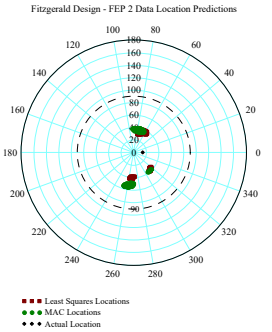

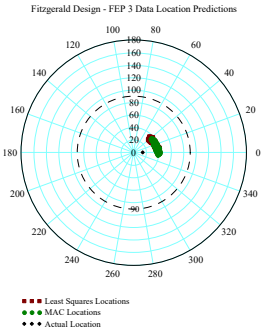

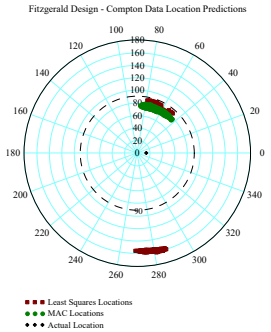

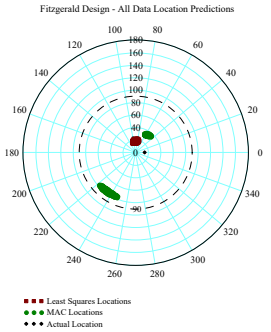

View Angle φ = 25° : Spectrum, Modulation Curve Data (No Smoothing), Library Curve, MAC and Least Squares Direction Predictions

Phi_ViewDegree = 25 Theta_ViewDegree = 0

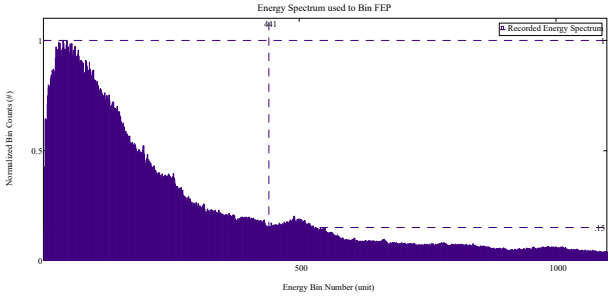

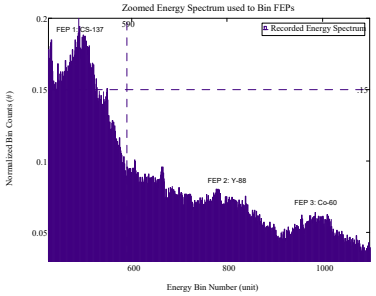

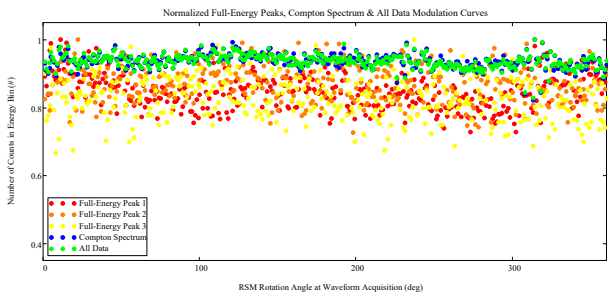

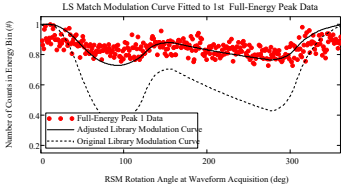

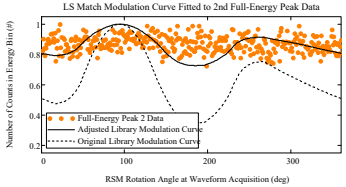

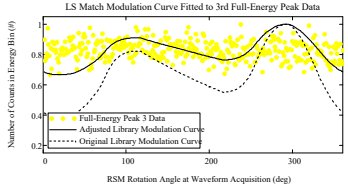

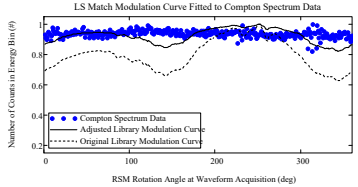

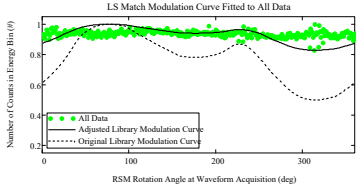

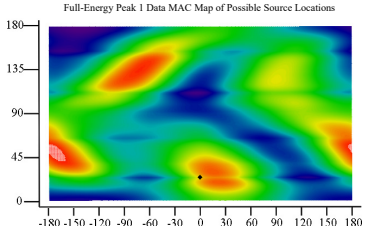

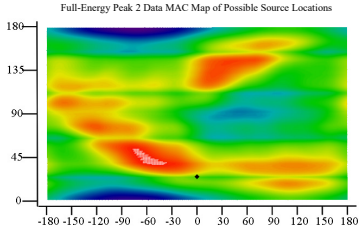

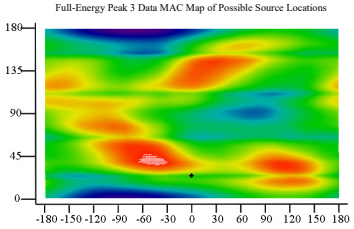

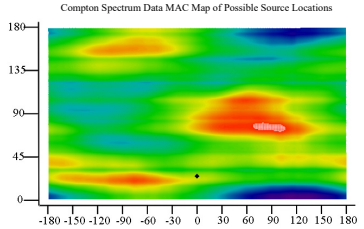

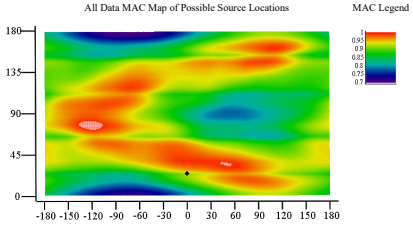

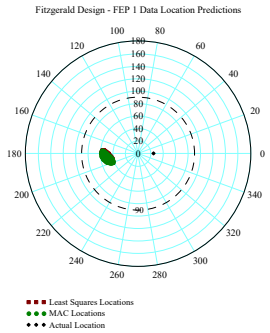

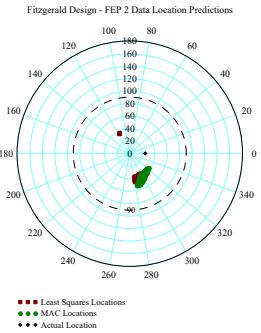

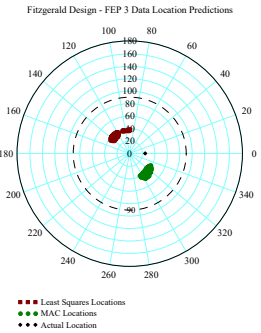

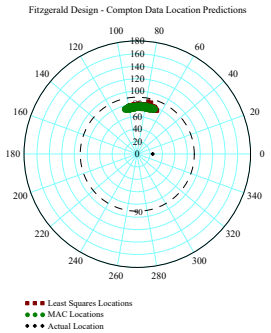

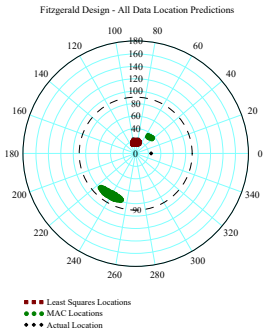

View Angle φ = 35° : Spectrum, Modulation Curve Data (No Smoothing), Library Curve, MAC and Least Squares Direction Predictions

Phi_ViewDegree = 35 Theta_ViewDegree = 0

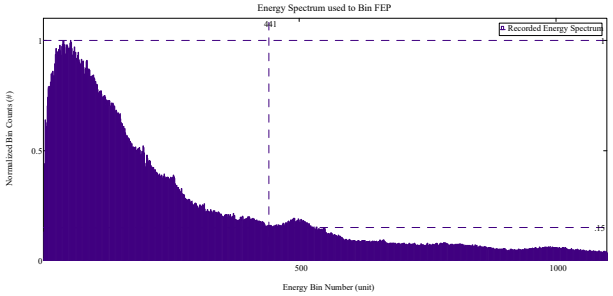

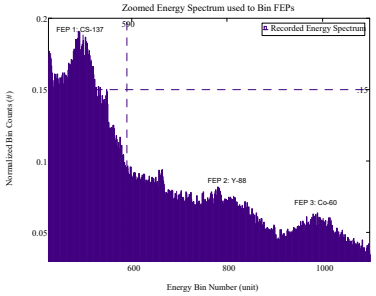

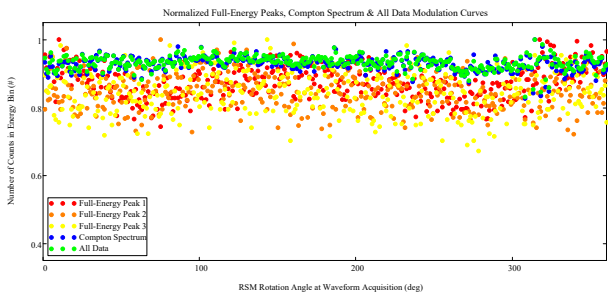

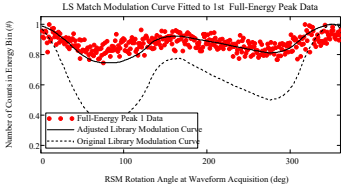

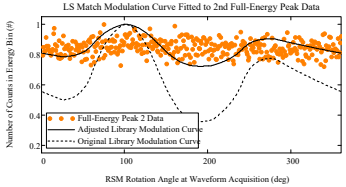

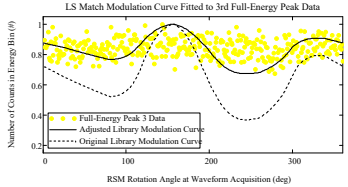

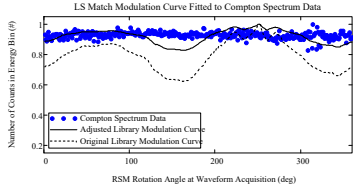

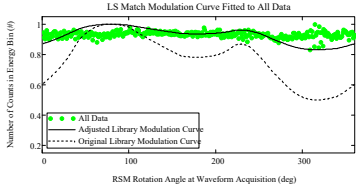

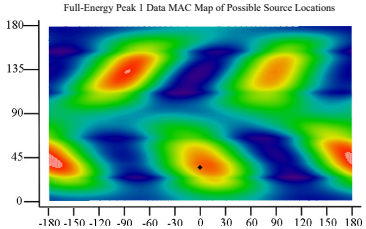

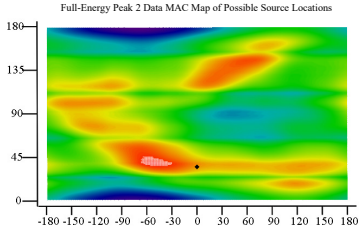

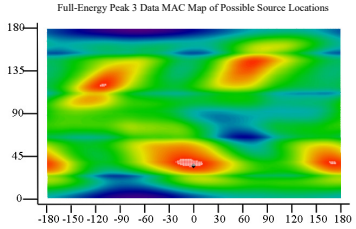

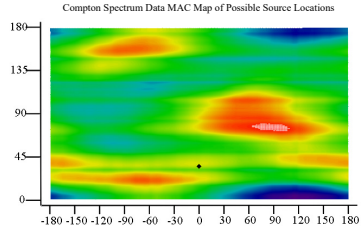

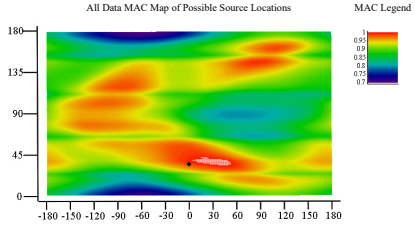

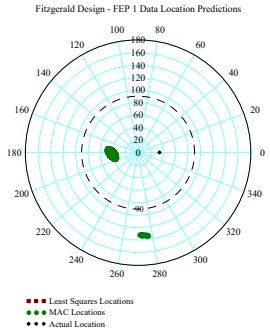

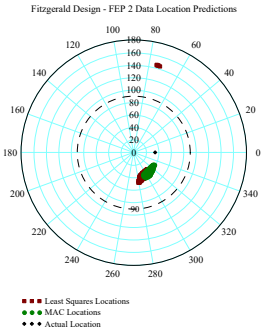

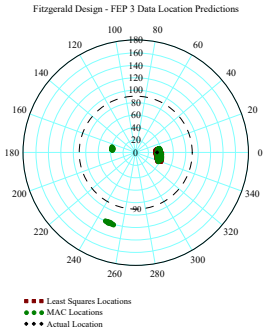

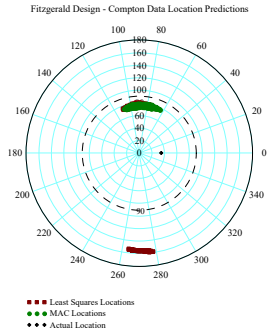

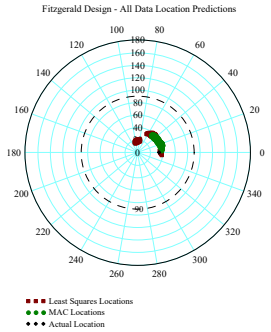

View Angle φ = 45° : Spectrum, Modulation Curve Data (No Smoothing), Library Curve, MAC and Least Squares Direction Predictions

Phi_ViewDegree = 45 Theta_ViewDegree = 0

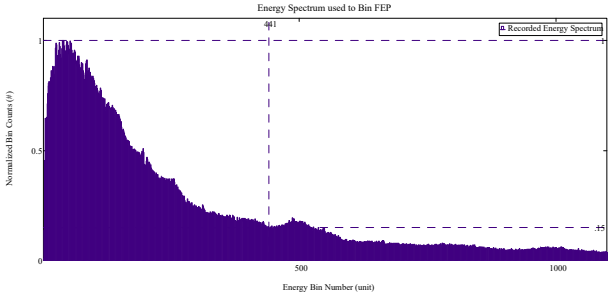

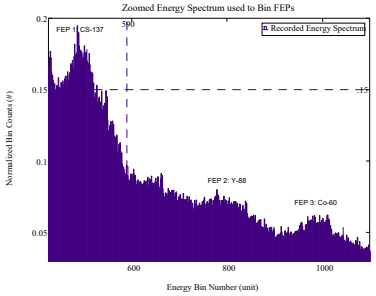

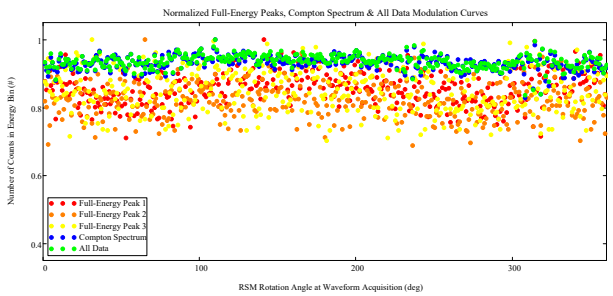

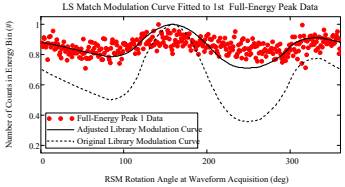

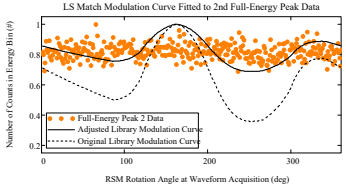

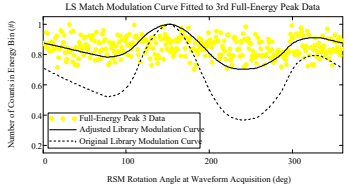

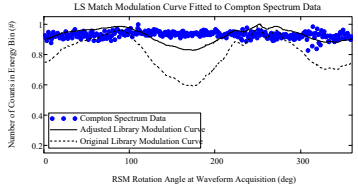

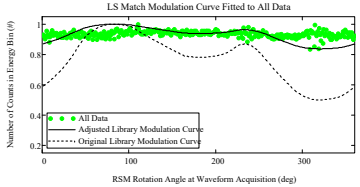

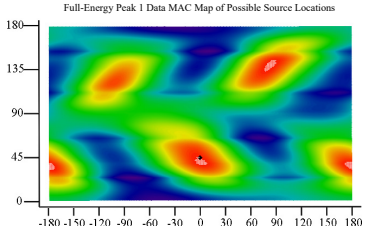

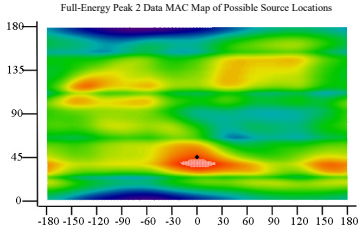

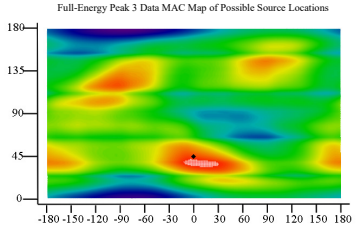

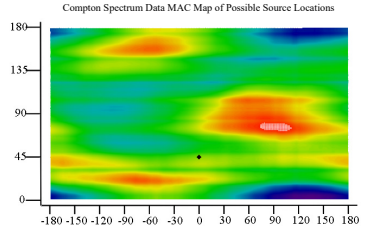

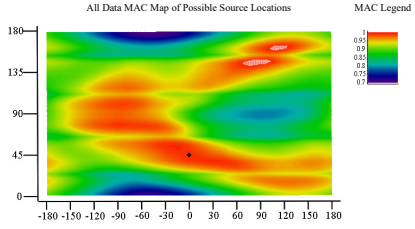

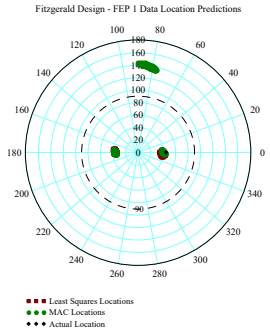

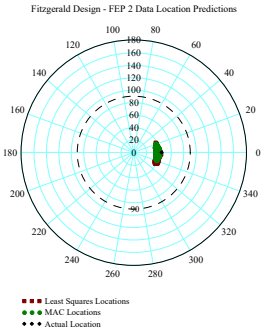

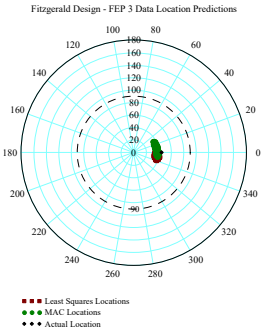

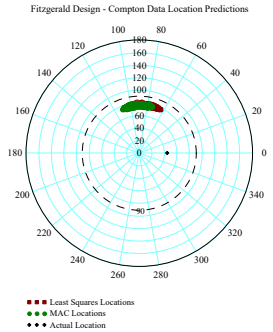

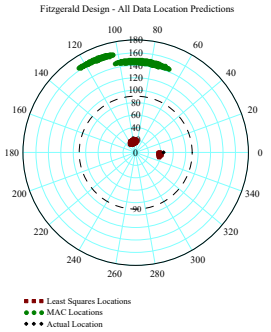

View Angle φ = 55° : Spectrum, Modulation Curve Data (No Smoothing), Library Curve, MAC and Least Squares Direction Predictions

Phi_ViewDegree = 55 Theta_ViewDegree = 0

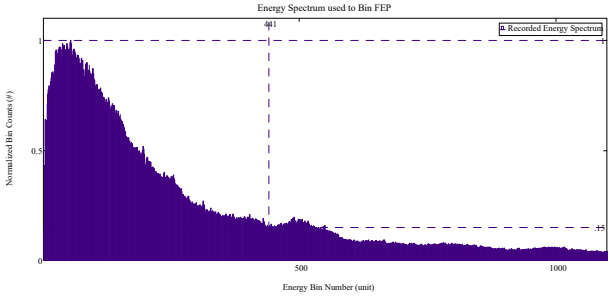

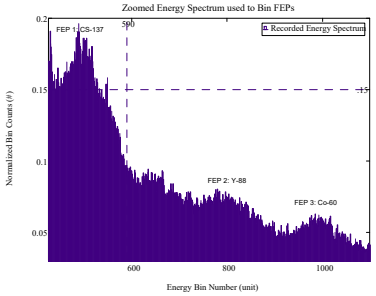

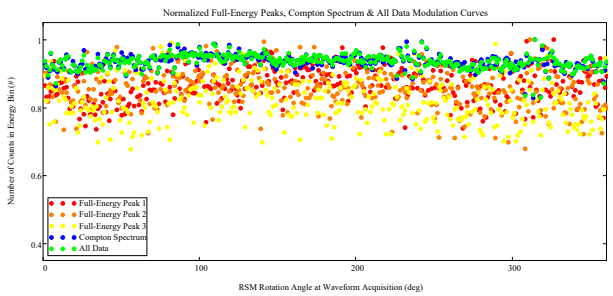

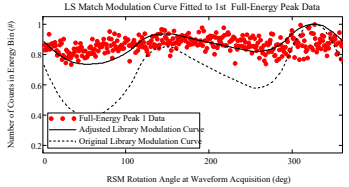

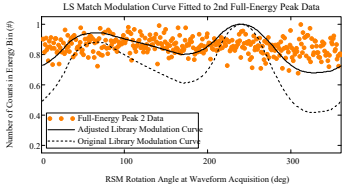

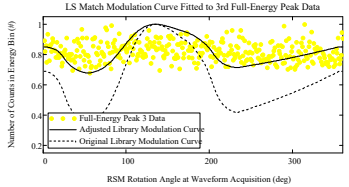

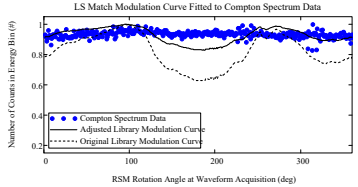

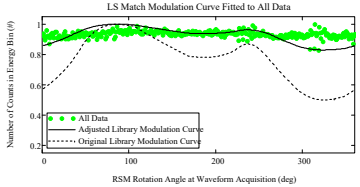

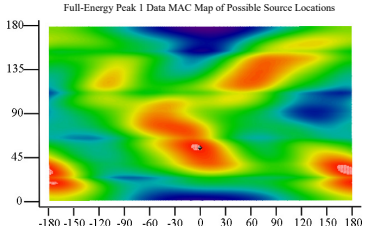

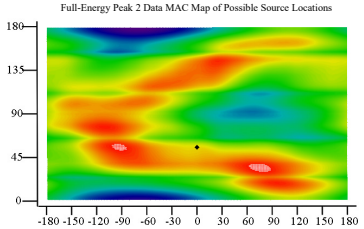

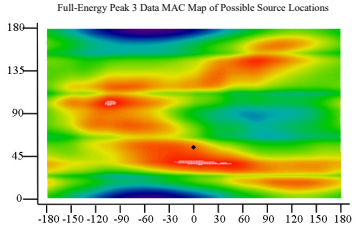

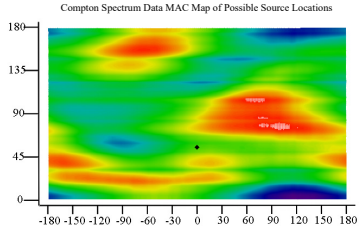

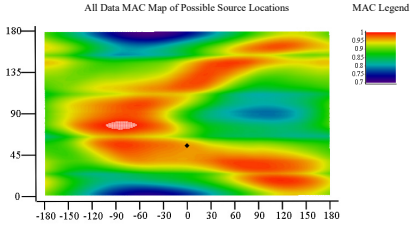

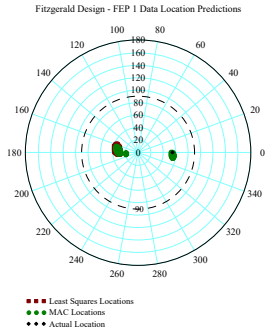

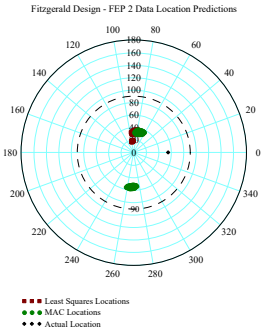

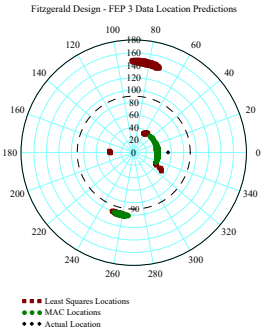

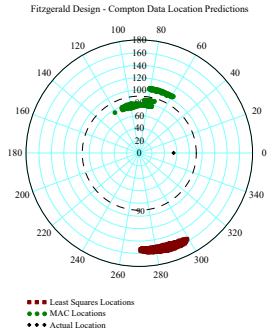

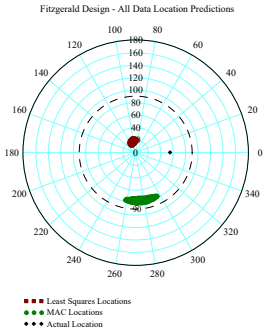

View Angle φ = 65° : Spectrum, Modulation Curve Data (No Smoothing), Library Curve, MAC and Least Squares Direction Predictions

Phi_ViewDegree = 65 Theta_ViewDegree = 0

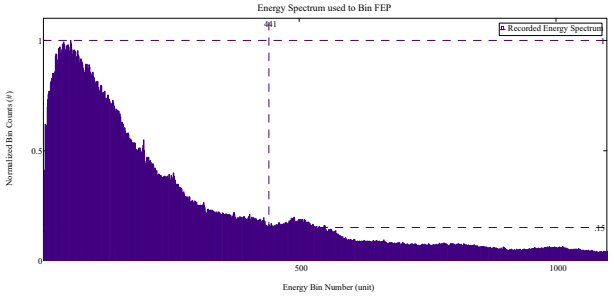

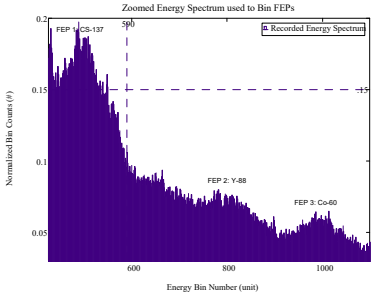

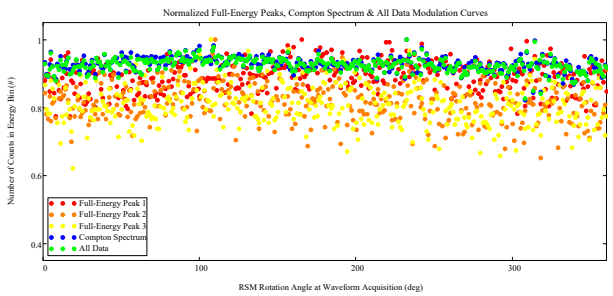

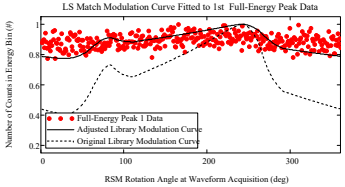

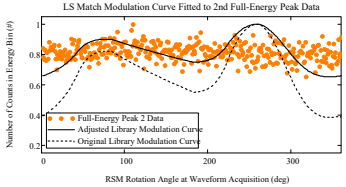

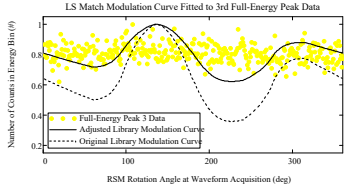

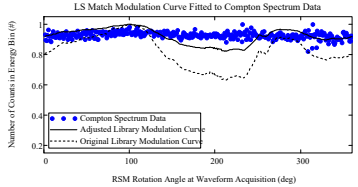

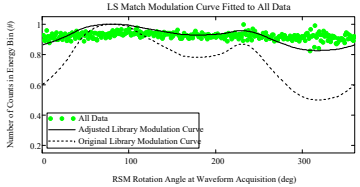

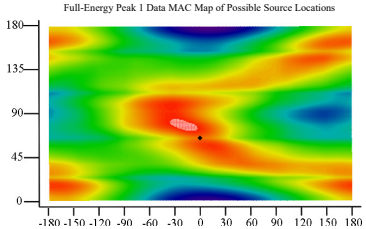

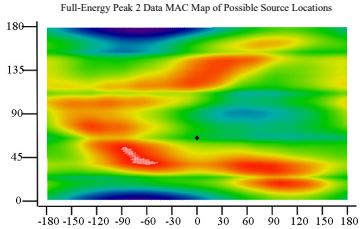

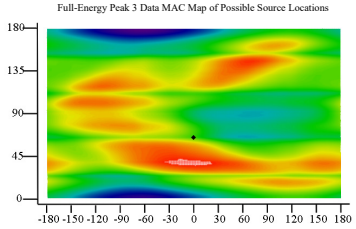

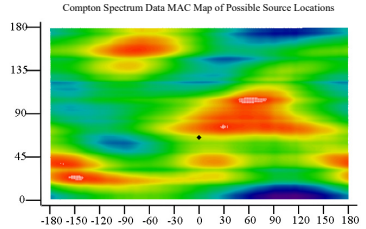

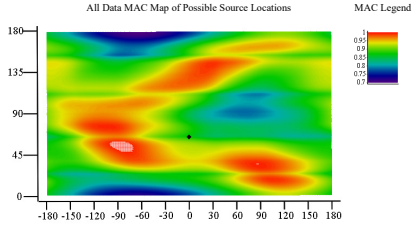

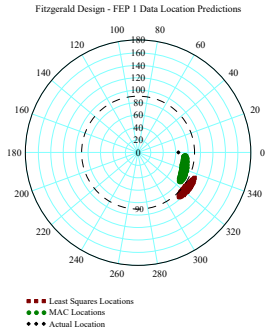

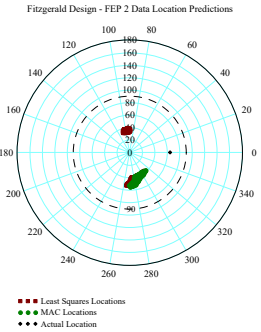

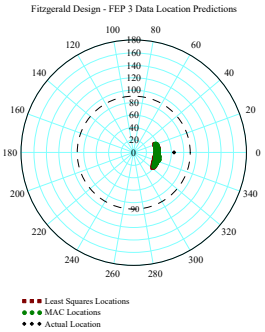

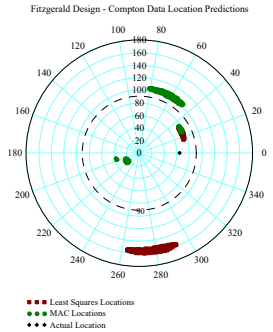

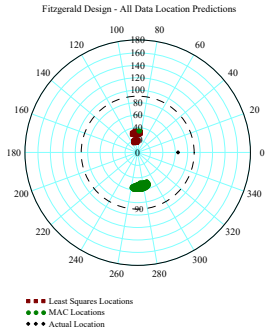

View Angle φ = 75° : Spectrum, Modulation Curve Data (No Smoothing), Library Curve, MAC and Least Squares Direction Predictions

Phi_ViewDegree = 75 Theta_ViewDegree = 0

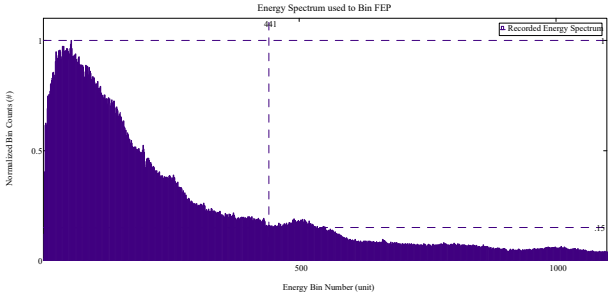

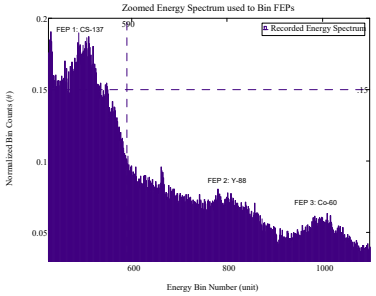

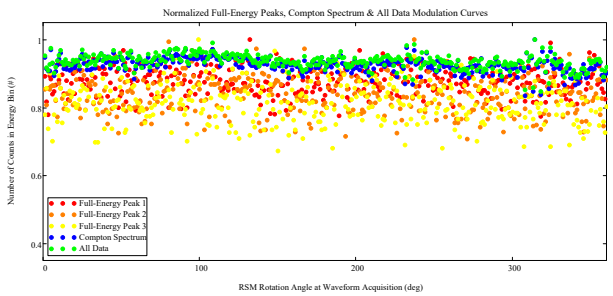

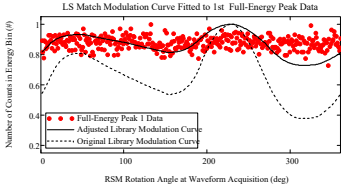

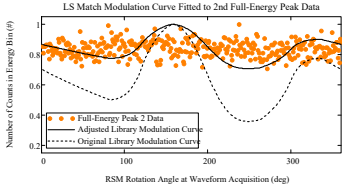

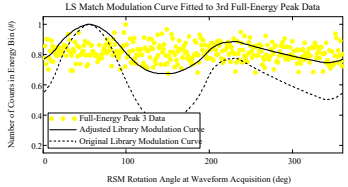

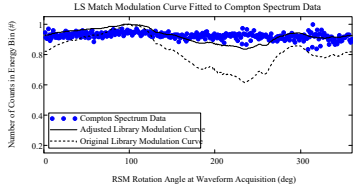

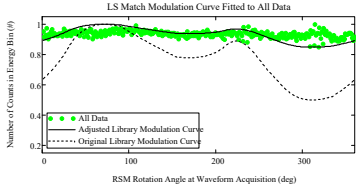

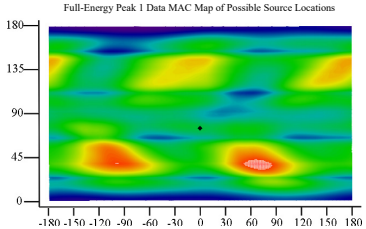

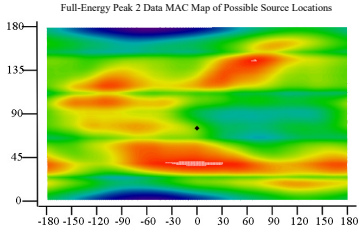

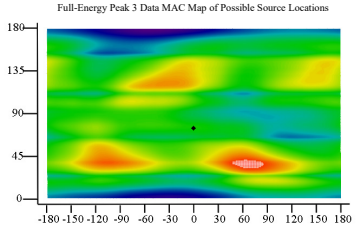

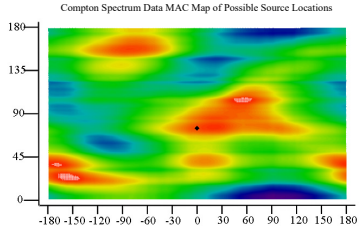

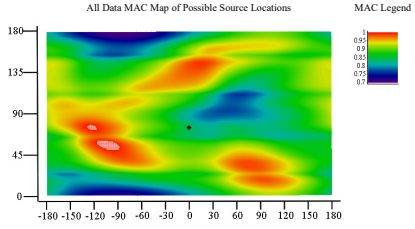

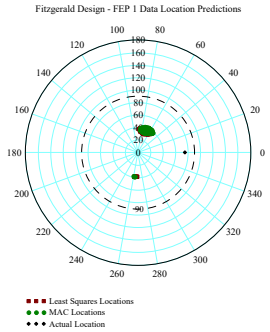

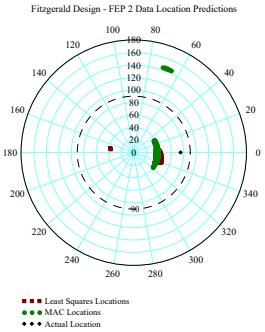

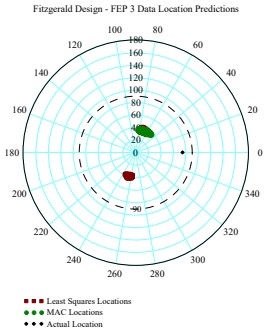

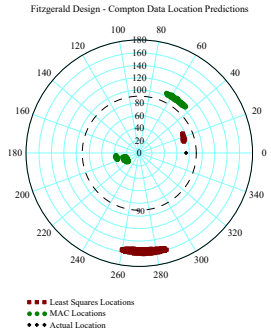

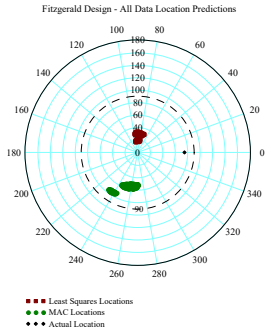

View Angle φ = 85° : Spectrum, Modulation Curve Data (No Smoothing), Library Curve, MAC and Least Squares Direction Predictions

Phi_ViewDegree = 85 Theta_ViewDegree = 0

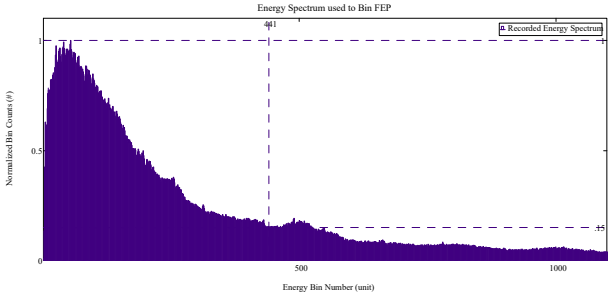

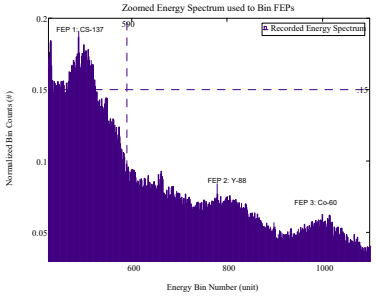

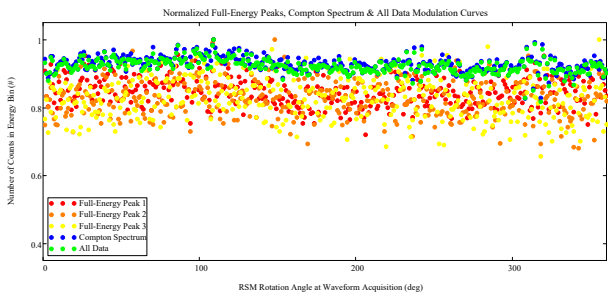

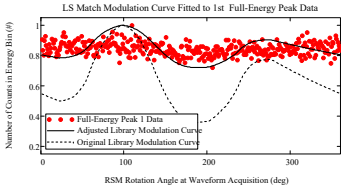

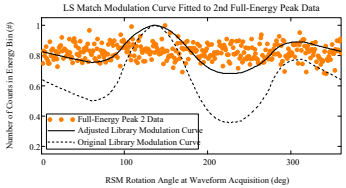

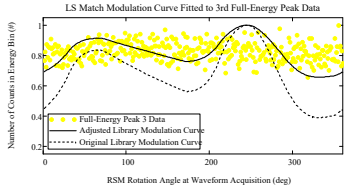

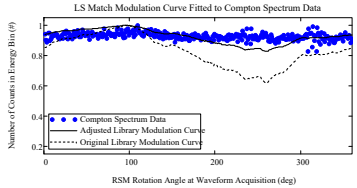

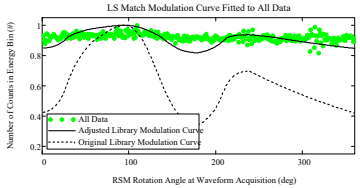

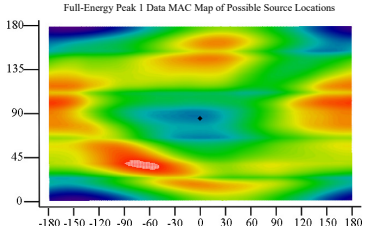

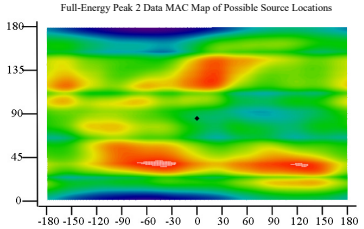

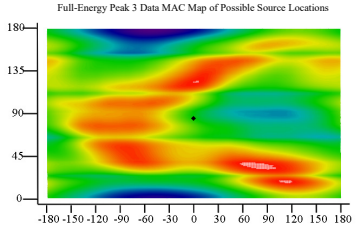

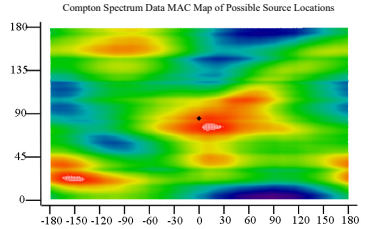

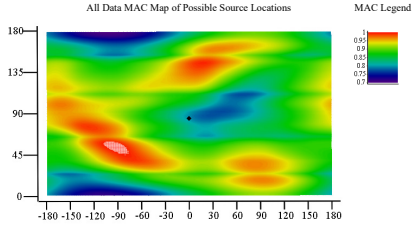

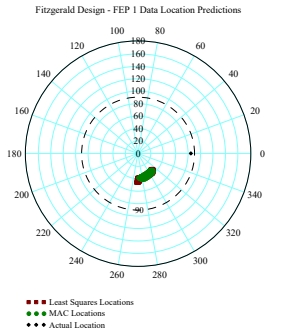

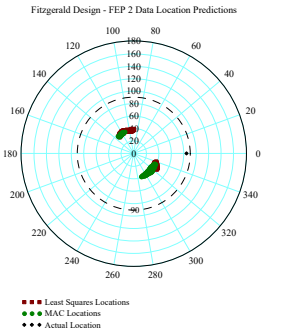

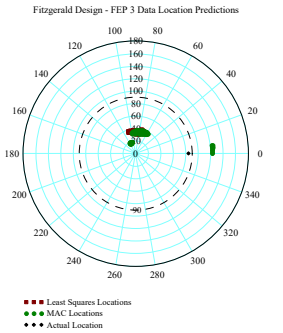

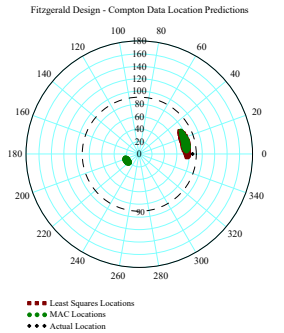

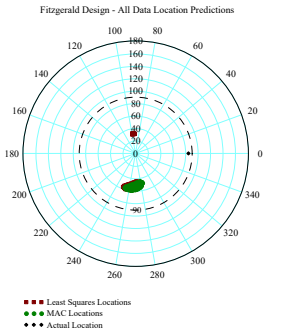

View Angle φ = 95° : Spectrum, Modulation Curve Data (No Smoothing), Library Curve, MAC and Least Squares Direction Predictions

Phi_ViewDegree = 95 Theta_ViewDegree = 0

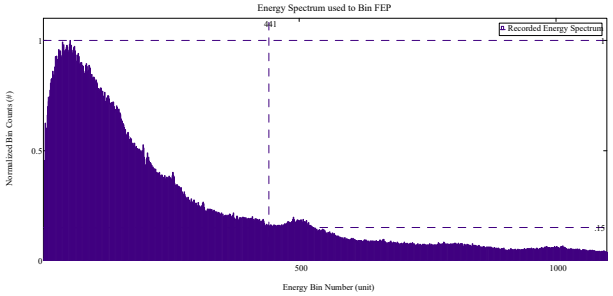

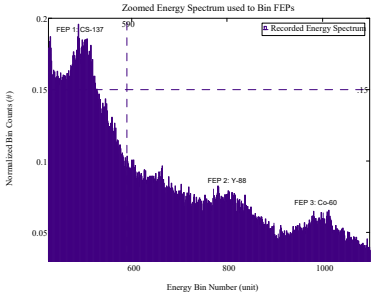

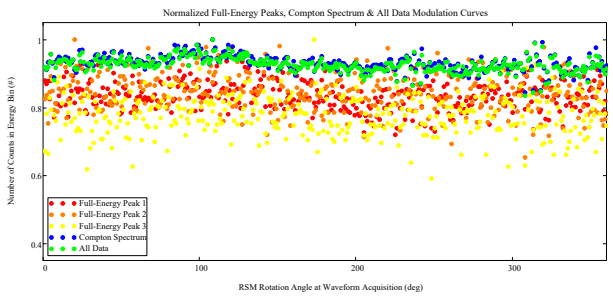

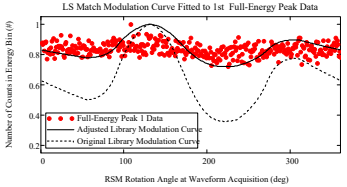

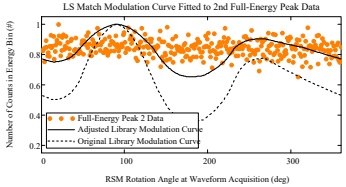

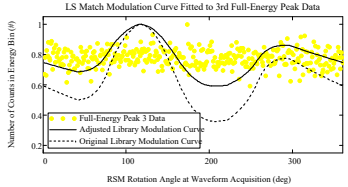

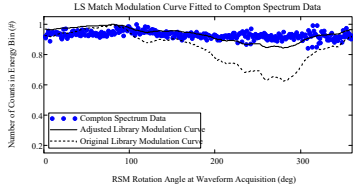

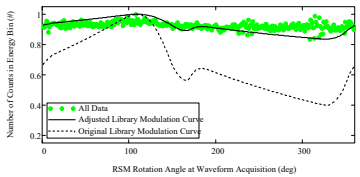

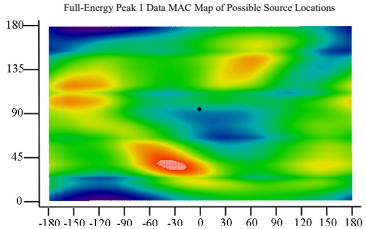

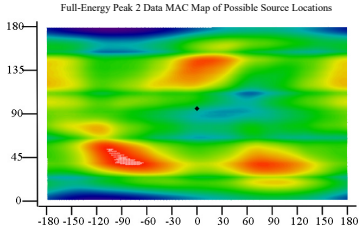

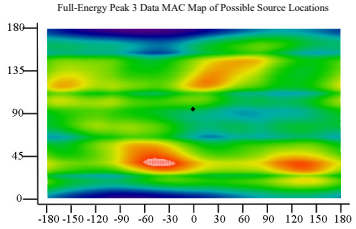

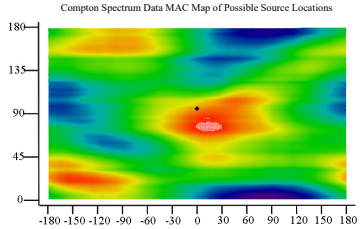

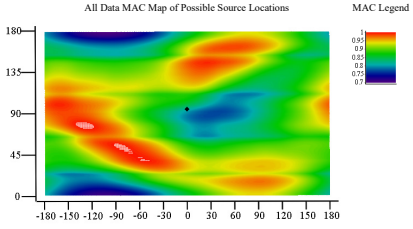

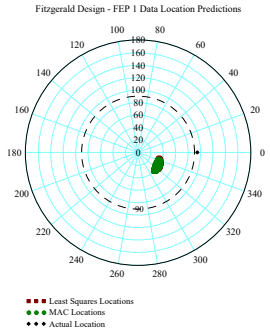

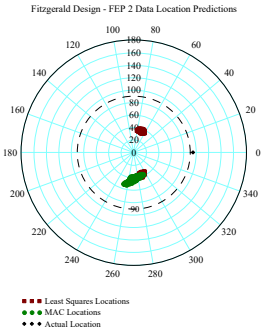

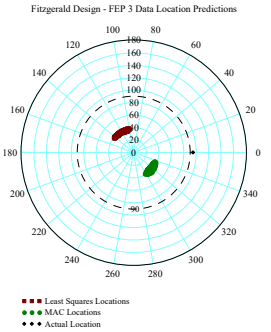

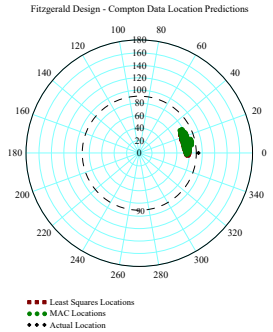

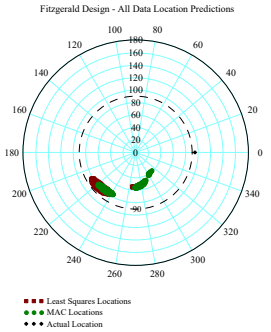

View Angle φ = 105° : Spectrum, Modulation Curve Data (No Smoothing), Library Curve, MAC and Least Squares Direction Predictions

Phi_ViewDegree = 105 Theta_ViewDegree = 0

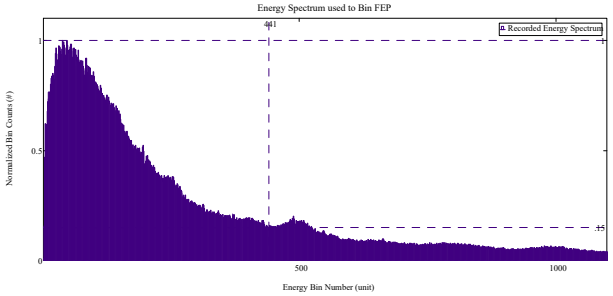

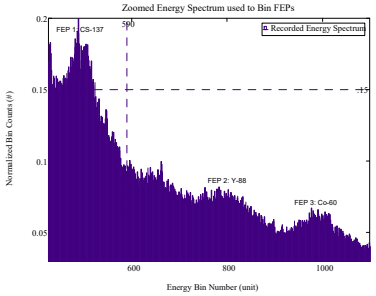

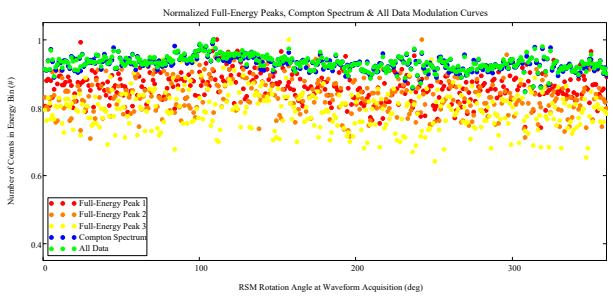

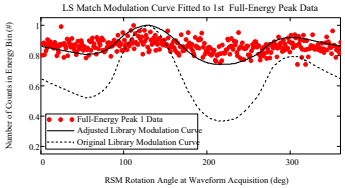

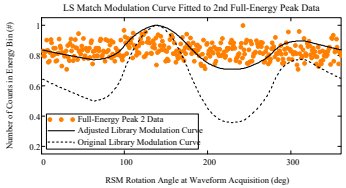

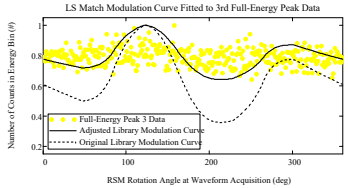

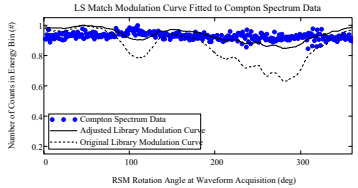

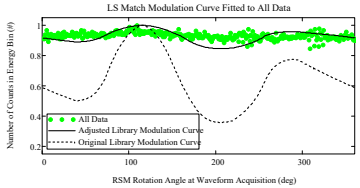

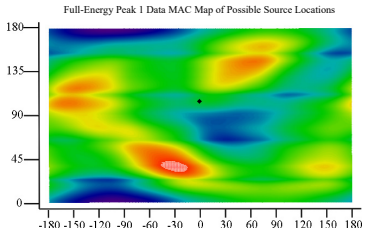

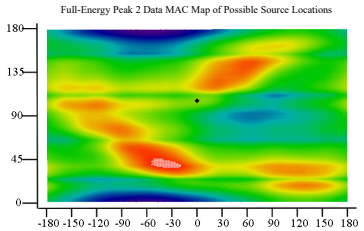

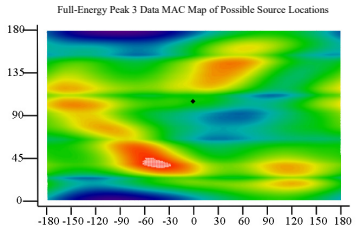

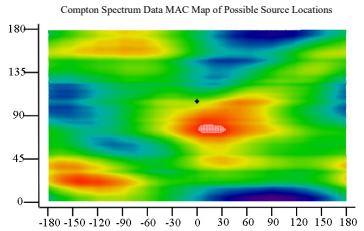

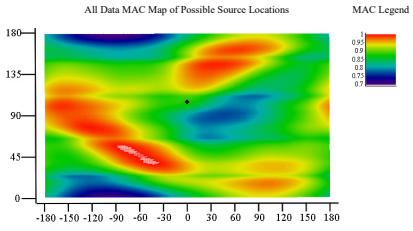

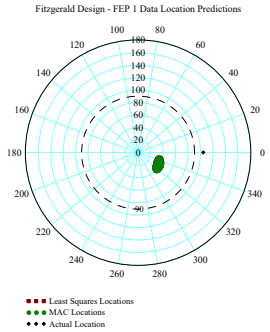

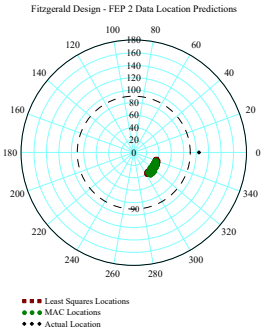

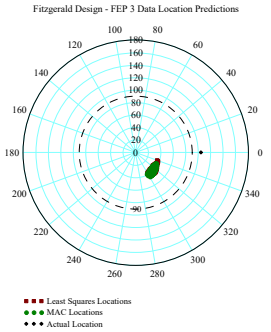

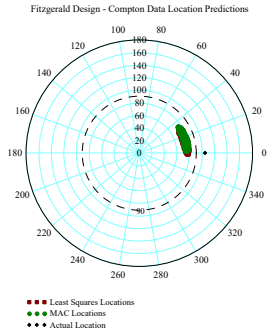

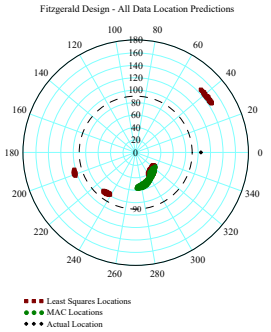

View Angle φ = 115° : Spectrum, Modulation Curve Data (No Smoothing), Library Curve, MAC and Least Squares Direction Predictions

Phi_ViewDegree = 115 Theta_ViewDegree = 0

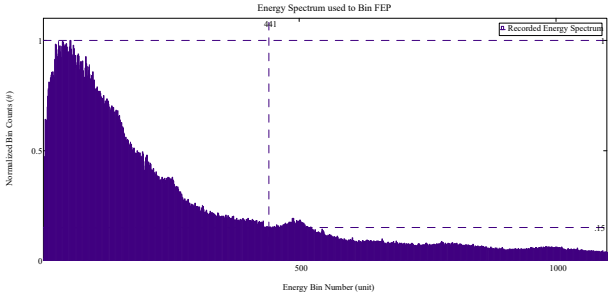

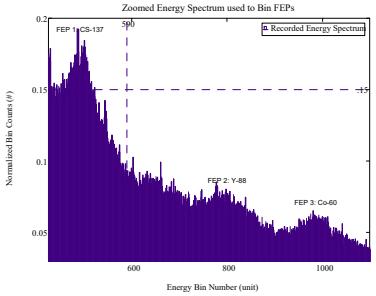

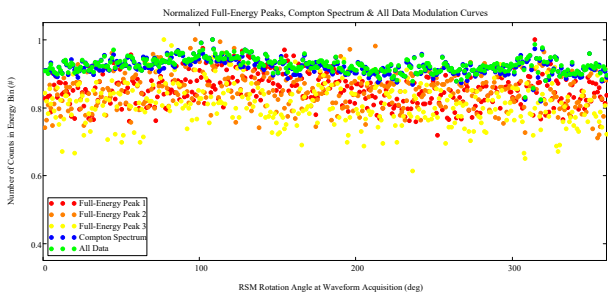

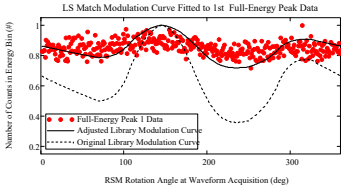

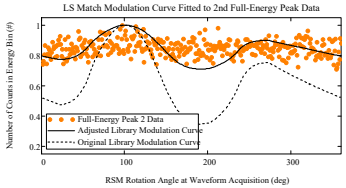

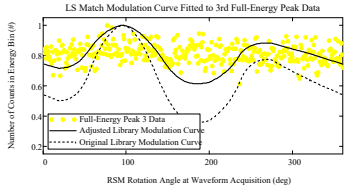

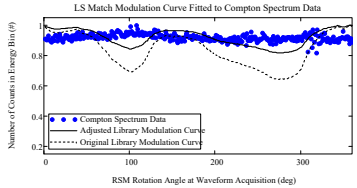

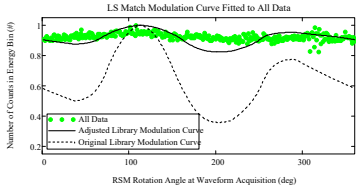

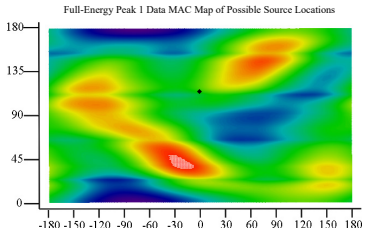

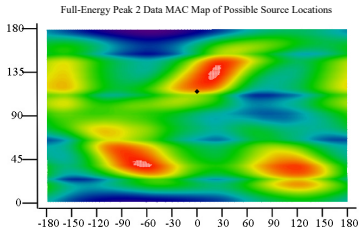

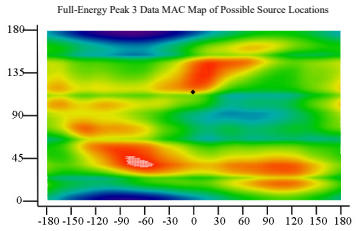

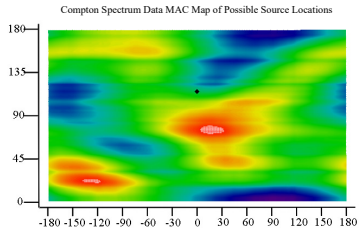

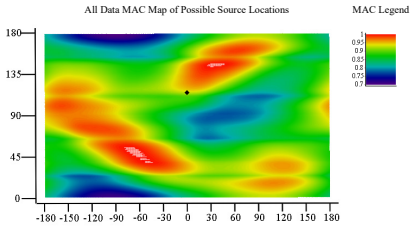

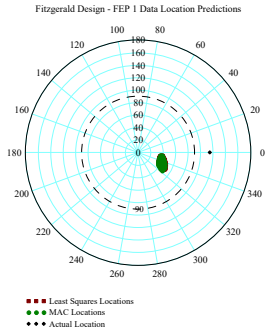

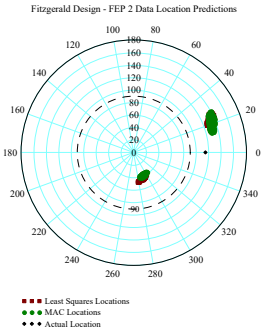

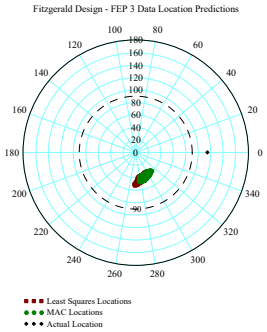

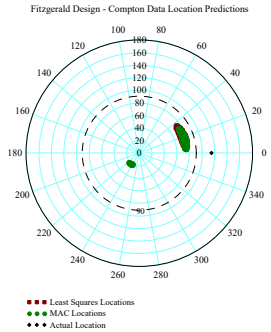

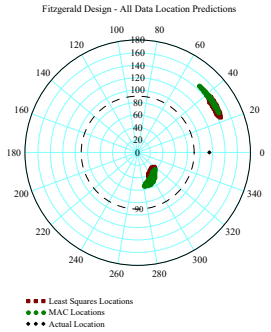

View Angle φ = 125° : Spectrum, Modulation Curve Data (No Smoothing), Library Curve, MAC and Least Squares Direction Predictions

Phi_ViewDegree = 125 Theta_ViewDegree = 0

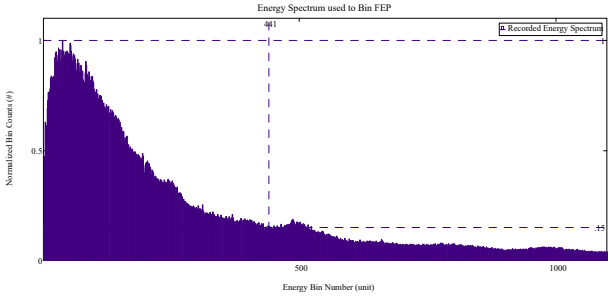

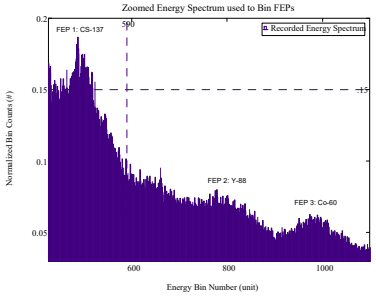

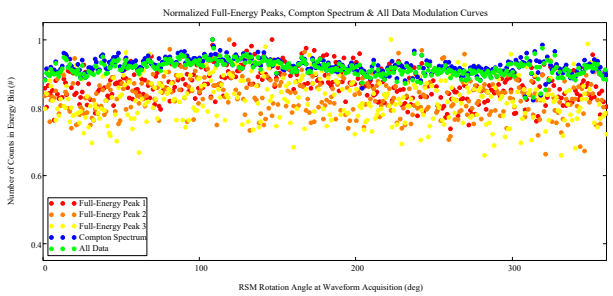

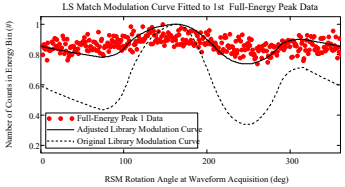

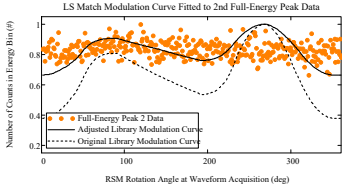

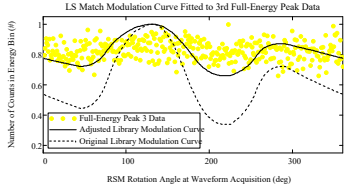

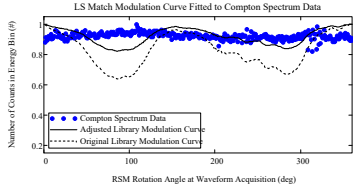

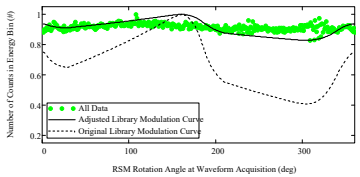

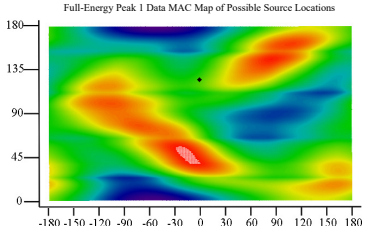

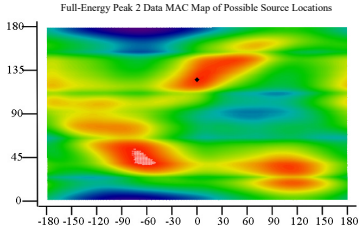

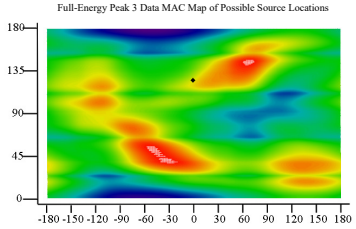

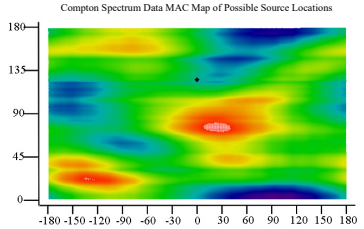

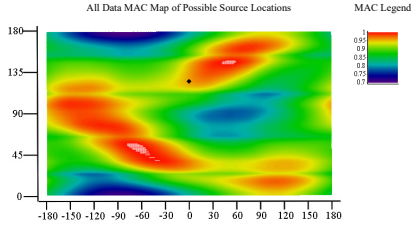

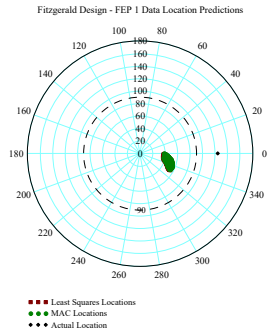

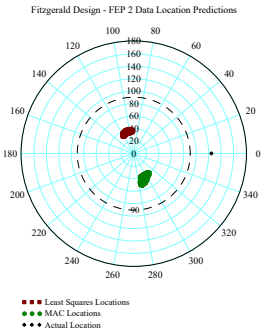

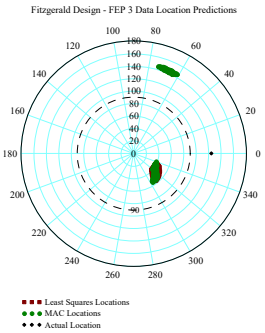

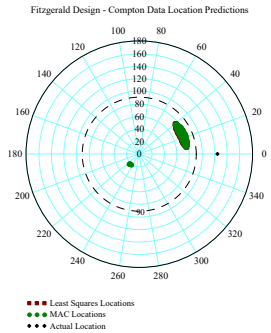

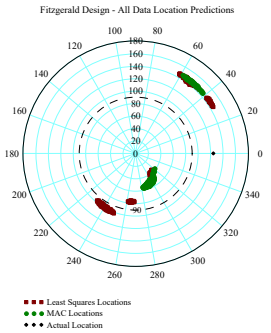

View Angle φ = 135° : Spectrum, Modulation Curve Data (No Smoothing), Library Curve, MAC and Least Squares Direction Predictions

Phi_ViewDegree = 135 Theta_ViewDegree = 0

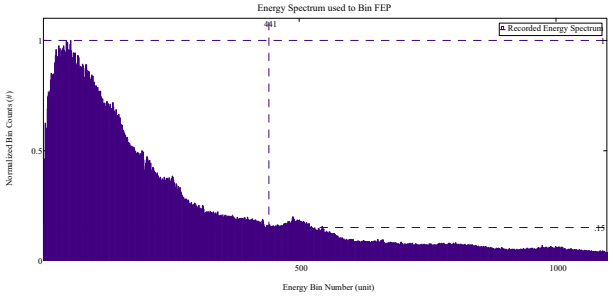

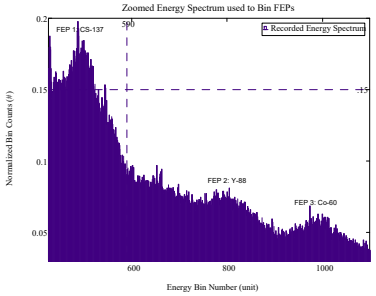

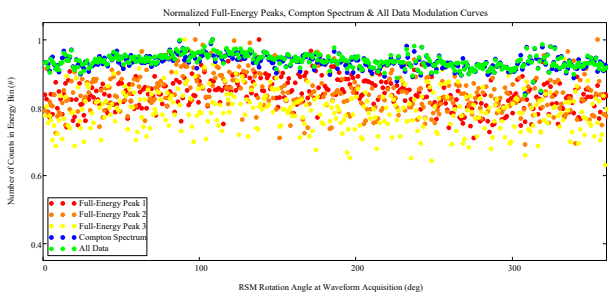

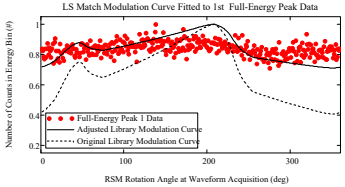

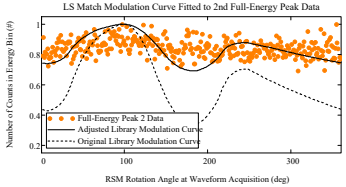

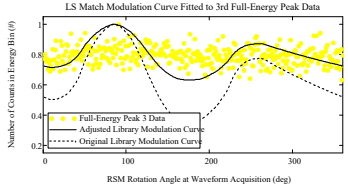

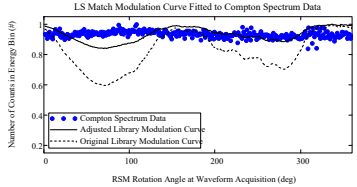

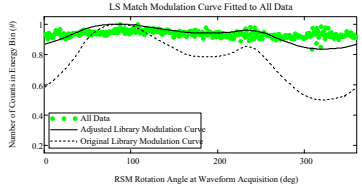

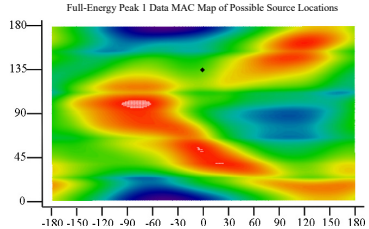

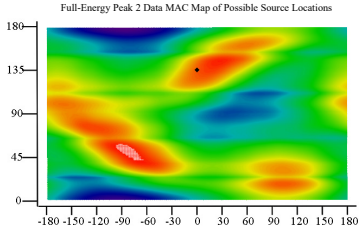

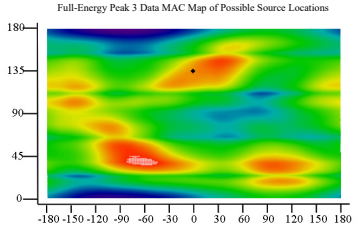

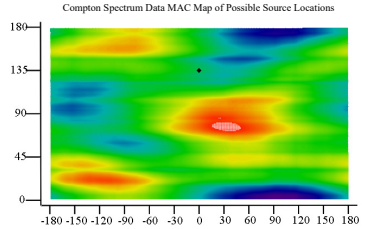

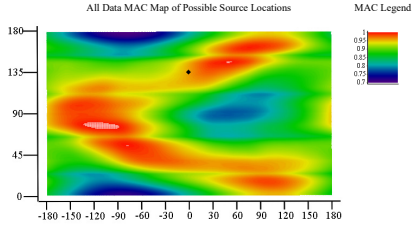

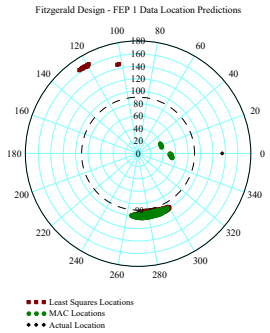

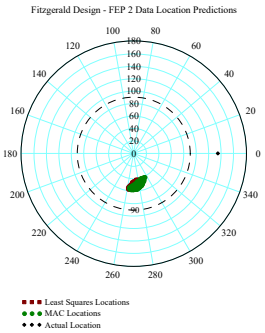

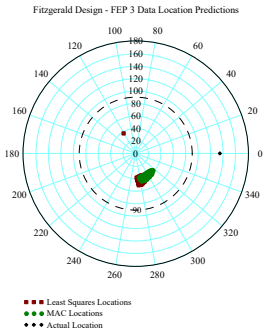

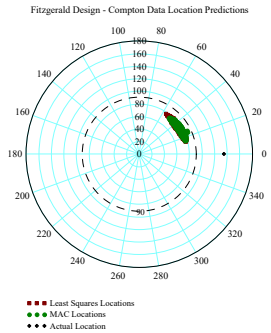

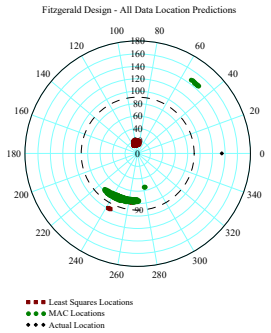

View Angle φ = 145° : Spectrum, Modulation Curve Data (No Smoothing), Library Curve, MAC and Least Squares Direction Predictions

Phi_ViewDegree = 145 Theta_ViewDegree = 0

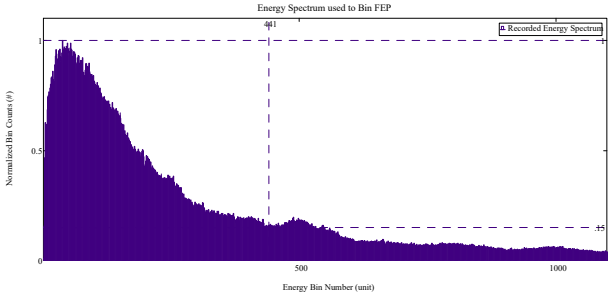

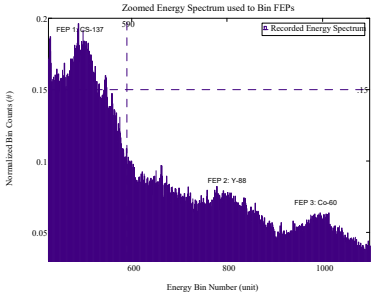

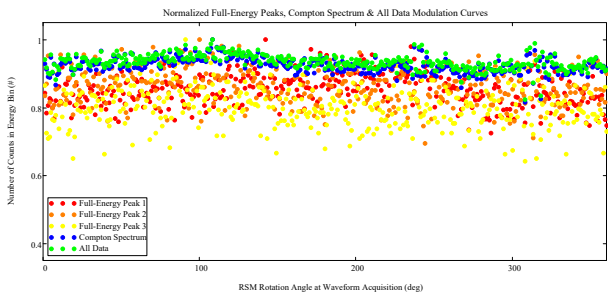

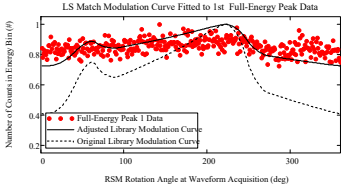

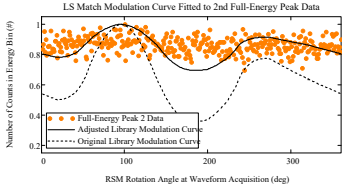

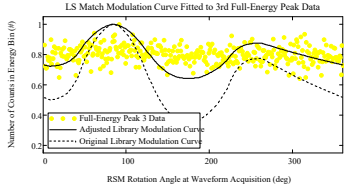

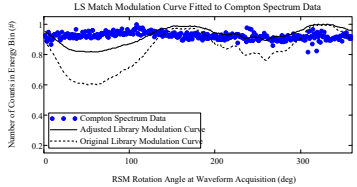

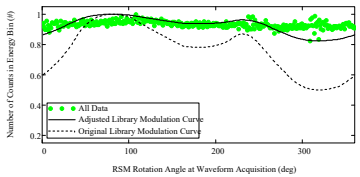

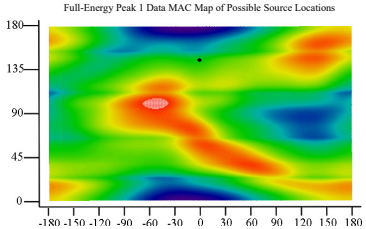

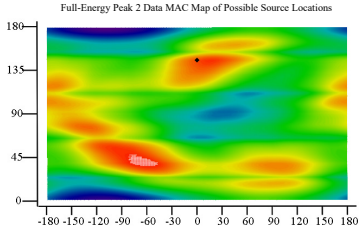

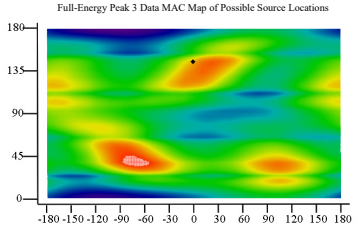

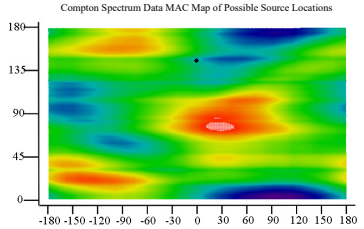

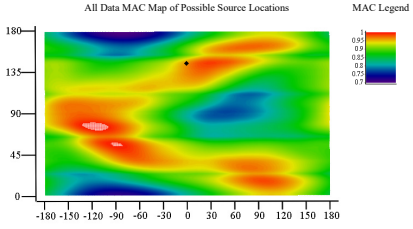

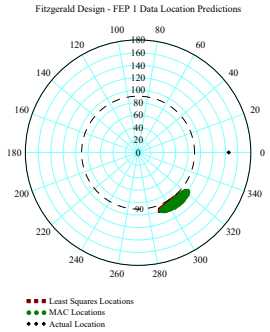

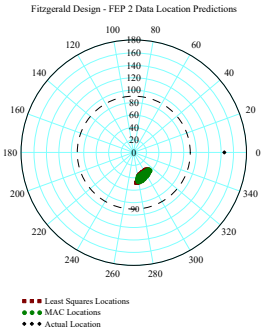

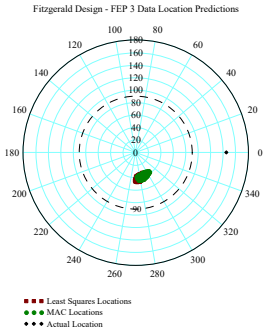

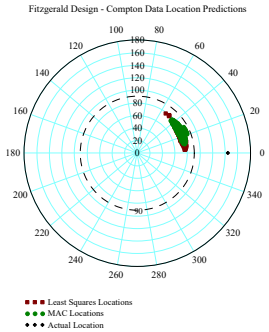

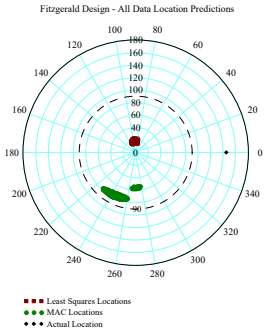

View Angle φ = 155° : Spectrum, Modulation Curve Data (No Smoothing), Library Curve, MAC and Least Squares Direction Predictions

Phi_ViewDegree = 155 Theta_ViewDegree = 0

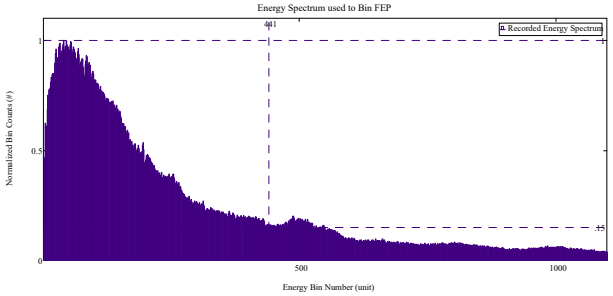

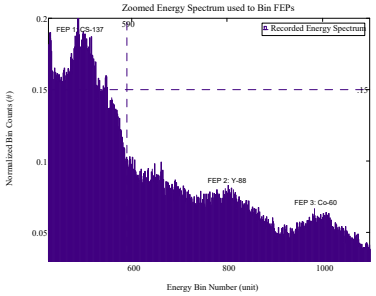

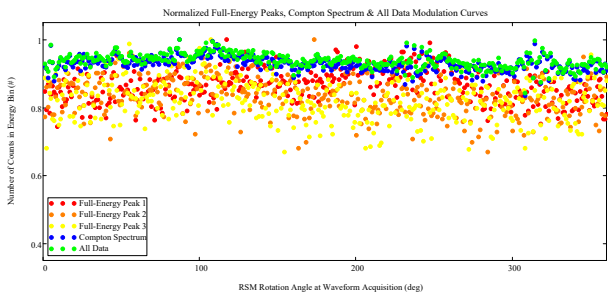

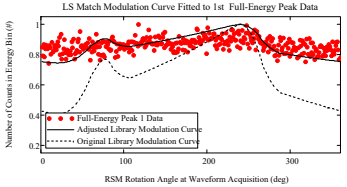

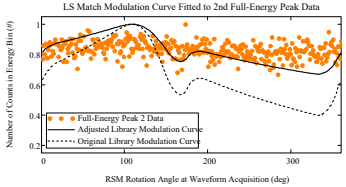

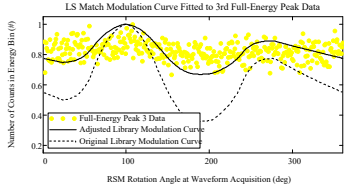

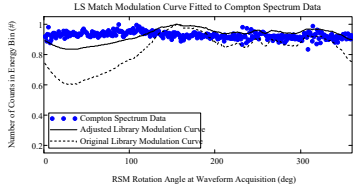

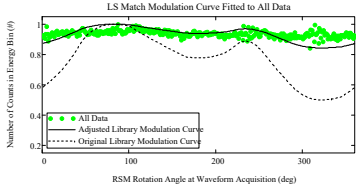

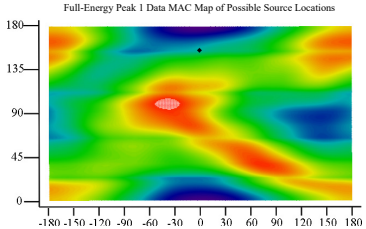

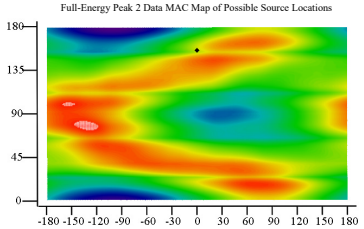

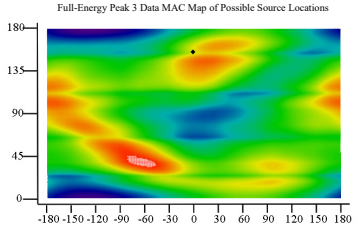

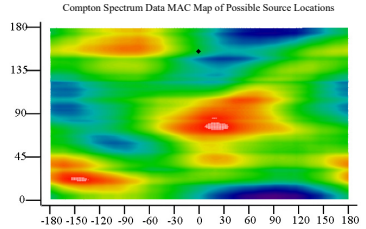

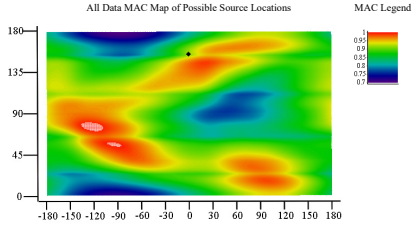

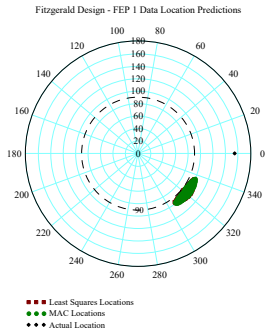

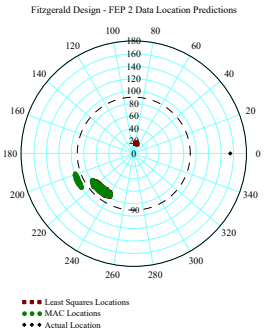

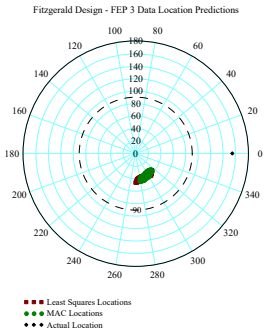

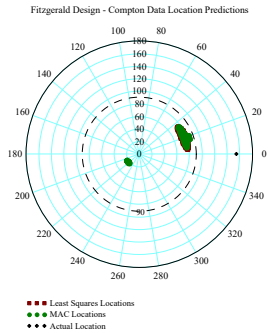

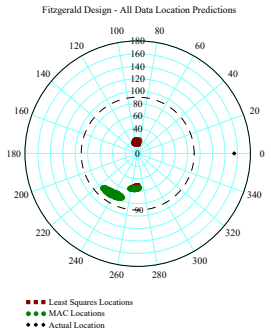

View Angle φ = 165° : Spectrum, Modulation Curve Data (No Smoothing), Library Curve, MAC and Least Squares Direction Predictions

Phi_ViewDegree = 165 Theta_ViewDegree = 0

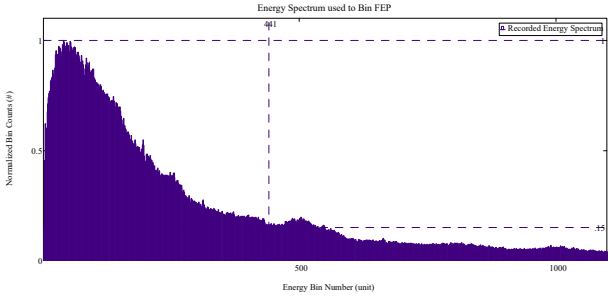

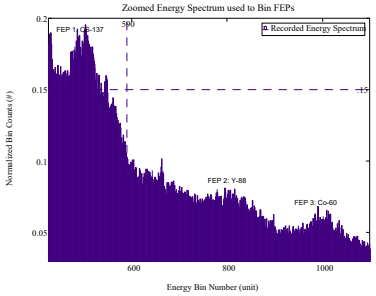

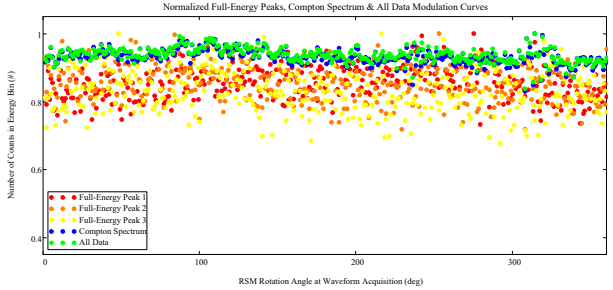

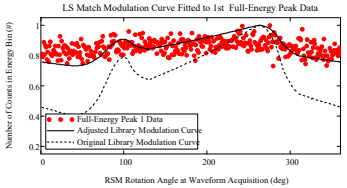

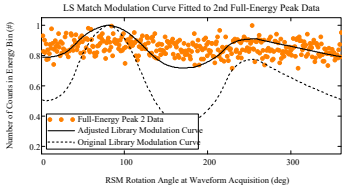

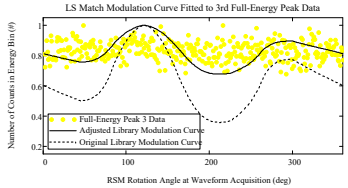

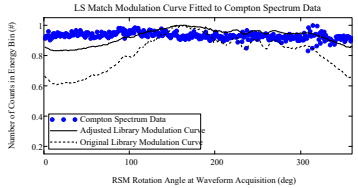

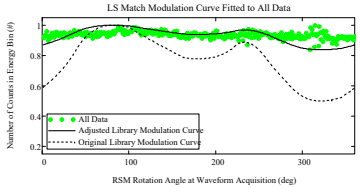

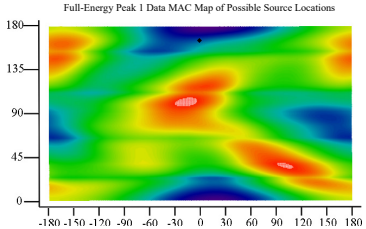

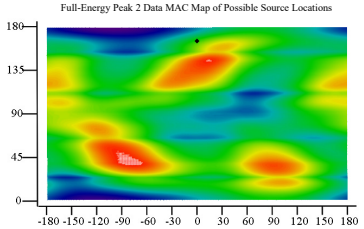

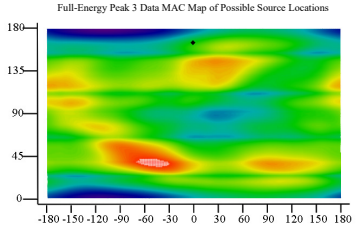

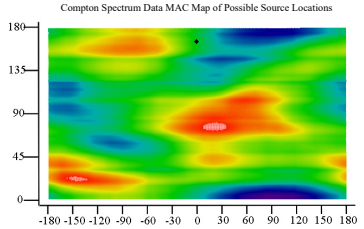

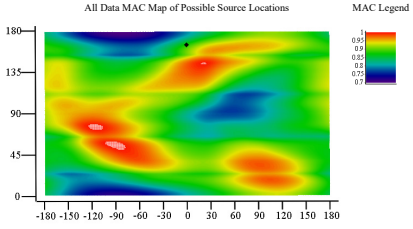

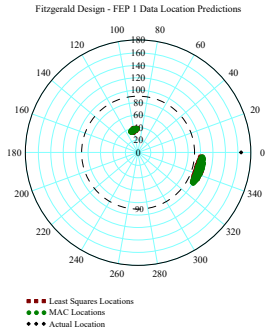

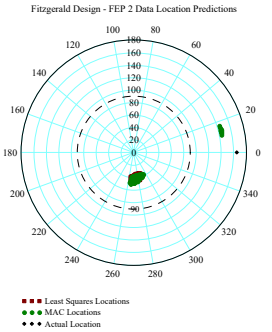

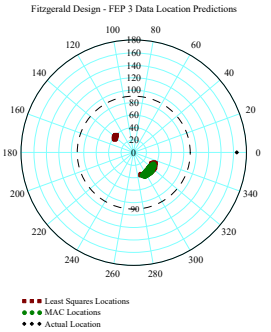

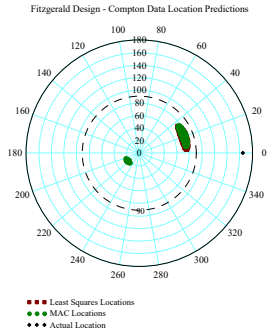

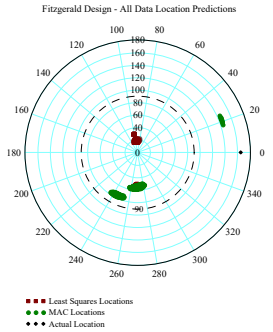

View Angle φ = 175° : Spectrum, Modulation Curve Data (No Smoothing), Library Curve, MAC and Least Squares Direction Predictions

Phi_ViewDegree = 175 Theta_ViewDegree = 0

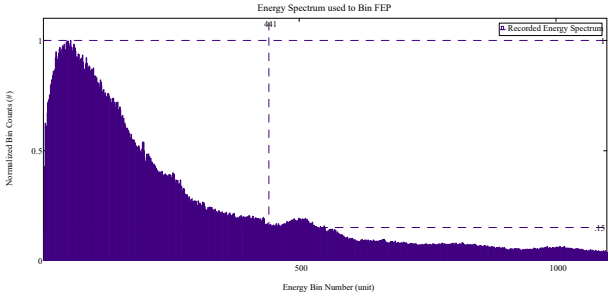

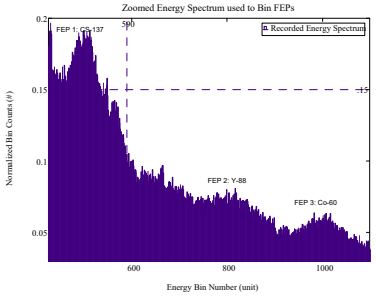

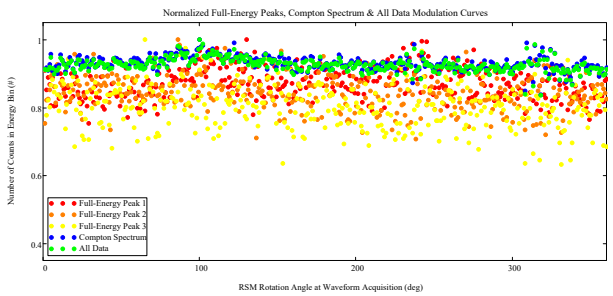

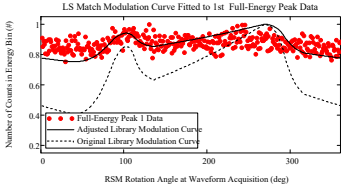

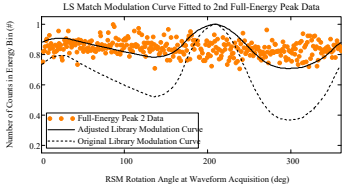

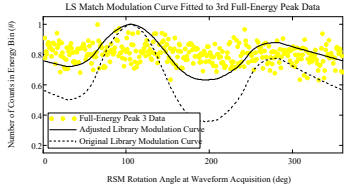

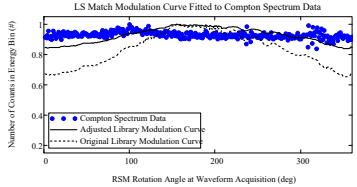

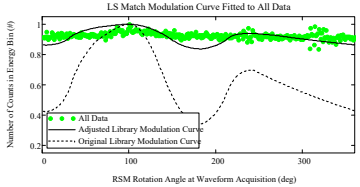

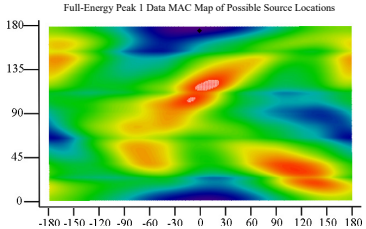

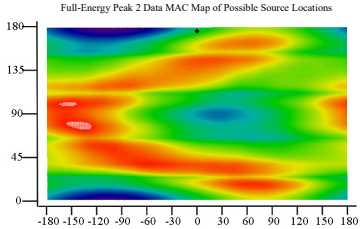

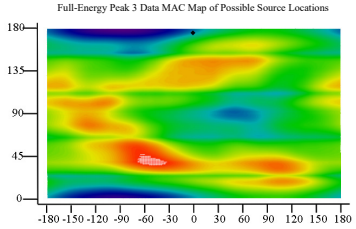

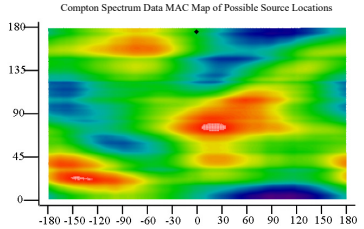

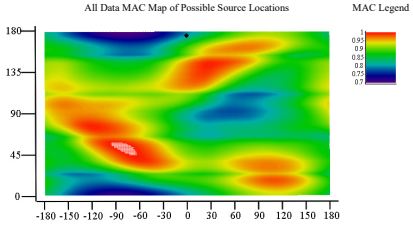

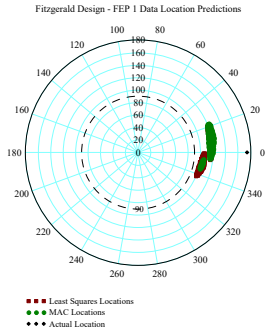

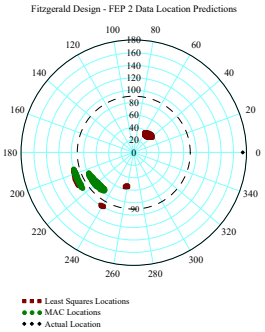

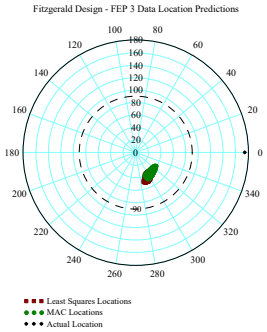

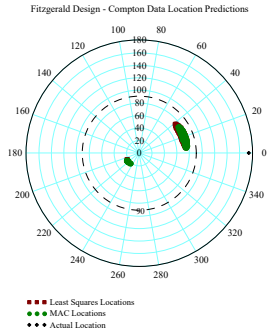

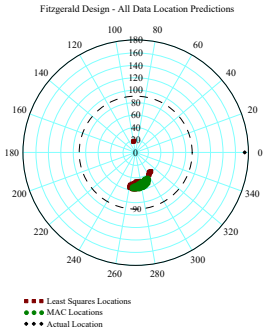

Appendix A.2.1: Large FitzGerald Design RSM Data, NaI Detector, Multinuclide Source; Experimentally Derived Library Matching Results Modulation Curve Smoothing Comparison for View Angle φ = 45°

View Angle φ = 45° : Spectrum, Modulation Curve Data (No Smoothing), Library Curve, MAC and Least Squares Direction Predictions

Phi_ViewDegree = 45 Theta_ViewDegree = 0

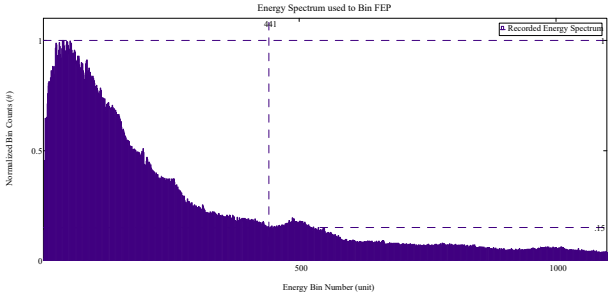

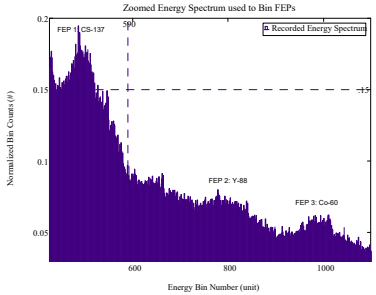

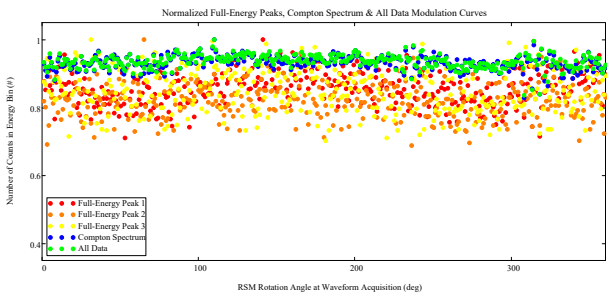

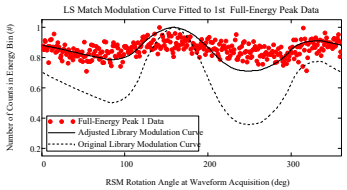

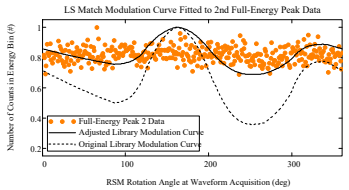

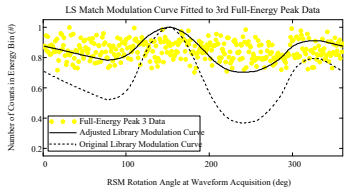

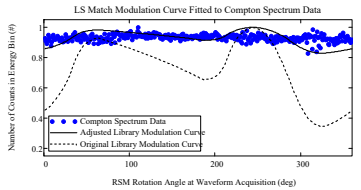

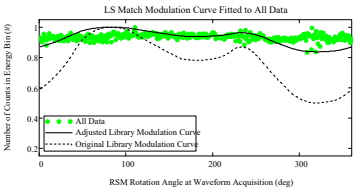

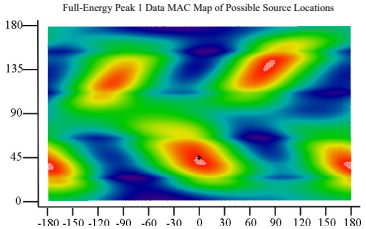

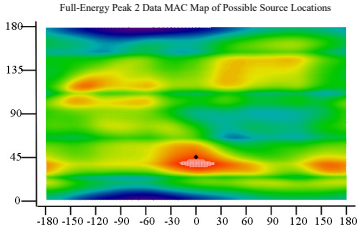

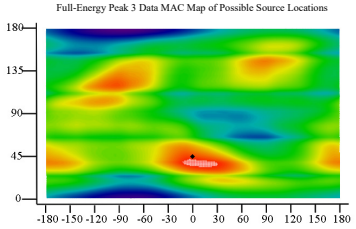

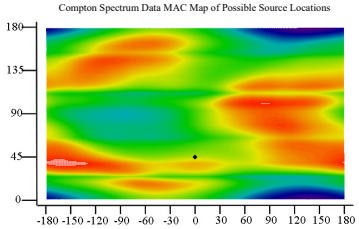

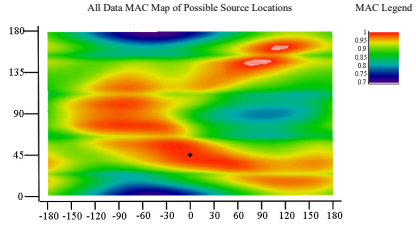

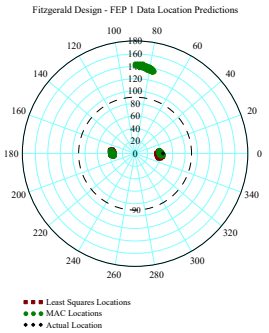

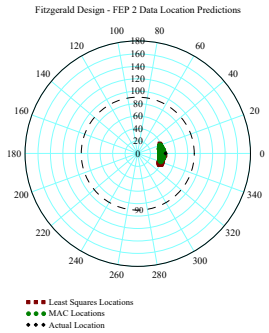

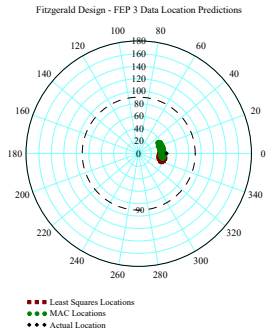

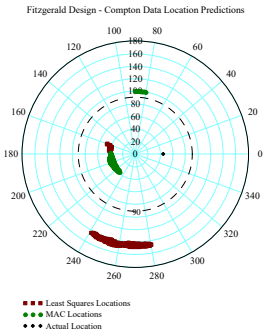

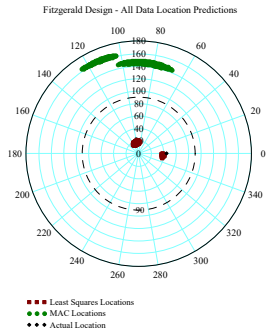

View Angle φ = 45° : Spectrum, Modulation Curve Data (5 Smoothing), Library Curve, MAC and Least Squares Direction Predictions

Phi_ViewDegree = 45 Theta_ViewDegree = 0

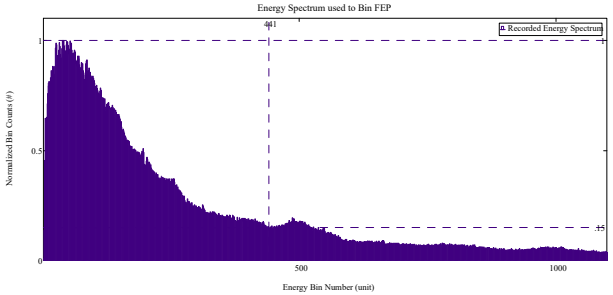

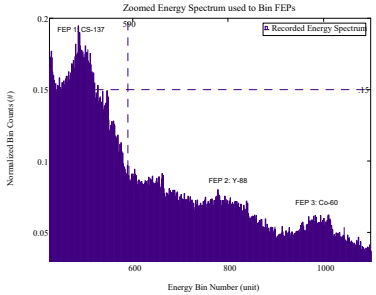

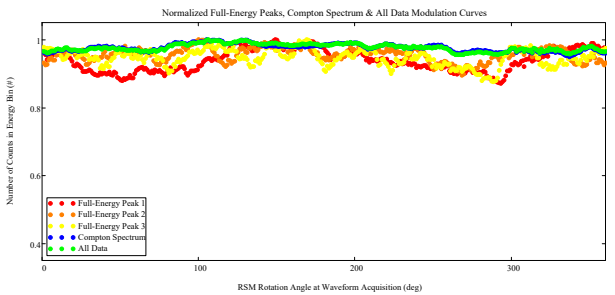

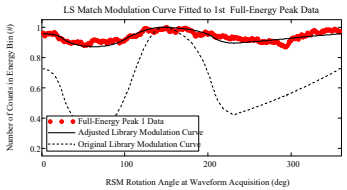

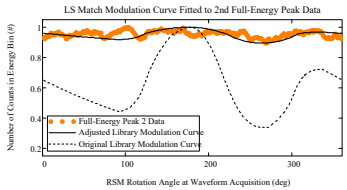

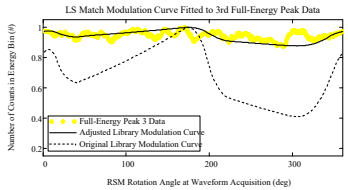

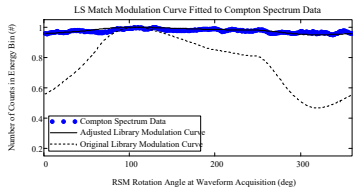

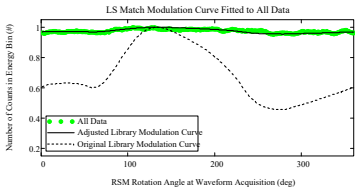

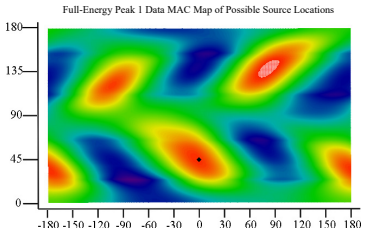

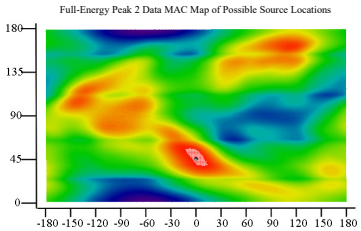

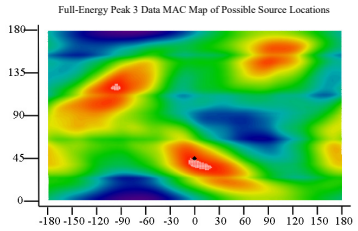

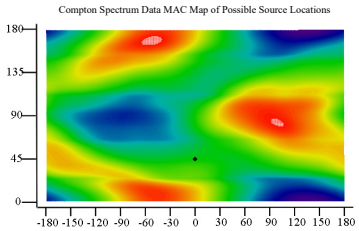

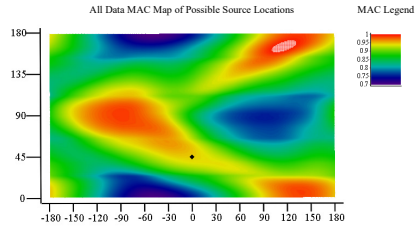

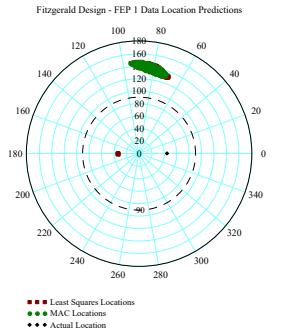

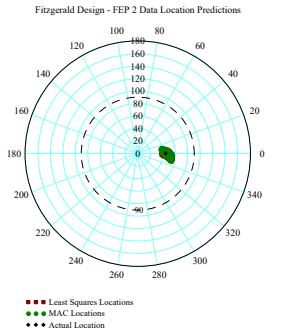

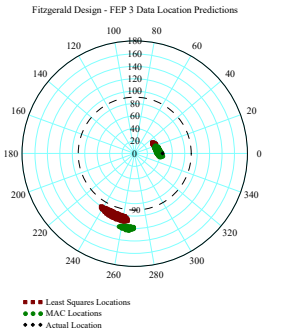

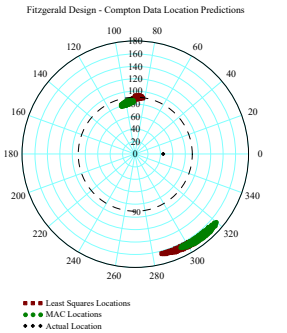

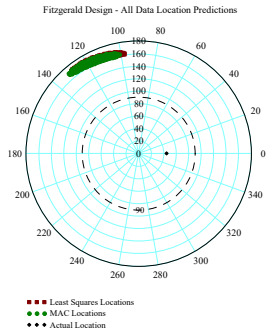

View Angle φ = 45° : Spectrum, Modulation Curve Data (10 Smoothing), Library Curve, MAC and Least Squares Direction Predictions

Phi_ViewDegree = 45 Theta_ViewDegree = 0

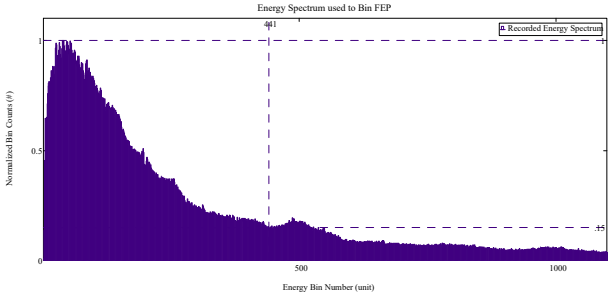

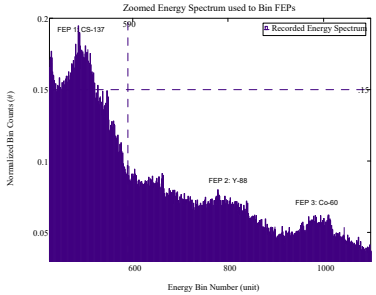

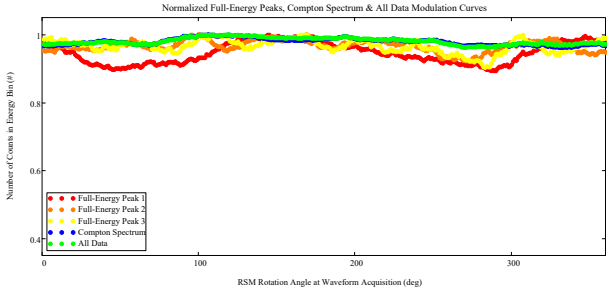

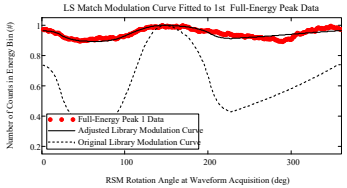

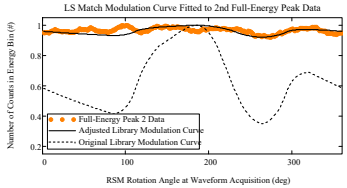

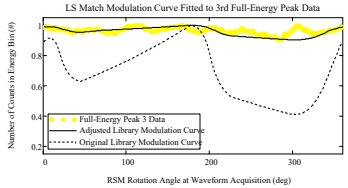

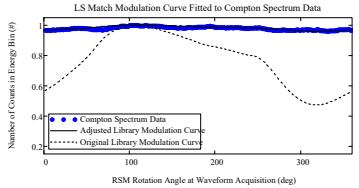

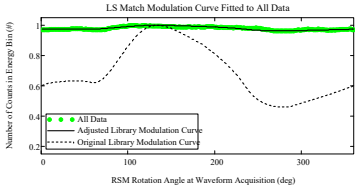

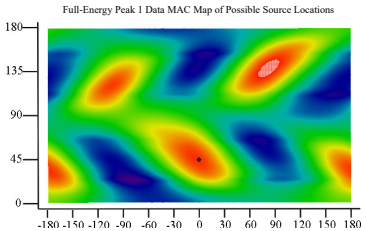

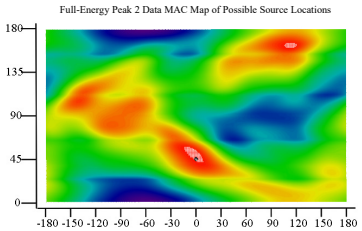

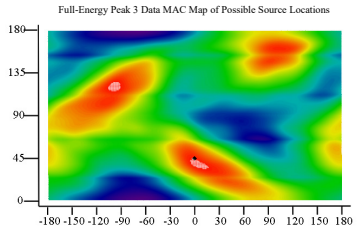

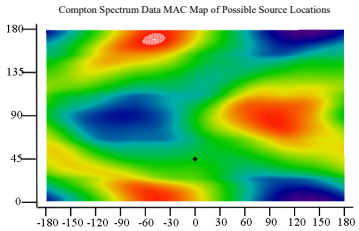

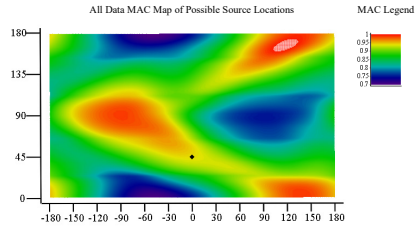

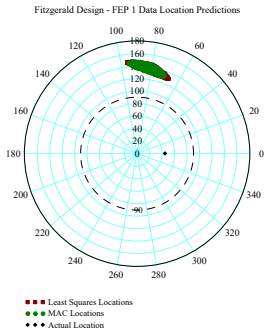

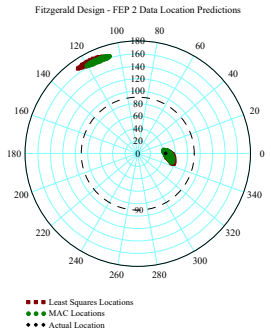

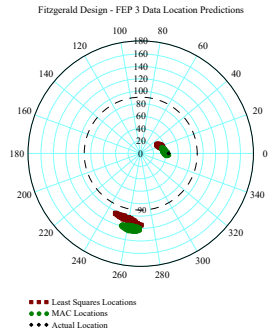

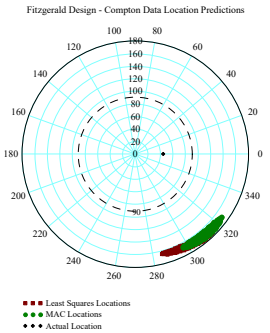

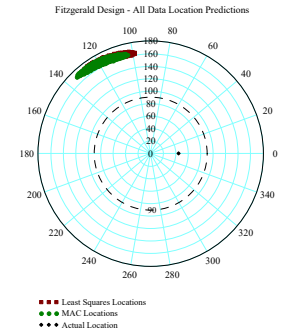

View Angle φ = 45° : Spectrum, Modulation Curve Data (20 Smoothing), Library Curve, MAC and Least Squares Direction Predictions

Phi_ViewDegree = 45 Theta_ViewDegree = 0

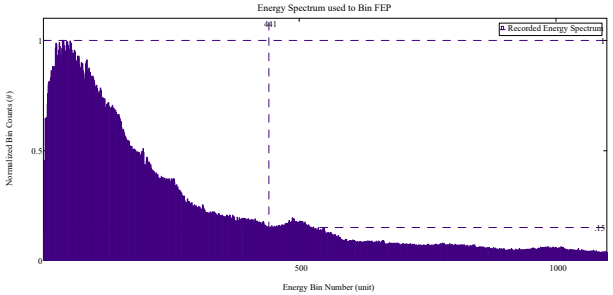

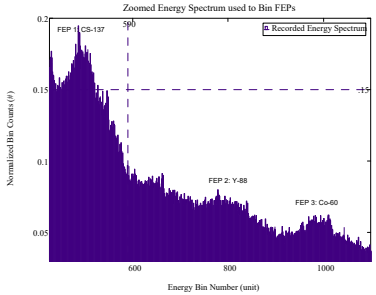

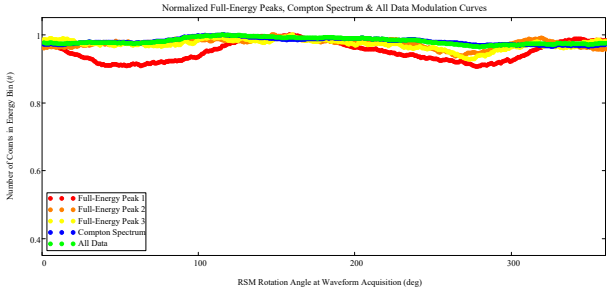

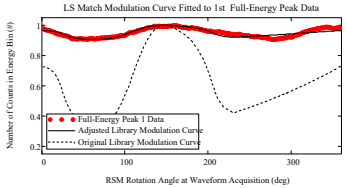

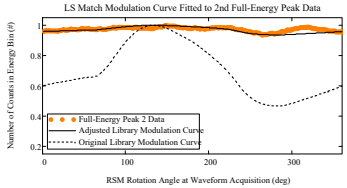

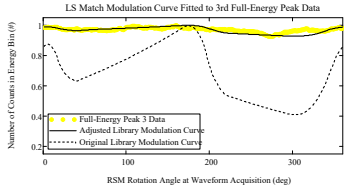

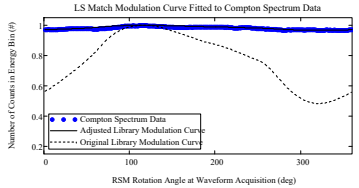

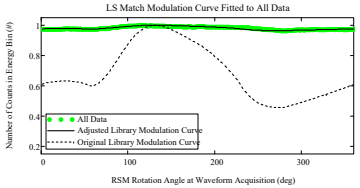

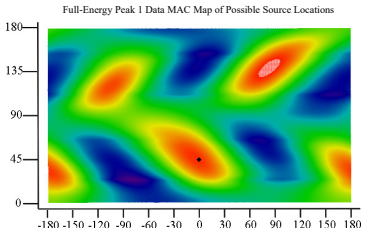

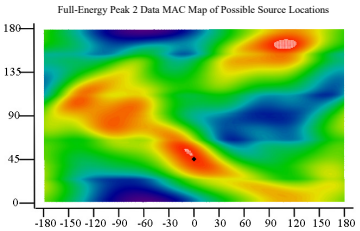

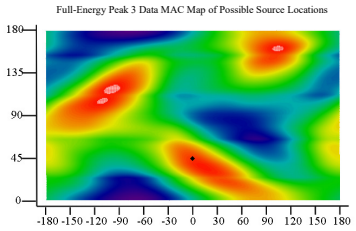

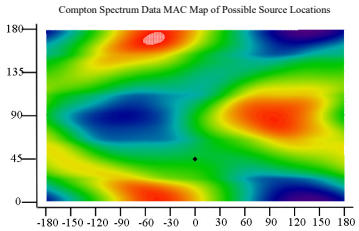

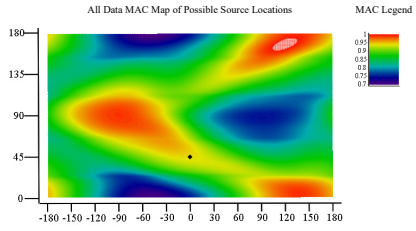

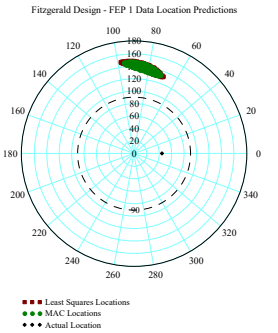

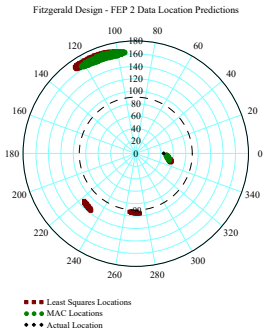

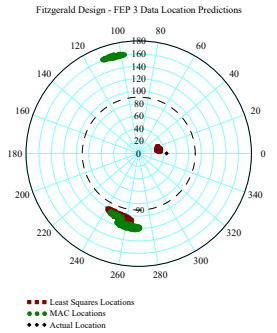

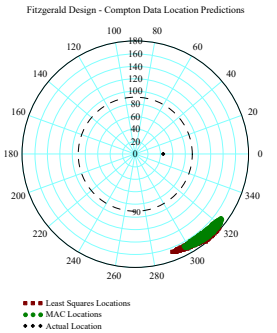

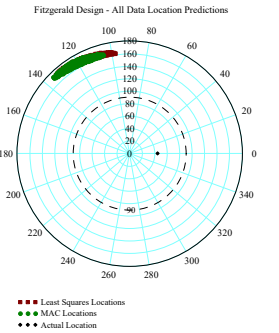

Appendix A.3: Large FitzGerald Design RSM Data, NaI Detector, Cs-137 Single Source, Encoder Ring Reader Equipment Failure; Experimentally Derived Library Matching Results for Missing/Stretched Modulation Curve Recovery Work

View Angle φ = 125° : Missing/Stretched Encoder Data Spectrum, Modulation Curve, Library Curve, MAC and LS Direction Predictions

Phi_ViewDegree= 125 theta = 0

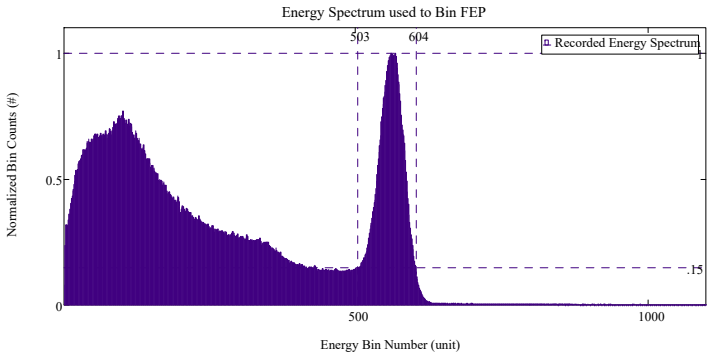

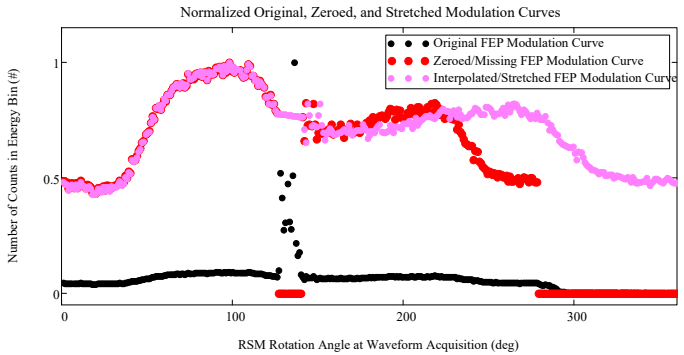

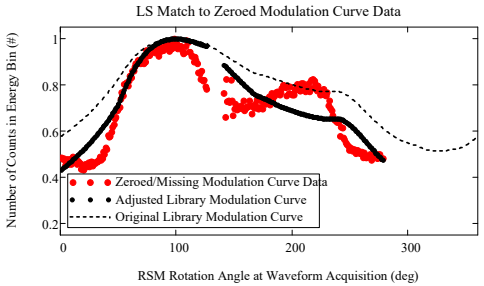

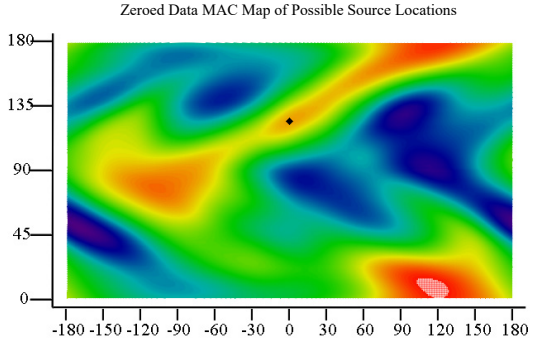

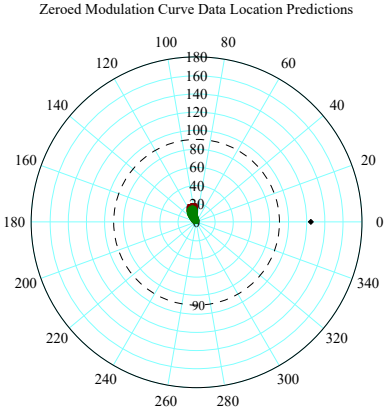

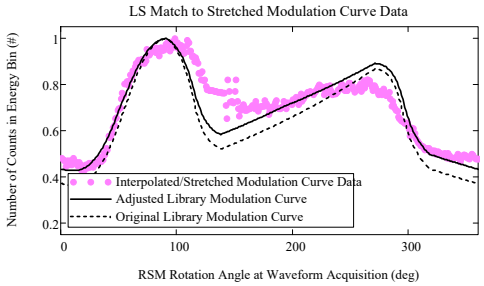

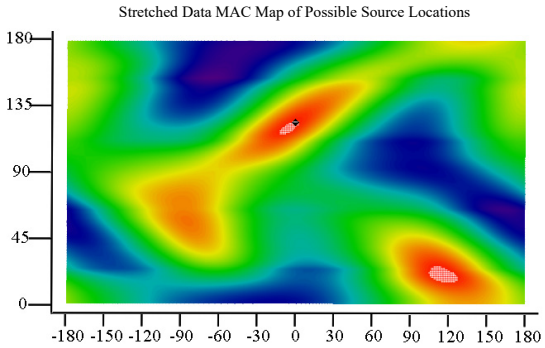

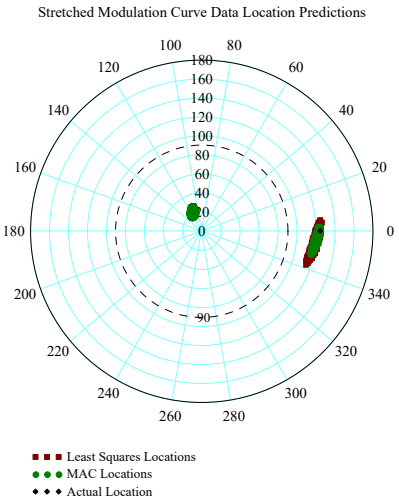

View Angle φ = 135° : Missing/Stretched Encoder Data Spectrum, Modulation Curve, Library Curve, MAC and LS Direction Predictions

Phi_ViewDegree= 135 theta = 0

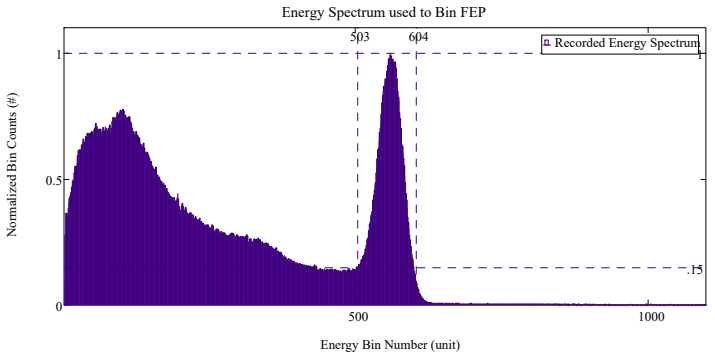

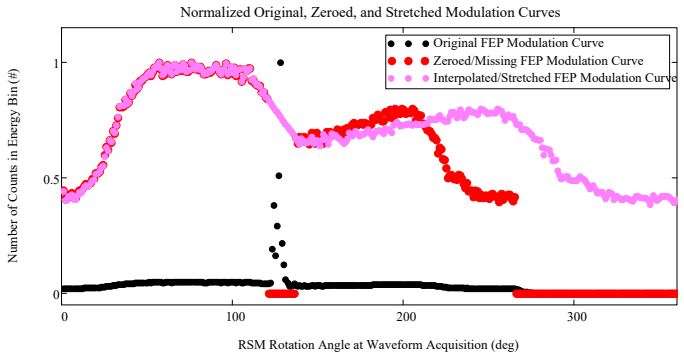

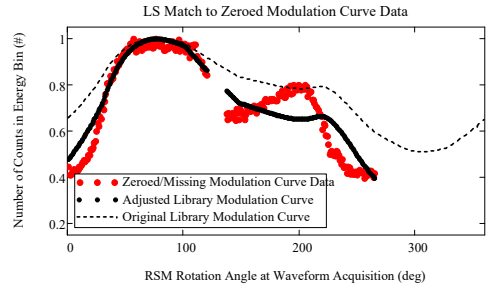

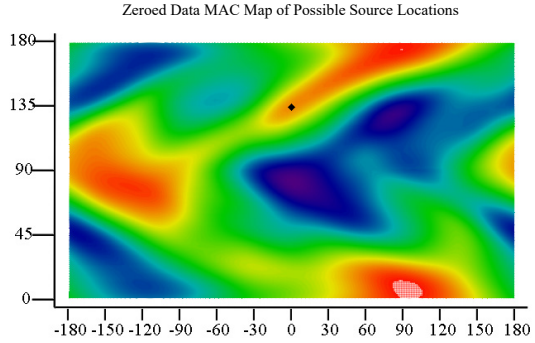

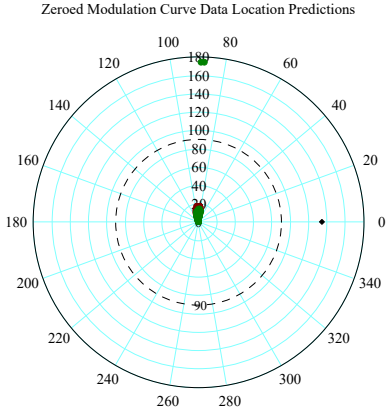

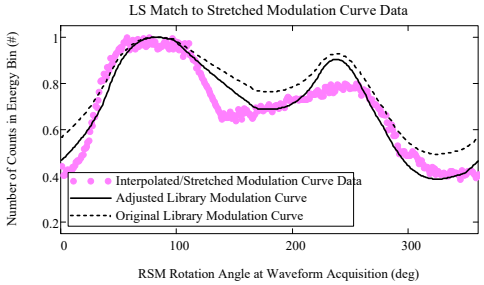

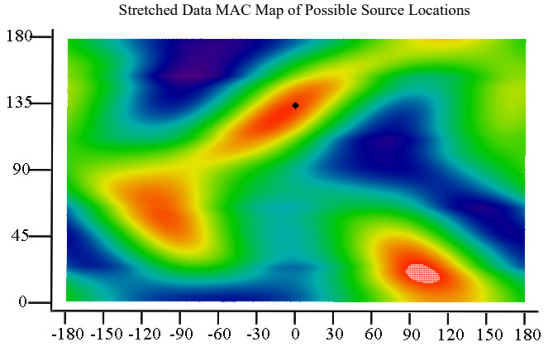

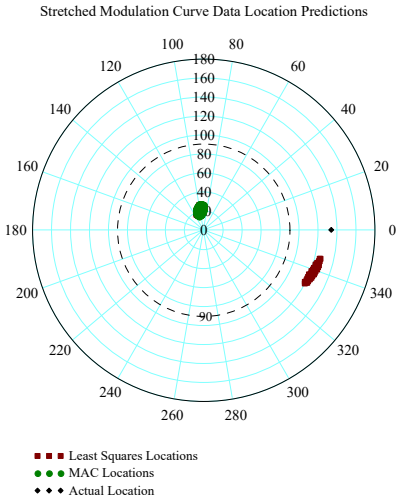

View Angle φ = 145° : Missing/Stretched Encoder Data Spectrum, Modulation Curve, Library Curve, MAC and LS Direction Predictions

Phi_ViewDegree= 145 theta = 0

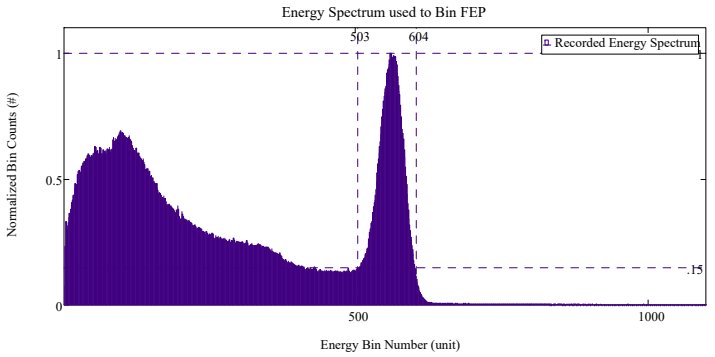

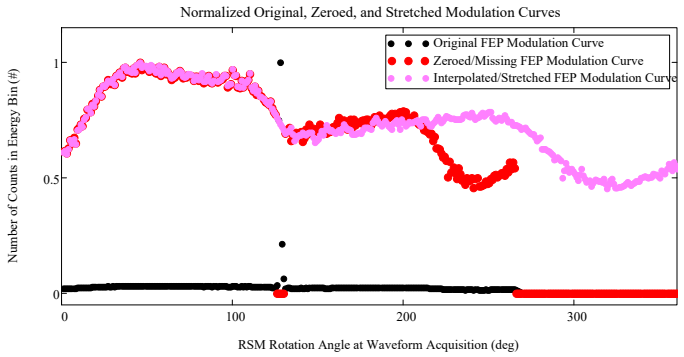

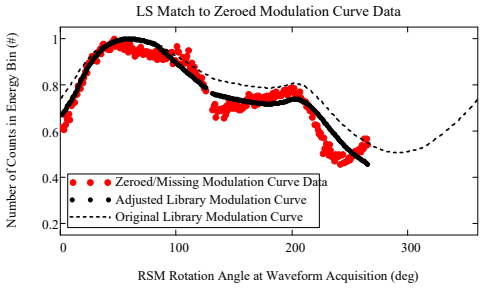

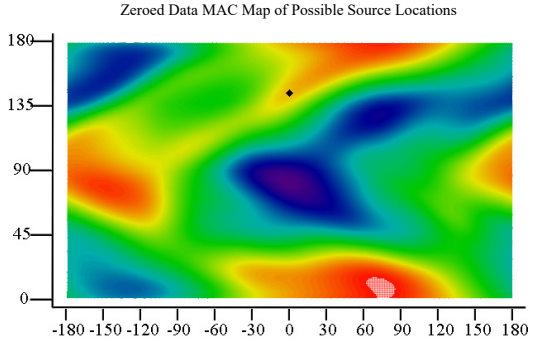

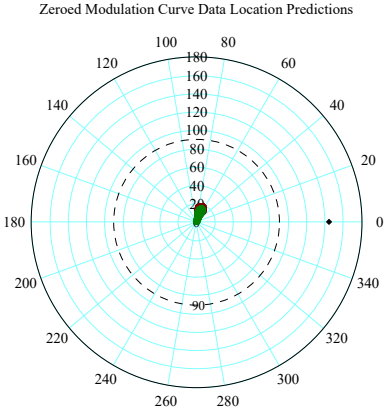

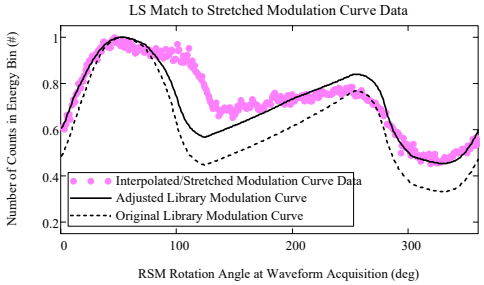

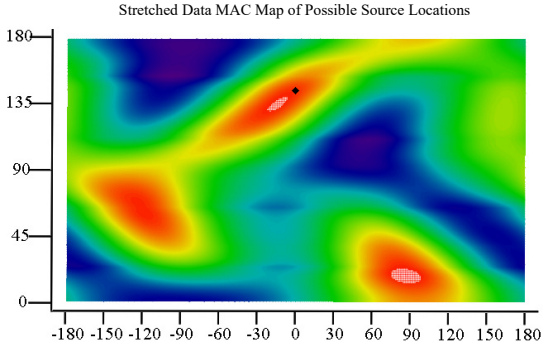

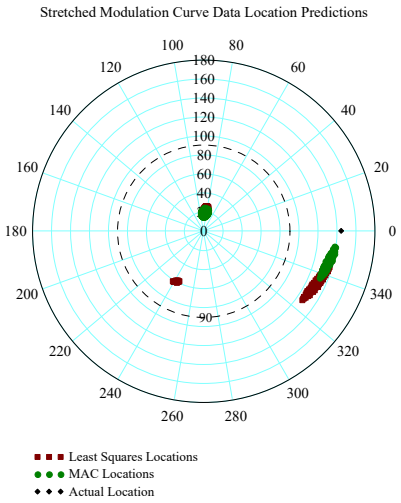

View Angle φ = 72° : Missing/Stretched Encoder Data Spectrum, Modulation Curve, Library Curve, MAC and LS Direction Predictions

Phi_ViewDegree= 72 theta = 0

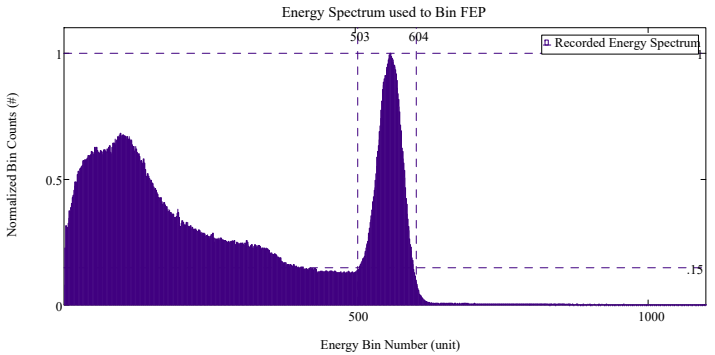

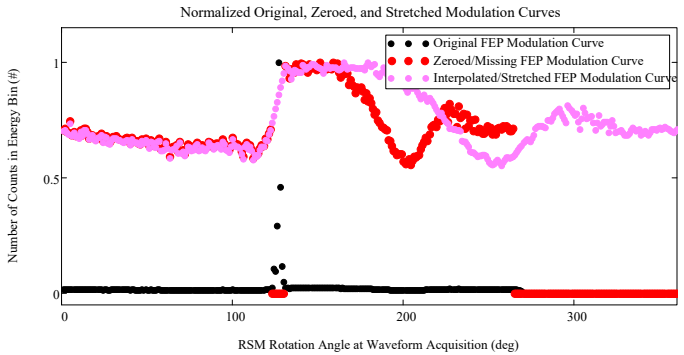

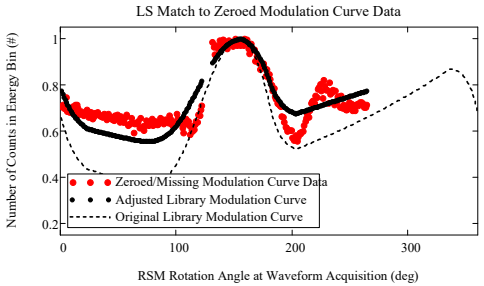

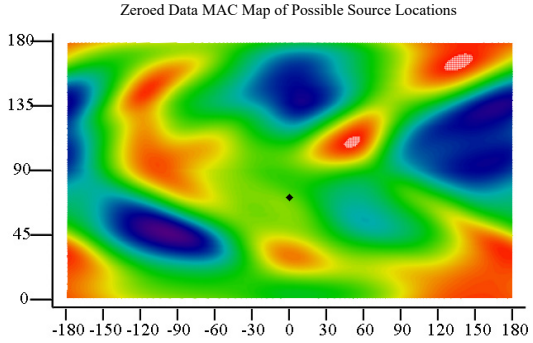

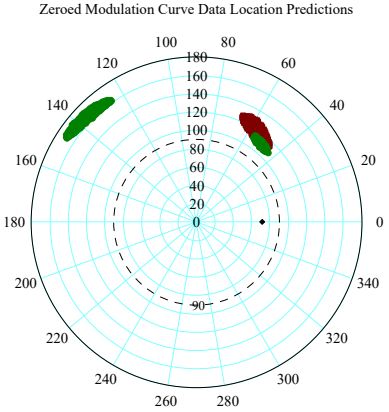

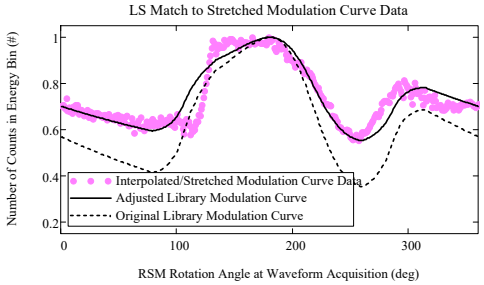

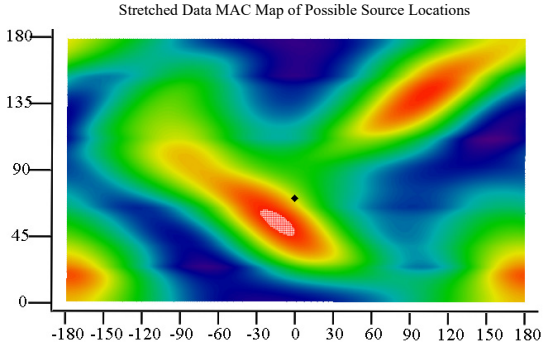

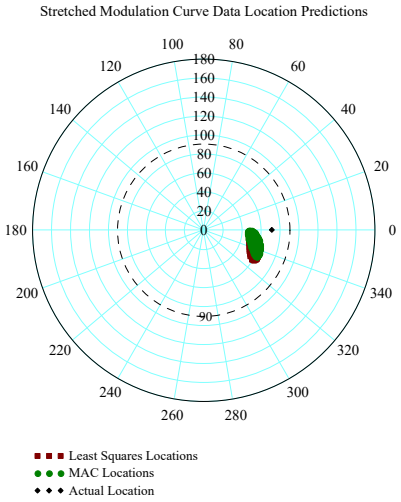

View Angle φ = 126° : Missing/Stretched Encoder Data Spectrum, Modulation Curve, Library Curve, MAC and LS Direction Predictions

Phi_ViewDegree= 126 theta = 0

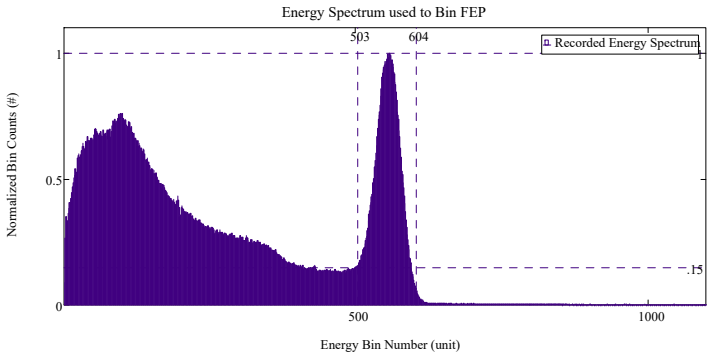

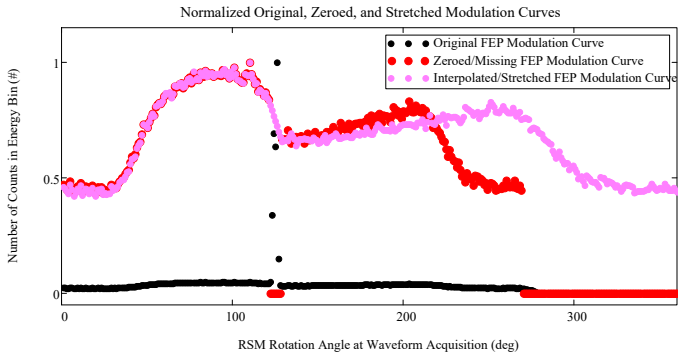

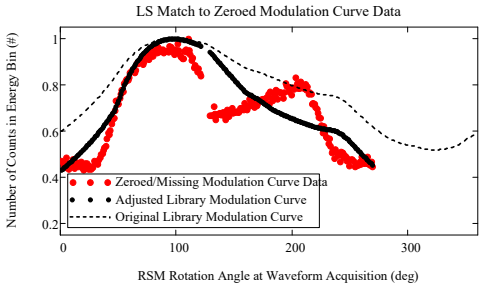

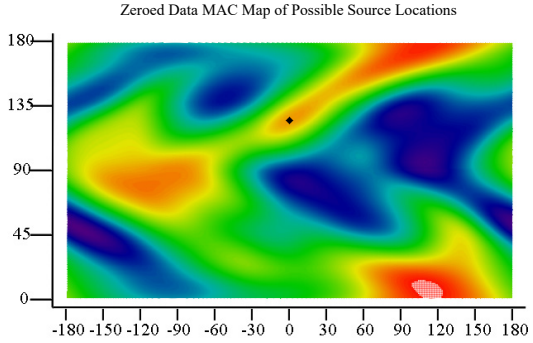

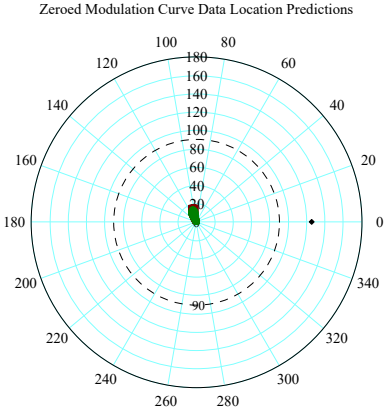

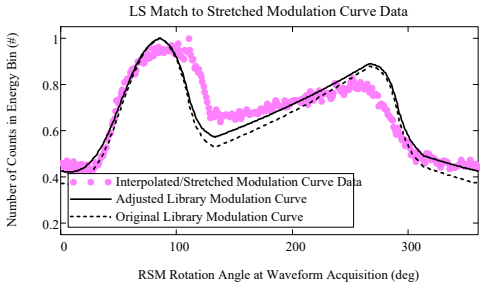

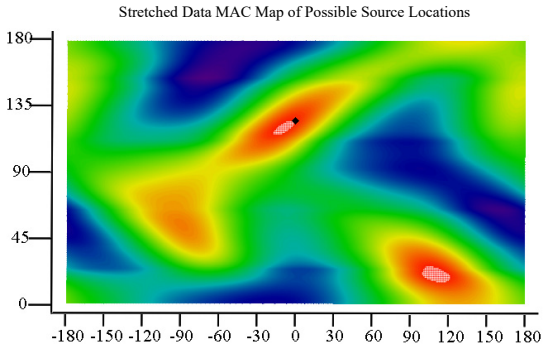

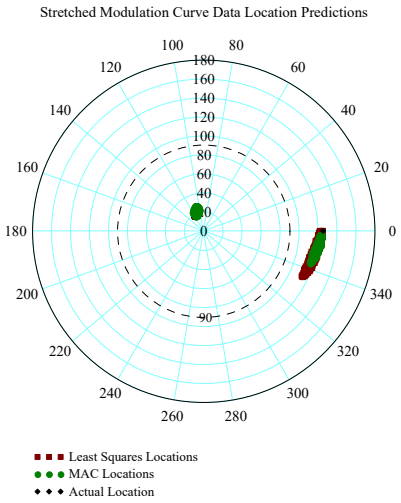

View Angle φ = 35° : Missing/Stretched Encoder Data Spectrum, Modulation Curve, Library Curve, MAC and LS Direction Predictions

Phi_ViewDegree = 35 theta = 0

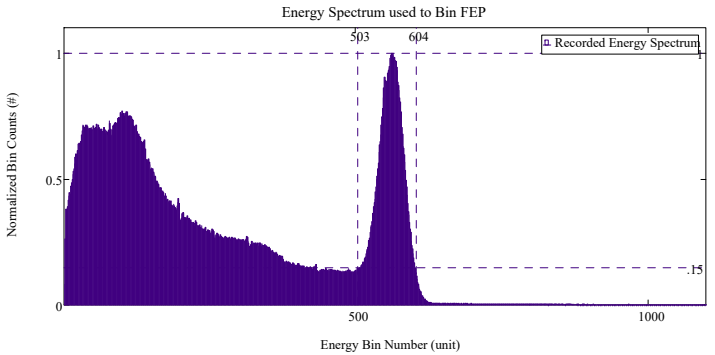

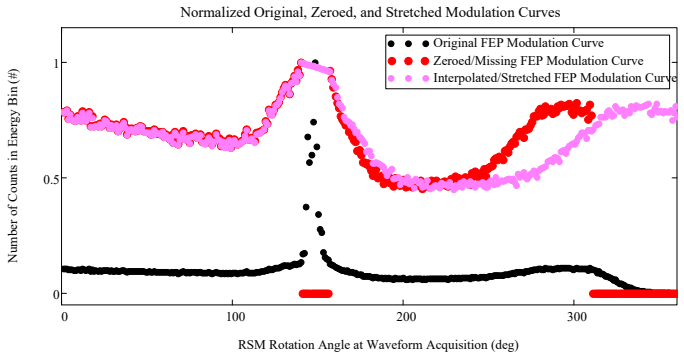

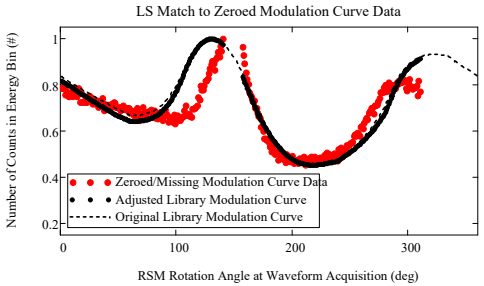

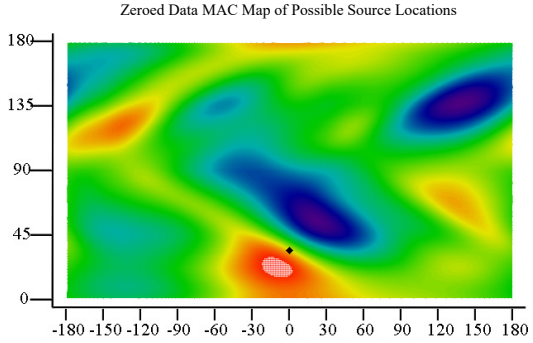

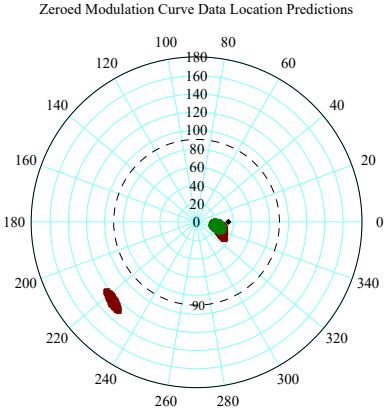

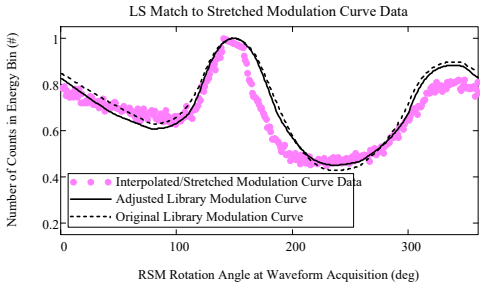

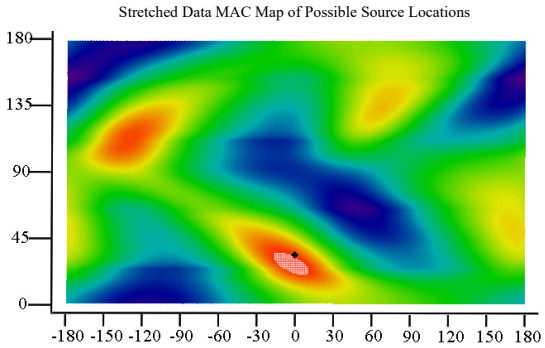

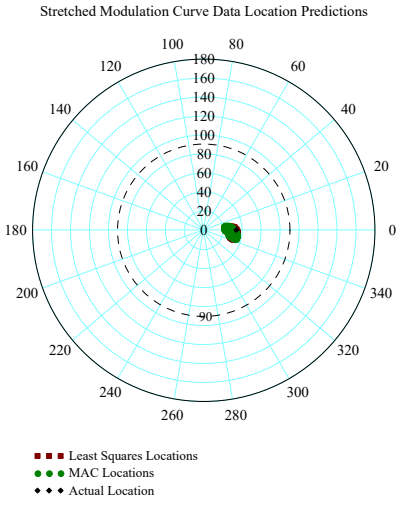

View Angle φ = 45° : Missing/Stretched Encoder Data Spectrum, Modulation Curve, Library Curve, MAC and LS Direction Predictions

Phi_ViewDegree = 45 theta = 0

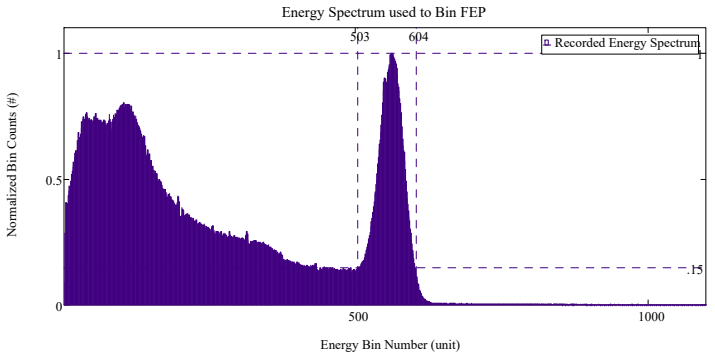

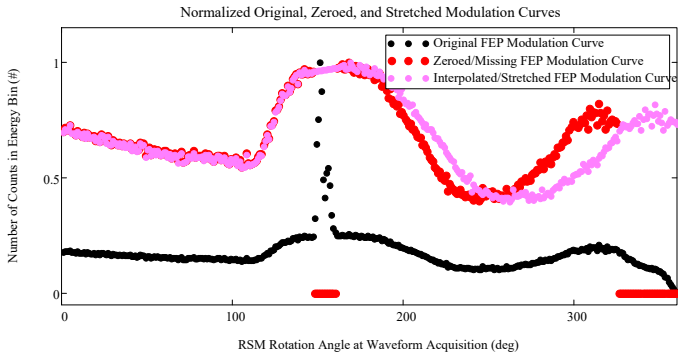

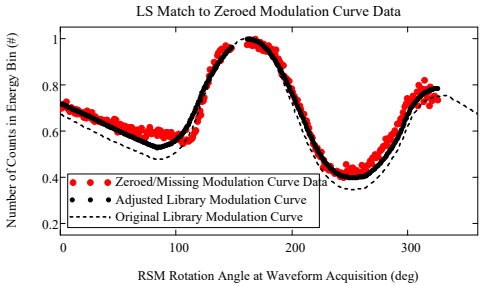

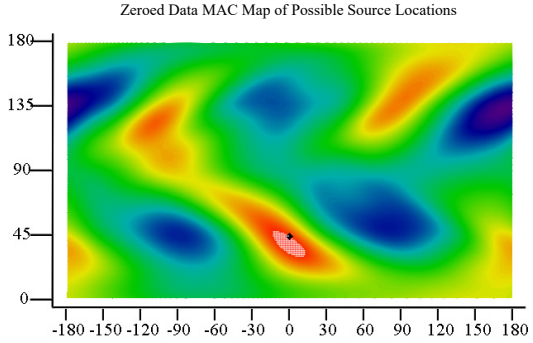

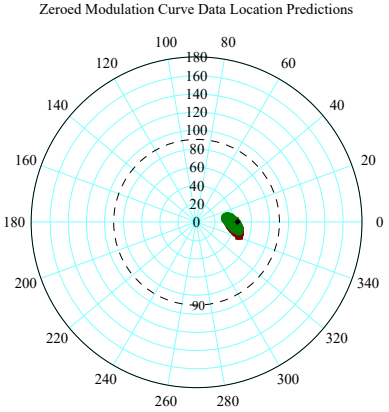

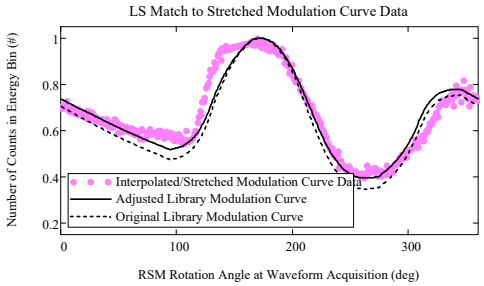

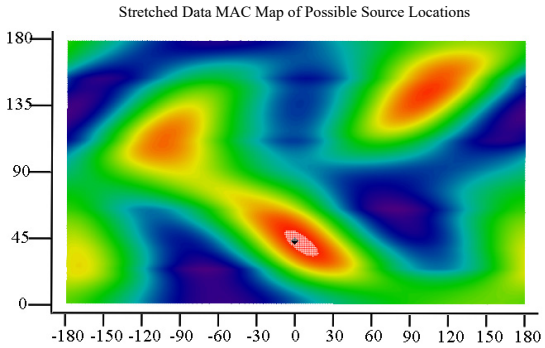

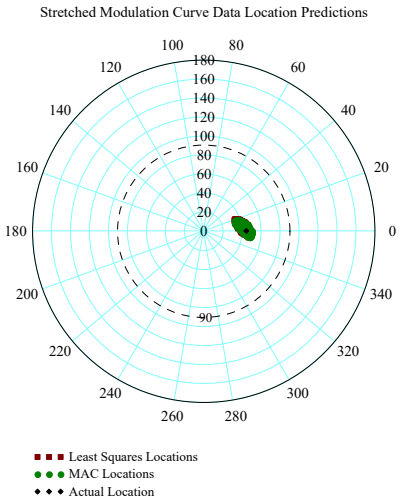

View Angle φ = 55° : Missing/Stretched Encoder Data Spectrum, Modulation Curve, Library Curve, MAC and LS Direction Predictions

Phi_ViewDegree= 55 theta = 0

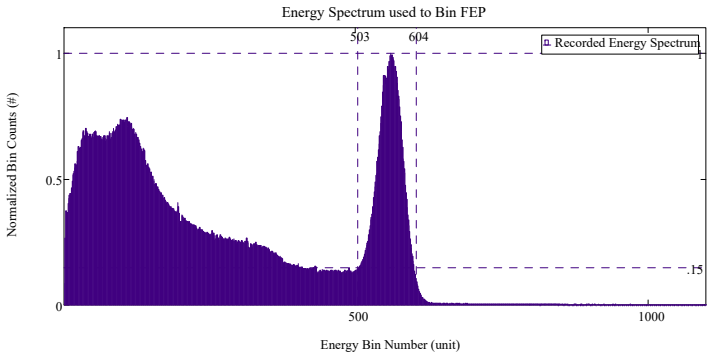

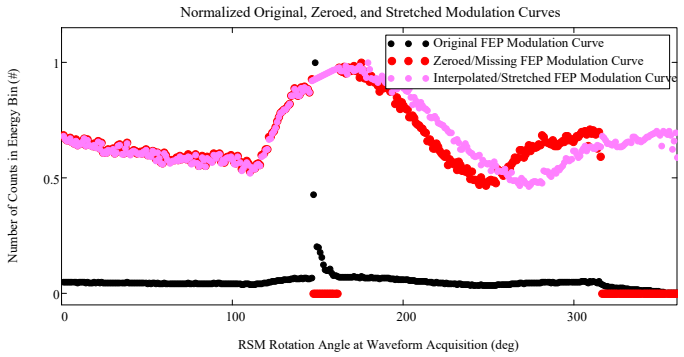

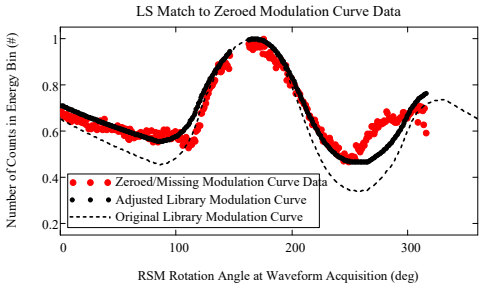

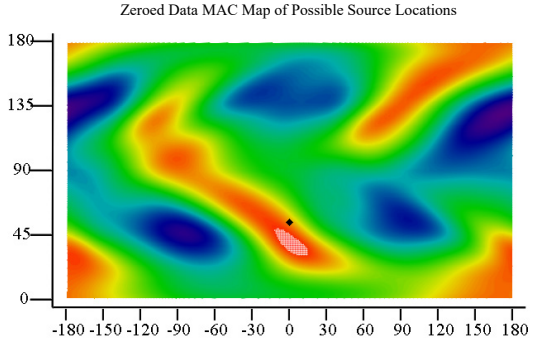

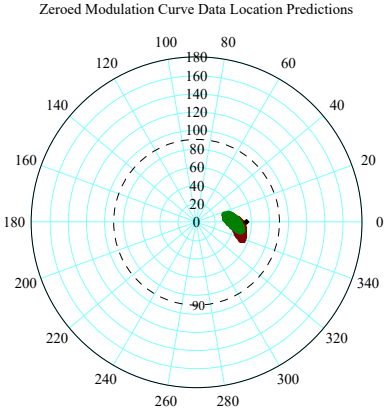

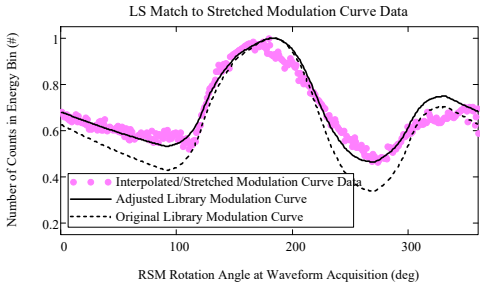

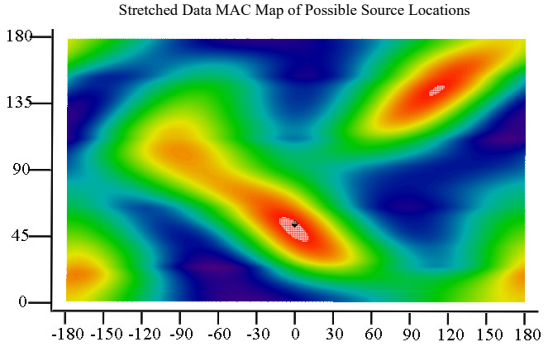

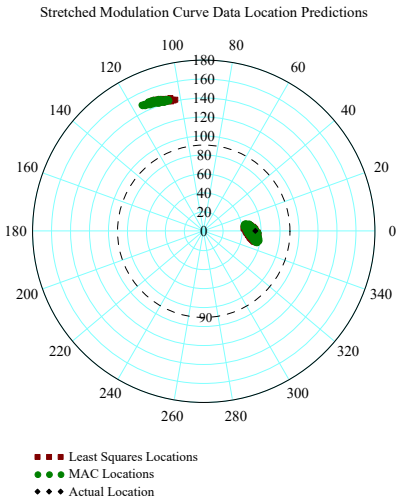

View Angle φ = 125° : Missing/Stretched Encoder Data Spectrum, Modulation Curve, Library Curve, MAC and LS Direction Predictions

Phi_ViewDegree = 125 theta = 0

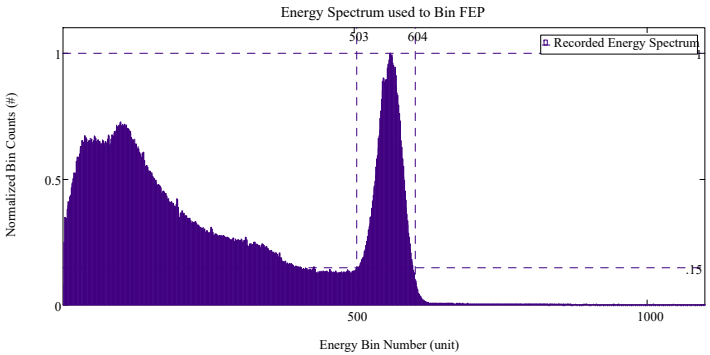

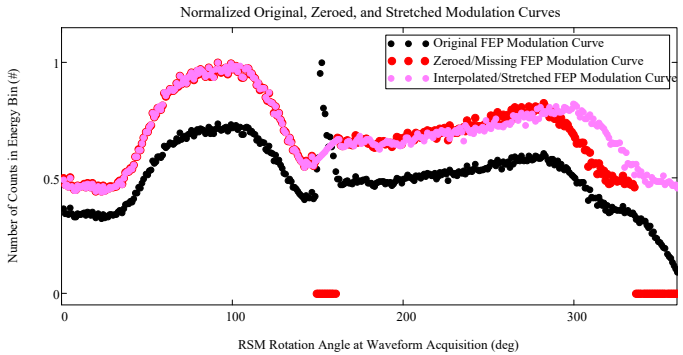

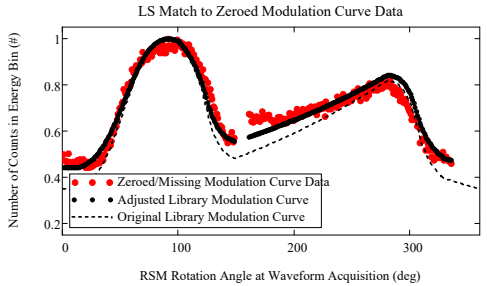

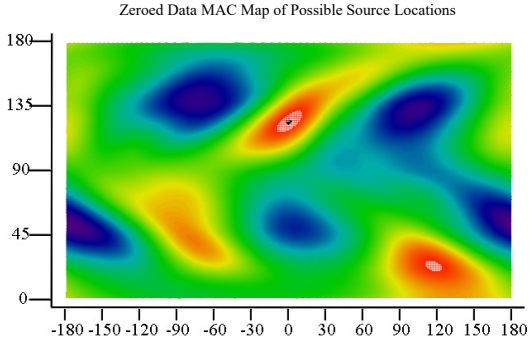

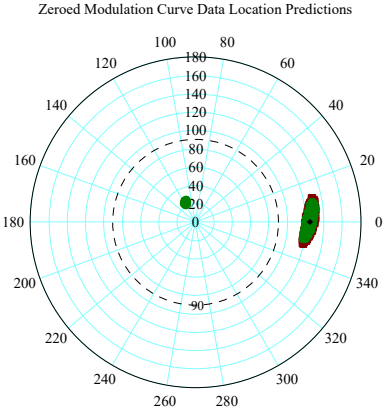

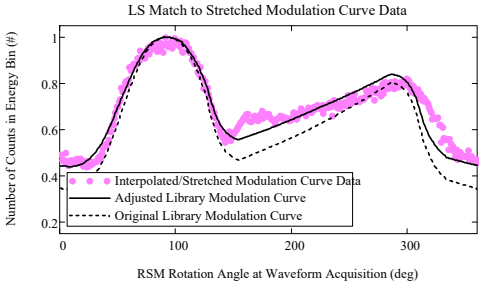

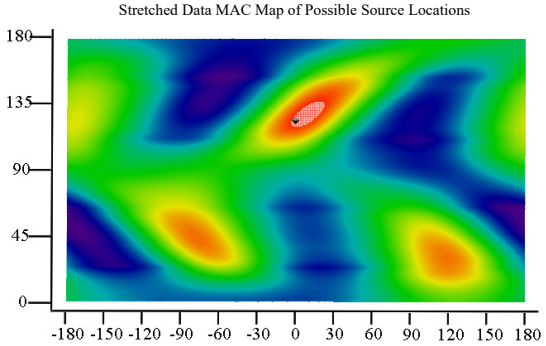

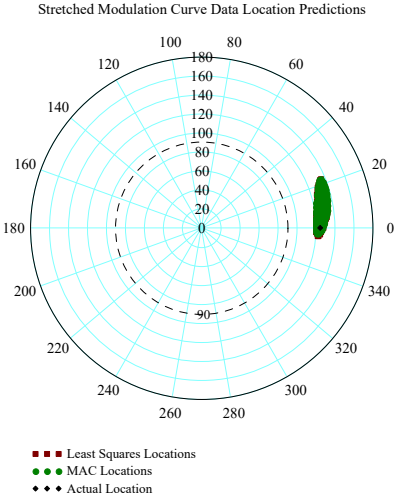

View Angle φ = 135° : Missing/Stretched Encoder Data Spectrum, Modulation Curve, Library Curve, MAC and LS Direction Predictions

Phi_ViewDegree= 135 theta = 0

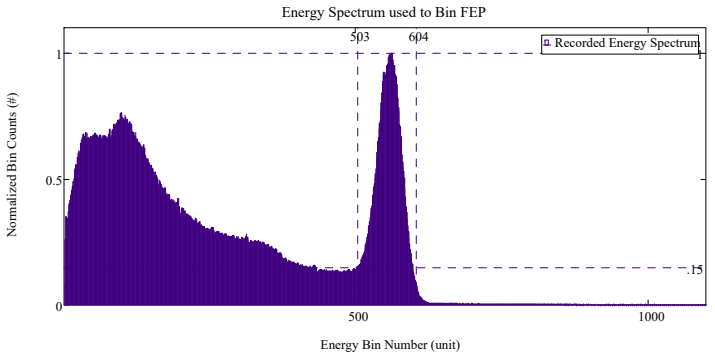

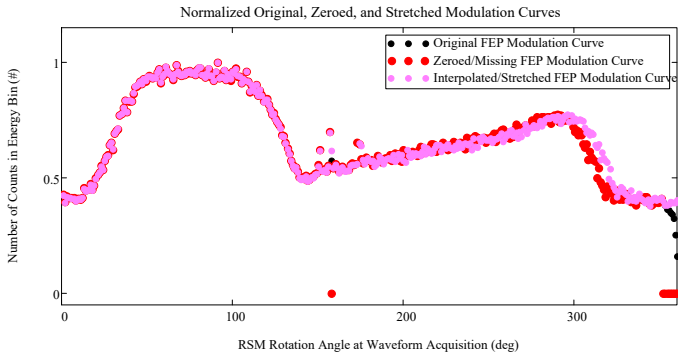

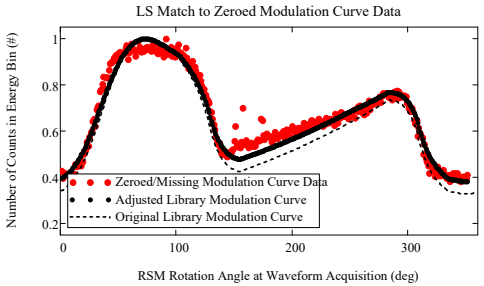

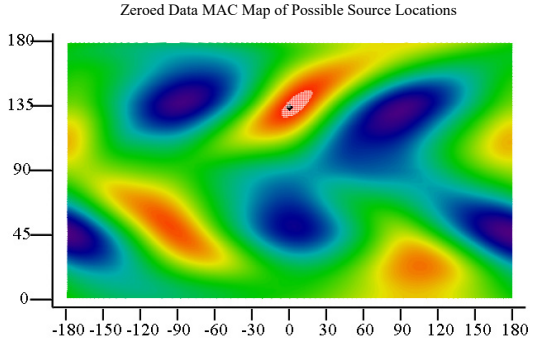

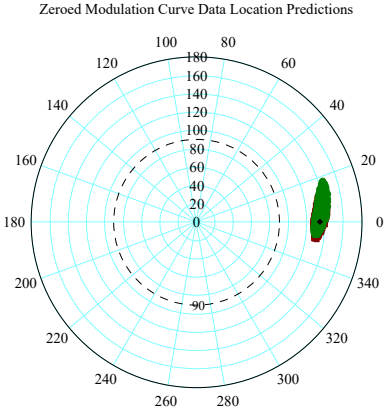

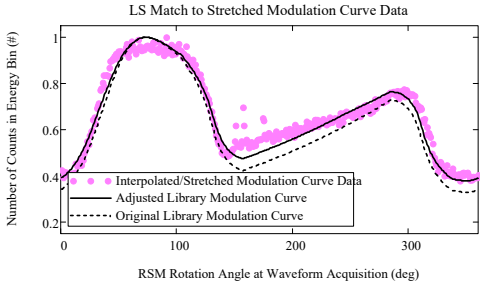

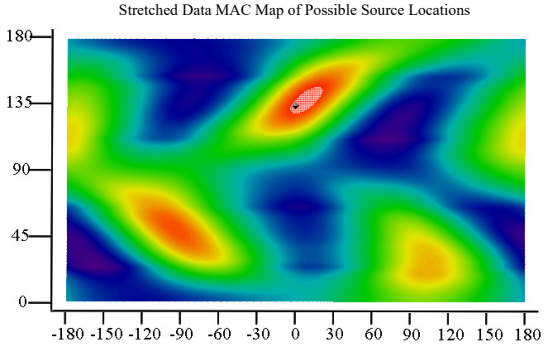

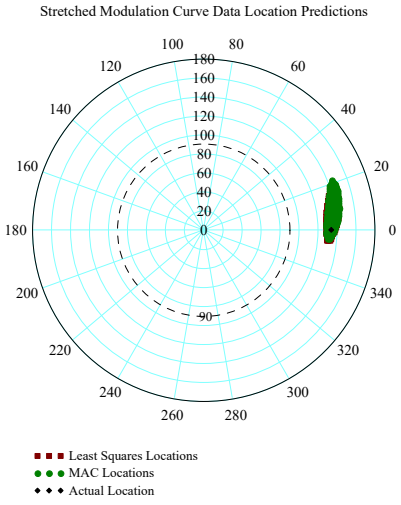

View Angle φ = 145° : Missing/Stretched Encoder Data Spectrum, Modulation Curve, Library Curve, MAC and LS Direction Predictions

Phi_ViewDegree = 145 theta = 0

Energy Spectrum used to Bin FEP

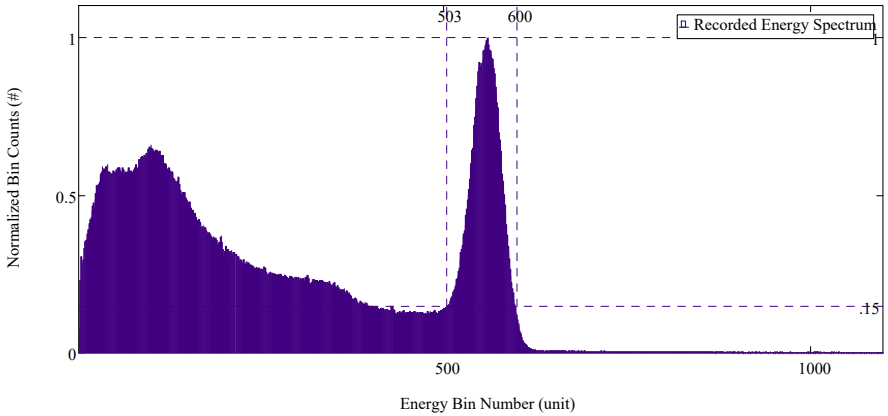

Normalized Original Modulation Curve

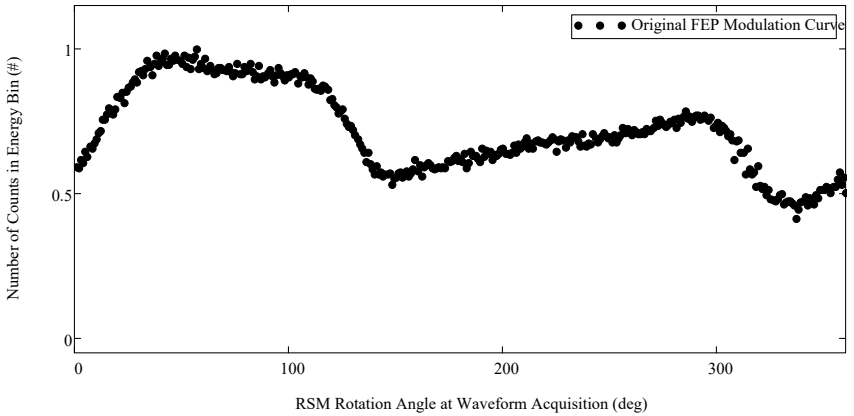

LS Match to Modulation Curve Data

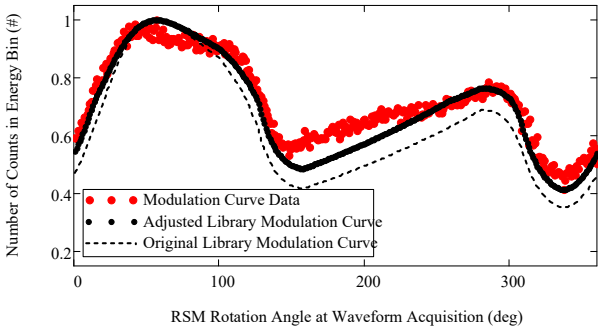

MAC Map of Possible Source Locations

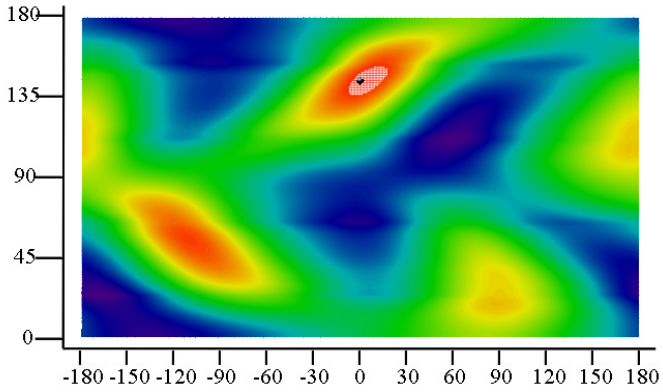

MAC Legend

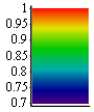

Modulation Curve Data Location Predictions

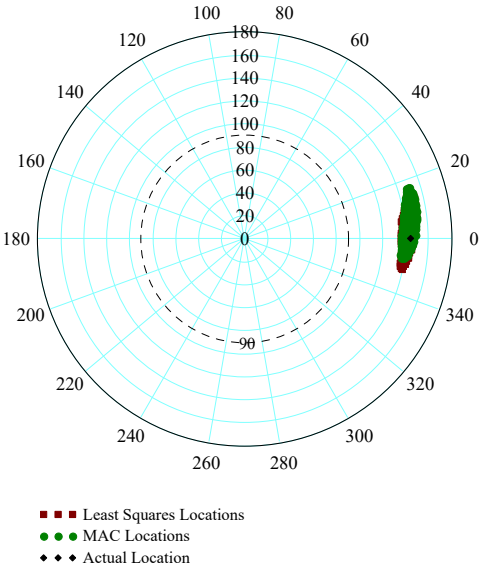

Appendix A.4: Large FitzGerald Design RSM Data, Phoswich Detector Cs-137 Single Source; Experimentally Derived Library Matching Results

View Angle φ = 35° : Original/Filtered Phoswich Data Spectra, Modulation Curves, Library Curves, MAC and LS Direction Predictions

Phi_ViewDegree = 35 Theta_ViewDegree = 0

Raw Phoswich Energy Spectrum used to Bin

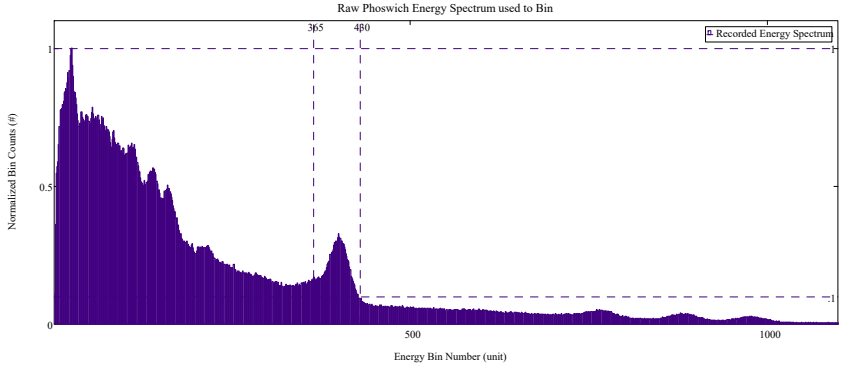

Filtered Phoswich Energy Spectrum used to Bin Compton Continuum

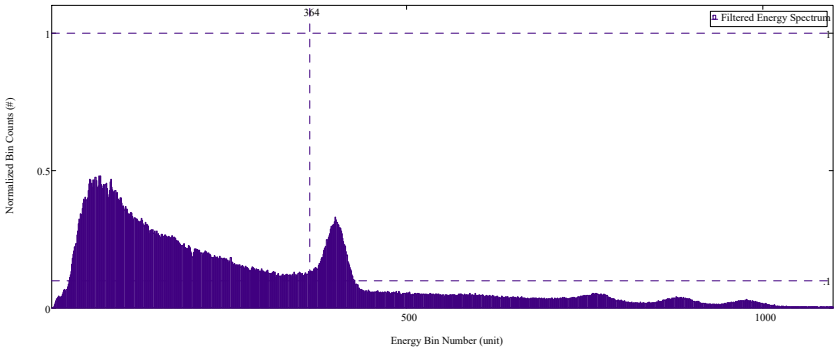

LS Match Modulation Curve Fitted to Raw Phoswich FEP Data

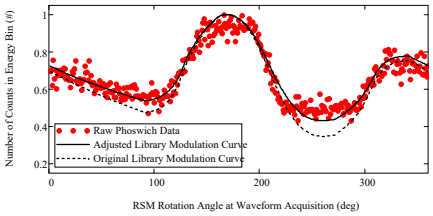

LS Match Modulation Curve Fitted to Filtered Phoswich FEP Data

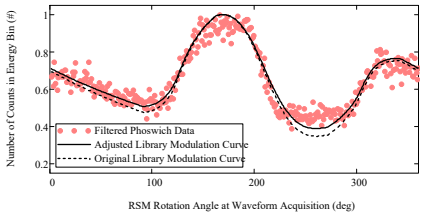

LS Match Modulation Curve Fitted to Raw Phoswich Compton Data

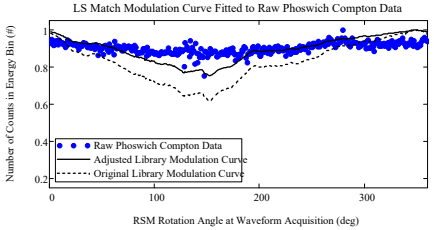

LS Match Modulation Curve Fitted to Filtered Phoswich Compton Data

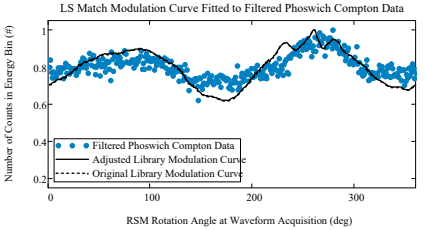

Raw Phoswich FEP Data MAC Map of Possible Source Locations

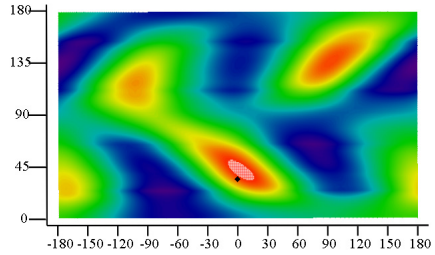

Filtered Phoswich FEP Data MAC Map of Possible Source Locations

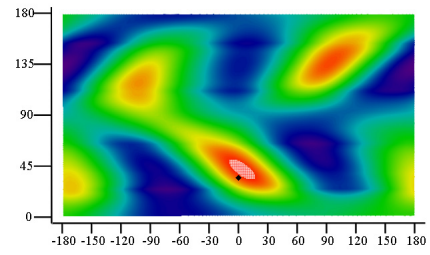

Raw Phoswich Compton Data MAC Map of Possible Source Locations

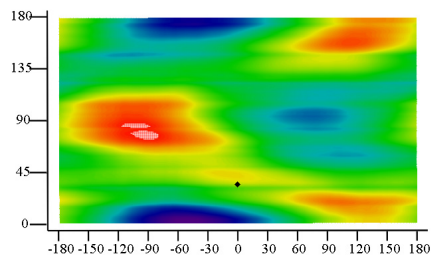

Filtered Phoswich Compton Data MAC Map of Possible Source Locations

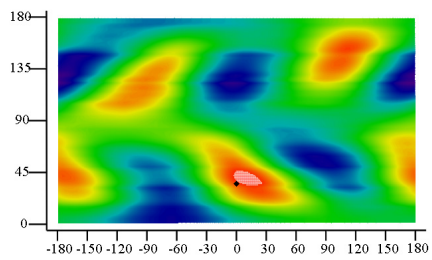

MAC Legend

Raw Phoswich FEP Data Location Predictions

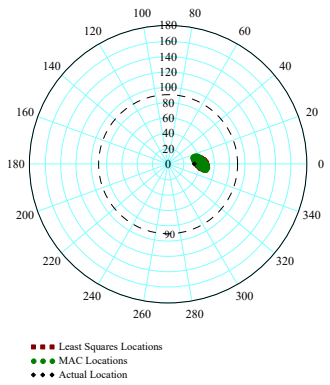

Filtered Phoswich FEP Data Location Predictions

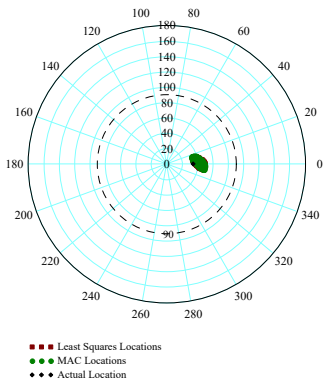

Raw Phoswich Compton Data Location Predictions

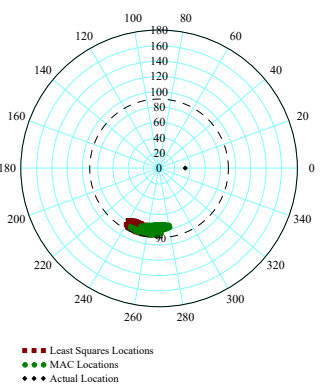

Filtered Phoswich Compton Data Location Predictions

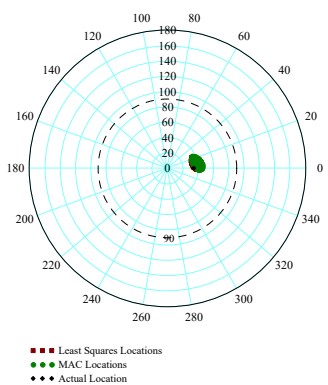

View Angle φ = 45° : Original/Filtered Phoswich Data Spectra, Modulation Curves, Library Curves, MAC and LS Direction Predictions

Phi_ViewDegree = 45 Theta_ViewDegree = 0

Raw Phoswich Energy Spectrum used to Bin

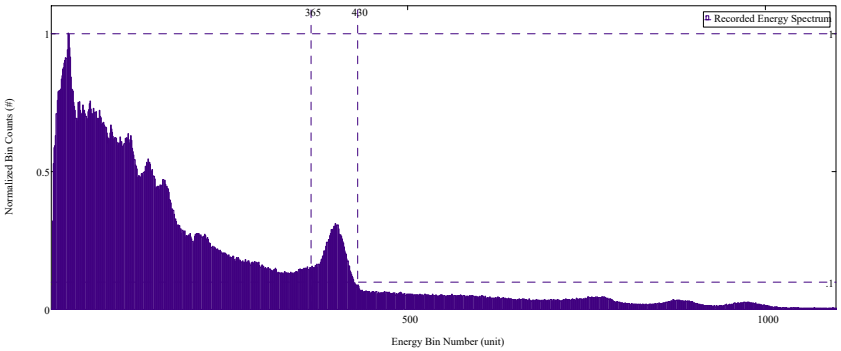

Filtered Phoswich Energy Spectrum used to Bin Compton Continuum

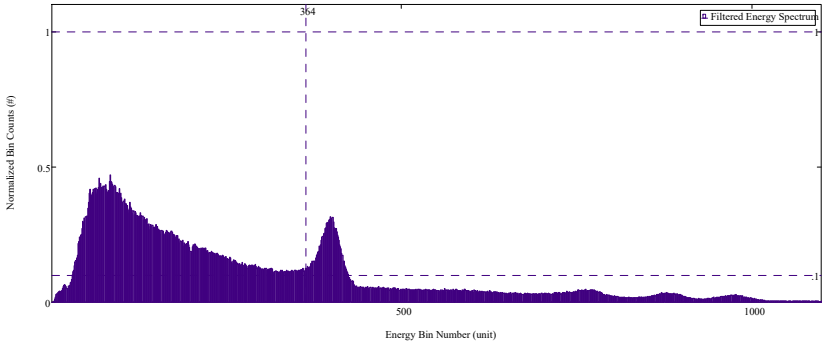

LS Match Modulation Curve Fitted to Raw Phoswich FEP Data

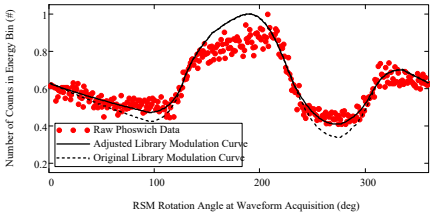

LS Match Modulation Curve Fitted to Filtered Phoswich FEP Data

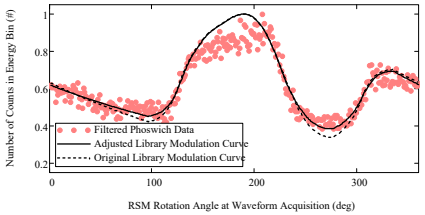

LS Match Modulation Curve Fitted to Raw Phoswich Compton Data

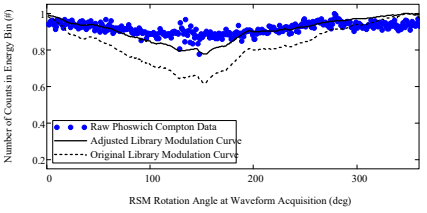

LS Match Modulation Curve Fitted to Filtered Phoswich Compton Data

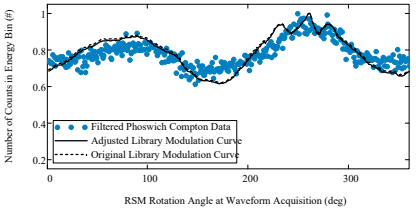

Raw Phoswich FEP Data MAC Map of Possible Source Locations

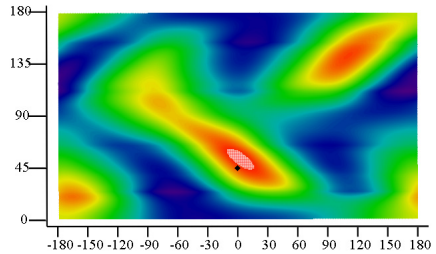

Filtered Phoswich FEP Data MAC Map of Possible Source Locations

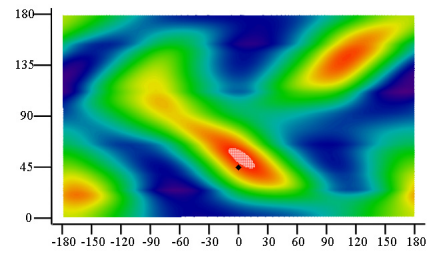

Raw Phoswich Compton Data MAC Map of Possible Source Locations

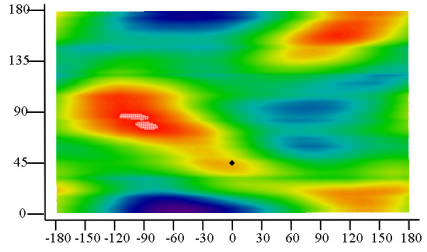

Filtered Phoswich Compton Data MAC Map of Possible Source Locations

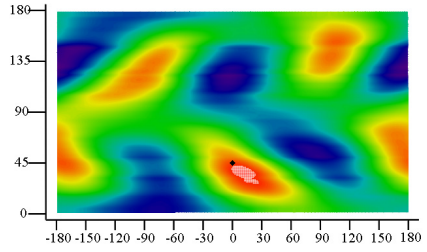

MAC Legend

Raw Phoswich FEP Data Location Predictions

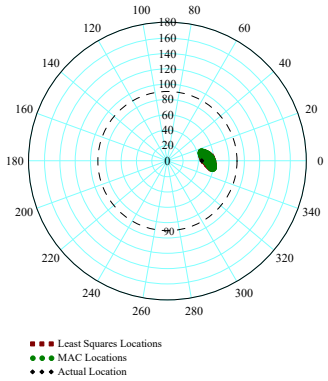

Filtered Phoswich FEP Data Location Predictions

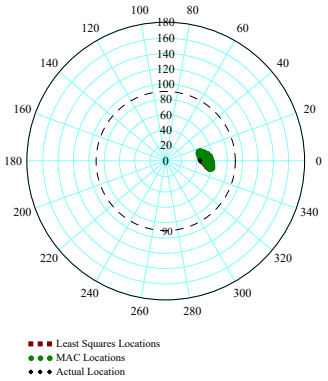

Raw Phoswich Compton Data Location Predictions

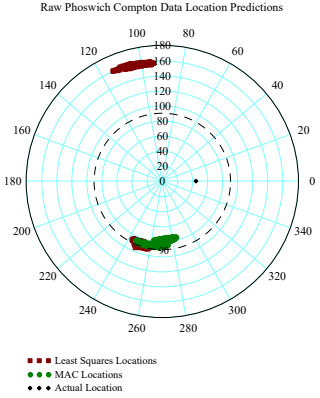

Filtered Phoswich Compton Data Location Predictions

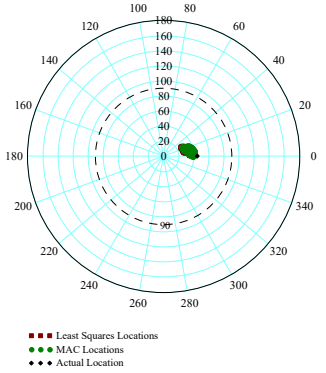

View Angle φ = 55° : Original/Filtered Phoswich Data Spectra, Modulation Curves, Library Curves, MAC and LS Direction Predictions

Phi_ViewDegree = 55 Theta_ViewDegree = 0

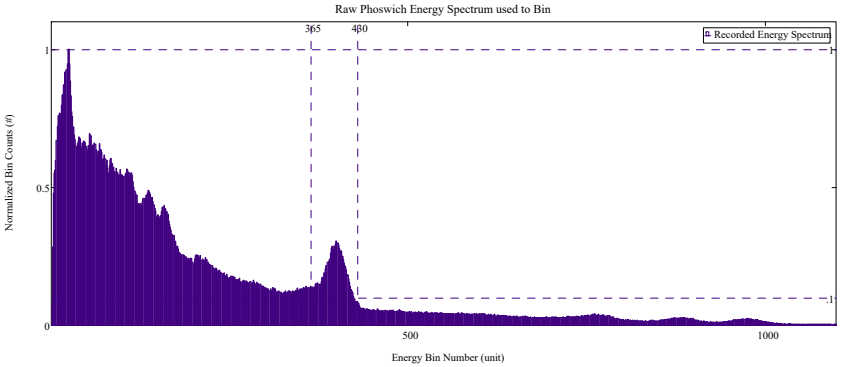

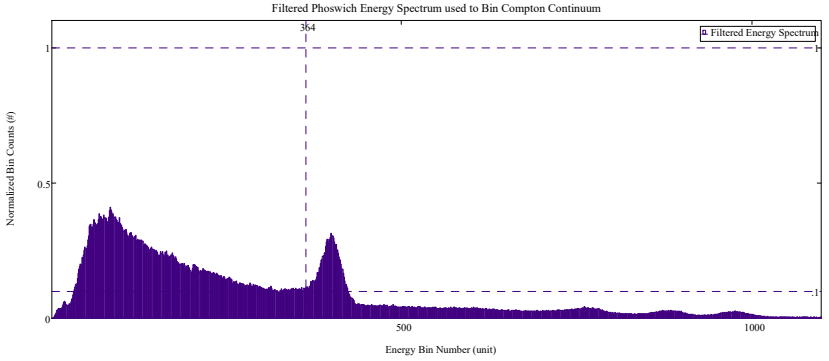

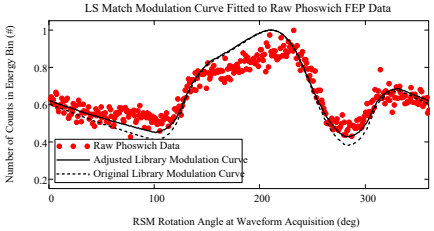

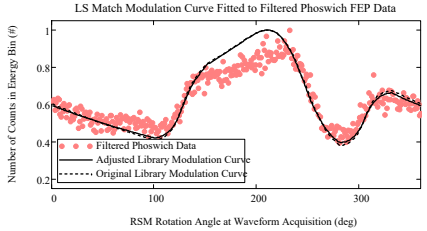

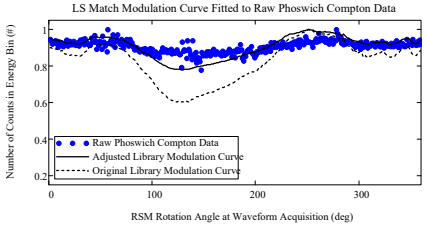

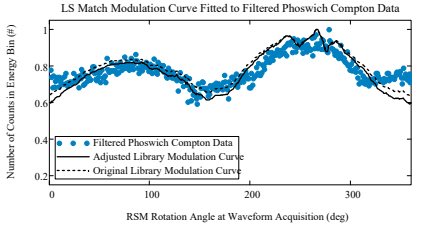

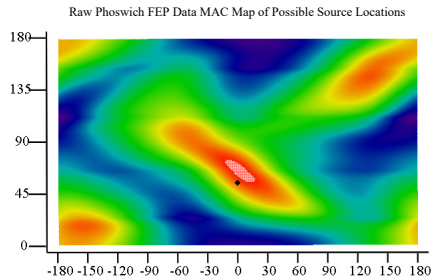

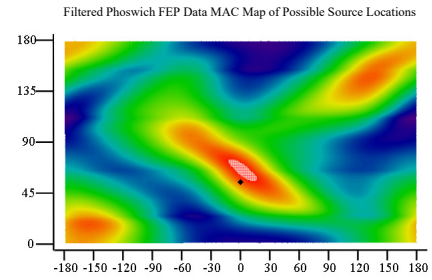

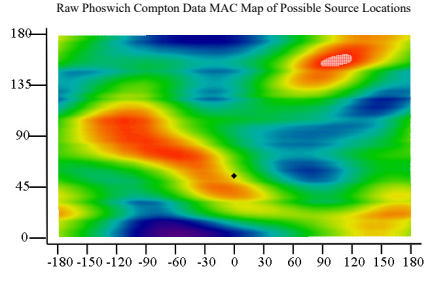

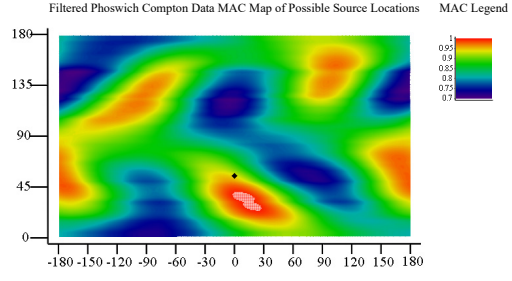

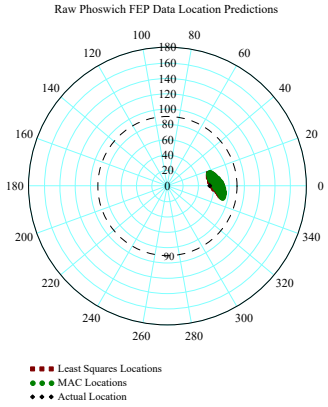

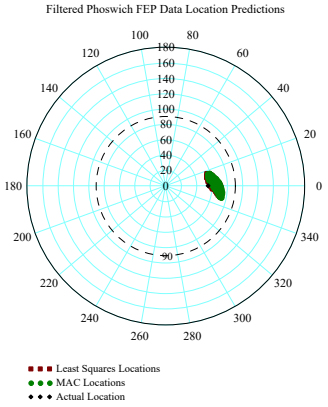

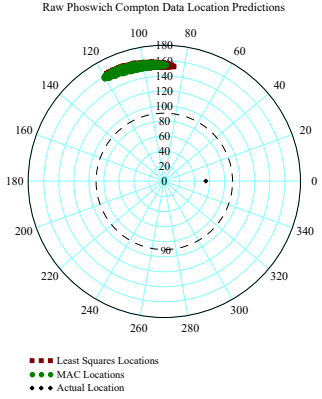

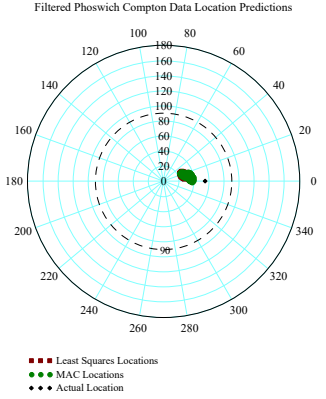

View Angle φ = 125° : Original/Filtered Phoswich Data Spectra, Modulation Curves, Library Curves, MAC and LS Direction Predictions

Phi_ViewDegree = 125 Theta_ViewDegree = 0

Raw Phoswich Energy Spectrum used to Bin

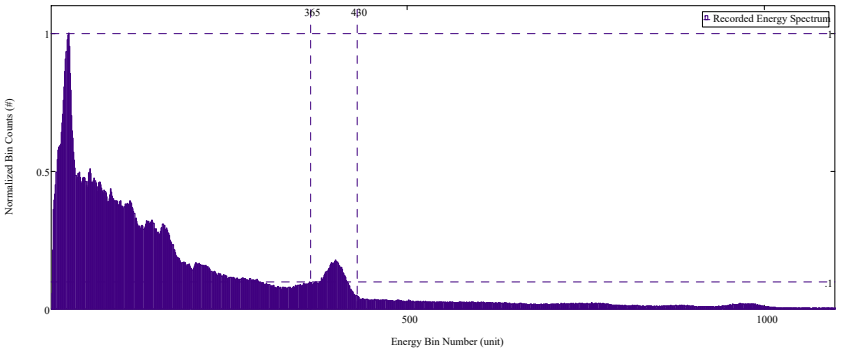

Filtered Phoswich Energy Spectrum used to Bin Compton Continuum

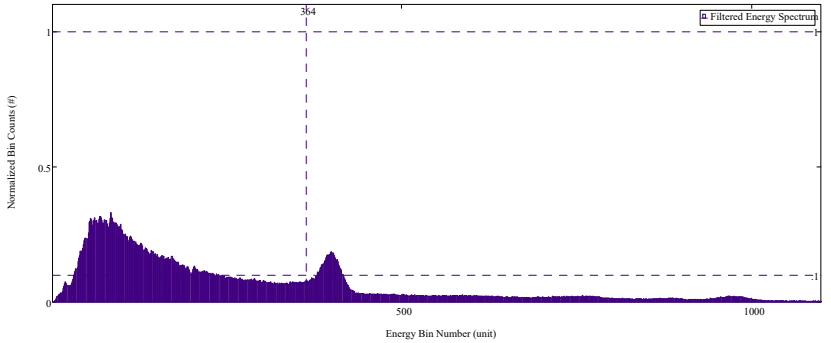

LS Match Modulation Curve Fitted to Raw Phoswich FEP Data

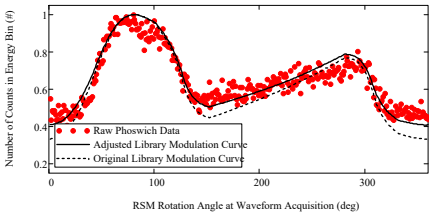

LS Match Modulation Curve Fitted to Filtered Phoswich FEP Data

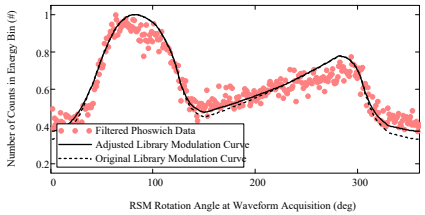

LS Match Modulation Curve Fitted to Raw Phoswich Compton Data

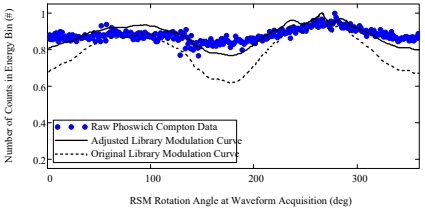

LS Match Modulation Curve Fitted to Filtered Phoswich Compton Data

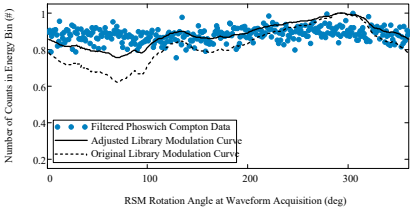

Raw Phoswich FEP Data MAC Map of Possible Source Locations

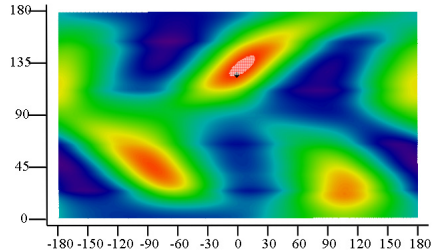

Filtered Phoswich FEP Data MAC Map of Possible Source Locations

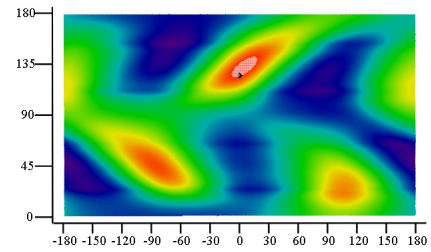

Raw Phoswich Compton Data MAC Map of Possible Source Locations

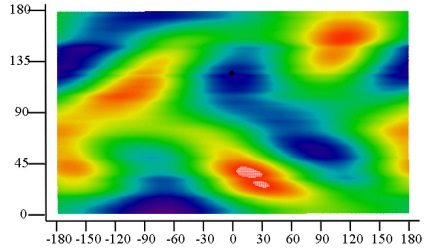

Filtered Phoswich Compton Data MAC Map of Possible Source Locations

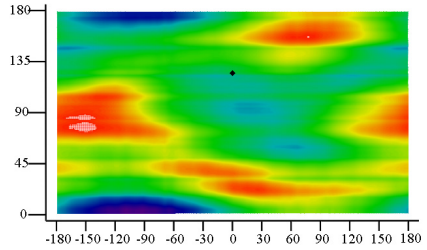

MAC Legend

Raw Phoswich FEP Data Location Predictions

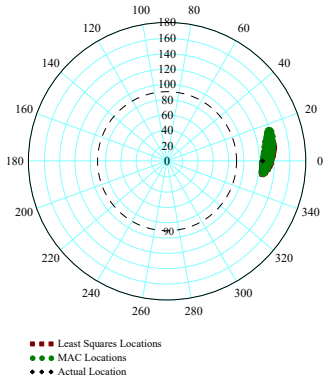

Filtered Phoswich FEP Data Location Predictions

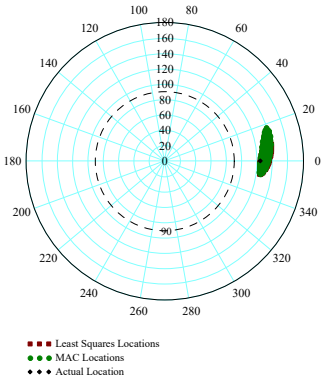

Raw Phoswich Compton Data Location Predictions

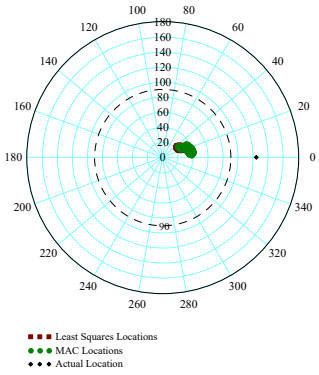

Filtered Phoswich Compton Data Location Predictions

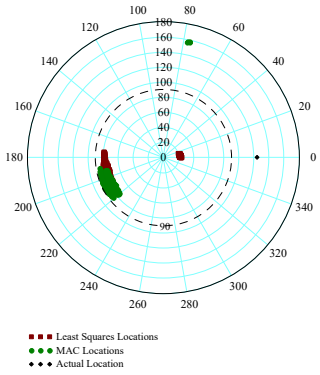

View Angle φ = 135° : Original/Filtered Phoswich Data Spectra, Modulation Curves, Library Curves, MAC and LS Direction Predictions

Phi_ViewDegree = 135 Theta_ViewDegree = 0

Raw Phoswich Energy Spectrum used to Bin

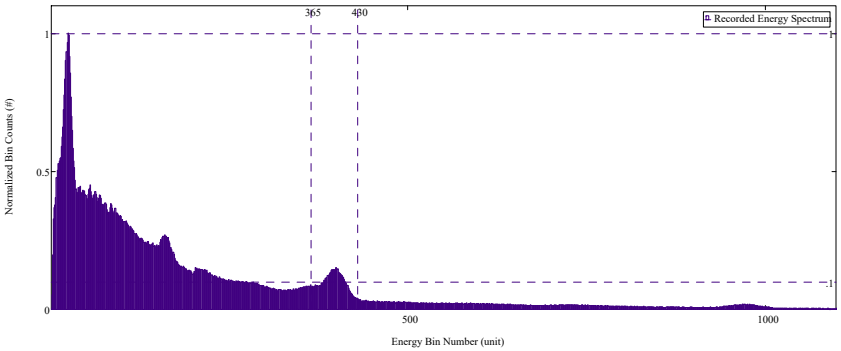

Filtered Phoswich Energy Spectrum used to Bin Compton Continuum

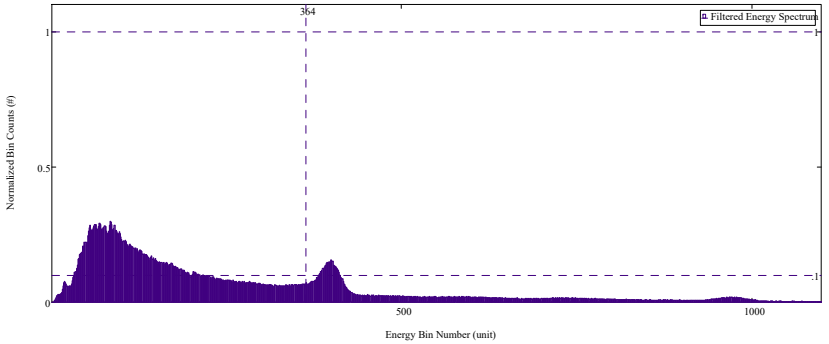

LS Match Modulation Curve Fitted to Raw Phoswich FEP Data

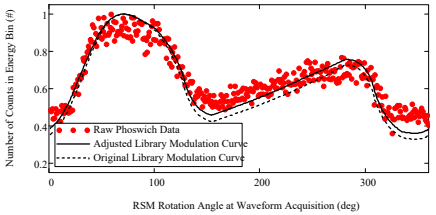

LS Match Modulation Curve Fitted to Filtered Phoswich FEP Data

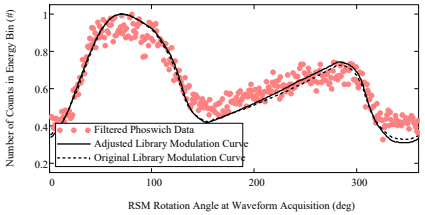

LS Match Modulation Curve Fitted to Raw Phoswich Compton Data

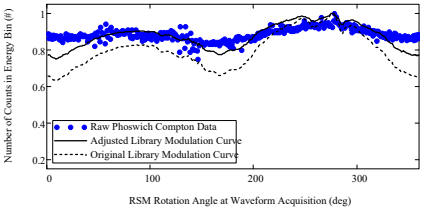

LS Match Modulation Curve Fitted to Filtered Phoswich Compton Data

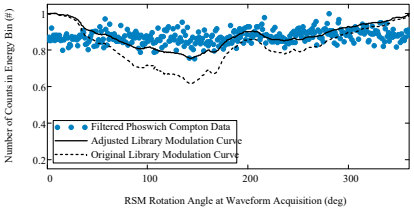

Raw Phoswich FEP Data MAC Map of Possible Source Locations

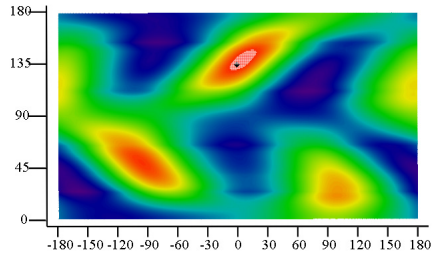

Filtered Phoswich FEP Data MAC Map of Possible Source Locations

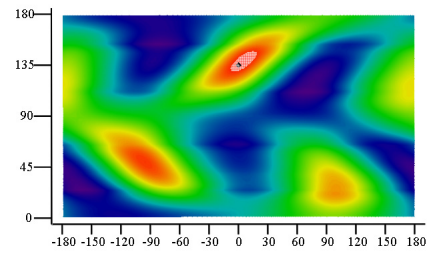

Raw Phoswich Compton Data MAC Map of Possible Source Locations

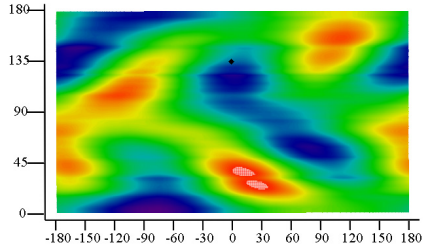

Filtered Phoswich Compton Data MAC Map of Possible Source Locations

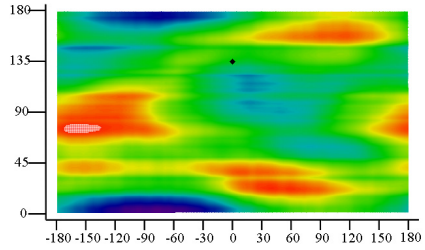

MAC Legend

Raw Phoswich FEP Data Location Predictions

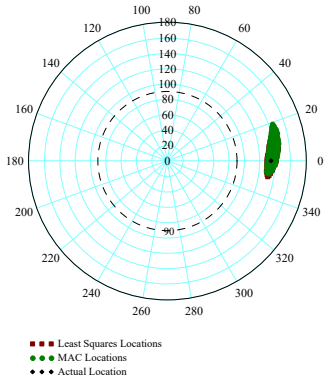

Filtered Phoswich FEP Data Location Predictions

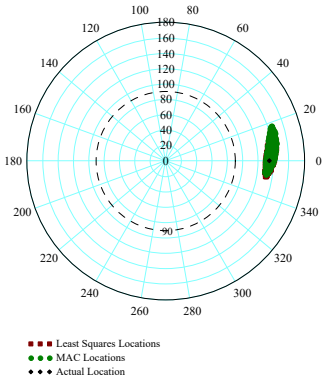

Raw Phoswich Compton Data Location Predictions

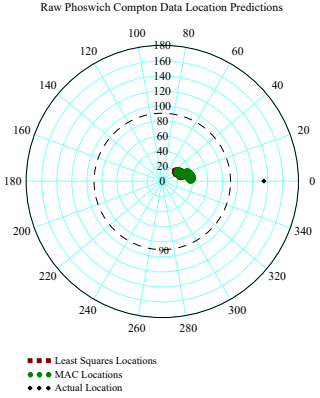

Filtered Phoswich Compton Data Location Predictions

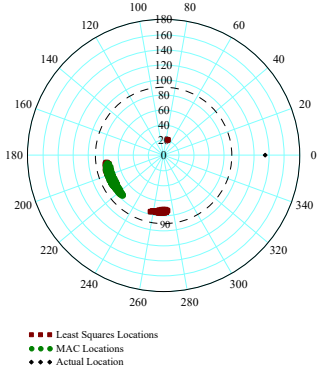

View Angle φ = 145° : Original/Filtered Phoswich Data Spectra, Modulation Curves, Library Curves, MAC and LS Direction Predictions

Phi_ViewDegree = 145 Theta_ViewDegree = 0

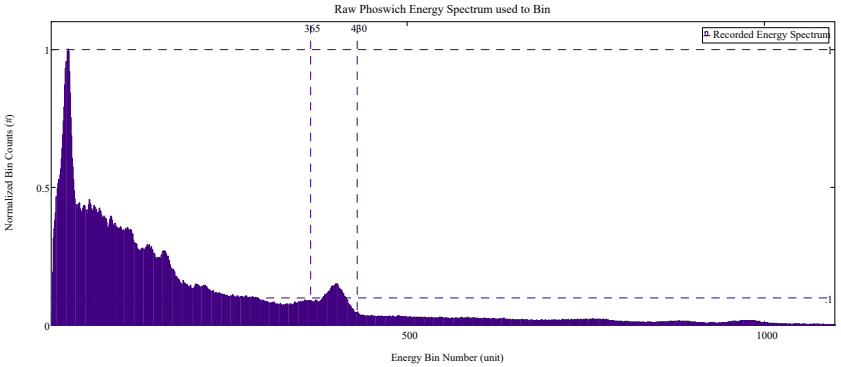

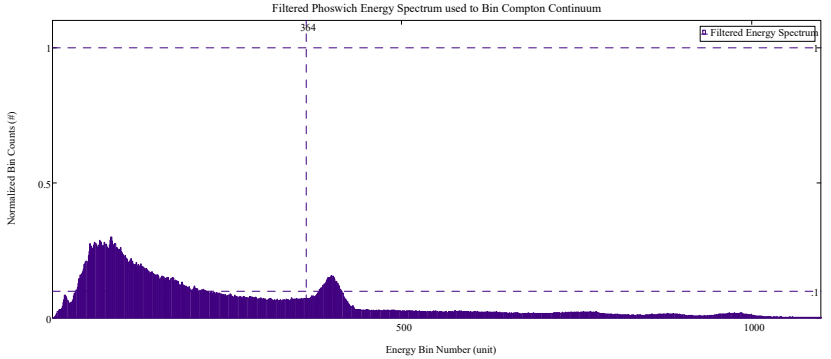

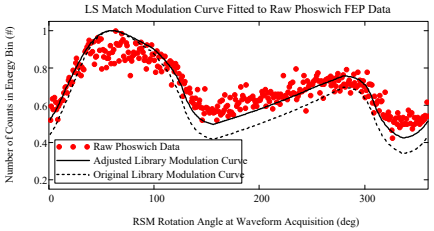

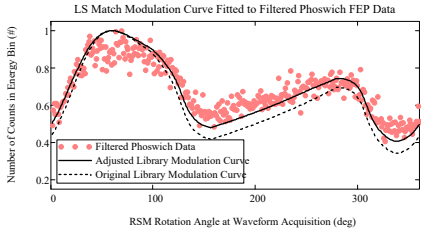

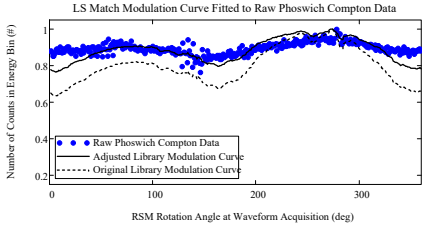

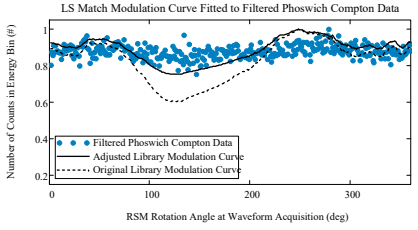

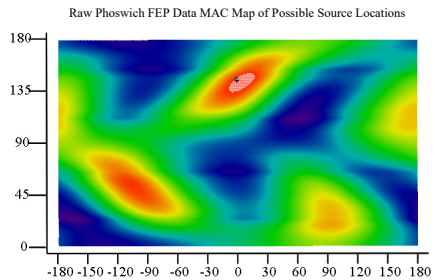

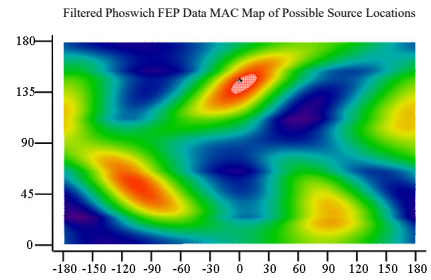

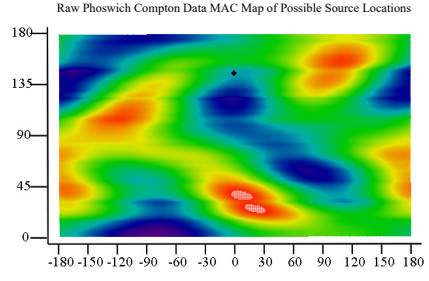

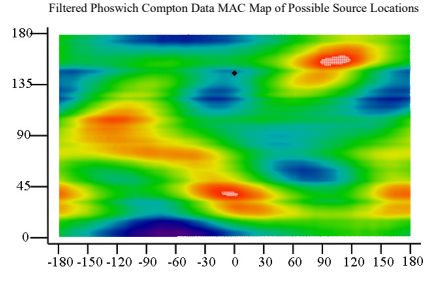

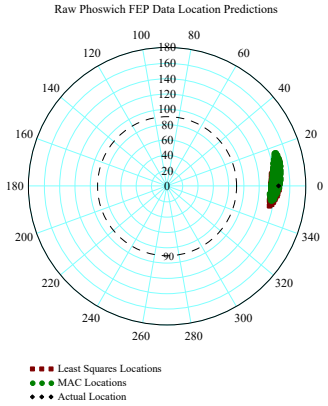

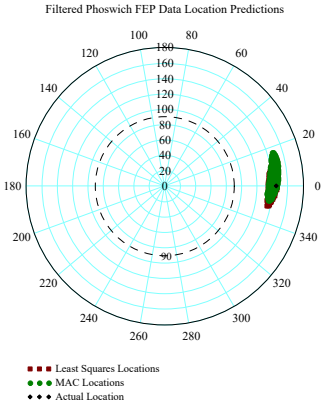

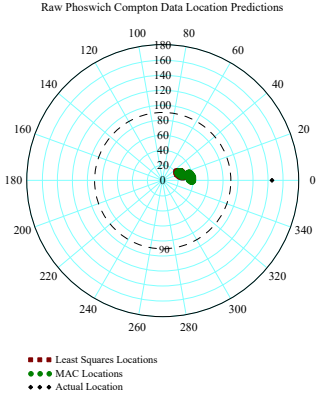

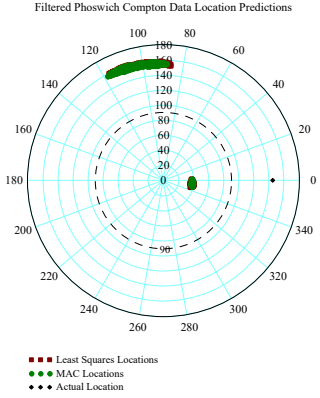

View Angle φ = 35° : Original/Filtered Phoswich w/Co-57 Rope Source Wrapped over θ = 0-359° and Placed at φ = 180° Data Spectra, Modulation Curves, Library Curves, MAC and LS Direction Predictions

Phi_ViewDegree = 35 Theta_ViewDegree = 0

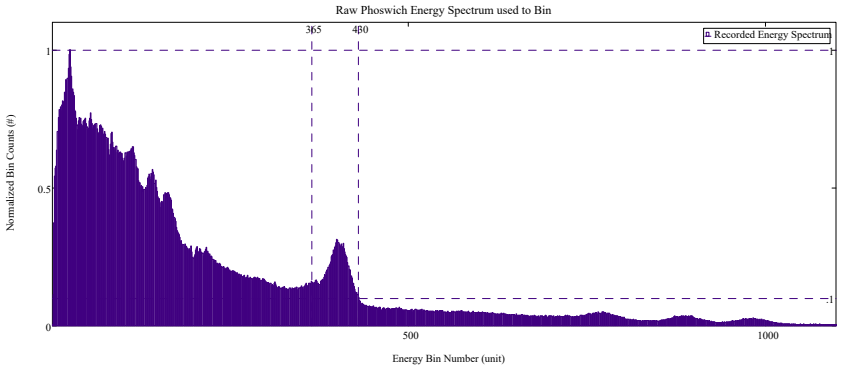

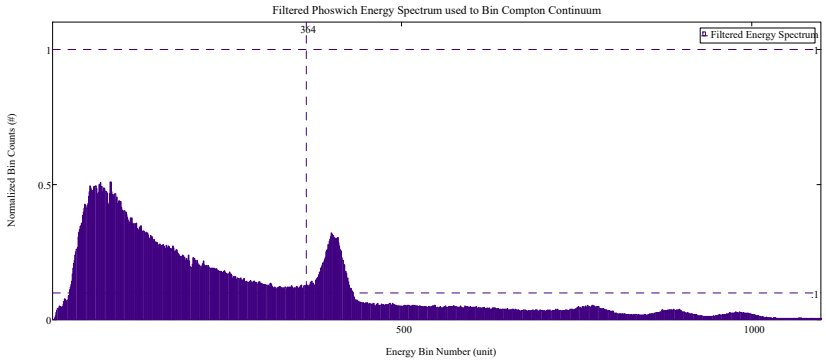

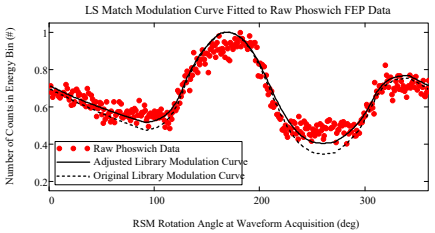

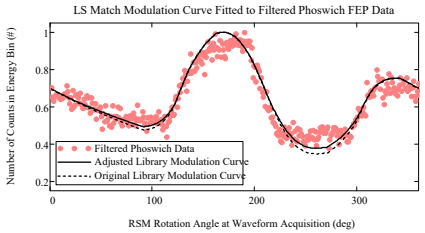

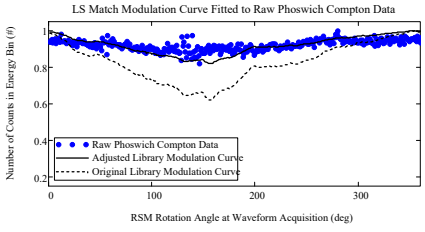

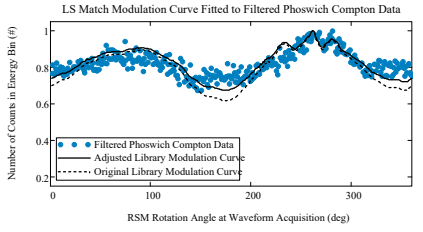

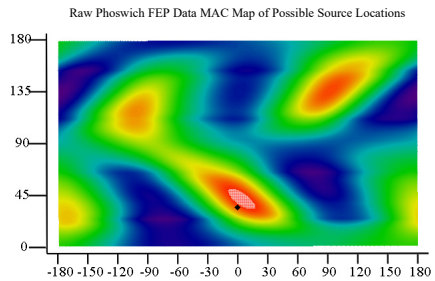

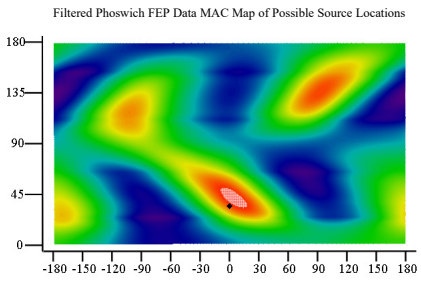

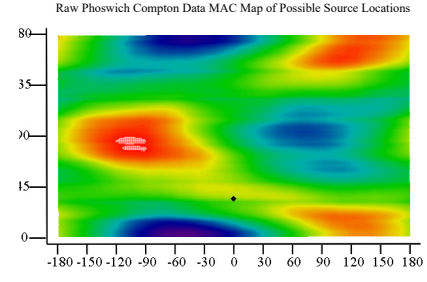

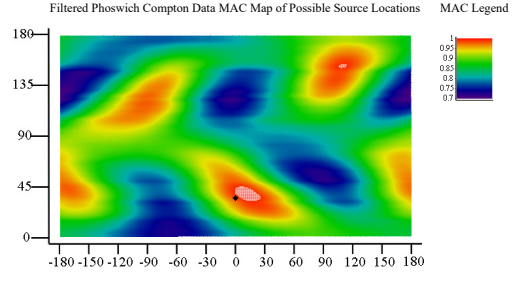

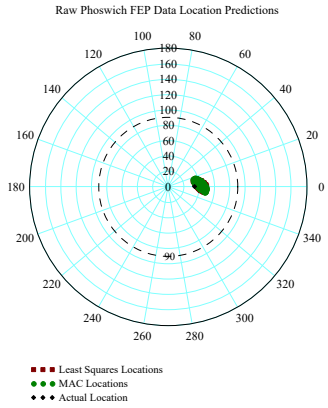

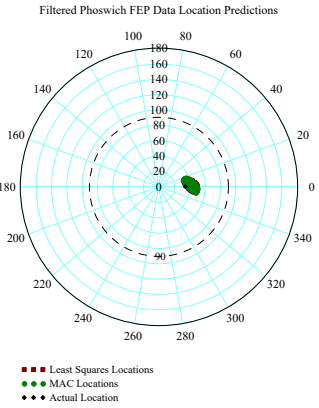

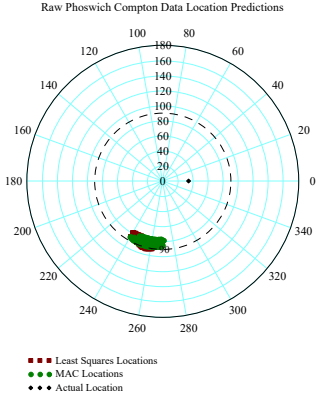

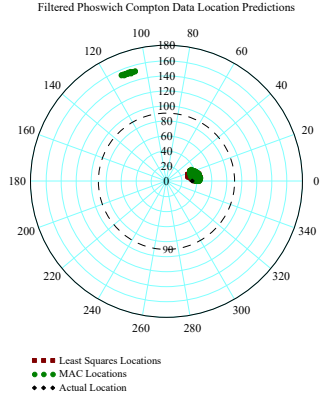

View Angle φ = 45° : Original/Filtered Phoswich w/Co-57 Rope Source Wrapped over θ = 0-359° and Placed at φ = 180° Data Spectra, Modulation Curves, Library Curves, MAC and LS Direction Predictions

Phi_ViewDegree = 45 Theta_ViewDegree = 0

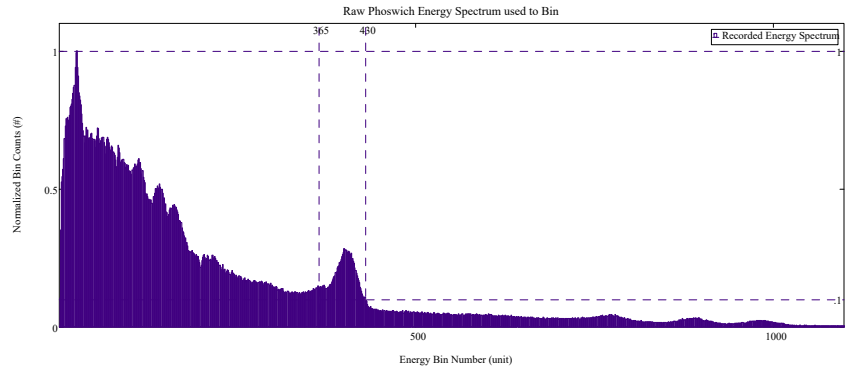

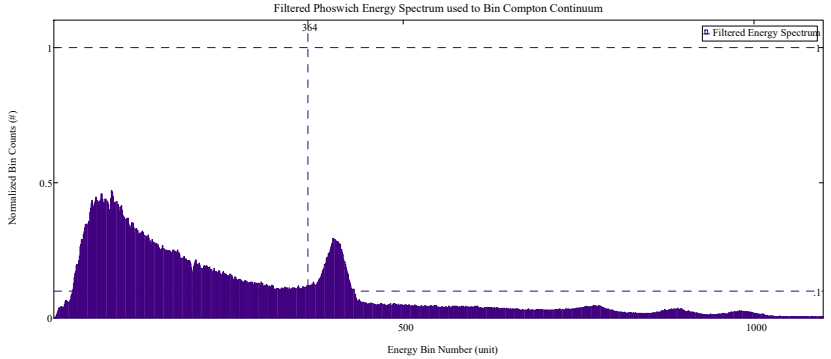

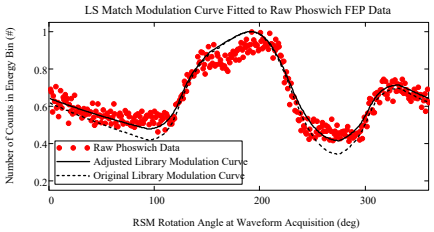

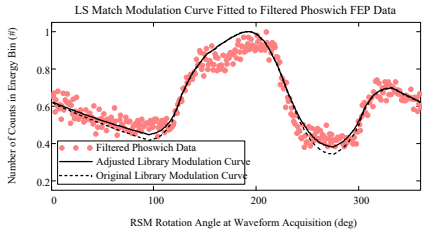

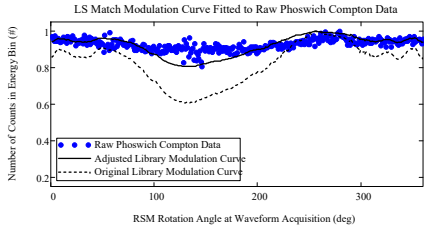

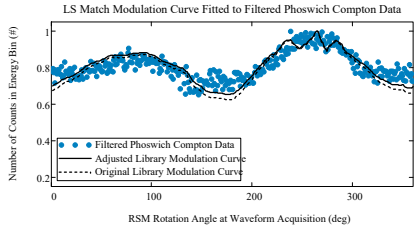

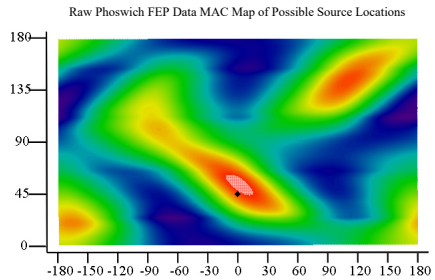

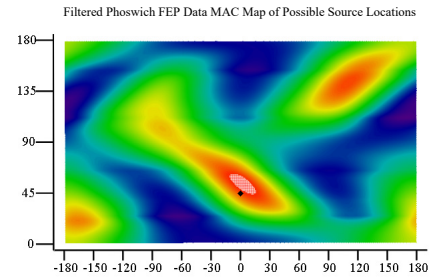

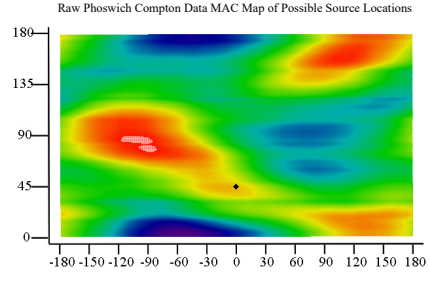

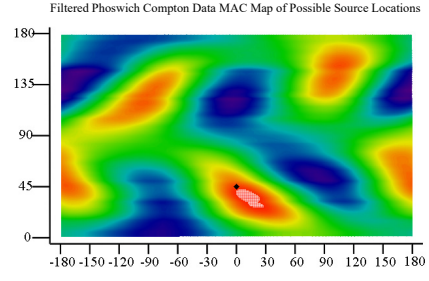

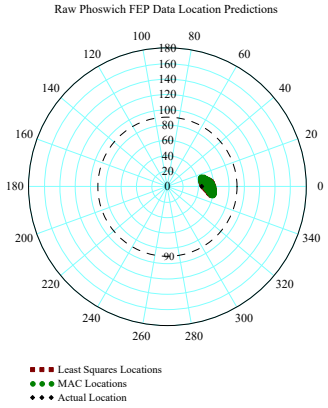

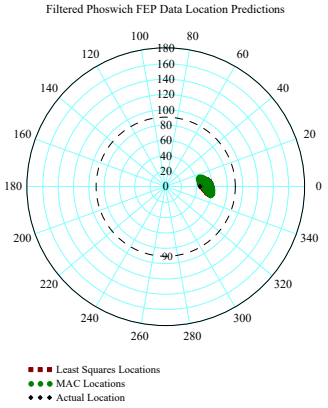

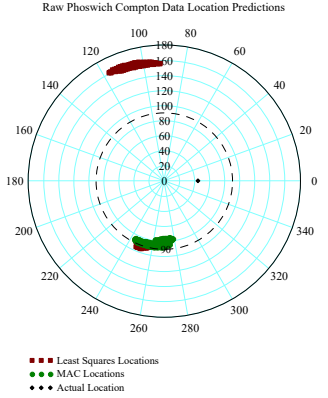

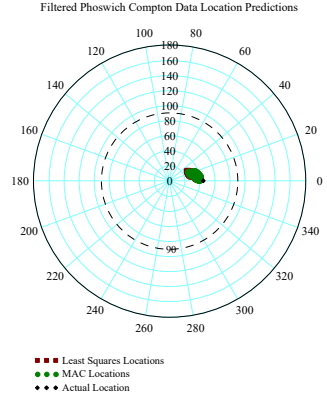

View Angle φ = 55° : Original/Filtered Phoswich w/Co-57 Rope Source Wrapped over θ = 0-359° and Placed at φ = 180° Data Spectra, Modulation Curves, Missing/Stretched Library Curves, MAC and LS Direction Predictions

Raw and Filtered Phoswich FEP Spectrum

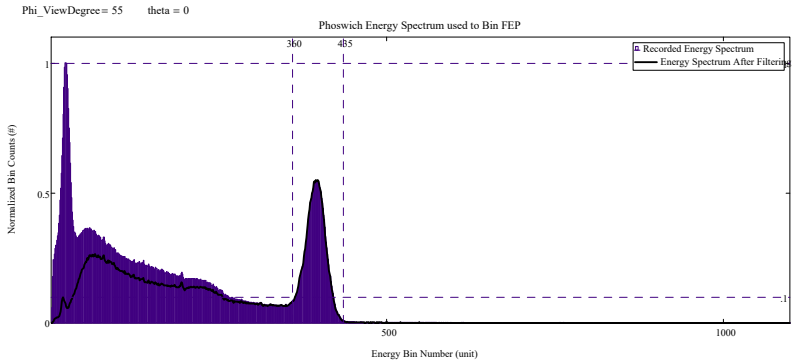

Original, Missing and Stretched Raw Phoswich FEP Modulation Curves

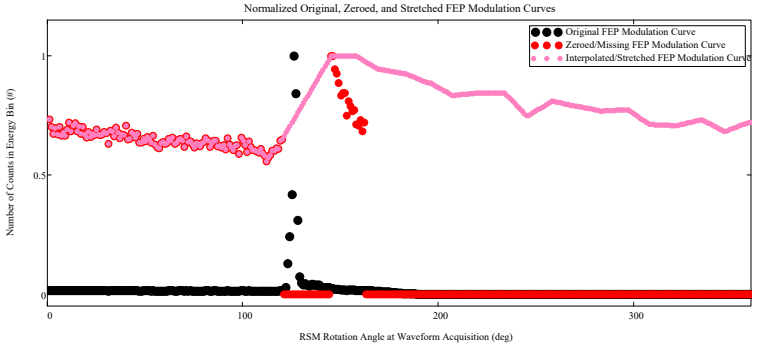

Missing Encoder Phoswich FEP Data Results:

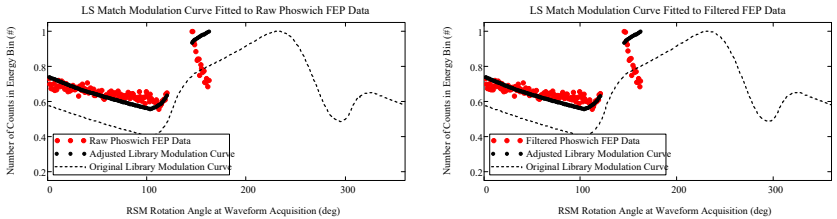

Stretched Encoder FEP Data Results:

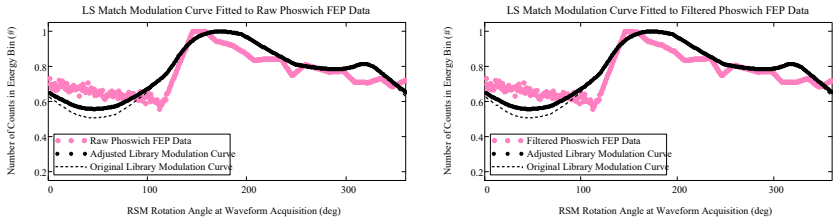

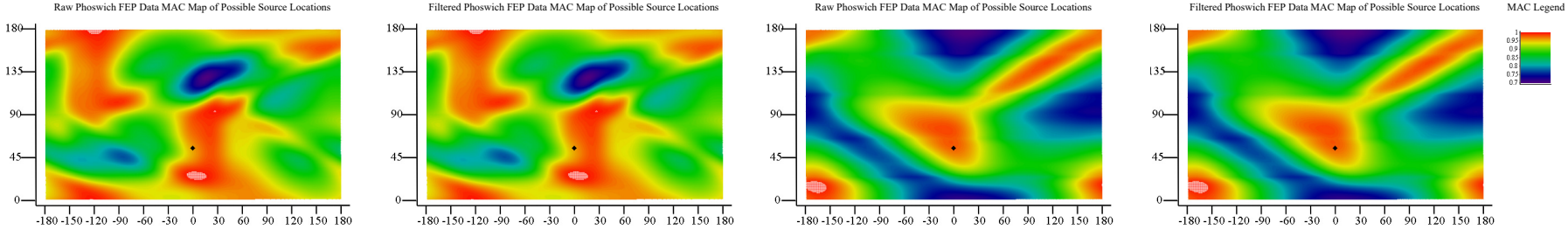

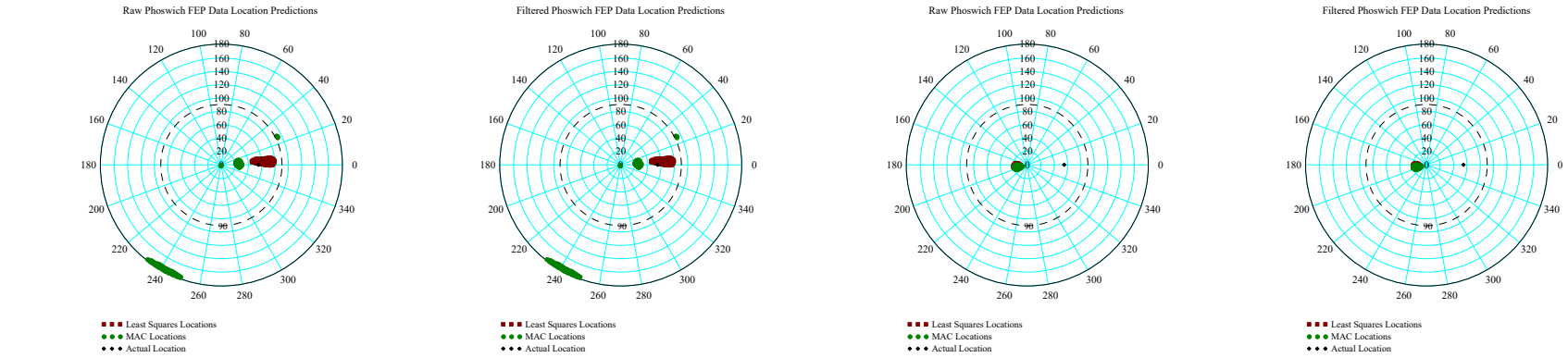

Raw and Filtered Phoswich Compton Spectrum

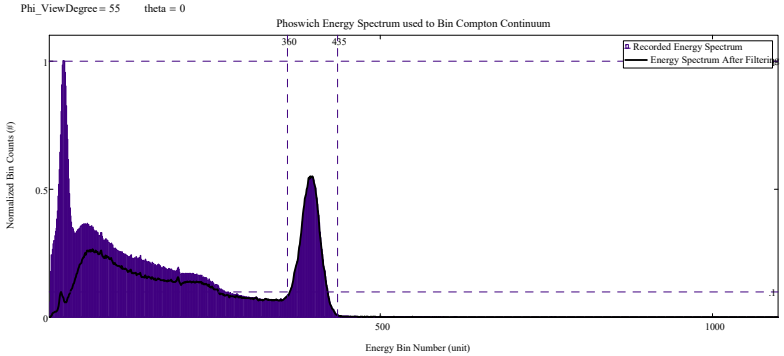

Original, Missing and Stretched Raw Phoswich Compton Modulation Curves

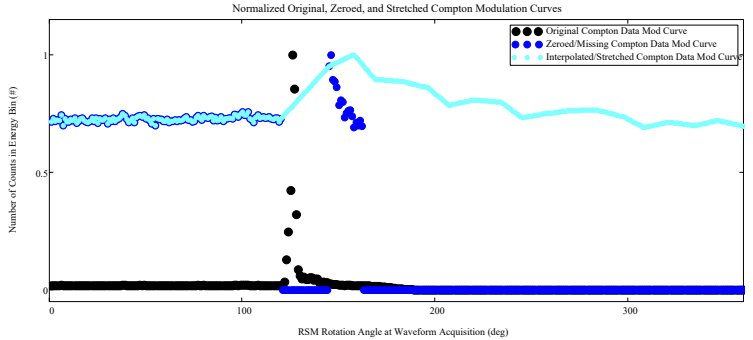

Missing Encoder Phoswich Compton Data Results:

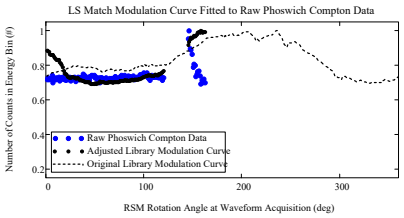

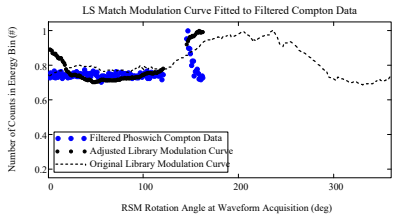

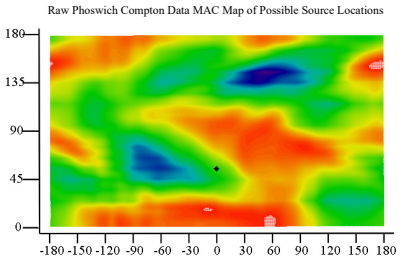

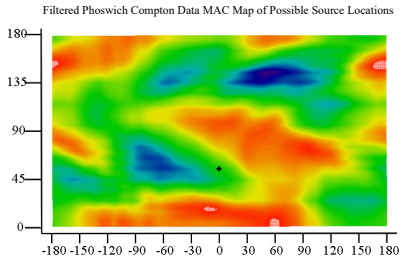

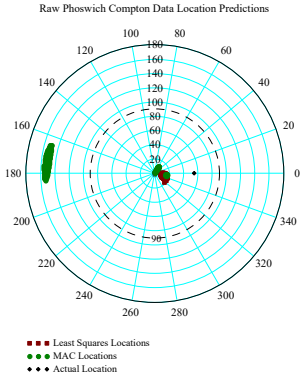

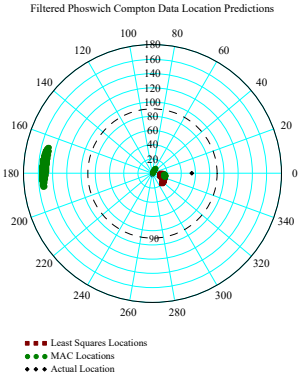

Stretched Encoder Compton Data Results:

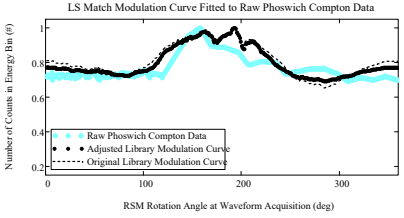

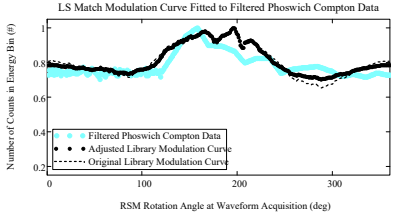

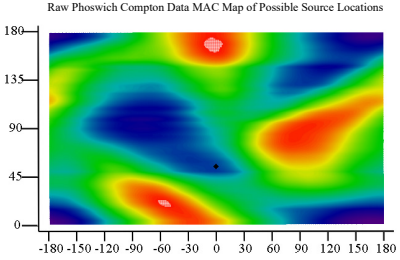

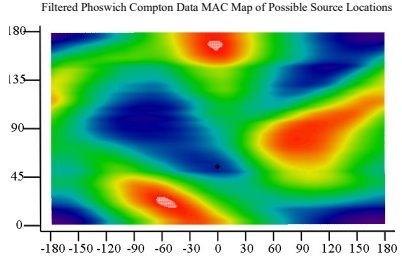

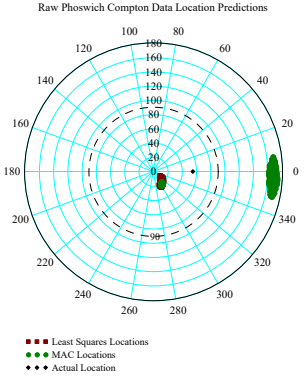

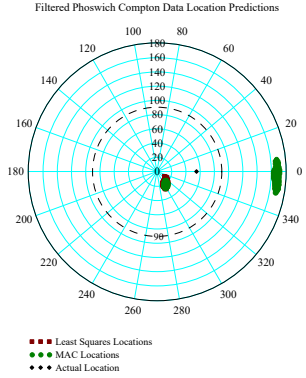

View Angle φ = 125° : Original/Filtered Phoswich w/Co-57 Rope Source Wrapped over θ = 0-359° and Placed at φ = 180° Data Spectra, Modulation Curves, Missing/Stretched Library Curves, MAC and LS Direction Predictions

Raw and Filtered Phoswich FEP Spectrum

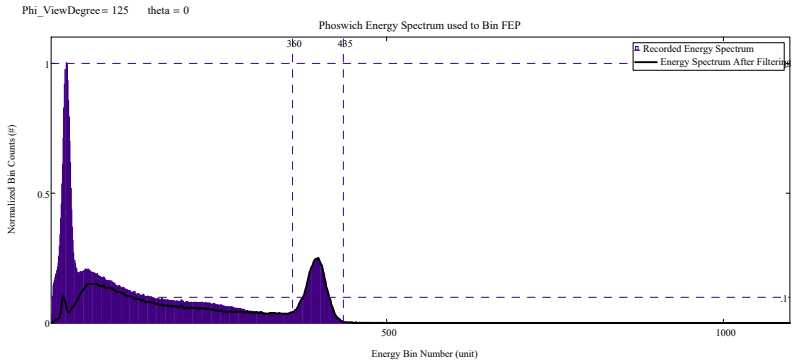

Original, Missing and Stretched Raw Phoswich FEP Modulation Curves

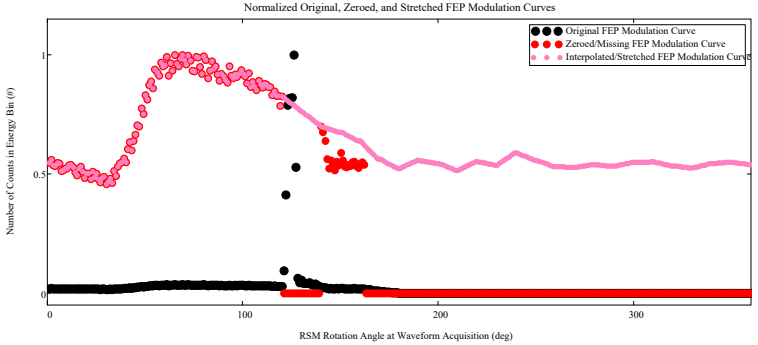

Missing Encoder Phoswich FEP Data Results:

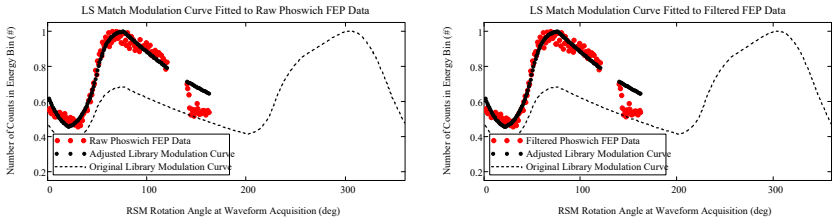

Stretched Encoder FEP Data Results:

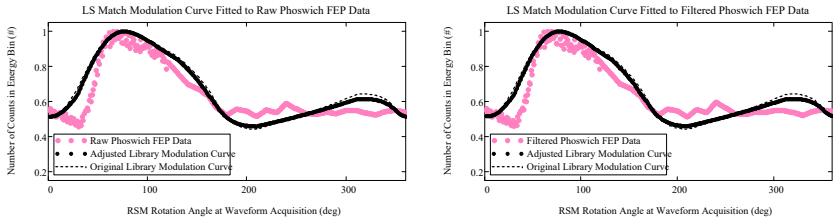

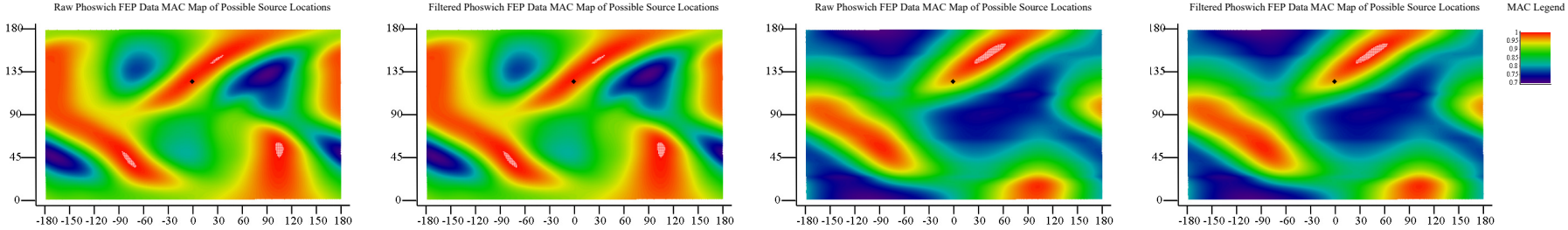

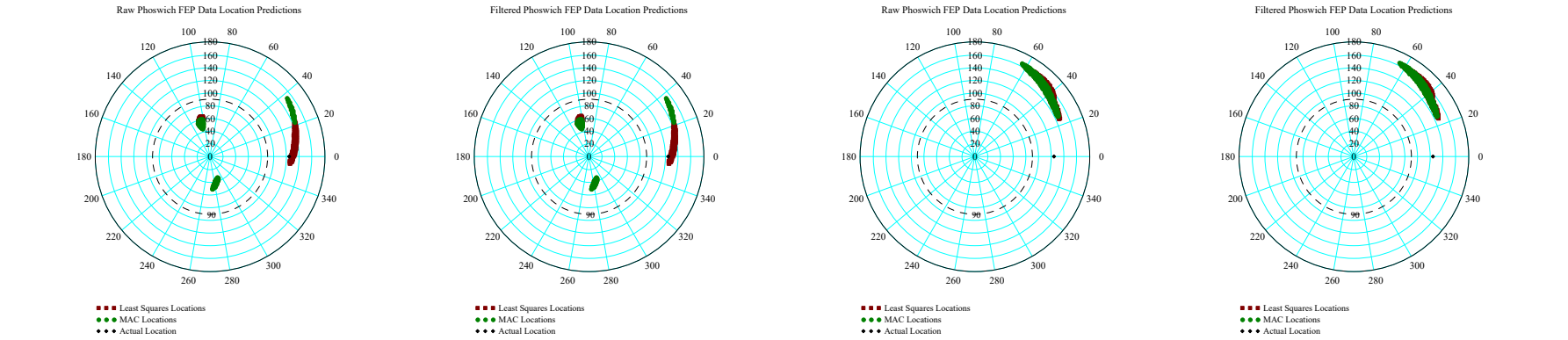

Raw and Filtered Phoswich Compton Spectrum

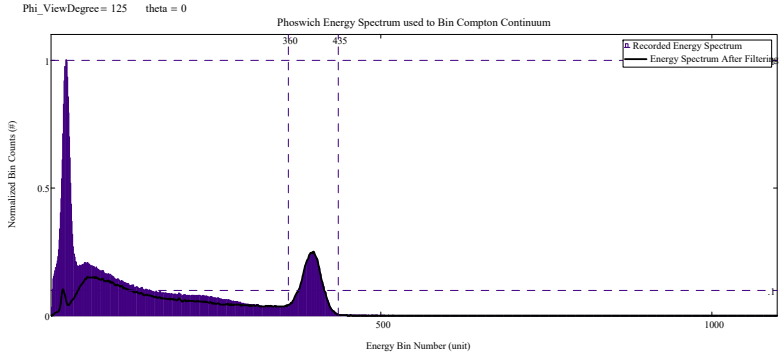

Original, Missing and Stretched Raw Phoswich Compton Modulation Curves

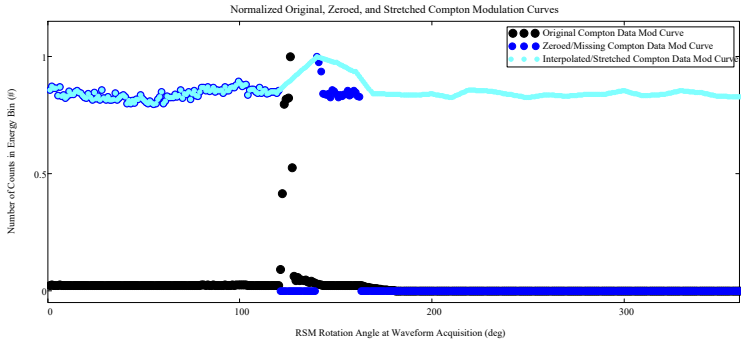

Missing Encoder Phoswich Compton Data Results:

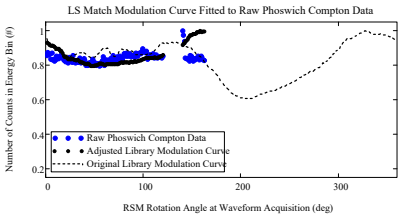

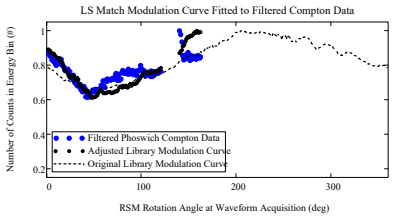

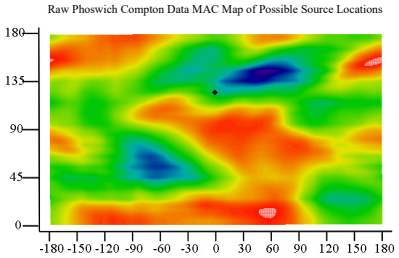

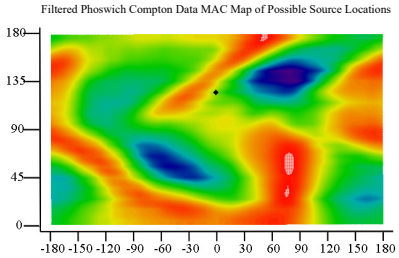

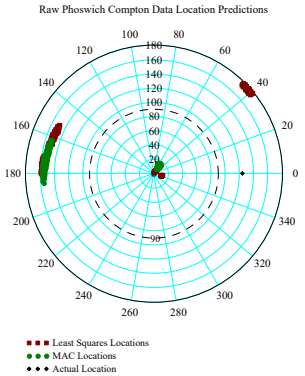

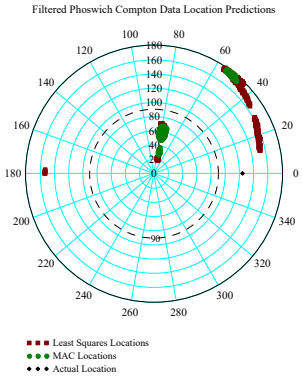

Stretched Encoder Compton Data Results:

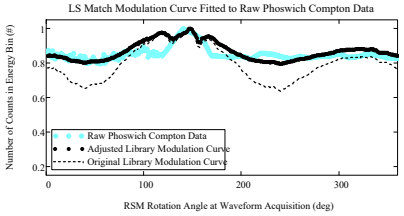

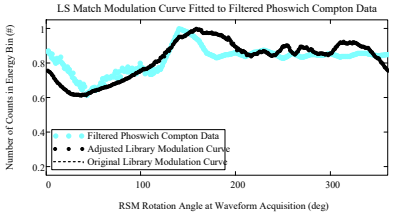

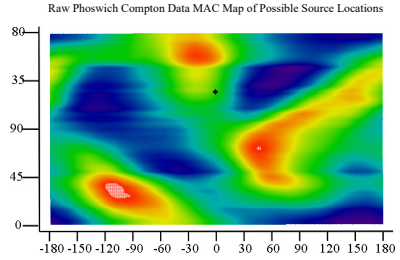

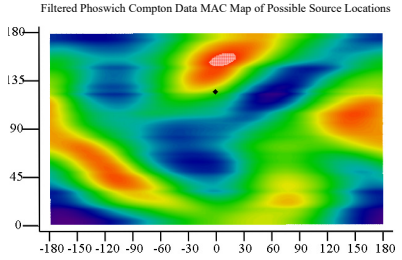

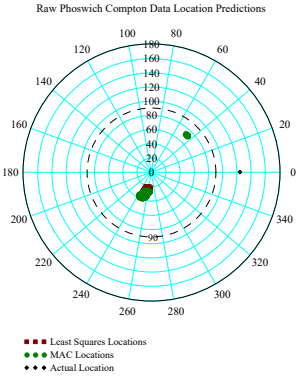

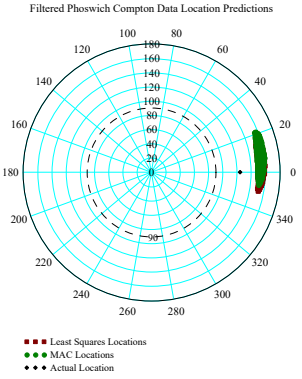

View Angle φ = 135° : Original/Filtered Phoswich w/Co-57 Rope Source Wrapped over θ = 0-359° and Placed at φ = 180° Data Spectra, Modulation Curves, Missing/Stretched Library Curves, MAC and LS Direction Predictions

Raw and Filtered Phoswich FEP Spectrum

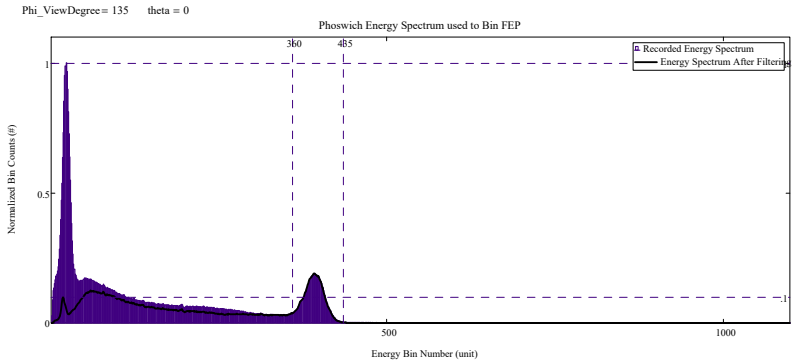

Original, Missing and Stretched Raw Phoswich FEP Modulation Curves

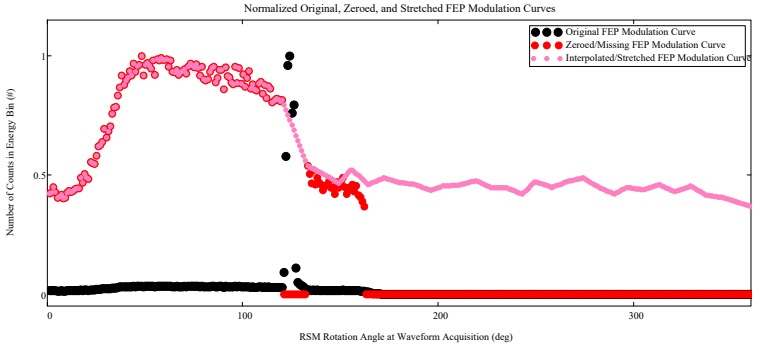

Missing Encoder Phoswich FEP Data Results:

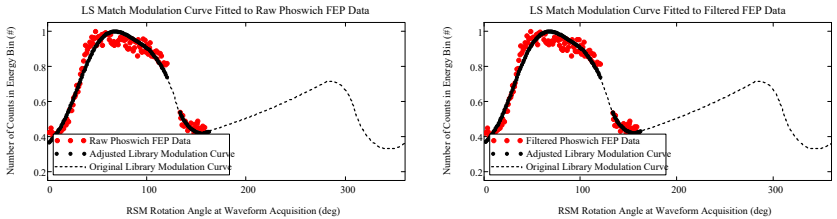

Stretched Encoder FEP Data Results:

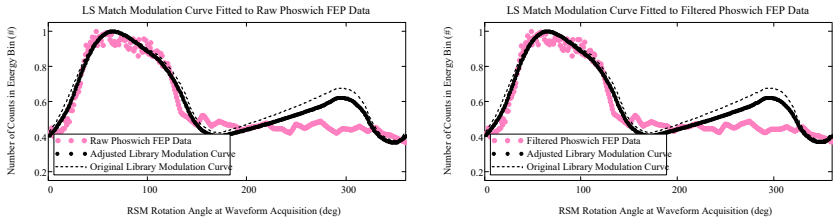

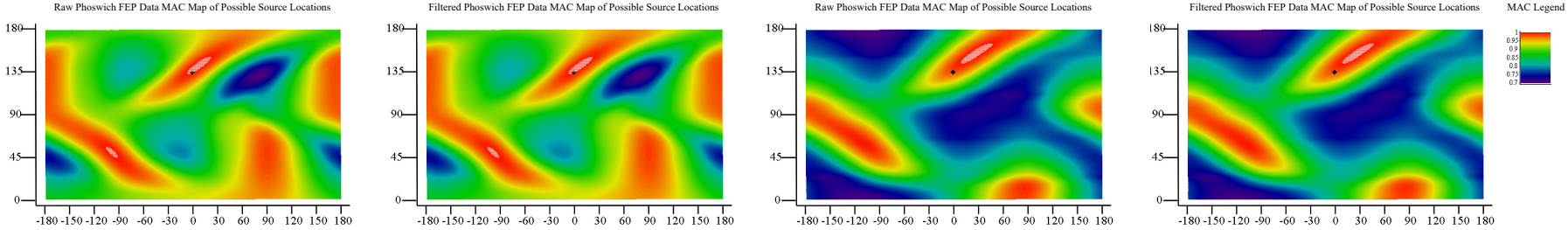

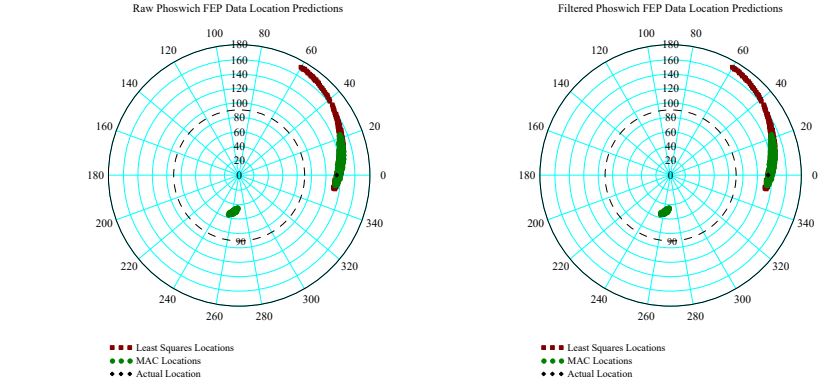

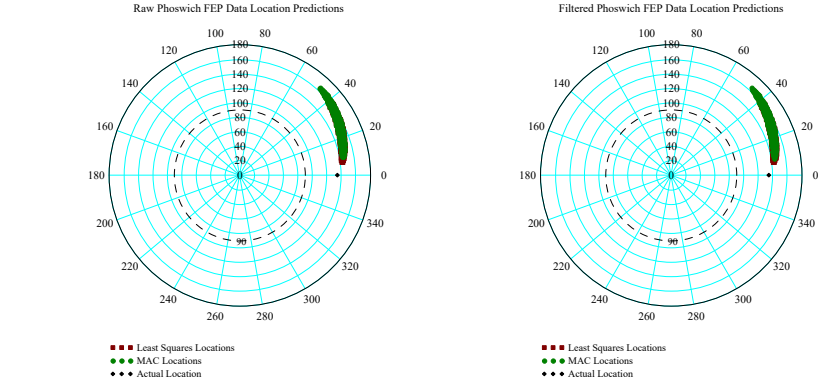

Raw and Filtered Phoswich Compton Spectrum

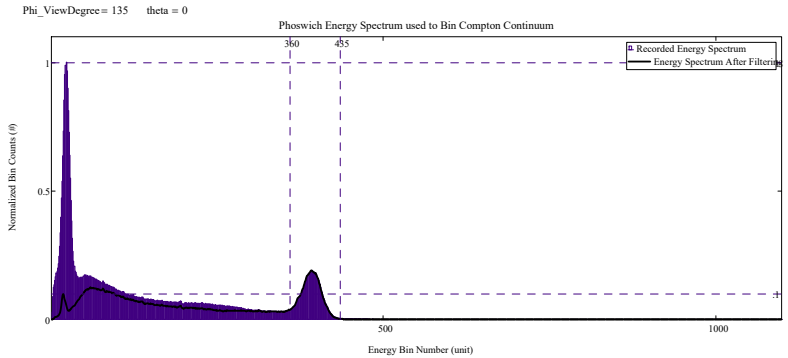

Original, Missing and Stretched Raw Phoswich Compton Modulation Curves

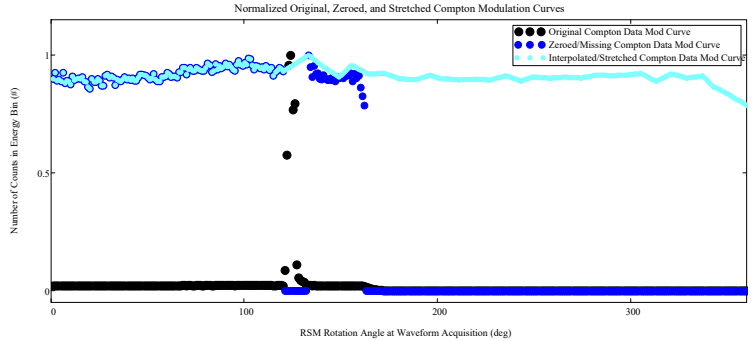

Missing Encoder Phoswich Compton Data Results:

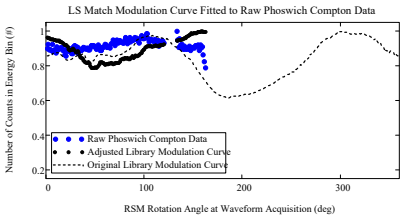

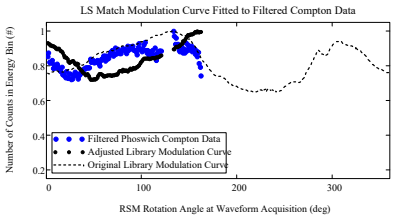

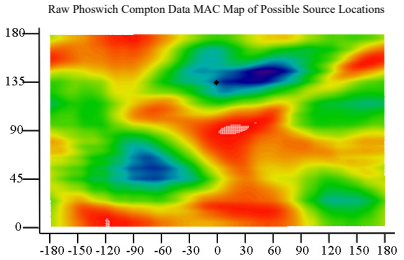

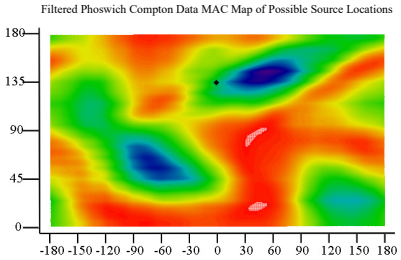

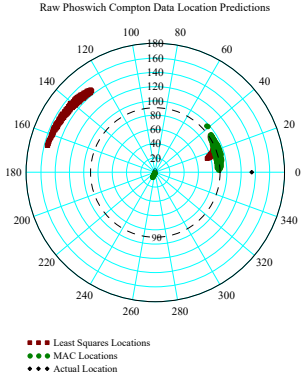

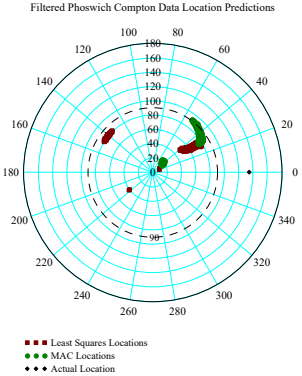

Stretched Encoder Compton Data Results:

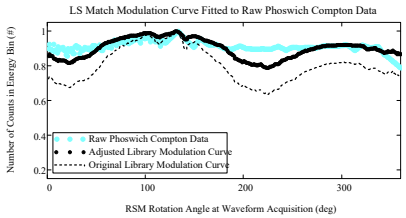

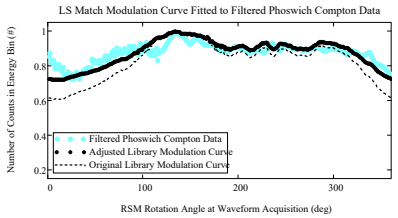

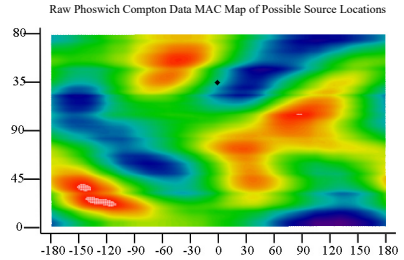

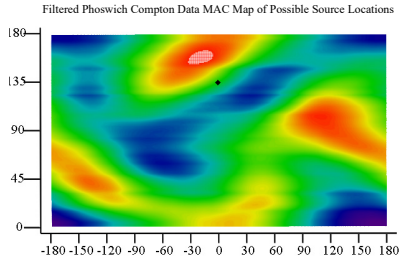

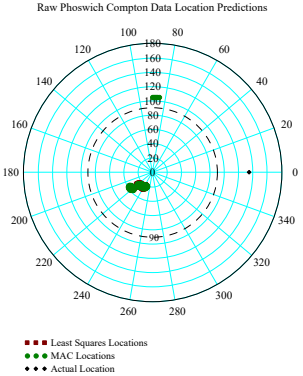

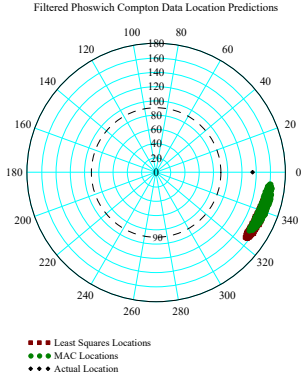

View Angle φ = 145° : Original/Filtered Phoswich w/Co-57 Rope Source Wrapped over θ = 0-359° and Placed at φ = 180° Data Spectra, Modulation Curves, Missing/Stretched Library Curves, MAC and LS Direction Predictions

Raw and Filtered Phoswich FEP Spectrum

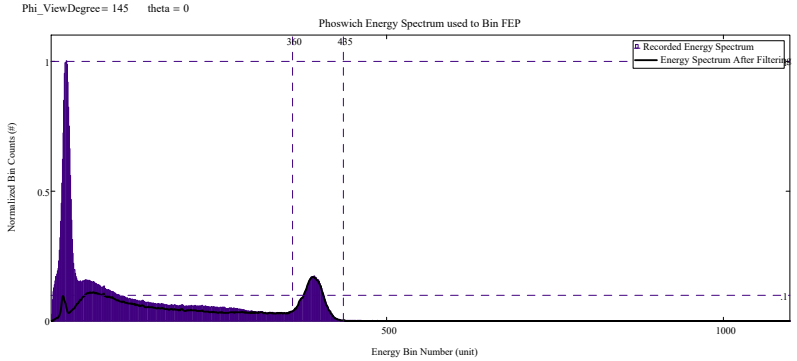

Original, Missing and Stretched Raw Phoswich FEP Modulation Curves

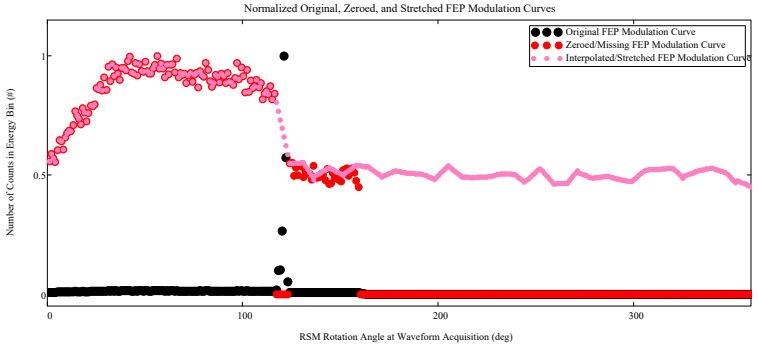

Missing Encoder Phoswich FEP Data Results:

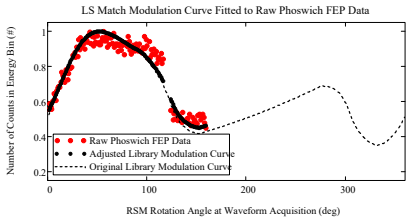

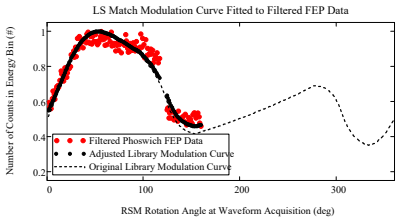

Stretched Encoder FEP Data Results:

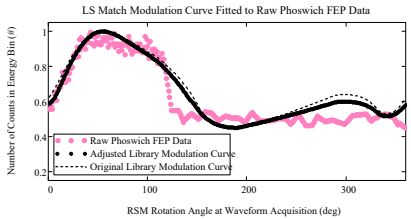

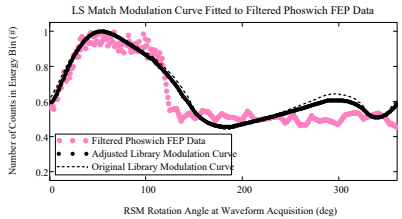

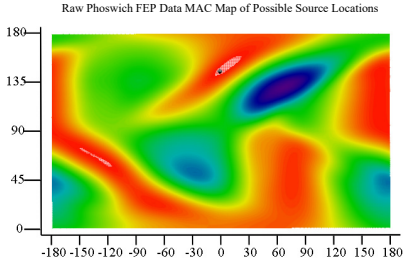

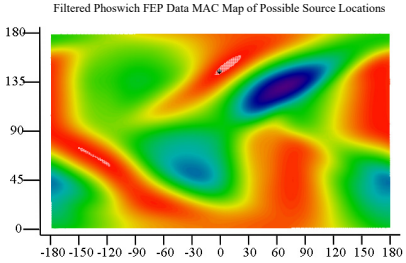

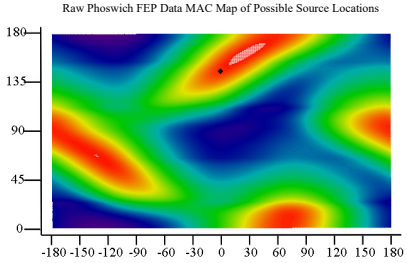

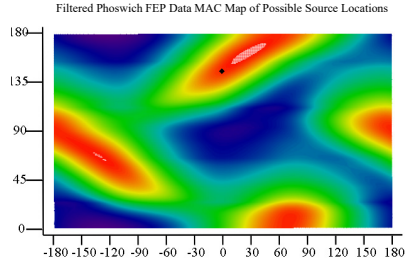

MAC Legend

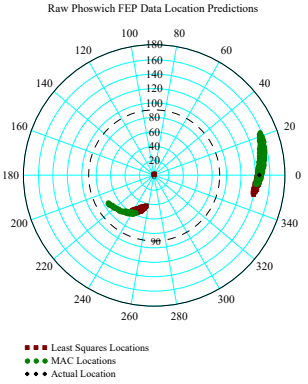

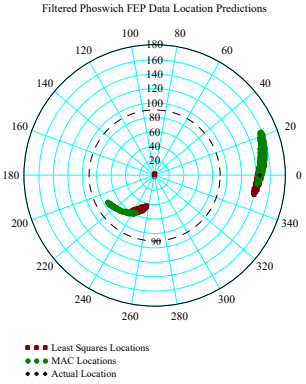

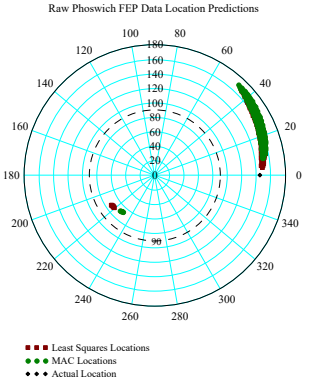

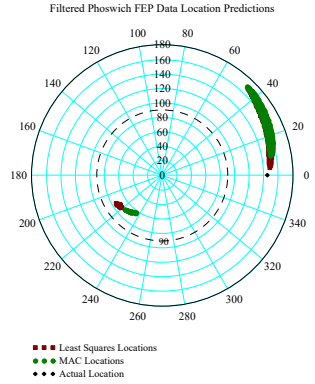

Raw and Filtered Phoswich Compton Spectrum

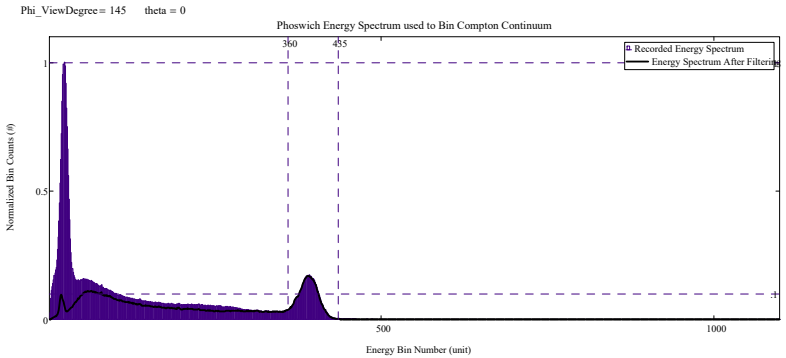

Original, Missing and Stretched Raw Phoswich Compton Modulation Curves

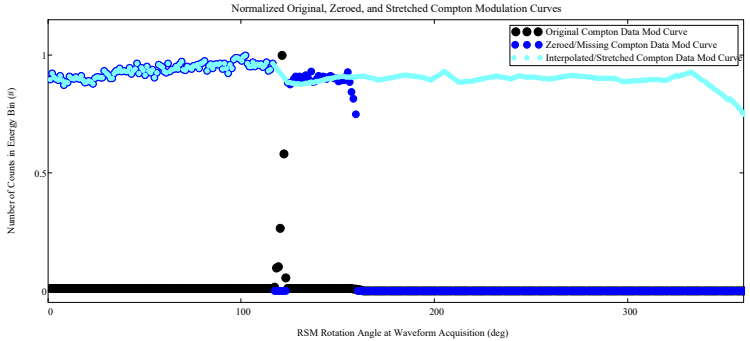

Missing Encoder Phoswich Compton Data Results:

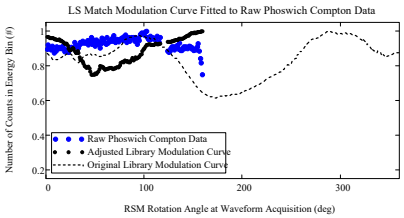

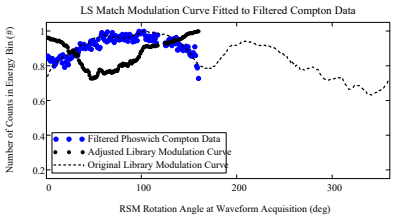

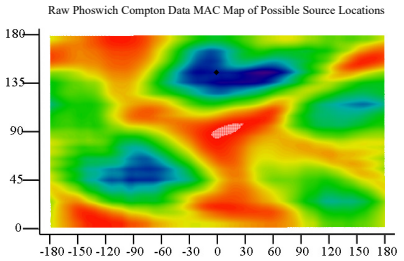

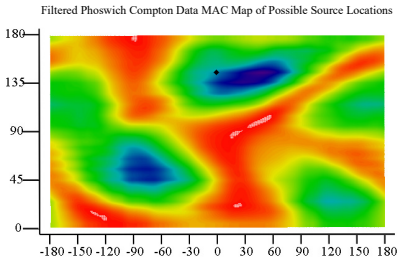

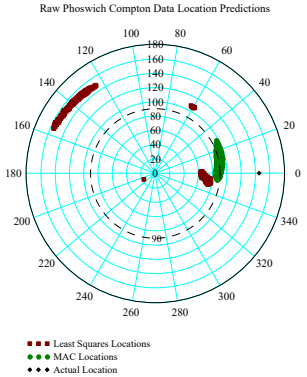

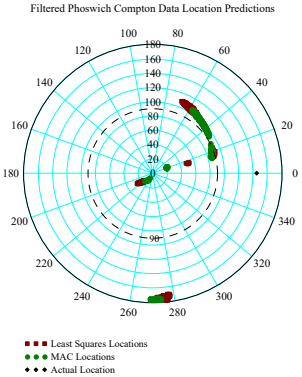

Stretched Encoder Compton Data Results:

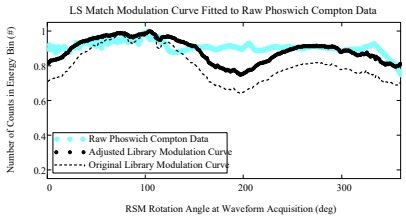

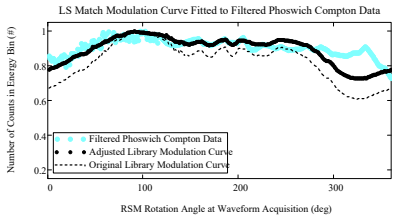

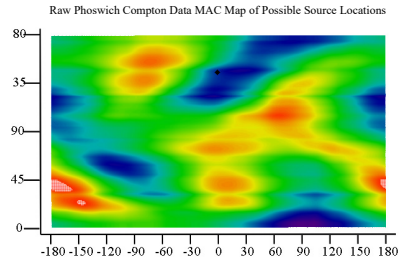

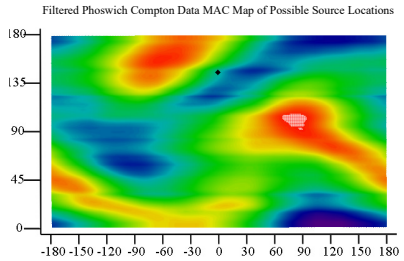

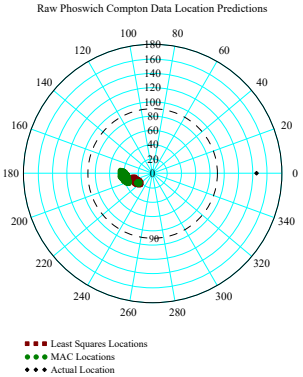

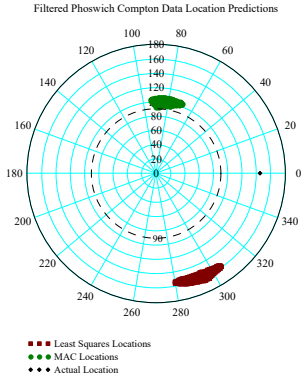

Appendix B.1: Small FitzGerald Design RSM Data, LaBr "Finger" Detector, Ba-133 & Cs-137 Single Sources; Experimentally Derived & Detector Shape Modified Library Matching Result

Page Intentionally Left Blank

View Angle φ = 5° : Small RSM FitzGerald Design Ba-133and Cs-137 Data Spectra for Original and Detector Shape Modified Libraries, Modulation Curves, Library Curves, MAC and LS Direction Predictions

Ba-133 Source Data Results: Phi_ViewDegree = 5 Theta_ViewDegree = 0

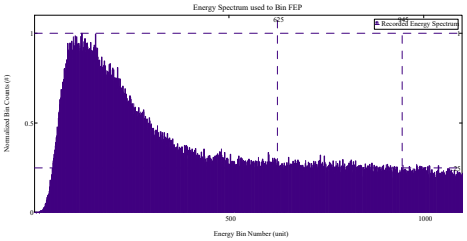

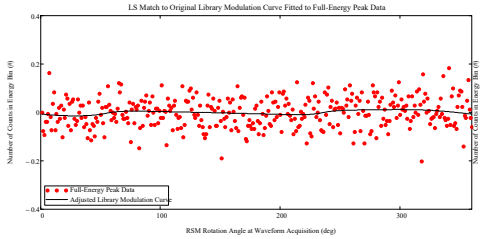

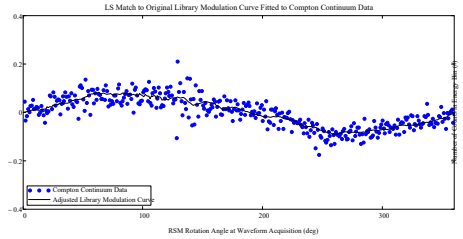

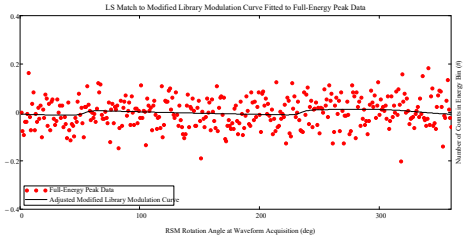

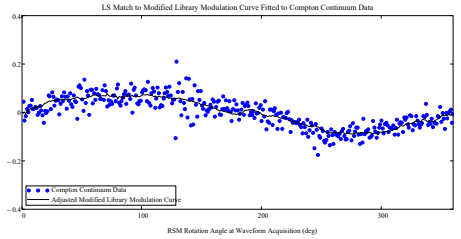

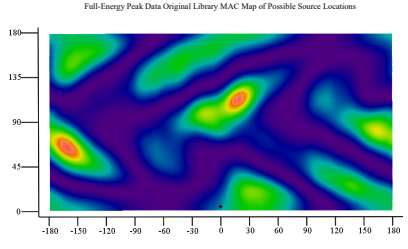

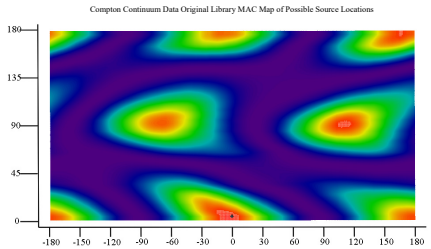

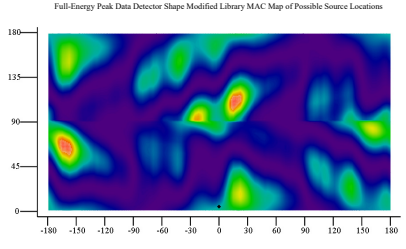

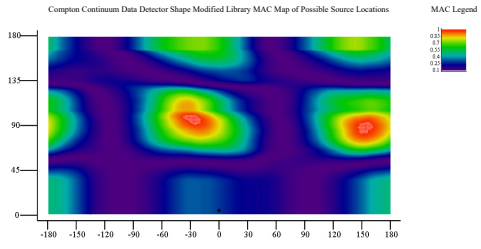

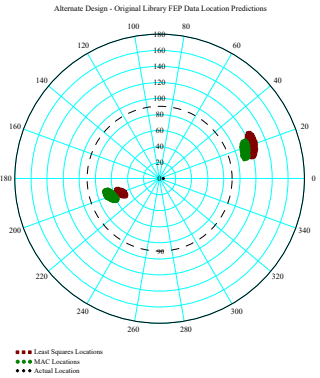

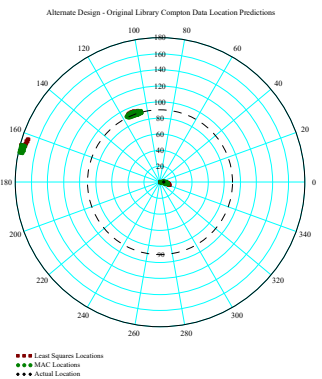

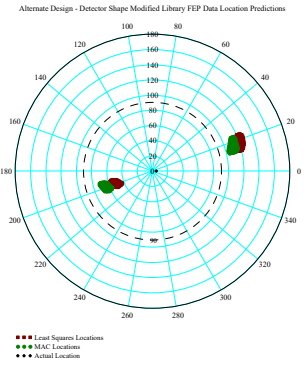

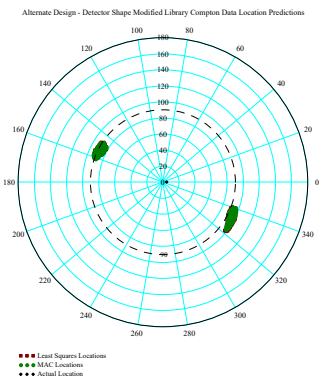

Cs-137 Source Data Results:

Phi_ViewDegree = 5
Theta_ViewDegree = 0

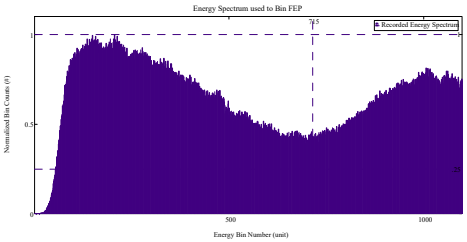

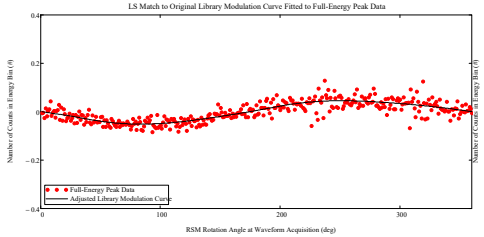

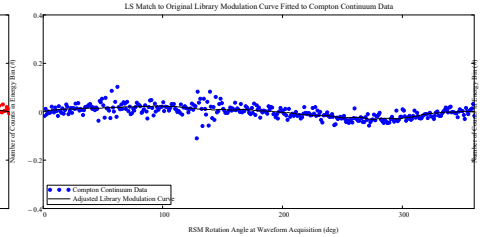

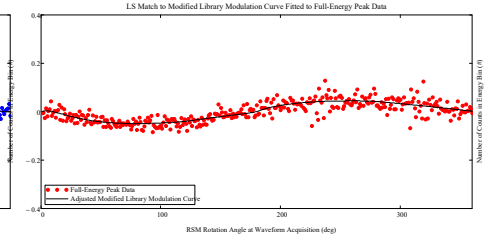

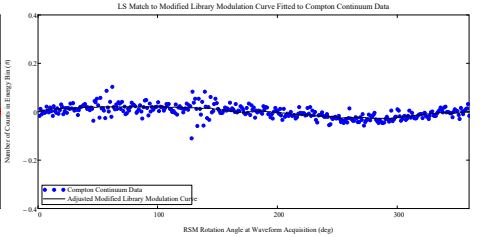

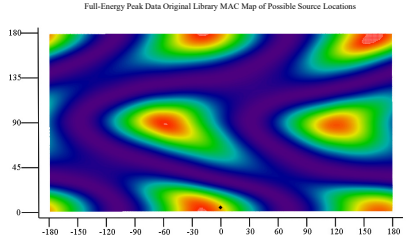

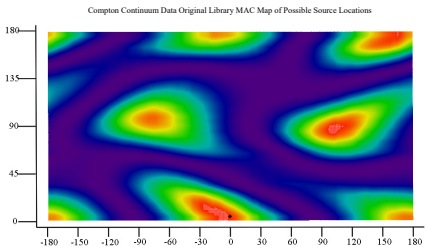

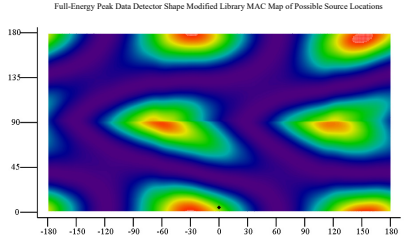

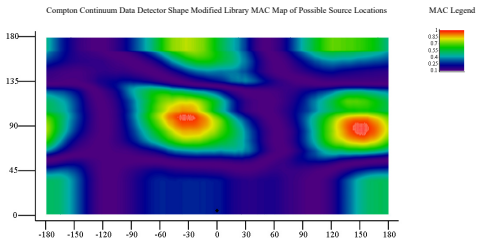

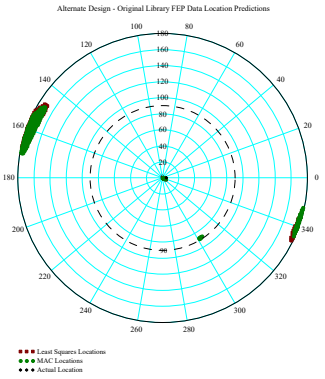

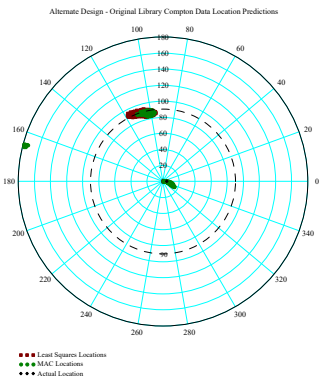

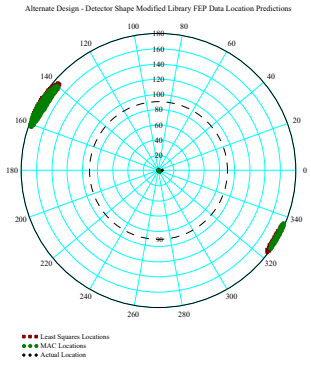

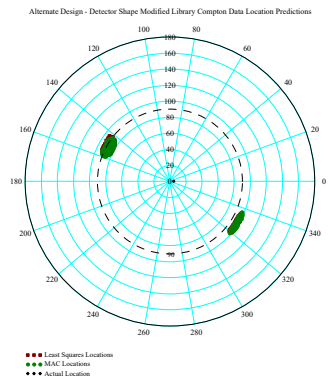

View Angle φ = 15° : Small RSM FitzGerald Design Ba-133and Cs-137 Data Spectra for Original and Detector Shape Modified Libraries, Modulation Curves, Library Curves, MAC and LS Direction Predictions

Ba-133 Source Data Results: Phi_ViewDegree = 15 Theta_ViewDegree = 0

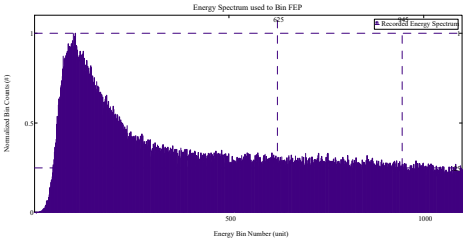

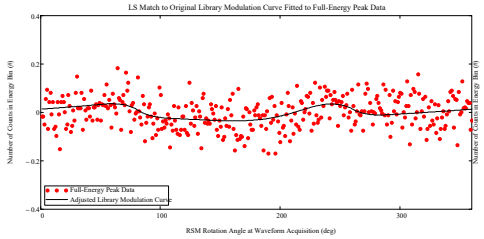

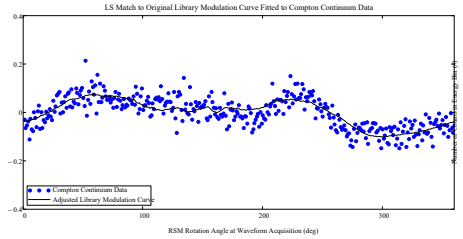

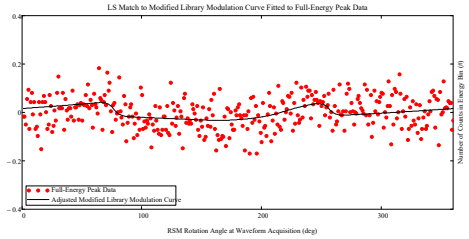

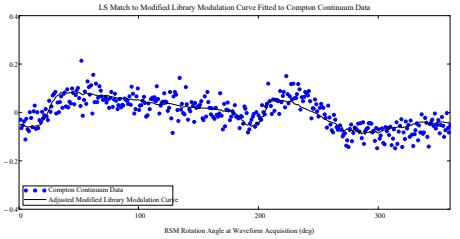

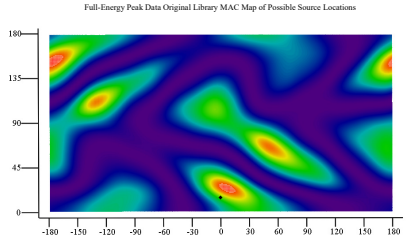

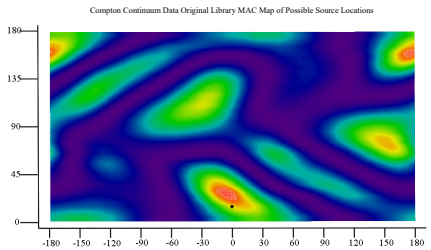

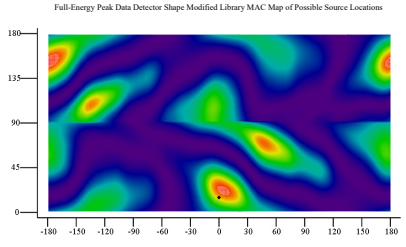

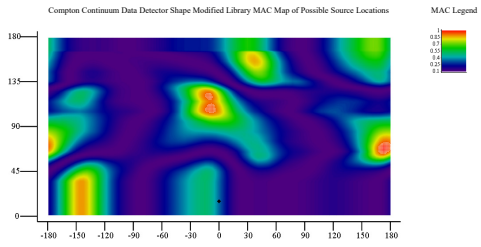

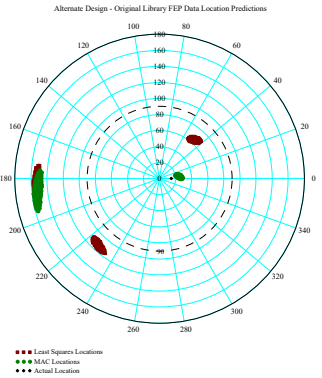

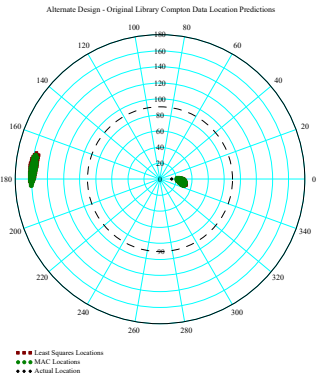

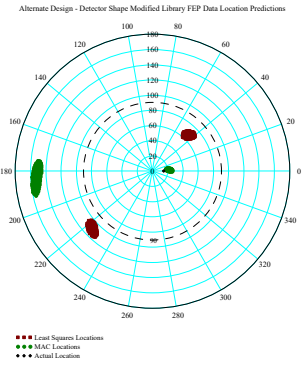

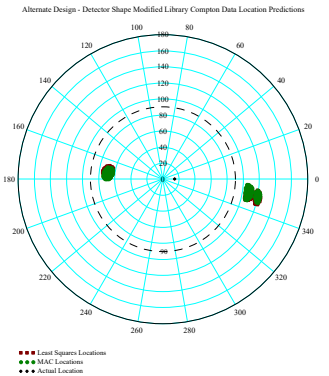

Cs-137 Source Data Results:

Phi_ViewDegree = 15
Theta_ViewDegree = 0

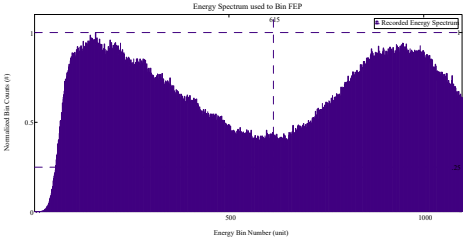

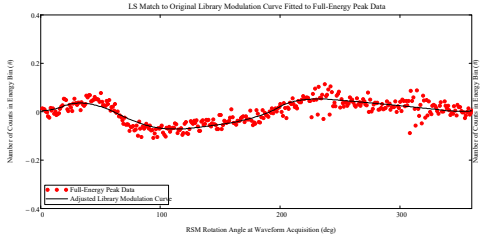

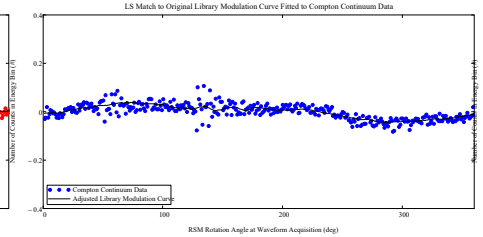

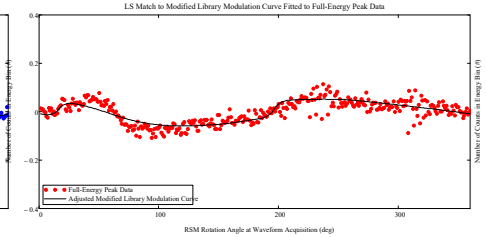

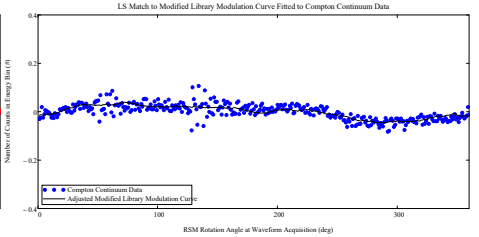

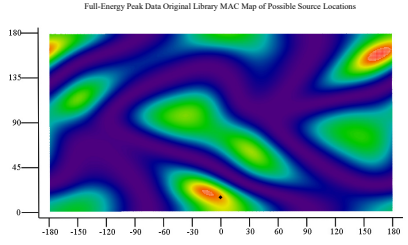

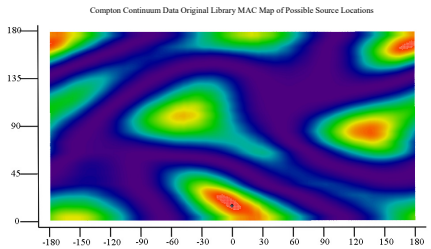

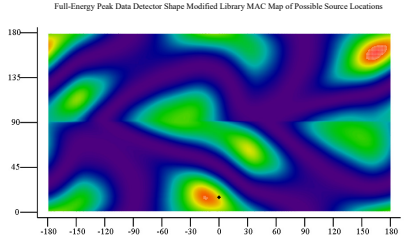

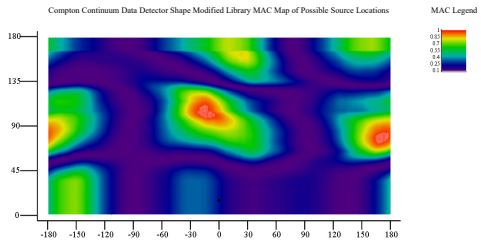

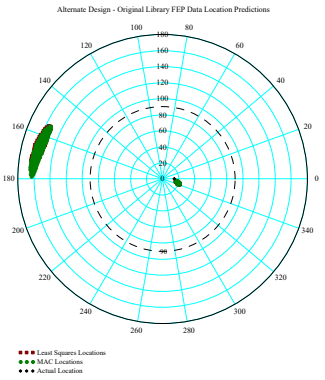

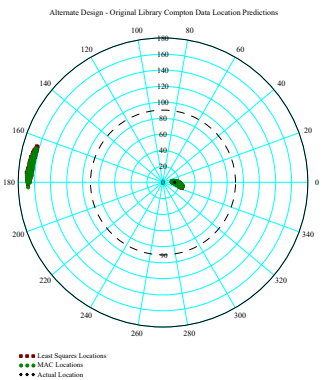

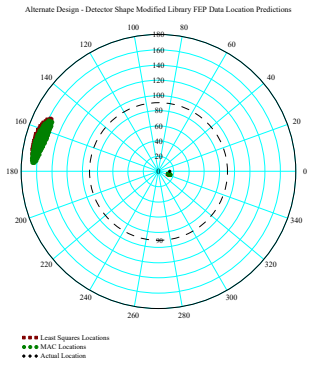

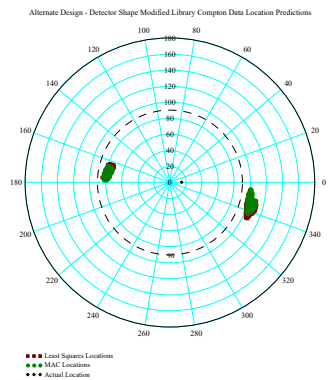

View Angle φ = 25° : Small RSM FitzGerald Design Ba-133and Cs-137 Data Spectra for Original and Detector Shape Modified Libraries, Modulation Curves, Library Curves, MAC and LS Direction Predictions

Ba-133 Source Data Results: Phi_ViewDegree = 25 Theta_ViewDegree = 0

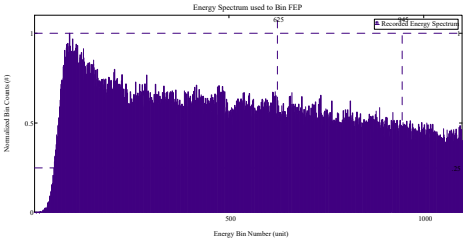

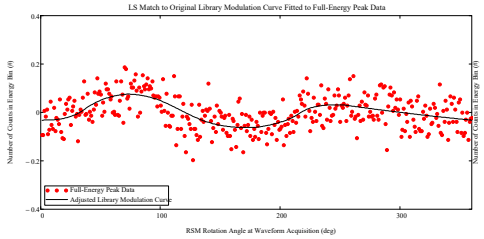

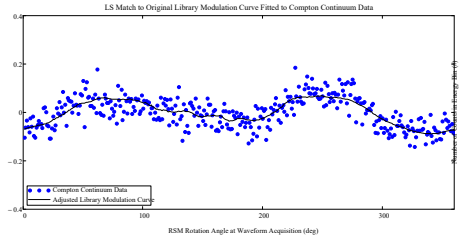

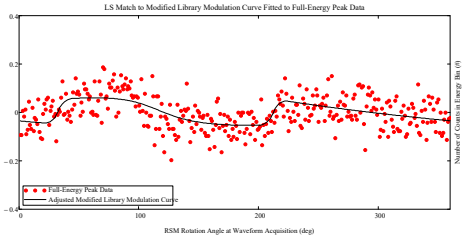

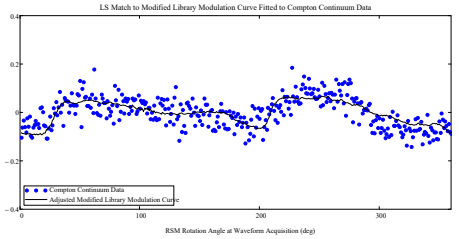

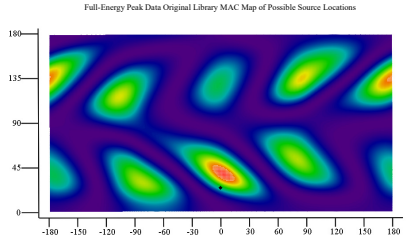

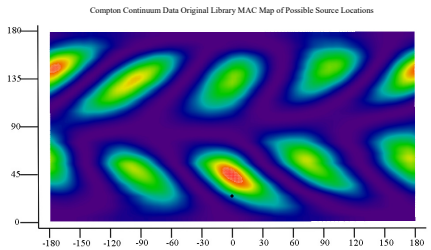

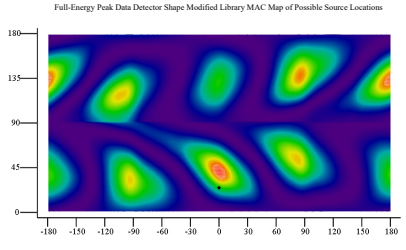

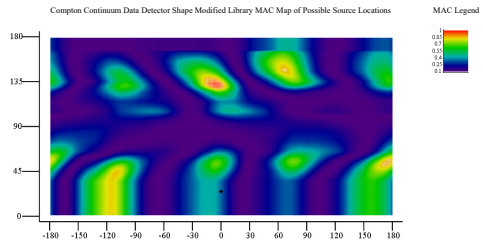

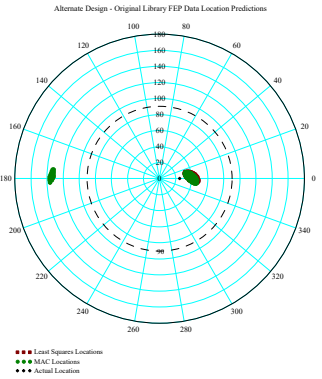

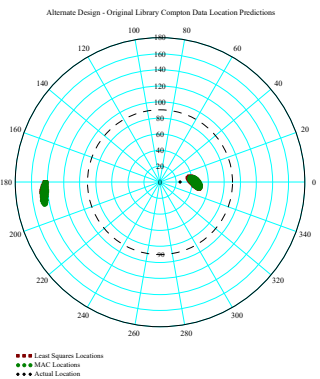

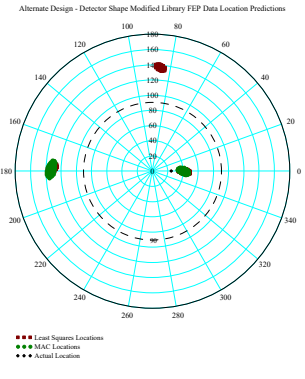

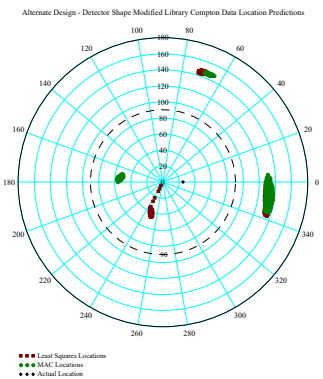

Cs-137 Source Data Results:

Phi_ViewDegree = 25
Theta_ViewDegree = 0

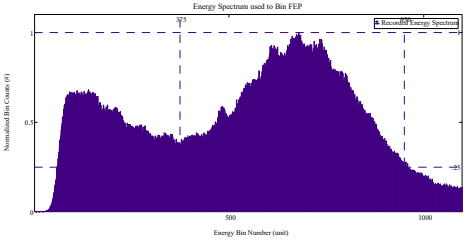

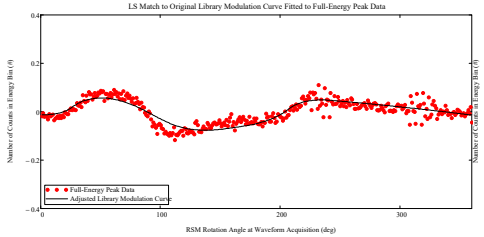

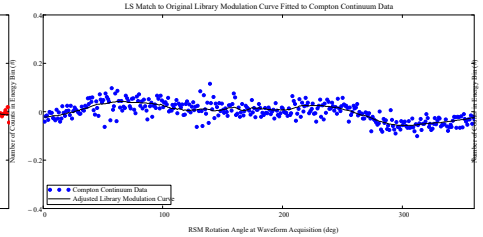

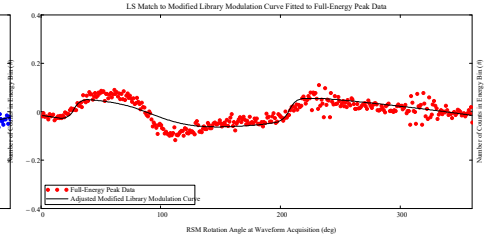

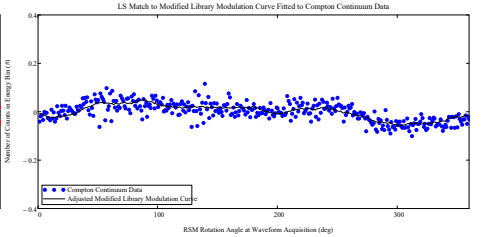

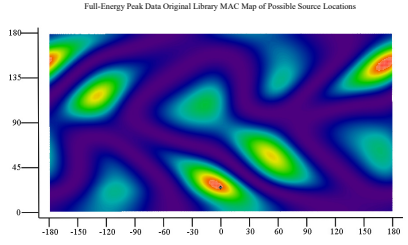

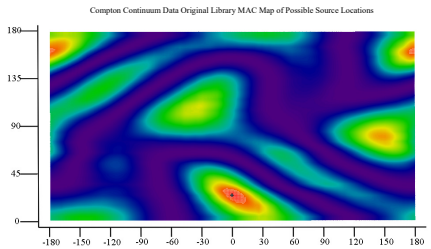

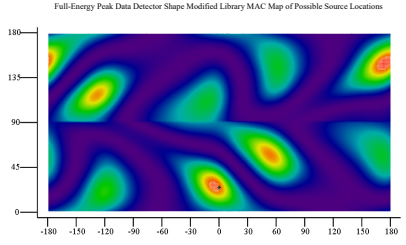

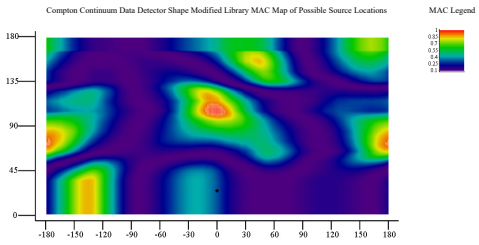

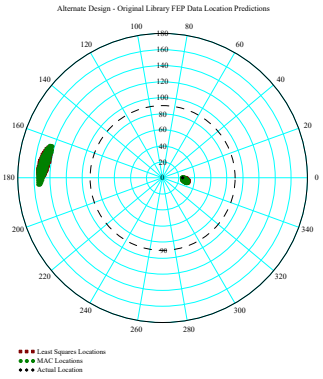

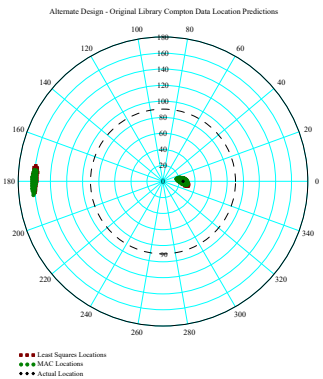

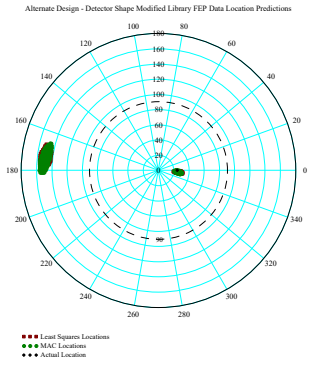

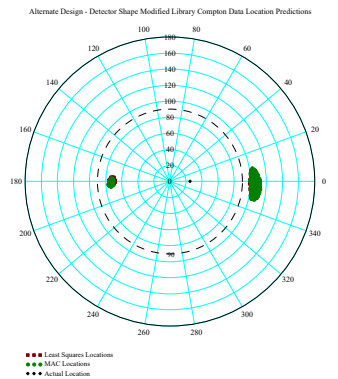

View Angle φ = 35° : Small RSM FitzGerald Design Ba-133and Cs-137 Data Spectra for Original and Detector Shape Modified Libraries, Modulation Curves, Library Curves, MAC and LS Direction Predictions

Ba-133 Source Data Results: Phi_ViewDegree = 35 Theta_ViewDegree = 0

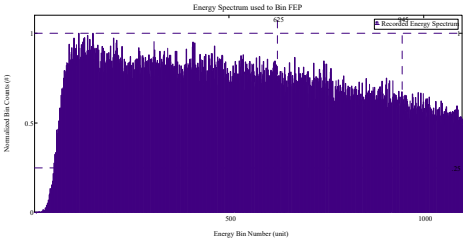

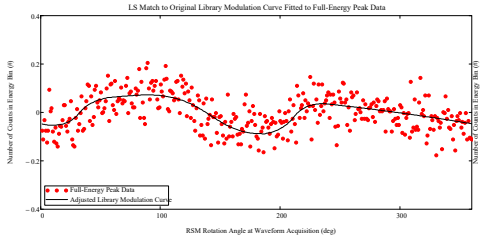

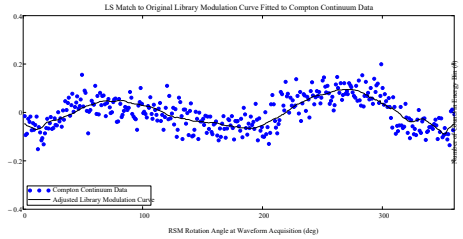

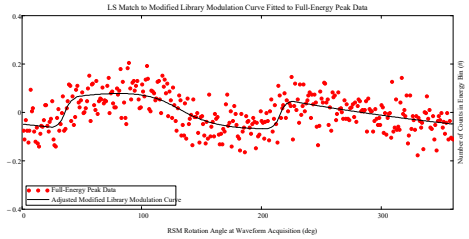

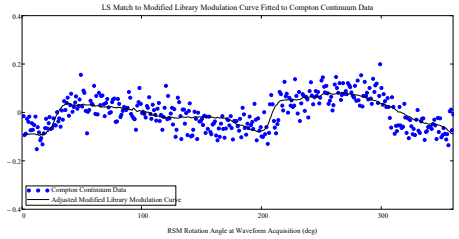

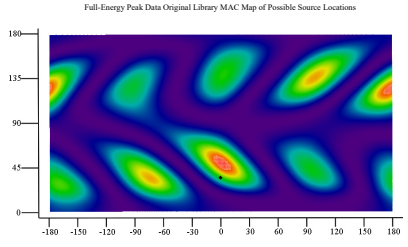

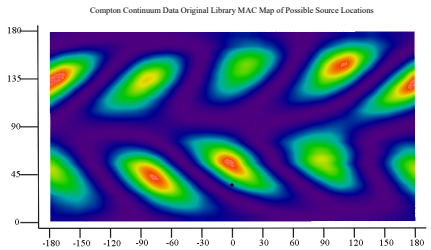

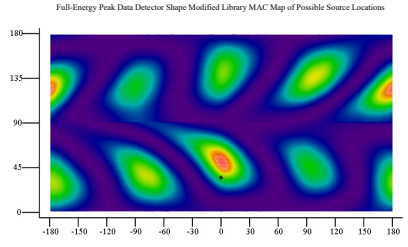

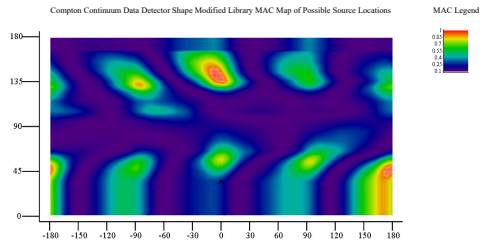

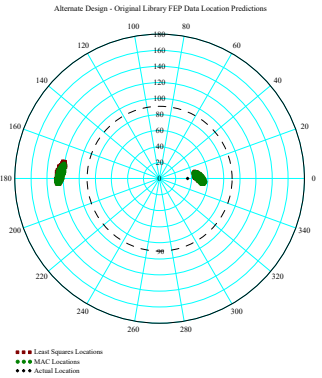

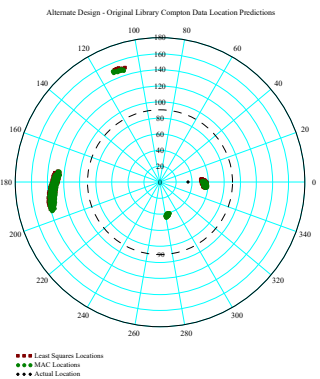

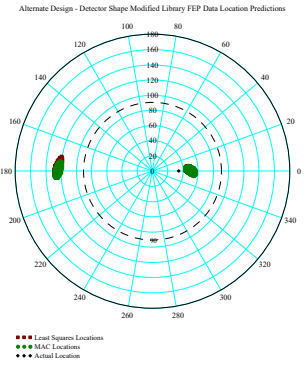

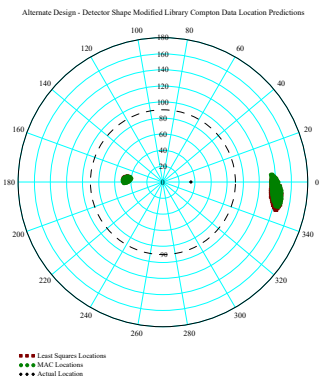

Cs-137 Source Data Results:

Phi_ViewDegree = 35
Theta_ViewDegree = 0

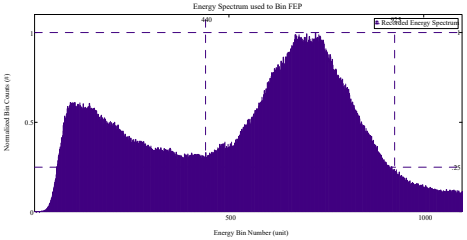

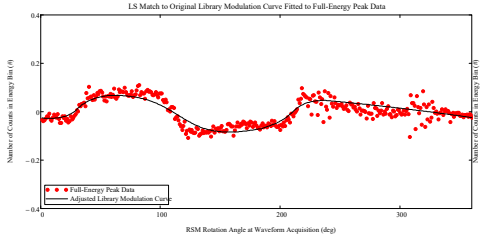

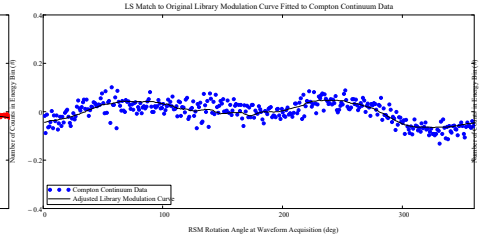

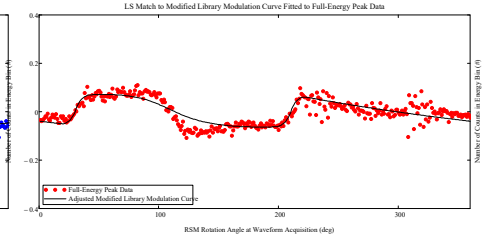

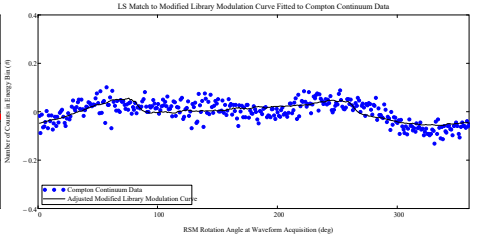

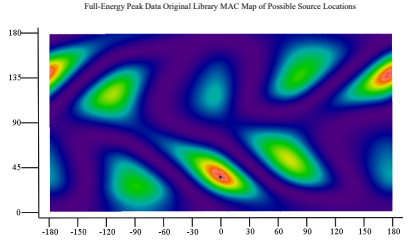

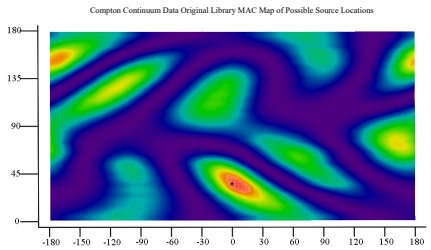

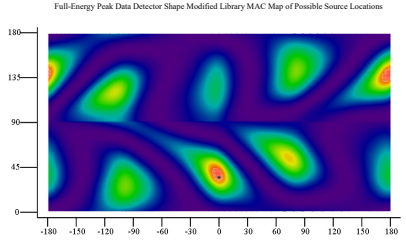

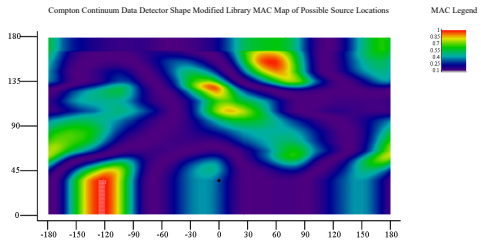

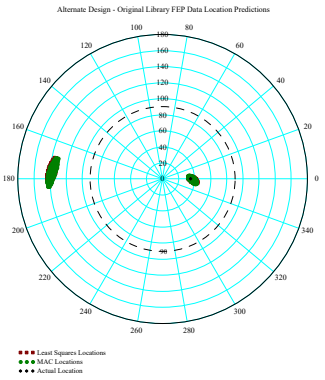

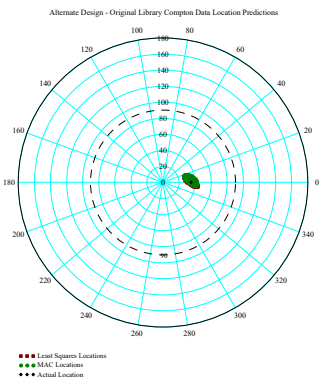

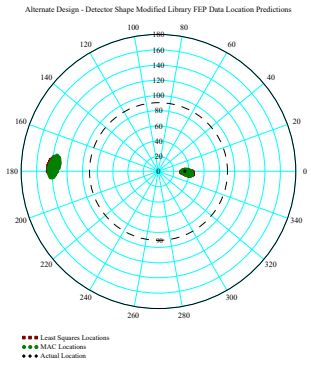

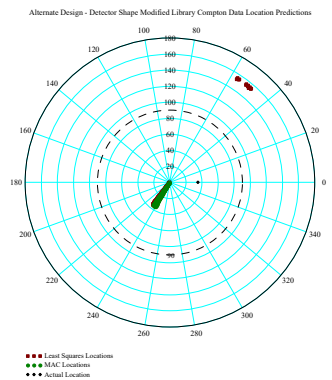

View Angle φ = 45° : Small RSM FitzGerald Design Ba-133and Cs-137 Data Spectra for Original and Detector Shape Modified Libraries, Modulation Curves, Library Curves, MAC and LS Direction Predictions

Ba-133 Source Data Results: Phi_ViewDegree = 45 Theta_ViewDegree = 0

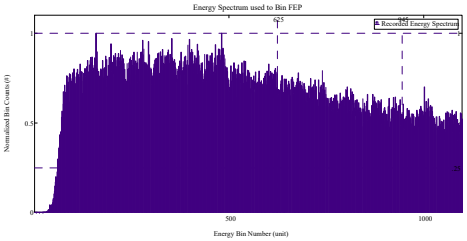

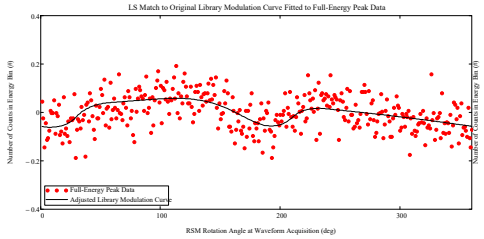

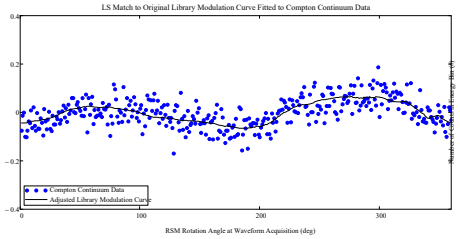

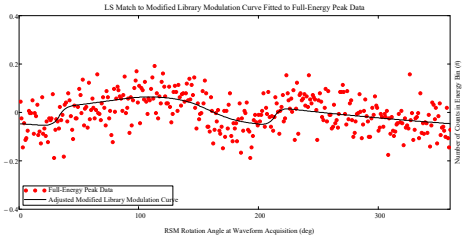

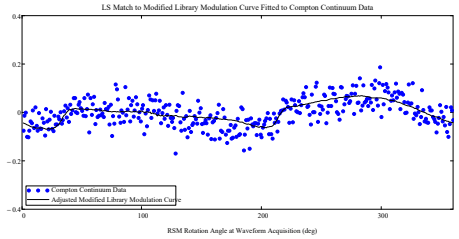

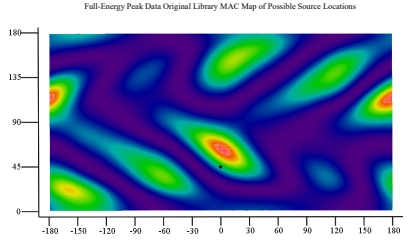

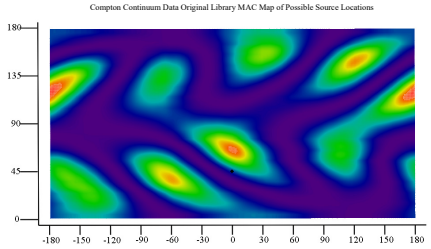

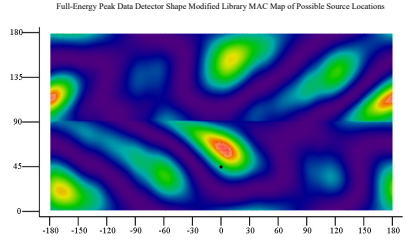

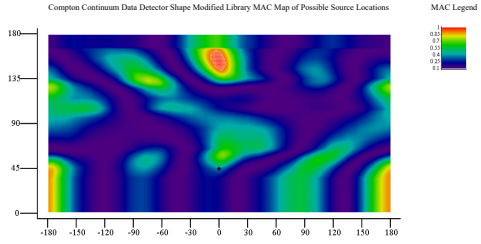

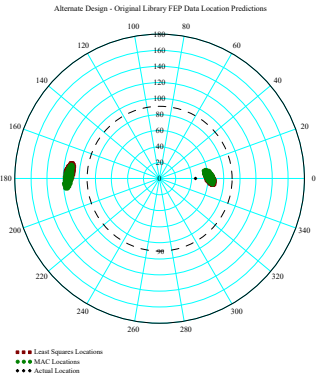

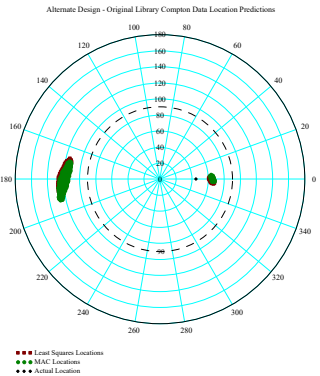

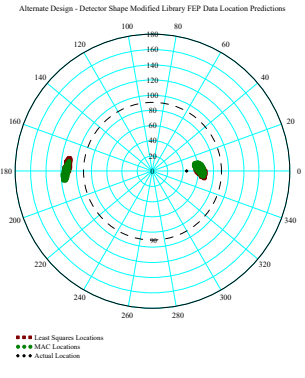

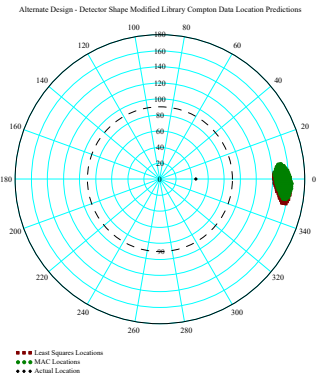

Cs-137 Source Data Results:

Phi_ViewDegree = 45
Theta_ViewDegree = 0

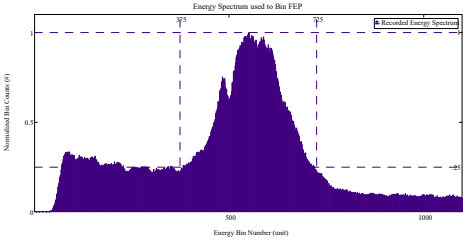

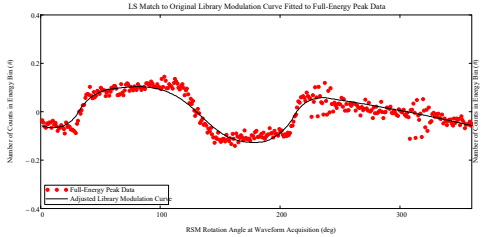

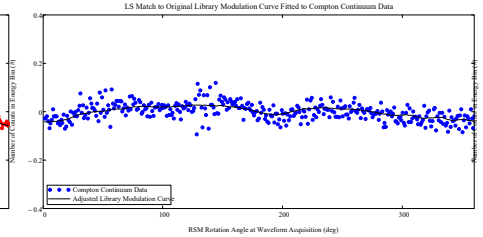

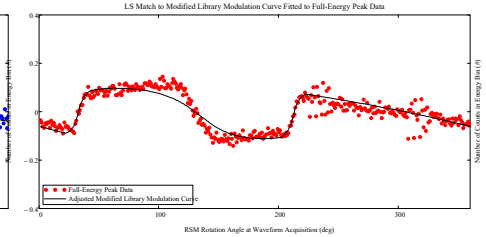

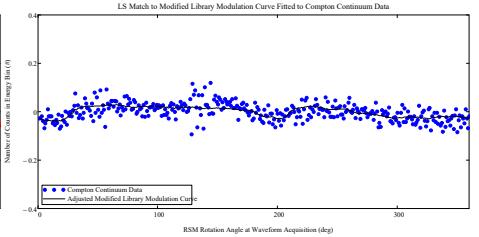

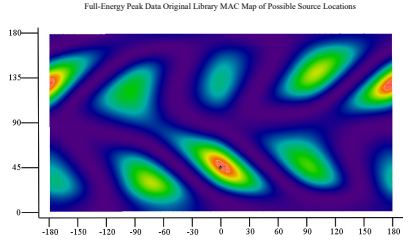

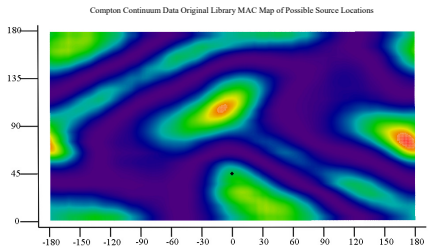

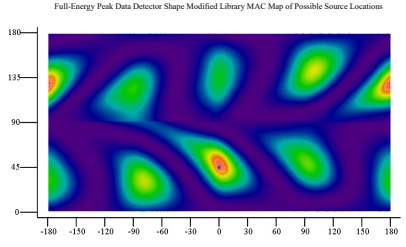

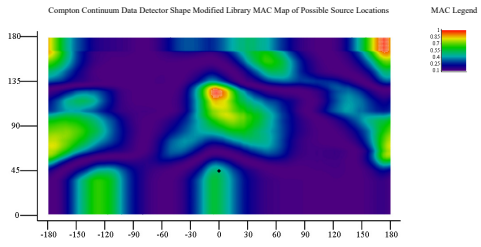

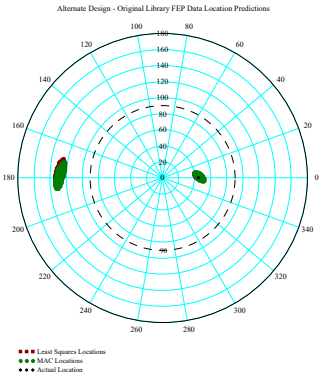

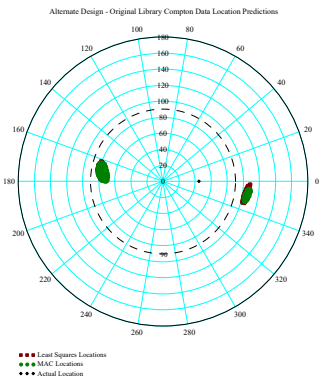

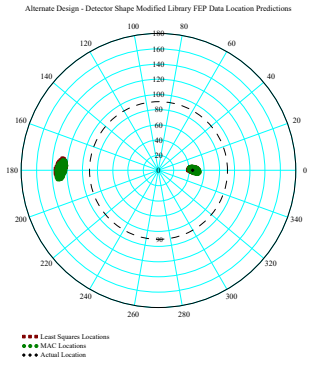

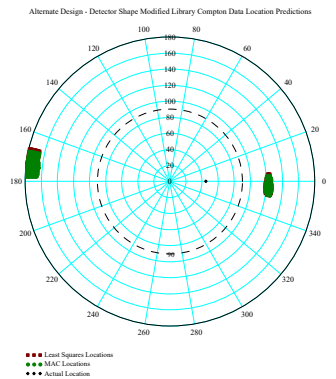

View Angle φ = 55° : Small RSM FitzGerald Design Ba-133and Cs-137 Data Spectra for Original and Detector Shape Modified Libraries, Modulation Curves, Library Curves, MAC and LS Direction Predictions

Ba-133 Source Data Results: Phi_ViewDegree = 55 Theta_ViewDegree = 0

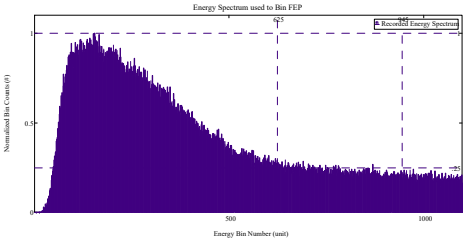

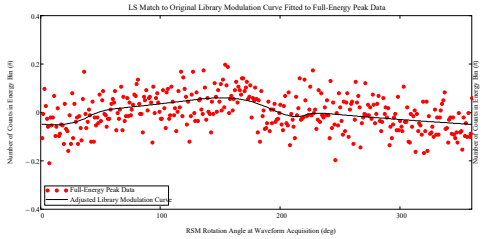

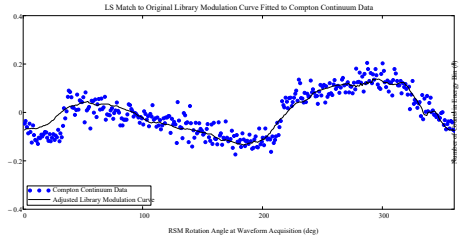

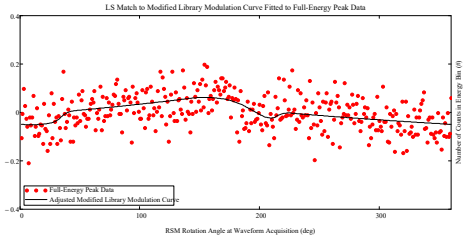

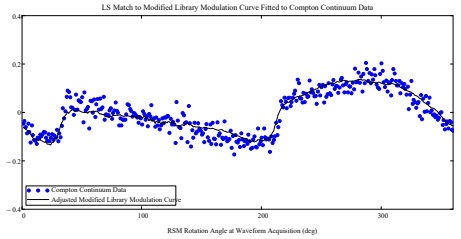

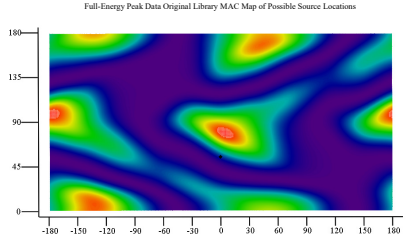

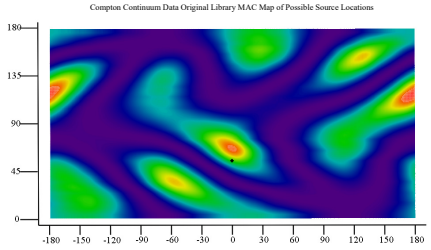

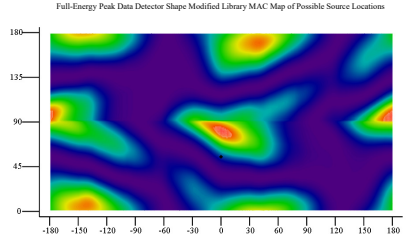

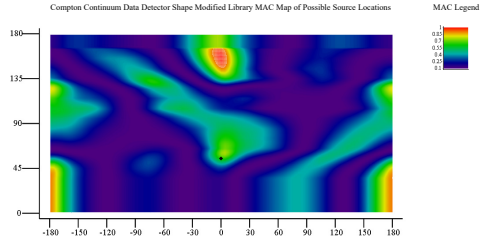

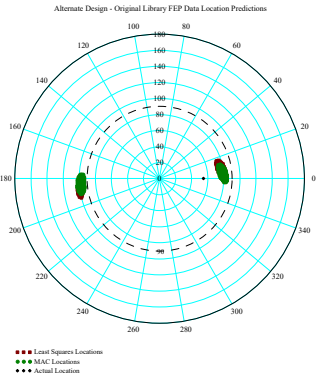

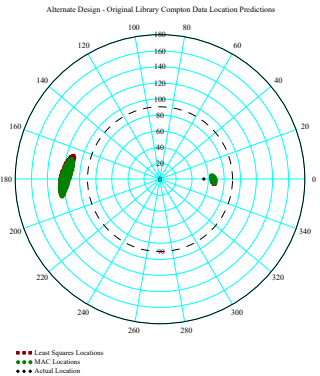

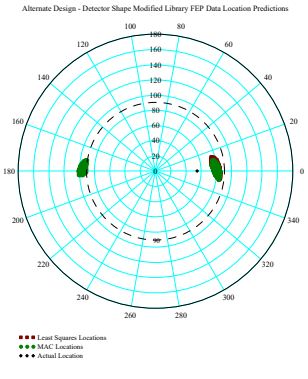

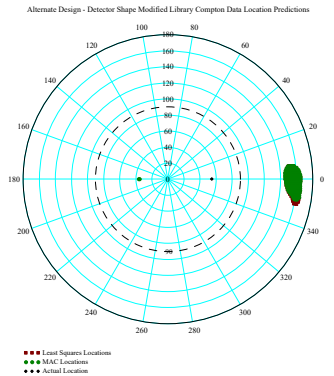

Cs-137 Source Data Results:

Phi_ViewDegree = 55
Theta_ViewDegree = 0

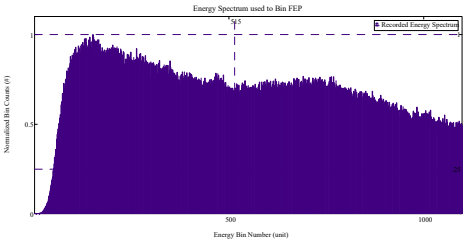

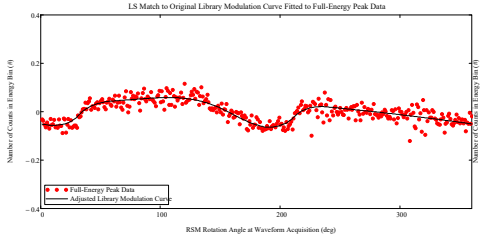

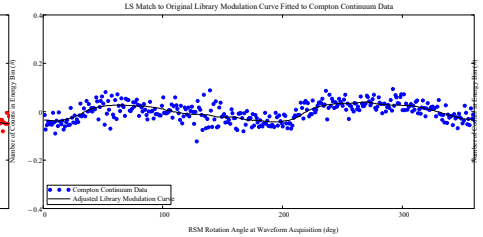

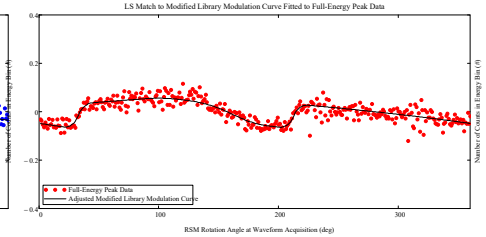

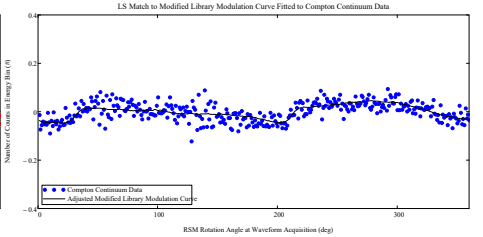

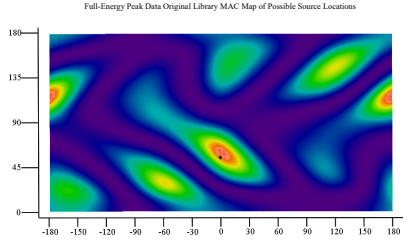

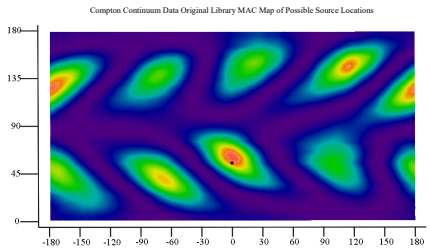

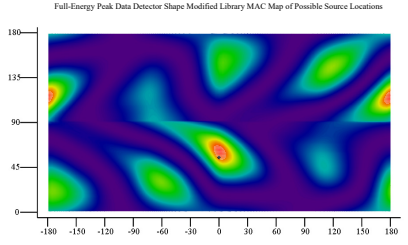

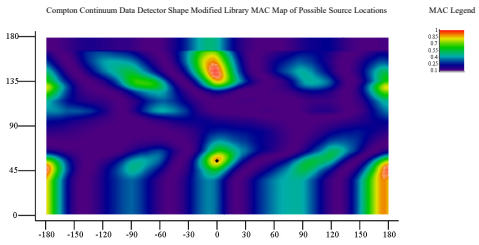

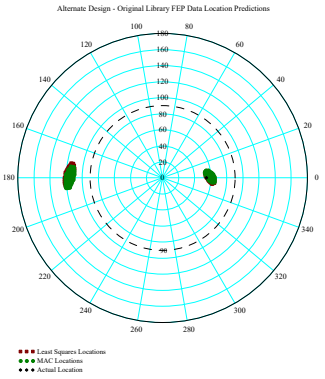

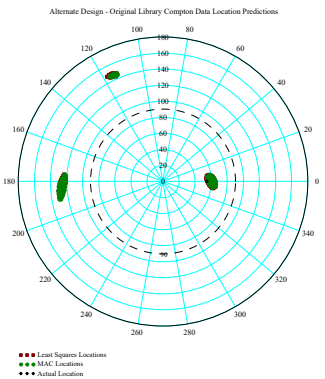

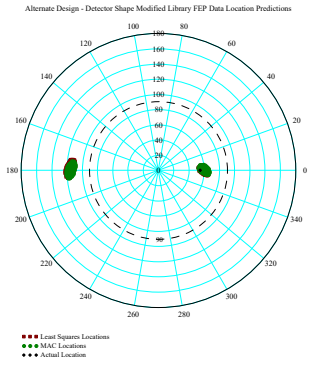

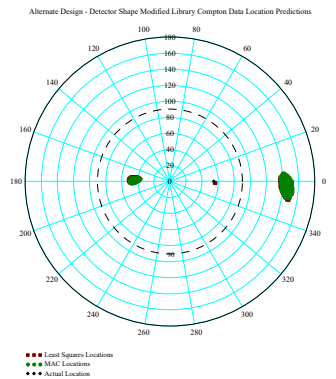

View Angle φ = 65° : Small RSM FitzGerald Design Ba-133and Cs-137 Data Spectra for Original and Detector Shape Modified Libraries, Modulation Curves, Library Curves, MAC and LS Direction Predictions

Ba-133 Source Data Results: Phi_ViewDegree = 65 Theta_ViewDegree = 0

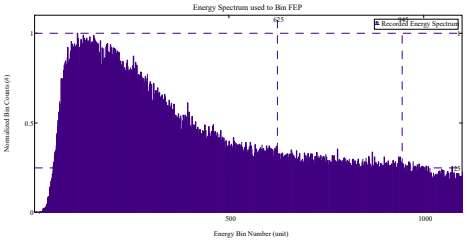

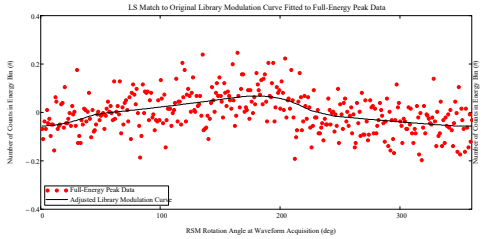

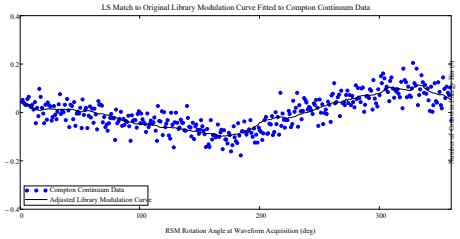

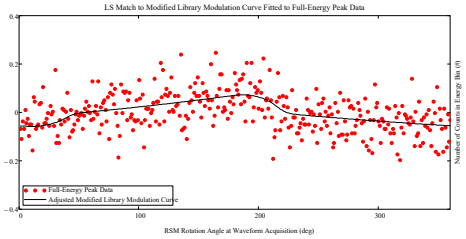

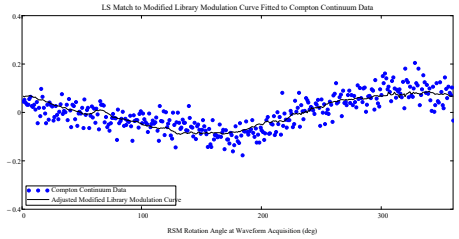

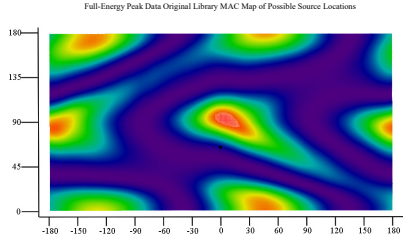

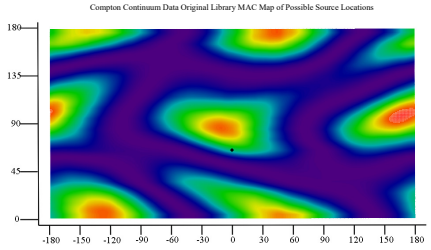

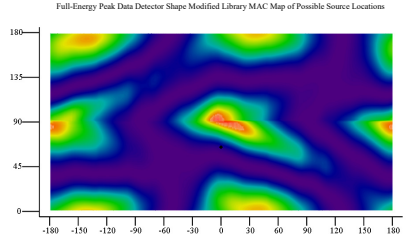

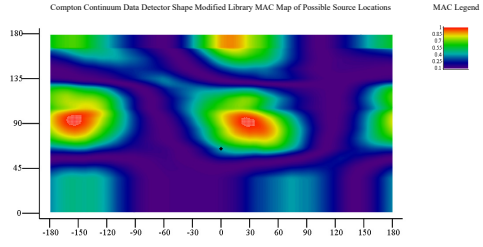

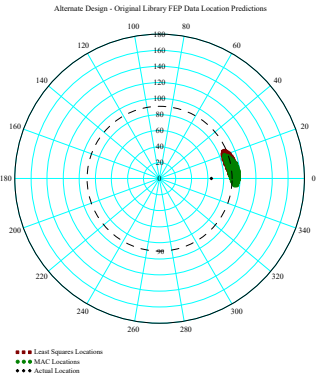

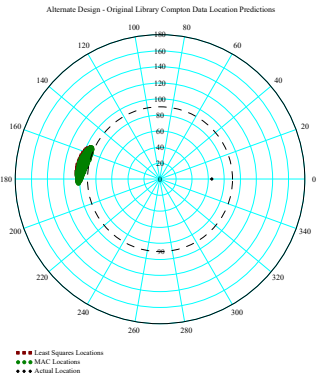

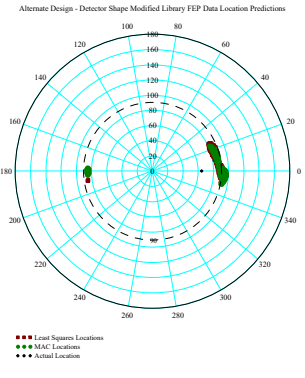

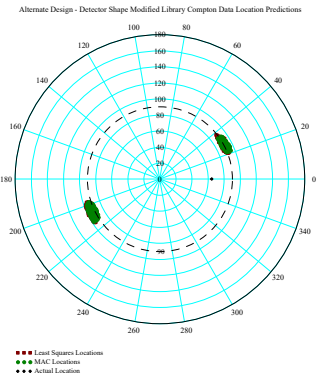

Cs-137 Source Data Results:

Phi_ViewDegree = 65
Theta_ViewDegree = 0

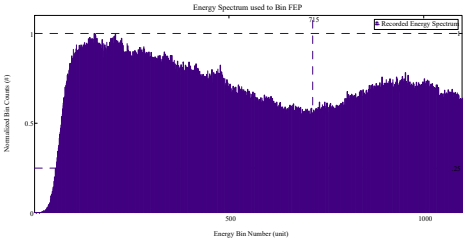

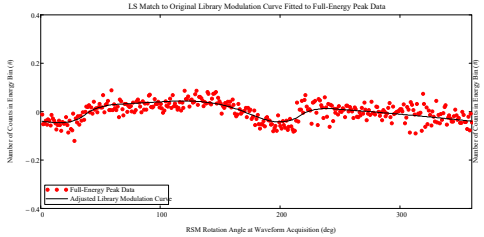

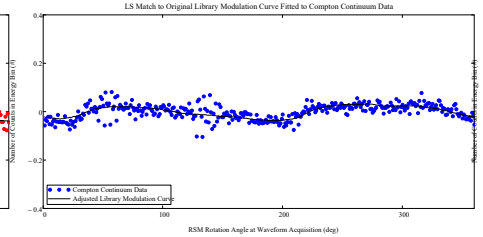

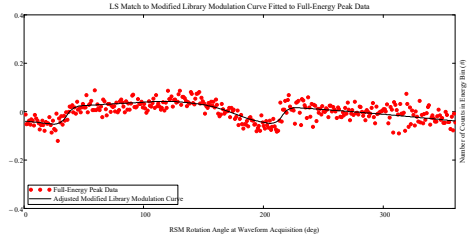

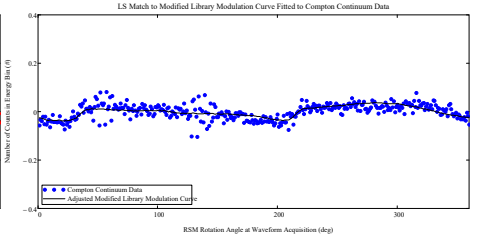

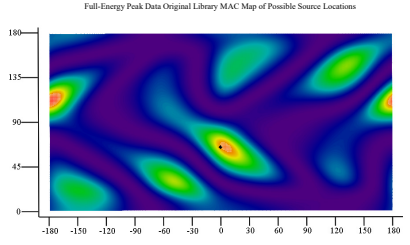

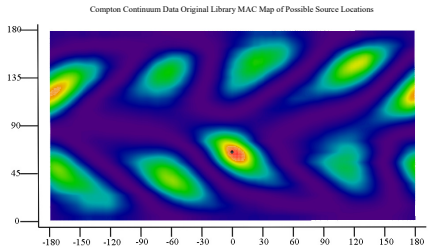

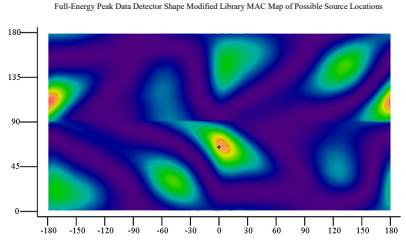

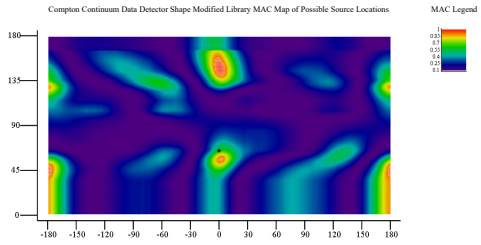

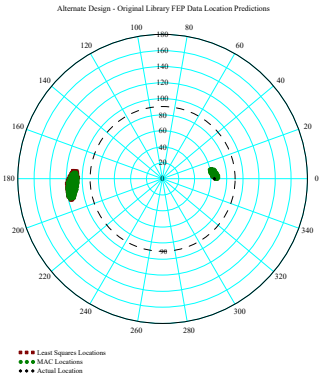

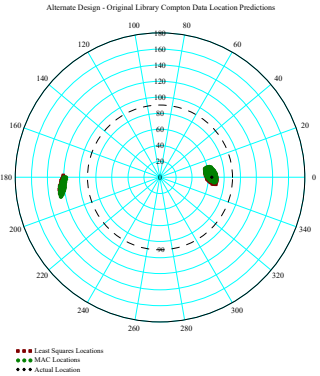

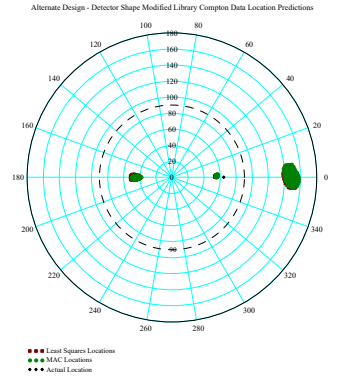

View Angle φ = 75° : Small RSM FitzGerald Design Ba-133and Cs-137 Data Spectra for Original and Detector Shape Modified Libraries, Modulation Curves, Library Curves, MAC and LS Direction Predictions

Ba-133 Source Data Results: Phi_ViewDegree = 75 Theta_ViewDegree = 0

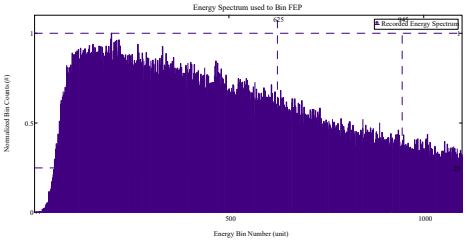

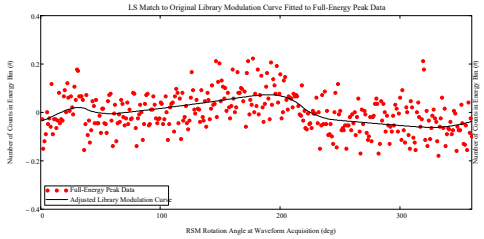

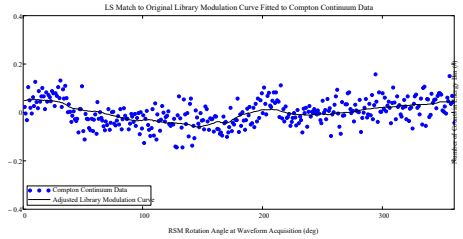

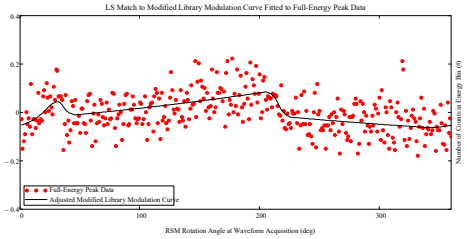

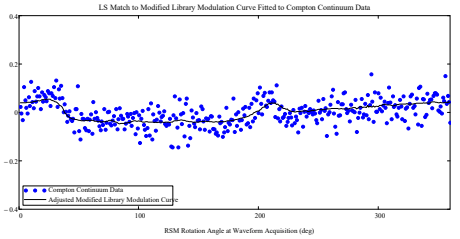

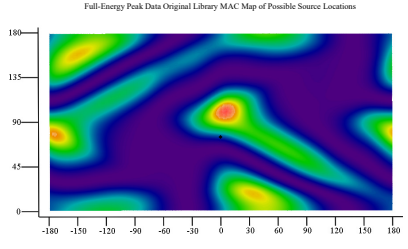

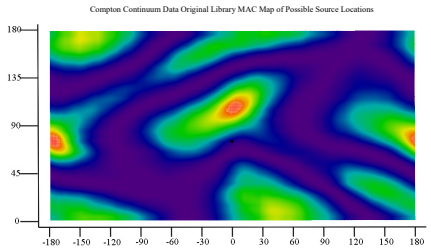

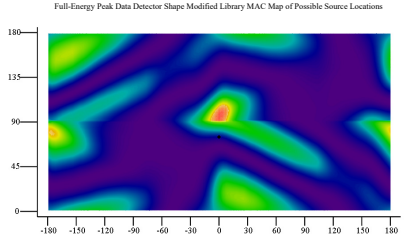

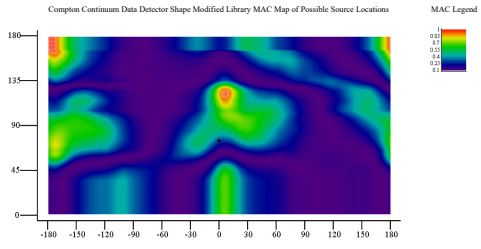

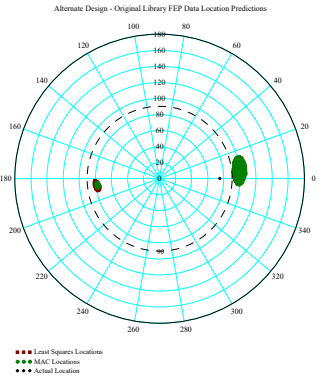

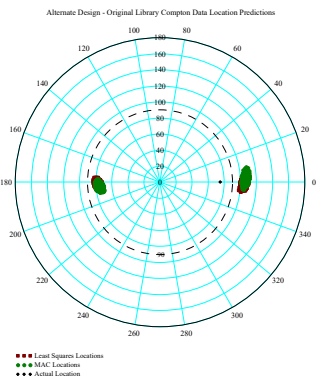

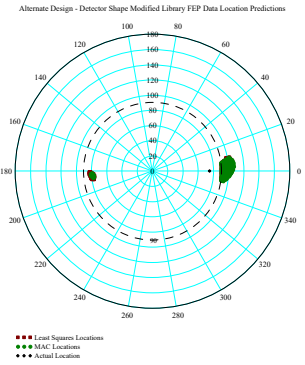

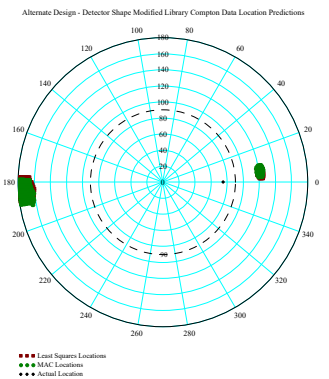

Cs-137 Source Data Results:

Phi_ViewDegree = 75
Theta_ViewDegree = 0

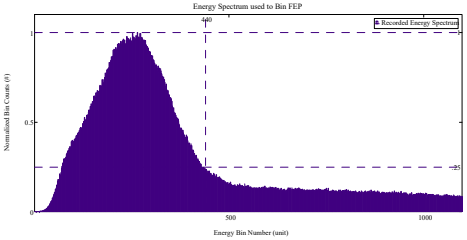

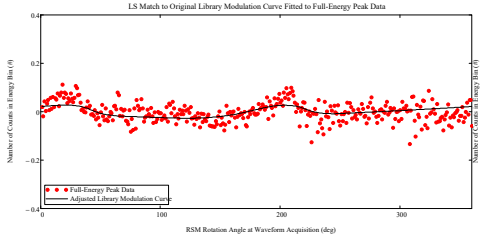

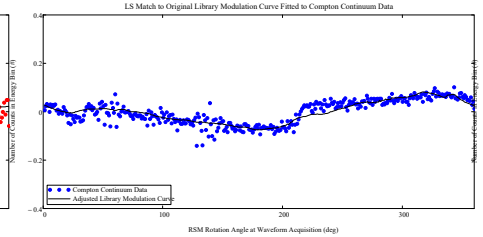

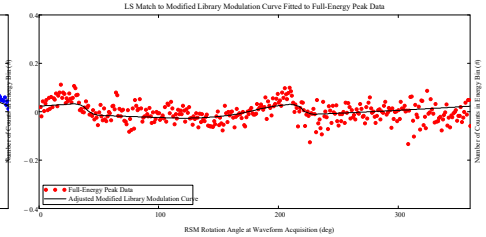

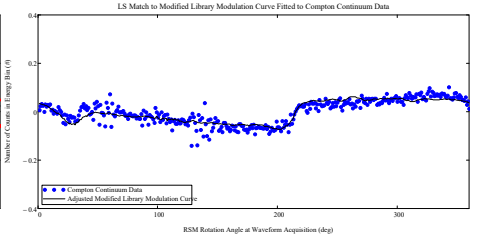

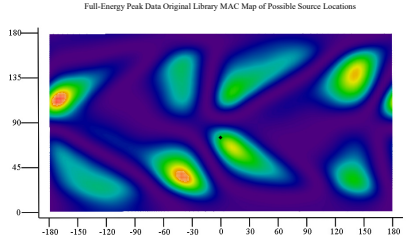

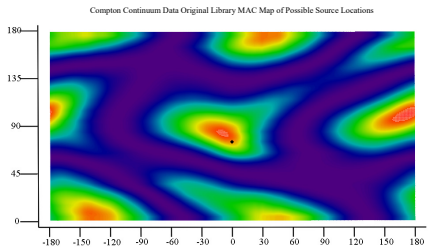

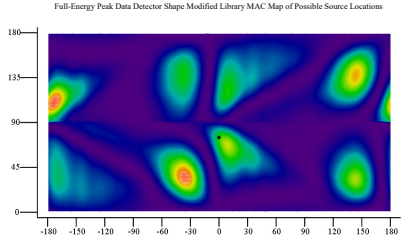

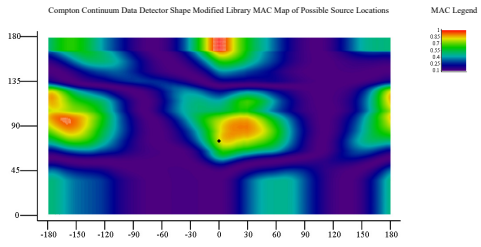

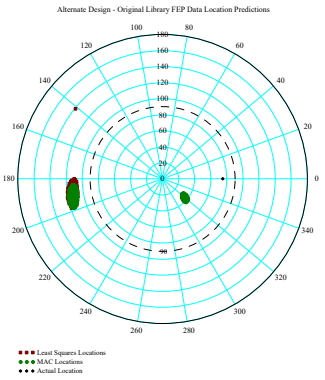

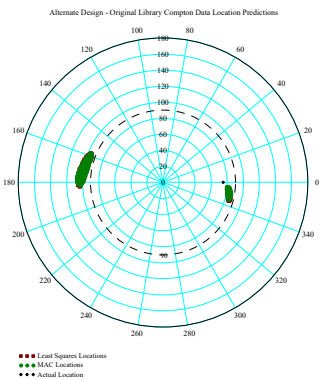

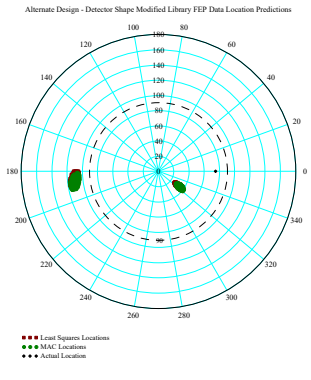

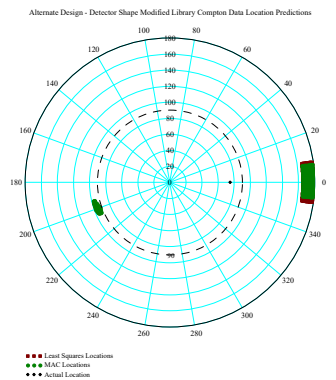

View Angle φ = 85° : Small RSM FitzGerald Design Ba-133and Cs-137 Data Spectra for Original and Detector Shape Modified Libraries, Modulation Curves, Library Curves, MAC and LS Direction Predictions

Ba-133 Source Data Results: Phi_ViewDegree = 85 Theta_ViewDegree = 0

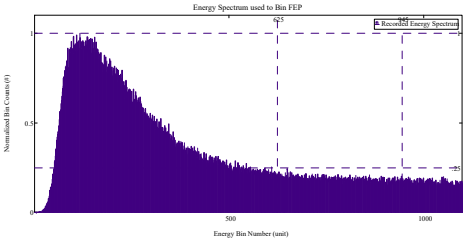

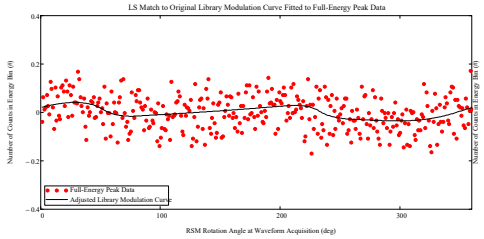

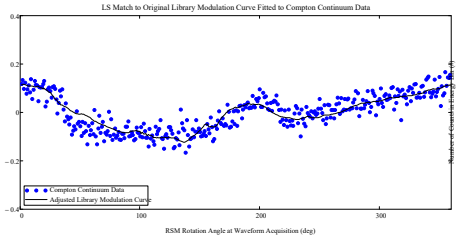

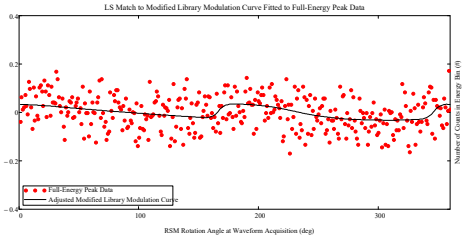

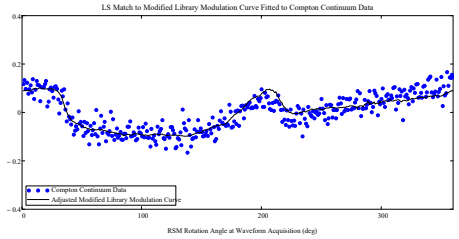

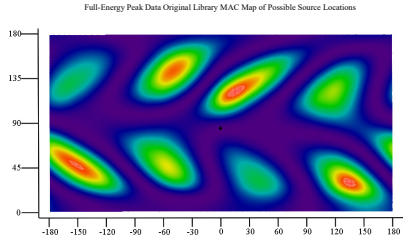

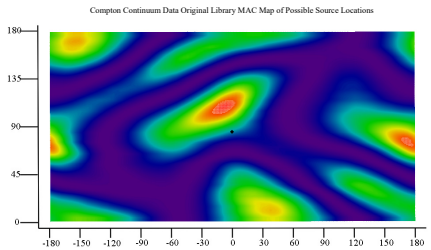

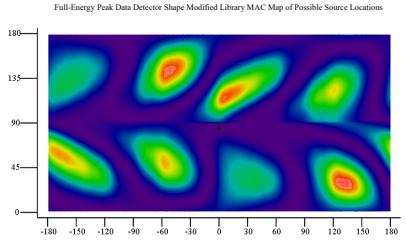

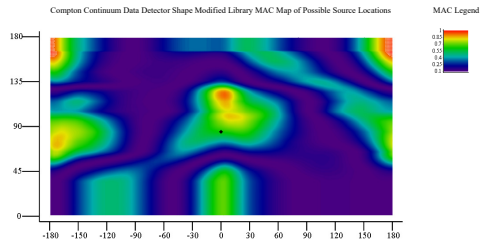

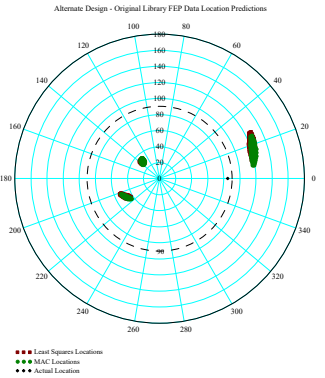

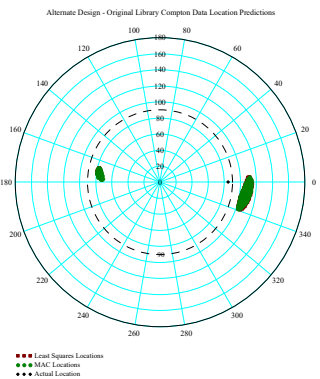

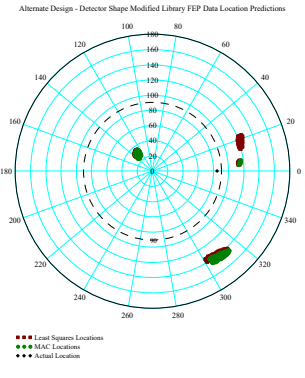

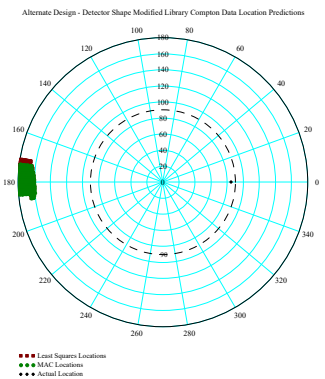

Cs-137 Source Data Results:

Phi_ViewDegree = 85
Theta_ViewDegree = 0

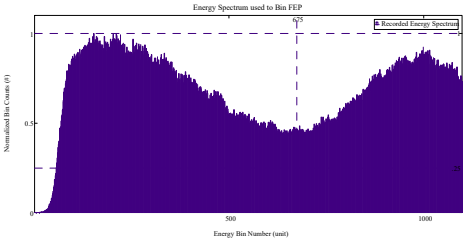

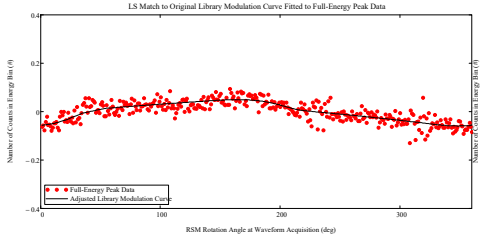

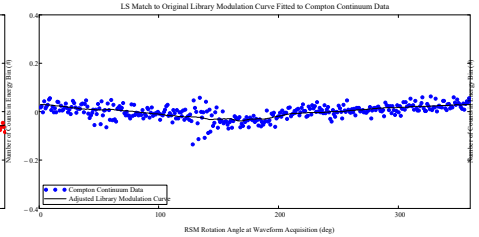

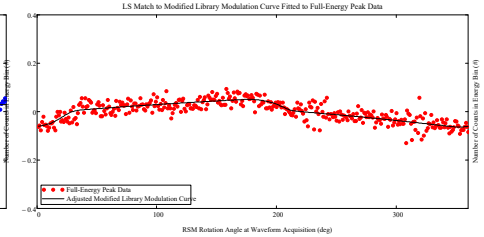

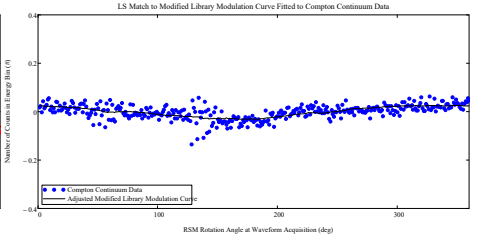

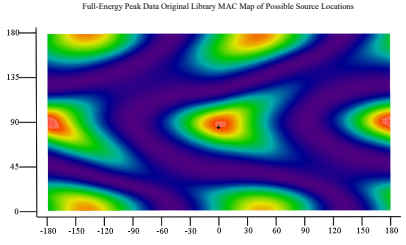

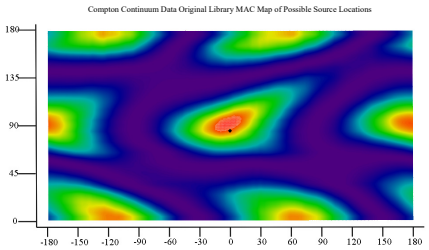

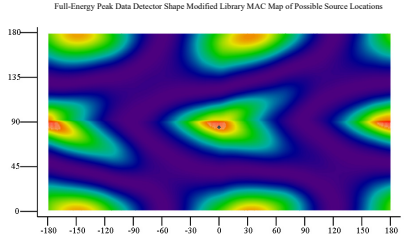

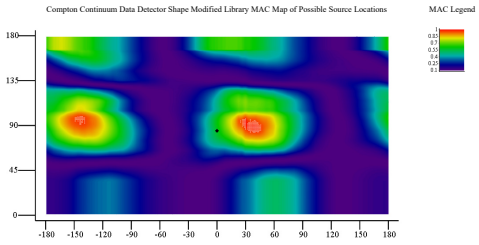

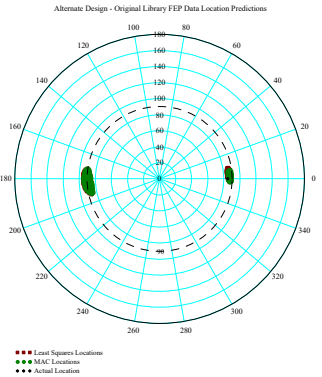

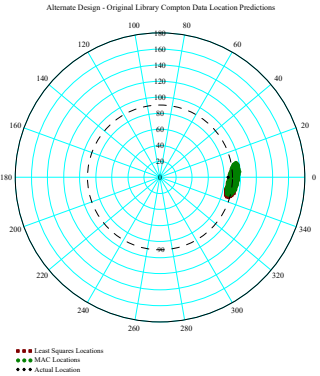

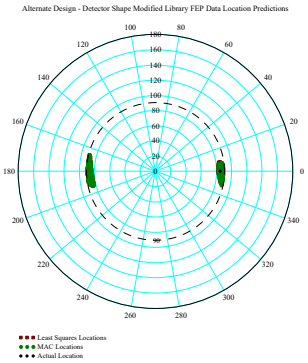

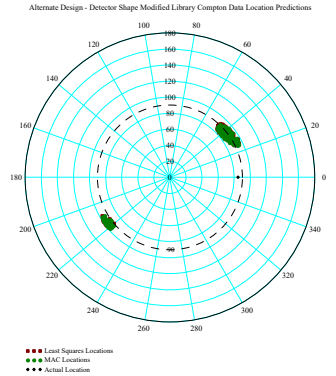

View Angle φ = 95° : Small RSM FitzGerald Design Ba-133and Cs-137 Data Spectra for Original and Detector Shape Modified Libraries, Modulation Curves, Library Curves, MAC and LS Direction Predictions

Ba-133 Source Data Results: Phi_ViewDegree = 95 Theta_ViewDegree = 0

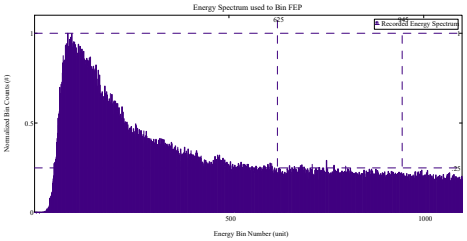

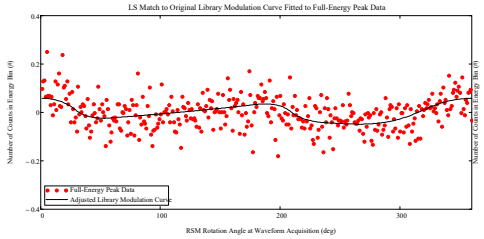

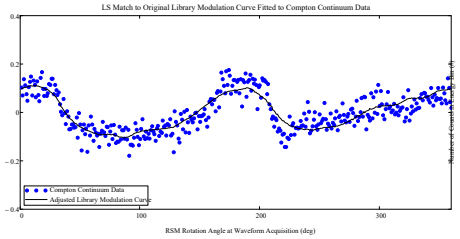

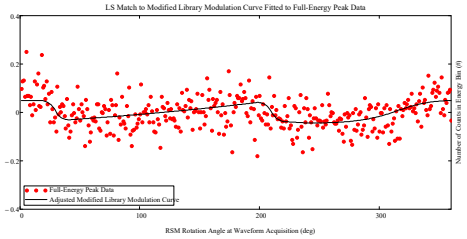

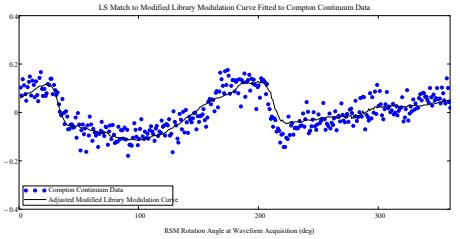

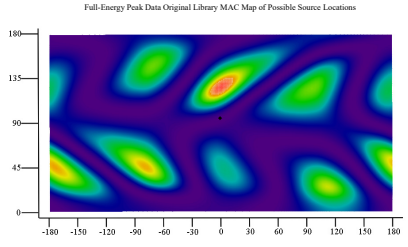

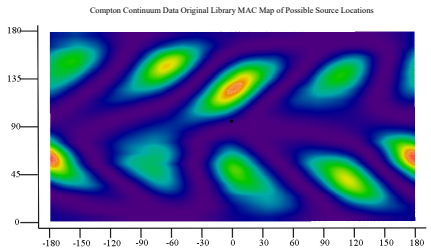

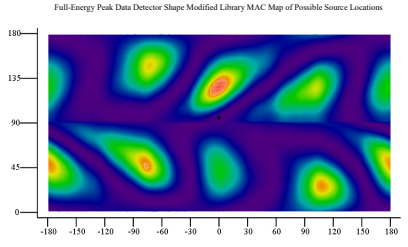

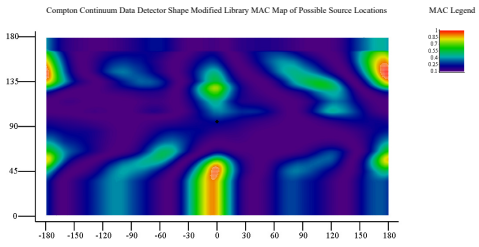

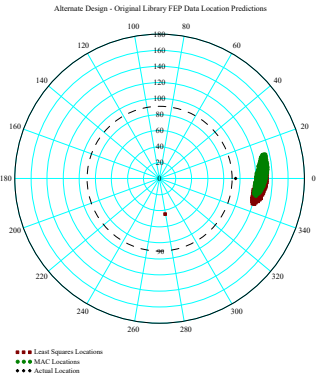

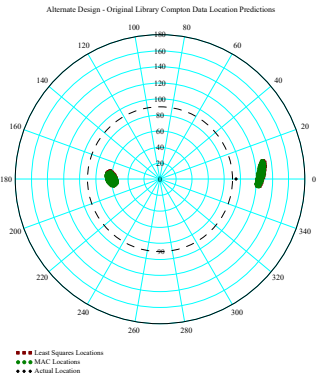

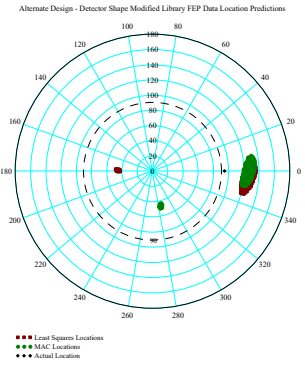

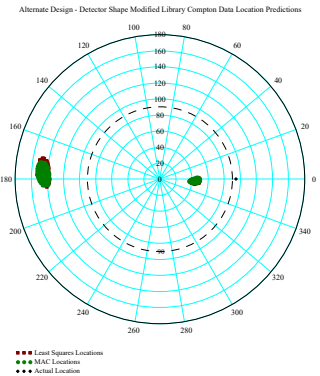

Cs-137 Source Data Results:

Phi_ViewDegree = 95
Theta_ViewDegree = 0

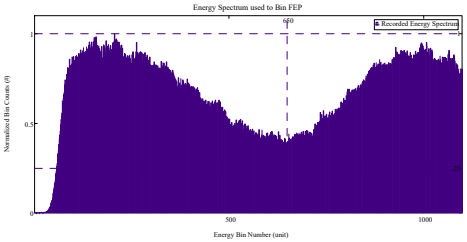

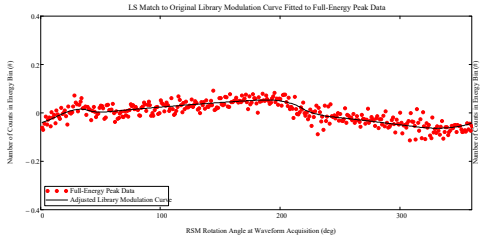

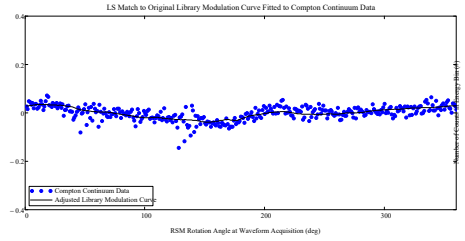

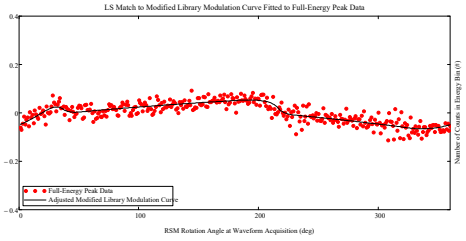

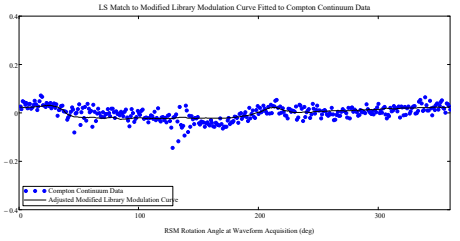

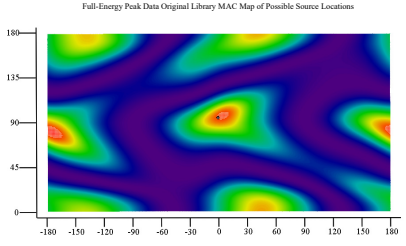

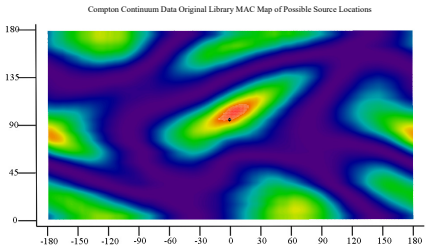

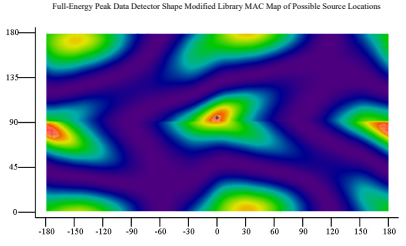

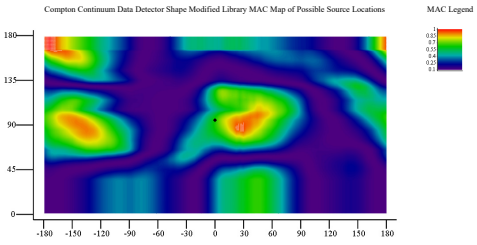

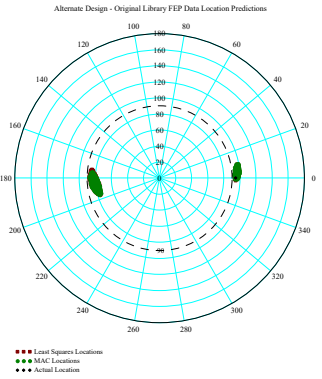

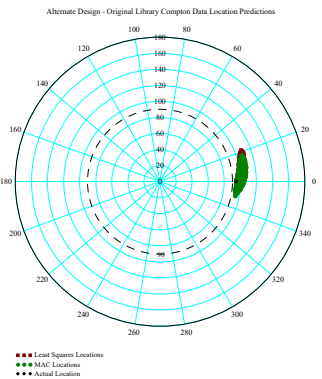

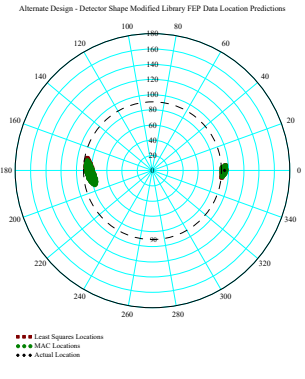

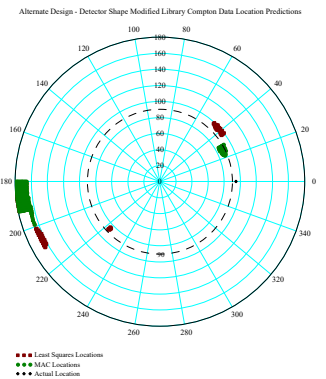

View Angle φ = 105° : Small RSM FitzGerald Design Ba-133and Cs-137 Data Spectra for Original and Detector Shape Modified Libraries, Modulation Curves, Library Curves, MAC and LS Direction Predictions

Ba-133 Source Data Results: Phi_ViewDegree = 105 Theta_ViewDegree = 0

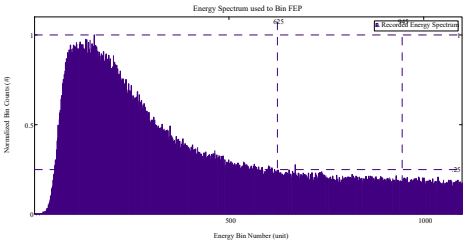

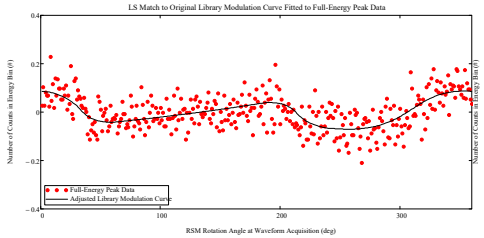

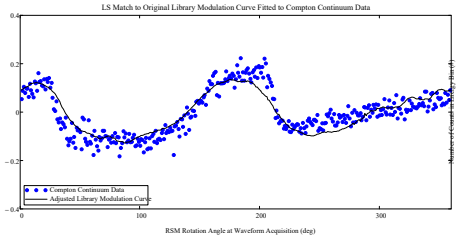

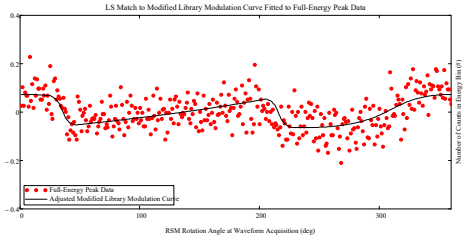

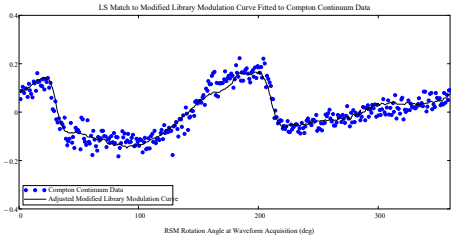

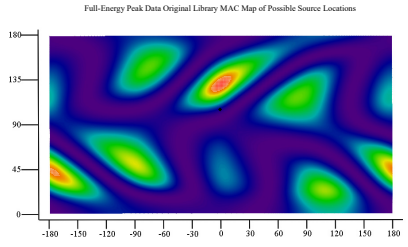

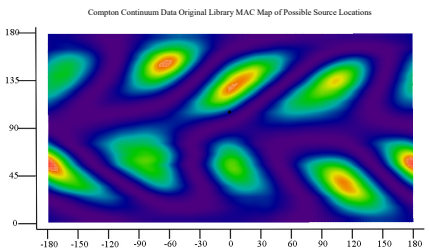

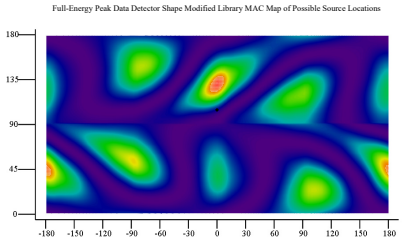

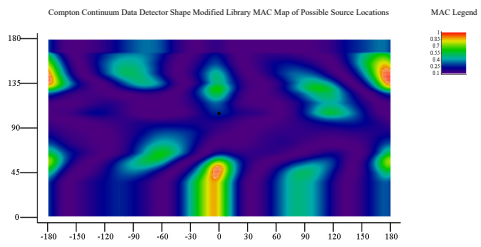

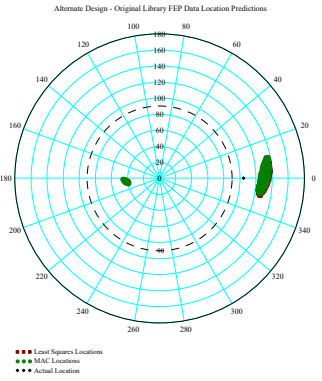

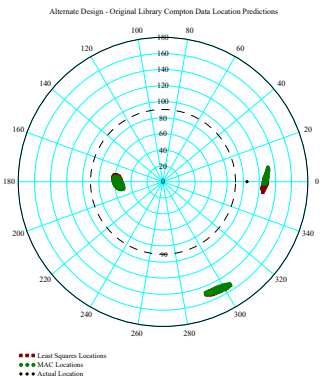

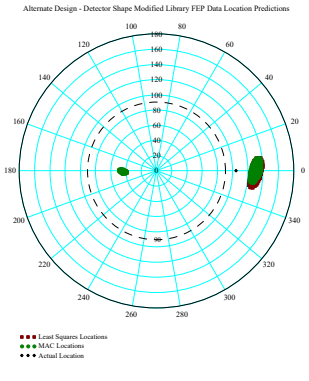

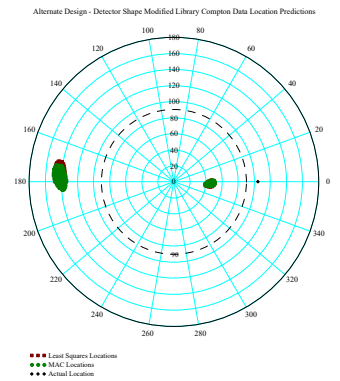

Cs-137 Source Data Results:

Phi_ViewDegree = 105
Theta_ViewDegree = 0

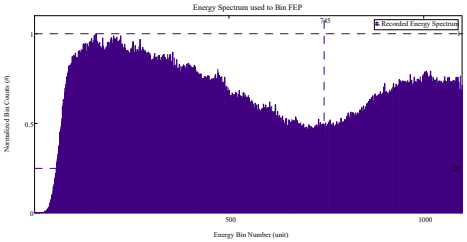

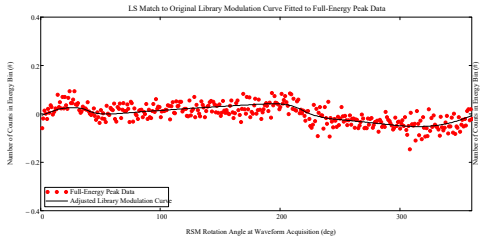

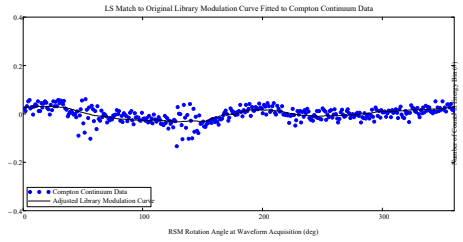

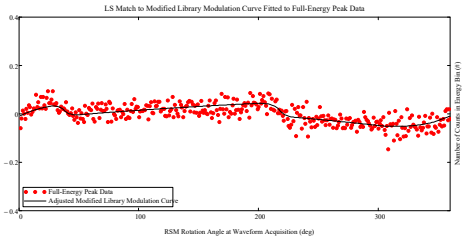

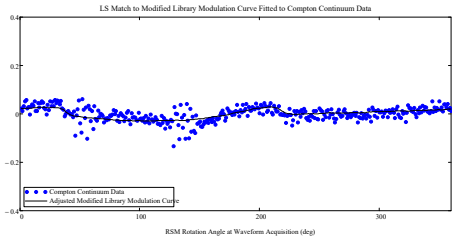

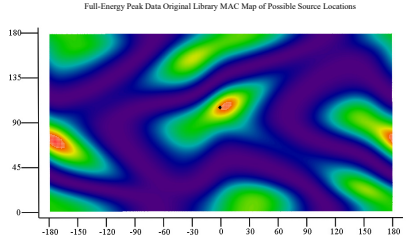

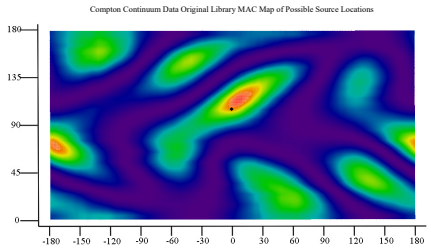

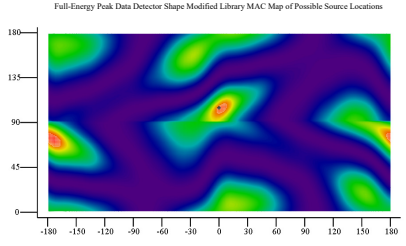

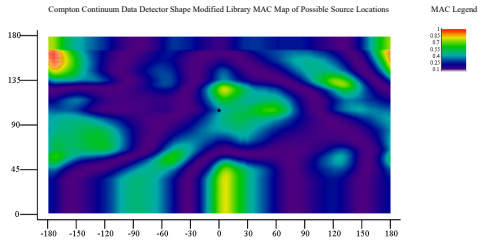

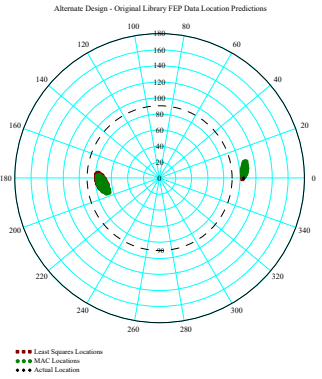

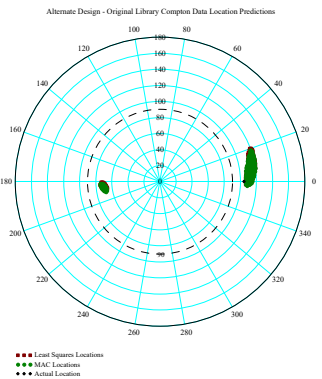

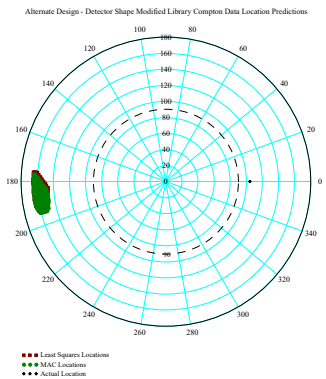

View Angle φ = 115° : Small RSM FitzGerald Design Ba-133and Cs-137 Data Spectra for Original and Detector Shape Modified Libraries, Modulation Curves, Library Curves, MAC and LS Direction Predictions

Ba-133 Source Data Results: Phi_ViewDegree = 115 Theta_ViewDegree = 0

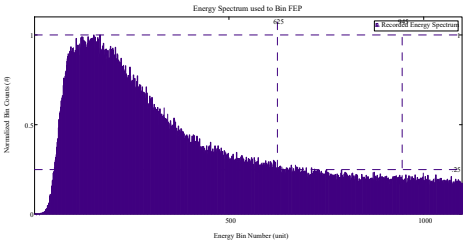

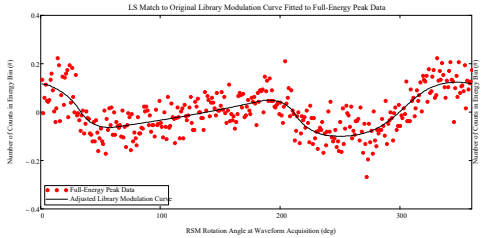

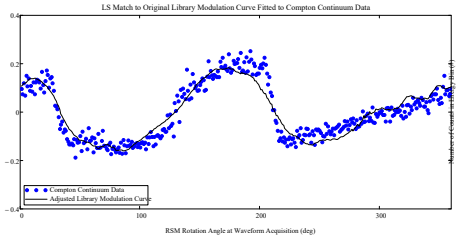

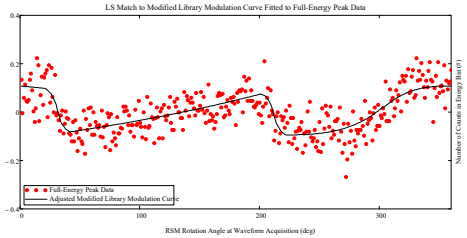

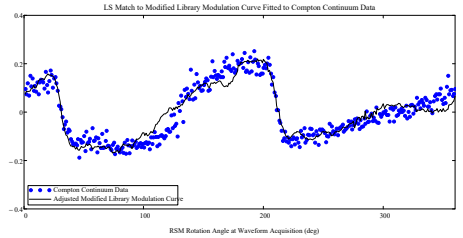

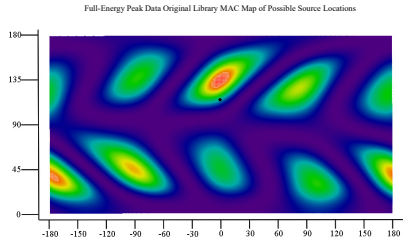

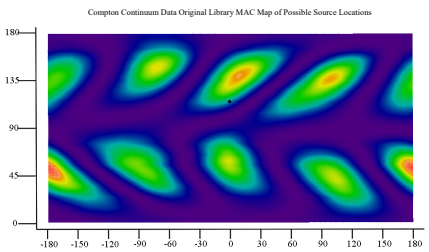

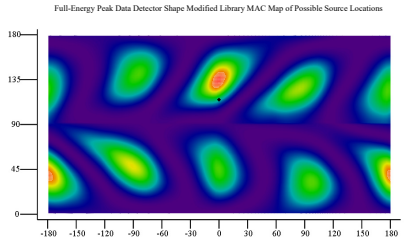

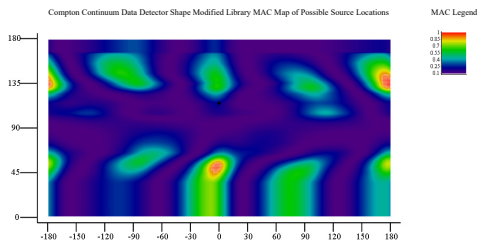

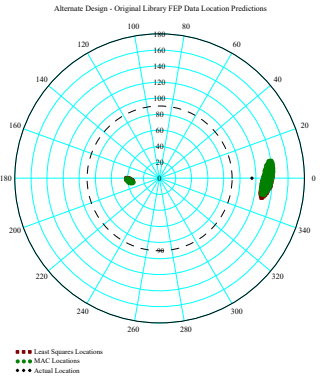

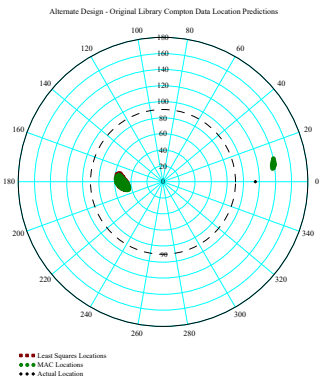

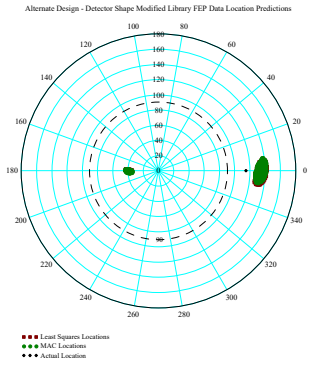

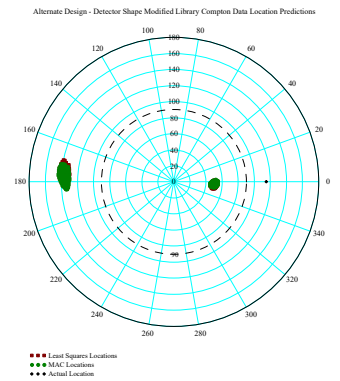

Cs-137 Source Data Results:

Phi_ViewDegree = 115
Theta_ViewDegree = 0

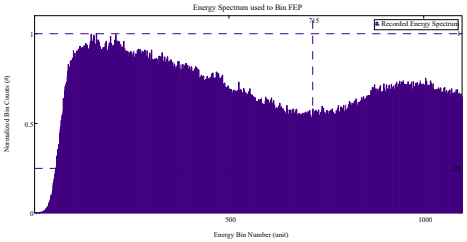

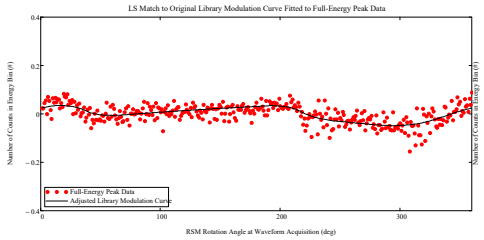

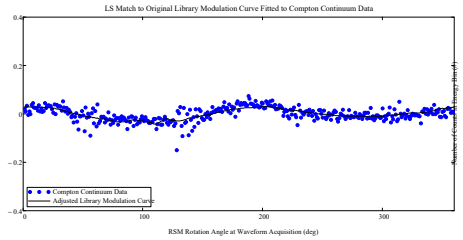

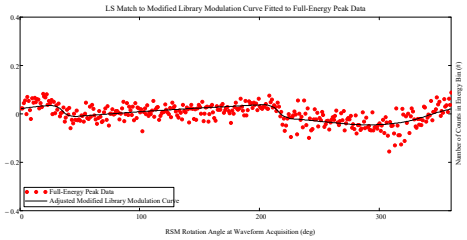

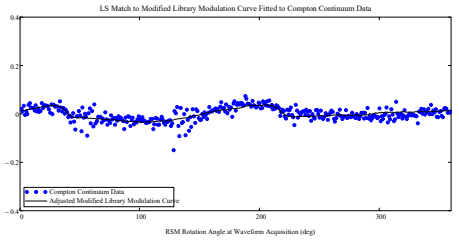

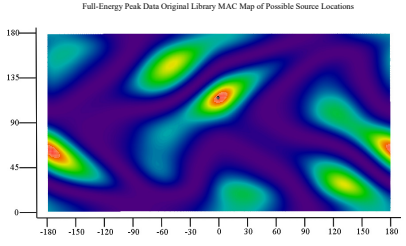

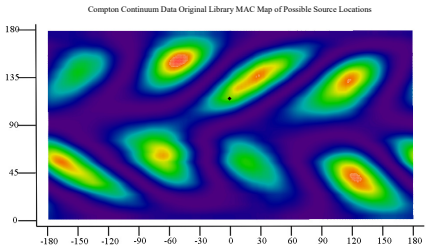

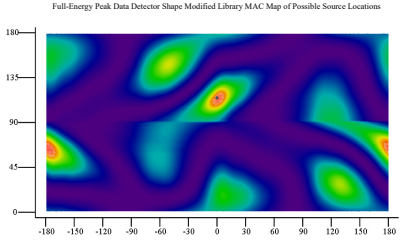

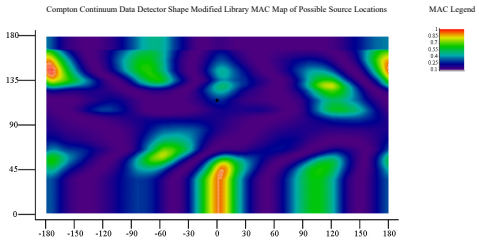

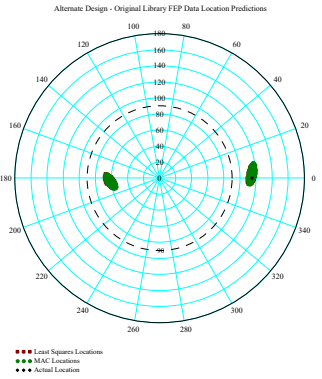

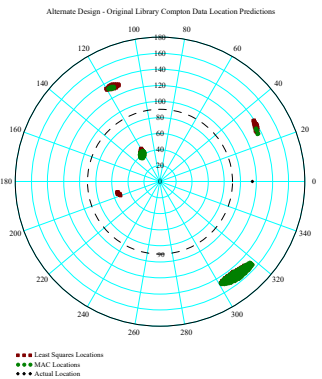

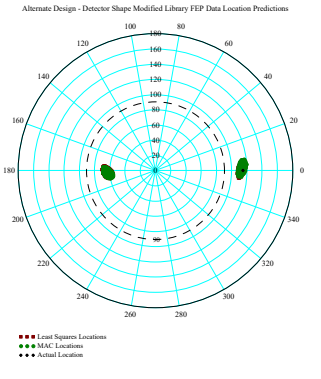

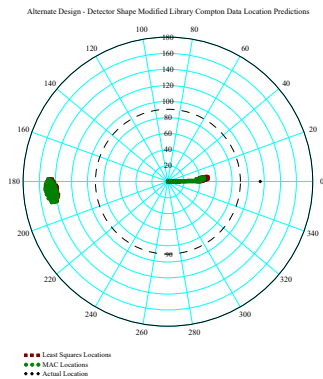

View Angle φ = 125° : Small RSM FitzGerald Design Ba-133and Cs-137 Data Spectra for Original and Detector Shape Modified Libraries, Modulation Curves, Library Curves, MAC and LS Direction Predictions

Ba-133 Source Data Results: Phi_ViewDegree = 125 Theta_ViewDegree = 0

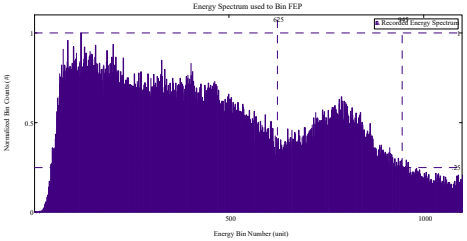

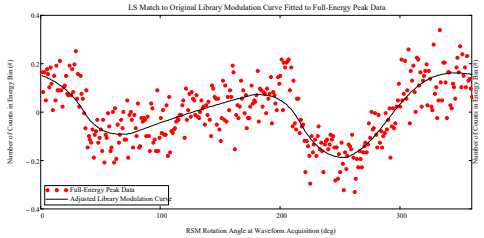

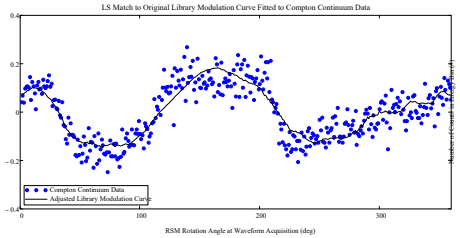

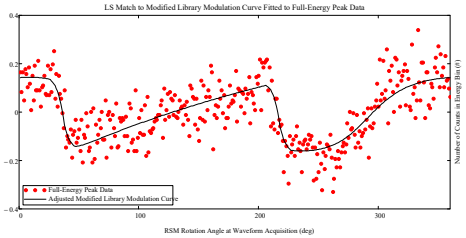

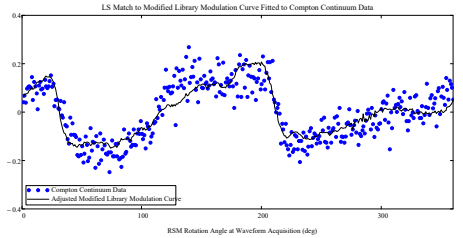

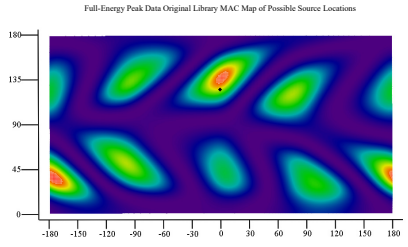

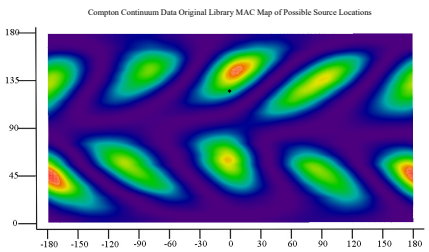

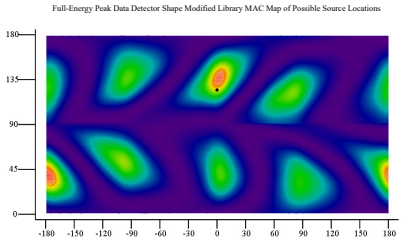

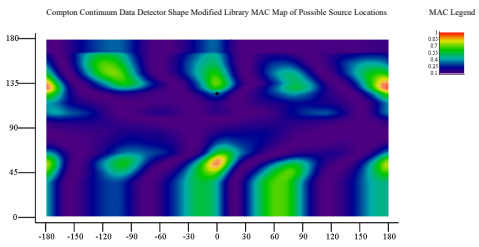

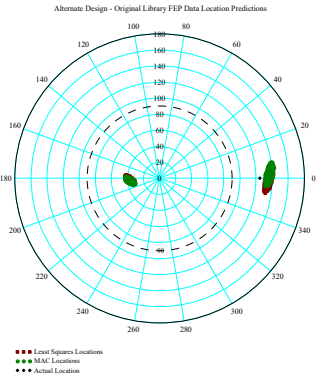

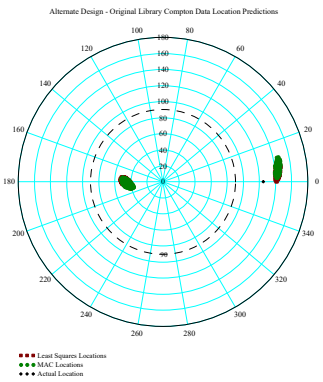

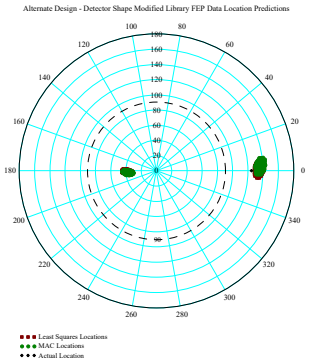

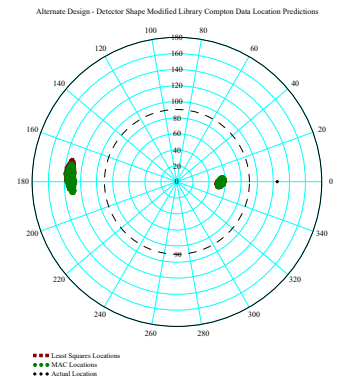

Cs-137 Source Data Results:

Phi_ViewDegree = 125
Theta_ViewDegree = 0

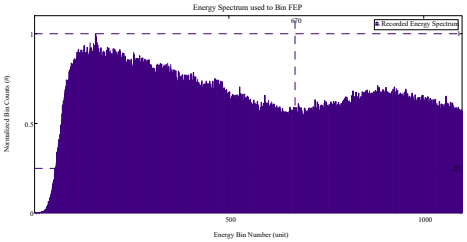

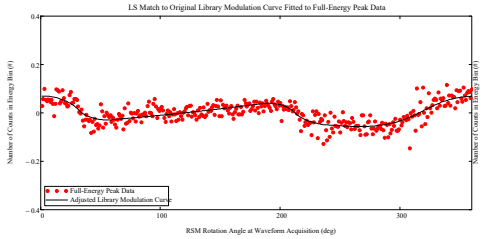

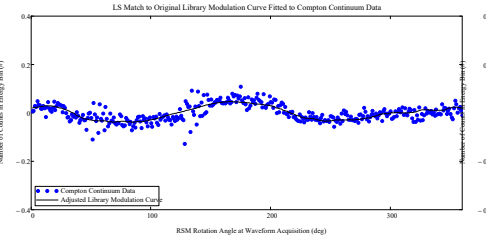

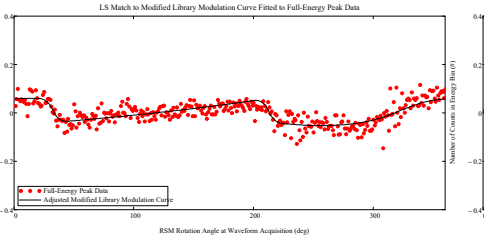

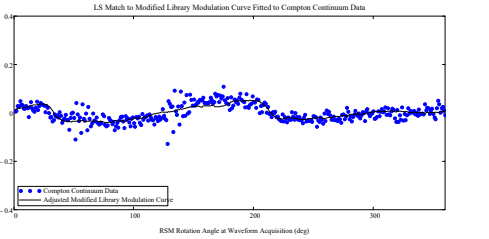

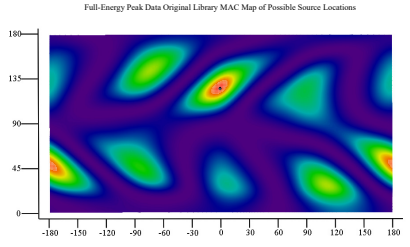

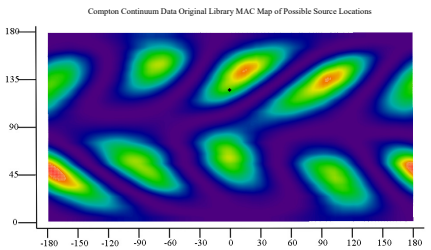

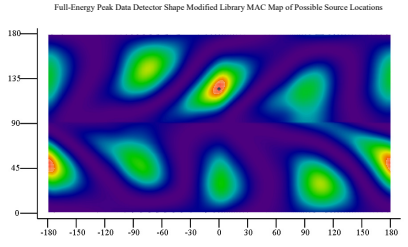

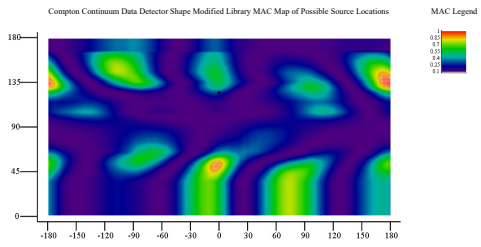

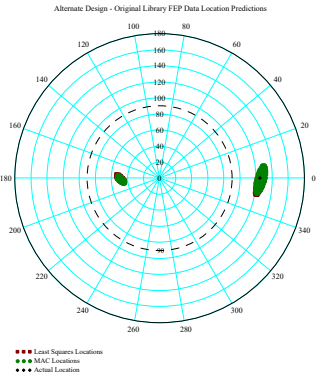

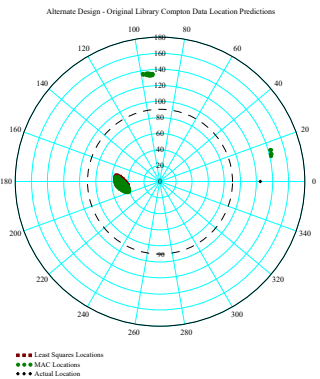

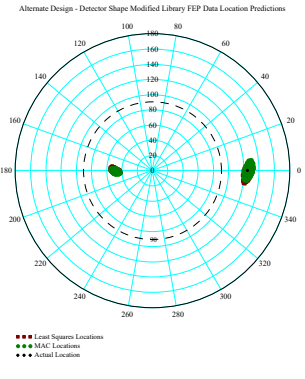

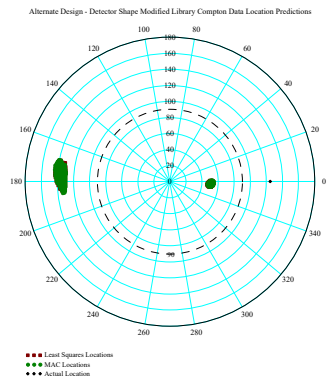

View Angle φ = 135° : Small RSM FitzGerald Design Ba-133and Cs-137 Data Spectra for Original and Detector Shape Modified Libraries, Modulation Curves, Library Curves, MAC and LS Direction Predictions

Ba-133 Source Data Results: Phi_ViewDegree = 135 Theta_ViewDegree = 0

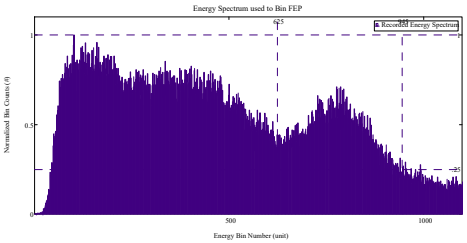

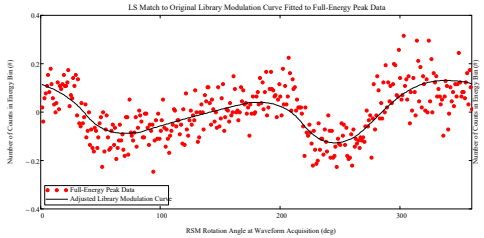

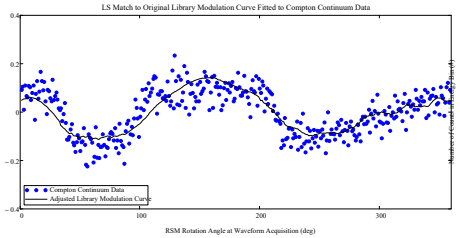

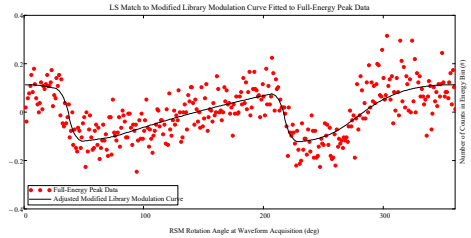

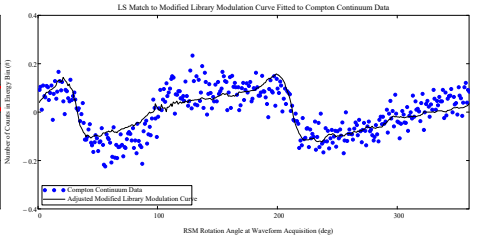

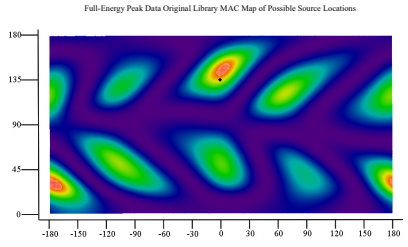

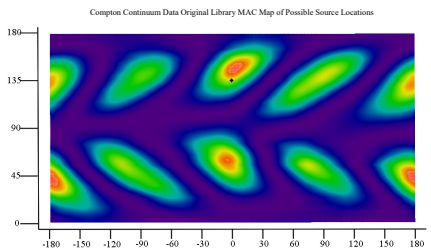

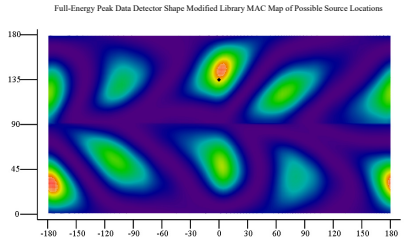

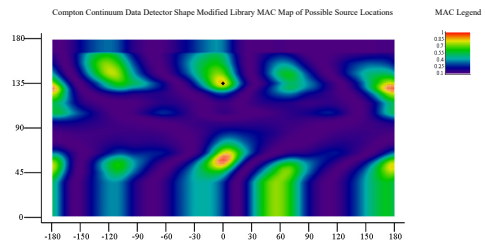

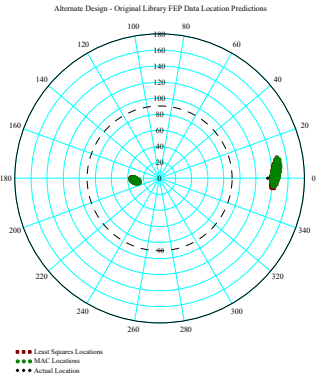

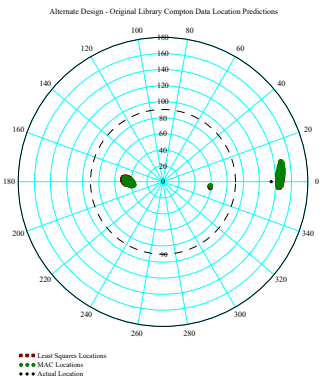

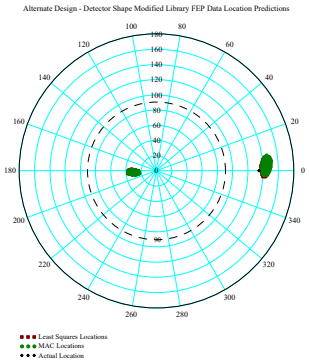

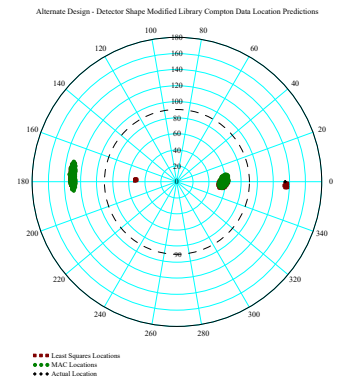

Cs-137 Source Data Results:

Phi_ViewDegree = 135
Theta_ViewDegree = 0

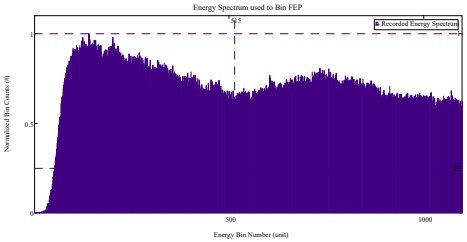

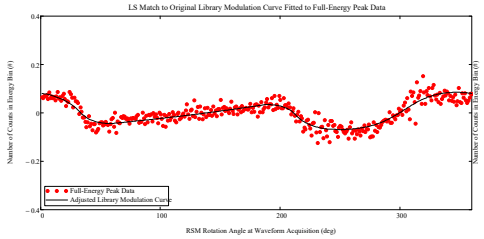

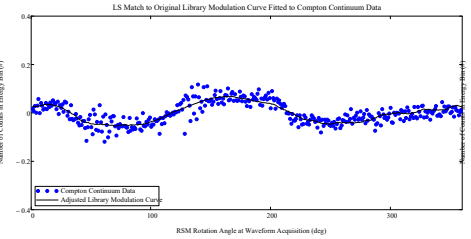

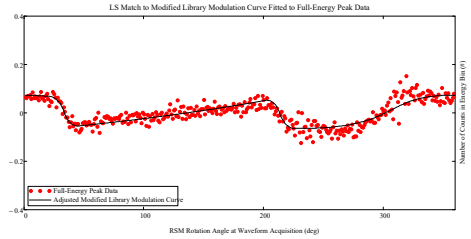

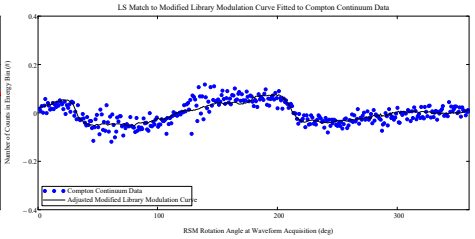

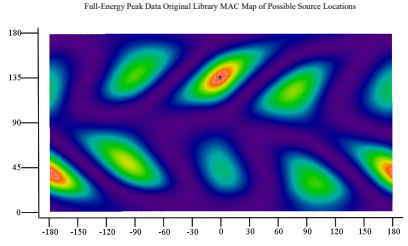

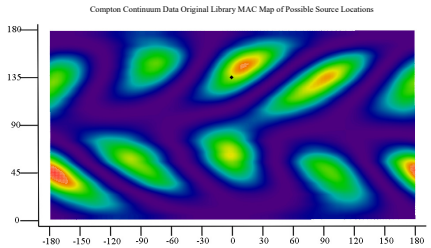

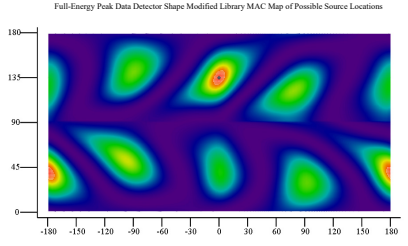

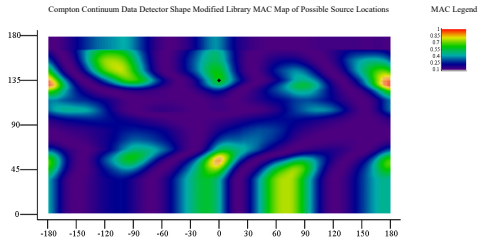

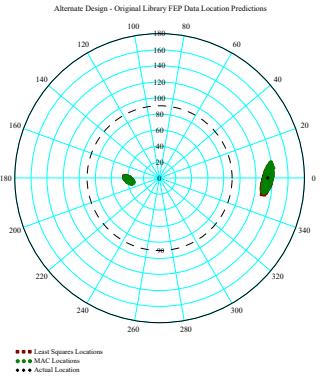

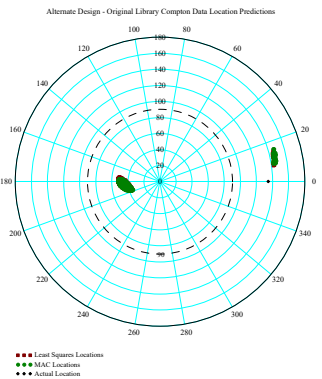

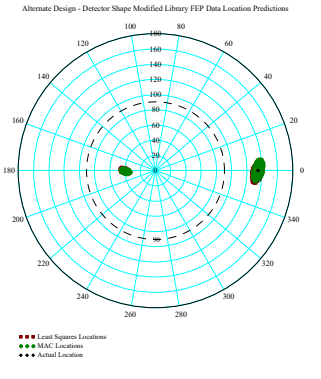

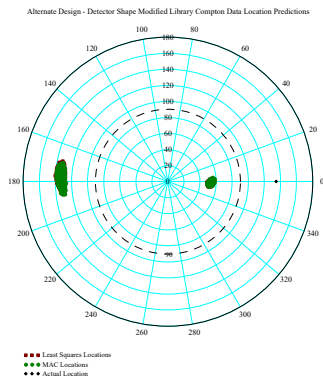

View Angle φ = 145° : Small RSM FitzGerald Design Ba-133and Cs-137 Data Spectra for Original and Detector Shape Modified Libraries, Modulation Curves, Library Curves, MAC and LS Direction Predictions

Ba-133 Source Data Results: Phi_ViewDegree = 145 Theta_ViewDegree = 0

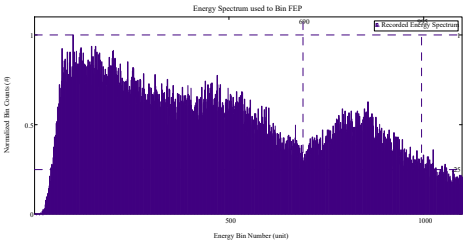

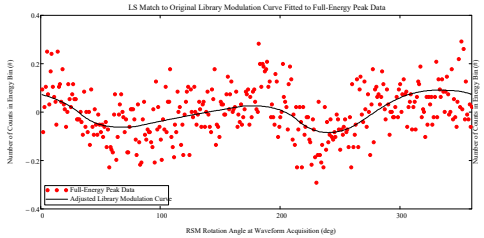

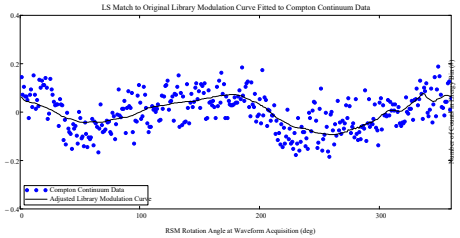

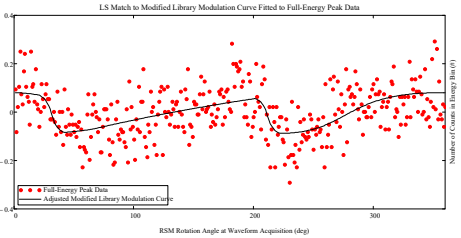

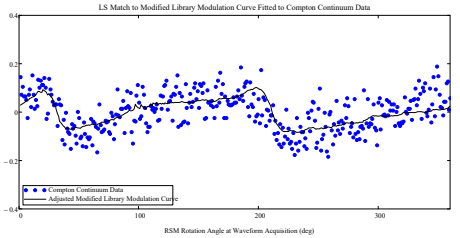

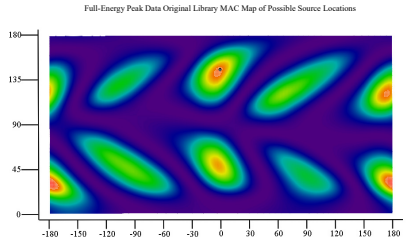

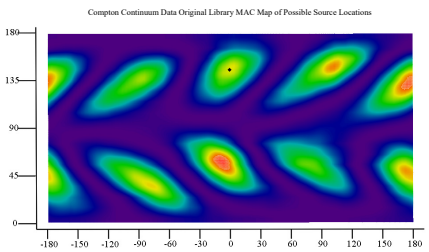

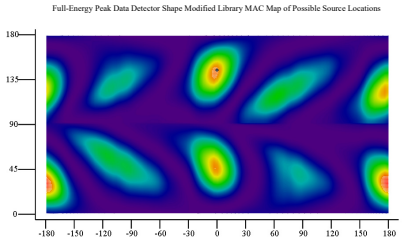

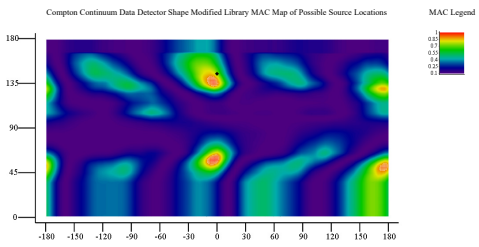

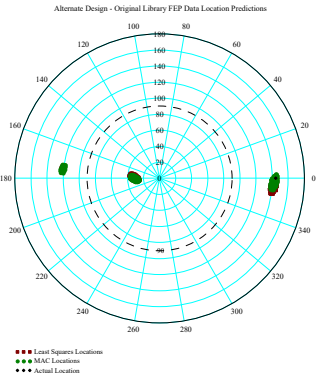

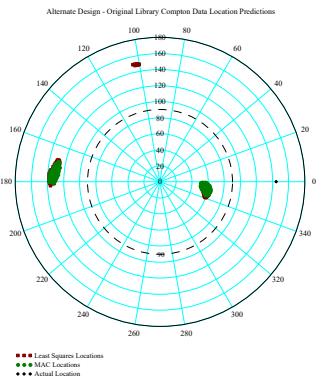

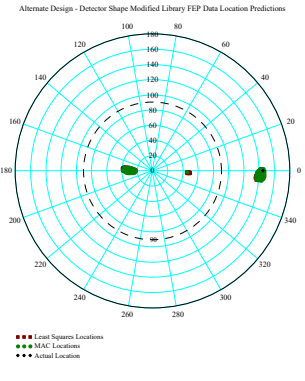

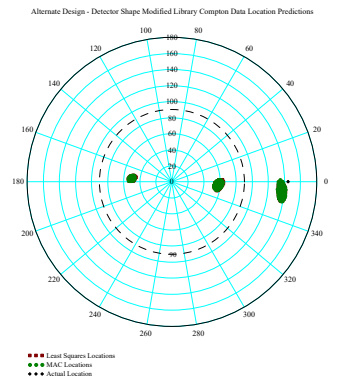

Cs-137 Source Data Results:

Phi_ViewDegree = 145
Theta_ViewDegree = 0

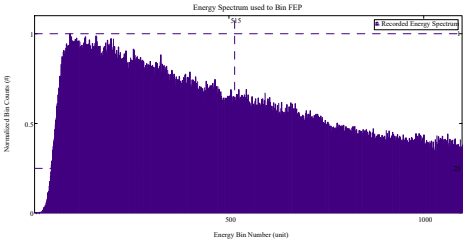

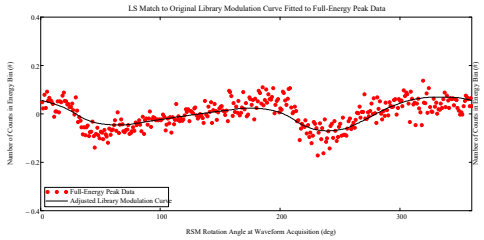

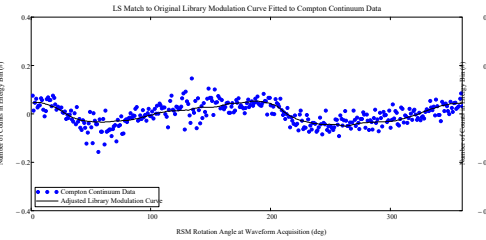

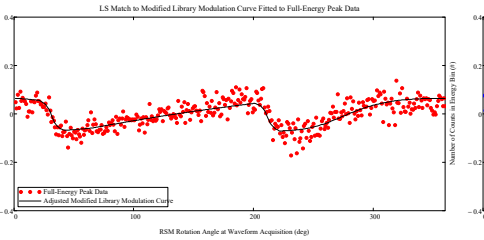

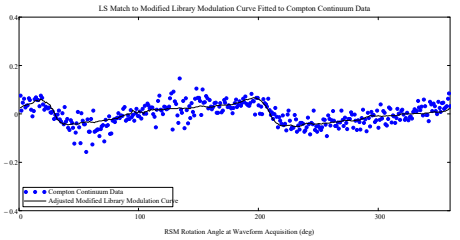

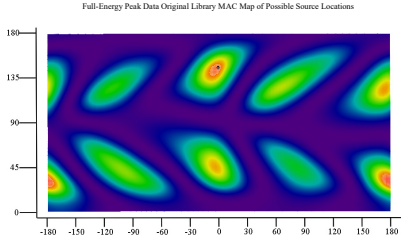

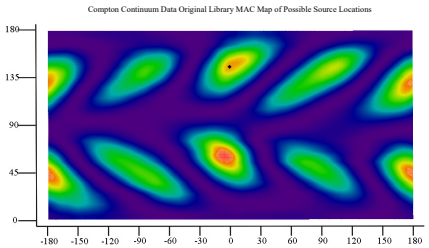

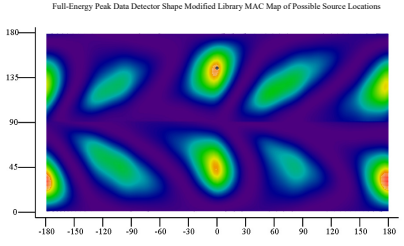

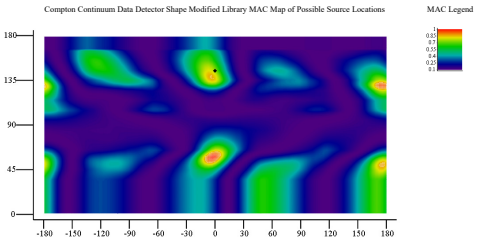

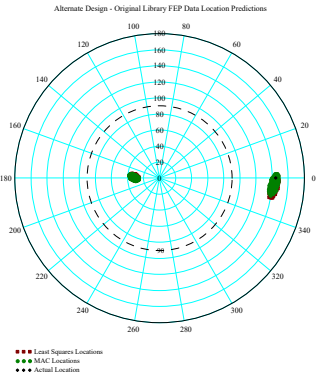

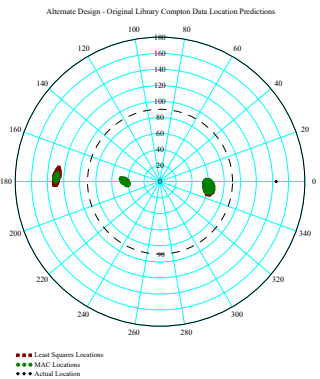

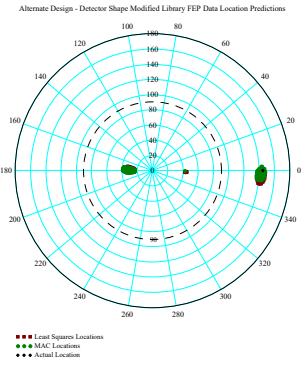

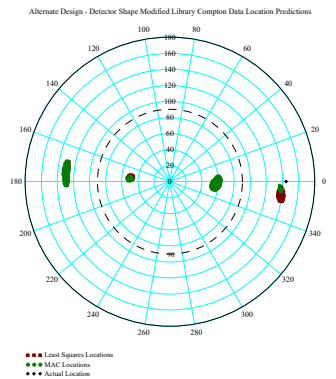

Appendix B.2: Small Alternate Design RSM Data, LaBr "Finger" Detector, Ba-133 & Cs-137 Single Sources; Experimentally Derived & Detector Shape Modified Library Matching Results

Page Intentionally Left Blank

View Angle φ = 5° : Small RSM Alternate Design Ba-133and Cs-137 Data Spectra for Original and Detector Shape Modified Libraries, Modulation Curves, Library Curves, MAC and LS Direction Predictions

Ba-133 Source Data Results: Phi_ViewDegree = 5 Theta_ViewDegree = 0

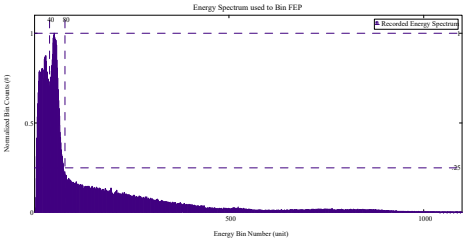

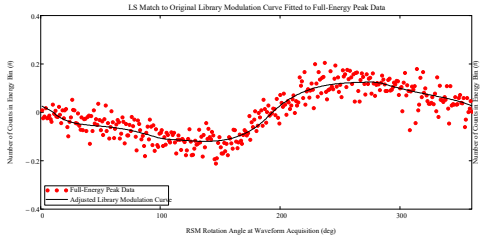

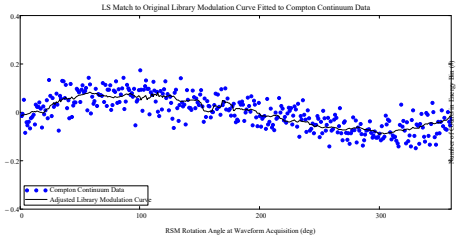

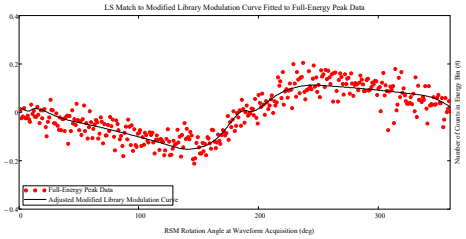

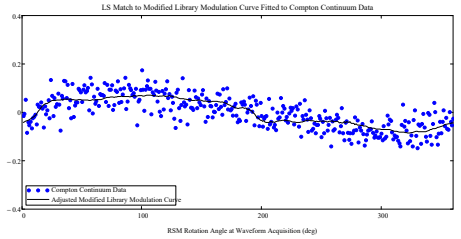

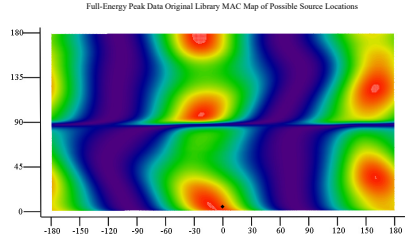

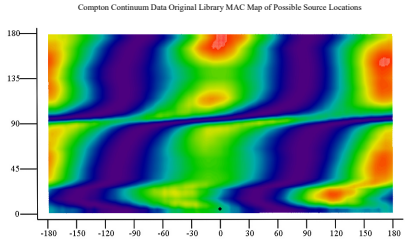

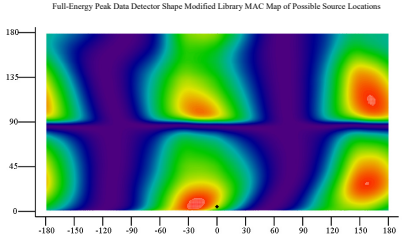

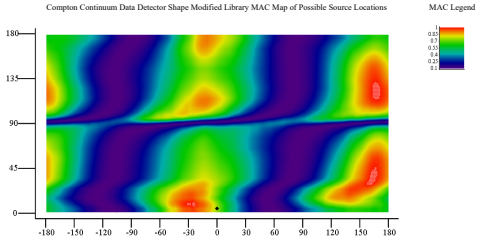

$(P1, P2, P3), \left(\text{thepoint}^{(1)}, \text{thepoint}^{(2)}, \text{thepoint}^{(3)}\right), \left(\text{Points}^{(1)}, \text{Points}^{(2)}, \text{Points}^{(3)}\right)$

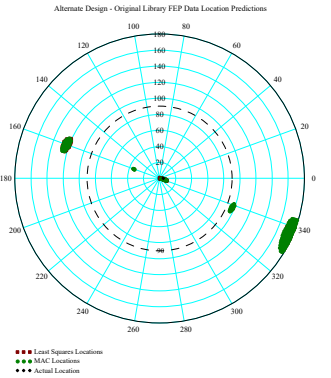

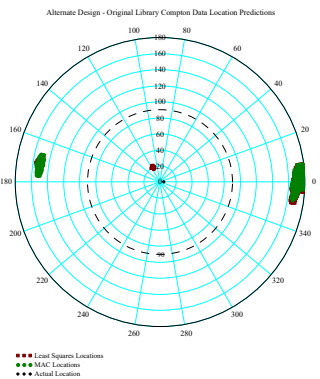

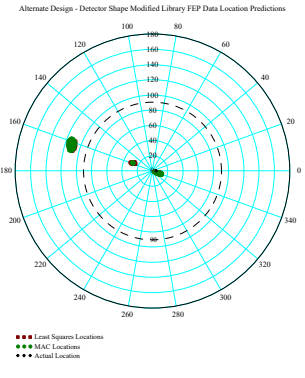

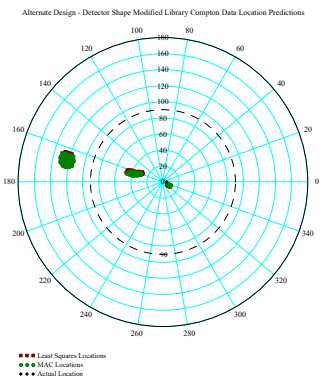

Cs-137 Source Data Results:

Phi_ViewDegree = 5
Theta_ViewDegree = 0

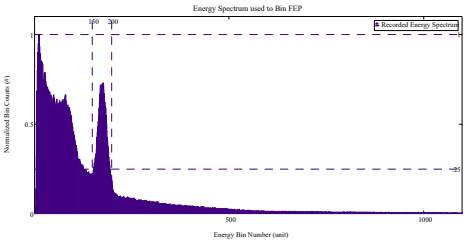

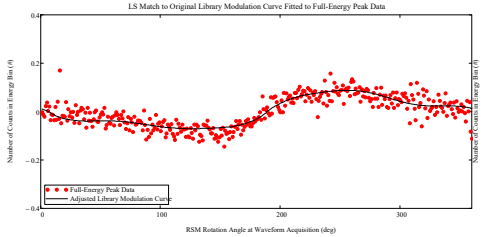

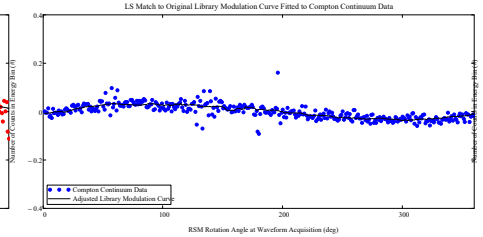

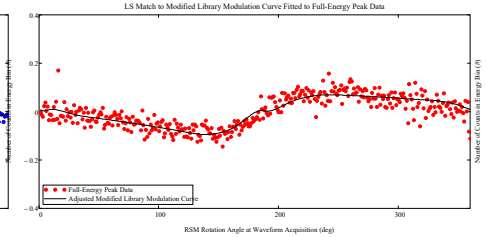

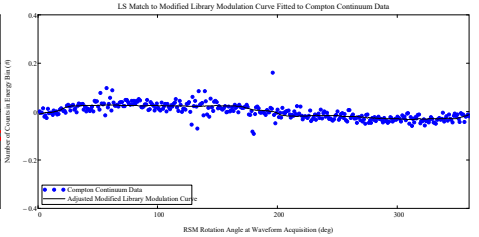

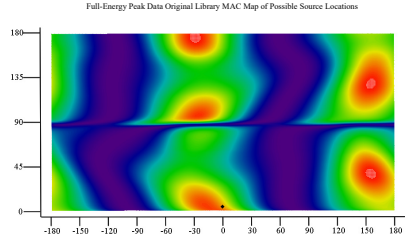

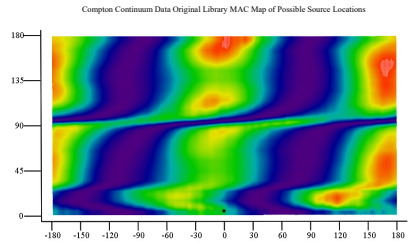

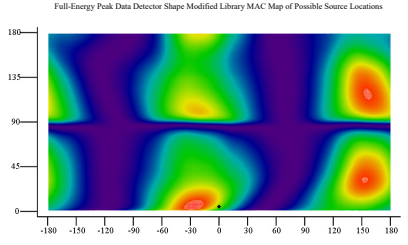

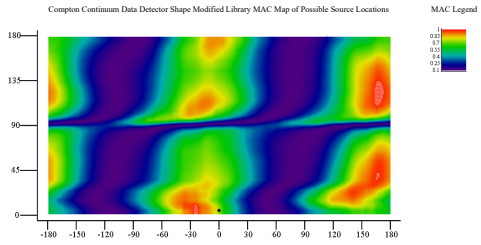

$(P1, P2, P3), \left(\text{thepoint}^{(1)}, \text{thepoint}^{(2)}, \text{thepoint}^{(3)}\right), \left(\text{Points}^{(1)}, \text{Points}^{(2)}, \text{Points}^{(3)}\right)$

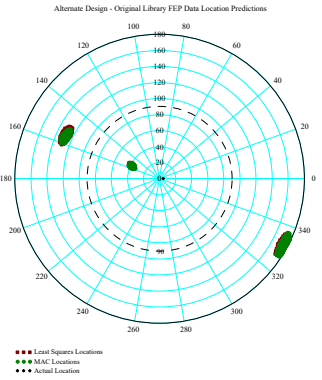

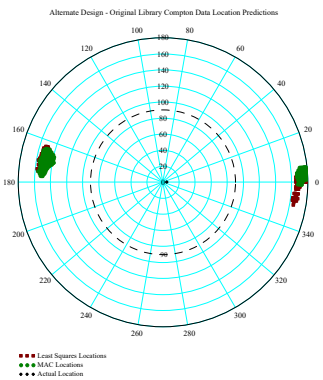

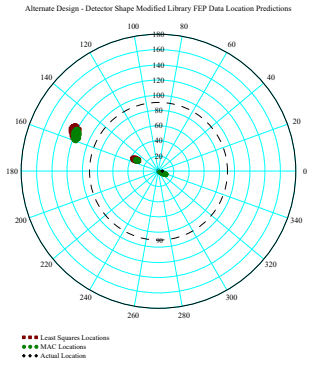

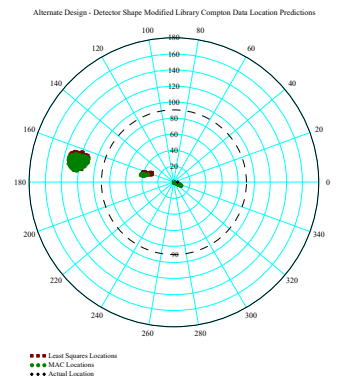

View Angle φ = 15° : Small RSM Alternate Design Ba-133and Cs-137 Data Spectra for Original and Detector Shape Modified Libraries, Modulation Curves, Library Curves, MAC and LS Direction Predictions

Ba-133 Source Data Results: Phi_ViewDegree = 15 Theta_ViewDegree = 0

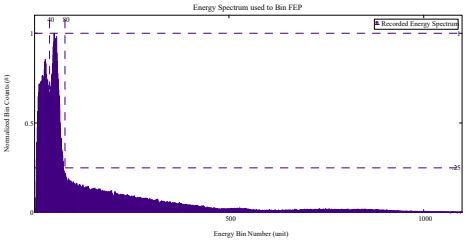

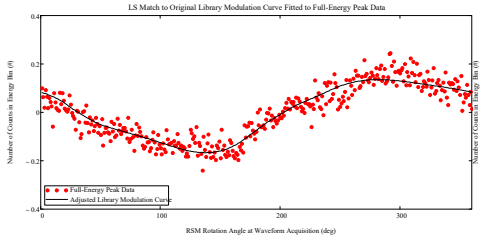

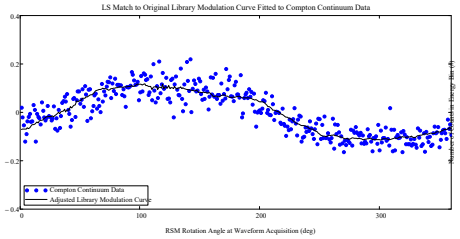

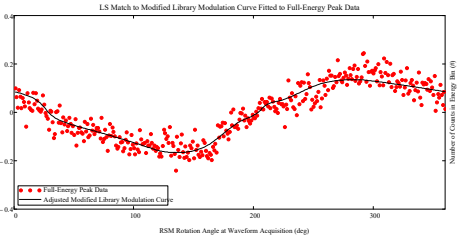

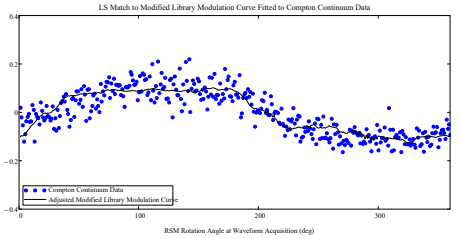

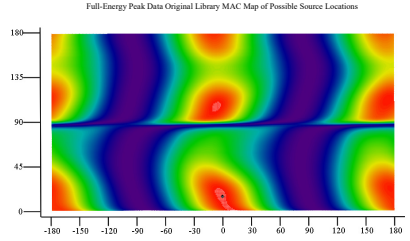

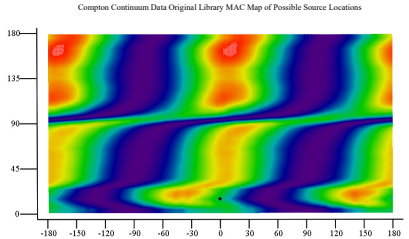

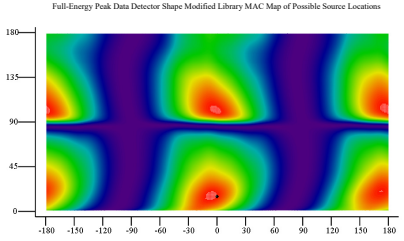

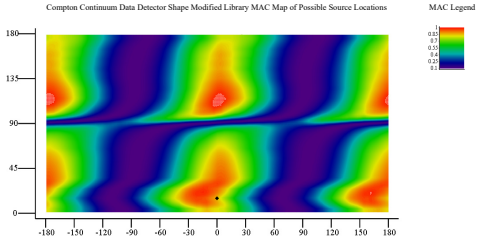

$(P1, P2, P3), \left(\text{thepoint}^{(1)}, \text{thepoint}^{(2)}, \text{thepoint}^{(3)}\right), \left(\text{Points}^{(1)}, \text{Points}^{(2)}, \text{Points}^{(3)}\right)$

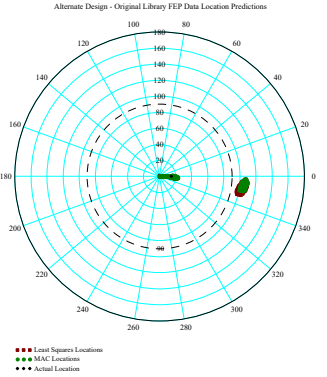

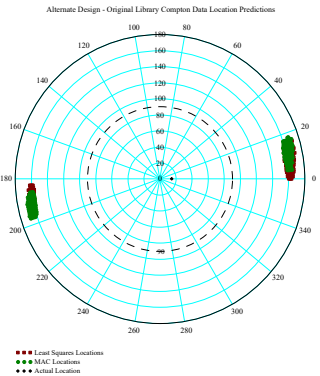

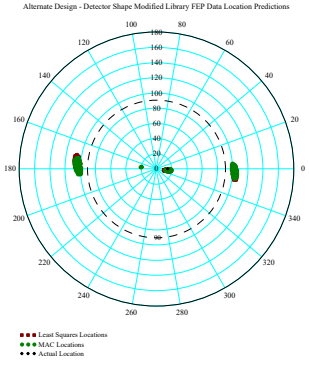

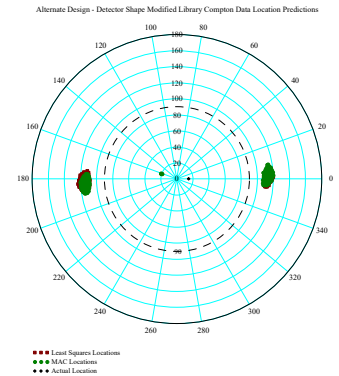

Cs-137 Source Data Results:

Phi_ViewDegree = 15
Theta_ViewDegree = 0

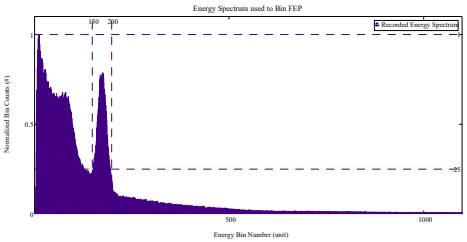

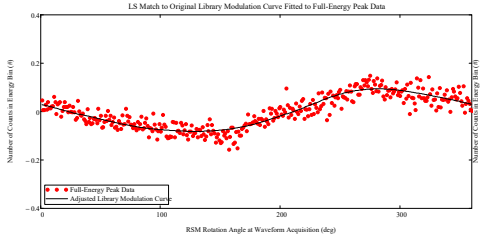

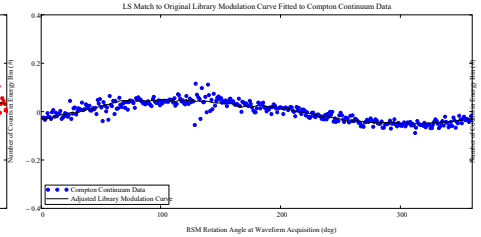

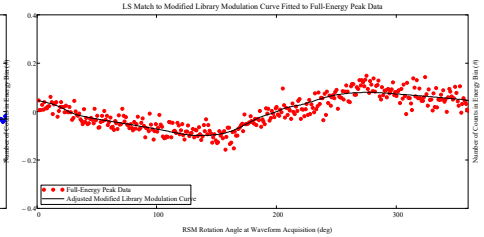

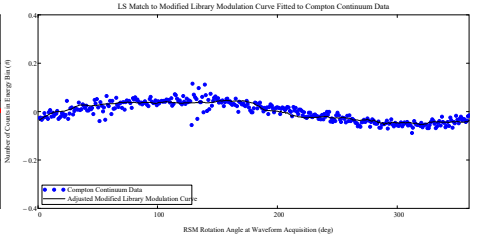

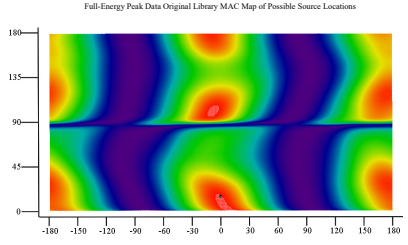

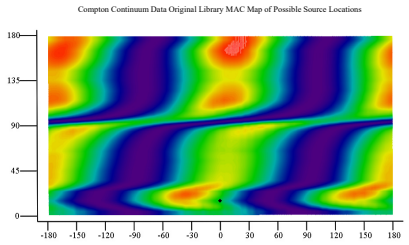

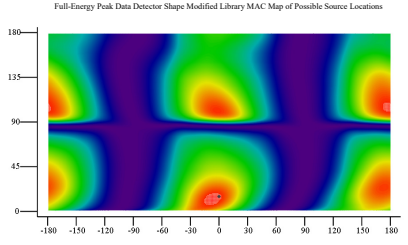

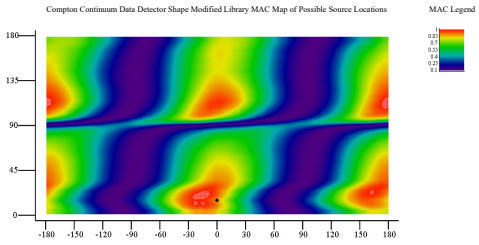

$(P1, P2, P3), \left(\text{thepoint}^{(1)}, \text{thepoint}^{(2)}, \text{thepoint}^{(3)}\right), \left(\text{Points}^{(1)}, \text{Points}^{(2)}, \text{Points}^{(3)}\right)$

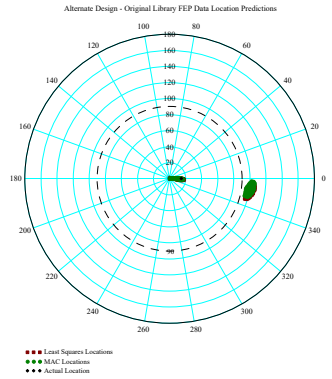

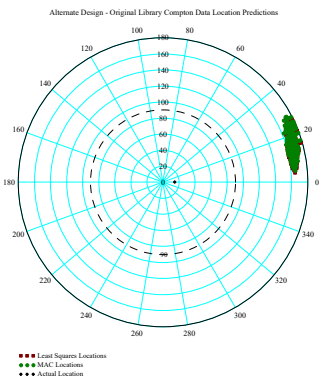

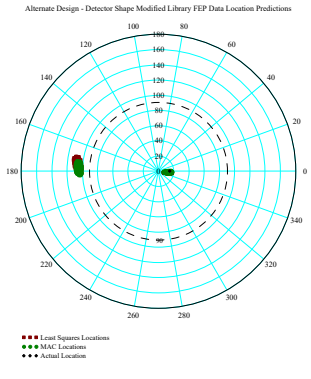

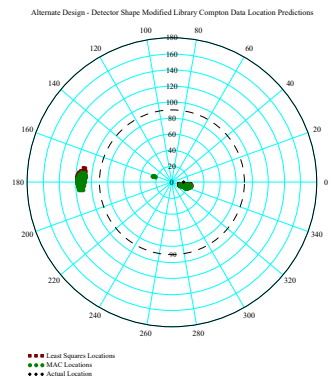

View Angle φ = 25° : Small RSM Alternate Design Ba-133and Cs-137 Data Spectra for Original and Detector Shape Modified Libraries, Modulation Curves, Library Curves, MAC and LS Direction Predictions

Ba-133 Source Data Results: Phi_ViewDegree = 25 Theta_ViewDegree = 0

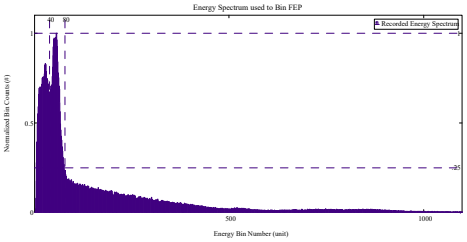

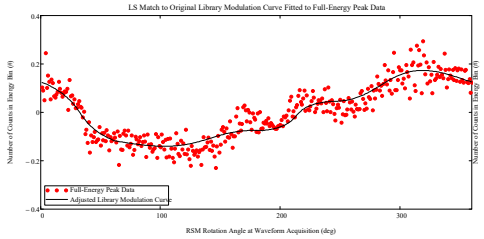

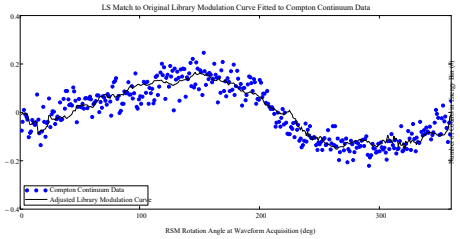

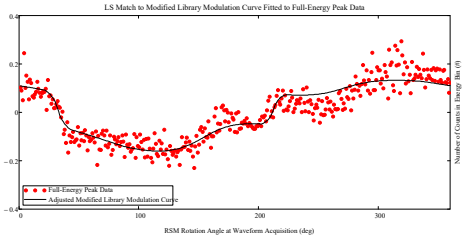

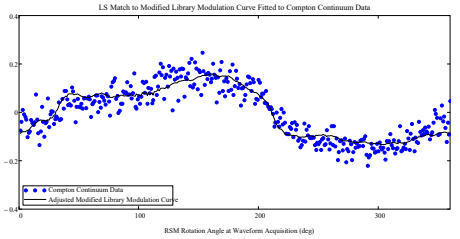

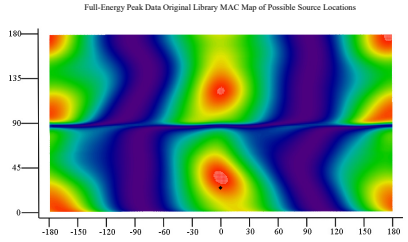

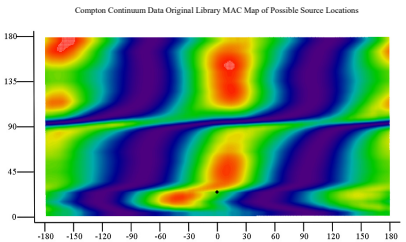

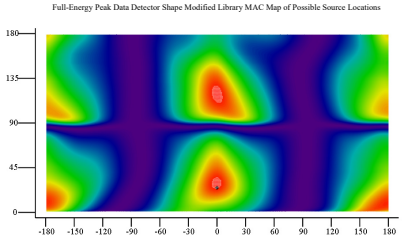

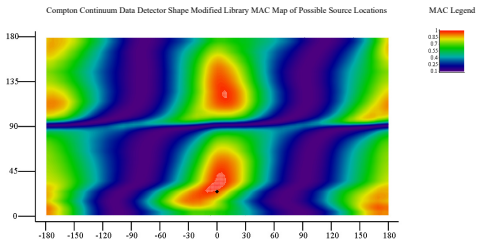

$(P1, P2, P3), \left(\text{thepoint}^{(1)}, \text{thepoint}^{(2)}, \text{thepoint}^{(3)}\right), \left(\text{Points}^{(1)}, \text{Points}^{(2)}, \text{Points}^{(3)}\right)$

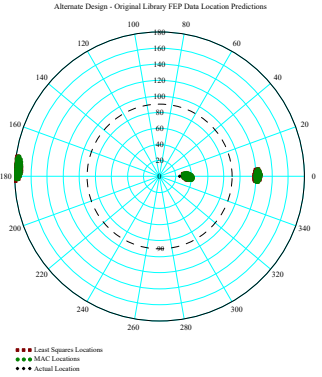

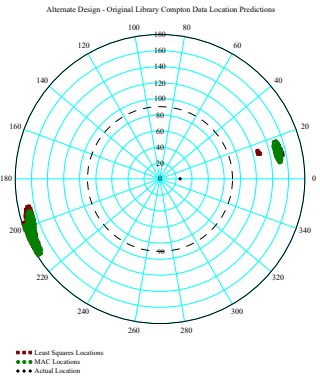

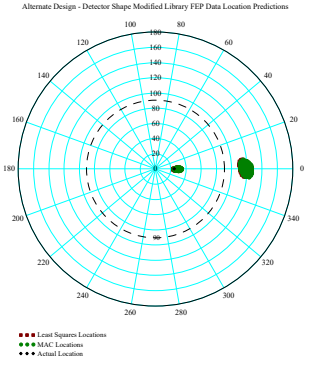

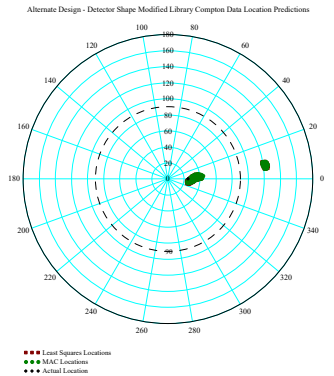

Cs-137 Source Data Results:

Phi_ViewDegree = 25
Theta_ViewDegree = 0

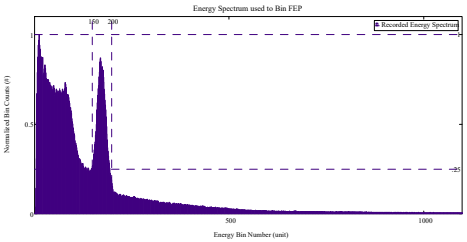

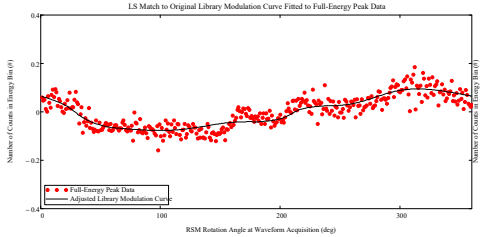

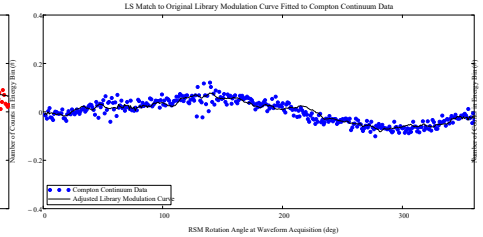

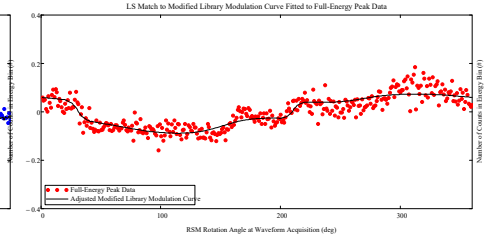

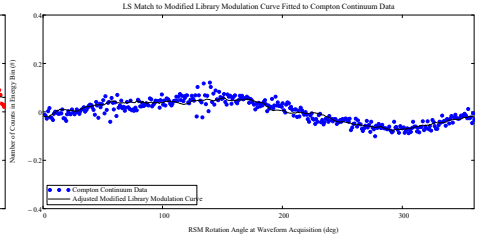

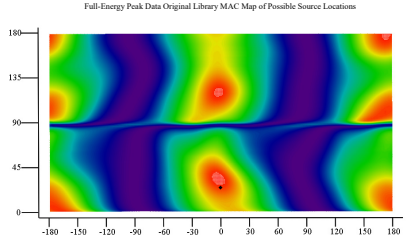

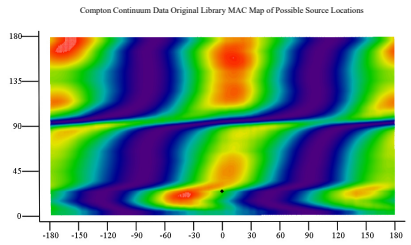

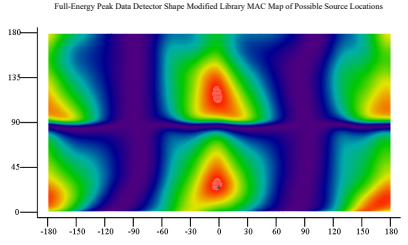

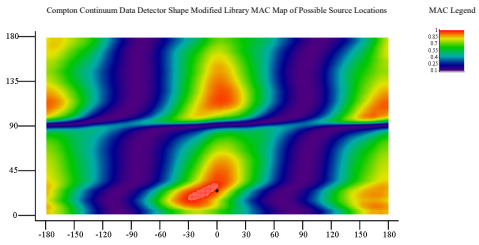

$(P1, P2, P3), (thepoint^{(1)}, thepoint^{(2)}, thepoint^{(3)}), (Points^{(1)}, Points^{(2)}, Points^{(3)})$

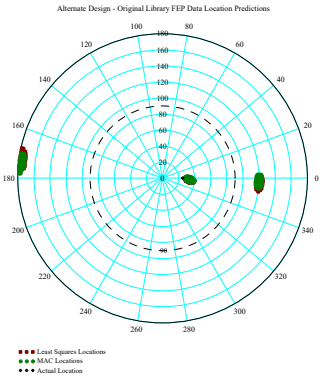

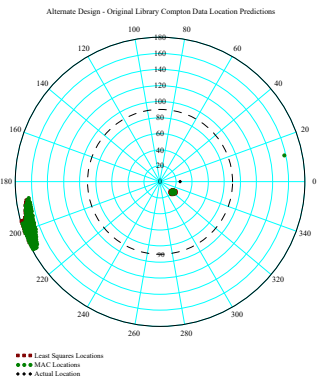

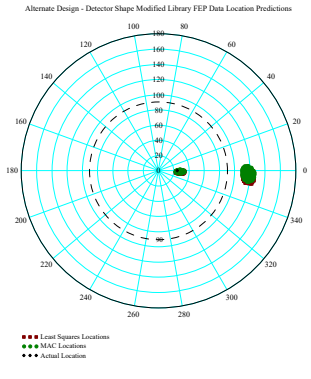

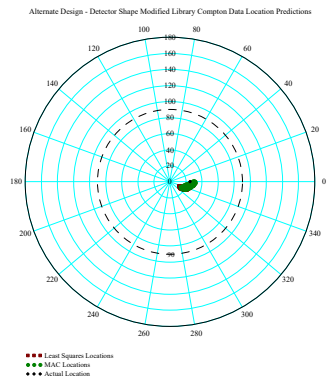

View Angle φ = 35° : Small RSM Alternate Design Ba-133and Cs-137 Data Spectra for Original and Detector Shape Modified Libraries, Modulation Curves, Library Curves, MAC and LS Direction Predictions

Ba-133 Source Data Results: Phi_ViewDegree = 35 Theta_ViewDegree = 0

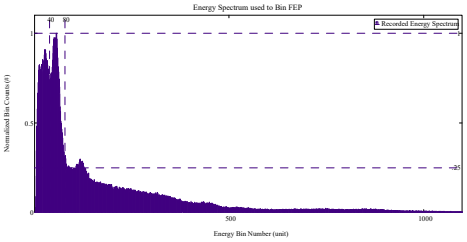

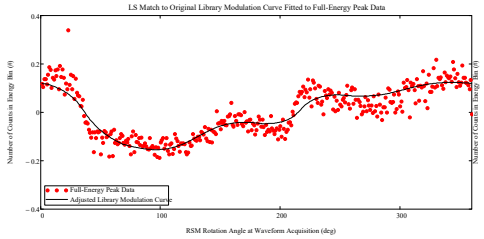

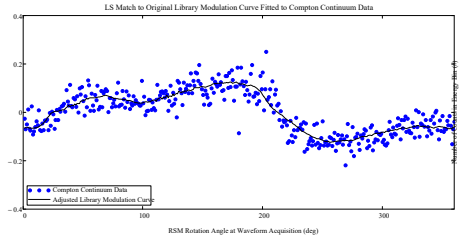

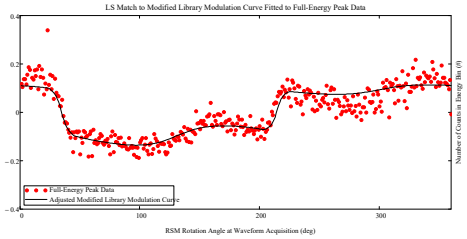

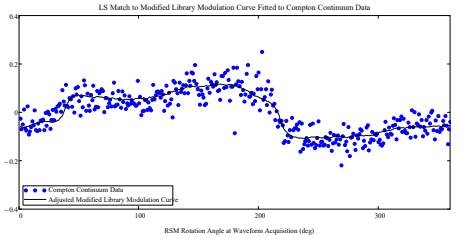

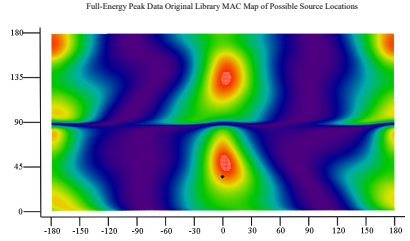

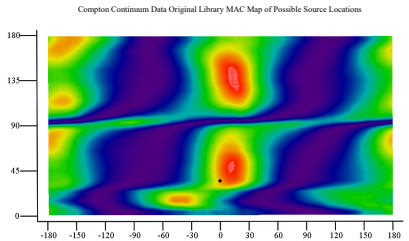

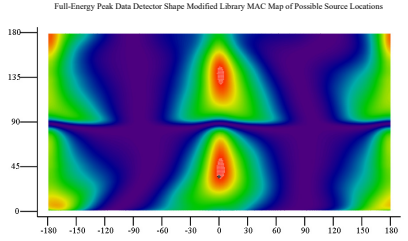

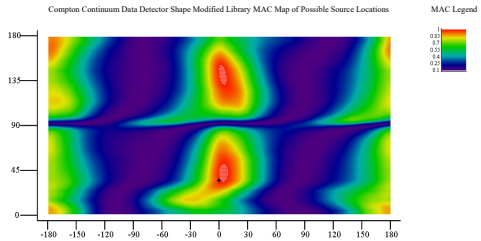

$(P1, P2, P3), \{thepoint^{(1)}, thepoint^{(2)}, thepoint^{(3)}\}, \{Points^{(1)}, Points^{(2)}, Points^{(3)}\}$

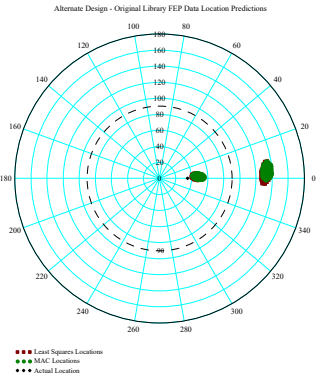

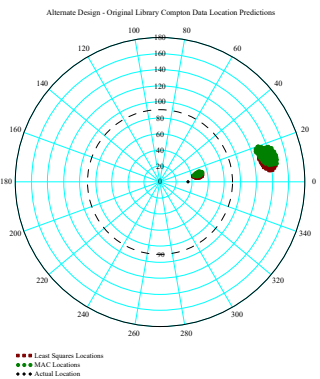

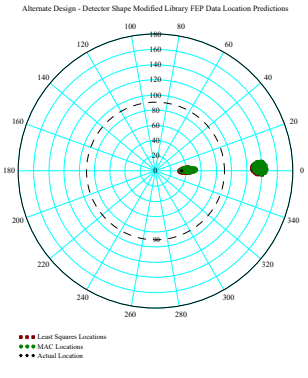

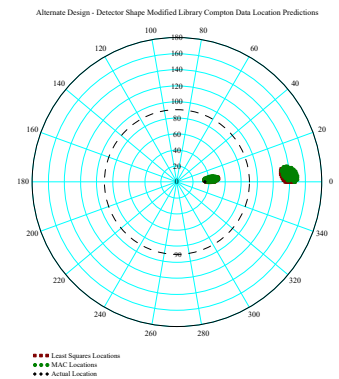

Cs-137 Source Data Results:

Phi_ViewDegree = 35
Theta_ViewDegree = 0

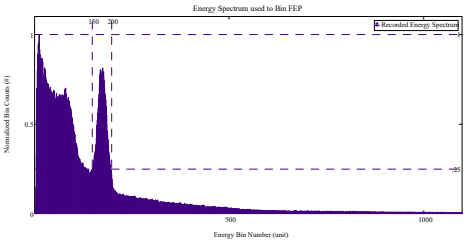

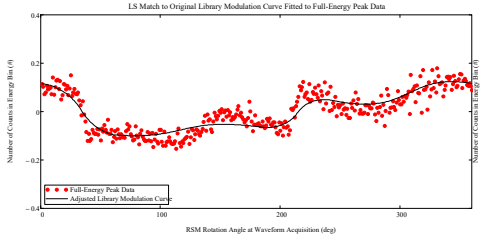

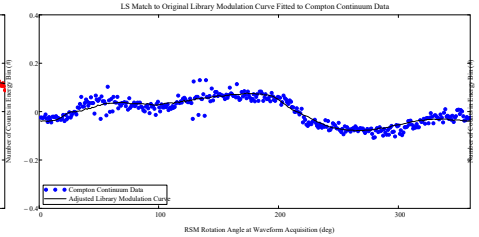

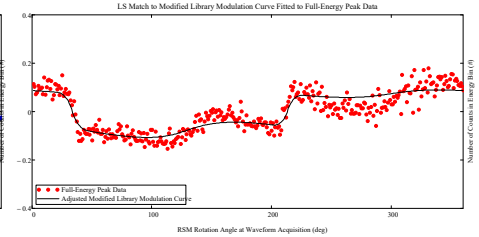

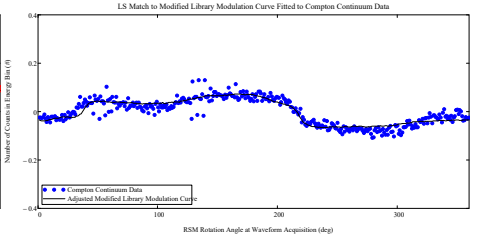

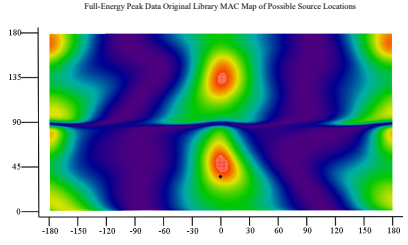

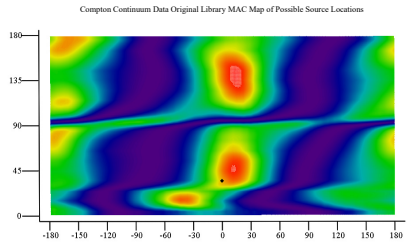

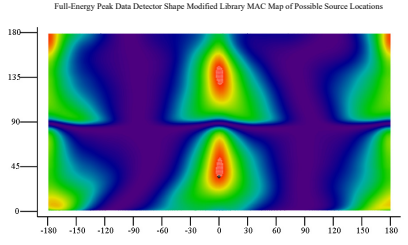

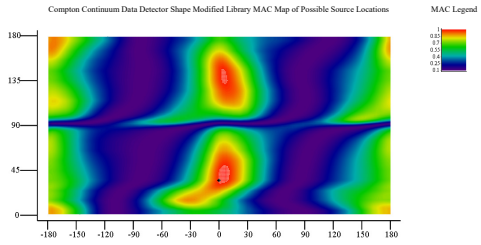

$(P1, P2, P3), \left(\text{thepoint}^{(1)}, \text{thepoint}^{(2)}, \text{thepoint}^{(3)}\right), \left(\text{Points}^{(1)}, \text{Points}^{(2)}, \text{Points}^{(3)}\right)$

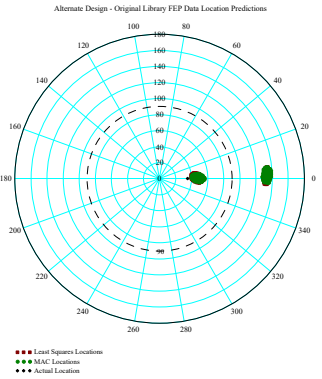

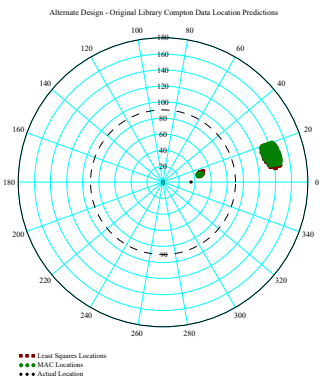

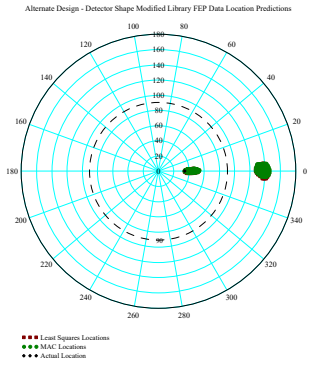

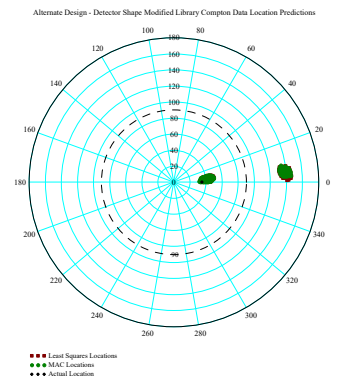

View Angle φ = 45° : Small RSM Alternate Design Ba-133and Cs-137 Data Spectra for Original and Detector Shape Modified Libraries, Modulation Curves, Library Curves, MAC and LS Direction Predictions

Ba-133 Source Data Results: Phi_ViewDegree = 45 Theta_ViewDegree = 0

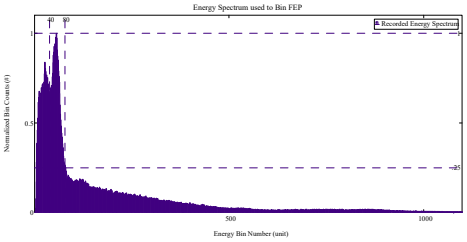

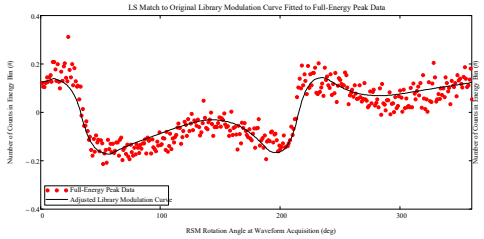

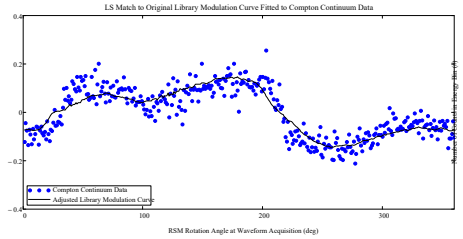

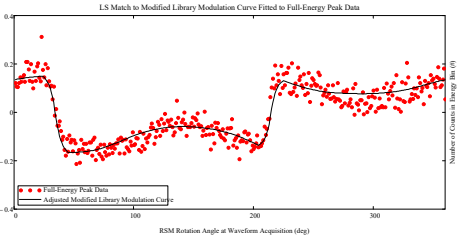

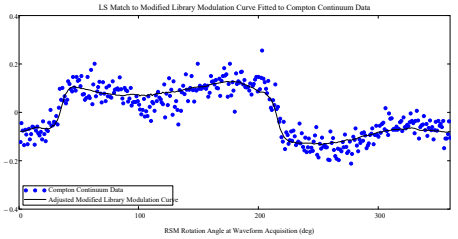

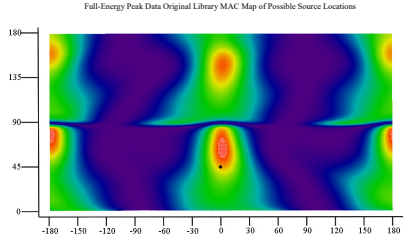

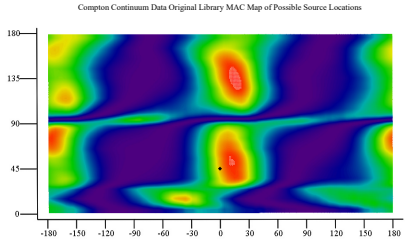

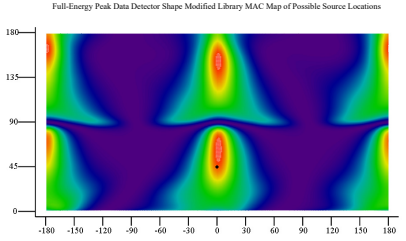

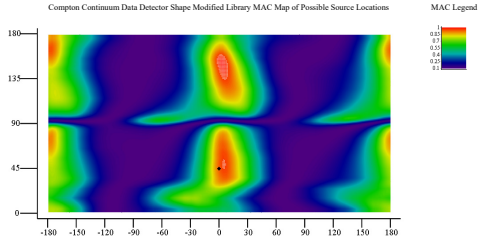

$(P1, P2, P3), \{thepoint^{(1)}, thepoint^{(2)}, thepoint^{(3)}\}, \{Points^{(1)}, Points^{(2)}, Points^{(3)}\}$

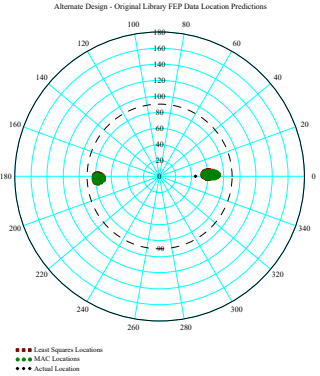

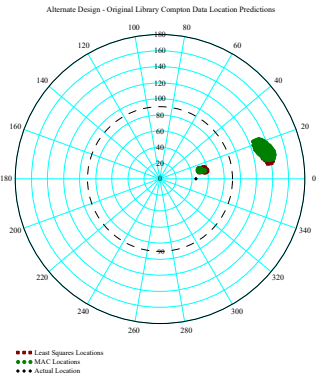

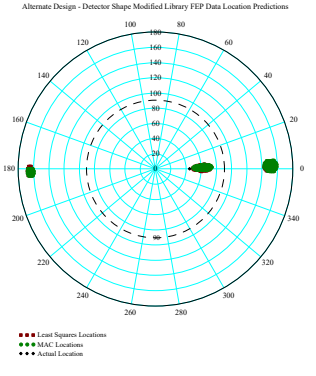

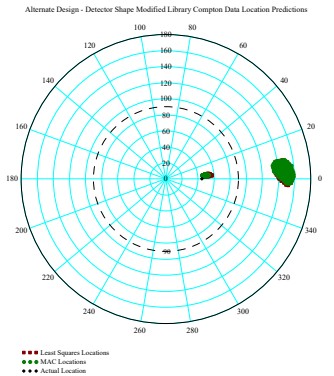

Cs-137 Source Data Results:

Phi_ViewDegree = 45
Theta_ViewDegree = 0

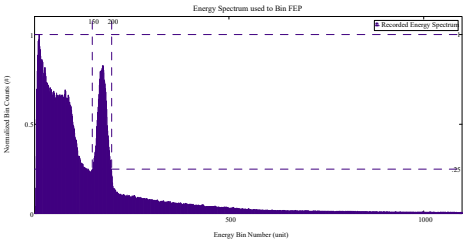

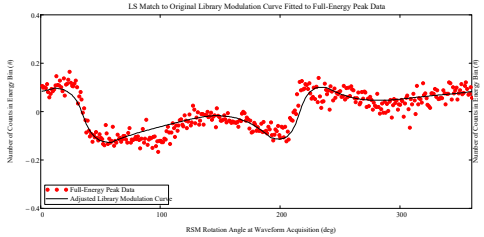

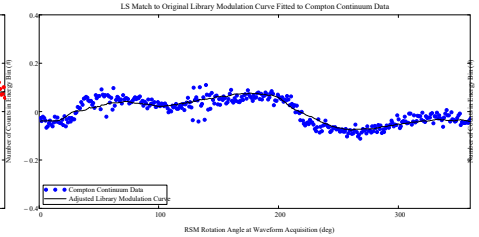

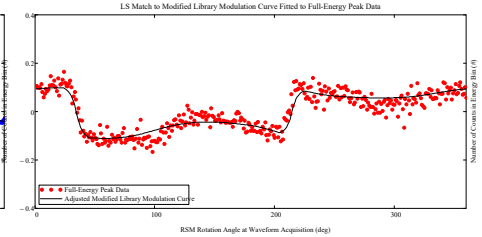

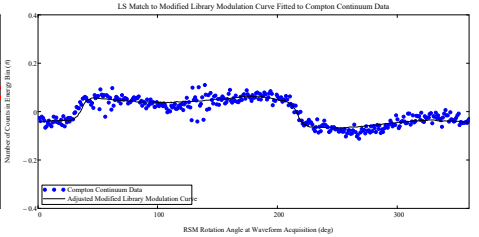

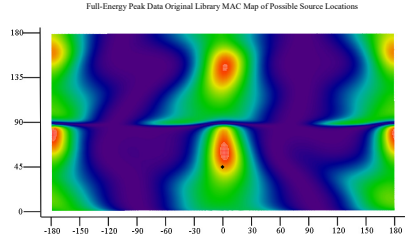

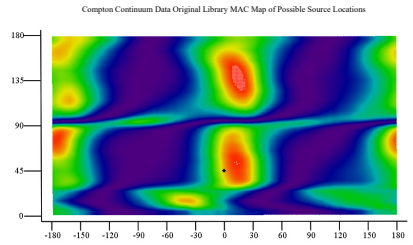

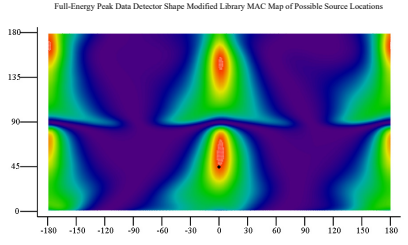

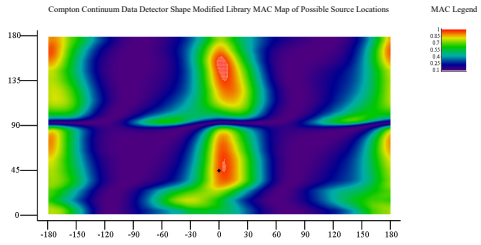

$(P1, P2, P3), \left(\text{thepoint}^{(1)}, \text{thepoint}^{(2)}, \text{thepoint}^{(3)}\right), \left(\text{Points}^{(1)}, \text{Points}^{(2)}, \text{Points}^{(3)}\right)$

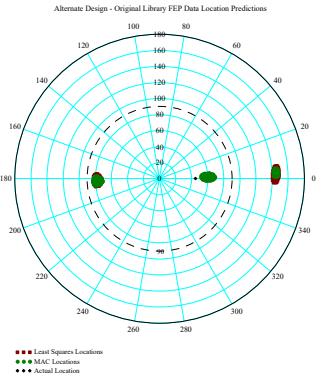

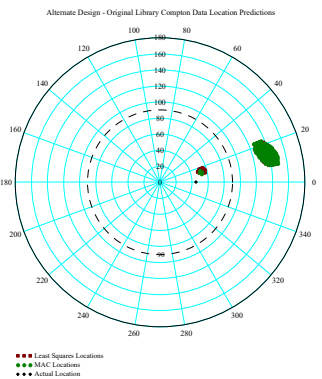

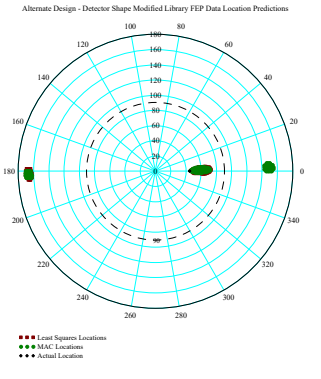

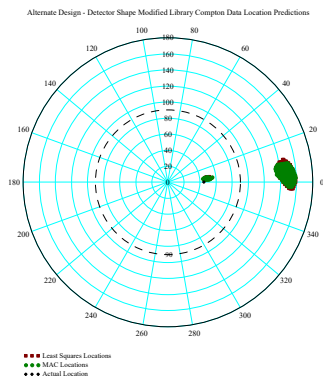

View Angle φ = 55° : Small RSM Alternate Design Ba-133and Cs-137 Data Spectra for Original and Detector Shape Modified Libraries, Modulation Curves, Library Curves, MAC and LS Direction Predictions

Ba-133 Source Data Results: Phi_ViewDegree = 55 Theta_ViewDegree = 0

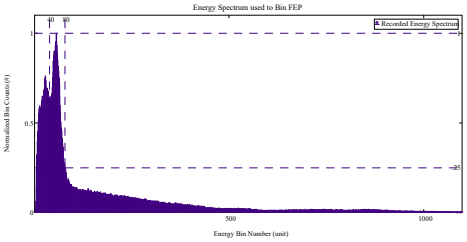

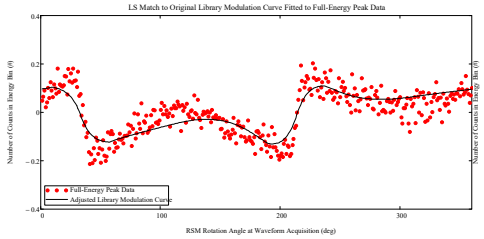

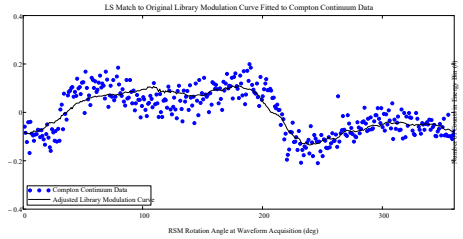

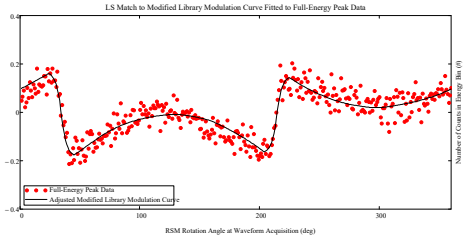

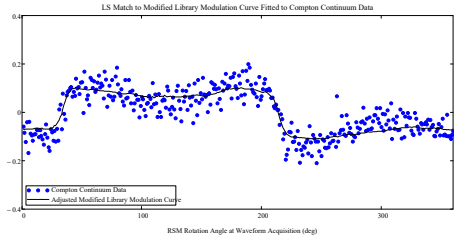

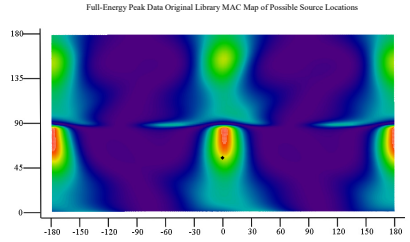

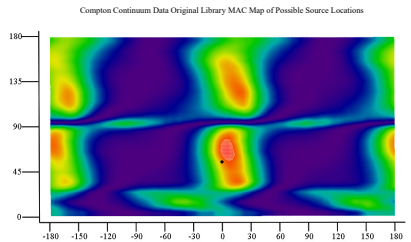

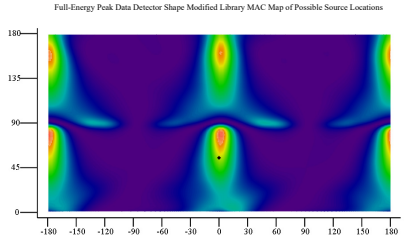

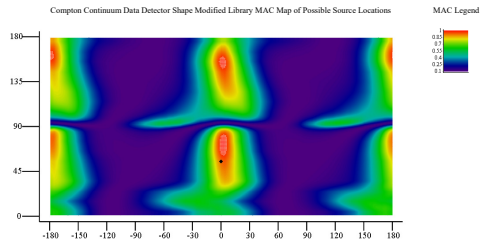

$(P1, P2, P3), \{thepoint^{(1)}, thepoint^{(2)}, thepoint^{(3)}\}, \{Points^{(1)}, Points^{(2)}, Points^{(3)}\}$

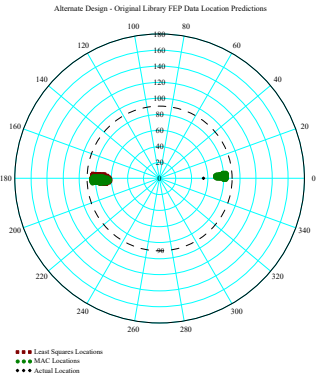

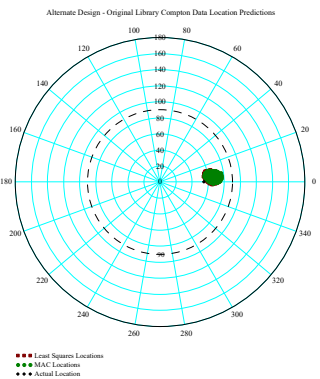

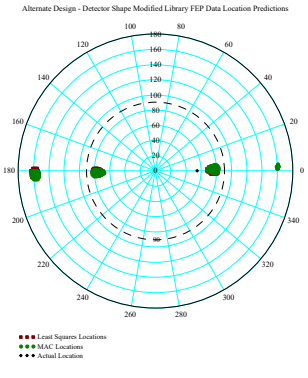

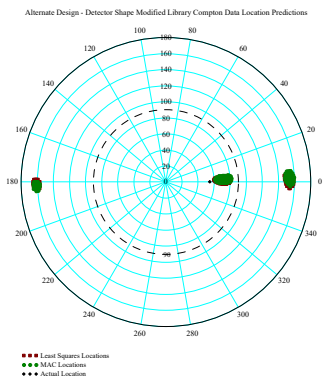

Cs-137 Source Data Results:

Phi_ViewDegree = 55
Theta_ViewDegree = 0

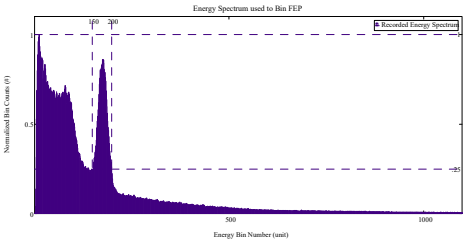

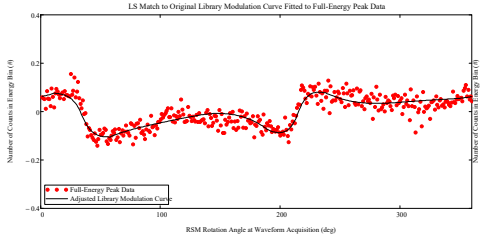

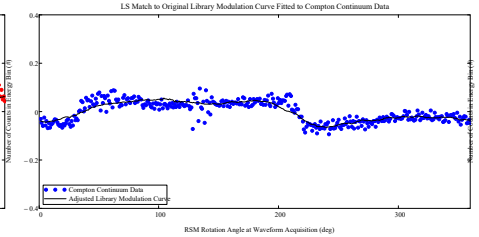

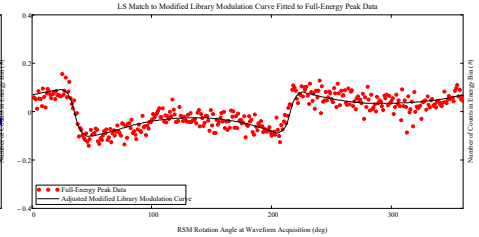

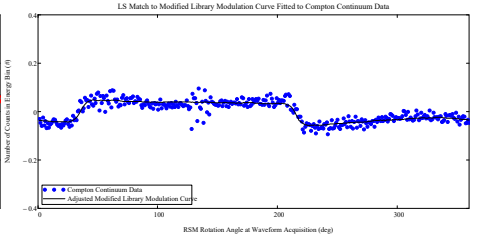

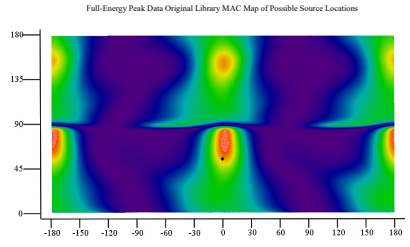

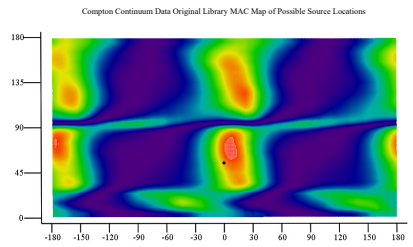

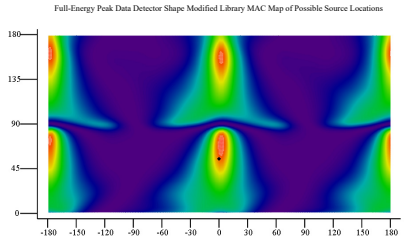

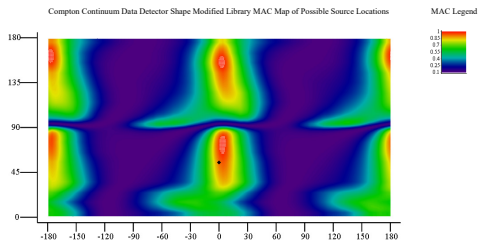

$(P1, P2, P3), \left(\text{thepoint}^{(1)}, \text{thepoint}^{(2)}, \text{thepoint}^{(3)}\right), \left(\text{Points}^{(1)}, \text{Points}^{(2)}, \text{Points}^{(3)}\right)$

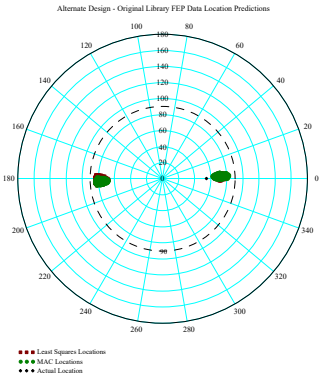

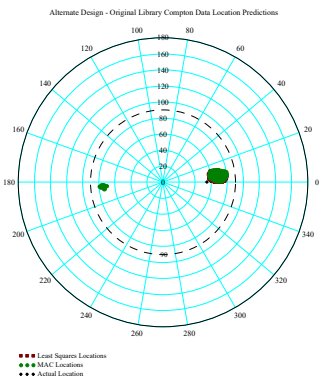

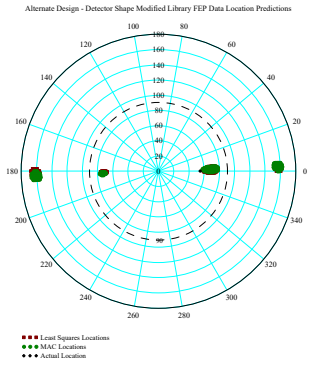

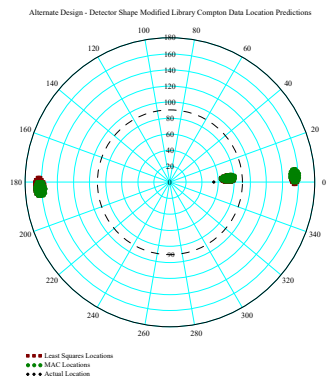

View Angle φ = 65° : Small RSM Alternate Design Ba-133and Cs-137 Data Spectra for Original and Detector Shape Modified Libraries, Modulation Curves, Library Curves, MAC and LS Direction Predictions

Ba-133 Source Data Results: Phi_ViewDegree = 65 Theta_ViewDegree = 0

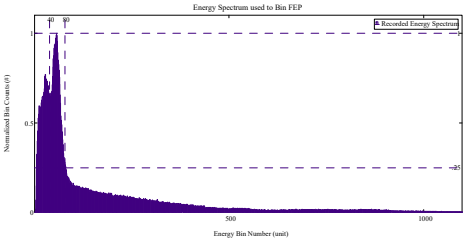

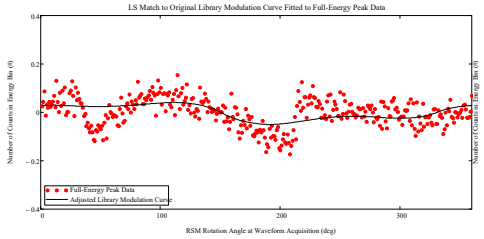

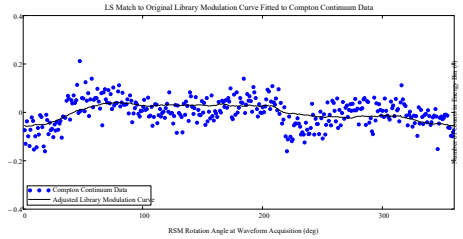

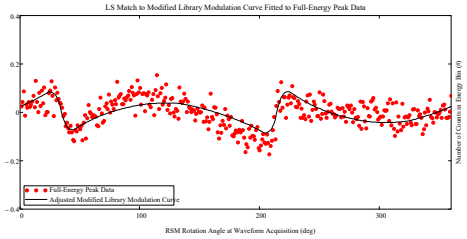

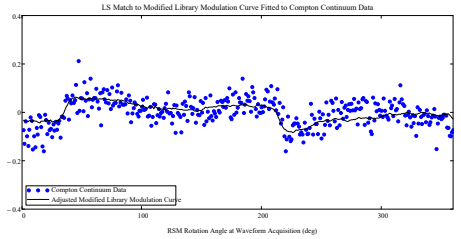

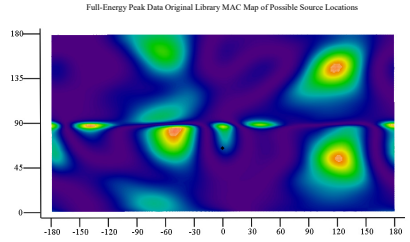

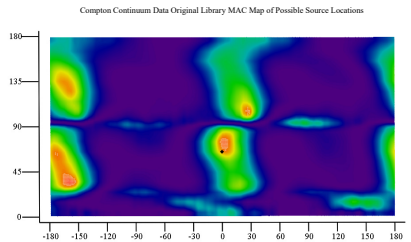

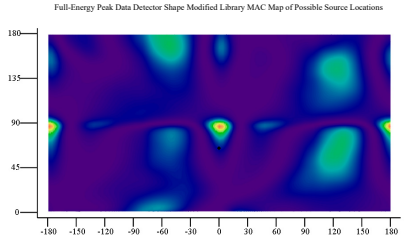

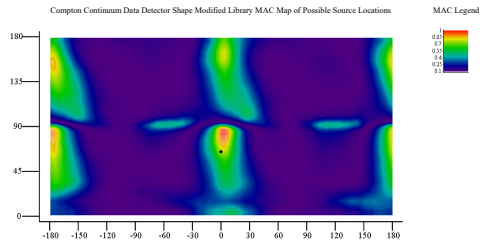

$(P1, P2, P3), \{thepoint^{(1)}, thepoint^{(2)}, thepoint^{(3)}\}, \{Points^{(1)}, Points^{(2)}, Points^{(3)}\}$

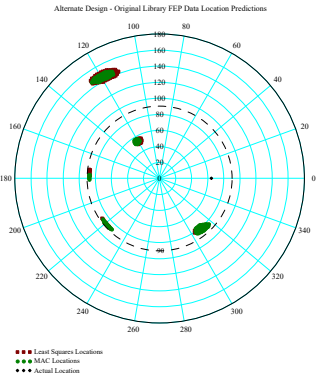

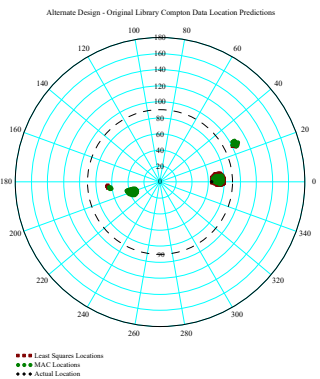

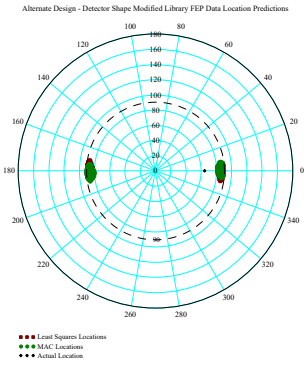

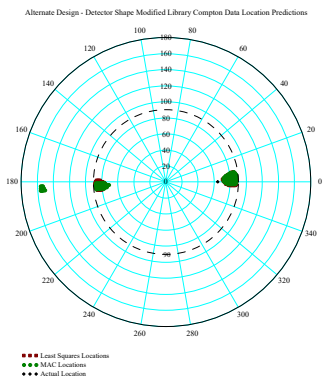

Cs-137 Source Data Results:

Phi_ViewDegree = 65
Theta_ViewDegree = 0

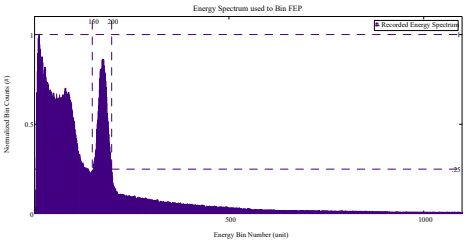

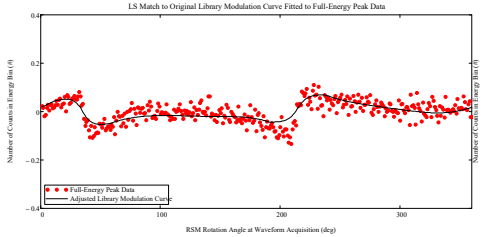

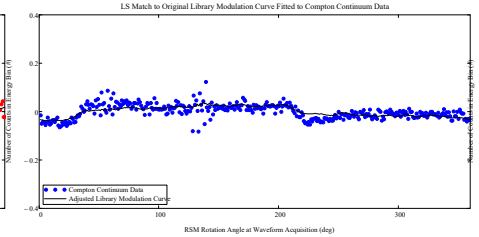

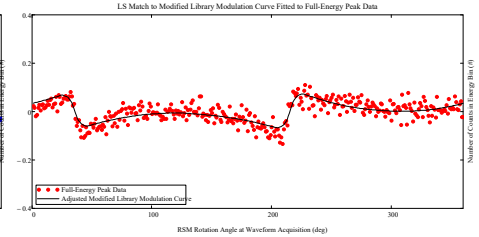

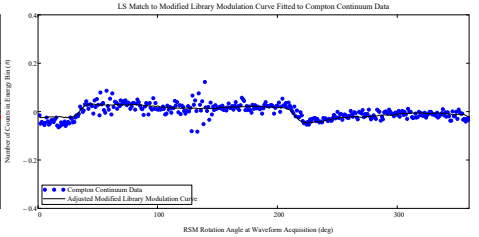

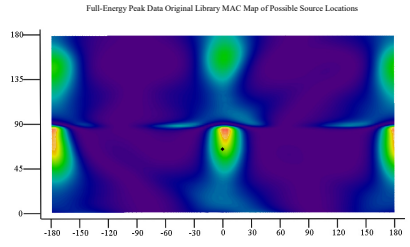

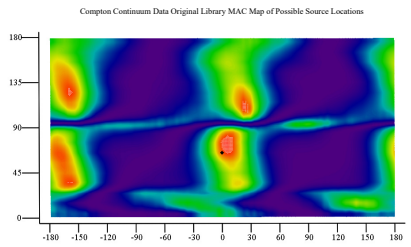

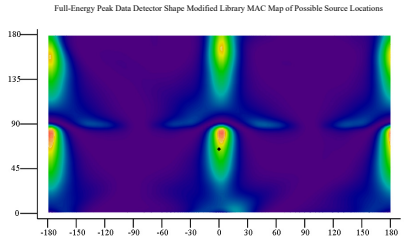

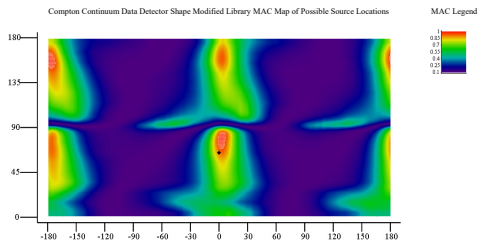

$(P1, P2, P3), \left(\text{thepoint}^{(1)}, \text{thepoint}^{(2)}, \text{thepoint}^{(3)}\right), \left(\text{Points}^{(1)}, \text{Points}^{(2)}, \text{Points}^{(3)}\right)$

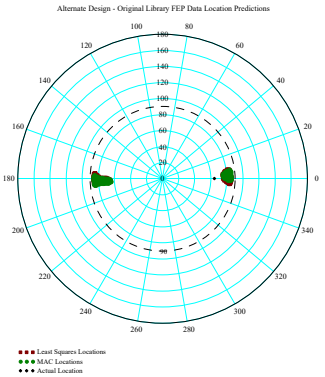

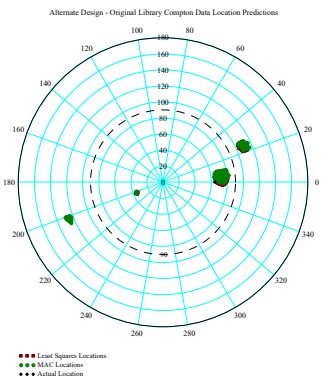

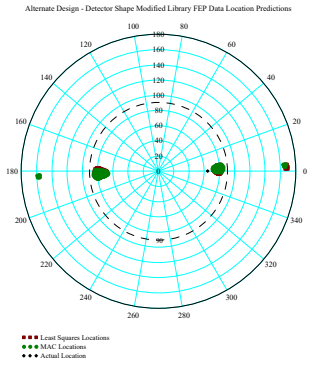

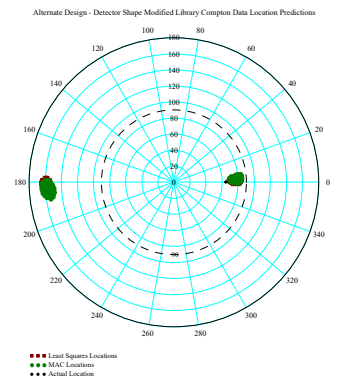

View Angle φ = 75° : Small RSM Alternate Design Ba-133and Cs-137 Data Spectra for Original and Detector Shape Modified Libraries, Modulation Curves, Library Curves, MAC and LS Direction Predictions

Ba-133 Source Data Results: Phi_ViewDegree = 75 Theta_ViewDegree = 0

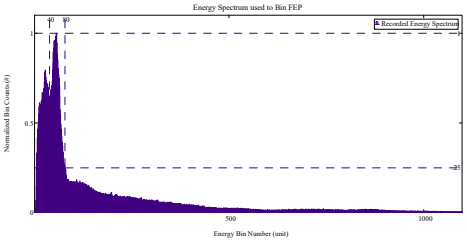

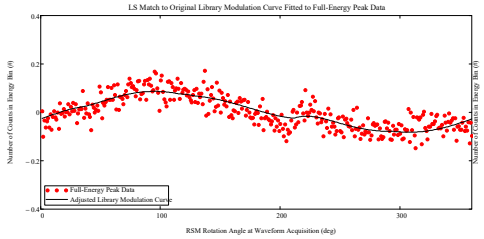

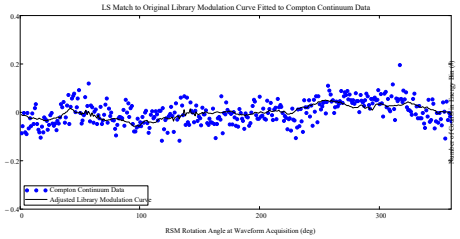

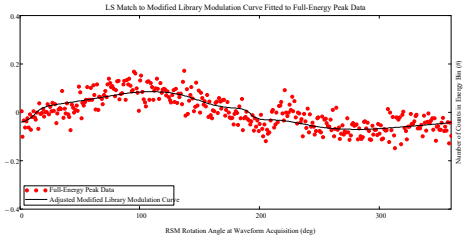

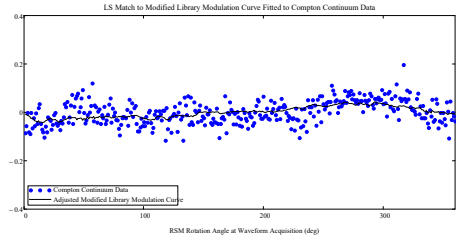

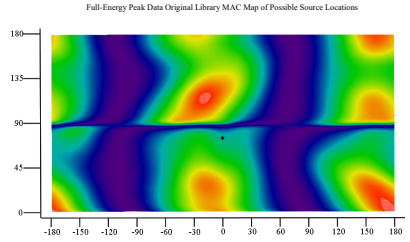

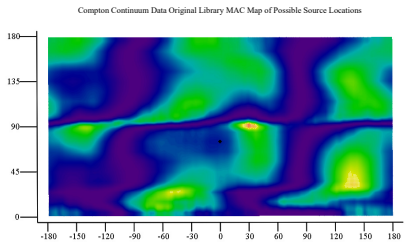

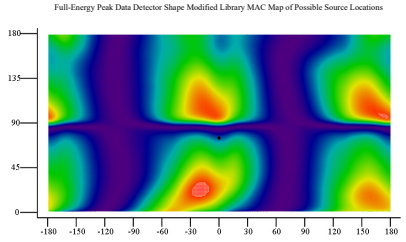

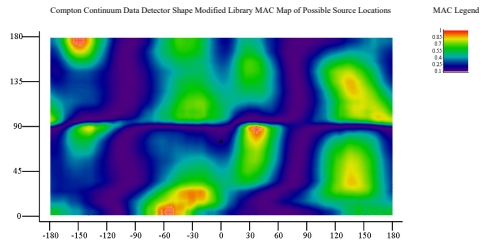

$(P1, P2, P3), \left(\text{thepoint}^{(1)}, \text{thepoint}^{(2)}, \text{thepoint}^{(3)}\right), \left(\text{Points}^{(1)}, \text{Points}^{(2)}, \text{Points}^{(3)}\right)$

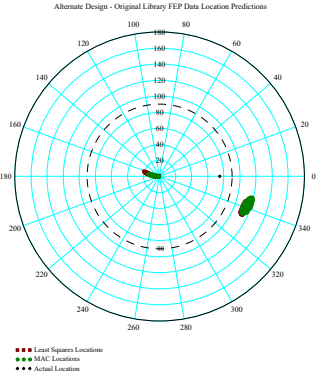

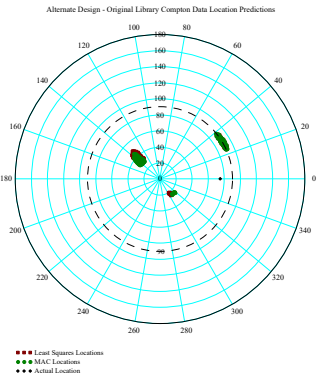

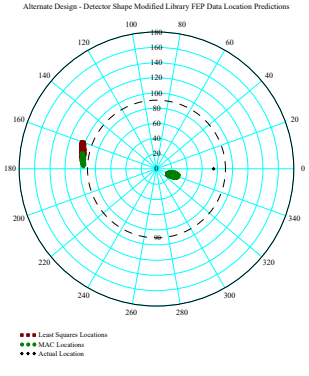

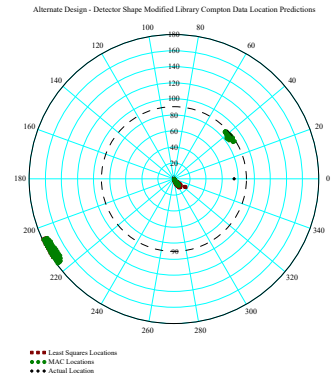

Cs-137 Source Data Results:

Phi_ViewDegree = 75
Theta_ViewDegree = 0

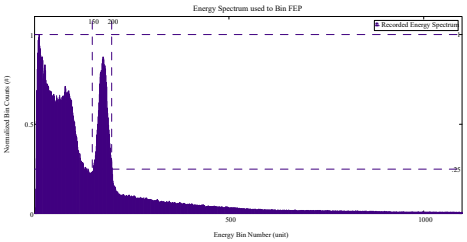

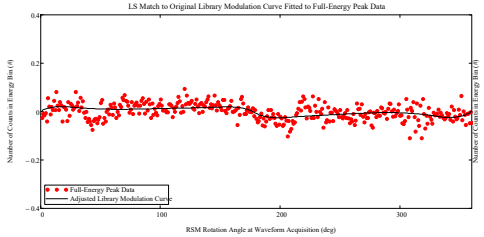

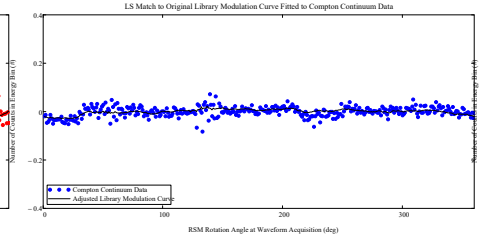

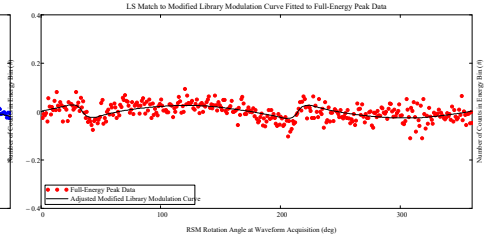

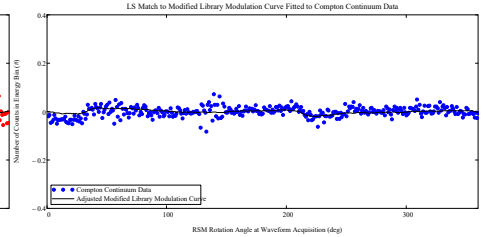

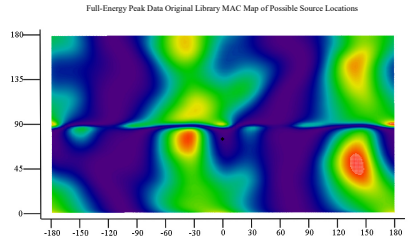

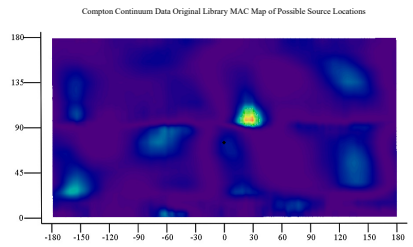

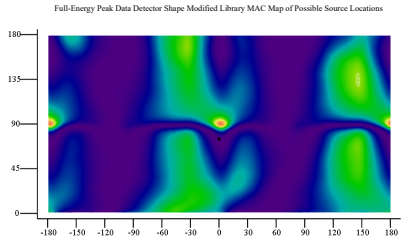

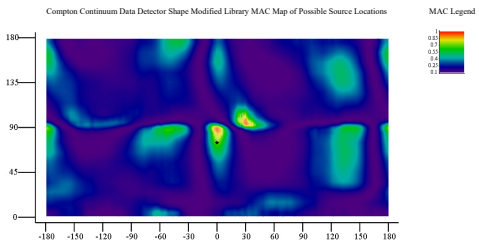

$(P1, P2, P3), \left(thepoint^{(1)}, thepoint^{(2)}, thepoint^{(3)}\right), \left(Points^{(1)}, Points^{(2)}, Points^{(3)}\right)$

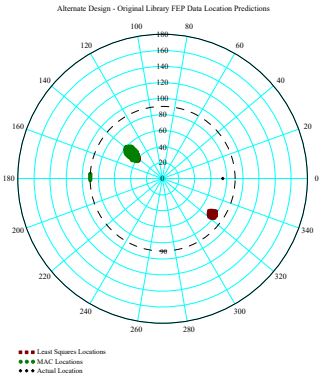

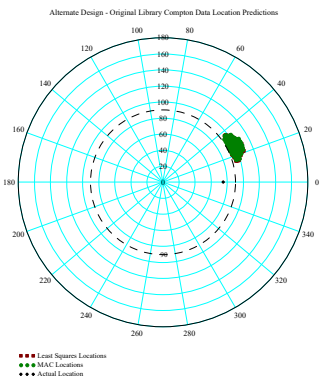

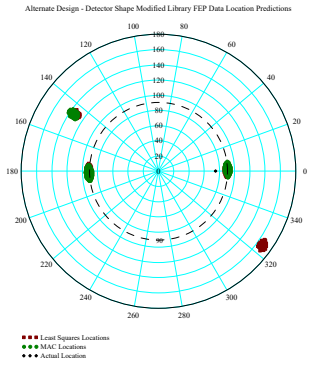

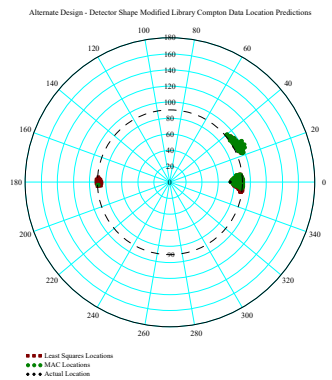

View Angle φ = 85° : Small RSM Alternate Design Ba-133and Cs-137 Data Spectra for Original and Detector Shape Modified Libraries, Modulation Curves, Library Curves, MAC and LS Direction Predictions

Ba-133 Source Data Results: Phi_ViewDegree = 85 Theta_ViewDegree = 0

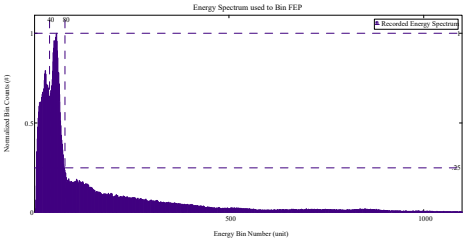

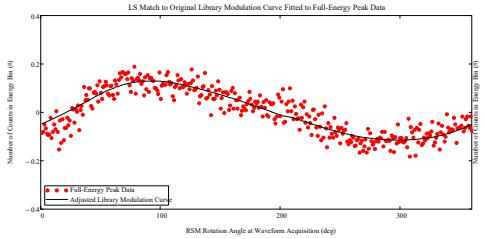

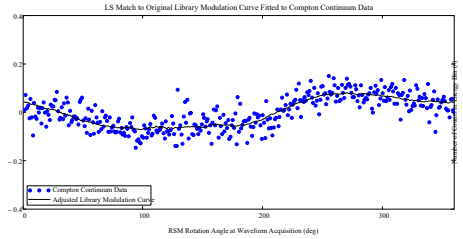

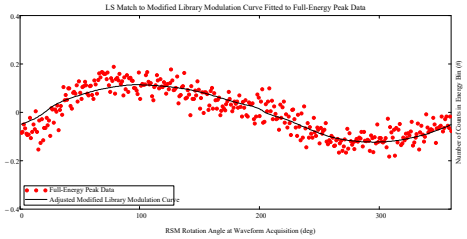

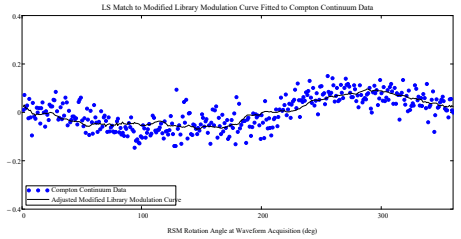

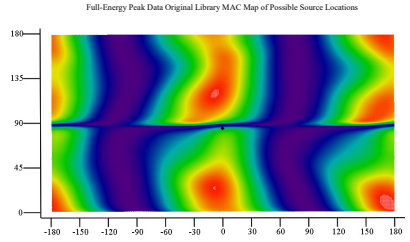

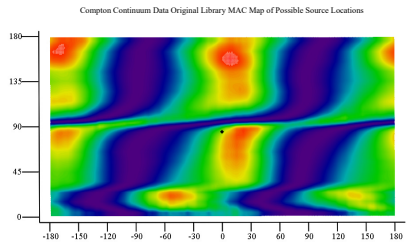

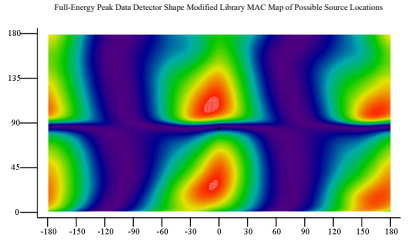

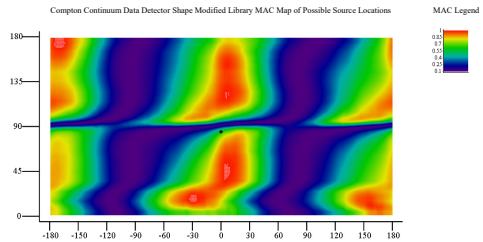

$(P1, P2, P3), \left(\text{thepoint}^{(1)}, \text{thepoint}^{(2)}, \text{thepoint}^{(3)}\right), \left(\text{Points}^{(1)}, \text{Points}^{(2)}, \text{Points}^{(3)}\right)$

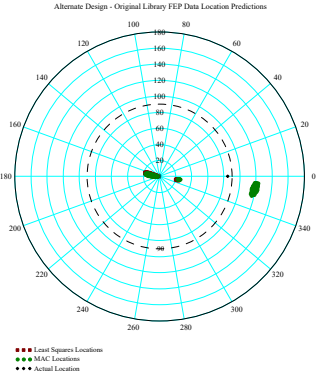

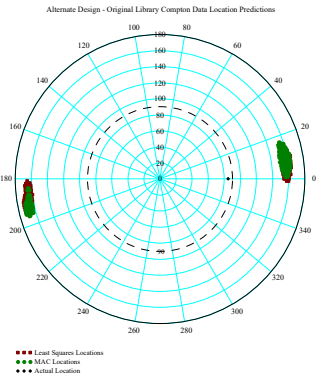

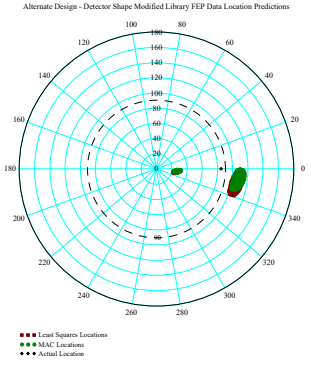

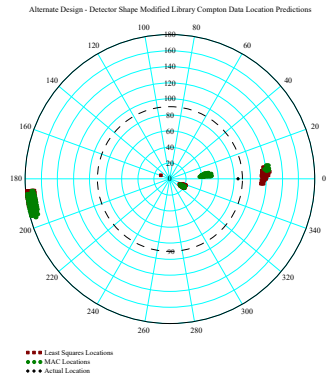

Cs-137 Source Data Results:

Phi_ViewDegree = 85
Theta_ViewDegree = 0

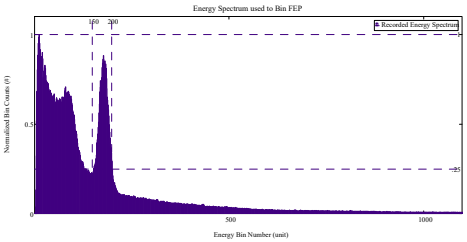

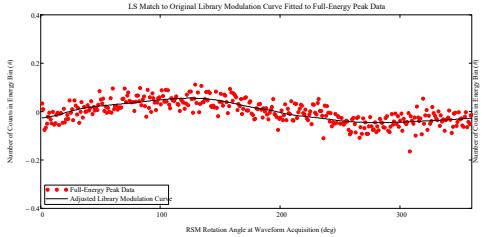

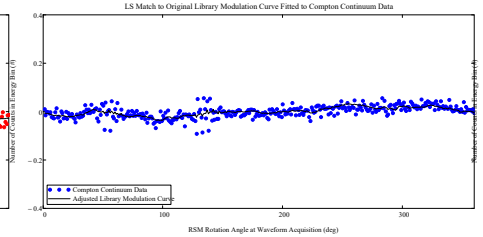

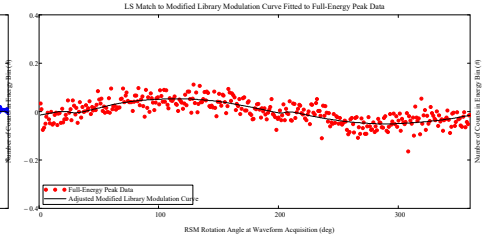

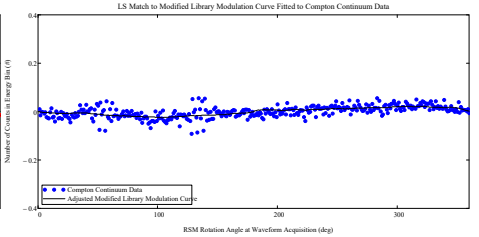

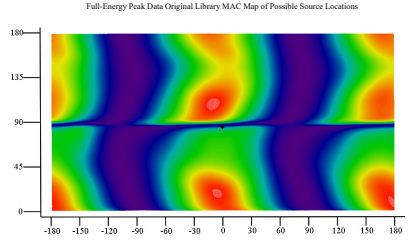

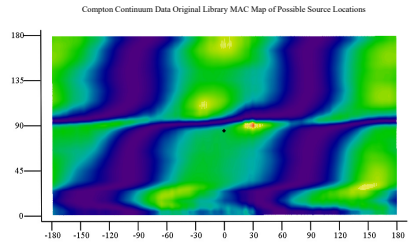

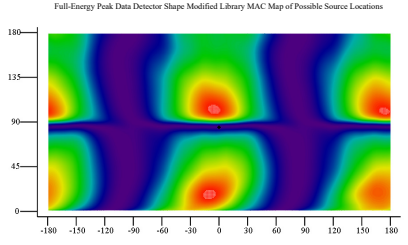

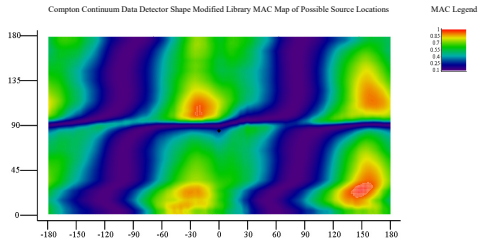

$(P1, P2, P3), \left(\text{thepoint}^{(1)}, \text{thepoint}^{(2)}, \text{thepoint}^{(3)}\right), \left(\text{Points}^{(1)}, \text{Points}^{(2)}, \text{Points}^{(3)}\right)$

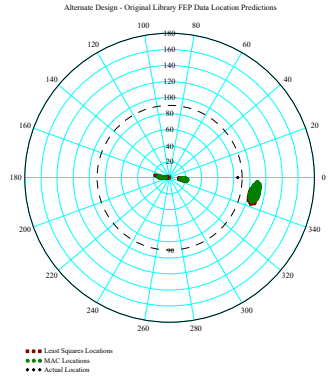

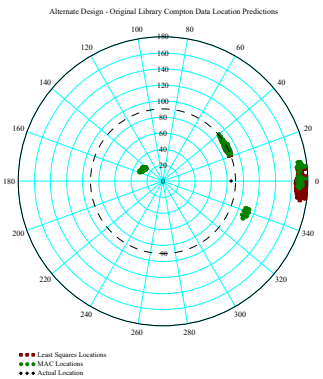

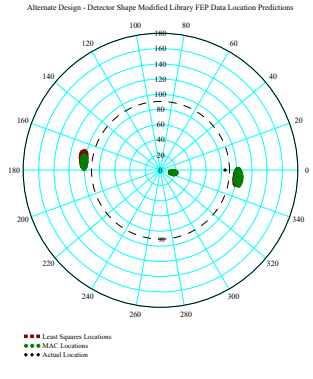

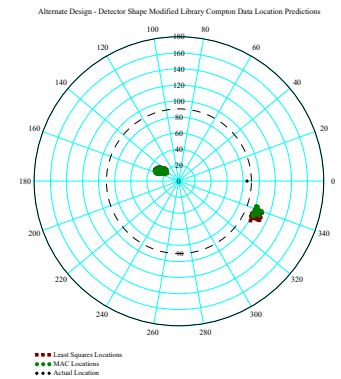

View Angle φ = 95° : Small RSM Alternate Design Ba-133and Cs-137 Data Spectra for Original and Detector Shape Modified Libraries, Modulation Curves, Library Curves, MAC and LS Direction Predictions

Ba-133 Source Data Results: Phi_ViewDegree = 95 Theta_ViewDegree = 0

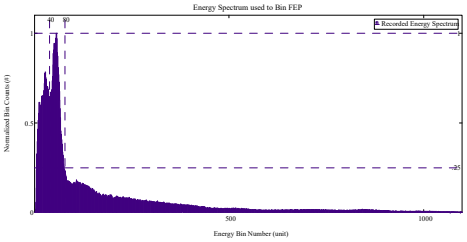

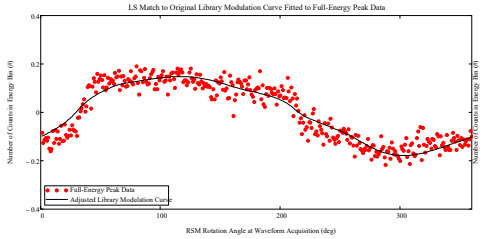

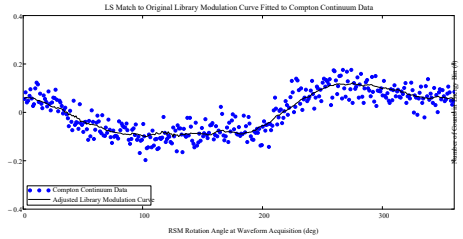

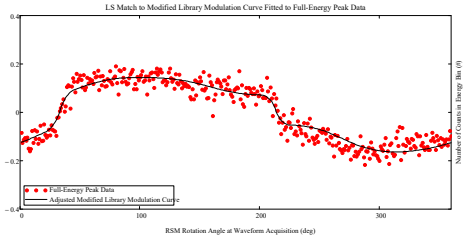

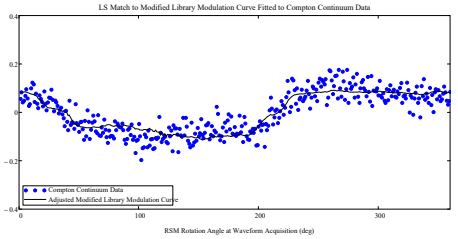

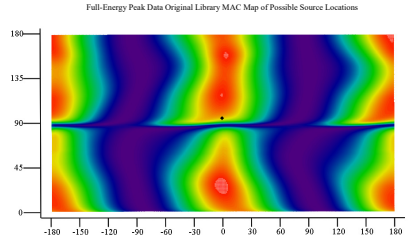

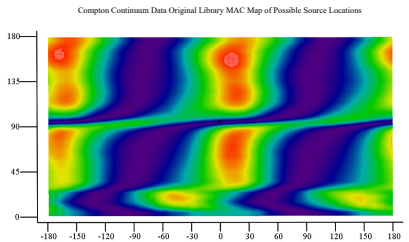

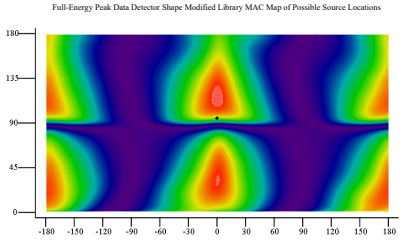

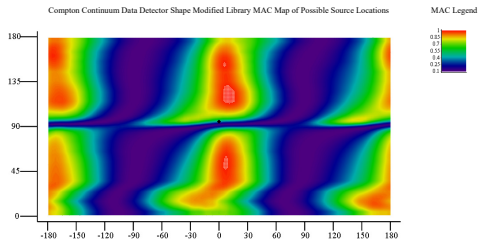

$(P1, P2, P3), \left(\text{thepoint}^{(1)}, \text{thepoint}^{(2)}, \text{thepoint}^{(3)}\right), \left(\text{Points}^{(1)}, \text{Points}^{(2)}, \text{Points}^{(3)}\right)$

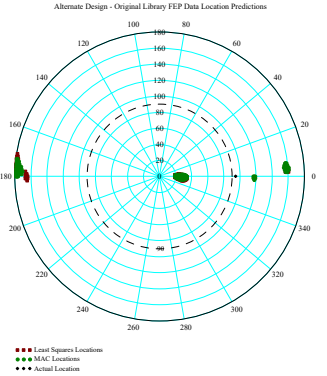

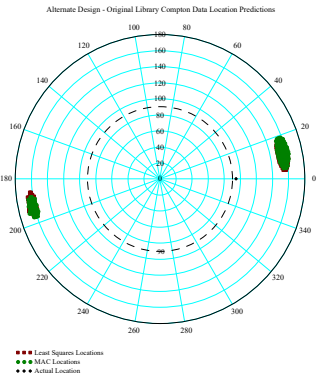

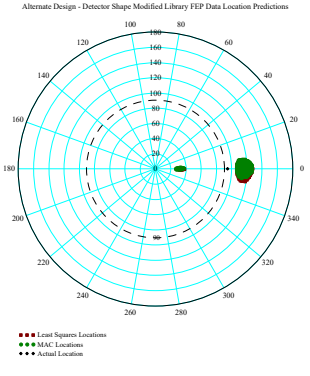

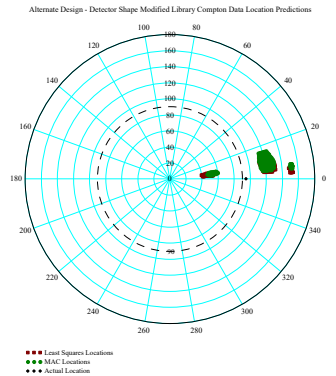

Cs-137 Source Data Results:

Phi_ViewDegree = 95
Theta_ViewDegree = 0

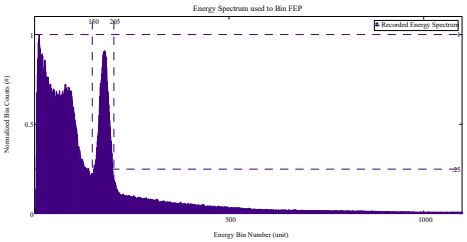

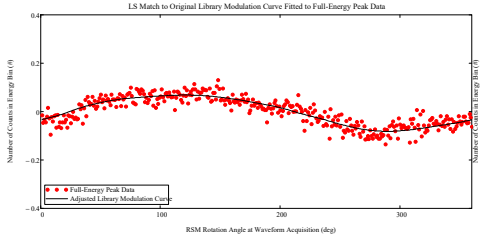

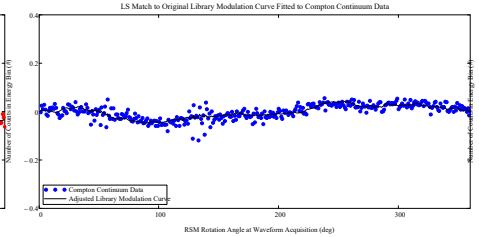

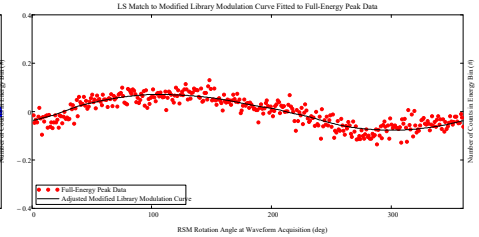

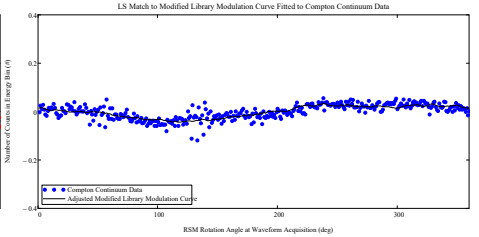

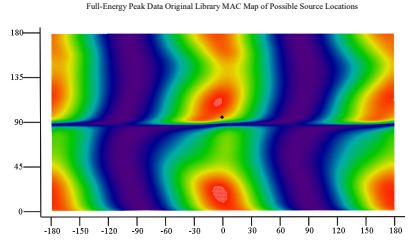

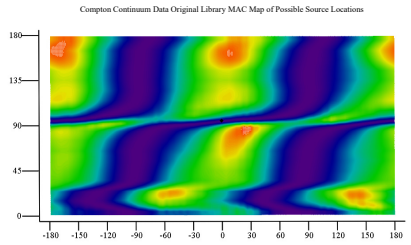

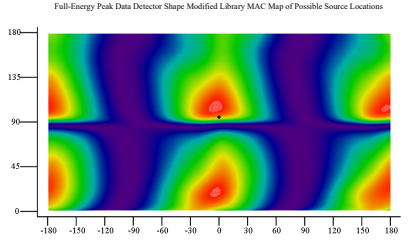

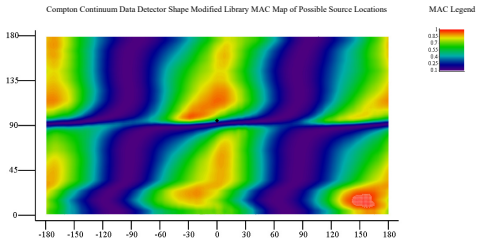

$(P1, P2, P3), \left(\text{thepoint}^{(1)}, \text{thepoint}^{(2)}, \text{thepoint}^{(3)}\right), \left(\text{Points}^{(1)}, \text{Points}^{(2)}, \text{Points}^{(3)}\right)$

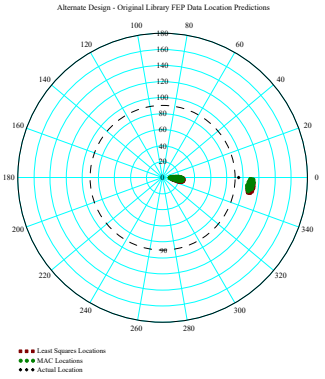

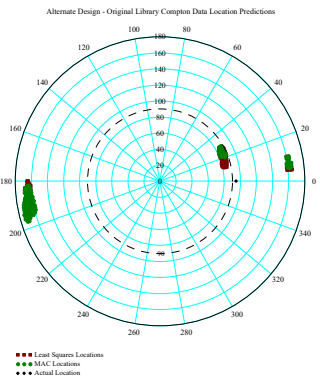

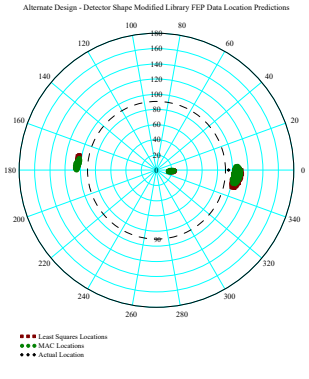

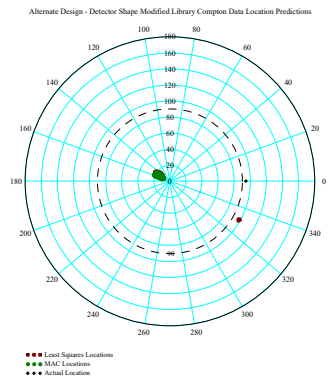

View Angle φ = 105° : Small RSM Alternate Design Ba-133and Cs-137 Data Spectra for Original and Detector Shape Modified Libraries, Modulation Curves, Library Curves, MAC and LS Direction Predictions

Ba-133 Source Data Results: Phi_ViewDegree = 105 Theta_ViewDegree = 0

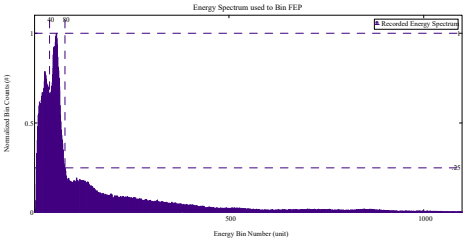

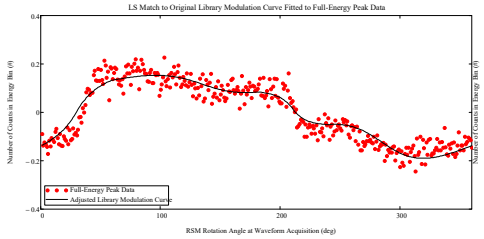

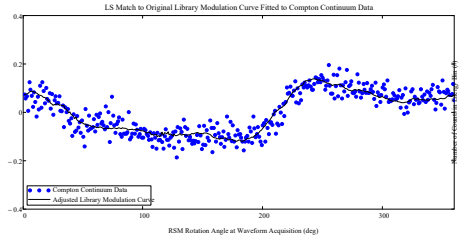

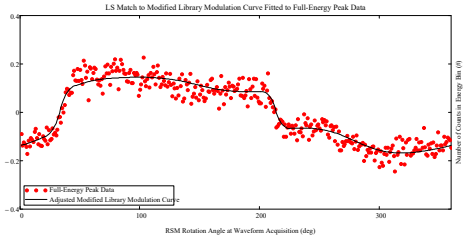

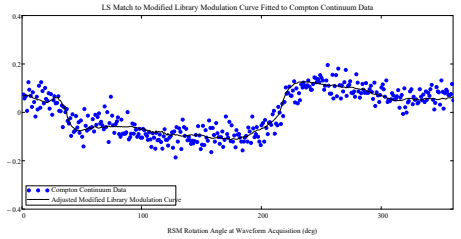

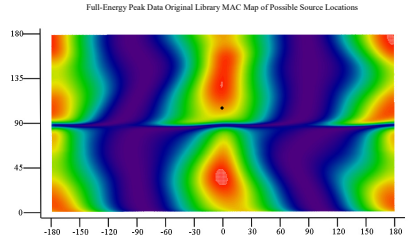

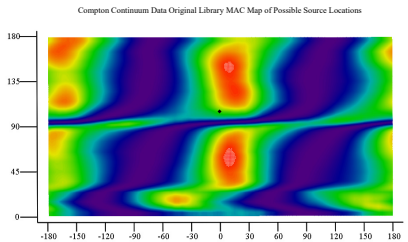

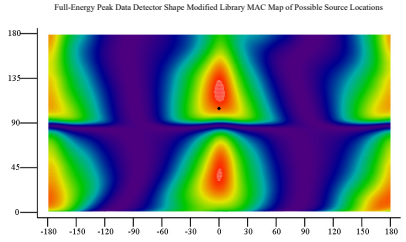

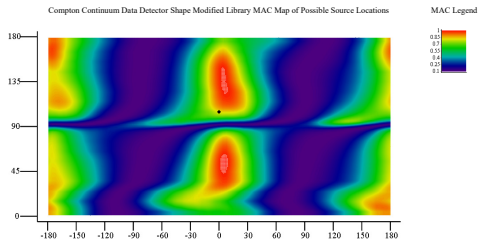

$(P1, P2, P3), \left(\text{thepoint}^{(1)}, \text{thepoint}^{(2)}, \text{thepoint}^{(3)}\right), \left(\text{Points}^{(1)}, \text{Points}^{(2)}, \text{Points}^{(3)}\right)$

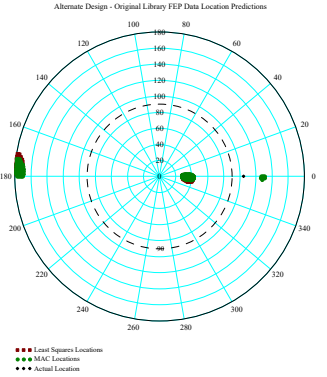

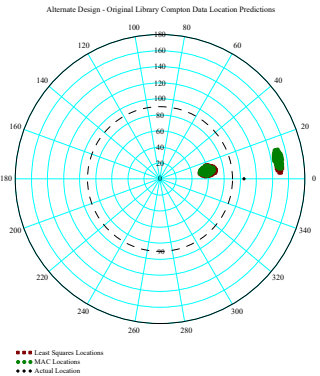

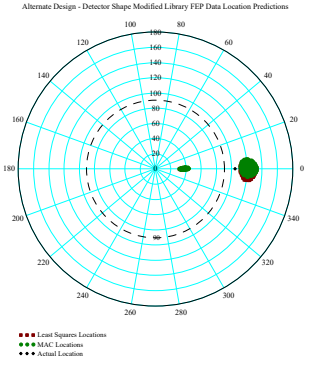

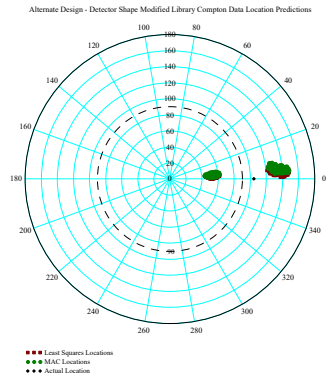

Cs-137 Source Data Results:

Phi_ViewDegree = 105
Theta_ViewDegree = 0

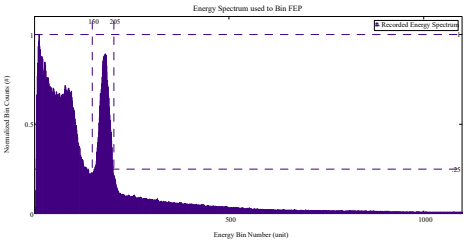

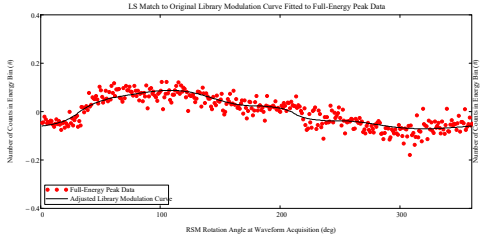

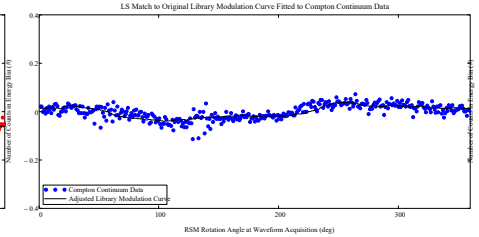

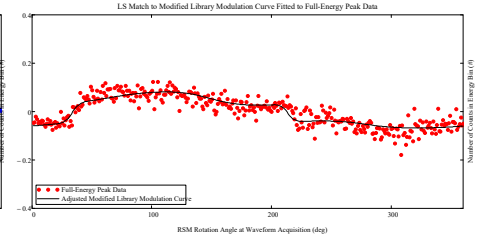

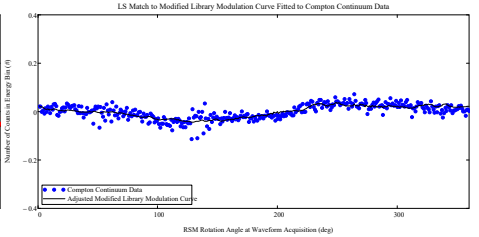

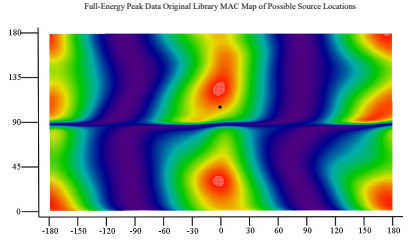

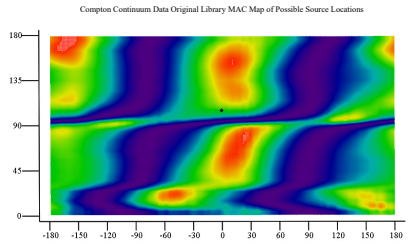

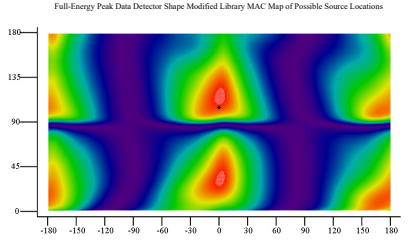

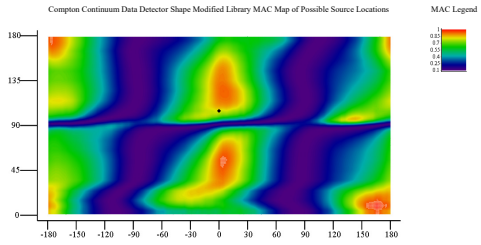

$(P1, P2, P3), \left(\text{thepoint}^{(1)}, \text{thepoint}^{(2)}, \text{thepoint}^{(3)}\right), \left(\text{Points}^{(1)}, \text{Points}^{(2)}, \text{Points}^{(3)}\right)$

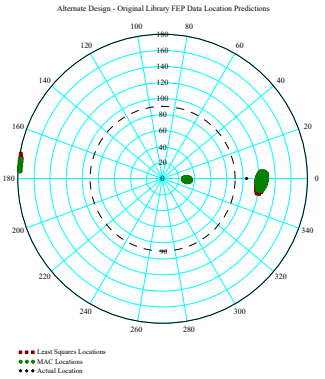

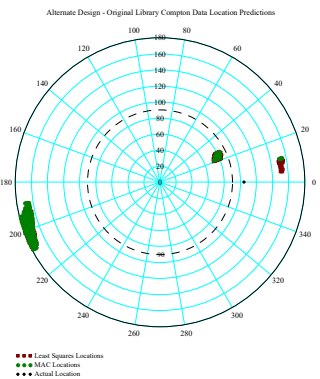

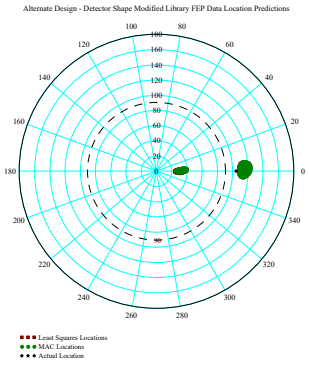

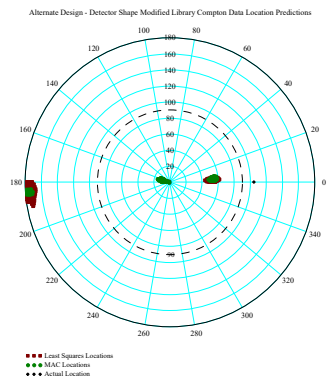

View Angle φ = 115° : Small RSM Alternate Design Ba-133and Cs-137 Data Spectra for Original and Detector Shape Modified Libraries, Modulation Curves, Library Curves, MAC and LS Direction Predictions

Ba-133 Source Data Results: Phi_ViewDegree = 115 Theta_ViewDegree = 0

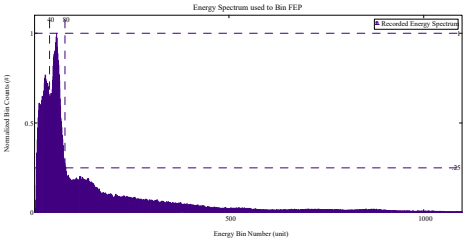

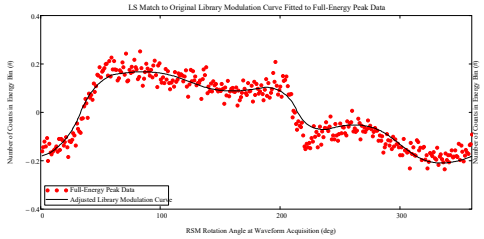

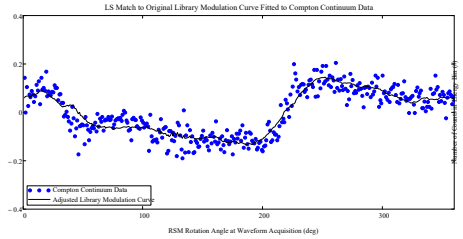

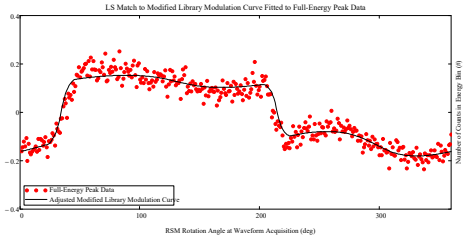

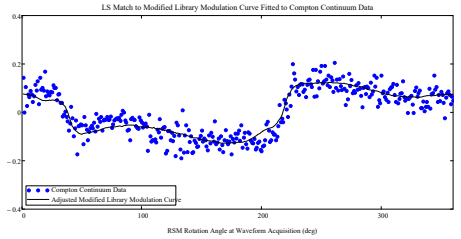

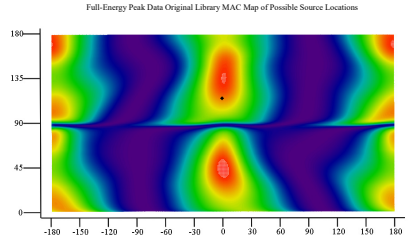

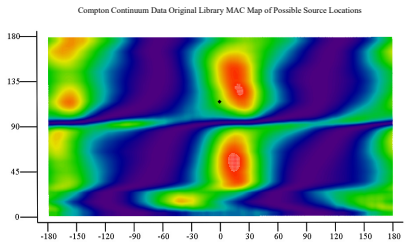

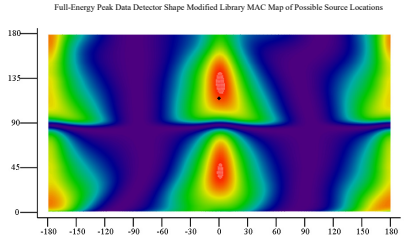

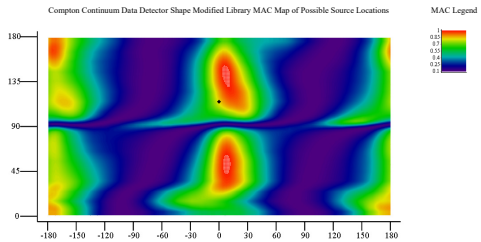

$(P1, P2, P3), \left(\text{thepoint}^{(1)}, \text{thepoint}^{(2)}, \text{thepoint}^{(3)}\right), \left(\text{Points}^{(1)}, \text{Points}^{(2)}, \text{Points}^{(3)}\right)$

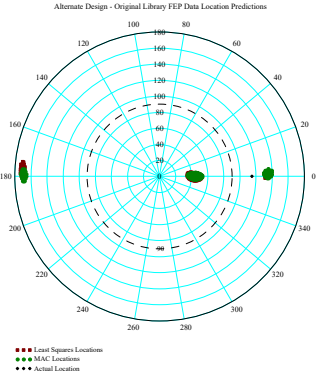

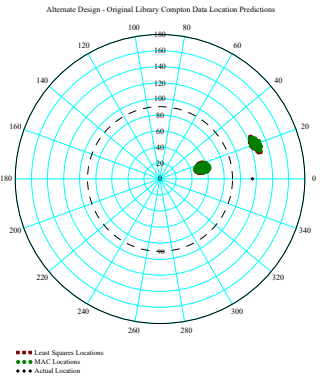

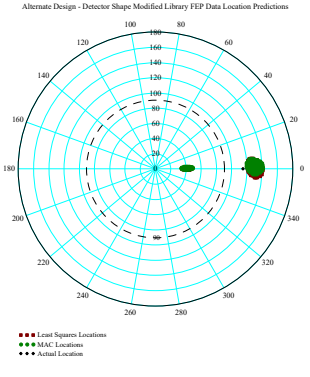

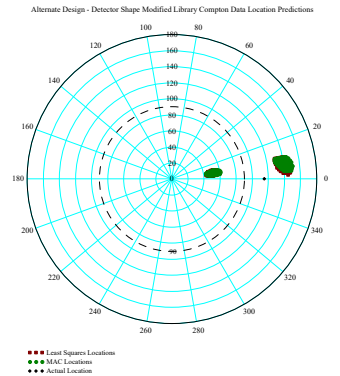

Cs-137 Source Data Results:

Phi_ViewDegree = 115
Theta_ViewDegree = 0

Energy Spectrum used to Bin FEP

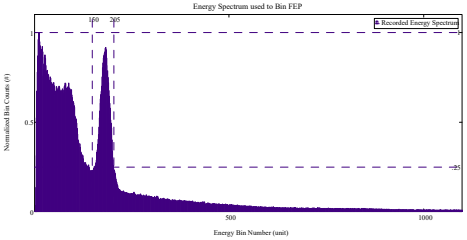

LS Match to Original Library Modulation Curve Fitted to Full-Energy Peak Data

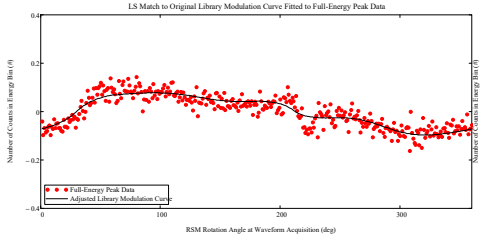

LS Match to Original Library Modulation Curve Fitted to Compton Continuum Data

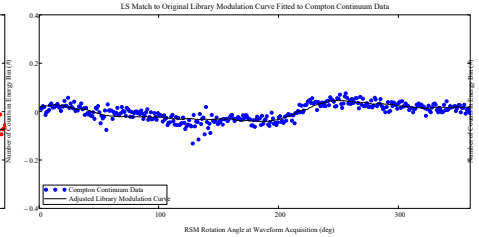

LS Match to Modified Library Modulation Curve Fitted to Full-Energy Peak Data

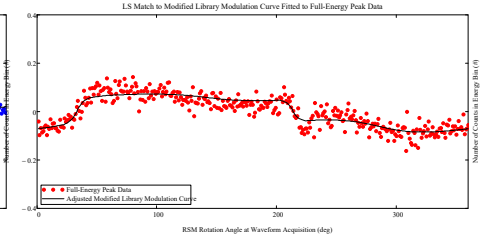

LS Match to Modified Library Modulation Curve Fitted to Compton Continuum Data

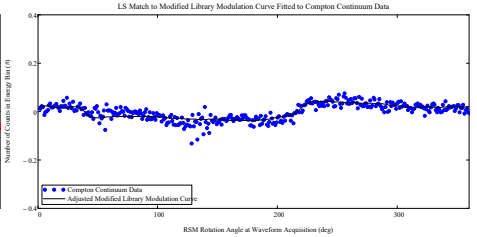

Full-Energy Peak Data Original Library MAC Map of Possible Source Locations

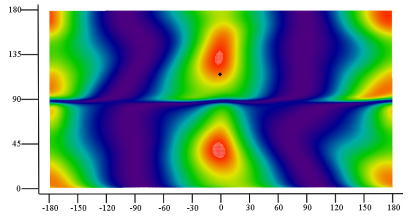

Compton Continuum Data Original Library MAC Map of Possible Source Locations

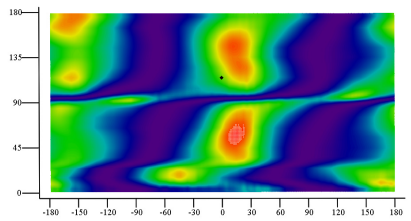

Full-Energy Peak Data Detector Shape Modified Library MAC Map of Possible Source Locations

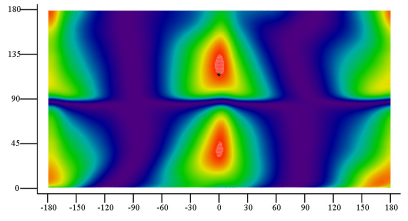

Compton Continuum Data Detector Shape Modified Library MAC Map of Possible Source Locations

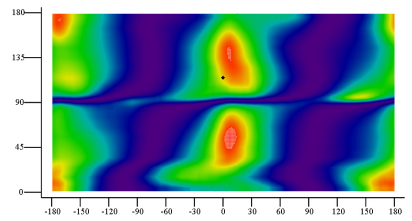

MAC Legend

$(P1, P2, P3), \left(thepoint^{(1)}, thepoint^{(2)}, thepoint^{(3)}\right), \left(Points^{(1)}, Points^{(2)}, Points^{(3)}\right)$

Alternate Design - Original Library FEP Data Location Predictions

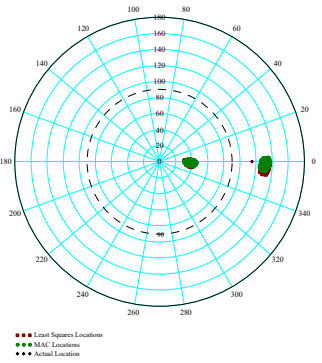

Alternate Design - Original Library Compton Data Location Predictions

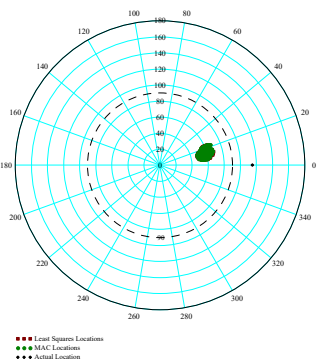

Alternate Design - Detector Shape Modified Library FEP Data Location Predictions

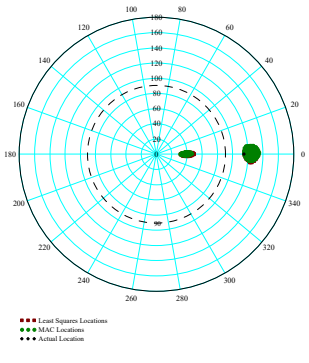

Alternate Design - Detector Shape Modified Library Compton Data Location Predictions

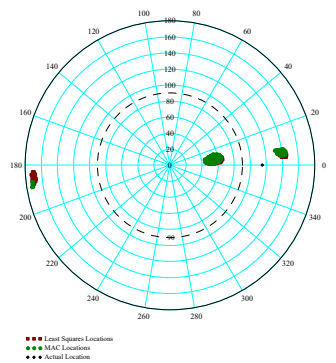

View Angle φ = 125° : Small RSM Alternate Design Ba-133and Cs-137 Data Spectra for Original and Detector Shape Modified Libraries, Modulation Curves, Library Curves, MAC and LS Direction Predictions

Ba-133 Source Data Results: Phi_ViewDegree = 125 Theta_ViewDegree = 0

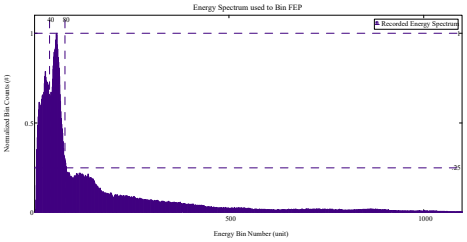

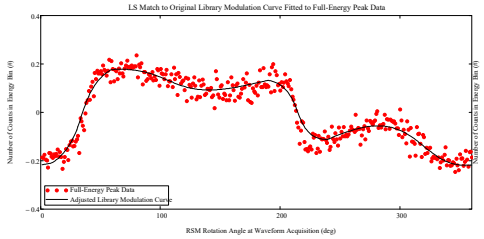

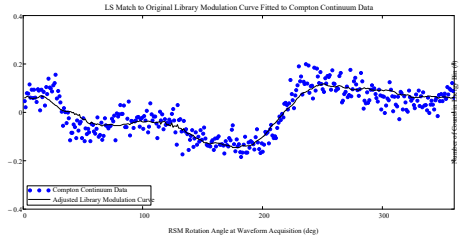

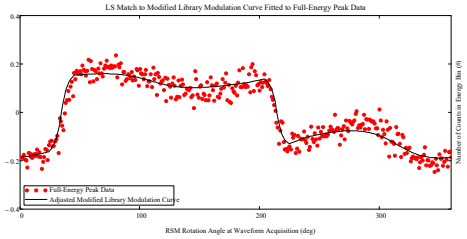

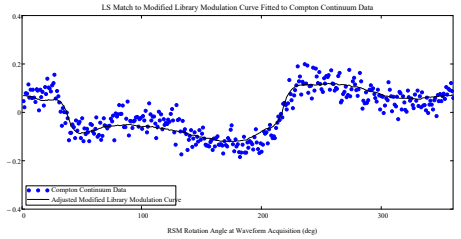

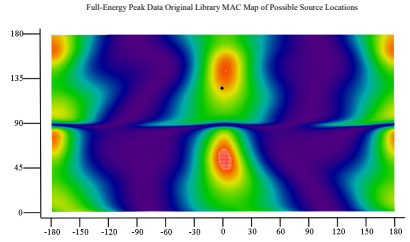

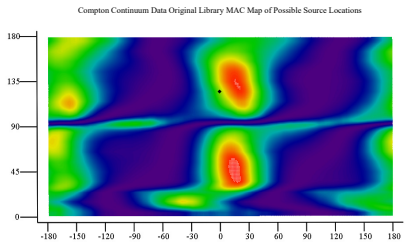

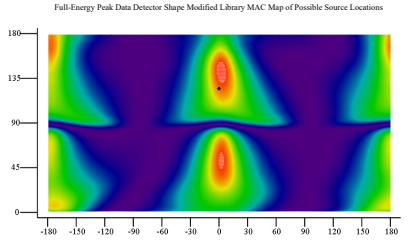

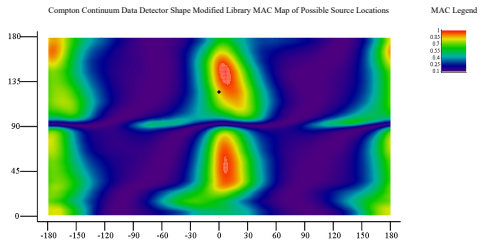

$(P1, P2, P3), \left(\text{thepoint}^{(1)}, \text{thepoint}^{(2)}, \text{thepoint}^{(3)}\right), \left(\text{Points}^{(1)}, \text{Points}^{(2)}, \text{Points}^{(3)}\right)$

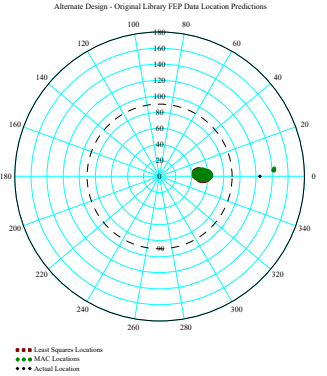

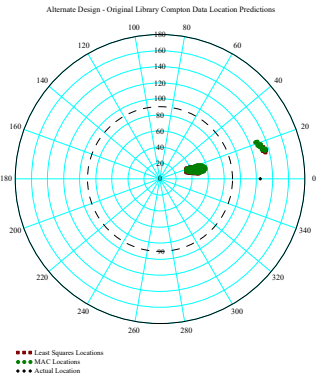

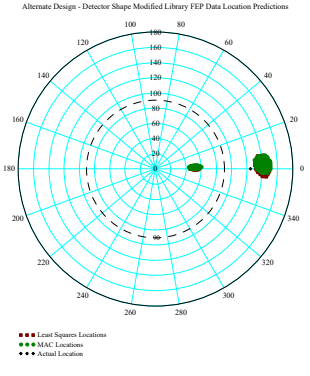

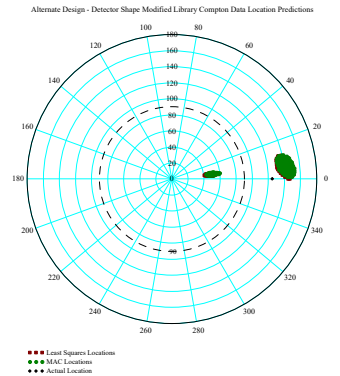

Cs-137 Source Data Results:

Phi_ViewDegree = 125
Theta_ViewDegree = 0

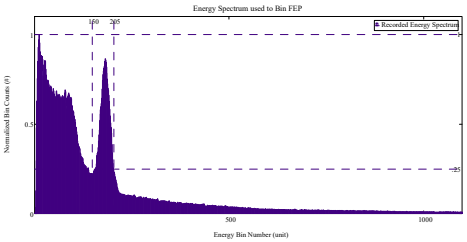

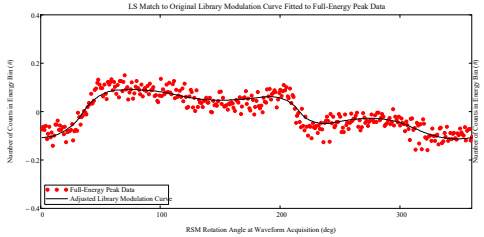

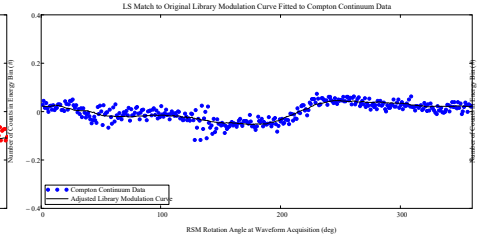

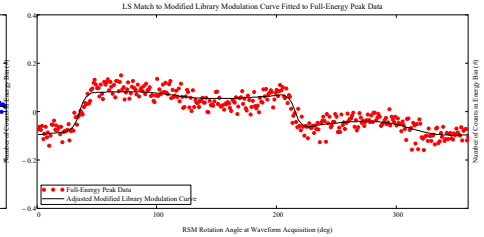

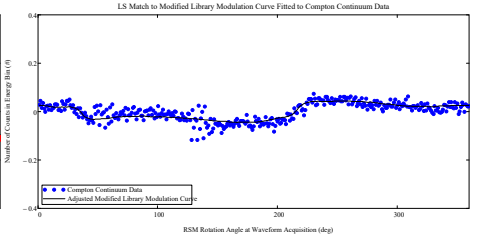

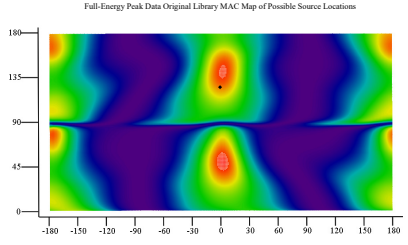

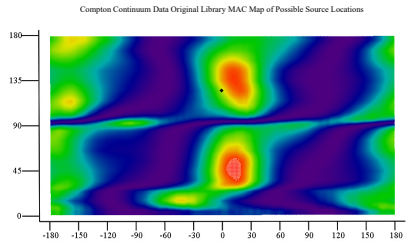

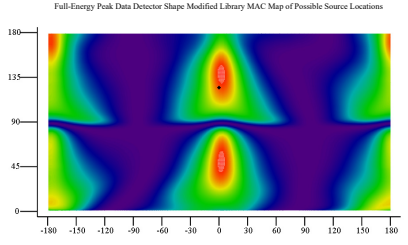

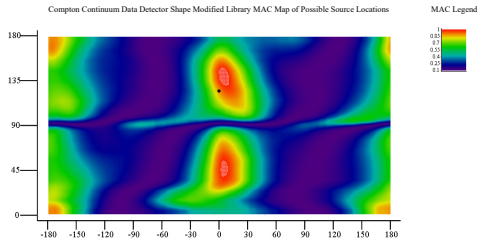

$(P1, P2, P3), \left(\text{thepoint}^{(1)}, \text{thepoint}^{(2)}, \text{thepoint}^{(3)}\right), \left(\text{Points}^{(1)}, \text{Points}^{(2)}, \text{Points}^{(3)}\right)$

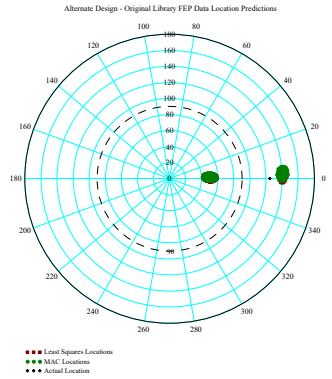

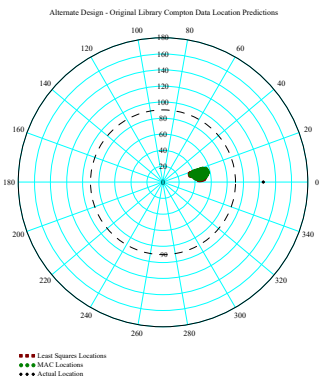

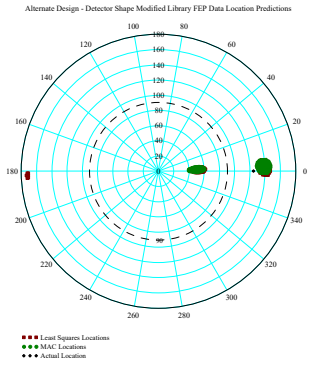

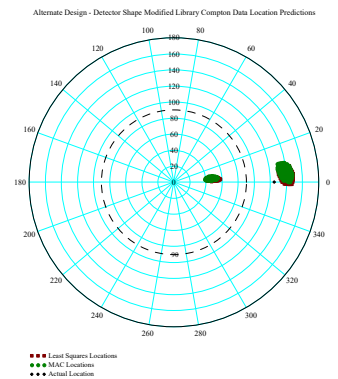

View Angle φ = 135° : Small RSM Alternate Design Ba-133and Cs-137 Data Spectra for Original and Detector Shape Modified Libraries, Modulation Curves, Library Curves, MAC and LS Direction Predictions

Ba-133 Source Data Results: Phi_ViewDegree = 135 Theta_ViewDegree = 0

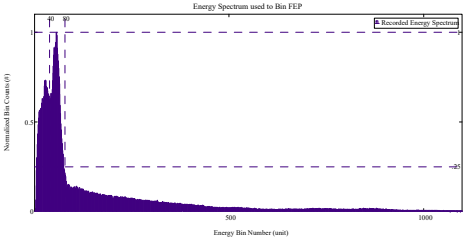

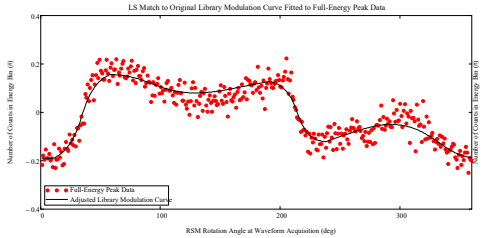

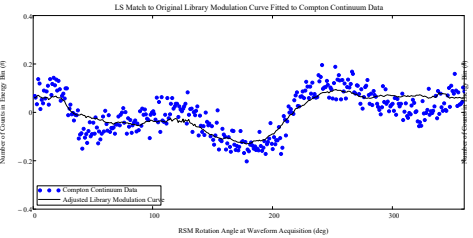

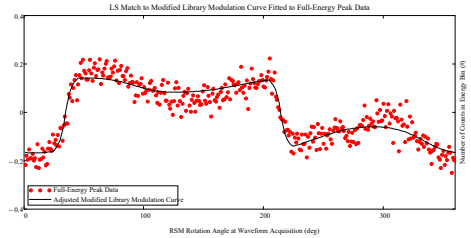

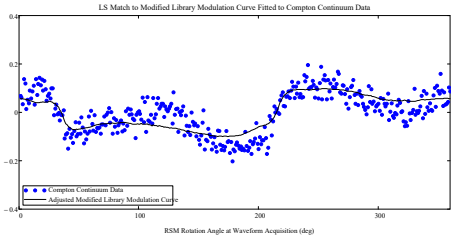

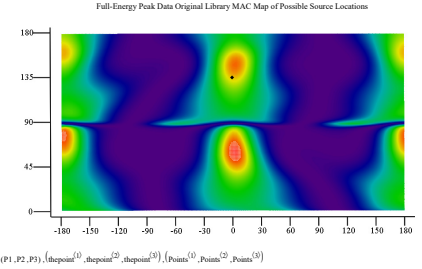

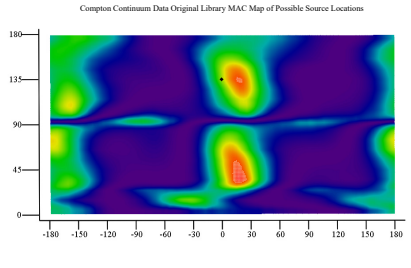

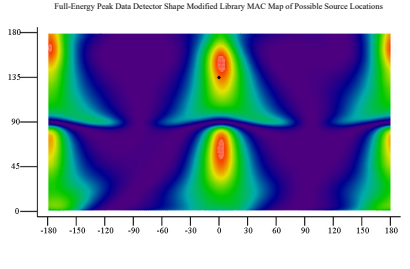

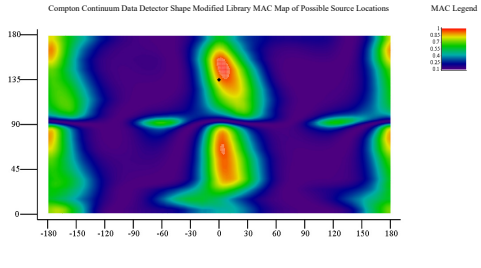

$(P1, P2, P3), \left(thepoint^{(1)}, thepoint^{(2)}, thepoint^{(3)}\right), \left(Points^{(1)}, Points^{(2)}, Points^{(3)}\right)$

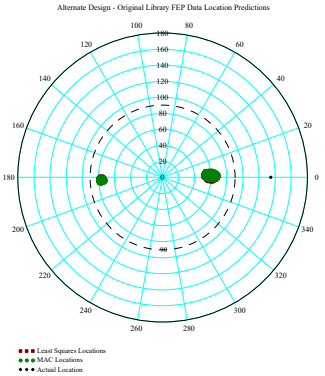

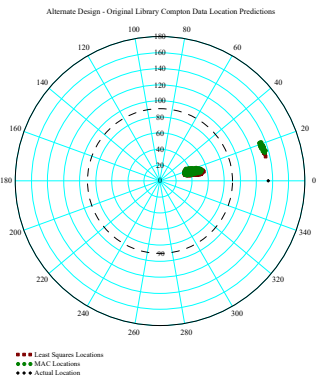

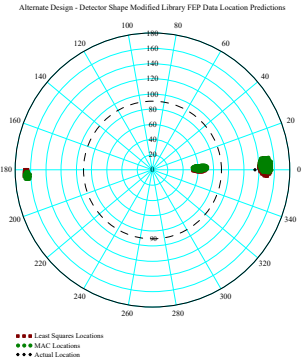

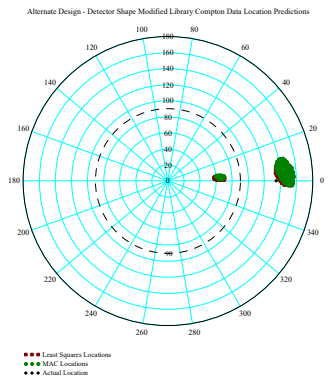

Cs-137 Source Data Results:

Phi_ViewDegree = 135
Theta_ViewDegree = 0

Energy Spectrum used to Bin FEP

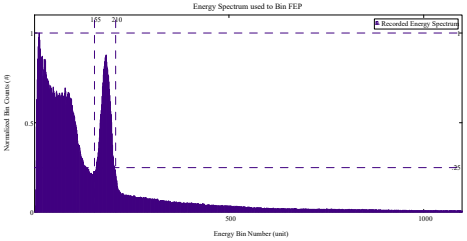

LS Match to Original Library Modulation Curve Fitted to Full-Energy Peak Data

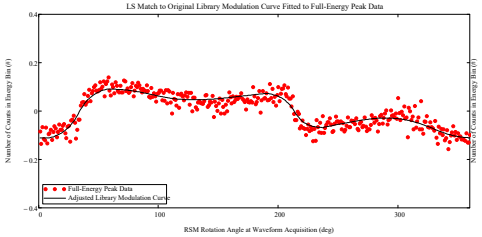

LS Match to Original Library Modulation Curve Fitted to Compton Continuum Data

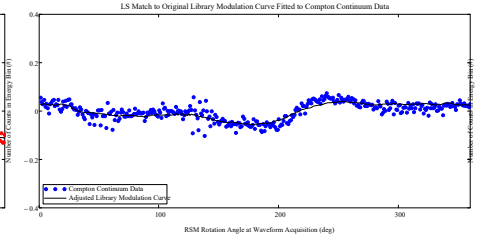

LS Match to Modified Library Modulation Curve Fitted to Full-Energy Peak Data

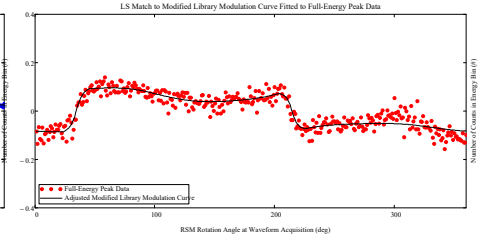

LS Match to Modified Library Modulation Curve Fitted to Compton Continuum Data

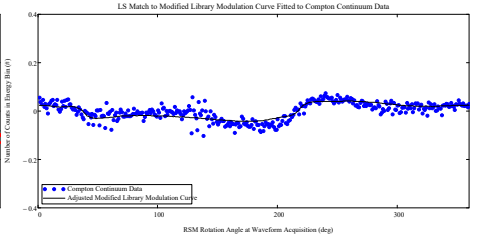

Full-Energy Peak Data Original Library MAC Map of Possible Source Locations

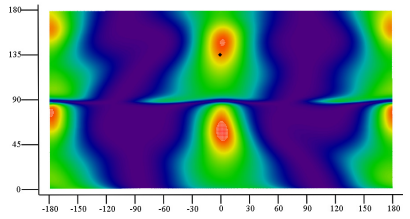

Compton Continuum Data Original Library MAC Map of Possible Source Locations

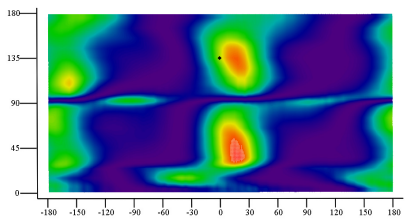

Full-Energy Peak Data Detector Shape Modified Library MAC Map of Possible Source Locations

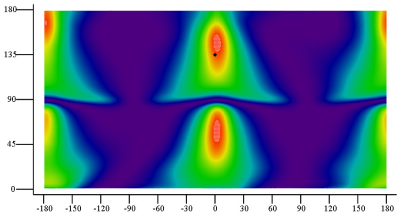

Compton Continuum Data Detector Shape Modified Library MAC Map of Possible Source Locations

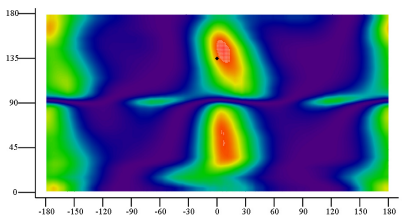

MAC Legend

$(P1, P2, P3), \left(\text{thepoint}^{(1)}, \text{thepoint}^{(2)}, \text{thepoint}^{(3)}\right), \left(\text{Points}^{(1)}, \text{Points}^{(2)}, \text{Points}^{(3)}\right)$

Alternate Design - Original Library FEP Data Location Predictions

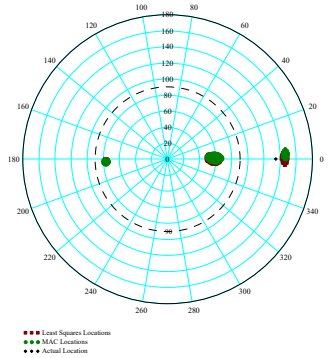

Alternate Design - Original Library Compton Data Location Predictions

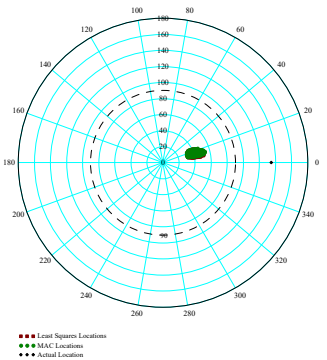

Alternate Design - Detector Shape Modified Library FEP Data Location Predictions

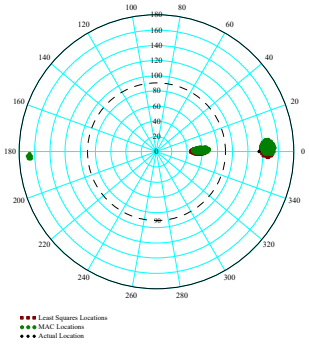

Alternate Design - Detector Shape Modified Library Compton Data Location Predictions

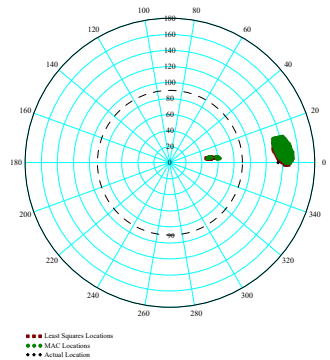

View Angle φ = 145° : Small RSM Alternate Design Ba-133and Cs-137 Data Spectra for Original and Detector Shape Modified Libraries, Modulation Curves, Library Curves, MAC and LS Direction Predictions

Ba-133 Source Data Results: Phi_ViewDegree = 145 Theta_ViewDegree = 0

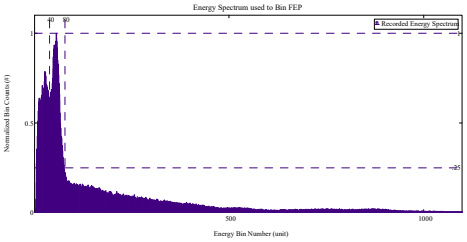

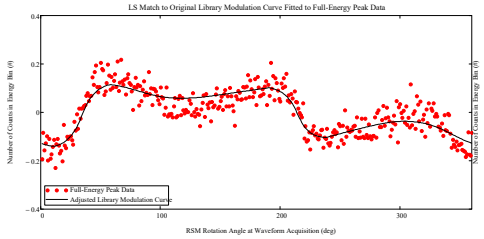

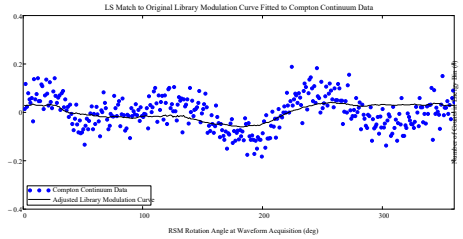

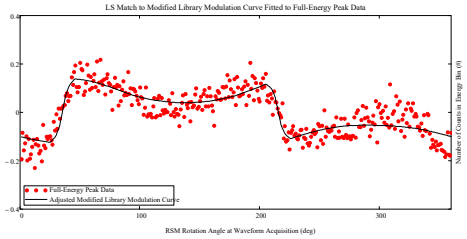

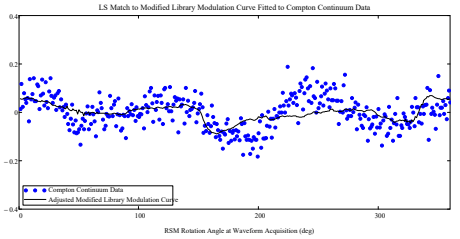

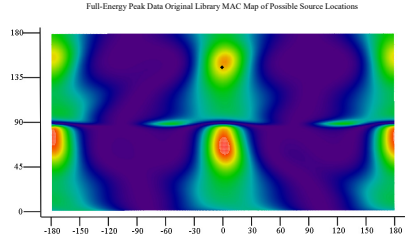

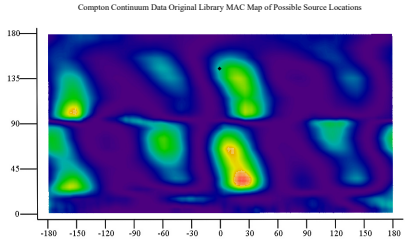

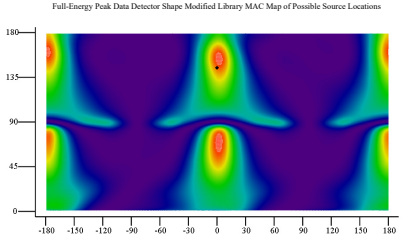

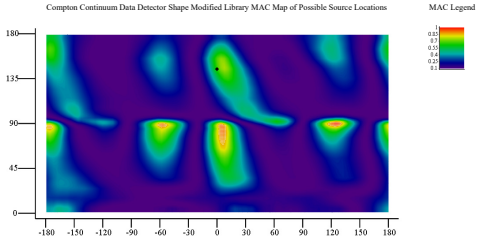

$(P1, P2, P3), \left(\text{thepoint}^{(1)}, \text{thepoint}^{(2)}, \text{thepoint}^{(3)}\right), \left(\text{Points}^{(1)}, \text{Points}^{(2)}, \text{Points}^{(3)}\right)$

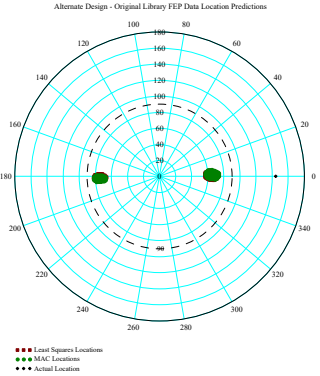

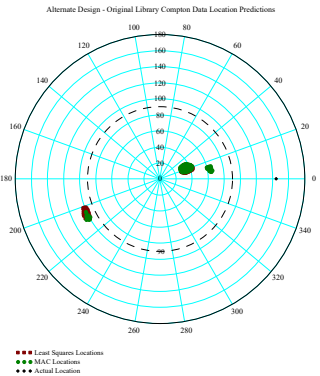

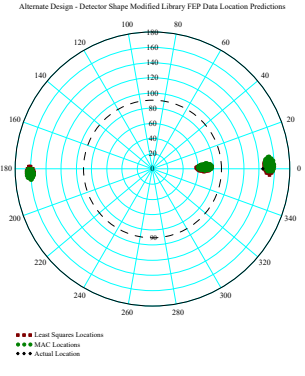

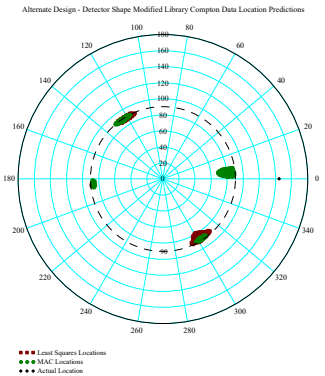

Cs-137 Source Data Results:

Phi_ViewDegree = 145
Theta_ViewDegree = 0

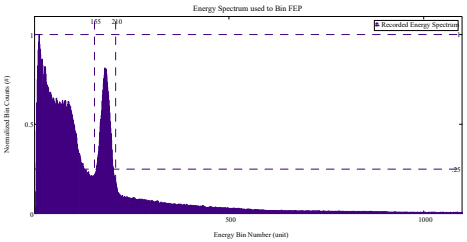

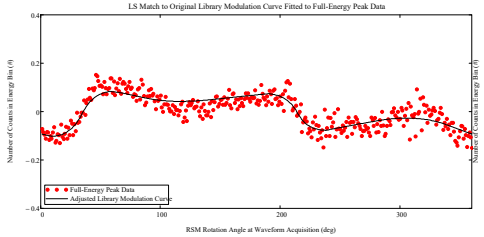

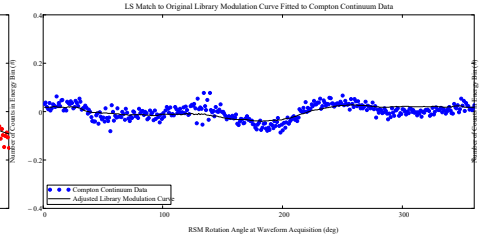

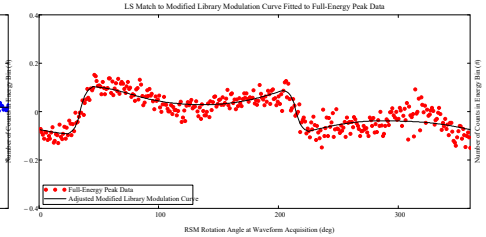

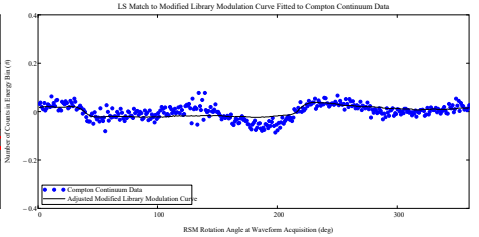

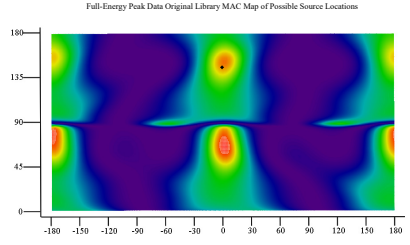

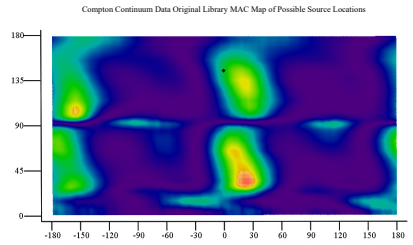

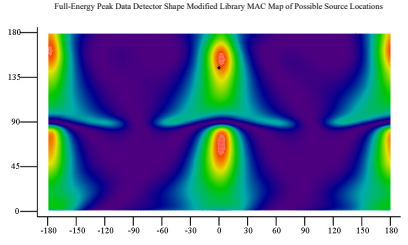

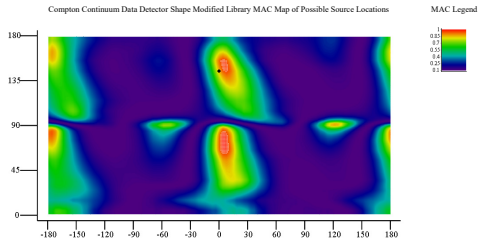

$(P1, P2, P3), \left(\text{thepoint}^{(1)}, \text{thepoint}^{(2)}, \text{thepoint}^{(3)}\right), \left(\text{Points}^{(1)}, \text{Points}^{(2)}, \text{Points}^{(3)}\right)$

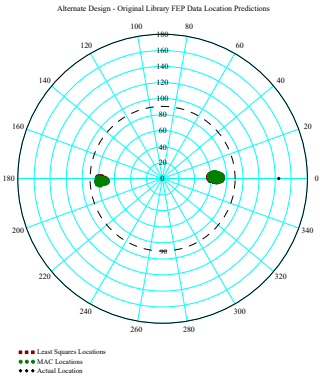

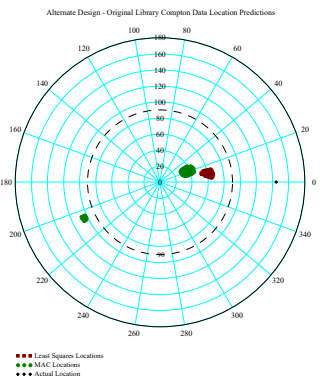

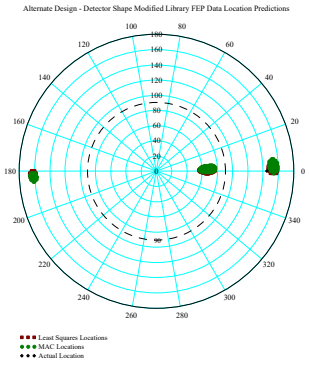

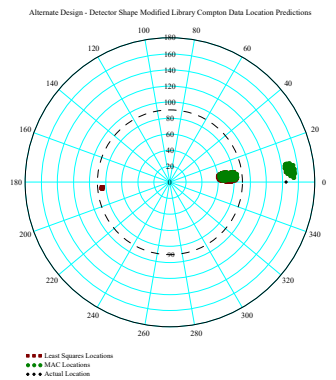

View Angle φ = 155° : Small RSM Alternate Design Ba-133and Cs-137 Data Spectra for Original and Detector Shape Modified Libraries, Modulation Curves, Library Curves, MAC and LS Direction Predictions

Ba-133 Source Data Results: Phi_ViewDegree = 155
Theta_ViewDegree = 0

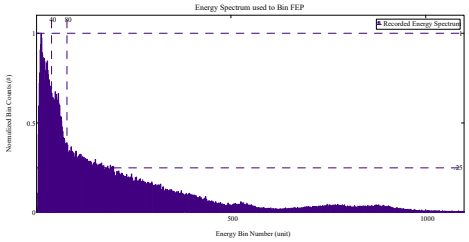

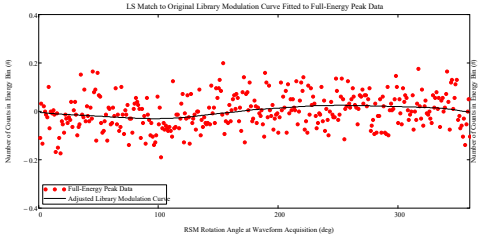

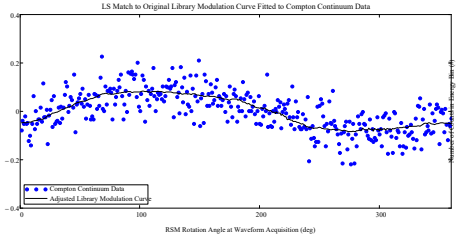

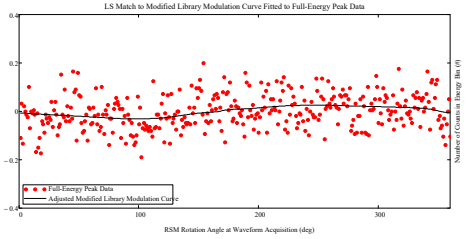

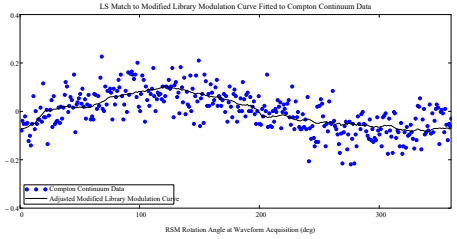

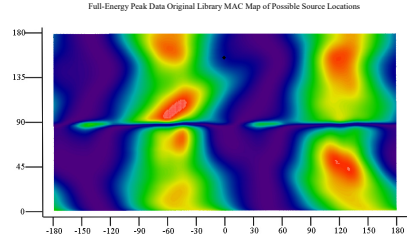

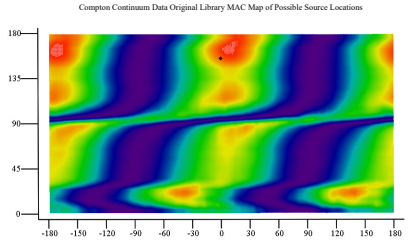

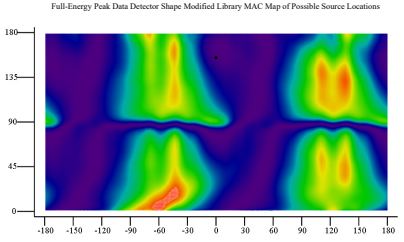

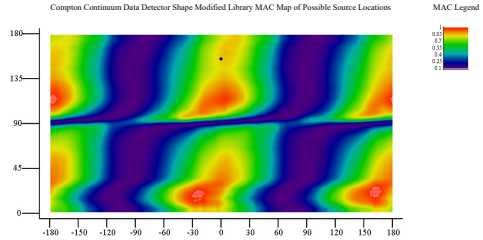

$(P1, P2, P3), \{thepoint^{(1)}, thepoint^{(2)}, thepoint^{(3)}\}, \{Points^{(1)}, Points^{(2)}, Points^{(3)}\}$

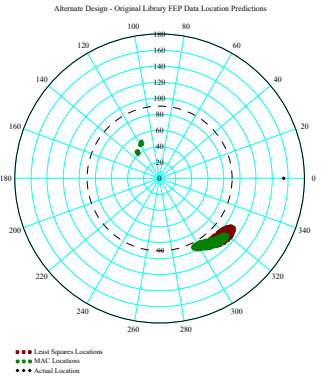

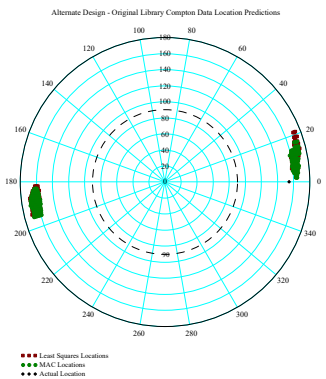

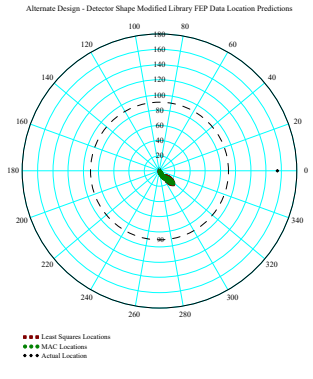

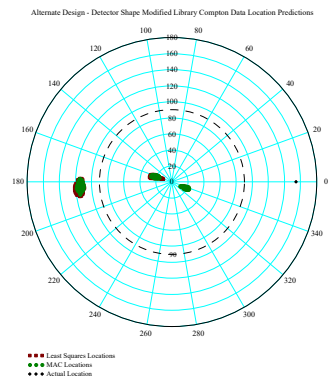

Cs-137 Source Data Results:

Phi_ViewDegree = 155
Theta_ViewDegree = 0

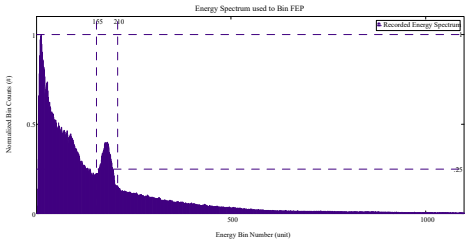

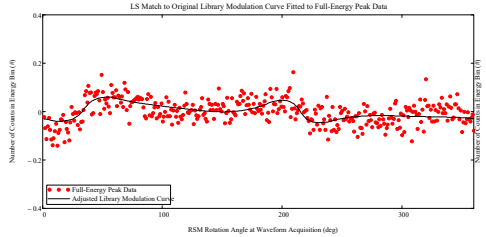

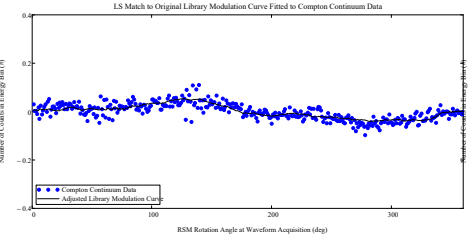

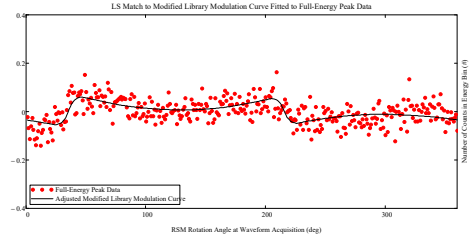

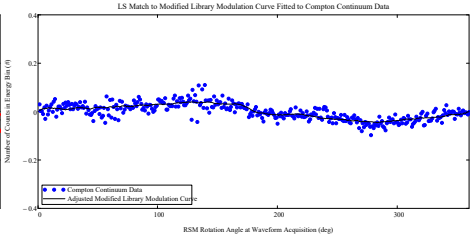

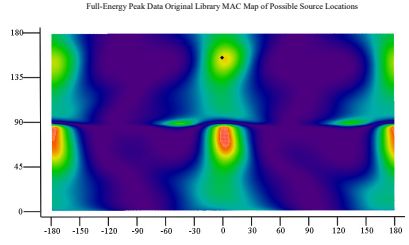

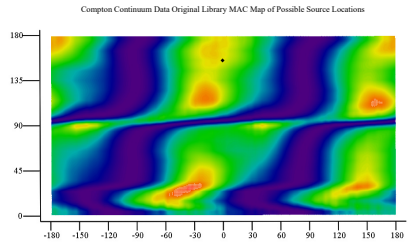

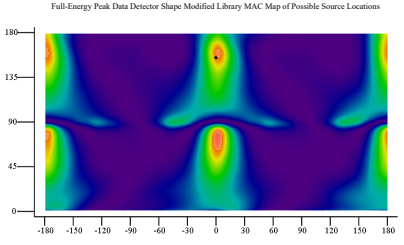

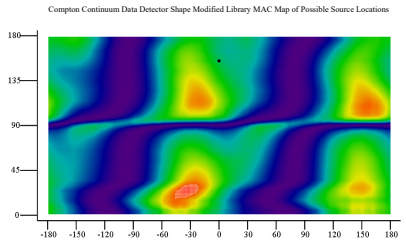

$(P1, P2, P3), (\text{thepoint}^{(1)}, \text{thepoint}^{(2)}, \text{thepoint}^{(3)}), (\text{Points}^{(1)}, \text{Points}^{(2)}, \text{Points}^{(3)})$

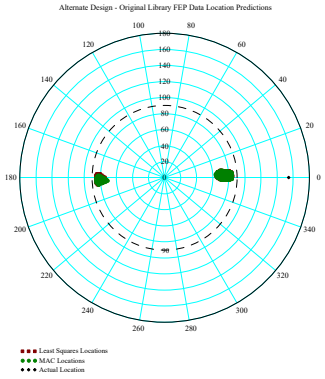

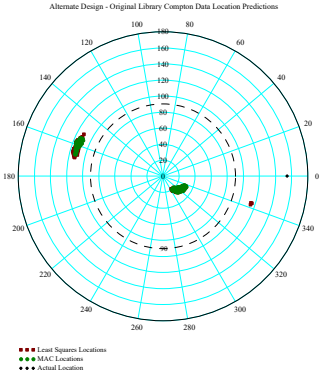

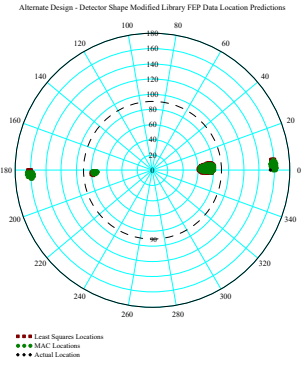

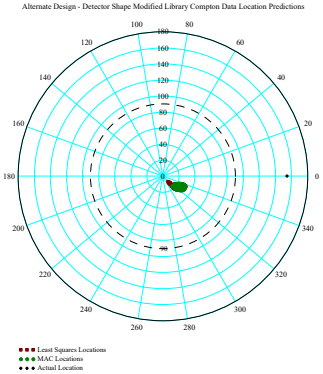

View Angle φ = 165° : Small RSM Alternate Design Ba-133and Cs-137 Data Spectra for Original and Detector Shape Modified Libraries, Modulation Curves, Library Curves, MAC and LS Direction Predictions

Ba-133 Source Data Results: Phi_ViewDegree = 165 Theta_ViewDegree = 0

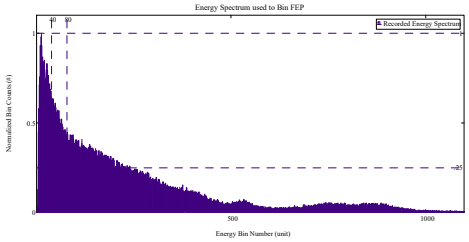

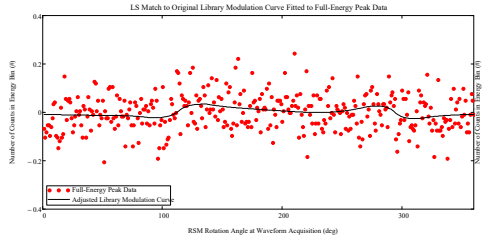

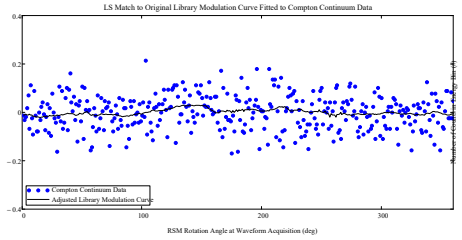

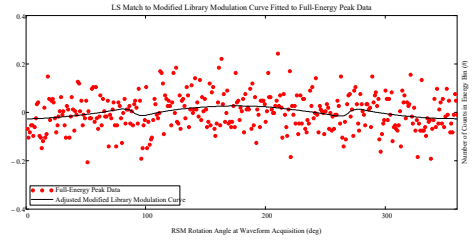

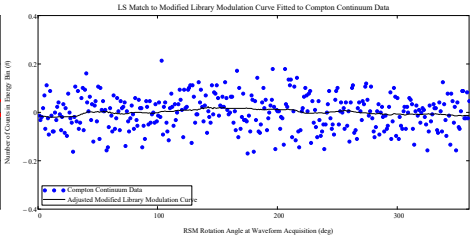

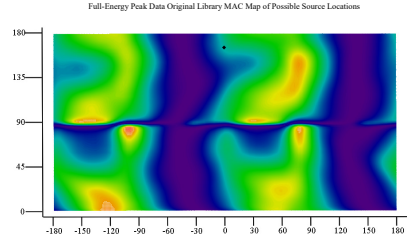

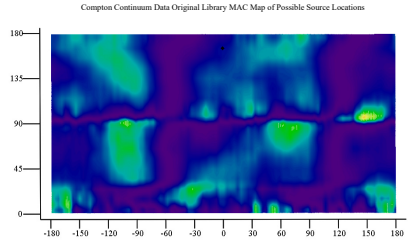

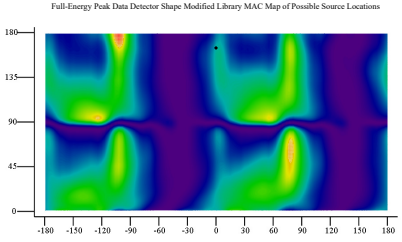

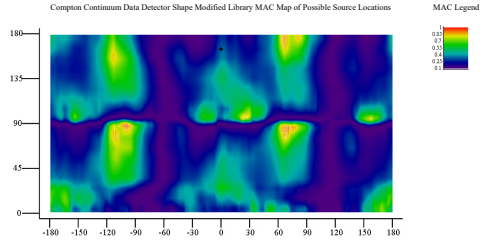

$(P1, P2, P3), \{thepoint^{(1)}, thepoint^{(2)}, thepoint^{(3)}\}, \{Points^{(1)}, Points^{(2)}, Points^{(3)}\}$

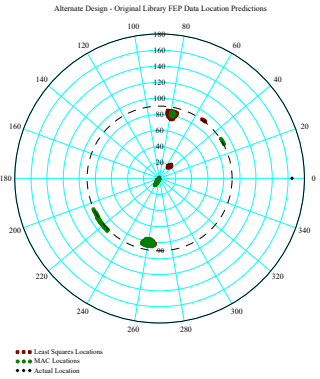

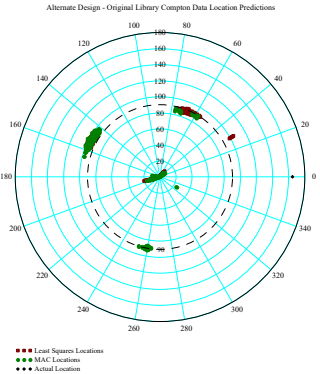

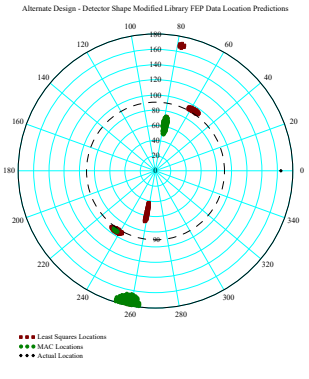

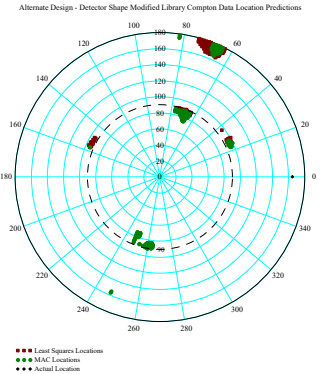

Cs-137 Source Data Results:

Phi_ViewDegree = 165
Theta_ViewDegree = 0

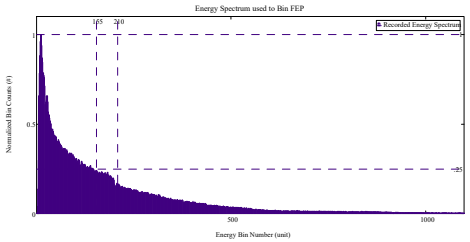

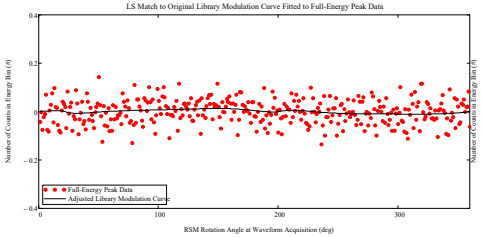

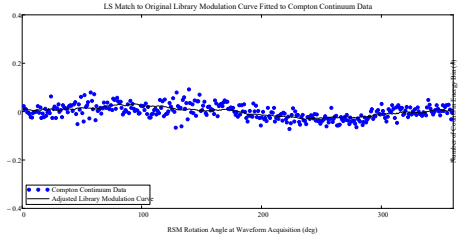

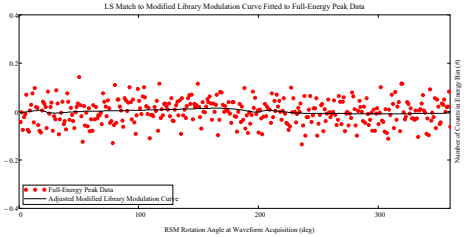

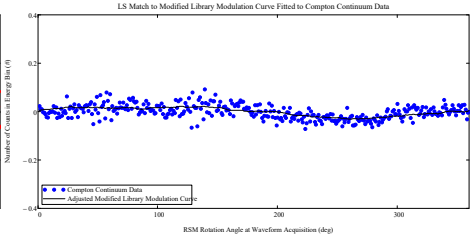

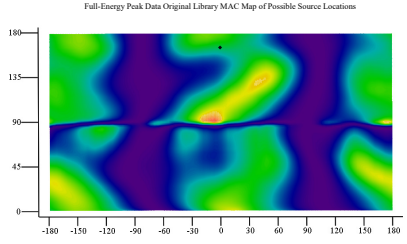

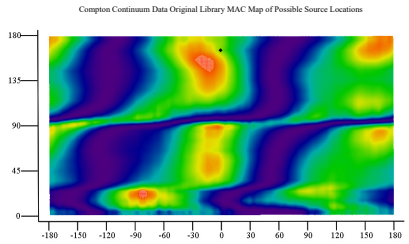

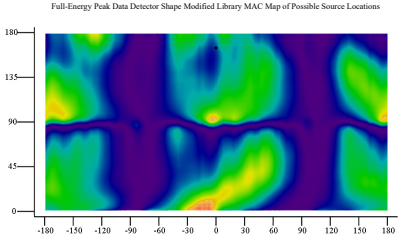

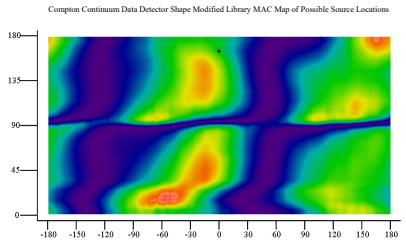

$(P1, P2, P3)$, $\langle \text{thepoint}^{\langle 1 \rangle}, \text{thepoint}^{\langle 2 \rangle}, \text{thepoint}^{\langle 3 \rangle} \rangle$, $\langle \text{Points}^{\langle 1 \rangle}, \text{Points}^{\langle 2 \rangle}, \text{Points}^{\langle 3 \rangle} \rangle$

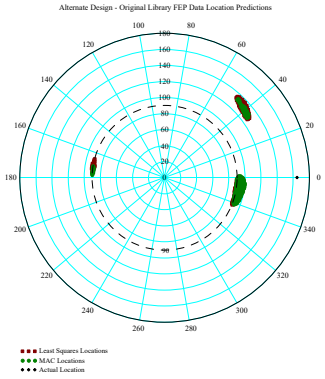

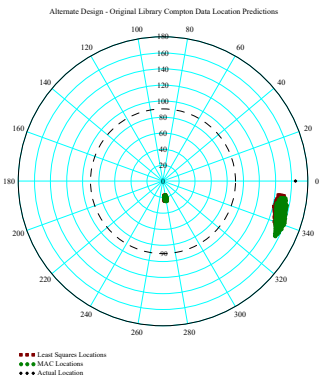

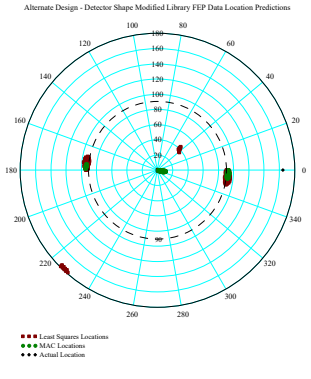

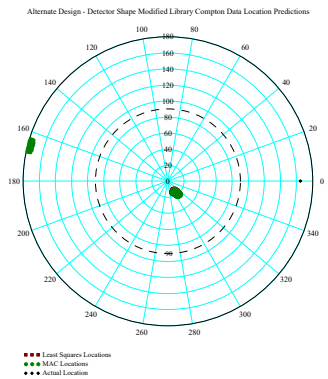

View Angle φ = 175° : Small RSM Alternate Design Ba-133and Cs-137 Data Spectra for Original and Detector Shape Modified Libraries, Modulation Curves, Library Curves, MAC and LS Direction Predictions

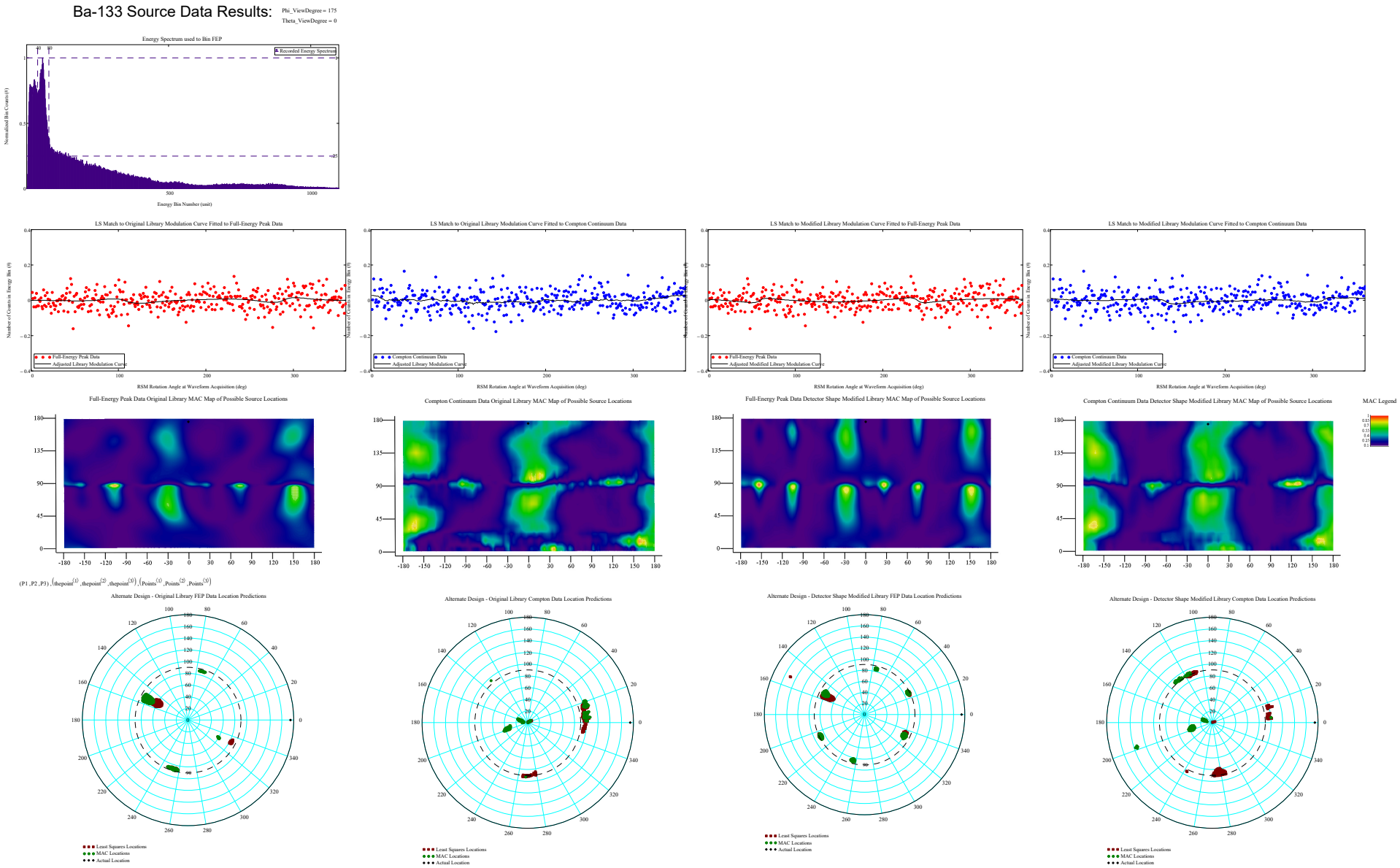

Cs-137 Source Data Results:

Phi_ViewDegree = 175
Theta_ViewDegree = 0

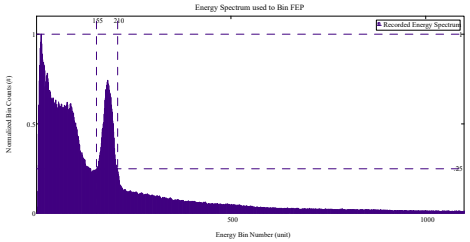

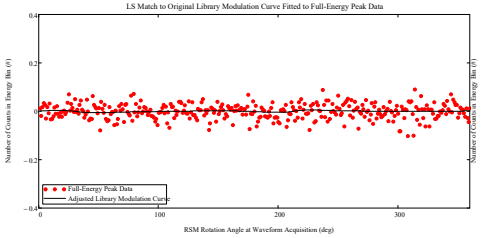

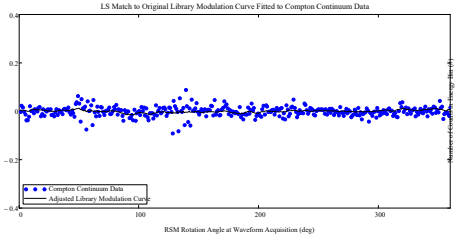

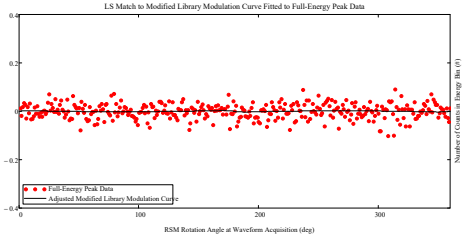

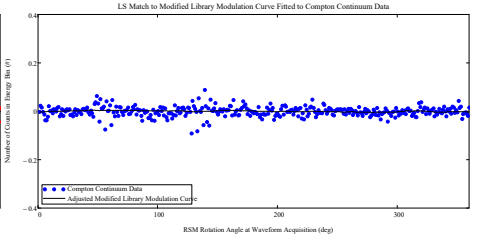

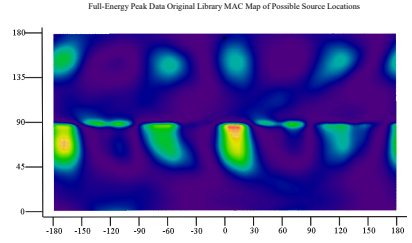

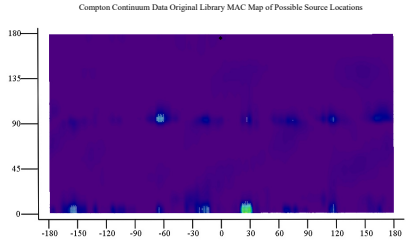

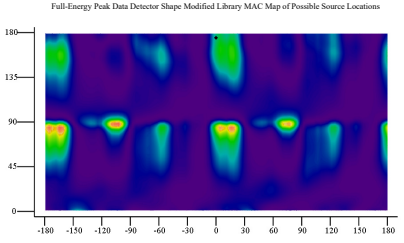

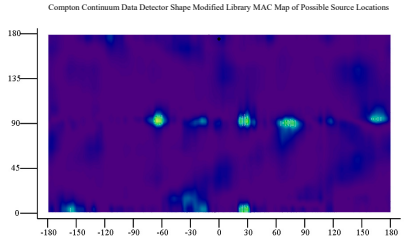

MAC Legend

$(P1, P2, P3), \{thepoint^{(1)}, thepoint^{(2)}, thepoint^{(3)}\}, \{Points^{(1)}, Points^{(2)}, Points^{(3)}\}$

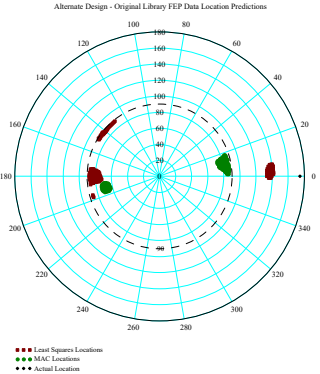

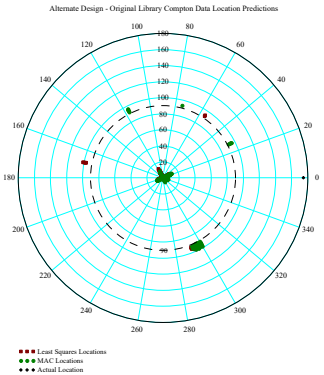

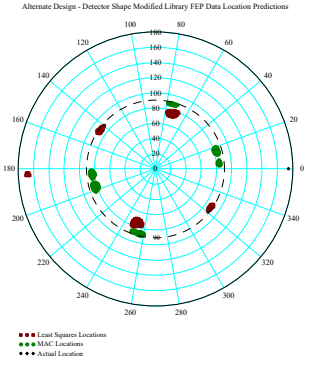

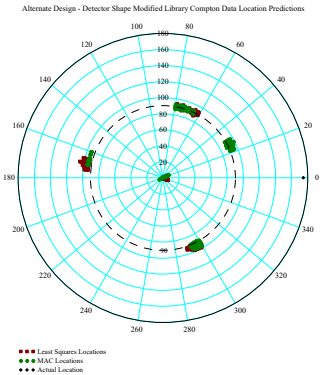

Appendix C: DTIC Information Page

REPORT DOCUMENTATION PAGE

Form Approved
OMB No. 074-0188

1. REPORT DATE *(DD-MM-YYYY)*	2. REPORT TYPE	3. DATES COVERED *(From – To)*
24-03-2022	Dissertation	August 2012 – March 2022

TITLE AND SUBTITLE

DIRECTIONALLY SENSITIVE GAMMA IMAGING USING ROTATING SCATTER MASKS AND INEXPENSIVE, SCINTILLATION DETECTORS

5a. CONTRACT NUMBER

5b. GRANT NUMBER

5c. PROGRAM ELEMENT NUMBER

6. AUTHOR(S)

Charles, Christopher S., Major, USAF

5d. PROJECT NUMBER

5e. TASK NUMBER

5f. WORK UNIT NUMBER

7. PERFORMING ORGANIZATION NAMES(S) AND ADDRESS(S)

Air Force Institute of Technology
Graduate School of Engineering and Management (AFIT/ENY)
2950 Hobson Way, Building 640
WPAFB OH 45433-8865

8. PERFORMING ORGANIZATION REPORT NUMBER

AFIT-ENP-DS-22-M-08

9. SPONSORING/MONITORING AGENCY NAME(S) AND ADDRESS(ES)

ATTN: LTC Nickolas Duncan (nickolas.duncan@westpoint.edu)
Defense Threat Reduction Agency
8725 John J. Kingman Rd. Stop 6201
Fort Belvoir, VA 22060-6201

10. SPONSOR/MONITOR'S ACRONYM(S)

DTRA

11. SPONSOR/MONITOR'S REPORT NUMBER(S)

12. DISTRIBUTION/AVAILABILITY STATEMENT

DISTRUBTION STATEMENT A. APPROVED FOR PUBLIC RELEASE; DISTRIBUTION UNLIMITED.

13. SUPPLEMENTARY NOTES

This material is declared a work of the U.S. Government and is not subject to copyright protection in the United States.

14. ABSTRACT

This work demonstrates the first instantiation of the FitzGerald Rotating Scatter Mask (RSM) as a proof-of-concept for two-dimensional source direction determination using a single, inexpensive, non-cooled scintillator, as well as an alternate mask design for comparison. A large RSM was additively manufactured from low-Z, acrylic like material, and rotated around the ubiquitous standard 3"x3" NaI(Tl) or NaI(Tl)/CsI(Tl) phoswich detector, set internally to the mask. Smaller versions of the FitzGerald and alternate RSM designs were 3D printed for testing and used in conjunction with a LaBr detector to characterize the RSM system with a size and weight reduction applied. A simplified, analytic, attenuation by Compton scatter of the Full-Energy Peak (FEP) model, based on a Beer-Lambert's law relationship was built, developed, and applied to the design geometry of the RSMs. This model is later parameterized and used in conjunction with experimental results to create detector response matrix (DRM) libraries for both the FEP and Compton continuum portions of the spectra. Source directions were successfully predicted over the 3π steradian acceptance angle of the system, with an average resolution determined to be ~4° when using the FEP attenuation by scatter-out based library for comparison.

15. SUBJECT TERMS

Rotating Scatter Mask, RSM, Compton scatter, phoswich, gamma source location, gamma imaging

16. SECURITY CLASSIFICATION OF:			17. LIMITATION OF ABSTRACT	18. NUMBER OF PAGES	19a. NAME OF RESPONSIBLE PERSON
a. REPORT	b. ABSTRACT	c. THIS PAGE			Larry W. Burggraf, AFIT/ENP
U	U	U	UU	409	19b. TELEPHONE NUMBER *(Include area code)* (937) 255-6565, ext 4507 (larry.burggraf@afit.edu)

Standard Form 298 (Rev. 8-98)
Prescribed by ANSI Std. Z39-18